ASSESSING STRUCTURAL INTEGRITY OF STEEL FIBRE REINFORCED CONCRETE ELEMENTS UNDER ELEVATED TEMPERATURE USING EMI TECHNIQUE

A THESIS

submitted in partial fulfillment of the requirements
for the degree of

DOCTOR OF PHILOSOPHY

in

CIVIL ENGINEERING

by

WESAM AL AGHA
(Roll No. 2K21/PHD/CE/16)

Under the supervision of

PROF. SHILPA PAL

PROF. NIRENDRA DEV

DEPARTMENT OF CIVIL ENGINEERING
DELHI TECHNOLOGICAL UNIVERSITY
(Formerly Delhi College of Engineering)
Shahbad Daulatpur, Main Bawana Road, Delhi-110042, India

October, 2026

ACKNOWLEDGEMENTS

The work presented in this thesis would not have been possible without the support, guidance, encouragement, and kindness of many people who stood by me throughout this journey. I take this opportunity to acknowledge them and to express my sincere gratitude for their contributions, which made the completion of this thesis possible.

At this important moment of accomplishment, I would first like to express my profound gratitude to the **Indian Council for Cultural Relations (ICCR)** for sponsoring me as a Ph.D. research fellow under the Atal Bihari Vajpayee Scholarship Scheme (A1201) of the Government of India. This support provided me with an invaluable opportunity to pursue my doctoral studies and research at Delhi Technological University. I also extend my sincere appreciation to the Vice Chancellor of Delhi Technological University, **Prof. Prateek Sharma**, for his leadership and for fostering an academic environment that promotes learning, research, scientific inquiry, and intellectual development.

First and foremost, I find it difficult to adequately express the magnitude of my gratitude to my supervisor, **Prof. Shilpa Pal**, for her unwavering support throughout my doctoral journey. Whether through critical guidance in my research or constant encouragement to remain strong and motivated while carrying out the many tasks required for the successful completion of this work, she has been one of my strongest pillars of support. I am deeply thankful to her for giving me the intellectual freedom to design and develop my research plan while always being available to provide valuable feedback, guidance, and mentorship.

I am equally and deeply grateful to my joint supervisor, **Prof. Nirendra Dev**, for his continuous guidance, enduring patience, encouragement, and nurturing support throughout this research. The successful completion of this work would not have been possible without his valuable contribution. It has been an honor and a privilege to work under the guidance of such experienced supervisors and to learn from their academic and professional expertise. Their scholarly suggestions, constructive criticism, immense interest in my work, constant support, and encouraging attitude have been a continuous source of inspiration. The knowledge and values I have gained from them will remain an inexhaustible source of scientific learning throughout my professional life.

I would also like to express my sincere and wholehearted gratitude to the members of my Doctoral Research Committee (DRC), particularly Prof. Awadhesh Kumar, Head of the Department of Civil Engineering, Delhi Technological University, Delhi, and Prof.

Raju Sarkar, DRC Chairman, Department of Civil Engineering, Delhi Technological University, for their valuable guidance, observations, and support throughout the course of my research.

I owe a great debt of gratitude to External Expert **Prof. Suresh Bhalla**, Professor (Higher Administrative Grade), Department of Civil Engineering, Indian Institute of Technology Delhi, for the consistent guidance and support he provided throughout my research work. I am particularly grateful for his insightful discussions during my SRC and Pre-Ph.D. presentations and for the valuable suggestions that helped me improve the quality and direction of my research.

I would also like to express my sincere thanks to External Expert **Prof. Dipendu Bhunia**, Professor & Head, Department of Civil Engineering, Birla Institute of Technology and Science (BITS) Pilani, for his valuable discussions during my Pre-Ph.D. presentation and for his constructive suggestions and observations.

I wish to express my heartfelt gratitude to **Dr. Tushar Bansal**, Post-Doctoral Fellow at King Fahd University of Petroleum and Minerals, Saudi Arabia, for his generous assistance, encouragement, and support. His timely help in several activities essential to the successful completion of my research work is sincerely appreciated and will always be remembered.

I would like to extend a special token of gratitude to **Dr. Indrajeet Singh**, Assistant Professor & Head, Department of Civil Engineering, Gautam Buddha University, Noida, for being an exceptional brainstorming partner, senior colleague, and mentor. I am particularly thankful to him for helping me develop the practical and technical skills required for working with the Electromechanical Impedance (EMI) technique and for sharing his knowledge and experience in the field of Structural Health Monitoring (SHM) during his Ph.D. period at Delhi Technological University. I will always remember the valuable time spent with him discussing scientific problems, experimental techniques, research ideas, and technological developments.

I would also like to express my sincere appreciation to **Dr. Prateek Roshan**, whose unwavering support from the early days of my Ph.D. until the submission of this thesis played a significant role in my journey. His remarkable ability to visualize problems, understand their underlying mechanisms, and approach their solutions systematically helped me gain a clearer understanding of many aspects of my research.

I am immensely grateful to **Ms. Khyati Saggu** for her continuous and unwavering support, particularly during my SRC and Pre-Ph.D. stages and throughout the documentation and administrative processes leading to the submission of my thesis. Her timely assistance played an important role in helping me successfully complete this journey.

I am grateful to my seniors, Dr. Abhishek Prakash Paswan, Dr. Nitin Lamba, Dr. Kiran Cholak, and Mr. Dharmendra Kumar, as well as my fellow researchers and friends, **Dr. Deepak Sharma**, Mr. Rishabh Tyagi, Ms. Shivangi Bharadwaj, and Ms. Payal Devi, for always being there for me and for sharing both the challenging and joyful moments of my Ph.D. journey. Their companionship, encouragement, and support made my years of research at Delhi Technological University truly memorable.

I am immensely grateful to the staff of the Earthquake Engineering Laboratory and the Concrete Engineering Laboratory within the Department of Civil Engineering for their cooperation and support. I extend my sincere thanks to laboratory technician Mr. Shashikant and laboratory assistants Mr. Sanjay and Mr. Rakesh for their unwavering assistance during the experimental and simulation phases of my research. Their cooperation and willingness to help contributed significantly to the successful execution of my research work.

I am also thankful to Ms. Arya Sajith (M.Tech), Ms. Janhvi Singh (M.Tech), Mr. Ashish Kumar (M.Tech), and Mr. Anshoo Yadav (M.Tech) for their constant support during the course of my Ph.D. work. I particularly appreciate their valuable assistance in formatting, organizing, and presenting the thesis in its final form. Their contribution helped me bring this thesis into the form in which it is presented today.

No acknowledgement would be complete without expressing my deepest gratitude to my family, whose unconditional love, prayers, sacrifices, patience, and unwavering belief in me have been the foundation upon which this entire journey was built. My achievements are inseparable from the strength, encouragement, and support that I have continuously received from them.

I owe an immeasurable debt of gratitude to my father, **Dr. Rateb Al Agha**, whose guidance, wisdom, strength, and constant belief in my abilities have always encouraged me to move forward, even during the most difficult stages of this journey. His support, advice, and reassuring presence have been a continuous source of confidence and determination throughout both my academic and personal life. His belief in me has always encouraged me to persevere and to face every challenge with patience and determination.

I am equally and profoundly grateful to my mother, **Ms. Laila Al Zahab**, whose endless love, prayers, patience, care, and sacrifices have accompanied me throughout every stage of my life. Her encouragement and emotional support gave me the strength to continue whenever the journey became difficult or demanding. Her prayers have always been a source of comfort and strength, and no words can adequately express my gratitude for everything she has done for me.

I extend my heartfelt appreciation to my maternal uncle, **Dr. Aymen Al Dahab**,

Specialist in Neurosurgery, for his constant encouragement, kindness, guidance, and sincere concern throughout my doctoral journey. His support, valuable advice, and genuine interest in my academic and personal progress have always meant a great deal to me. I am deeply grateful for the encouragement and family support he has continuously extended to me throughout the years.

My deepest and most heartfelt thanks go to my brother, **Dr. Bashar Al Agha**, whose unwavering support throughout my Ph.D. journey has been invaluable. He has always stood beside me, offering encouragement, understanding, practical assistance, and support whenever I needed it. During both the most demanding periods and the happiest moments of this journey, I knew that I could depend on him. His constant encouragement, confidence in me, and readiness to help gave me tremendous strength to continue moving forward. His own professional and academic achievements have also been a source of inspiration and motivation to me. I will always be grateful for his presence, support, and the many ways in which he contributed to making this long journey easier.

I also express my deepest love and appreciation to my younger sister, **Ms. Shaza Al Agha**, for her affection, patience, encouragement, and continuous support. Her kindness, positive spirit, and loving presence have always brought warmth and happiness to my life, particularly during the demanding periods of my Ph.D. journey. Her encouragement and sincere concern have meant more to me than words can adequately express.

To my entire family, words will never be sufficient to express how much their love, prayers, sacrifices, patience, encouragement, and confidence in me have contributed to this achievement. They remained beside me throughout the challenges, uncertainties, and accomplishments of this long journey. This achievement is therefore not mine alone; in many ways, it also belongs to them.

Finally, and above all, I humbly offer my deepest gratitude to **Almighty Allah** for His countless blessings, guidance, mercy, strength, and patience throughout this journey. I remain forever grateful for the ability, opportunities, and people He placed in my path, which enabled me to overcome the challenges of this journey and reach this important milestone in my life.

WESAM AL AGHA

DELHI TECHNOLOGICAL UNIVERSITY
(Formerly Delhi College of Engineering)
Shahbad Daulatpur, Main Bawana Road, Delhi-110042

CANDIDATE'S DECLARATION

I, **Wesam Al Agha**, hereby certify that the work which is being presented in the thesis entitled **"Assessing Structural Integrity of Steel Fibre Reinforced Concrete Elements under Elevated Temperature using EMI Technique"** in partial fulfillment of the requirements for the award of the Degree of Doctor of Philosophy, submitted in the **Department of Civil Engineering**, Delhi Technological University is an authentic record of my own work carried out during the period from August 2021 to July 2026 under the supervision of **Prof. Shilpa Pal** and **Prof. Nirendra Dev**.

The matter presented in the thesis has not been submitted by me for the award of any other degree of this or any other Institute.

Candidate's Signature

This is to certify that the student has incorporated all corrections suggested by the examiners in the thesis and that the statement made by the candidate is correct to the best of our knowledge.

Shilpa Pal 15/10/26 Nirendra Dev

Signature of Supervisor(s)

13.10.26

Signature of External Examiner

DELHI TECHNOLOGICAL UNIVERSITY

(Formerly Delhi College of Engineering)

Shahbad Daulatpur, Main Bawana Road, Delhi-110042

CERTIFICATE BY THE SUPERVISOR(S)

Certified that **WESAM AL AGHA** (2K21/PHD/CE/16) has carried out the research work presented in this thesis entitled **"Assessing Structural Integrity of Steel Fibre Reinforced Concrete Elements under Elevated Temperature using EMI Technique"** for the award of **Doctor of Philosophy** from the Department of Civil Engineering, Delhi Technological University, Delhi, under our supervision. The thesis embodies original work carried out by the candidate, and its contents do not form the basis for the award of any other degree to the candidate or to any other person at this or any other University/Institution.

Nirendra Dev

Prof. Nirendra Dev
Professor
Department of Civil Engineering
Delhi Technological University
Shahbad Daulatpur, Bawana Road
Delhi - 110042

Prof. Shilpa Pal
Professor
Department of Civil Engineering
Delhi Technological University
Shahbad Daulatpur, Bawana Road
Delhi - 110042

Place:

Date:

ABSTRACT

Steel Fibre Reinforced Concrete (SFRC) improves the post-cracking behaviour of concrete because the steel fibres bridge developing cracks. However, the interaction among the cementitious matrix, fibres and cracks makes its condition difficult to assess. Destructive tests determine material properties at specified ages or after loading, whereas non-destructive tests record the response at the chosen test times and points. This thesis evaluates the Electromechanical Impedance (EMI) technique as a laboratory Structural Health Monitoring (SHM) method for monitoring SFRC during curing, mechanical loading and heating. The analysis combines piezoelectric measurements, resonance characteristics, statistical indices, Equivalent Structural Parameters (EPS) and data-driven prediction.

The research addresses three objectives. The first assesses piezoelectric sensing for monitoring material development and mechanically induced change in fibre-reinforced concrete. The second examines how heating time and temperature affect the measured EMI response and evaluates a compensation procedure for separating temperature effects from structural changes. The third investigates data-driven models that relate EMI measurements to the mechanical responses obtained in the experiments. Four connected experimental studies were conducted using two sensor configurations. Jacketed Piezo Sensors (JPS) were embedded and retained in four monitored SFRC cubes. A Non-Bonded Piezo Sensor (NBPS) was coupled at a fixed test point and removed before destructive testing, allowing the same sensing arrangement to be used with separate specimens.

The curing study considered four SFRC configurations containing hooked-end steel fibres with aspect ratios of 55 and 65 and dosages of 0.50% and 0.75%. One JPS was embedded in each monitored cube, and EMI measurements were recorded at ten curing ages from 1 to 180 days. Separate cubes were tested in compression to provide age-dependent mechanical reference data. Changes in resonance frequency, peak conductance, statistical indices and the extracted equivalent mass, stiffness and damping were examined together. The changes depended on the fibre configuration and were largest during the early curing period. For two monitored configurations, equivalent stiffness had a linear relationship with the corresponding compressive strength, with reported R^2 values of 0.94 and 0.96. Within the tested specimens, these results show that the local coupled sensor–concrete response changed as curing progressed.

Mechanical-damage assessment used separate groups of 39 cubes and 39 cylinders. Each group contained thirteen material configurations with three specimens per configuration. The reusable NBPS was positioned before the compression and splitting-tensile tests and returned to the same point after loading to obtain paired EMI signatures. The highest measured mean compressive strengths in the cube group were 60.95 MPa for aspect ratio 65 and 59.90 MPa for aspect ratio 55, both at 0.75% fibre dosage. In the cylinder group, the highest measured mean splitting-tensile strengths were 6.68 MPa and 6.34 MPa for aspect ratios 65 and 55, respectively, at the upper tested dosage of 1.50%. The paired signatures, statistical indices and EPS responses varied with material configuration and loading mode. Selected high-dosage cylinder records also showed an increase in local resonance frequency after splitting-tensile loading. Because the

response was measured at one sensor position, these results identify local condition changes but do not locate damage throughout the structural element.

The same four JPS-instrumented cubes used for curing monitoring were subsequently tested under controlled heating. EMI signatures were recorded from 75 to 250 °C at 25 °C intervals and after three holding periods, first in the intact condition and then after introducing a 3-mm-wide and 30-mm-deep saw cut. The two configurations containing 0.75% fibre have saw-cut records only up to 175 °C, whereas the 0.50% configurations extend to 250 °C. Temperature changed the frequency and amplitude of the conductance and susceptance features. An uncompensated signature therefore cannot be treated as a damage response without comparison at the same temperature. The evaluated Enhanced Effective Frequency Shift (E–EFS) procedure combines interpolated frequency alignment, a joint conductance–susceptance shift search and correction of the mean offset in each channel. It reduced the RMSD value for every available comparison within the same structural condition, although the remaining difference generally increased at the higher temperatures. The procedure improves comparison of the tested records but does not establish a universal compensation limit or damage threshold.

Three data-driven studies were conducted separately for the hydration, compression and splitting-tensile experiments. The methods included conventional Machine Learning regressors and Deep Learning models based on Convolutional Neural Networks, Long Short-Term Memory networks, Bidirectional Long Short-Term Memory networks and their hybrid combinations. Model ranking depended on the measured response and material configuration. The cube-compression study favoured squared-exponential Gaussian Process Regression, whereas the splitting-tensile studies identified different neural-network models for the two aspect-ratio groups. The hydration models also related EMI inputs to compressive strength with high reported coefficients of determination. These results show that study-specific regression can be performed for the available experimental data. The conclusions remain limited to the training and test divisions used in each study; validation based on independent specimen groups and external data is required before application to other structures.

The principal contribution of the thesis is the combined use of retained embedded sensing and reusable non-bonded sensing in curing, mechanical-loading and thermal studies of SFRC. Resonance features, statistical measures and model-derived EPS provide different measures of change in the local coupled response. The work also establishes an experimental basis for comparison at different temperatures and for estimating mechanical responses from EMI measurements. Potential applications include laboratory material development, construction-stage monitoring and comparative condition assessment where repeatable sensor coupling and suitable baselines can be maintained.

The conclusions apply to the investigated materials, specimen geometries, fibre configurations, sensor arrangements, excitation ranges, loading procedures and temperature conditions. The monitored JPS configurations represent individual physical specimens, and the NBPS findings were obtained from controlled groups of laboratory specimens rather than full-scale structures. Future work should therefore examine replicated embedded specimens, long-term coupling stability, larger structural elements,

combined mechanical and environmental actions, independent data and validation based on separate specimen groups. Such studies are required to establish repeatability, transferability and reliable criteria for field application.

LIST OF PUBLICATIONS

Journal

1. W. Al Agha, S. Pal, and N. Dev, "Electro-mechanical impedance-based equivalent structural health monitoring of steel fibre cementitious materials under long curing age effect," *Construction and Building Materials*, vol. 489, p. 142296, 2025, doi: 10.1016/j.conbuildmat.2025.142296. *Journal Impact Factor: 8.0.*
2. W. Al Agha, N. Dev, and S. Pal, "ML-integrated reusable piezoceramic sensors for steel fibre concrete structural health monitoring," *Measurement*, vol. 258, p. 119201, 2026, doi: 10.1016/j.measurement.2025.119201. *Journal Impact Factor: 6.1.*
3. W. Al Agha, S. Pal, and N. Dev, "Electromechanical Impedance-Based Tensile Damage Assessment of Steel Fibre Concrete Using Reusable Piezoceramic Sensors: An Experimental and Deep Learning Approach," *Journal of Vibration Engineering & Technologies*, vol. 14, p. 164, 2026, doi: 10.1007/s42417-025-02311-9. *Journal Impact Factor: 3.5 (2025).*

Conference Proceedings

W. Al Agha, S. Pal, and N. Dev, "Challenges for structural health monitoring of concrete curing using piezoelectric sensor and electromechanical impedance (EMI) technique: A critical review," *Materials Today: Proceedings*, in press, corrected proof, available online 18 July 2023, doi: 10.1016/j.matpr.2023.06.451. *Journal Impact Factor: not listed by the publisher.*

Conference Participated

W. Al Agha, N. Dev, and S. Pal, "Investigation of Steel Fibre Reinforced Concrete Elements under Elevated Temperature," Paper Conference Presentation at the *International Conference on Atomic, Molecular, Material, Nano, and Optical Physics with Applications (ICAMNOP-2023)*, organised by the Department of Applied Physics, Delhi Technological University, Delhi, India, 20–22 December 2023.

Journal Papers Communicated

1. W. Al Agha, S. Pal, N. Dev, and T. Bansal, "Thermal drift of embedded piezoelectric sensors in steel-fibre-reinforced concrete heated to 250 °C and evaluation of frequency-shift compensation."
2. W. Al Agha, S. Pal, N. Dev, and T. Bansal, "Bayesian assessment of electromechanical impedance indices in heated steel-fibre-reinforced concrete."

Contents

Acknowledgements **i**

Candidate's Declaration **v**

Certificate **vi**

Abstract **vii**

List of Publications **x**

List of Tables **xix**

List of Figures **xxx**

List of Symbols, Abbreviations and Nomenclature **xxxviii**

1 INTRODUCTION **1**

1.1 Background 1
1.2 The Role of Structural Health Monitoring 2
1.3 The Electromechanical Impedance Technique 3
1.4 Piezoelectric Sensor Configurations 4
1.5 Temperature Effects and the Need for an Enhanced EFS 5
1.6 Data-Driven Analytics in SHM 5
1.7 Research Motivation and Objectives 6
1.8 Scope and Contributions 7
1.9 Organisation of the Thesis 8

2 LITERATURE REVIEW **9**

2.1 General Background 9
2.2 Historical and Theoretical Foundations of the EMI Technique 9
2.3 Evolution of Piezoelectric Sensor Configurations 11
2.3.1 SBPS Configuration 11

2.3.2 Embedded PZT and the JPS Configuration 12
2.3.3 NBPS Configuration 12
2.4 Statistical Damage Indices for the EMI Signature 13
2.5 Equivalent Structural Parameters and Lumped-Parameter Representations 13
2.6 Steel Fibre Reinforced Concrete: Mechanics and Durability 14
2.7 Hydration and Early-Age Monitoring with EMI 15
2.8 Mechanical Damage Assessment using EMI 16
2.8.1 Compressive Damage 16
2.8.2 Split-Tensile Damage and Frequency Hardening 17
2.9 Thermal Effects and Compensation Methodologies 17
2.9.1 Classical EFS Compensation 17
2.9.2 Advanced Compensation Strategies 18
2.10 Machine Learning and Deep Learning for EMI-SHM 19
2.10.1 Classical Regressors 19
2.10.2 CNN Architectures 20
2.10.3 LSTM and Bi-LSTM Architectures 20
2.10.4 Hybrid CNN-LSTM and CNN-Bi-LSTM Architectures 20
2.11 Synthesis and Research Gaps 21
2.12 Research Gap to Objective Mapping 22

3 EXPERIMENTAL METHODOLOGY 24
3.1 General 24
3.2 Material Properties 24
3.2.1 Ordinary Portland Cement 25
3.3 Mix Design and Specimen Preparation 25
3.3.1 M30-Grade Mix Design 25
3.3.2 Cube Specimen Programme 26
3.3.3 Cylindrical Specimen Programme 26
3.3.4 Initial Fibre-Dosage Selection 27
3.4 Sensor Development 27
3.4.1 Jacketed Piezo Sensor 27
3.4.2 Non-Bonded Piezo Sensor 27
3.5 Study 1: Hydration and Curing-Age Monitoring Setup 29
3.5.1 Specimen Matrix 29
3.5.2 Hydration EMI Measurement Procedure 29
3.6 Study 2: Compressive Damage Detection Setup 30
3.6.1 Thirteen-Configuration Experimental Matrix 30

3.6.2 Compressive Loading and EMI Acquisition Procedure 30
3.7 Study 3: Split-Tensile Damage Detection Setup 31
3.7.1 Cylindrical Specimen Matrix 31
3.7.2 Split-Tensile Loading and EMI Acquisition Procedure 31
3.8 Study 4: Thermal Loading Setup 32
3.8.1 Thermal Loading Protocol 32
3.8.2 Thermal EMI Measurement Procedure 33
3.8.3 Saw-Cut Damage Introduction 34
3.9 Common Instrumentation: Keysight E4980A LCR Meter 34
3.10 Theoretical Framework of the Electromechanical Impedance Technique 34
3.11 Lumped-Parameter Mechanical Impedance Modelling 36
3.12 Statistical Damage Metrics for Structural Health Assessment 37
3.12.1 Root Mean Square Deviation 37
3.12.2 Mean Absolute Percentage Deviation 38
3.12.3 Cross-Correlation Coefficient 38
3.12.4 Covariance 38
3.13 Quality Assurance and Statistical Reliability 38
3.13.1 PZT Screening and Consistent Sensor Mapping 38
3.13.2 Experimental Units and Replication 39
3.14 Summary 39

4 HYDRATION AND CURING-AGE MONITORING USING JACKETED PIEZO SENSORS 40
4.1 General 40
4.2 Experimental Programme and Measurement Records 41
4.3 Measured Conductance and Susceptance Signatures 42
4.4 Resonant Frequency and Peak Conductance during Curing 47
4.5 Comparison with Compressive-Strength Growth 49
4.6 Assessment Based on Statistical Indices 53
4.7 EPS from JPS Signatures 56
4.8 Comparison of Equivalent Stiffness with Compressive Strength 67
4.9 Summary 72

5 MECHANICAL DAMAGE DETECTION IN STEEL FIBRE CONCRETE USING NON-BONDED PIEZO SENSORS 73
5.1 General 73
5.2 Common Experimental and Analytical Basis 73

5.2.1 Specimen Matrix 73
5.2.2 NBPS Measurement Protocol 74
5.2.3 EMI Measures Used in the Analysis 74
5.3 Compressive Damage Assessment 75
5.3.1 Compressive Strength Results 75
5.3.2 Healthy and Post-Damage Spectra 76
5.3.3 Statistical Signature-Difference Metrics 78
5.3.4 Equivalent Stiffness and Normalised Stiffness Change 79
5.3.5 Stiffness-Based Damage Index 83
5.4 Split-Tensile Damage Assessment 85
5.4.1 Split-Tensile Loading Programme (Cylinders) 85
5.4.2 Comparison with Destructive Splitting-Tensile Tests 85
5.4.3 Tensile Conductance Signatures 86
5.4.4 Rightward Peak Shifts after Split-Tensile Loading 86
5.4.5 Quantitative Peak Tracking 87
5.4.6 Statistical Quantification of Tensile Damage 88
5.4.7 Equivalent Structural Parameters for the Cylinder Geometry . 90
5.4.8 Compressive Stiffness–Strength Relationship 91
5.4.9 Tensile Stiffness–Strength Relationship 92
5.4.10 Stiffness-Based Damage Index for Cylinders 94
5.5 Comparative Interpretation of Compressive and Split-Tensile Response 95
5.6 Experimental Limitations and Repeatability 96
5.7 Summary 96

6 TEMPERATURE EFFECTS AND THE ENHANCED EFS COMPENSATION ALGORITHM 97
6.1 General 97
6.2 Enhanced EFS Compensation Algorithm 98
6.3 Worked Example: Before and After EFS Compensation 99
6.3.1 Motivation and Algorithmic Overview 99
6.3.2 High-Resolution Cubic-Spline Interpolation 100
6.3.3 Joint Conductance–Susceptance Correlation Metric 100
6.3.4 Two-Stage Coarse-to-Fine Search 101
6.3.5 Horizontal Alignment and Mean-Offset Correction 101
6.3.6 Quality Metrics of the Compensation 102
6.4 Overview of Experimental Cases 102
6.4.1 Research Objective and Experimental Framework 102

6.4.2 Analysis Matrix . . . 103
6.4.3 Temperature Testing Protocol . . . 104
6.5 Measurement Parameters Overview . . . 106
6.5.1 Signal Types: Conductance and Susceptance . . . 106
6.5.2 Calculated Parameters: SHM Indices and EPS . . . 107
6.6 Signature Response Under Heating . . . 109
6.6.1 Without Compensation Signatures . . . 109
6.6.2 With Compensation Signatures . . . 112
6.7 Equivalent Structural Parameters (EPS) Under Intact Heating . . . 115
6.7.1 Equivalent Mass Parameter . . . 115
6.7.2 Equivalent Stiffness Parameter . . . 120
6.7.3 Equivalent Damping Parameter . . . 123
6.8 SHM Indices Under Intact Heating . . . 125
6.8.1 RMSD Index Analysis . . . 125
6.8.2 MAPD Index Analysis . . . 127
6.8.3 AMPD Index Analysis . . . 130
6.8.4 Correlation Coefficient (CC) Index Analysis . . . 132
6.8.5 CCD Index Analysis . . . 135
6.8.6 CCD^3 Index Analysis . . . 138
6.8.7 CCV Index Analysis . . . 140
6.8.8 MSE Index Analysis . . . 143
6.8.9 Variance Index Analysis . . . 145
6.8.10 RMS Index Analysis . . . 148
6.8.11 Skewness Index Analysis . . . 150
6.8.12 Peak-to-Peak Index Analysis . . . 153
6.8.13 Covariance Index Analysis . . . 156
6.8.14 Consolidated Performance of Secondary SHM Indices (Intact Heating) . . . 159
6.8.15 Effect of Compensation for the Intact Condition . . . 159
6.9 Signature Response in the Saw-Cut State under Heating . . . 164
6.9.1 Without Compensation Signatures (Cut Condition) . . . 164
6.9.2 With Compensation Signatures (Cut Condition) . . . 167
6.10 Equivalent Structural Parameters in the Saw-Cut State under Heating . 171
6.10.1 Equivalent Mass Parameter (Cut Condition) . . . 171
6.10.2 Equivalent Stiffness Parameter (Cut Condition) . . . 176
6.10.3 Equivalent Damping Parameter (Cut Condition) . . . 178
6.11 SHM Indices in the Saw-Cut State under Heating . . . 181

6.11.1 RMSD Index Analysis (Cut Condition) 181
6.11.2 MAPD Index Analysis (Cut Condition) 184
6.11.3 AMPD Index Analysis (Cut Condition) 187
6.11.4 Correlation Coefficient (CC) Index Analysis (Cut Condition) . 190
6.11.5 CCD Index Analysis (Cut Condition) 193
6.11.6 CCD^3 Index Analysis (Cut Condition) 196
6.11.7 CCV Index Analysis (Cut Condition) 200
6.11.8 MSE Index Analysis (Cut Condition) 203
6.11.9 Variance Index Analysis (Cut Condition) 206
6.11.10 RMS Index Analysis (Cut Condition) 209
6.11.11 Skewness Index Analysis (Cut Condition) 212
6.11.12 Peak-to-Peak Index Analysis (Cut Condition) 216
6.11.13 Covariance Index Analysis (Cut Condition) 219
6.11.14 Consolidated Performance of Secondary SHM Indices (Cut Heating) 222
6.11.15 Effect of Compensation for the Saw-Cut Condition 223
6.12 Intact vs Cut Comparison 228
6.12.1 EPS Parameter Changes Due to Cut 228
6.12.2 SHM Index Sensitivity to Cut Damage 236
6.12.3 Consolidated Matched Changes of the Secondary SHM Indices 278
6.12.4 Material Effects on Damage Detection 278
6.12.5 Temperature Effects on Damage Detection 285
6.13 Histogram and Statistical Analysis 290
6.13.1 Distribution Analysis 290
6.13.2 Threshold Determination 301
6.13.3 Statistical Evaluation Summary 307
6.14 Conclusions 309
6.14.1 Temperature Effect Conclusions 309
6.14.2 Compensation Algorithm Conclusions 310
6.14.3 Damage Detection Conclusions 311
6.14.4 Material Configuration Conclusions 313
6.14.5 PZT Sensor Performance Conclusions 314
6.15 Recommendations 315
6.15.1 Recommendations for Researchers 315
6.15.2 Conditions for Future Implementation 316
6.16 Potential Applications and Transfer Requirements 317
6.16.1 Infrastructure Applications 317

6.16.2 Industrial Applications 318
6.16.3 Future Technology Integration 319

7 MACHINE LEARNING AND DEEP LEARNING FOR STRENGTH PREDICTION 320
7.1 General 320
7.2 Unified ML/DL Framework and Data Pipeline 320
7.2.1 Dataset Construction 321
7.2.2 Feature Engineering and Normalisation 321
7.2.3 Training and Validation Protocol 322
7.3 Classical Machine Learning Models 322
7.3.1 Linear Regression Family 322
7.3.2 Support Vector Machines 322
7.3.3 Ensemble Boosted Trees 323
7.3.4 Gaussian Process Regression 323
7.4 Deep Learning Architectures 324
7.4.1 2D Convolutional Neural Network (2D CNN) 324
7.4.2 2D Long Short-Term Memory (2D LSTM) 324
7.4.3 2D Bidirectional LSTM (2D Bi-LSTM) 325
7.4.4 Hybrid DL Architectures 326
7.5 Evaluation Metrics 327
7.6 Predictive Modelling of the Compressive Programme 328
7.6.1 Comparative Analysis of Support Vector Machine Kernels . . 330
7.7 Predictive Modelling of the Hydration Programme 333
7.8 Predictive Modelling of the Split-Tensile Programme 338
7.9 Physical Interpretability of the AI Framework 342
7.10 Comparative Analysis and Computational Cost 342
7.11 Summary 343

8 CONCLUSIONS, LIMITATIONS AND FUTURE SCOPE 344
8.1 Conclusion 344
8.1.1 Conclusions on Objective 1 344
8.1.2 Conclusions on Objective 2 346
8.1.3 Conclusions on Objective 3 347
8.1.4 Principal Contributions of the Thesis 348
8.2 Limitations 349
8.3 Future Scope 350

8.4 Social, Economic and Environmental Relevance 350
8.4.1 Social Relevance 350
8.4.2 Economic Relevance 351
8.4.3 Environmental Relevance 351
8.4.4 Alignment with the Sustainable Development Goals 352
8.5 Closing Remarks 352

References **353**

A SUPPLEMENTARY TEMPERATURE-STUDY RESULTS **363**
A.1 Scope of the Supplementary Results 363
A.2 Additional SHM-Index Equations 363
A.3 Temperature-Averaged EPS Results 364
A.4 Experimental Coverage and Interpretation Limits 366

Annexure: Replies to the Examiners' Comments **368**

Proofs of Publications and Certificates **378**

List of Tables

Table No.	Description	Page No.
2.1	Selected developments in EMI-based SHM for civil infrastructure	10
2.2	Comparison of PZT sensor configurations reported for concrete monitoring	11
2.3	Comparison of the main thermal-compensation methods reported for EMI	19
2.4	Summary of machine learning and deep learning architectures applied to EMI-based SHM datasets	21
2.5	Traceability between research gaps, thesis objectives and evidence chapters	23
3.1	M30-grade concrete constituent quantities per cubic metre	26
3.2	Full thermal loading protocol for intact specimens and the 0.50% cut configurations	33
4.1	Specimen-sensor mapping and fibre configurations for the long-term monitoring programme	42
4.2	Compressive strength (f_c) of the separately tested cubes versus curing age for the four SFRC configurations	50
5.1	The thirteen-configuration experimental matrix evaluated for both compressive (cube) and split-tensile (cylinder) loading	74
5.2	Mean 28-day compressive strength for three cubes per SFRC configuration	76
5.3	Descriptive quartic interpolations of SFRC conductance and resonant-frequency data over the tested dosages	78
5.4	Descriptive quadratic fits for Δs versus fibre dosage over 0–1.50%	84
5.5	Mean 28-day splitting-tensile strength for three cylinders per SFRC configuration	85
5.6	Descriptive quartic interpolations of NBPS peak conductance and resonance frequency over the tested dosages	89

5.7 Descriptive quartic fits for cylinder Δs over the tested 0–1.50% dosage range 94

6.1 Steel Fibre Properties Used in SFRC Specimens 103
6.2 Analysis matrix: four specimens, two structural states and two processing branches 103
6.3 Temperature Testing Protocol 104
6.4 SHM Indices Calculated in This Study 108
6.5 Equivalent Structural Parameters (EPS) Derived from Impedance Signatures 108
6.6 Thermal Drift Quantification for All Four Intact SFRC Specimens (Without Compensation) 111
6.7 Comparison of Thermal Drift Before and After Compensation for All Four Specimens 112
6.8 Descriptive ordering of residual peak shifts after compensation. 114
6.9 Equivalent Mass (kg) at Each Temperature for All Four Intact SFRC Specimens (Without Compensation) 115
6.10 Equivalent Mass Change Summary for All Four Intact SFRC Specimens (Without Compensation) 118
6.11 Equivalent Mass (kg) at Each Temperature for All Four Intact SFRC Specimens (With Compensation) 119
6.12 Comparison of Mass Parameter Changes Before and After Temperature Compensation (All 4 specimens) 119
6.13 Equivalent Stiffness (MN/m) at Each Temperature for All Four Intact SFRC Specimens (Without Compensation) 121
6.14 Equivalent Stiffness Change Summary for All Four Intact SFRC Specimens (Without Compensation) 121
6.15 Equivalent Stiffness (MN/m) at Each Temperature for All Four Intact SFRC Specimens (With Compensation) 122
6.16 Comparison of Stiffness Changes Before and After Temperature Compensation (All 4 specimens) 122
6.17 Equivalent Damping Change Summary for All Four Intact SFRC Specimens (Without Compensation) 123
6.18 Equivalent Damping Change Summary for All Four Intact SFRC Specimens (With Compensation) 124
6.19 Comparison of Damping Changes Before and After Temperature Compensation (All 4 specimens) 124

6.20 RMSD Values at Each Temperature for All Four Intact SFRC Specimens 125
6.21 RMSD Statistical Summary for All Four Intact SFRC Specimens . . . 127
6.22 MAPD (%) Values at Each Temperature for All Four Intact SFRC Specimens 128
6.23 MAPD Statistical Summary for All Four Intact SFRC Specimens . . . 128
6.24 AMPD (%) Values at Each Temperature for All Four Intact SFRC Specimens 130
6.25 AMPD Statistical Summary for All Four Intact SFRC Specimens . . . 132
6.26 Correlation Coefficient Values at Each Temperature for All Four Intact SFRC Specimens 134
6.27 Correlation Coefficient Statistical Summary for All Four Intact SFRC Specimens 134
6.28 CCD Values at Each Temperature for All Four Intact SFRC Specimens 135
6.29 CCD Statistical Summary for All Four Intact SFRC Specimens 137
6.30 CCD^3 Values at Each Temperature for All Four Intact SFRC Specimens 138
6.31 CCD^3 Statistical Summary for All Four Intact SFRC Specimens . . . 138
6.32 CCV Values at Each Temperature for All Four Intact SFRC Specimens 142
6.33 CCV Statistical Summary for All Four Intact SFRC Specimens 142
6.34 MSE Values ($\times 10^{-5}$) at Each Temperature for All Four Intact SFRC Specimens 143
6.35 MSE Statistical Summary for All Four Intact SFRC Specimens 143
6.36 Variance Values ($\times 10^{-7}$) at Each Temperature for All Four Intact SFRC Specimens 147
6.37 Variance Statistical Summary for All Four Intact SFRC Specimens . . 147
6.38 RMS Values at Each Temperature for All Four Intact SFRC Specimens 148
6.39 RMS Statistical Summary for All Four Intact SFRC Specimens 150
6.40 Skewness Values at Each Temperature for All Four Intact SFRC Specimens 151
6.41 Skewness Statistical Summary for All Four Intact SFRC Specimens . 151
6.42 Peak-to-Peak (%) Values at Each Temperature for All Four Intact SFRC Specimens 153
6.43 Peak-to-Peak Statistical Summary for All Four Intact SFRC Specimens 155
6.44 Covariance Values ($\times 10^{-7}$) at Each Temperature for All Four Intact SFRC Specimens 156
6.45 Covariance Statistical Summary for All Four Intact SFRC Specimens 156
6.46 Consolidated performance of the ten secondary SHM indices under intact heating for all four SFRC specimens. 159

6.47 Reported end-to-end EPS changes before and after compensation for the intact records (75°C to 250°C). 160
6.48 Specimen-level summary of the reported EPS changes after compensation. 160
6.49 SHM-index ranges before and after compensation for the intact records. 161
6.50 Descriptive ordering of the reported SHM-index range changes after compensation. 162
6.51 Aggregate changes in the reported intact-state summaries after compensation. 163
6.52 Representative before–after comparisons for Enhanced EFS processing. 163
6.53 Thermal Drift Quantification for All Four SFRC Specimens with Saw-Notch Damage (Without Compensation) 165
6.54 Compensated Signature Characteristics for All Four SFRC Specimens with Saw-Notch Damage 168
6.55 Equivalent Mass (kg) at Each Temperature for All Four SFRC Specimens with Saw-Notch (Without Compensation) 173
6.56 Equivalent Mass Change Summary for All Four SFRC Specimens with Saw-Notch (Without Compensation) 174
6.57 Equivalent Mass (kg) at Each Temperature for All Four SFRC Specimens with Saw-Notch (With Compensation) 175
6.58 Comparison of Mass Parameter Changes Before and After Temperature Compensation (Cut Condition) 175
6.59 Equivalent Stiffness (MN/m) at Each Temperature for All Four SFRC Specimens with Saw-Notch (Without Compensation) 176
6.60 Equivalent Stiffness Change Summary for All Four SFRC Specimens with Saw-Notch (Without Compensation) 176
6.61 Equivalent Stiffness (MN/m) at Each Temperature for All Four SFRC Specimens with Saw-Notch (With Compensation) 178
6.62 Comparison of Stiffness Parameter Changes Before and After Temperature Compensation (Cut Condition) 178
6.63 Equivalent Damping Change Summary for All Four SFRC Specimens with Saw-Notch (Without Compensation) 179
6.64 Comparison of Damping Parameter Changes Before and After Temperature Compensation (Cut Condition) 180
6.65 RMSD Values at Each Temperature for All Four SFRC Specimens with Saw-Notch 181
6.66 RMSD Statistical Summary for All Four SFRC Specimens with Saw-Notch 183

6.67 RMSD comparison between the matched intact and saw-cut states . . 183
6.68 MAPD Values (%) at Each Temperature for All Four SFRC Specimens with Saw-Notch 184
6.69 MAPD Statistical Summary for All Four SFRC Specimens with Saw-Notch 186
6.70 MAPD comparison between the matched intact and saw-cut states . . 186
6.71 AMPD Values (%) at Each Temperature for All Four SFRC Specimens with Saw-Notch 187
6.72 AMPD Statistical Summary for All Four SFRC Specimens with Saw-Notch 187
6.73 AMPD comparison between the matched intact and saw-cut states . . 189
6.74 Correlation Coefficient at Each Temperature for All Four SFRC Specimens with Saw-Notch 190
6.75 Correlation Coefficient Statistical Summary for All Four SFRC Specimens with Saw-Notch 192
6.76 Correlation Coefficient Comparison between the matched intact and saw-cut states 192
6.77 CCD Values at Each Temperature for All Four SFRC Specimens with Saw-Notch 195
6.78 CCD Statistical Summary for All Four SFRC Specimens with Saw-Notch 195
6.79 CCD Comparison between the matched intact and saw-cut states . . . 195
6.80 CCD^3 Values at Each Temperature for All Four SFRC Specimens with Saw-Notch 198
6.81 CCD^3 Statistical Summary for All Four SFRC Specimens with Saw-Notch 198
6.82 CCD^3 Comparison between the matched intact and saw-cut states . . 199
6.83 CCV Values at Each Temperature for All Four SFRC Specimens with Saw-Notch 200
6.84 CCV Statistical Summary for All Four SFRC Specimens with Saw-Notch 200
6.85 CCV Comparison between the matched intact and saw-cut states . . . 202
6.86 MSE Values ($\times 10^{-5}$) at Each Temperature for All Four SFRC Specimens with Saw-Notch 203
6.87 MSE Statistical Summary for All Four SFRC Specimens with Saw-Notch 205
6.88 MSE Comparison between the matched intact and saw-cut states . . . 205
6.89 Variance Values ($\times 10^{-10}$) at Each Temperature for All Four SFRC Specimens with Saw-Notch 206
6.90 Variance Statistical Summary for All Four SFRC Specimens with Saw-Notch 208

6.91 Variance Comparison between the matched intact and saw-cut states . 208
6.92 RMS Values at Each Temperature for All Four SFRC Specimens with Saw-Notch 211
6.93 RMS Statistical Summary for All Four SFRC Specimens with Saw-Notch 211
6.94 RMS Comparison between the matched intact and saw-cut states . . . 211
6.95 Skewness Values at Each Temperature for All Four SFRC Specimens with Saw-Notch 214
6.96 Skewness Statistical Summary for All Four SFRC Specimens with Saw-Notch 214
6.97 Skewness Comparison between the matched intact and saw-cut states 215
6.98 Peak-to-Peak (%) Values at Each Temperature for All Four SFRC Specimens with Saw-Notch 216
6.99 Peak-to-Peak Statistical Summary for All Four SFRC Specimens with Saw-Notch 216
6.100 Peak-to-Peak Comparison between the matched intact and saw-cut states 218
6.101 Covariance Values ($\times 10^{-10}$) at Each Temperature for All Four SFRC Specimens with Saw-Notch 219
6.102 Covariance Statistical Summary for All Four SFRC Specimens with Saw-Notch 221
6.103 Covariance Comparison between the matched intact and saw-cut states 221
6.104 Consolidated performance of the ten secondary SHM indices under cut heating for all four SFRC specimens. 222
6.105 Reported end-to-end EPS changes before and after compensation for the saw-cut records. 223
6.106 Specimen-level summary of the reported EPS changes for the saw-cut records. 224
6.107 Comparison of reported EPS processing effects in the intact and saw-cut states. 224
6.108 SHM Index Range Comparison Before vs After Compensation (Cut Condition) 225
6.109 SHM Compensation Effectiveness: Intact vs Cut Condition 226
6.110 Descriptive ordering of reported SHM-index range changes for the saw-cut records. 226
6.111 Aggregate changes in the reported saw-cut summaries after compensation. 227
6.112 Overall Compensation Effectiveness: Intact vs Cut Condition 227
6.113 Representative before–after comparisons for Enhanced EFS processing of the saw-cut records. 227

6.114Equivalent Mass Parameter: Intact vs Cut Comparison (After Compensation) 231
6.115Mass Temperature Drift: Intact vs Cut (75°C to End Temperature) . . 231
6.116Material Configuration Effect on Mass Change Due to Damage 232
6.117Equivalent Stiffness Parameter: Intact vs Cut Comparison (After Compensation) 233
6.118Stiffness Temperature Drift: Intact vs Cut (75°C to End Temperature) 233
6.119Material Configuration Effect on Stiffness Change Due to Damage . . 234
6.120Damping Temperature Drift: Intact vs Cut (75°C to End Temperature) 234
6.121Damping Behaviour vs Mass/Stiffness Under Damage 235
6.122Material Configuration Effect on Damping Change Due to Damage . . 236
6.123Matched EPS changes between the intact and saw-cut states 236
6.124RMSD Damage Sensitivity: Conductance Signal (After Compensation) 238
6.125RMSD Damage Sensitivity: Susceptance Signal (After Compensation) 238
6.126RMSD Damage Sensitivity: Signal Type Comparison 239
6.127RMSD temperature progression for matched intact and saw-cut conductance records 239
6.128RMSD: Material Configuration Effect on Damage Sensitivity 240
6.129MAPD Damage Sensitivity: Conductance Signal (After Compensation) 240
6.130MAPD Damage Sensitivity: Susceptance Signal (After Compensation) 242
6.131MAPD Damage Sensitivity: Signal Type Comparison 242
6.132MAPD temperature progression for matched intact and saw-cut conductance records 242
6.133MAPD vs RMSD: Damage Sensitivity Pattern Comparison 243
6.134AMPD Damage Sensitivity: Conductance Signal (After Compensation) 245
6.135AMPD Damage Sensitivity: Susceptance Signal (After Compensation) 245
6.136AMPD matched intact–saw-cut comparison by signal type 245
6.137AMPD temperature progression for matched intact and saw-cut conductance records 246
6.138AMPD vs RMSD/MAPD: Pattern Comparison 246
6.139Correlation Coefficient Damage Sensitivity: Conductance Signal (After Compensation) 248
6.140Correlation Coefficient Damage Sensitivity: Susceptance Signal (After Compensation) 248
6.141Correlation Coefficient Damage Sensitivity: Signal Type Comparison 249
6.142Correlation-coefficient temperature progression for matched intact and saw-cut conductance records 249

6.143 Observed directions of the correlation coefficient and RMSD in the matched records 250
6.144 CCD Damage Sensitivity: Conductance Signal (After Compensation) 252
6.145 CCD Damage Sensitivity: Susceptance Signal (After Compensation) . 252
6.146 CCD Damage Sensitivity: Signal Type Comparison 252
6.147 CCD temperature progression for matched intact and saw-cut conductance records 252
6.148 CCD vs RMSD: Pattern Consistency 253
6.149 CCD^3 Damage Sensitivity: Conductance Signal (After Compensation) 255
6.150 CCD^3 Damage Sensitivity: Susceptance Signal (After Compensation) 255
6.151 CCV Damage Sensitivity: Conductance Signal (After Compensation) 256
6.152 CCV Damage Sensitivity: Susceptance Signal (After Compensation) . 257
6.153 CCV intact–saw-cut comparison by signal type 258
6.154 Direction of CCV and other deviation-index changes in the tested specimens 258
6.155 MSE Damage Sensitivity: Conductance Signal (After Compensation) 259
6.156 MSE Damage Sensitivity: Susceptance Signal (After Compensation) . 260
6.157 MSE Damage Sensitivity: Signal Type Comparison 260
6.158 MSE vs RMSD: Pattern Consistency 261
6.159 Variance Damage Sensitivity: Conductance Signal (After Compensation) – REVERSED PATTERN 263
6.160 Variance Damage Sensitivity: Susceptance Signal (After Compensation) 263
6.161 Variance Damage Sensitivity: Signal Type Comparison – Complementary Pattern 263
6.162 Observed variance and RMSD directions in the matched records . . . 264
6.163 Conductance RMS comparison after compensation 266
6.164 Susceptance RMS comparison after compensation 266
6.165 RMS intact–saw-cut comparison by signal type 266
6.166 RMS vs RMSD: Opposite Sensitivity Patterns by SF Content 267
6.167 Skewness Damage Sensitivity: Conductance Signal (After Compensation) 269
6.168 Skewness Damage Sensitivity: Susceptance Signal (After Compensation) 269
6.169 Skewness Damage Sensitivity: Signal Type Comparison 269
6.170 Skewness Interpretation: Shape vs Magnitude Information 270
6.171 Peak-to-Peak Damage Sensitivity: Conductance Signal (After Compensation) 272
6.172 Peak-to-Peak Damage Sensitivity: Susceptance Signal (After Compensation) 272

6.173Peak-to-Peak Damage Sensitivity: Signal Type Comparison 272
6.174Peak-to-Peak vs RMSD: Pattern Comparison 273
6.175Covariance Damage Sensitivity: Conductance Signal (After Compensation) – REVERSED PATTERN 275
6.176Covariance Damage Sensitivity: Susceptance Signal (After Compensation) 275
6.177Covariance Damage Sensitivity: Signal Type Comparison – Complementary Pattern 275
6.178Covariance vs Variance: Identical Patterns 276
6.179Indices with a Consistent Direction in the Four Tested Specimens: Performance Across All Configurations 277
6.180Observed dosage-group direction of selected deviation indices 277
6.181Within-dataset comparison of the thirteen SHM indices 278
6.182Consolidated matched changes of the ten secondary SHM indices for all four SFRC specimens 279
6.183Matched changes of deviation-based indices for the 0.50% fibre pair . 280
6.184Matched CCV and RMS changes for the two aspect ratios and fibre dosages 280
6.185Matched changes of selected correlation-based indices by aspect ratio 281
6.186Matched Variance and Covariance changes for the 0.75% fibre pair . . 281
6.187Observed index-direction reversal between the two dosage groups . . 282
6.188Deviation-Based Indices: SF Dose Effect (Conductance Signal) . . . 282
6.189Reversed conductance-index directions in the two fibre-dosage groups 282
6.190Indices retaining one direction across the four tested specimens 283
6.191Reported index effects for SFC2 (AR 55/SF 0.50%) 283
6.192Within-dataset index directions grouped by fibre dosage 284
6.193Signal channel associated with the reported within-dataset effects . . . 284
6.194Within-dataset ordering of selected indices 284
6.195Selected temperature-dependent intact–saw-cut differences 285
6.196Endpoint ratios of selected intact–saw-cut differences 286
6.197Observed curve separation over 75–125°C. 286
6.198Observed curve separation over 125–200°C. 287
6.199Observed curve separation over 200–250°C for SFC1 and SFC2. . . . 287
6.200Configuration-specific ranges associated with the reported separation . 288
6.201Temperature Effect vs Matched direction: Magnitude Comparison . . 288
6.202Reported changes in matched separation after compensation for selected indices. 289

6.203 Selected index behaviour with and without compensation in the analysed records. 290
6.204 Histogram Analysis Overview: Matched direction by Index (Conductance Signal) 291
6.205 Configuration-Specific RMSD Statistics (Conductance) 292
6.206 Indices with a Consistent Direction in the Four Tested Specimens: Distribution Separation Metrics 295
6.207 Deviation-Based Indices: Distribution Separation by SF Content . . . 296
6.208 Distribution Separation Summary: All Indices (Conductance) 298
6.209 Matched intact–saw-cut effect summary for the thirteen SHM indices 299
6.210 Configuration with the largest reported separation by index category . 299
6.211 Reported coefficient-of-variation summaries for compensated index records 300
6.212 Temperature-associated endpoint changes for compensated intact SFC2 records 300
6.213 Preliminary screening values retained from the source summaries . . . 301
6.214 Illustrative one-sided normal probabilities for threshold multipliers . . 302
6.215 Exploratory conductance thresholds calculated from intact records . . 302
6.216 Within-dataset threshold exceedance rates for the saw-cut records . . . 303
6.217 Aspect Ratio-Specific Thresholds (0.5% SF, Conductance) 304
6.218 Fibre-dosage group comparison of empirical index directions 304
6.219 Configuration-specific threshold matrix for conductance 305
6.220 Pooled Within-Dataset Threshold Performance Across All Configurations 305
6.221 Within-dataset classification summary for configuration-specific and pooled thresholds 306
6.222 Descriptive comparison of pooled and configuration-specific threshold constructions 306
6.223 Candidate pooled thresholds derived from the present dataset 307
6.224 Within-dataset separation metrics for selected SHM indices 307
6.225 Within-dataset classification summaries for candidate threshold strategies 308
6.226 Within-dataset classification summaries before and after compensation 311
6.227 Within-dataset index summaries by material configuration 313

7.1 Performance comparison of classical ML algorithms for the aspect ratio 65 SFRC cube series. 329
7.2 Performance comparison of classical ML algorithms for the aspect ratio 55 SFRC cube series. 329

7.3 Validation performance of the three deep learning architectures for hydration compressive strength prediction 333
7.4 Validation performance boundaries of the applied DL architectures for split-tensile strength prediction 339
7.5 Computational benchmarking and architectural training durations for the deep learning models 342

A.1 Intact-state mean equivalent mass-like parameter after compensation (kg). 364
A.2 Intact-state mean equivalent stiffness-like parameter after compensation ($\mathrm{N\,m^{-1}}$). 365
A.3 Intact-state mean equivalent damping-like parameter after compensation. 365
A.4 Saw-cut-state mean equivalent mass-like parameter after compensation (kg). 365
A.5 Saw-cut-state mean equivalent stiffness-like parameter after compensation ($\mathrm{N\,m^{-1}}$). 366
A.6 Saw-cut-state mean equivalent damping-like parameter after compensation. 366

List of Figures

Fig. No.	Description	Page No.
1.1	Schematic distinction among the PZT sensor configurations relevant to this thesis.	4
3.1	Fabrication sequence and principal components of the JPS	28
3.2	Fabrication sequence and structural components of the reusable NBPS	28
3.3	Data-acquisition arrangement for the 180-day curing-age monitoring study.	29
3.4	Data-acquisition arrangement for the compressive damage detection study.	31
3.5	Data-acquisition arrangement for the split-tensile damage study.	32
3.6	Data-acquisition arrangement for the thermal-loading study.	33
3.7	Saw-cut damage introduced in the four SFRC cubes before the damaged thermal sequence	34
3.8	Series spring–damper–mass equivalent network used for EPS extraction	37
4.1	Measurement sequence for the repeated JPS records and the separately obtained compressive-strength results.	41
4.2	Conductance (G) signatures recorded over 30–1000 kHz at representative curing ages for the four JPS configurations (Part 1).	43
4.2	Conductance (G) signatures recorded over 30–1000 kHz at representative curing ages for the four JPS configurations (continued).	44
4.3	Susceptance (B) signatures recorded over 30–1000 kHz at representative curing ages for the four JPS configurations (Part 1).	45
4.3	Susceptance (B) signatures recorded over 30–1000 kHz at representative curing ages for the four JPS configurations (continued).	46
4.4	Resonant frequency and peak conductance during the 1–180 day curing period for the four JPS configurations (Part 1).	48
4.4	Resonant frequency and peak conductance during the 1–180 day curing period for the four JPS configurations (continued).	49

4.5 Combined compressive-strength results over 1–180 days for the four SFRC configurations obtained from separately tested cubes. 50
4.6 Individual compressive-strength records and fitted exponential age–strength curves for the four SFRC configurations (Part 1). 51
4.6 Individual compressive-strength records and fitted exponential age–strength curves for the four SFRC configurations (continued). 52
4.7 RMSD and MAPD values across curing ages (Part 1). 54
4.7 CC and covariance values across curing ages (continued). 55
4.8 Computed real (x) and imaginary (y) mechanical-impedance components across curing ages for SFC1 (Part 1). 57
4.8 Computed real (x) and imaginary (y) mechanical-impedance components across curing ages for SFC2 (continued). 58
4.8 Computed real (x) and imaginary (y) mechanical-impedance components across curing ages for SFC3 (continued). 59
4.9 Computed real (x) and imaginary (y) mechanical-impedance components across curing ages for SFC4. 60
4.10 EPS for the four SFRC configurations across the curing period (Part 1). 61
4.10 EPS for the four SFRC configurations across the curing period (continued). 62
4.11 Reconstructed and experimental (x, y) spectra for SFC1 (Part 1). . . . 63
4.11 Reconstructed and experimental (x, y) spectra for SFC2 (continued). . 64
4.11 Reconstructed and experimental (x, y) spectra for SFC3 (continued). . 65
4.12 Reconstructed and experimental (x, y) spectra for SFC4. 66
4.13 Equivalent stiffness in relation to compressive strength and curing age for SFC1 (Part 1). 68
4.13 Equivalent stiffness in relation to compressive strength and curing age for SFC2 (continued). 69
4.13 Equivalent stiffness in relation to compressive strength and curing age for SFC3 (continued). 70
4.14 Equivalent stiffness in relation to compressive strength and curing age for SFC4. 71

5.1 Compressive strength development in SFRC specimens as a function of steel fibre dosage and aspect ratio (28 days). 75
5.2 NBPS resonant frequency and peak conductance shifts for the AR 65 SFRC series. 77
5.3 NBPS resonant frequency and peak conductance shifts for the AR 55 SFRC series. 77

5.4 RMSD for the thirteen SFRC cube configurations. 78
5.5 MAPD for the thirteen SFRC cube configurations. 79
5.6 Mechanical-impedance components for the SFRC–NBPS cube series. 80
5.7 Fitted EPS parameters for healthy and damaged SFRC cubes. 80
5.8 Measured and reconstructed spectra for the AR 65 cubes. 82
5.8 Measured and reconstructed spectra for the AR 55 cubes (continued). 83
5.9 Normalised equivalent-stiffness change Δs for the SFRC cubes. 84
5.10 Destructive splitting-tensile strengths of the 39-cylinder matrix at 28 days. 86
5.11 Comparative NBPS conductance spectra contrasting healthy and post-tensile-test damaged states (AR 65 series). 87
5.11 Comparative NBPS conductance spectra contrasting healthy and post-tensile-test damaged states (continued: AR 55 series). 88
5.12 Detailed view of Peak 1 at the two upper tested dosages, contrasting healthy and damaged states. 89
5.13 Peak conductance versus resonance frequency for the AR 65 SFRC cylinders after splitting-tensile loading. 89
5.14 Peak conductance versus resonance frequency for the AR 55 SFRC cylinders after splitting-tensile loading. 90
5.15 RMSD index of NBPS signatures as a function of fibre dosage for both aspect ratios. 90
5.16 Mechanical-impedance components for the NBPS–cylinder system at varying fibre dosages. 91
5.17 Derived Equivalent Structural Parameters (c, m, k) for SFRC cylinders across healthy and damaged conditions. 92
5.18 Comparison of experimental and equivalent-system $x(f)$ and $y(f)$ responses for the SFRC cylinders. 93
5.19 Relationship between NBPS-derived equivalent stiffness k and compressive strength over the tested configurations 93
5.20 Relationship between NBPS-derived stiffness k and splitting-tensile strength over the tested configurations 94
5.21 Magnitude of normalised equivalent-stiffness change Δs across the SFRC cylinder configurations 95

6.1 Four-panel comparison of conductance signatures before and after applying the Enhanced-EFS compensation algorithm at 150°C and 175°C. 99

6.2 Integrated thermal-study workflow linking the specimen configurations, structural states, progressive temperature protocol, processing branches and reported comparisons. 105
6.3 Uncompensated intact conductance signatures for SFC1 and SFC3 (AR 65). 109
6.4 Uncompensated intact conductance signatures for SFC2 and SFC4 (AR 55). 110
6.5 Compensated intact conductance signatures for SFC1 and SFC3 (AR 65). 113
6.6 Compensated intact conductance signatures for SFC2 and SFC4 (AR 55). 114
6.7 Intact EPS transitions before and after compensation for SFC1 (AR 65, 0.50% fibre). 116
6.8 Intact EPS transitions before and after compensation for SFC3 (AR 65, 0.75% fibre). 116
6.9 Intact EPS transitions before and after compensation for SFC2 (AR 55, 0.50% fibre). 117
6.10 Intact EPS transitions before and after compensation for SFC4 (AR 55, 0.75% fibre). 117
6.11 RMSD index comparison for all four intact SFRC specimens. 126
6.12 MAPD index comparison for all four intact SFRC specimens. 129
6.13 AMPD index comparison for all four intact SFRC specimens. 131
6.14 Correlation Coefficient comparison for all four intact SFRC specimens. 133
6.15 CCD index comparison for all four intact SFRC specimens. 136
6.16 CCD^3 index comparison for all four intact SFRC specimens. 139
6.17 CCV index comparison for all four intact SFRC specimens. 141
6.18 MSE index comparison for all four intact SFRC specimens. 144
6.19 Variance index comparison for all four intact SFRC specimens. 146
6.20 RMS index comparison for all four intact SFRC specimens. 149
6.21 Skewness index comparison for all four intact SFRC specimens. . . . 152
6.22 Peak-to-Peak index comparison for all four intact SFRC specimens. . 154
6.23 Covariance index comparison for all four intact SFRC specimens. . . 157
6.24 Uncompensated saw-cut conductance signatures for SFC1 and SFC3 (AR 65). 165
6.25 Uncompensated saw-cut conductance signatures for SFC2 and SFC4 (AR 55). 166
6.26 Compensated saw-cut conductance signatures for SFC1 and SFC3 (AR 65). 168

6.27 Compensated saw-cut conductance signatures for SFC2 and SFC4 (AR 55). 169
6.28 Saw-cut EPS transitions before and after compensation for SFC1 (AR 65, 0.50% fibre). 171
6.29 Saw-cut EPS transitions before and after compensation for SFC3 (AR 65, 0.75% fibre; data to 175 °C). 172
6.30 Saw-cut EPS transitions before and after compensation for SFC2 (AR 55, 0.50% fibre). 172
6.31 Saw-cut EPS transitions before and after compensation for SFC4 (AR 55, 0.75% fibre; data to 175 °C). 173
6.32 RMSD index comparison for all four SFRC specimens with saw-notch damage. 182
6.33 MAPD index comparison for all four SFRC specimens with saw-notch damage. 185
6.34 AMPD index comparison for all four SFRC specimens with saw-notch damage. 188
6.35 Correlation Coefficient comparison for all four SFRC specimens with saw-notch damage. 191
6.36 CCD index comparison for all four SFRC specimens with saw-notch damage. 194
6.37 CCD^3 index comparison for all four SFRC specimens with saw-notch damage. 197
6.38 CCV index comparison for all four SFRC specimens with saw-notch damage. 201
6.39 MSE index comparison for all four SFRC specimens with saw-notch damage. 204
6.40 Variance index comparison for all four SFRC specimens with saw-notch damage. 207
6.41 RMS index comparison for all four SFRC specimens with saw-notch damage. 210
6.42 Skewness index comparison for all four SFRC specimens with saw-notch damage. 213
6.43 Peak-to-Peak index comparison for all four SFRC specimens with saw-notch damage. 217
6.44 Covariance index comparison for all four SFRC specimens with saw-notch damage. 220
6.45 Matched intact and saw-cut EPS trajectories for SFC1 after compensation. 229

6.46 Matched intact and saw-cut EPS trajectories for SFC3 after compensation. 230
6.47 Matched intact and saw-cut EPS trajectories for SFC2 after compensation. 230
6.48 Matched intact and saw-cut EPS trajectories for SFC4 after compensation. 231
6.49 RMSD response after compensation: matched intact and saw-cut conductance records. 237
6.50 RMSD response after compensation: matched intact and saw-cut susceptance records. 238
6.51 MAPD response after compensation: matched intact and saw-cut conductance records. 241
6.52 MAPD response after compensation: matched intact and saw-cut susceptance records. 241
6.53 AMPD response after compensation: matched intact and saw-cut conductance records. 244
6.54 AMPD response after compensation: matched intact and saw-cut susceptance records. 244
6.55 Correlation Coefficient (CC) response after compensation: matched intact and saw-cut conductance records. 247
6.56 Correlation Coefficient (CC) response after compensation: matched intact and saw-cut susceptance records. 248
6.57 CCD response after compensation: matched intact and saw-cut conductance records. 251
6.58 CCD response after compensation: matched intact and saw-cut susceptance records. 251
6.59 CCD^3 response after compensation: matched intact and saw-cut conductance records. 254
6.60 CCD^3 response after compensation: matched intact and saw-cut susceptance records. 254
6.61 CCV response after compensation: matched intact and saw-cut conductance records. 256
6.62 CCV response after compensation: matched intact and saw-cut susceptance records. 257
6.63 MSE response after compensation: matched intact and saw-cut conductance records. 259
6.64 MSE response after compensation: matched intact and saw-cut susceptance records. 260
6.65 Variance response after compensation: matched intact and saw-cut conductance records. 262

6.66 Variance response after compensation: matched intact and saw-cut susceptance records. 262
6.67 RMS response after compensation: matched intact and saw-cut conductance records. 265
6.68 RMS response after compensation: matched intact and saw-cut susceptance records. 265
6.69 Skewness response after compensation: matched intact and saw-cut conductance records. 268
6.70 Skewness response after compensation: matched intact and saw-cut susceptance records. 268
6.71 Peak-to-Peak response after compensation: matched intact and saw-cut conductance records. 271
6.72 Peak-to-Peak response after compensation: matched intact and saw-cut susceptance records. 271
6.73 Covariance response after compensation: matched intact and saw-cut conductance records. 274
6.74 Covariance response after compensation: matched intact and saw-cut susceptance records. 274
6.75 RMSD distributions for the pooled intact and saw-cut records. 291
6.76 CCV Histogram Distribution for intact and saw-cut record distributions. 292
6.77 CCV distributions for the matched intact and saw-cut records. 294
6.78 RMS distributions for the matched intact and saw-cut records. 294
6.79 Peak-to-Peak distributions for the matched intact and saw-cut records. 295
6.80 MAPD distributions for the matched intact and saw-cut records. . . . 296
6.81 Variance Index Distribution: intact and saw-cut record distributions. . 297
6.82 Correlation Coefficient Distribution: intact and saw-cut record distributions. 297

7.1 Unified ML/DL framework for EMI-based SHM of SFRC. 321
7.2 Workflow for the development and validation of machine learning algorithms for SFRC strength prediction. 323
7.3 Schematic of the 2D Convolutional Neural Network (2D CNN) architecture implemented for strength prediction. 325
7.4 Block diagram of the 2D LSTM architecture illustrating internal cell gate operations. 326
7.5 2D Bidirectional Long Short-Term Memory (2D Bi-LSTM) architecture configured for sequential sensor data evaluation. 326

7.6 Predicted versus actual compressive strength of SFRC cubes (AR 65 series) demonstrating tracking error across three Gaussian kernel scales. 331
7.7 Predicted versus actual compressive strength of SFRC cubes (AR 55 series) demonstrating tracking error across three Gaussian kernel scales. 332
7.8 SFC1 training and prediction performance: 2D CNN. 334
7.9 SFC1 training and prediction performance: 2D CNN–LSTM. 335
7.10 SFC1 training and prediction performance: 2D CNN–Bi-LSTM. . . . 336
7.11 MSE and R^2 comparison across the four JPS hydration datasets. . . . 337
7.12 Network-predicted versus destructively measured tensile strength for SFRC cylinders (AR 65 series). 339
7.13 Network-predicted versus destructively measured tensile strength for SFRC cylinders (AR 55 series). 340
7.14 Quantitative evaluation of deep learning architectures based on MSE and R^2 for both split-tensile cylinder series. 341

LIST OF SYMBOLS, ABBREVIATIONS AND NOMENCLATURE

Notation	Meaning
	Mathematical Symbols
$B(f)$	Susceptance, the imaginary component of electrical admittance at frequency f
c	Equivalent damping parameter in the adopted series-mobility representation
$C(s)$	Joint conductance–susceptance correlation objective evaluated at trial shift s
d	Steel-fibre diameter
d_{31}	Piezoelectric strain coefficient
f	Excitation frequency
$f_c(t)$	Compressive strength at curing age t
$F(t)$	Harmonic excitation force
F_0	Amplitude of the harmonic excitation force
$G(f)$	Conductance, the real component of electrical admittance at frequency f
G_{bl}	Baseline conductance
G_i	Conductance at the i-th frequency bin of a comparison signature
h	PZT-patch thickness
l	PZT-patch in-plane dimension
i	Frequency-bin or observation index
j	Imaginary unit, $j^2 = -1$
k	Equivalent stiffness parameter; other local uses are defined with their equations
m	Equivalent mass parameter
M	Generic equivalent mass notation
K	Generic equivalent stiffness notation
C	Generic equivalent damping notation
$\mathscr{M}(\omega)$	Total mechanical mobility
N	Number of frequency bins
n	Number of evaluated observations
R^2	Coefficient of determination
s	Trial frequency shift in the enhanced EFS search
$s^\star$	Selected frequency shift in the enhanced EFS search
t	Curing age or time, as defined in the relevant experiment
w_G	Conductance weight in the joint correlation objective
w_B	Susceptance weight in the joint correlation objective

Notation	Meaning
$x(\omega)$	Real component of equivalent mechanical impedance
$y(\omega)$	Imaginary component of equivalent mechanical impedance
$Y(\omega)$	Complex electrical admittance
y_i	Measured response
$\hat{y}_i$	Predicted response
$\bar{y}$	Sample-mean response
$Z_{s,\text{eff}}$	Effective mechanical impedance of the structure
$Z_{a,\text{eff}}$	Effective mechanical impedance of the PZT actuator
Δf	Effective frequency shift
Δs	Magnitude of normalised equivalent-stiffness change
δ_G	Conductance mean offset
δ_B	Susceptance mean offset
η	Mechanical loss factor
ν	Poisson's ratio
ρ	Density
ω	Angular frequency
	Abbreviations and Identifiers
AC	Alternating Current
AI	Artificial Intelligence
AMPD	Absolute Mean Percentage Deviation
ANN	Artificial Neural Network
AR	Steel-fibre aspect ratio; AR55 and AR65 identify the two investigated fibre families
Bi-LSTM	Bidirectional Long Short-Term Memory network
CC	Cross-Correlation Coefficient
CCD	Cross-Correlation Deviation, $1 - \text{CC}$
CNN	Convolutional Neural Network
CNN–Bi-LSTM	Hybrid Convolutional Neural Network–Bidirectional Long Short-Term Memory model
CNN–LSTM	Hybrid Convolutional Neural Network–Long Short-Term Memory model
Cov	Covariance
CTM	Compression Testing Machine
DL	Deep Learning
E–EFS	Enhanced Effective Frequency Shift procedure
EFS	Effective Frequency Shift
EMI	Electromechanical Impedance
EPS	Equivalent Structural Parameter(s)

Notation	Meaning
E4980A	Keysight precision LCR-meter model used for EMI acquisition
FRC	Fibre Reinforced Concrete
GPR	Gaussian Process Regression
GPU	Graphics Processing Unit
IS	Indian Standard
JPS	Jacketed Piezo Sensor
JPS1–JPS4	Identifiers of the four embedded jacketed sensors
LCR	Inductance–Capacitance–Resistance meter
LSTM	Long Short-Term Memory network
MAE	Mean Absolute Error
MAPD	Mean Absolute Percentage Deviation
ML	Machine Learning
MSE	Mean Squared Error
M30	Nominal concrete strength-grade designation used in the experimental programme
NBPS	Non-Bonded Piezo Sensor
NDE	Non-Destructive Evaluation
NDT	Non-Destructive Testing
OPC	Ordinary Portland Cement
PTFE	Polytetrafluoroethylene
PVDF	Polyvinylidene fluoride
PZT	Lead Zirconate Titanate piezoceramic
PZT-5H	PZT material grade used for the transducers
PZT-PIC151	PZT material/product designation reported for a transducer
ReLU	Rectified Linear Unit
RMS	Root Mean Square
RMSD	Root Mean Square Deviation
RMSE	Root Mean Squared Error
SA	Smart Aggregate
SBPS	Surface-Bonded Piezo Sensor
SDOF	Single Degree of Freedom
SFC	Steel Fibre Concrete configuration identifier
SFC1–SFC4	Identifiers of the four monitored SFRC configurations
SFCM	Steel Fibre Cementitious Material
SFRC	Steel Fibre Reinforced Concrete
SHM	Structural Health Monitoring
SVM	Support Vector Machine

Notation	Meaning
VEE Pro	Keysight measurement-control and data-acquisition software used with the LCR meter

CHAPTER 1

INTRODUCTION

1.1 Background

Concrete is widely used in civil infrastructure because its materials are generally available and it can be cast into many structural forms. Its tensile strength and post-cracking capacity are, however, much lower than its compressive strength. Steel Fibre Reinforced Concrete (SFRC) addresses this limitation through short fibres distributed within the cementitious matrix. After cracking begins, well-distributed fibres bridge the crack surfaces, transfer tensile stress and contribute to toughness and energy absorption. This behaviour depends on the matrix, fibre geometry, aspect ratio, volume fraction, orientation and fibre–matrix bond rather than on fibre addition alone (Banthia and Gupta, 2004; Bentur and Mindess, 2007; Naaman, 2006).

Hooked-end fibres are used in the present work. Their end geometry increases pull-out resistance after a crack crosses a fibre, while the aspect ratio affects the anchorage length and reinforcing action. Increasing the fibre content does not always produce the same improvement because workability, fibre orientation and local distribution also affect the response. The experimental programme therefore identifies every specimen by fibre aspect ratio and dosage (Chen et al., 2024; di Prisco et al., 2021; Lantsoght, 2019).

These benefits do not remove the need to evaluate structural condition. Hydration changes the mechanical properties of young concrete, mechanical loading causes cracking and changes in stiffness, and high temperature affects both the material and the sensing system. Aggregate and randomly distributed fibres also make it difficult to relate a local measurement to the condition of the whole SFRC specimen. Structural assessment must distinguish changes due to material development, loading or temperature from those caused by the sensor, its attachment or the measurement environment (Farrar and Worden, 2007; Na and Baek, 2018; Sohn et al., 2003).

Structural Health Monitoring (SHM) uses measured responses to evaluate changes

in structural condition. In the Electromechanical Impedance (EMI) technique, a piezoelectric transducer excites the host and records an electrical response that is influenced by their mechanical interaction. The method is suited to local measurements, but it does not replace visual inspection, material testing or other non-destructive methods. Its results depend on the sensor configuration, the test conditions and the method used for interpretation (Bhalla and Soh, 2004b; Gopalakrishnan et al., 2019; Park et al., 2003).

This thesis investigates EMI-based monitoring of SFRC during curing, mechanical loading and heating, together with data-driven interpretation of the measured signatures. The experimental programme uses two piezoelectric sensor configurations and evaluates resonance characteristics, statistical indices and Equivalent Structural Parameters (EPS). The research context, measurement challenges, objectives and boundaries of the work are introduced below.

1.2 The Role of Structural Health Monitoring

Farrar and Worden (2007) describe SHM as a process in which periodically sampled dynamic-response measurements are used to extract damage-sensitive features and support statistical decisions about structural condition. This definition emphasises a sequence rather than a single sensor: a monitoring question is translated into a measurement strategy, the acquired signal is conditioned, features are extracted, and the features are interpreted with respect to an appropriate baseline. Sohn et al. (2003) similarly show that environmental and operational variability must be considered before a change in a measured feature can be assigned to damage.

The conclusions supported by an SHM system depend on the available evidence. Detecting a change in response is not the same as locating damage, determining its severity or estimating the remaining service life. These tasks require additional measurement coverage, calibration and validation. The laboratory investigations in this thesis therefore use controlled specimen groups, defined baselines and separate mechanical tests. The results apply to the tested conditions and are not used to claim a universal field-monitoring threshold.

Lead Zirconate Titanate (PZT) transducers are used because of their coupled electrical and mechanical behaviour. Mechanical deformation produces an electrical response, while an applied electric field causes the PZT to deform. A PZT element can therefore act as both actuator and sensor. When it is coupled to concrete, the measured response is influenced by the PZT, its protective or mounting layers, the interface and the surrounding host material (Giurgiutiu and Zagrai, 2005; Liang et al., 1994; Park et al., 2003). This coupling is the basis of EMI monitoring and is also a principal source

of uncertainty.

Other inspection and monitoring methods remain valuable because they measure different physical phenomena over different regions. Ultrasonic methods, acoustic emission and radar-based methods, for example, may be used to assess material quality, active cracking or internal features under suitable conditions. EMI measures the local high-frequency interaction with the host, but its response is sensitive to installation and environmental conditions. It is therefore used alongside other evidence rather than ranked as universally better or worse than other non-destructive methods (Malhotra and Carino, 2004; Na and Baek, 2018; Ohtsu, 2010).

1.3 The Electromechanical Impedance Technique

The EMI technique applies a variable-frequency electrical excitation to a PZT transducer and records the resulting complex electrical admittance. The real component is the conductance G, and the imaginary component is the susceptance B. Liang et al. (1994) established a coupled formulation linking the electrical response of a piezoelectric actuator to the mechanical impedance of the host structure. Subsequent work by Park et al. (2003) and Bhalla and Soh (2004b) developed the technique for structural monitoring and clarified the influence of the transducer–host interaction.

An EMI signature contains resonances whose frequencies, amplitudes and shapes can change with the coupled system. In cementitious materials, these changes may result from hydration, cracking, stiffness loss, temperature variation or sensor coupling. The signature is therefore not a direct image of damage. It must be compared with a defined baseline and interpreted for the particular experiment. Statistical indices quantify differences between signatures, while resonance characteristics describe changes in peak frequency or conductance. Each measure represents the frequency response differently and must be used within its validated range (Lim et al., 2018; Park et al., 1999; Singh et al., 2022).

Selection of the frequency range is part of the experimental procedure. The range must contain stable resonance information and avoid regions dominated by measurement noise or inadequate sensor contact. The selected range and sampling interval are therefore specific to each study and cannot be transferred automatically to every structure. Baseline selection is equally important because curing continuously changes the host, whereas a mechanical-damage test compares defined conditions before and after loading.

This thesis also uses EPS to represent the equivalent mass, stiffness and damping in the adopted lumped-parameter model of the PZT–structure interaction. These are

model-dependent parameters of the coupled measurement system, not direct measurements of the bulk concrete properties. They are interpreted only with the corresponding experimental records (Singh et al., 2022; Talakokula et al., 2018).

EMI monitoring offers high sensitivity to local changes, but this sensitivity also makes repeatability important. Sensor geometry, bonding or contact, frequency range, acquisition settings and temperature can influence the recorded spectrum. Reliable interpretation therefore requires consistent instrumentation, a traceable baseline and comparison with independent mechanical evidence. These requirements guide the experimental design adopted in this thesis and prevent a spectral difference from being labelled as damage without supporting context.

1.4 Piezoelectric Sensor Configurations

The physical installation of the PZT determines how excitation is transferred to the concrete and how the host response returns to the transducer. Surface-bonded sensors are attached to hardened concrete and allow direct access for installation and replacement. Embedded sensors can operate from an early age but are retained within the specimen and are difficult to inspect after casting. Non-bonded arrangements place the PZT on an intermediate element that is brought into mechanical contact with the specimen, allowing reuse while introducing an additional coupling interface (Divsholi and Yang, 2009; Gu et al., 2006; Narayanan and Subramaniam, 2016).

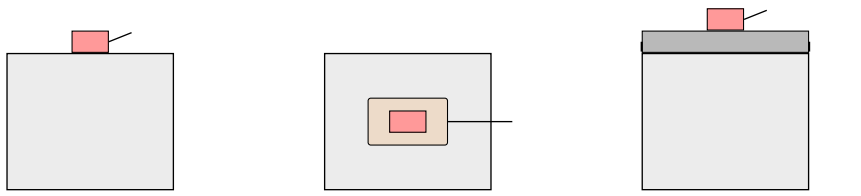

(a) SBPS surface-bonded

(b) JPS embedded and retained

(c) NBPS non-bonded and reusable

Figure 1.1: Schematic distinction among the PZT sensor configurations relevant to this thesis.

Figure 1.1 shows the three configurations considered in this thesis. A Surface-Bonded Piezo Sensor (SBPS) is bonded to the external surface of hardened concrete. In the present study, the Jacketed Piezo Sensor (JPS) is the embedded arrangement: a protective jacket allows the sensor to be placed in fresh concrete and retained in the specimen. The Non-Bonded Piezo Sensor (NBPS) is the reusable external arrangement used before and after mechanical testing.

The three configurations differ in installation and maintenance. An SBPS can be

inspected directly but normally requires a hardened surface for bonding. A JPS permits measurements from an early age because it is cast with the concrete, although the transducer and jacket remain part of that specimen. An NBPS can be moved between specimens, but repeatable measurements require the same contact pressure, position and surface condition (Bhalla and Gupta, 2022; Divsholi and Yang, 2009; Wu and Chang, 2006).

The two sensor arrangements serve different experimental purposes in this work. JPS supports measurements from casting onward using a sensor retained in the concrete, whereas NBPS supports repeated measurements of hardened specimens using a removable sensor (Aulakh and Bhalla, 2022, 2025).

1.5 Temperature Effects and the Need for an Enhanced EFS

Temperature affects several parts of the EMI measurement system. It can change the mechanical behaviour of concrete, the dielectric and piezoelectric properties of the PZT, and the properties of the sensor jacket, bond or contact surface. Even without structural damage, an admittance signature may therefore change in frequency, amplitude or shape as the temperature varies. Unless these effects are separated from changes caused by damage, temperature can produce a false damage indication or hide a genuine change (Huynh and Kim, 2017; Park et al., 1999; Rabelo and others, 2017).

Koo et al. (2009) proposed the Effective Frequency Shift (EFS) approach to align a temperature-affected conductance signature with a reference before damage indices are evaluated. The present thermal study examines an enhanced procedure using both conductance and susceptance. It accounts for frequency displacement and the mean amplitude offset in each channel. Its validity is assessed only for the measured temperature stages and frequency resolution.

The thermal assessment compares intact and saw-cut conditions using the available conductance, susceptance, statistical-index and EPS records. These measures are examined together so that the effect of temperature is not judged from a single indicator.

1.6 Data-Driven Analytics in SHM

An EMI measurement contains many correlated conductance and susceptance samples. When measurements are repeated across specimens, ages and loading conditions, the resulting data are high-dimensional and the relation between a signature and a mechanical response may be nonlinear. Statistical features and physics-based parameters provide interpretable summaries, while machine- learning and deep-learning

methods can examine relationships within the measured data.

Gaussian Process Regression (GPR), for example, provides a probabilistic regression framework, whereas Convolutional Neural Networks (CNNs) can extract local patterns from structured inputs (LeCun et al., 2015; Rasmussen and Williams, 2006). Long Short-Term Memory (LSTM) and Bidirectional LSTM architectures were developed to represent dependencies in sequential data (Hochreiter and Schmidhuber, 1997; Schuster and Paliwal, 1997). Their suitability in an SHM study nevertheless depends on sample construction, partitioning, pre-processing and the relationship between training and test specimens. Model accuracy alone does not establish a physical cause or prove that the model will perform under field conditions.

The data-driven investigations are evaluated separately for the curing, compression and splitting-tensile studies using their reported divisions of training and test data and their stated performance measures. The models are treated as study-specific regression tools supported by the corresponding EMI and mechanical records. They have not been validated for independent structures, real-time field use, untested materials or different sensor installations (Parida et al., 2022; Zhang et al., 2024).

1.7 Research Motivation and Objectives

The preceding discussion identifies a connected research need. EMI offers local sensitivity to changes in an SFRC–sensor system, but its interpretation depends on sensor configuration, baseline definition, mechanical state, temperature and data-processing method. Studies addressing only one of these elements cannot by themselves establish how the method behaves across curing, mechanical damage and elevated-temperature exposure. The present work therefore combines retained and reusable sensing, conventional mechanical tests, statistical and EPS-based interpretation, thermal compensation and study-specific data-driven models within one laboratory programme.

The research is governed by the following objectives:

- Objective 1: To assess and investigate damage detection and localization in fibre-reinforced concrete using piezoelectric sensors.
- Objective 2: To investigate the heating-time effect on fibre-reinforced concrete using a PZT sensor.
- Objective 3: To computationally model the damage progression of fibre-reinforced concrete by an advanced data-driven modeling framework based on PZT sensor monitoring.

1.8 Scope and Contributions

The experimental scope is limited to the materials, sensor configurations, specimen geometries, loading procedures, temperature stages and acquisition settings used in the experimental programme. The investigated material is SFRC incorporating hooked-end steel fibres with the aspect ratios and volume fractions assigned to each study. The work uses PZT-based EMI measurements under laboratory conditions. Other fibre families, sensor technologies, long-term field environments, fatigue, impact, freeze–thaw and chemical exposure are not experimentally validated in this thesis.

Within these boundaries, the principal contributions are:

1. Two sensor configurations for SFRC: Embedded JPS are used for curing and thermal monitoring, while reusable NBPS are used for the mechanical tests. Each configuration is evaluated for its intended use.

2. Experimental evidence across material conditions: EMI signatures are examined during curing, before and after compression and splitting-tensile loading, and during heating. The measurements are compared with the relevant mechanical tests and experimental limits.

3. Different measures of EMI response: Resonance characteristics and statistical indices are considered together with model-dependent EPS. No single parameter is treated as a universal direct measure of structural damage.

4. Assessment and compensation of temperature effects: The thermal study evaluates conductance and susceptance changes and an enhanced EFS procedure for the available intact and saw-cut records.

5. Study-specific data-driven evaluation: Machine-learning and deep-learning models are assessed separately for each experiment, and the reported performance is limited to the adopted training, testing and validation procedures.

The contributions are methodological and experimental rather than evidence of universal field use. Local sensitivity, specimen variability, sensor coupling, environmental effects and the amount of available data remain limitations.

The curing, mechanical and thermal studies are analysed separately because they use different specimens, baselines, loading or temperature conditions and validation measurements. The common EMI method allows their interpretation approaches to be compared, while each conclusion remains linked to the experiment that produced the measurement.

1.9 Organisation of the Thesis

The remainder of the thesis is organised as follows. Chapter 2 reviews EMI-based SHM, piezoelectric sensor configurations, statistical and EPS-based interpretation, temperature effects and compensation, and data-driven modelling, and concludes by identifying the research gaps addressed in this thesis. Chapter 3 presents the materials, sensor configurations, specimen matrices, instrumentation and experimental and analytical procedures used in the curing, mechanical-loading and thermal studies.

Chapter 4 presents the 180-day JPS hydration study and the associated strength, resonance, statistical-index and EPS results. Chapter 5 presents the NBPS measurements obtained before and after compression of the cube specimens and splitting-tensile loading of the cylinder specimens. Chapter 6 examines the effects of temperature and dwell time on the intact and saw-cut JPS records and evaluates E–EFS compensation together with the statistical-index and EPS responses. Chapter 7 evaluates study-specific machine-learning and deep-learning models for strength prediction using the hydration, compression and splitting-tensile datasets. Chapter 8 presents the conclusions for the three research objectives, followed by the principal contributions, limitations, future scope and social, economic and environmental relevance of the work.

CHAPTER 2

LITERATURE REVIEW

2.1 General Background

The published EMI literature combines piezoelectric coupling, sensor installation, concrete behaviour and signal interpretation. In SFRC, the measured signature reflects the coupled PZT–interface–host system rather than a single material property. Consequently, a spectral change must be interpreted with reference to the sensor configuration, baseline, loading or environmental condition, and the scale of the supporting mechanical evidence (Bhalla and Soh, 2004b; Farrar and Worden, 2007; Park et al., 2003).

Two forms of interpretation are prominent in previous studies. Statistical indices quantify differences between signatures, whereas EPS express the response through an assumed equivalent mechanical model. Both depend on the selected frequency range and reference condition. Studies of hydration, mechanical loading and elevated temperature further show that changes caused by material development, damage and temperature cannot be distinguished from the electrical signature without suitable experimental controls. More recent data-driven methods extend the analysis of EMI measurements, but their conclusions remain dependent on the structure and independence of the data used for training and evaluation.

2.2 Historical and Theoretical Foundations of the EMI Technique

Liang et al. (1994) formalised the electromechanical coupling used in EMI through a closed-form one-dimensional model. The electrical admittance of a surface-bonded PZT is expressed in relation to the mechanical impedance of the host through the piezoelectric strain coefficient d_{31}, the complex dielectric permittivity $\bar{\varepsilon}_{33}^{T}$, and the complex Young's modulus $\bar{Y}_{11}^{E}$. Resonance features in the electrical signature can therefore respond to changes in the coupled PZT–interface–host system; they do not measure a single property of the host directly.

Bhalla and Soh (2004a,b) extended the formulation to two-dimensional PZT patches and included additional coupling effects. Park et al. (1999, 2003) examined the technique under structural and environmental changes, while Giurgiutiu and Zagrai (2005) developed related high-frequency piezoelectric sensing methods. These studies established the importance of selecting a frequency band that contains stable, damage-sensitive resonances. The suitable band depends on the transducer, attachment, host and acquisition system and should not be treated as one universal range. Reviews by Sohn et al. (2003), Na and Baek (2018), and Gomasa et al. (2023) document the later development of EMI for structural monitoring.

EMI records a local response generated by active PZT excitation and can be implemented with surface-mounted or protected sensors. Ultrasonic testing, acoustic emission and digital image correlation observe different phenomena and spatial scales, so they serve different diagnostic purposes rather than a single performance hierarchy (Malhotra and Carino, 2004; Ohtsu, 2010; Sutton et al., 2009). For EMI, temperature, coupling condition, sensor ageing and instrument settings can all alter the signature (Lim et al., 2018; Park et al., 1999; Wu and Chang, 2006). These dependencies explain why baseline control and environmental compensation recur throughout the literature. A reported frequency shift or index is therefore meaningful only when the sensor, coupling, host, frequency band and reference measurement are specified. This requirement links the theoretical formulations to the experimental practices adopted in later concrete-monitoring studies. Selected developments are summarised in Table 2.1.

Table 2.1: Selected developments in EMI-based SHM for civil infrastructure

Period	**Development**	**Representative studies**
1990s	Closed-form coupled electromechanical-impedance model and early structural demonstrations.	Liang et al. (1994); Park et al. (1999)
Early 2000s	Extension to two-dimensional PZT patches, civil-structure applications and consolidated EMI reviews.	Bhalla and Soh (2004b); Park et al. (2003); Sohn et al. (2003)
Late 2000s	Embedded PZT devices applied to cement hydration and strength-development monitoring.	Divsholi and Yang (2009); Gu et al. (2006); Talakokula et al. (2018)
2010s	Wider concrete applications, environmental-effect studies and temperature compensation through EFS.	Huynh and Kim (2017); Koo et al. (2009); Narayanan and Subramaniam (2016); Rabelo and others (2017)
Late 2010s	Deep-learning architectures established generally and introduced progressively into signal-based SHM analysis.	Hochreiter and Schmidhuber (1997); LeCun et al. (2015); Schuster and Paliwal (1997)
2020s	Reusable coupling, parameter-based interpretation, heating-time studies and hybrid data-driven models.	Ai et al. (2021a); Aulakh and Bhalla (2022); Singh et al. (2022); Zhang et al. (2024)

2.3 Evolution of Piezoelectric Sensor Configurations

The measured EMI signature depends on how the PZT is coupled to the host. The literature describes three broad installation categories relevant here: surface-bonded devices, protected devices embedded during casting, and non-bonded devices coupled through a reusable carrier. Published SFRC curing studies use the JPS as a protected embedded configuration, while SBPS and NBPS represent the two external arrangements (Aulakh and Bhalla, 2022; Gu et al., 2006; Narayanan and Subramaniam, 2016; Park et al., 2003).

Table 2.2: Comparison of PZT sensor configurations reported for concrete monitoring

Attribute	SBPS	JPS	NBPS	Refs
Deployment stage	Applied to a hardened surface prepared for bonding	Embedded during casting	Coupled to a hardened surface	Aulakh and Bhalla (2022); Gu et al. (2006); Park et al. (2003)
Retrieval after testing	Accessible, but the bonded patch is not normally reused	Retained within the concrete	Retrievable when the carrier and PZT remain intact	Aulakh and Bhalla (2022); Parpe and Jothi Saravanan (2024)
Coupling route	Adhesive bond to the host surface	Protective jacket interacting with the surrounding concrete	Mechanical contact through a metallic carrier	Aulakh and Bhalla (2022); Narayanan and Subramaniam (2016); Wu and Chang (2006)
Main measurement consideration	Bond quality and surface preparation	Protective enclosure and embedment position	Contact position, pressure and surface condition	Aulakh and Bhalla (2025); Lim et al. (2018)
Early-age access	Not available before a suitable surface hardens	Available from early age after casting	Not available before a suitable contact surface exists	Bhalla and Gupta (2022); Gu et al. (2006); Narayanan and Subramaniam (2016)
Use after destructive testing	Replacement may be required after destructive testing or debonding	Embedded hardware remains with the specimen	Controlled reuse can reduce sensor consumption	Aulakh and Bhalla (2022); Gupta et al. (2024); Parpe and Jothi Saravanan (2024)

2.3.1 SBPS Configuration

SBPS are widely used because the PZT can be attached directly to an accessible hardened surface and inspected or replaced when necessary. A thin adhesive layer transfers the actuation and response between the transducer and the host; consequently, adhesive properties, bond thickness and debonding affect repeatability (Lim et al., 2018; Park et al., 2003; Wu and Chang, 2006). Surface bonding also requires a hardened

surface prepared for bonding and is therefore not available during the earliest stage after concrete casting (Divsholi and Yang, 2009; Gu et al., 2006; Narayanan and Subramaniam, 2016). Published applications on metallic and concrete elements establish the usefulness of SBPS under controlled coupling, but they also show that installation and environmental changes must be separated from changes in the host (Bhalla and Soh, 2004b; Giurgiutiu and Zagrai, 2005).

2.3.2 Embedded PZT and the JPS Configuration

The need for measurements from the time of casting led to protected embedded PZT devices (Divsholi and Yang, 2009; Gu et al., 2006; Narayanan and Subramaniam, 2016). The piezoceramic element is encapsulated within mortar, epoxy or a composite enclosure to isolate it from fresh concrete while maintaining mechanical interaction with the host. Representative developments include the smart aggregate of Gu et al. (2006), the smart probe reported by Divsholi and Yang (2009), and later embeddable composite sensors (Bhalla and Gupta, 2022). These devices permit early-age measurements, but the protective enclosure becomes part of the coupled system and the embedded unit is not normally retrieved after casting.

Within this category, SFRC studies using an epoxy-jacketed PZT reported measurements from 1 to 180 days. This interval is the duration of those experiments and is not a general service-life rating for jacketed sensors. Other protected concepts based on polyvinylidene fluoride, macro-fibre composites and printed piezoelectric elements broaden the available design space, but their materials and coupling mechanisms are not interchangeable (Naderi and Zhang, 2022; Zou et al., 2024).

2.3.3 NBPS Configuration

NBPS arrangements place the PZT on a metallic carrier that is brought into mechanical contact with the host rather than bonded permanently to it. Reported carriers include aluminium foil, steel plates and partially embedded or clamped elements (Aulakh and Bhalla, 2022; Divsholi and Yang, 2009; Gupta et al., 2024). The sensor can be recovered after measurement and reused on another specimen, which can reduce the number of PZT units required in laboratory programmes. This benefit is accompanied by a measurement requirement: position, contact pressure, surface condition and the carrier itself affect the measured signature and must be controlled when baselines are compared (Aulakh and Bhalla, 2022, 2025; Parpe and Jothi Saravanan, 2024).

Taken together, the configuration literature shows that protection, access, coupling

repeatability and reuse must be balanced for the intended monitoring stage. The sensor geometries are already introduced in Figure 1.1; their literature-based measurement characteristics are compared here in Table 2.2.

2.4 Statistical Damage Indices for the EMI Signature

After an admittance signature $Y(\omega) = G(\omega) + jB(\omega)$ is acquired, its difference from a reference can be summarised through statistical indices. Root Mean Square Deviation (RMSD) is widely used to express the normalised point-by-point separation between a reference and a later signature (Giurgiutiu and Zagrai, 2005; Park et al., 2003). Mean Absolute Percentage Deviation (MAPD) and Absolute Mean Percentage Deviation (AMPD) provide related amplitude-based summaries, while the Correlation Coefficient (CC) and correlation-deviation forms describe similarity of spectral shape (Naoum et al., 2023, 2024).

Other published measures include Mean Squared Error (MSE), Root Mean Square (RMS), variance, skewness, peak-to-peak amplitude, covariance and coefficient-of-variation measures. These quantities emphasise different features of a spectrum and are affected differently by amplitude scaling, frequency shift and local peak changes (Parida et al., 2022; Parida and Moharana, 2024). A larger index value is therefore not automatically evidence of a more severe or more spatially extensive damage state; its meaning depends on the definition, baseline and selected frequency band.

Statistical indices reduce a high-dimensional signature to a small number of comparison values. However, they are not physically unique: the same statistical change can arise from damage, temperature, coupling or another change in the measured system (Aulakh and Bhalla, 2022; Singh et al., 2022; Talakokula et al., 2018). Studies of concrete and embedded-sensor platforms consequently report different index rankings under different conditions rather than one universally dominant metric (Bansal and Talakokula, 2024; Naoum et al., 2024; Sun et al., 2023). Model-based quantities provide a second level of analysis by representing the PZT–host interaction through equivalent mechanical parameters.

2.5 Equivalent Structural Parameters and Lumped-Parameter Representations

A model-based representation describes the PZT–host interaction with a lumped-parameter mechanical system. The measured response is expressed in terms of equivalent mass, stiffness, and damping, collectively denoted EPS. Different formulations appear in the literature, so their structure and assumptions must be stated explicitly

before the extracted quantities are compared.

In the lumped-parameter representation the mechanical impedance of the host is modelled by three scalars, namely an equivalent mass M, an equivalent stiffness K, and an equivalent damping C. The three parameters are related to the electrical admittance of the PZT through the closed-form coupling derived by Liang et al. (1994) and refined for two-dimensional patches by Bhalla and Soh (2004a,b). Under the assumption that the PZT is operated in its first in-plane resonance mode the admittance reads

$$Y(\omega) = j\,\omega\,\overline{C}_{\mathrm{PZT}} + \frac{d_{31}^2\,\omega^2\,\bar{Y}_{11}^E}{K - \omega^2 M + j\,\omega\,C} \tag{2.1}$$

where $\overline{C}_{\mathrm{PZT}}$ is the constant-strain (blocked) capacitance of the transducer, and d_{31} and $\bar{Y}_{11}^E$ are respectively the strain coefficient and complex in-plane Young's modulus of the PZT. The stiffness-loss index Δs is defined as the fractional reduction of K relative to its healthy baseline value, and in the literature has been shown to correlate directly with compressive strength loss (Bansal and Talakokula, 2021, 2024; Singh et al., 2022, 2023; Talakokula et al., 2018). The corresponding mass-change index Δm and damping-change index Δc describe changes in the corresponding equivalent quantities but do not, by themselves, identify a unique physical cause. Talakokula et al. (2018) demonstrated a linear correlation $R^2 > 0.9$ between K and the compressive strength gain of plain concrete during the first 28 days of hydration. Later studies (Bansal and Talakokula, 2021, 2024; Singh et al., 2022, 2023) have extended the EPS framework to progressive damage in beams, plates, and shear walls.

EPS complement statistical indices by expressing spectral change through a mechanical triad (M, K, C). The resulting values remain model-dependent: changes in an equivalent quantity cannot be assigned to a single damage mechanism without additional evidence. Temperature-dependent PZT and host properties also affect the extracted parameters and must be considered when thermal and damage effects occur together.

2.6 Steel Fibre Reinforced Concrete: Mechanics and Durability

SFRC contains short steel fibres distributed through a cementitious matrix. After cracking, fibres that intersect a crack can transfer tensile stress, limit crack opening and contribute to toughness and post-peak energy absorption (Banthia and Gupta, 2004; Bentur and Mindess, 2007; Naaman, 2006). Hooked-end and crimped fibres develop this action through a combination of interfacial bond, friction and mechanical anchorage.

Aspect ratio l/d, where l is the fibre length and d is its diameter, is an important descriptor, but it does not determine performance independently of fibre shape, dosage, orientation, matrix strength and workability (di Prisco et al., 2013, 2021; Lantsoght, 2019).

Published mechanical studies show that fibre addition affects compressive, tensile and flexural responses differently. Increasing dosage may improve post-cracking resistance while also reducing workability or increasing the likelihood of non-uniform dispersion. Consequently, the dosage associated with a favourable response is specific to the material, geometry and target property; the literature does not establish one universal optimum (Chen et al., 2024; Guo et al., 2024; Jia et al., 2024). Dispersion, orientation and fibre–matrix bond also contribute to specimen-to-specimen scatter, particularly when a local measurement is compared with a bulk mechanical test (Di Prisco et al., 2009; Gribniak et al., 2019).

This heterogeneity is directly relevant to SHM. A local EMI response is influenced by the material and cracking within the sensing region, whereas a global test or whole-specimen strength represents a different spatial scale. Agreement between them must therefore be demonstrated experimentally rather than assumed from fibre dosage or aspect ratio (Ai and Cheng, 2023; Farrar and Worden, 2007; Sohn et al., 2003). The same requirement applies when corrosion, alkali–silica reaction, freeze–thaw exposure or elevated temperature changes the matrix, fibres, interface or sensor coupling (Ai et al., 2021a; Antolik and Jo, 2023; Zhang et al., 2022).

Collectively, the SFRC literature establishes the mechanical importance of fibre bridging but also shows that local variability and environmental dependence cannot be reduced to one material parameter. Standards govern material testing and structural design, but they do not provide an EMI interpretation rule (IS 8112, 2013; IS 383, 2016; IS 10262, 2019). This distinction motivates the following review of EMI observations during hydration and mechanical loading.

2.7 Hydration and Early-Age Monitoring with EMI

Early-age monitoring is difficult because hydration changes temperature, pore structure and mechanical properties while the concrete is developing. An embedded PZT can record the coupled response during this period because it is installed before a hardened external surface is available (Bhalla and Gupta, 2022; Gu et al., 2006; Narayanan and Subramaniam, 2016). Gu et al. (2006) and Divsholi and Yang (2009) reported systematic evolution of embedded-sensor signatures during setting and hardening. Later studies extended the monitoring interval and examined relationships among

resonance features, equivalent stiffness and companion strength measurements (Lim et al., 2021; Narayanan and Subramaniam, 2016; Talakokula et al., 2018).

The reported observations are not identical across sensors and materials. Resonance features may shift in frequency, amplitude and shape as hydration proceeds, and a later reduction in the rate of change is not a universal fixed-age plateau. Studies of SFRC, self-compacting concrete and other cementitious systems show that housing, local material composition and baseline selection affect the measured trajectory (Gayakwad and Thiyagarajan, 2022; Mishra and Lourencc, 2022). Published regressions between EMI features and compressive strength are therefore calibrations for the tested specimens rather than transferable material laws.

The hydration literature establishes that protected embedded PZT devices can follow changes in the local coupled response from early age. Because the reported studies use different protective enclosures, mixtures, specimens and baselines, their calibrations cannot be transferred directly between systems. Mechanical-damage studies provide a separate evidence base in which a defined loading event produces the condition change.

2.8 Mechanical Damage Assessment using EMI

Published EMI studies have considered cracking, stiffness reduction, debonding and load-induced change in concrete (Park et al., 2003; Singh et al., 2022; Zhang et al., 2022). For SFRC, compressive loading and split-tensile loading involve different crack patterns and fibre-bridging mechanisms, so their signatures should not be assumed to evolve in the same manner.

2.8.1 Compressive Damage

Uniaxial compression produces distributed microcracking followed by localisation and macrocracking. EMI studies report changes in resonance frequency, amplitude and statistical indices as this process develops, but the direction and magnitude of those changes depend on sensor location, coupling, frequency band and loading sequence (Bansal and Talakokula, 2021, 2024; Bhalla and Soh, 2004b). Equivalent stiffness and damping can provide a model-based description of signature change, while statistical indices describe spectral separation; neither identifies a unique crack state without mechanical evidence (Singh et al., 2022; Talakokula et al., 2018).

For SFRC, fibre bridging alters crack opening and post-peak behaviour and may also change the local EMI response near a crack (Banthia and Gupta, 2004; di Prisco et

al., 2013; Gao et al., 2023). The literature is more developed for plain concrete than for systematic SFRC comparisons across fibre geometry and dosage. Replicated studies with controlled reusable coupling remain limited.

2.8.2 Split-Tensile Damage and Frequency Hardening

The split-tensile test promotes a dominant crack plane rather than the more distributed damage associated with compression. Mechanical studies show that steel fibres bridge the opening crack and modify the tensile post-cracking response (Chen et al., 2024; Guo et al., 2024; Jia et al., 2024). EMI evidence for this loading mode is comparatively limited, particularly when a reusable external sensor is removed before destructive loading and returned afterwards. Published data do not establish a universal direction of resonance shift or a transferable statistical threshold for split-tensile damage in SFRC. The available evidence is also insufficient to isolate the respective effects of crack opening, fibre bridging and local sensor coupling on the measured spectrum.

2.9 Thermal Effects and Compensation Methodologies

Temperature affects the entire coupled EMI measurement. Changes in the dielectric permittivity, piezoelectric coefficient and elastic properties of the PZT alter its electrical and mechanical response. Temperature also changes the host material and the adhesive, jacket or mechanical interface (Huynh and Kim, 2017; Park et al., 1999; Rabelo and others, 2017). The result is an environmental change in the admittance signature even when the structural condition is unchanged.

Two effects are commonly distinguished. A horizontal drift shifts resonance features along the frequency axis as the effective dynamic properties of the coupled system change. A vertical drift changes conductance or susceptance amplitude through temperature-dependent electrical properties and coupling. Heating duration and the preceding temperature path can add further differences between measurements taken at the same nominal temperature (Ai et al., 2021a, 2022b). Because statistical damage indices respond to these spectral differences, an uncompensated comparison can confuse an environmental change with damage. Thermal compensation is therefore required before residual signature differences are interpreted.

2.9.1 Classical EFS Compensation

Koo et al. (2009) proposed the EFS method, and later studies adapted it to concrete

and related EMI applications (Huynh and Kim, 2017; Rabelo and others, 2017). In the classical procedure, a temperature-affected conductance signature is shifted along the frequency axis and compared with a reference. The selected shift maximises their correlation or minimises a defined difference. The residual difference is then evaluated for possible condition change.

This procedure addresses horizontal shift but depends on the reference, frequency increment and similarity criterion. Its limitations become important when the signature changes in more than one way (Ai et al., 2021a, 2022a). Three recurring cases are identified in the literature.

(i) Vertical amplitude distortion: Temperature-dependent electrical properties can change the conductance and susceptance levels as well as their resonance positions (Huynh and Kim, 2017; Park et al., 1999; Rabelo and others, 2017). A horizontal-only shift leaves this amplitude difference in the compensated signature, where it can contribute to the resulting damage index.

(ii) Heating-time dependence: Ai et al. (2021a) reported that EMI signatures depend on heating duration and the preceding temperature path as well as the nominal temperature. A reference indexed only by temperature may therefore be insufficient when holding times or temperature paths differ.

(iii) Sub-bin frequency resolution: A resonance may move by less than the acquisition frequency increment. Integer-bin alignment cannot represent that shift exactly, so frequency-resolution error remains in the comparison (Ai et al., 2021a; Huynh and Kim, 2017).

2.9.2 Advanced Compensation Strategies

Later strategies supplement horizontal alignment with amplitude correction, interpolation or a temperature-dependent model of the sensing system (Ai et al., 2022a,b; Parpe and Jothi Saravanan, 2024). Interpolation can represent shifts smaller than one acquired frequency increment, while amplitude normalisation addresses part of the vertical drift. Parameter-based methods instead incorporate temperature-dependent PZT or concrete-host properties (Bhalla and Soh, 2004a; Park et al., 1999). Data-driven compensators have also been proposed, but they require training data that represent the sensor, concrete host and temperature range of interest (Ai and Cheng, 2023; Hocaoug, 2024; Zhang et al., 2024).

The literature therefore establishes that frequency alignment alone may be insufficient when amplitude and heating duration also change. It does not establish one compensation procedure that transfers unchanged across sensor types, concrete materi-

als and temperature ranges. The main strategies and their limitations are compared in Table 2.3.

Table 2.3: Comparison of the main thermal-compensation methods reported for EMI

Methodology	Correction Mechanism	Operational Limitation	Refs
Baseline look-up	Comparison with stored temperature-tagged reference signatures	Requires representative prior measurements for the monitored system	Park et al. (1999); Rabelo and others (2017)
Classical EFS	Horizontal alignment of the conductance signature	Does not by itself correct amplitude drift, heating-duration effects or sub-bin shifts	Ai et al. (2021a); Huynh and Kim (2017); Koo et al. (2009)
Parameter-based method	Represents temperature-dependent PZT, concrete-host or equivalent mechanical properties	Requires appropriate and traceable temperature-dependent material data	Bhalla and Soh (2004a); Park et al. (1999); Singh et al. (2022)
Data-driven compensator	Models temperature-associated variation from labelled data	Transfer depends on the training sensor, concrete host and temperature range	Ai and Cheng (2023); Hocaoug (2024); Zhang et al. (2024)
Multi-stage EFS variant	Combines frequency alignment with amplitude correction and, where used, interpolation	Requires a stable reference and a defined procedure validated over the target range	Ai et al. (2022a); Alazzawi and Wang (2024); Parpe and Jothi Saravanan (2024)

2.10 Machine Learning and Deep Learning for EMI-SHM

Data-driven analysis complements statistical and model-based interpretation when EMI datasets contain many correlated frequency samples. Published methods either use engineered features, such as resonance values or statistical indices, or extract features from structured conductance and susceptance inputs (Ai and Cheng, 2023; Parida et al., 2022; Rasmussen and Williams, 2006). Their reported performance depends on how specimens, repeated measurements and target labels are divided between training and evaluation. The main model categories are reviewed below.

2.10.1 Classical Regressors

GPR is suitable for nonlinear regression with datasets of modest size and can provide a predictive distribution when its uncertainty is retained and assessed (Parida et al., 2022; Rasmussen and Williams, 2006; Zhu et al., 2023). Support Vector Machines and tree-based ensembles provide alternative regression or classification models for compact feature vectors (Abambres and Lantsoght, 2019; Nematzadeh et al., 2021; Pan and Yang, 2009). These methods normally operate on selected EMI features rather than

the complete raw signature. Their comparison therefore depends on both the model and the feature-construction process.

2.10.2 CNN Architectures

CNNs determine local filters during training rather than relying exclusively on hand-selected features (Ai and Cheng, 2023; LeCun et al., 2015). One-dimensional representations can preserve frequency order, while two-dimensional arrangements can combine channels or reshape measurements for convolution (Parida et al., 2022; Zhang et al., 2024). The physical meaning of each input axis must be stated; reshaping a vector into an image does not make the resulting relation intrinsically spatial.

2.10.3 LSTM and Bi-LSTM Architectures

LSTM and Bi-LSTM networks represent dependencies along an ordered input axis (Hochreiter and Schmidhuber, 1997; Schuster and Paliwal, 1997). A temporal interpretation is justified only when that axis contains chronological observations with preserved sequence identity. If the sequence consists of frequency bins, recurrence represents spectral ordering rather than time (Parida et al., 2022; Zhang et al., 2024).

2.10.4 Hybrid CNN-LSTM and CNN-Bi-LSTM Architectures

Hybrid CNN–LSTM and CNN–Bi-LSTM architectures combine convolutional feature extraction with recurrent processing along the chosen sequence axis (Parida et al., 2022; Zhang et al., 2024, 2025). This combination can represent local and ordered dependencies, but it does not by itself prove that the ordering is temporal or that the learned relation transfers between specimens. Reported accuracy remains dependent on dataset size, partitioning, specimen independence and target definition (Cui et al., 2024; Yan et al., 2022). In practical terms, the convolutional layers extract local spectral features from the admittance signature while the recurrent layers capture their sequential arrangement across frequency bins. Whether this sequential processing improves prediction over a standalone CNN depends on how the input is structured and whether the ordering carries physical information relevant to the target property. The main model categories and their literature roles are compared in Table 2.4.

Table 2.4: Summary of machine learning and deep learning architectures applied to EMI-based SHM datasets

Architecture	Analytical role	Reported use with EMI data	Refs
GPR	Nonlinear probabilistic regression for modest datasets	Regression from selected EMI features; uncertainty available when retained and calibrated	Parida et al. (2022); Rasmussen and Williams (2006); Zhu et al. (2023)
Support Vector Machine / tree ensemble	Regression or classification from compact feature vectors	Condition classification and mechanical-response estimation from engineered EMI features	Abambres and Lantsoght (2019); Nematzadeh et al. (2021); Pan and Yang (2009)
One- or two-dimensional CNN	Filters fitted on structured input arrays	Signature-based classification or regression using defined frequency and channel axes	Ai and Cheng (2023); Parida et al. (2022); Zhang et al. (2024)
LSTM / Bi-LSTM	Dependency modelling along an ordered input axis	Chronological modelling when sequence identity is preserved; spectral-order modelling otherwise	Hochreiter and Schmidhuber (1997); Parida et al. (2022); Schuster and Paliwal (1997)
CNN–LSTM / CNN–Bi-LSTM	Convolutional feature extraction followed by ordered processing	Sequence-axis regression or classification, subject to the physical meaning of the ordering	Parida et al. (2022); Zhang et al. (2024, 2025)

2.11 Synthesis and Research Gaps

The literature establishes EMI as a sensitive laboratory method for detecting local changes in the electromechanical response of concrete. Surface-bonded, jacketed embedded, and non-bonded sensors differ in coupling, protection, access, and reuse. Statistical indices provide compact measures of spectral change, while EPS adds a model-based mechanical interpretation; neither class identifies a unique damage cause without supporting evidence. Temperature changes both frequency and amplitude and may also introduce heating-duration effects, so compensation must be evaluated for the relevant sensor, concrete host, and temperature range. Data-driven models expand the available interpretation tools, but their reported performance depends strongly on specimen independence and data partitioning. Against this background, six literature gaps motivate the research objectives.

1. Research Gap 1: EMI evidence for SFRC remains limited compared with plain concrete, particularly for reusable coupling under progressive mechanical loading and across combined changes in fibre geometry and dosage (Aulakh and Bhalla, 2022; Banthia and Gupta, 2004; Lantsoght, 2019; Naderi and Zhang, 2022).

2. Research Gap 2: Statistical indices detect spectral change but provide lim-

ited physical interpretation, whereas lumped-parameter indices remain model-dependent. Their relationship to compressive and split-tensile damage in SFRC, and their ability to support localisation rather than specimen-level detection, require clearer evidence (Chen et al., 2024; Guo et al., 2024; Singh et al., 2022; Talakokula et al., 2018).

3. Research Gap 3: Classical EFS primarily addresses horizontal frequency shift. Compensation that also accounts for amplitude distortion, heating duration, and sub-bin shifts has not been demonstrated as transferable across PZT configurations, concrete mixes, and elevated-temperature ranges (Ai et al., 2021a; Huynh and Kim, 2017; Koo et al., 2009; Rabelo and others, 2017).

4. Research Gap 4: The combined influence of temperature, holding time, and controlled mechanical damage on both statistical indices and EPS remains insufficiently separated in the published literature, particularly for SFRC and embedded sensors (Ai et al., 2021a; Jena et al., 2025).

5. Research Gap 5: Data-driven EMI studies commonly treat hydration, compressive damage, and tensile damage as separate tasks. The extent to which modelling choices can be compared across these tasks without conflating different sensors, specimens, and sampling structures remains uncertain (Jena et al., 2025; LeCun et al., 2015; Parida et al., 2022; Zhang et al., 2024).

6. Research Gap 6: Comparisons between classical probabilistic regressors and deep temporal networks often use small or highly correlated datasets. Transparent specimen-level partitioning, uncertainty reporting, and testing on independent specimens remain necessary for credible performance assessment (Parida et al., 2022; Rasmussen and Williams, 2006; Zhang et al., 2024, 2025).

2.12 Research Gap to Objective Mapping

The six gaps form three connected groups. The first pair concerns the interpretation of EMI measurements during mechanical loading, the second pair concerns temperature and heating duration, and the third pair concerns the reliability of data-driven prediction. Table 2.5 links each group to the objective that addresses it and to the chapters containing the corresponding methods and results.

This mapping maintains a direct connection between the reviewed evidence and the investigations undertaken in the thesis. Gaps 1 and 2 are examined through the mechanical programmes, Gaps 3 and 4 through the thermal programme, and Gaps 5

Table 2.5: Traceability between research gaps, thesis objectives and evidence chapters

Research Gap	**Thesis Objective**	**Chapter**
Research Gap 1: Characterisation of SFRC NBPS response under load	Investigate damage detection and localisation using PZT sensors (Objective 1)	Chapters 3 and 5
Research Gap 2: Mechanics-based stiffness-loss index (Δs)	Investigate damage detection and localisation using PZT sensors (Objective 1)	Chapters 3 and 5
Research Gap 3: High-temperature Enhanced EFS compensation	Investigate heating-time effect using PZT sensors (Objective 2)	Chapters 3 and 6
Research Gap 4: Heating-time hysteresis quantification	Investigate heating-time effect using PZT sensors (Objective 2)	Chapters 3 and 6
Research Gap 5: Study-specific prediction across three experimental domains	Computational modelling of damage progression (Objective 3)	Chapters 3 and 7
Research Gap 6: Classical and deep model benchmarks with validation limits	Computational modelling of damage progression (Objective 3)	Chapters 3 and 7

and 6 through the modelling analyses. The common methodology defines the specimens, measurements and analysis procedures used to address all three groups. This structured approach ensures that every experimental finding directly contributes to resolving the identified limitations. The specific material selections and measurement protocols required to execute this framework are detailed in the subsequent methodology chapter.

CHAPTER 3

EXPERIMENTAL METHODOLOGY

3.1 General

This chapter presents the experimental methodology shared by four connected studies: hydration and curing-age monitoring, compressive damage detection, split-tensile damage detection, and thermal-loading assessment. The constituent materials, mix designs, specimen preparation, sensor arrangements, instrumentation, loading procedures, and analytical formulations are described once so that the experimental programme can be followed without repeating the same methods in each results chapter.

The hydration study followed four JPS-instrumented cubes from casting to 180 days, and the same specimens were subsequently used in the thermal study. The compressive and split-tensile studies used the complete thirteen-configuration matrix with an NBPS on separate cube and cylinder specimens. All four studies used the Keysight E4980A LCR meter, while the measurement schedule and loading procedure were selected for the purpose of each study. The sections that follow present the materials and specimen allocation first, followed by sensor preparation, the four experimental procedures, the common instrumentation, and the analytical methods.

3.2 Material Properties

The four studies used the same aggregate sources, laboratory water, superplasticizer, hooked-end steel-fibre families, and PZT patch type. The specimens were cast in separate laboratory campaigns, however, and the hydration–thermal and mechanical programmes used two M30 mix designs with different OPC grades. The allocation of the two mixes to the four studies is specified below so that the experimental basis of each result is clear.

3.2.1 Ordinary Portland Cement

The experimental programme was executed in two independent phases. Mix A used OPC 53 conforming to IS 12269:2013 (IS 12269, 2013) for the hydration study and the subsequent thermal study on the same specimens. Mix B used OPC 43 conforming to IS 8112:2013 (IS 8112, 2013) for the compressive and split-tensile studies. Both cement grades were supplied by UltraTech Cement Ltd., India, and both mixtures were proportioned for M30 concrete with a water-to-binder ratio of 0.44.

The selection of the cement grades was based on the physical requirements of the specific tests. Mix A utilised OPC 53 because its finer grinding and higher early-age hydration rate yield a clear physical development for time-dependent monitoring. Its denser microstructure also provides a rigorous condition for evaluating thermal degradation. Mix B utilised OPC 43 for the mechanical studies. OPC 43 provides a gradual strength development and represents a standard baseline matrix. This allows the mechanical tests to evaluate the fibre-matrix interfacial bond, toughness, and post-cracking behaviour characteristic of the hooked-end steel fibres without the heightened early brittleness seen in higher-grade cements. The properties of both cement grades are those reported by the manufacturer.

The piezoelectric patches used in both sensor types are described in Section 3.4; their material properties were not measured in the present programme.

3.3 Mix Design and Specimen Preparation

3.3.1 M30-Grade Mix Design

Two M30 mix designs were prepared in accordance with IS 10262:2019 (IS 10262, 2019), with a target mean strength of 38.25 MPa and a water-to-binder ratio of 0.44. Mix A, containing OPC 53 with a proportion of 1:1.66:3.69 and 167 L/m^3 of water, was used for the hydration and thermal studies. Mix B, containing OPC 43 with a proportion of 1:1.63:3.63 and 170 L/m^3 of water, was used for the compressive and split-tensile studies. These mixes belong to the two campaign groups described in Section 3.2.1; they were not introduced as levels of a cement-grade comparison. Fibre dosage ranged from 0% to 1.50% in 0.25% increments. Table 3.1 gives the constituent quantities per cubic metre for the two mixes.

The same fibre-addition sequence was used for both mixtures. Cement, sand, and aggregates were dry mixed for 90 s before the fibres were introduced; water and superplasticizer were then added, followed by 120 s of mixing and 30 s of vibration after

Table 3.1: M30-grade concrete constituent quantities per cubic metre

Constituent	**Mix A (OPC 53)**	**Mix B (OPC 43)**
Ordinary Portland Cement (kg)	380	386
Fine aggregate (M-sand, Zone II) (kg)	631	631
Coarse aggregate (20–12.5 mm) (kg)	840	840
Coarse aggregate (12.5–10 mm) (kg)	560	560
Water (L)	167	170
Superplasticizer (SikaPlast-5061 NS2) (kg)	3.80	3.86
Water-to-binder ratio	0.44	0.44
Mix proportion (c:fa:ca)	1:1.66:3.69	1:1.63:3.63
Steel fibres @ 0.25% (kg)	19.6	19.6
Steel fibres @ 0.50% (kg)	39.3	39.3
Steel fibres @ 0.75% (kg)	58.9	58.9
Steel fibres @ 1.00% (kg)	78.5	78.5
Steel fibres @ 1.25% (kg)	98.2	98.2
Steel fibres @ 1.50% (kg)	117.8	117.8

casting. The fibres were introduced without an imposed alignment direction. Specimens were demoulded after 24 h and placed in water curing. The mechanical-test specimens were cured for 28 days, whereas the JPS specimens were measured at scheduled ages throughout the 1–180-day hydration programme.

3.3.2 Cube Specimen Programme

The cube programme comprised three applications. Four JPS-instrumented 150 mm cubes were used for hydration monitoring and were retained for the subsequent thermal sequence. A separate set of 39 cubes was used for the compressive study: one plain-concrete control and six fibre dosages for each of AR 55 and AR 65, with three physical specimens per configuration. The study-specific allocation and measurements are given in Sections 3.5, 3.6, and 3.8.

3.3.3 Cylindrical Specimen Programme

The split-tensile study used 150 mm-diameter, 300 mm-high cylinders. Its thirteen configurations followed the mechanical-study matrix defined for the cubes: one plain-concrete control and six dosages for each fibre aspect ratio. Three physical specimens per configuration produced 39 cylinders.

3.3.4 Initial Fibre-Dosage Selection

Before long-term hydration monitoring, the six fibre dosages from 0.25% to 1.50% were screened at 28 days for both aspect ratios using three cubes per configuration. The screening results were used to select the 0.50% and 0.75% dosages for extended monitoring; retaining both aspect ratios at each dosage produced the four JPS configurations listed in Section 3.5.1. The control and all six dosages for both aspect ratios remained in the separate NBPS compressive and split-tensile matrices. The screening is used here only to explain specimen selection; the strength results are interpreted with the mechanical-study results.

3.4 Sensor Development

Two PZT sensor arrangements were matched to the experimental requirements. The JPS remained embedded in the same four cubes during hydration and thermal loading, whereas the removable NBPS was used on hardened cubes and cylinders before and after mechanical loading.

3.4.1 Jacketed Piezo Sensor

The Jacketed Piezo Sensor was used for the hydration study and was retained in the same four specimens for the subsequent thermal study. A 10 mm $\times$ 10 mm $\times$ 0.2 mm PZT patch was housed within a cylindrical epoxy shell of 25 mm diameter and 20 mm height, and waterproofing with a resin-and-hardener blend was applied to limit moisture ingress and electrical leakage. The epoxy coating was allowed to cure for 24 h prior to embedment, and the JPS was inserted into the cube mould only after the adhesive had cured. This encapsulation follows the general embeddable-sensor concept described by Bhalla et al. Bhalla and Gupta (2022). Figure 3.1 shows the manufacturing sequence.

3.4.2 Non-Bonded Piezo Sensor

The NBPS was used to obtain removable measurements on hardened specimens without bonding a PZT patch directly to each specimen. A centrally positioned 10 mm $\times$ 10 mm $\times$ 0.2 mm PZT patch was bonded with high-strength epoxy onto a 100 mm $\times$ 10 mm $\times$ 1 mm aluminium carrier strip, as illustrated in Figure 3.2. The aluminium strip protected one face of the piezoceramic element and provided the removable contact surface. The electrical leads were soldered to the PZT faces and

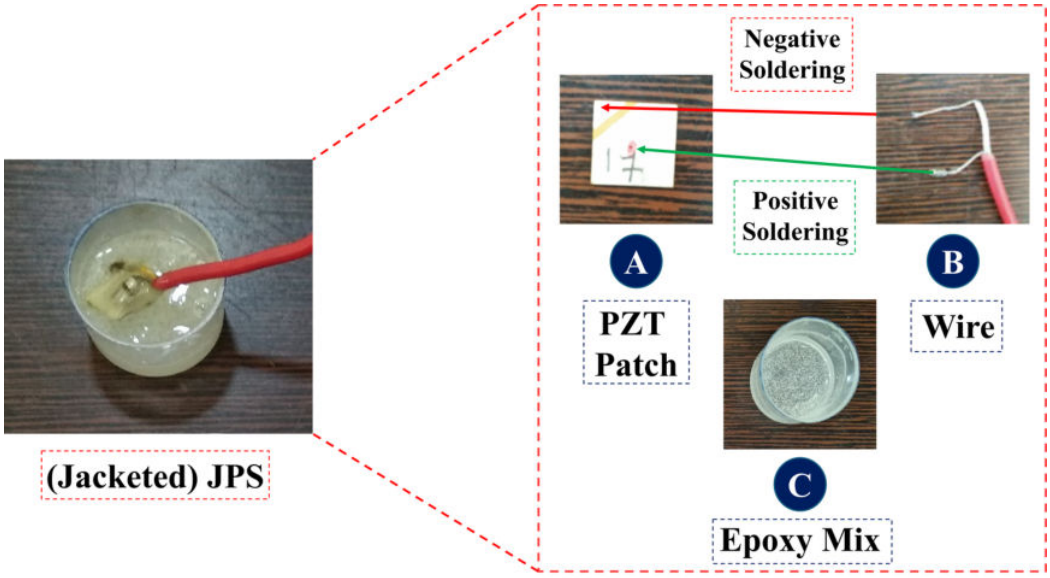

Figure 3.1: Fabrication sequence and principal components of the JPS

encapsulated with a thin protective coating for electrical insulation under laboratory conditions.

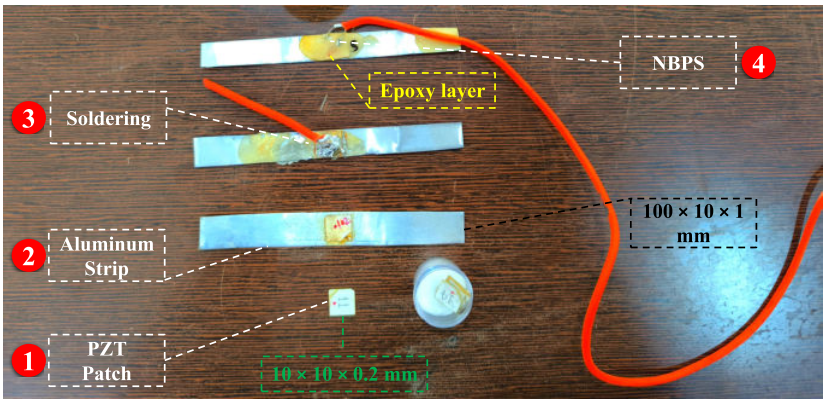

Figure 3.2: Fabrication sequence and structural components of the reusable NBPS

The NBPS was deployed in the compressive campaign on cubes and the split-tensile campaign on cylinders. Mechanical contact was maintained with polytetrafluoroethylene (PTFE) tape shims placed symmetrically at both ends of the aluminium strip, outside the active PZT region. For each specimen, the baseline and post-damage signatures were recorded using the same marked position, shims, and holding procedure. This consistent arrangement reduced changes associated with sensor repositioning without assuming that contact effects were eliminated.

3.5 Study 1: Hydration and Curing-Age Monitoring Setup

3.5.1 Specimen Matrix

The hydration and curing-age monitoring study employed four 150 mm cubes, each containing one embedded JPS. The four configurations were mapped as follows:

- SFC1 (JPS1): AR 65 at 0.50% dosage
- SFC2 (JPS2): AR 55 at 0.50% dosage
- SFC3 (JPS3): AR 65 at 0.75% dosage
- SFC4 (JPS4): AR 55 at 0.75% dosage

Each JPS was placed inside the cube mould before casting, and its coaxial lead was routed through the mould wall for connection to the LCR meter.

3.5.2 Hydration EMI Measurement Procedure

After casting and demoulding, the JPS-instrumented cubes were maintained in the curing tank at 25 ± 1 °C. Conductance (G) and susceptance (B) signatures were recorded at ten curing ages: 1, 3, 7, 14, 28, 60, 90, 120, 150, and 180 days. Figure 3.3 shows the data-acquisition arrangement used throughout the 180-day curing window, with the four cubes continuously connected to the common instrumentation described in Section 3.9.

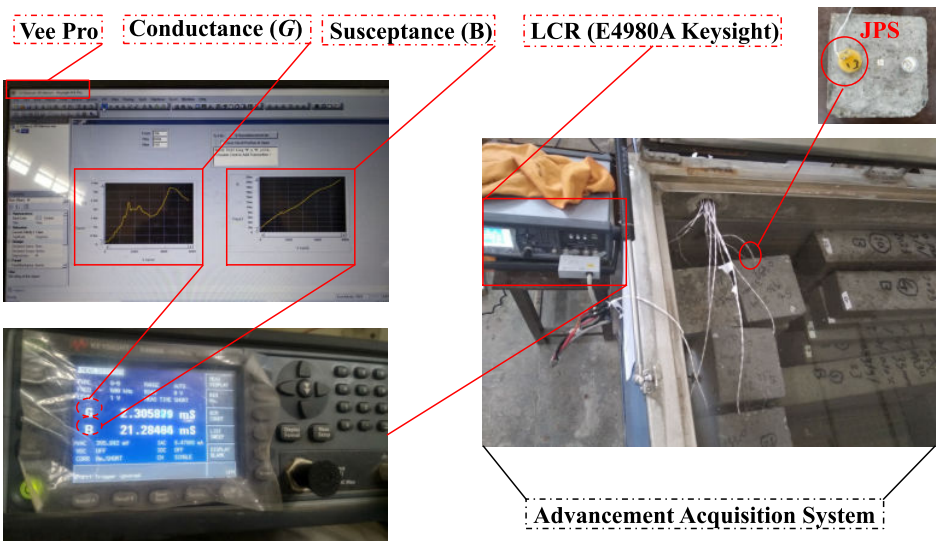

Figure 3.3: Data-acquisition arrangement for the 180-day curing-age monitoring study.

3.6 Study 2: Compressive Damage Detection Setup

3.6.1 Thirteen-Configuration Experimental Matrix

The compressive damage detection study employed a thirteen-configuration matrix of 150 mm SFRC cubes measured with the NBPS. The matrix comprises one control mix (0% fibre dosage) plus six fibre dosages (0.25%, 0.50%, 0.75%, 1.00%, 1.25%, 1.50%) for each of the two aspect ratios (AR 55 and AR 65), yielding thirteen distinct configurations. The 0% control was counted once because fibre aspect ratio is not applicable to plain concrete. Three replicate cubes per configuration produced a total of 39 cubes.

3.6.2 Compressive Loading and EMI Acquisition Procedure

After 28-day water curing at 25 $\pm$ 1 °C, each cube was surface-finished with fine sandpaper to remove laitance, and the NBPS was secured centrally on one of the two cast faces using the PTFE-shim arrangement described in Section 3.4.2. A baseline electromechanical admittance signature was acquired on the healthy cube, after which the cube was loaded in a 2000 kN Compression Testing Machine (CTM) following the recorded IS 516-1959 procedure (IS 516, 1959). The NBPS was removed during mechanical loading and secured again at the marked position for the post-damage acquisition. EMI signatures were therefore compared at two states, baseline and post-damage; no intermediate EMI acquisition is assumed. Figure 3.4 shows the test arrangement used for the compressive damage study. A reusable NBPS was coupled to the marked cube face through symmetric PTFE shims to record signatures in the baseline and post-damage states via the common instrumentation.

The measurement sequence maintained a direct connection between the electrical response and the mechanical test. For every cube, the healthy-state signature was recorded before loading, the destructive compressive strength was obtained from the CTM, and the post-damage signature was then recorded after returning the NBPS to the marked face. Thus, the baseline and post-damage spectra belong to the same physical specimen, while the three cubes in each configuration provide the replicate mechanical results for that mix. This distinction is retained throughout the subsequent damage analysis.

The fixed NBPS location and common frequency settings make the two electrical states directly comparable. Conductance and susceptance were recorded together, so changes in resonance position and amplitude could be examined using the same

acquisition window. The protocol does not represent intermediate loading stages: it provides one matched electrical comparison across the destructive event for each cube. The arrangement in Figure 3.4 therefore summarises the complete sequence from healthy-state acquisition through compressive loading to the final post-damage measurement.

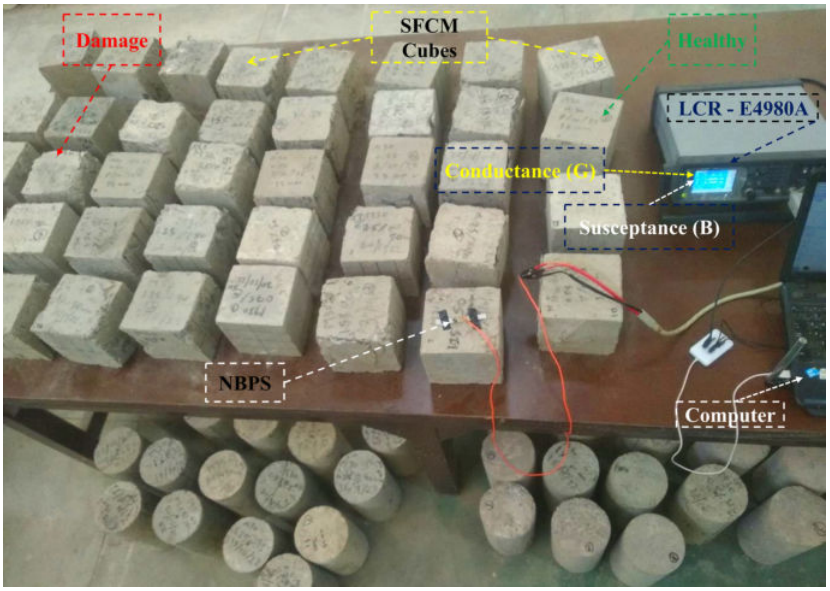

Figure 3.4: Data-acquisition arrangement for the compressive damage detection study.

3.7 Study 3: Split-Tensile Damage Detection Setup

3.7.1 Cylindrical Specimen Matrix

The split-tensile damage detection study employed the same thirteen-configuration matrix as the compressive study, but on cylindrical specimens of 150 mm diameter and 300 mm height. Three replicate cylinders per system produce a total of 39 cylinders. The common matrix structure (one control mix plus six dosages for each of two aspect ratios) permits comparison of trends across the compressive and split-tensile campaigns; the measurements are from separate specimens and are not paired specimen observations.

3.7.2 Split-Tensile Loading and EMI Acquisition Procedure

After 28-day water curing, each cylinder was surface-finished along the longitudinal axis on the plane where the NBPS would be secured. A baseline electromechanical admittance signature was acquired in the healthy state, and the cylinder was then loaded

destructively in split-tensile mode on the CTM following IS 516-1959 (IS 516, 1959) to produce the recorded damaged state. The NBPS was demounted during the mechanical loading and secured again in the same position for the post-damage acquisition. Figure 3.5 shows the test arrangement used for the split-tensile study. The cylinder was positioned horizontally on the CTM, with the NBPS secured on the marked lateral plane to record the baseline and post-damage states.

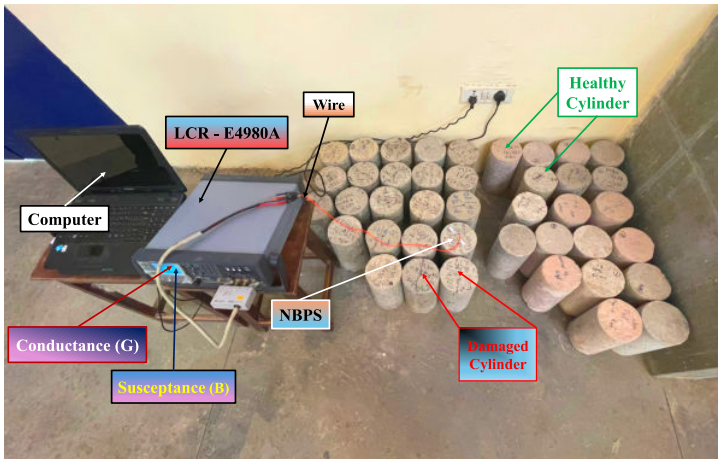

Figure 3.5: Data-acquisition arrangement for the split-tensile damage study.

3.8 Study 4: Thermal Loading Setup

3.8.1 Thermal Loading Protocol

A controlled electric furnace with a temperature accuracy of ± 2 °C was used to impose the recorded thermal loading programme. Eight nominal temperature stages (75, 100, 125, 150, 175, 200, 225, and 250 °C) were imposed consecutively without intermediate cooling. At each stage the specimen was held at the target temperature for 30 minutes, and conductance and susceptance signatures were recorded at three dwell intervals (10, 20, and 30 minutes) to document the response during each heating stage. A baseline signature was also acquired at ambient temperature (≈ 25 °C) prior to heating. A detailed summary of the thermal protocol is presented in Table 3.2.

The full sequence in Table 3.2 yields one ambient baseline plus 24 heated signatures per specimen. It was used for the intact campaign and for the saw-cut 0.50% configurations (SFC1/JPS1, AR 65, and SFC2/JPS2, AR 55). For the saw-cut 0.75% configurations (SFC3/JPS3, AR 65, and SFC4/JPS4, AR 55), measurements are available only through 175 °C, corresponding to the baseline and five heated stages. The absence of higher-temperature measurements is reported as a data limitation; no failure

Table 3.2: Full thermal loading protocol for intact specimens and the 0.50% cut configurations

Stage	Temperature (°C)	Dwell	Recording Points	Signatures
Baseline	≈ 25	Reference	Initial	1
1	75	30 min	10, 20, 30 min	3
2	100	30 min	10, 20, 30 min	3
3	125	30 min	10, 20, 30 min	3
4	150	30 min	10, 20, 30 min	3
5	175	30 min	10, 20, 30 min	3
6	200	30 min	10, 20, 30 min	3
7	225	30 min	10, 20, 30 min	3
8	250	30 min	10, 20, 30 min	3
		Signatures per specimen per condition:		**25**

mechanism is assigned without direct evidence.

3.8.2 Thermal EMI Measurement Procedure

Each cube in the four-specimen matrix was seated on a refractory support inside the electric furnace. The JPS lead was routed out of the furnace and connected to the LCR meter. At each prescribed temperature stage, signatures were acquired after 10, 20, and 30 minutes using the thermal frequency sweep specified in Section 3.9. Figure 3.6 shows the furnace, controller, specimen, and measurement arrangement.

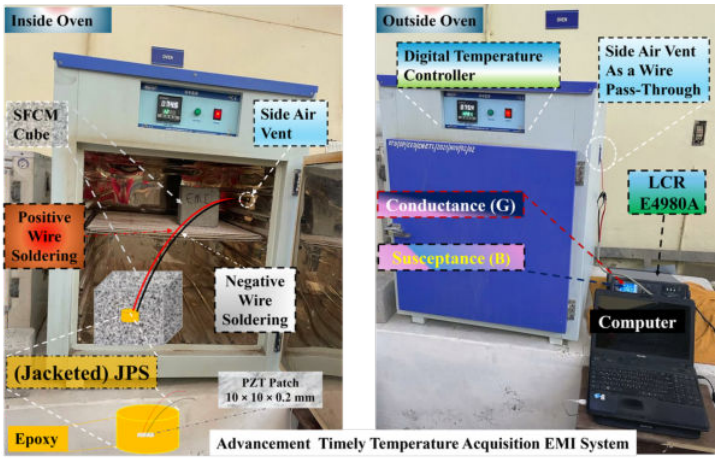

Figure 3.6: Data-acquisition arrangement for the thermal-loading study.

3.8.3 Saw-Cut Damage Introduction

For the damaged-state measurements, an artificial saw-cut was introduced into each hardened cube before the second thermal sequence. A 3 mm-wide diamond saw blade cut a 30 mm-deep slot across one face of the cube, in a plane orthogonal to the embedded JPS. The saw-cut geometry is shown in Figure 3.7. The JPS remained connected for the subsequent damaged-state electromechanical admittance acquisitions over the available temperature stages.

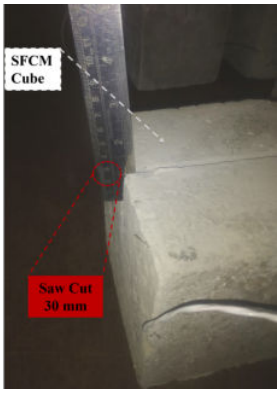

Figure 3.7: Saw-cut damage introduced in the four SFRC cubes before the damaged thermal sequence

3.9 Common Instrumentation: Keysight E4980A LCR Meter

Electromechanical admittance data across all four studies were acquired with a single Keysight E4980A precision LCR meter operating over the 20 Hz–2 MHz range. For the hydration, compression, and tension studies, the excitation frequency was swept from 30 kHz to 1000 kHz at a resolution of 100 Hz under a 1 V AC driving signal. For the thermal study, a denser sweep of 30–557.4 kHz at 5275 points per signature was adopted to resolve the frequency shifts used by the thermal-compensation procedure. Conductance (G) and susceptance (B) were recorded simultaneously through shielded coaxial cables soldered to the sensor terminals, and Keysight VEE Pro software was used for automated logging and real-time visualisation. The same LCR meter was used throughout the four studies.

3.10 Theoretical Framework of the Electromechanical Impedance Technique

The electromechanical impedance technique relies on the dynamic coupling between a piezoelectric transducer and the host structure. When the PZT patch is

electrically excited across a high-frequency range (typically 30–1000 kHz), the resulting electromechanical admittance signature captures the combined electrical impedance of the PZT transducer and the mechanical impedance of the substrate. Variations in the admittance signature thus reflect changes in the mechanical state of the host structure, enabling damage detection and quantification without direct mechanical intervention.

The one-dimensional constitutive relation that governs the complex admittance $\bar{Y}$ of the coupled PZT–structure system is expressed in Equation 3.1:

$$\bar{Y} = G + jB = 4\omega j \frac{l^2}{h}\left[\overline{\varepsilon_{33}^{T}} - \frac{2d_{31}^2\overline{Y^E}}{1-\nu} + \frac{2d_{31}^2\overline{Y^E}}{1+\nu}\left(\frac{Z_{a,\text{eff}}}{Z_{s,\text{eff}}+Z_{a,\text{eff}}}\right)\bar{T}\right] \tag{3.1}$$

where G and B denote the real (conductance) and imaginary (susceptance) components of the complex admittance; j is the imaginary unit; ω is the angular frequency; l and h are the in-plane dimension and thickness of the PZT patch; $Z_{s,\text{eff}}$ and $Z_{a,\text{eff}}$ are the effective mechanical impedances of the structure and of the PZT patch, respectively; $\overline{\varepsilon_{33}^{T}}$ is the complex electric permittivity under constant stress; d_{31} is the piezoelectric strain coefficient; $\bar{T}$ is the complex tangent ratio; and ν denotes the Poisson ratio of the PZT patch.

The complex Young modulus $\overline{Y^E}$ and the complex permittivity $\overline{\varepsilon_{33}^{T}}$ incorporate the mechanical loss factor η and the dielectric loss factor δ through Equations 3.2 and 3.3:

$$\overline{Y^E} = Y^E(1 + j\eta) \tag{3.2}$$

$$\overline{\varepsilon_{33}^{T}} = \varepsilon_{33}^{T}(1 - j\delta) \tag{3.3}$$

The complex tangent ratio $\bar{T}$ is given by Equation 3.4:

$$\bar{T} = \frac{\tan(kl)}{kl} \tag{3.4}$$

where k is the two-dimensional wave number that depends on the density ρ and the elastic properties of the PZT patch, as expressed in Equation 3.5:

$$k = \sqrt{\frac{\rho(1-\nu^2)}{\overline{Y^E}}} \tag{3.5}$$

Changes in the measured conductance and susceptance signatures describe changes in the coupled PZT–sensor-interface–specimen response. The model-based interpretation of that response is presented next, followed by the statistical indices used for

comparison with the corresponding baseline signature.

3.11 Lumped-Parameter Mechanical Impedance Modelling

The PZT–concrete system is represented as a single-degree-of-freedom (SDOF) series spring–damper–mass network formulated in terms of mechanical mobility. Under harmonic excitation $F(t) = F_0 e^{j\omega t}$, the transmitted force is common to the three elements, whereas their velocities and mobilities are additive. The summed mobility is therefore inverted to obtain the mechanical impedance of the coupled system. The extracted mass (m), stiffness (k), and damping (c) are local, model-dependent EPS rather than unique global properties of a concrete specimen.

The total mechanical mobility and its corresponding impedance are

$$\mathscr{M}(\omega) = \frac{1}{c} + j\left(\frac{\omega}{k} - \frac{1}{\omega m}\right), \qquad Z(\omega) = \frac{1}{\mathscr{M}(\omega)} = x(\omega) + j\,y(\omega). \tag{3.6}$$

At each frequency, the additive mobility in Equation 3.6 is inverted to obtain impedance. Using the established extraction procedure and its resonance boundary condition, the three parameters are obtained as follows:

$$m = \frac{(\omega_0^2 - \omega^2)(x^2 + y^2)}{\omega_0 \omega^2 y} \tag{3.7}$$

$$k = \frac{(\omega_0^2 - \omega^2)(x^2 + y^2)}{\omega y} \tag{3.8}$$

$$c = \frac{x^2 + y^2}{x} \tag{3.9}$$

where x and y are the real and imaginary components of the mechanical impedance $Z(\omega)$, ω is the angular excitation frequency, and the extraction boundary condition is $\omega = \omega_0$ when $y = 0$.

The real and imaginary impedance components reconstructed from the extracted parameters were compared with the corresponding measured components:

$$x = \frac{c^{-1}}{c^{-2} + \left(\dfrac{\omega}{k} - \dfrac{1}{\omega m}\right)^2} \tag{3.10}$$

$$y = \frac{-\left(\frac{\omega}{k} - \frac{1}{\omega m}\right)}{c^{-2} + \left(\frac{\omega}{k} - \frac{1}{\omega m}\right)^2} \tag{3.11}$$

Figure 3.8 shows the series mechanical network represented by Equations 3.6–3.11.

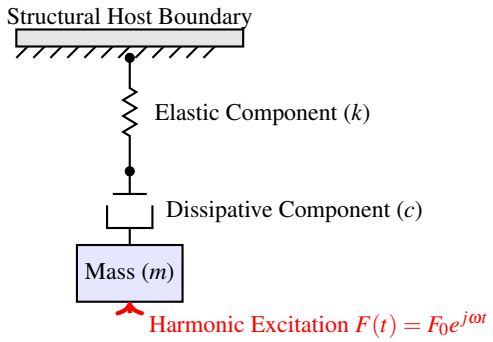

Figure 3.8: Series spring–damper–mass equivalent network used for EPS extraction

3.12 Statistical Damage Metrics for Structural Health Assessment

Four classical indices were used to compare a measured conductance signature with its corresponding baseline: Root Mean Square Deviation (RMSD), Mean Absolute Percentage Deviation (MAPD), the Cross-Correlation Coefficient (CC), and covariance. In the following definitions, G_i is the conductance at the i-th frequency bin of the measured signature and G_{bl} is the conductance at the same bin of the baseline signature.

3.12.1 Root Mean Square Deviation

RMSD relates the squared spectral difference to the energy of the baseline signature:

$$\mathrm{RMSD}(\%) = \sqrt{\frac{\sum_{i=1}^{N}(G_i - G_{bl})^2}{\sum_{i=1}^{N}(G_{bl})^2}} \tag{3.12}$$

where N is the number of frequency bins included in the comparison.

3.12.2 Mean Absolute Percentage Deviation

MAPD is the mean absolute value of the relative difference evaluated at each frequency bin:

$$\mathrm{MAPD}(\%) = \frac{1}{N}\sum_{i=1}^{N}\left|\frac{G_i - G_{bl}}{G_{bl}}\right| \tag{3.13}$$

3.12.3 Cross-Correlation Coefficient

The CC quantifies the linear similarity between the baseline and the test signature:

$$\mathrm{CC} = \frac{\frac{1}{N}\sum_{i=1}^{N}(G_{bl} - \overline{G_{bl}})(G_i - \overline{G_i})}{\sigma_{bl}\,\sigma_i} \tag{3.14}$$

where σ_{bl} and σ_i denote the standard deviations of the baseline and current signatures, respectively.

3.12.4 Covariance

Covariance provides an unnormalised measure of the joint variation of the baseline and current signatures:

$$\mathrm{Cov} = \frac{1}{N}\sum_{i=1}^{N}(G_{bl} - \overline{G_{bl}})(G_i - \overline{G_i}) \tag{3.15}$$

3.13 Quality Assurance and Statistical Reliability

3.13.1 PZT Screening and Consistent Sensor Mapping

Each PZT patch was checked before deployment, and a fixed sensor-to-specimen mapping was maintained throughout each monitoring sequence. The same JPS remained in each hydration–thermal specimen, while the same NBPS assembly and positioning procedure were used for the baseline and post-damage measurements. This practice reduces sensor-to-sensor and repositioning variability but does not remove all sensor, contact, cable, or environmental effects.

3.13.2 Experimental Units and Replication

The physical specimen is the experimental unit in the mechanical studies. Three independently cast specimens were tested for each of the thirteen configurations, giving 39 cubes and 39 cylinders. The hydration study used four separately cast JPS-instrumented cubes, and the thermal study reused those same four specimens. Repeated curing ages, temperature stages, intact/saw-cut states, and compensated/uncompensated analyses are repeated observations or derived states of those specimens; they are not additional physical replicates.

3.14 Summary

This chapter establishes the experimental basis of the four studies. The hydration and thermal studies used the same four JPS-instrumented cubes, whereas the compressive and split-tensile studies used separate thirteen-configuration matrices containing 39 cubes and 39 cylinders, respectively. The chapter also defines the common LCR-meter acquisition, the coupled EMI formulation, the local EPS model, the baseline-comparison indices, and the controls applied to sensor mapping and replication. These methods provide a consistent basis for interpreting the hydration, mechanical-damage, and thermal results.

CHAPTER 4

HYDRATION AND CURING-AGE MONITORING USING JACKETED PIEZO SENSORS

4.1 General

This chapter addresses the first research objective by examining changes in the measured JPS signatures during the 180-day curing programme. Four SFRC cubes were measured at Days 1, 3, 7, 14, 28, 60, 90, 120, 150, and 180. The analysis uses the conductance (G) and susceptance (B) spectra, features obtained from the selected resonance band, statistical comparisons with the Day-1 signature, and EPS calculated by the method established in Chapter 3.

The four monitored configurations combine AR 65 and AR 55 hooked-end fibres with volume fractions of 0.50% and 0.75%: SFC1 (AR 65, 0.50%), SFC2 (AR 55, 0.50%), SFC3 (AR 65, 0.75%), and SFC4 (AR 55, 0.75%). One JPS-instrumented cube was retained for each configuration. Repeated measurements on each cube provide a record of change within the same installation. Comparisons among SFC1–SFC4 are descriptive because the monitoring programme does not include replicate JPS cubes for estimating the separate effects of aspect ratio and fibre dosage.

The results are presented in the order in which the measurements were interpreted. The complete 30–1000 kHz records are examined first, after which the common 150–300 kHz region is used to follow resonant frequency and peak conductance. These observations are compared with separately obtained compressive-strength results at the same curing ages. The analysis then considers the statistical indices and the EPS results, including the in-sample relation between equivalent stiffness and compressive strength. This sequence links the measured electrical response to the independent mechanical observations without treating either measurement as a direct substitute for the other.

4.2 Experimental Programme and Measurement Records

The results combine two types of record: repeated, non-destructive measurements on the four JPS-instrumented cubes and destructive compressive-strength measurements from separately tested cubes. Figure 4.1 shows how the two measurement streams enter the comparison.

- JPS monitoring cubes: Four $150 \times 150 \times 150$ mm cubes, each containing one JPS (JPS1–JPS4), were retained for measurements at the ten scheduled curing ages.
- Strength-test cubes: The reported compressive-strength values were obtained from separate cubes corresponding to the four SFRC configurations and curing ages. They provide an age- and mixture-matched mechanical reference and were not obtained from the monitored cubes.

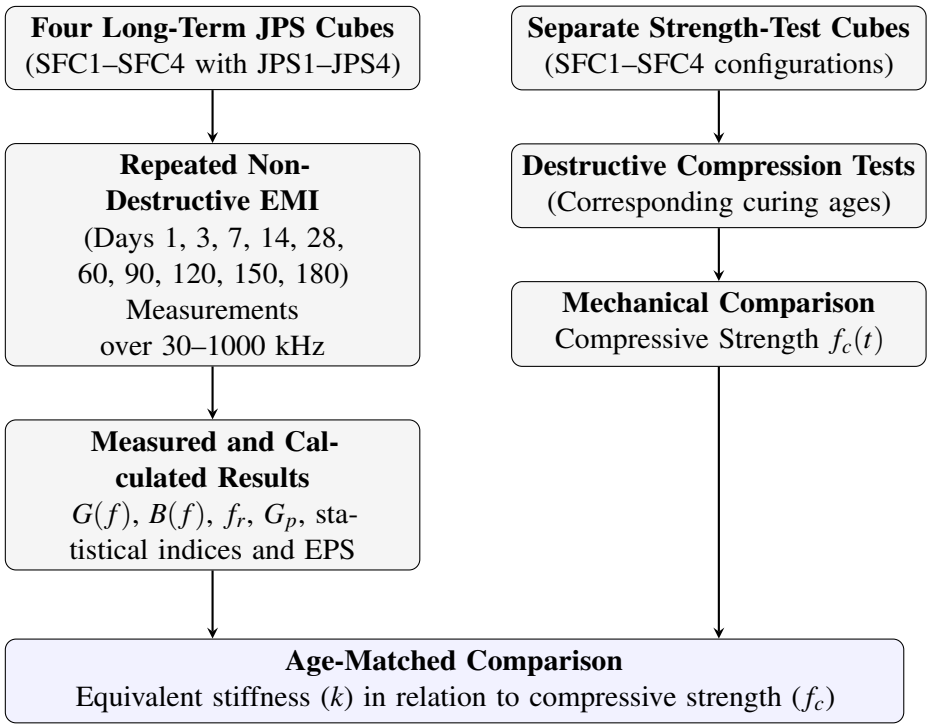

Figure 4.1: Measurement sequence for the repeated JPS records and the separately obtained compressive-strength results.

The specimen–sensor mapping is given in Table 4.1. The curing conditions, JPS construction, specimen preparation, and acquisition procedure are documented in Sections 3.5 and 3.9. In brief, the cubes were water-cured at 25 ± 1 °C, and $G(f)$ and $B(f)$ were recorded from 30 to 1000 kHz at 100 Hz intervals under a 1 V excitation.

Table 4.1: Specimen-sensor mapping and fibre configurations for the long-term monitoring programme

Specimen	Sensor	AR	Dosage	Monitoring Period	Measured Signals
SFC1	JPS1	65	0.50%	1–180 days	Conductance (G), Susceptance (B)
SFC2	JPS2	55	0.50%	1–180 days	Conductance (G), Susceptance (B)
SFC3	JPS3	65	0.75%	1–180 days	Conductance (G), Susceptance (B)
SFC4	JPS4	55	0.75%	1–180 days	Conductance (G), Susceptance (B)

Because each strength test is destructive, the values in this chapter are treated as separate age-matched mechanical results. They are compared with the JPS-derived quantities at corresponding ages, but they are not interpreted as direct strength measurements of the four instrumented cubes. The repeated JPS records and the strength results therefore answer complementary questions: the former show change in each unchanged sensor installation, whereas the latter provide the measured mechanical response of the corresponding SFRC mixtures.

4.3 Measured Conductance and Susceptance Signatures

The measured $G(f)$ and $B(f)$ spectra reflect the coupled response of the JPS, its protective jacket and interface, and the surrounding concrete. Changes in the curves are therefore interpreted within each sensor–specimen installation rather than as direct measurements of a single concrete property. The complete recorded range is retained to show the available resonances, while the enlarged 150–300 kHz panels identify the common range used in the subsequent calculations.

All ten curing-age measurements were acquired with the same frequency increment and excitation setting described in Chapter 3. The comparison therefore preserves a common frequency grid from Day 1 to Day 180 for every installation. This is important because the observed differences can be located at the same frequencies without interpolation or a change of acquisition range. It does not, however, make the four sensors interchangeable: each later curve is interpreted against the earlier response of the same JPS–specimen system.

The 150–300 kHz interval contains the first labelled resonance region in all four conductance records and the corresponding portion of the susceptance response. Retaining this common interval gives one consistent basis for peak extraction, statistical comparison and EPS calculation. The complete 30–1000 kHz views remain alongside the enlarged panels so that changes within the selected interval can be checked against the other measured resonance regions.

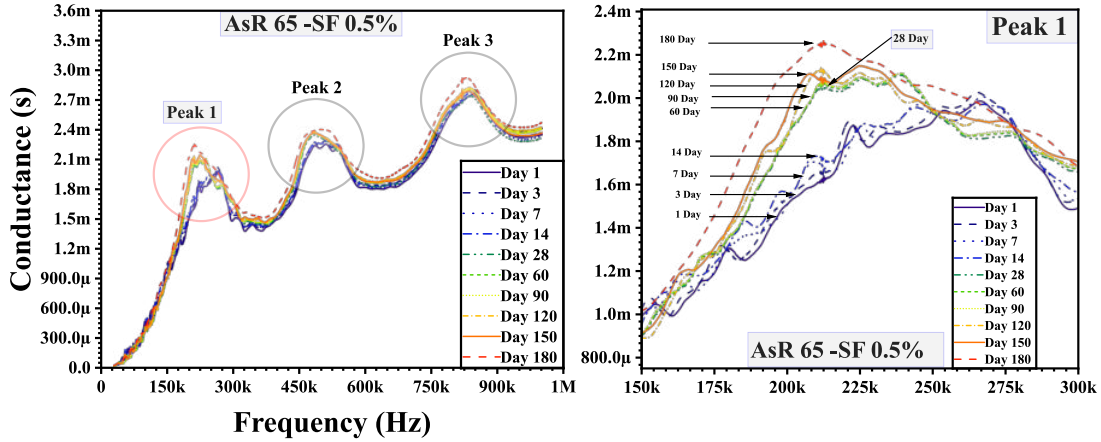

(a) JPS1: SFC1 (AR 65, 0.50% dosage).

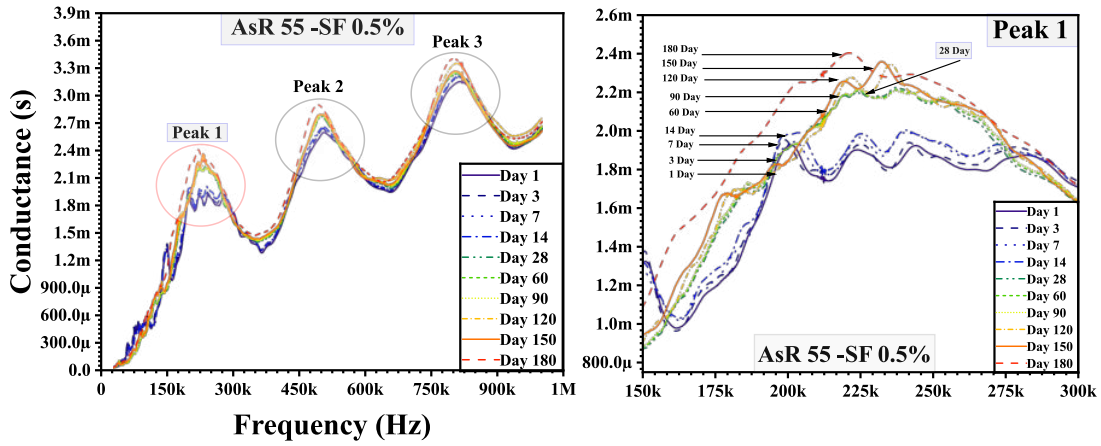

(b) JPS2: SFC2 (AR 55, 0.50% dosage).

Figure 4.2: Conductance (G) signatures recorded over 30–1000 kHz at representative curing ages for the four JPS configurations (Part 1).

For JPS1 and JPS2, the complete records in Figures 4.2(a) and 4.2(b) contain three principal resonance regions. The enlarged 150–300 kHz views show that the first region remains identifiable at every recorded age, while both its frequency position and conductance magnitude change. The neighbouring curve shape also changes, so the retained peak is interpreted together with the surrounding response rather than as an isolated scalar measurement.

The full-range panels show that curing-age differences are not confined to the first labelled region. Changes are also visible around the second and third regions, although their magnitude and detailed form differ between JPS1 and JPS2. The enlarged panels are therefore used to examine the selected first region more clearly, not to imply that the remaining measured spectrum is unchanged. This distinction supports use of a consistent analysis band while preserving the information supplied by the complete

signatures.

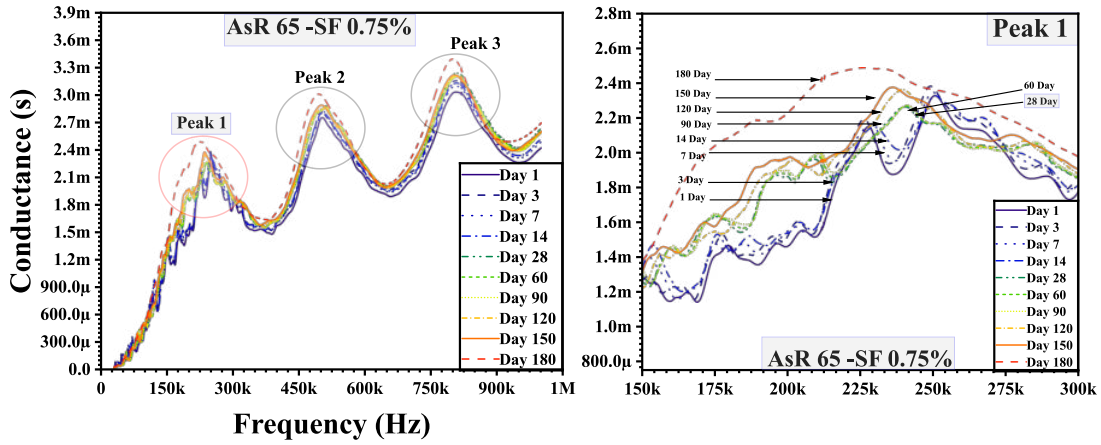

(c) JPS3: SFC3 (AR 65, 0.75% dosage).

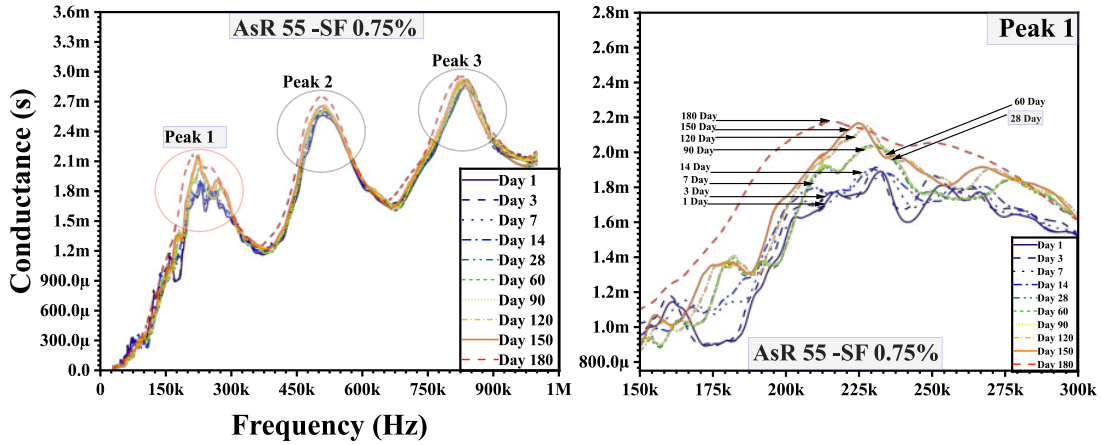

(d) JPS4: SFC4 (AR 55, 0.75% dosage).

Figure 4.2: Conductance (G) signatures recorded over 30–1000 kHz at representative curing ages for the four JPS configurations (continued).

The corresponding JPS3 and JPS4 records show the same three-region structure but not the same peak magnitudes or detailed curve shapes. Across all four installations, the retained peak moves to a higher frequency from Day 1 to Day 7, occurs at a lower frequency at Day 14, and then moves to higher frequencies through Day 180. The complete and enlarged views make that selection visible; however, absolute differences between sensors cannot be assigned solely to fibre aspect ratio or dosage because the separate contributions of the concrete, interface, protective jacket, moisture and PZT response were not measured independently.

The susceptance records are examined over the same frequency ranges because both measured components are used in the EPS calculation. The comparison below focuses on whether the curve background and local features change consistently with

age within each installation; it is not used to assign a unique dielectric or hydration mechanism.

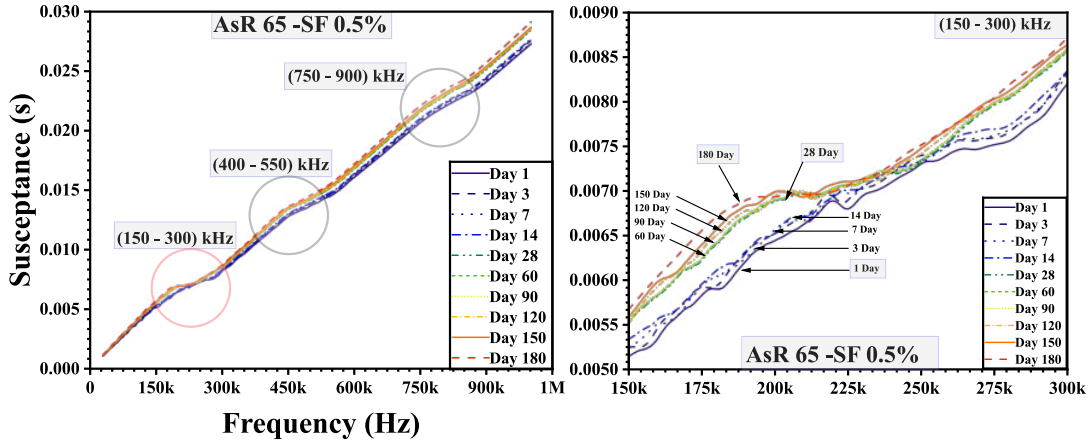

(a) JPS1: SFC1 (AR 65, 0.50% dosage).

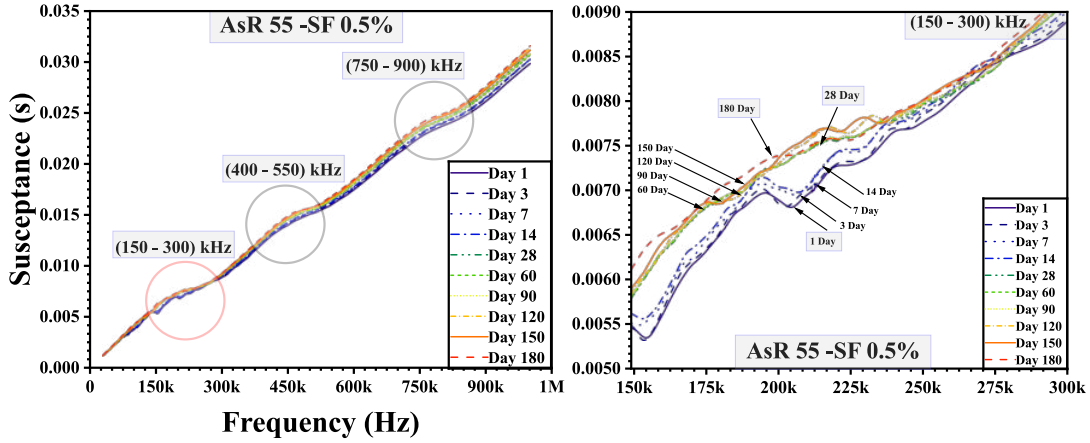

(b) JPS2: SFC2 (AR 55, 0.50% dosage).

Figure 4.3: Susceptance (B) signatures recorded over 30–1000 kHz at representative curing ages for the four JPS configurations (Part 1).

For JPS1 and JPS2, susceptance increases across most of the complete frequency range, with local changes in slope in the same three regions highlighted in the source plots. In the 150–300 kHz panels, the later-age curves generally lie above the early-age curves, although their spacing is not uniform across frequency. This shows why a single susceptance value cannot represent the full measured change.

Within the enlarged interval, separation among the age-dependent curves is clearest through portions of approximately 150–225 kHz, whereas the curves draw closer together and locally cross at higher frequencies. The direction and magnitude of the difference therefore depend on frequency as well as curing age. Using the complete set of frequency ordinates preserves this behaviour for the subsequent impedance

calculation and avoids selecting one susceptance reading as representative of the entire band.

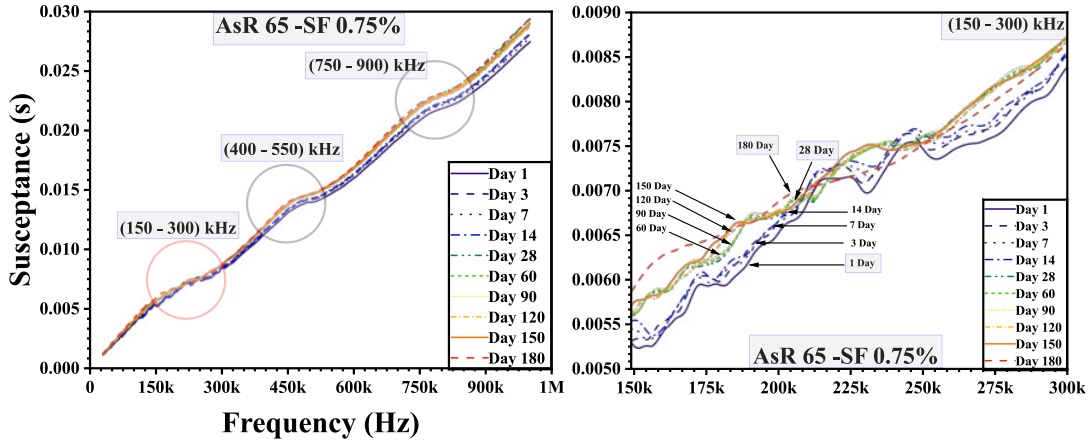

(c) JPS3: SFC3 (AR 65, 0.75% dosage).

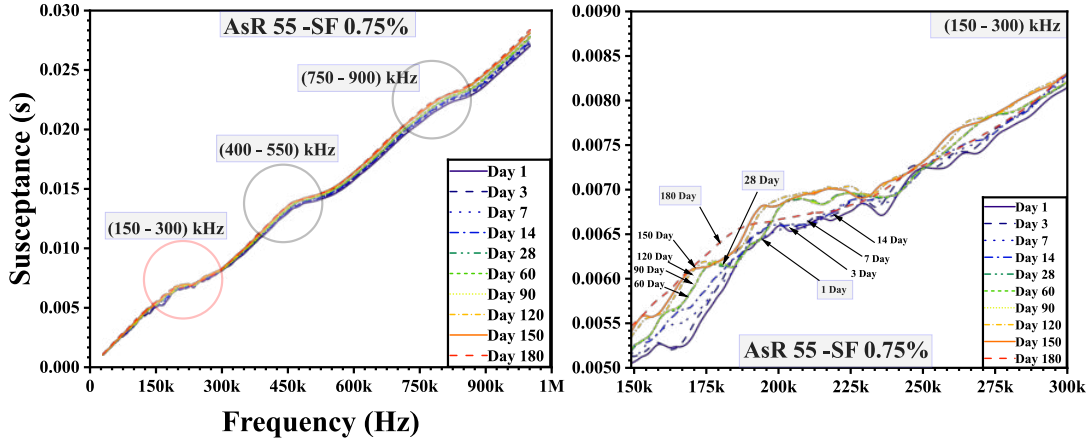

(d) JPS4: SFC4 (AR 55, 0.75% dosage).

Figure 4.3: Susceptance (B) signatures recorded over 30–1000 kHz at representative curing ages for the four JPS configurations (continued).

JPS3 and JPS4 exhibit the same rising background, but the local curve separation within 150–300 kHz differs from that of JPS1 and JPS2. For all four installations, the age-dependent curves change in both level and local form. These differences confirm that the measured imaginary component is age dependent, but their magnitude cannot be interpreted independently of the JPS electrical response and its local coupling to the concrete.

Taken together, the two sets of spectra show that curing affects more than the height of one conductance peak. Frequency position, conductance magnitude, the surrounding resonance pattern and the susceptance background all change with age. The following analysis reduces these records to two traceable peak quantities before

considering multi-frequency indices and EPS.

4.4 Resonant Frequency and Peak Conductance during Curing

Feature extraction was applied to the 150–300 kHz region highlighted in Figures 4.2 and 4.3. The original study used this common range for the four JPS records and for the statistical comparisons reported below. Restricting the analysis to the same range at every age prevents the numerical comparison from being dominated by unrelated resonances elsewhere in the 30–1000 kHz record.

At each curing age, the retained resonance frequency (f_r) and its conductance magnitude (G_p, in S) were extracted. The same bounded range was used throughout the 180-day series. The source records do not document a separate automated peak-switching criterion; consequently, the results are reported as the retained peak within the stated range rather than as proof that it is the unique most-sensitive resonance. Figure 4.4 presents both quantities for the four monitored configurations.

The age-dependent records show larger changes during the early measurements and smaller changes later in the programme. The paired records for JPS1 and JPS2 in Figure 4.4(a) and (b) show that the retained resonant frequency increases through Day 7, is lower at Day 14, and resumes its upward tendency thereafter. Peak conductance follows a comparable early-age pattern, although the magnitude of change differs between the two installations. These configuration-level observations are consistent with the larger early-age changes noted in the complete conductance signatures of Section 4.3.

For JPS3 and JPS4, the same Day-14 frequency dip appears in Figure 4.4(c) and (d), but neither the absolute frequency nor the conductance magnitude matches those of JPS1 and JPS2. The fitted lines in Figure 4.4 are descriptive summaries of ten observations from each individual sensor–specimen system. The frequency-fit R^2 values are 0.6499, 0.6756, 0.6835, and 0.3060 for JPS1–JPS4, while the linear conductance-fit values are 0.8372, 0.8531, 0.2792, and 0.8898. The wide variation in fit quality across the four installations confirms that one empirical function cannot be treated as a general curing law for all four installations.

The two fitted quantities do not show the same fit quality for a given installation. JPS1 and JPS2 have moderate frequency fits and comparatively high conductance fits, whereas JPS3 has a moderate frequency fit but a low conductance fit. JPS4 shows the reverse combination, with the lowest frequency-fit value and the highest conductance-fit value. Thus, neither frequency nor peak magnitude alone provides a consistent description across SFC1–SFC4; both measured features must be retained

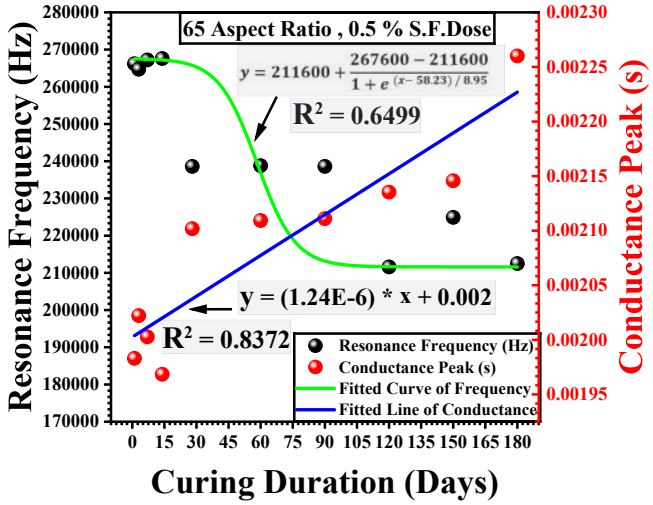

(a) JPS1: SFC1 (AR 65, 0.50% dosage).

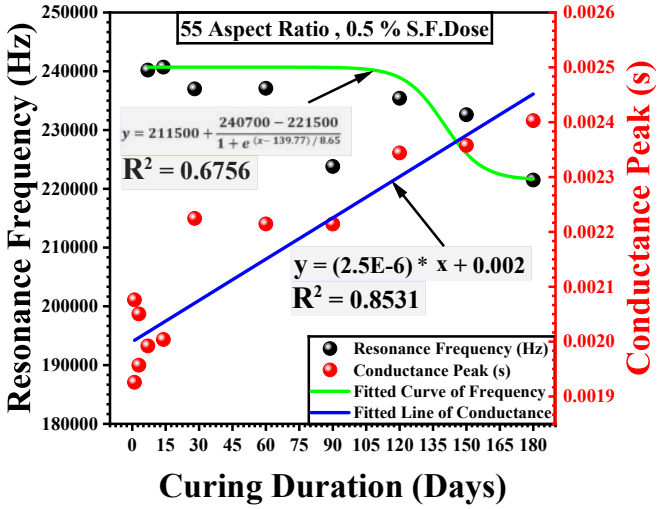

(b) JPS2: SFC2 (AR 55, 0.50% dosage).

Figure 4.4: Resonant frequency and peak conductance during the 1–180 day curing period for the four JPS configurations (Part 1).

when comparing the curing records.

Differences among SFC1–SFC4 are visible, but aspect ratio and fibre dosage cannot be isolated statistically because each configuration contains one monitored cube and one sensor installation. The comparisons are therefore retained as specimen-level observations rather than causal fibre-effect estimates.

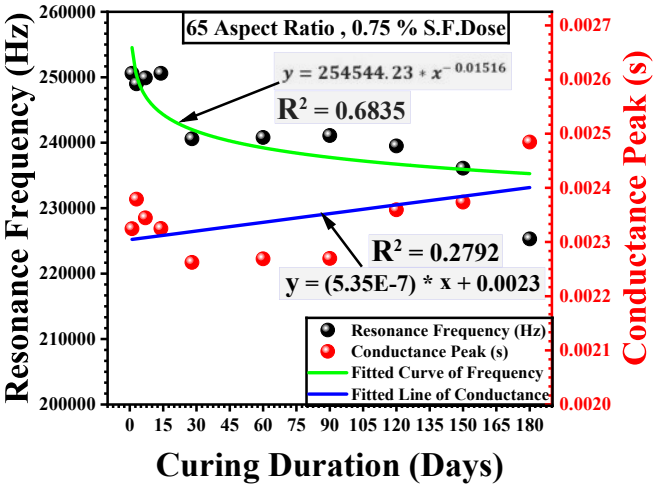

(c) JPS3: SFC3 (AR 65, 0.75% dosage).

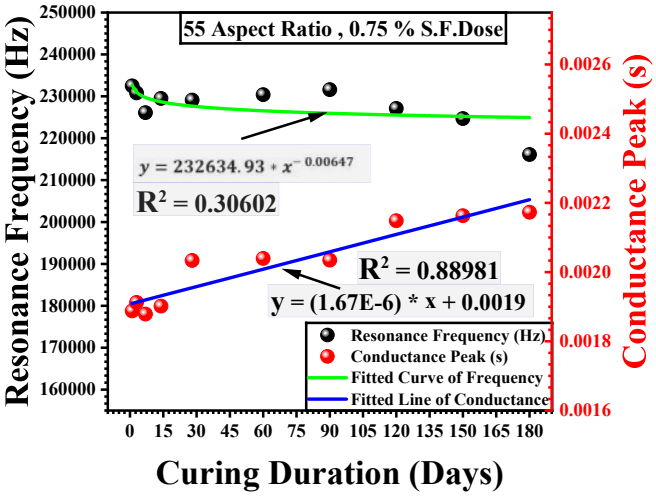

(d) JPS4: SFC4 (AR 55, 0.75% dosage).

Figure 4.4: Resonant frequency and peak conductance during the 1–180 day curing period for the four JPS configurations (continued).

4.5 Comparison with Compressive-Strength Growth

The separately obtained compressive-strength results provide an age- and mixture-matched mechanical comparison for the JPS observations. Table 4.2 reports the source values (f_c, in MPa) at the ten curing ages for the four SFRC configurations.

Figure 4.5 compares the strength records. The measured strength increases rapidly between Days 1 and 28 for all four mixtures. By Day 28, the values reach 58.80–61.06 MPa, corresponding to approximately 88.6–89.3% of the respective measured Day-180 values. Subsequent gains are smaller, and the Day-180 strengths range from 66.15 to 68.69 MPa. The Day-180 measurements are the final observations in this

Table 4.2: Compressive strength (f_c) of the separately tested cubes versus curing age for the four SFRC configurations

Curing Age (Days)	SFC1 (MPa)	SFC2 (MPa)	SFC3 (MPa)	SFC4 (MPa)
1	5.98	5.58	6.71	5.78
3	14.95	14.99	15.87	15.53
7	20.93	20.28	21.98	21.05
14	26.91	27.63	28.10	29.73
28	59.98	58.80	61.06	60.68
60	61.17	60.21	62.58	62.19
90	61.80	60.79	63.19	62.92
120	62.36	61.50	63.80	63.59
150	65.98	66.44	70.21	69.78
180	67.15	66.15	68.69	68.50

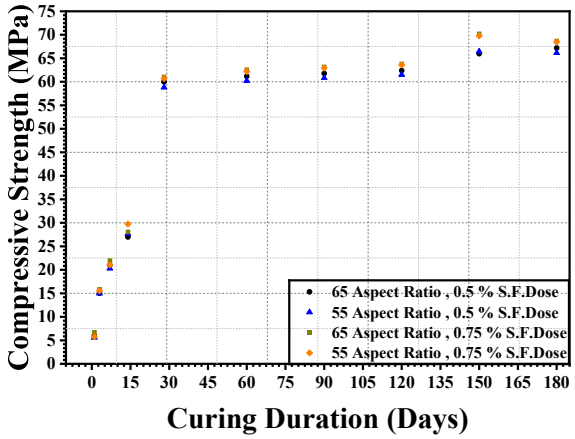

Figure 4.5: Combined compressive-strength results over 1–180 days for the four SFRC configurations obtained from separately tested cubes.

programme, not estimates of ultimate strength.

The measured range increases from 5.58–6.71 MPa at Day 1 to 20.28–21.98 MPa at Day 7 and 26.91–29.73 MPa at Day 14. The largest interval increase occurs from Day 14 to Day 28: 33.07, 31.17, 32.96, and 30.95 MPa for SFC1–SFC4, respectively. From Day 28 to Day 180, the corresponding net increases are 7.17, 7.35, 7.63, and 7.82 MPa. This numerical comparison distinguishes the rapid pre-28-day increase from the smaller net change recorded over the longer subsequent interval.

The late-age observations are not strictly monotonic for every mixture. SFC3 and SFC4 reach 70.21 and 69.78 MPa at Day 150 before measuring 68.69 and 68.50 MPa at Day 180. These source values are retained as measured rather than adjusted to impose a monotonic curve. Consequently, the fitted functions summarize the overall age-related pattern and do not replace the individual observations in Table 4.2.

The four curves remain close in magnitude at the common test ages. Small

differences between the configurations are visible in Table 4.2, but the available source does not establish the number and variability of strength-test replicates at every age. The comparison is therefore used to describe the measured age-dependent response and to provide the independent mechanical values paired with the JPS results; it is not used here to claim a statistically isolated fibre effect.

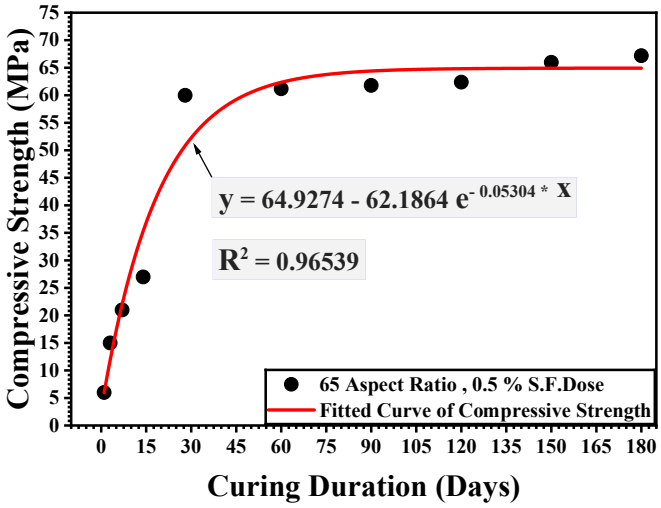

(a) SFC1 (AR 65, 0.50% dosage).

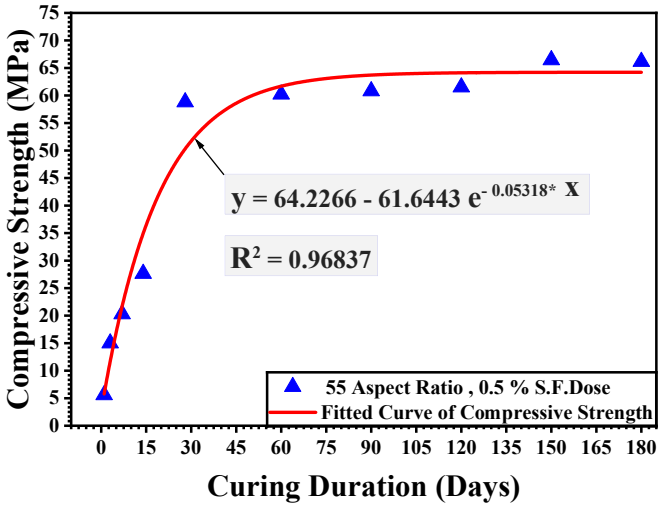

(b) SFC2 (AR 55, 0.50% dosage).

Figure 4.6: Individual compressive-strength records and fitted exponential age–strength curves for the four SFRC configurations (Part 1).

The strength records were modelled empirically using the three-parameter exponential age–strength function in Equation 4.1:

$$f_c(t) = a - be^{-ct} \tag{4.1}$$

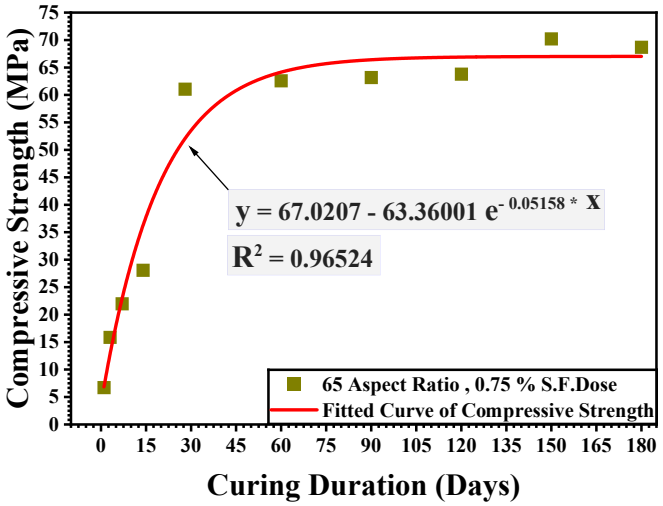

(c) SFC3 (AR 65, 0.75% dosage).

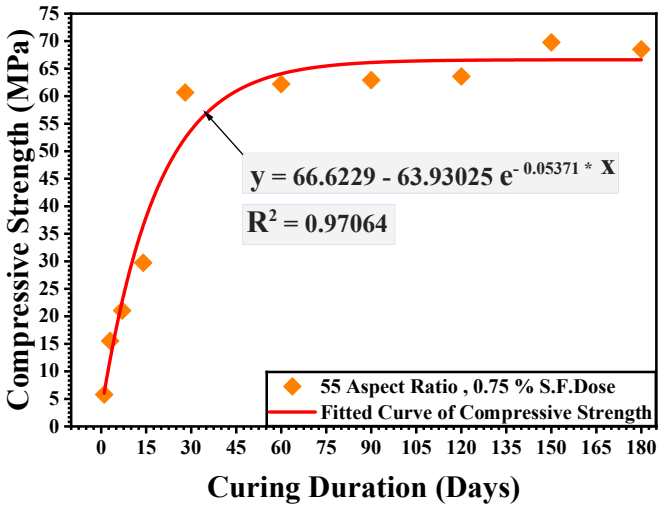

(d) SFC4 (AR 55, 0.75% dosage).

Figure 4.6: Individual compressive-strength records and fitted exponential age–strength curves for the four SFRC configurations (continued).

where $f_c(t)$ is the compressive strength at curing age t (days); a is the fitted asymptotic upper-bound strength parameter (MPa); b is the fitted initial strength offset (MPa); and c is the fitted rate parameter (day^{-1}).

The three-parameter empirical models for SFC1 and SFC2 summarise the measured strength records with coefficients of determination exceeding 0.965. The fitted curves in Figure 4.6(a) and (b) show that the rate of measured strength increase is highest during the 1–28 day interval and diminishes thereafter, consistent with the combined records in Figure 4.5. These functions are descriptive summaries of the ten source observations and are not extrapolated beyond the measured 180-day range.

For SFC3 and SFC4, the fitted asymptotic parameters and rate constants follow

a similar pattern. The corresponding R^2 values confirm close in-sample agreement, although the Day-150 and Day-180 measurements are not strictly monotonic for every configuration, as noted in the discussion of Table 4.2. The fitted curves therefore represent the overall age-dependent pattern without adjusting the individual source values. Both the strength measurements and the JPS feature records change more during the early curing period than after Day 28. This agreement concerns their timing and overall pattern; the two measurements were obtained from different cubes and do not establish a unique hydration mechanism or a specimen-independent transfer function.

4.6 Assessment Based on Statistical Indices

Statistical indices were used to describe multi-frequency differences that are not represented by a single tracked peak. The Day-1 measurement is the reference signature, and the later values quantify the difference from that measured state. In this curing study, the indices describe change with age rather than structural damage.

The four indices and their equations are defined in Section 3.12. RMSD and MAPD quantify the magnitude of pointwise differences over 150–300 kHz, CC describes similarity in curve shape, and covariance retains the scale of the paired conductance values. The fourth source plot is labelled “CoV”, although the implemented expression in Equation 3.15 is covariance rather than coefficient of variation. Retaining these complementary quantities avoids interpreting the response from one peak or one comparison measure alone.

Every comparison uses the same 150–300 kHz limits and the same 100 Hz sampling interval as the Day-1 record. This common frequency grid is essential for pointwise comparison: a change in an index then arises from the measured signatures rather than from unequal frequency locations. Because all later ages share the same Day-1 reference, the resulting values are age-referenced observations within each installation; they are not independent replicate measurements and are not compared as though they formed four interchangeable sensor populations.

Figure 4.7 presents the four age-dependent index series:

- RMSD and MAPD: Both indices increase relative to the Day-1 reference signature, with larger changes during the early curing period and configuration-dependent changes thereafter. The source discussion reports values of approximately 30% to 40% at Day 28 and 85% to 95% at Day 180 across these deviation measures.

- CC: Similarity to the Day-1 signature generally decreases as the resonance pattern

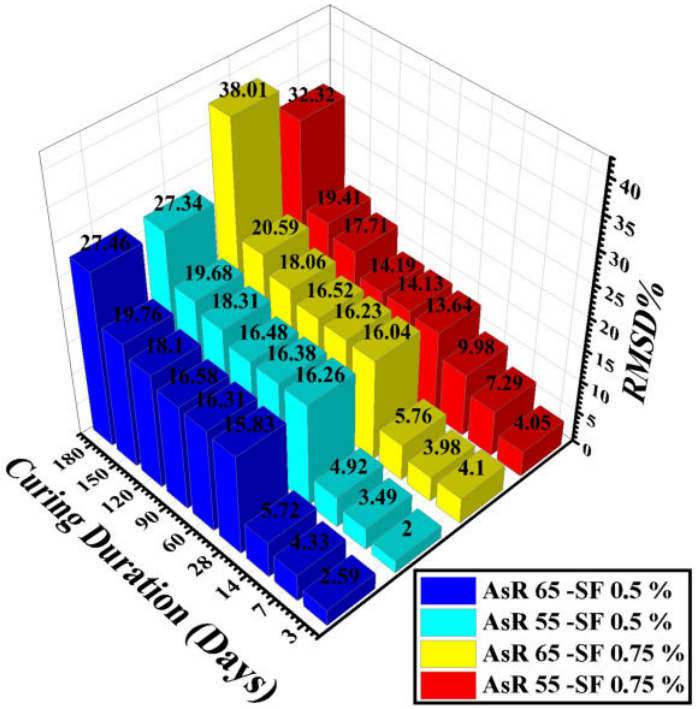

(a) RMSD relative to the Day-1 signature.

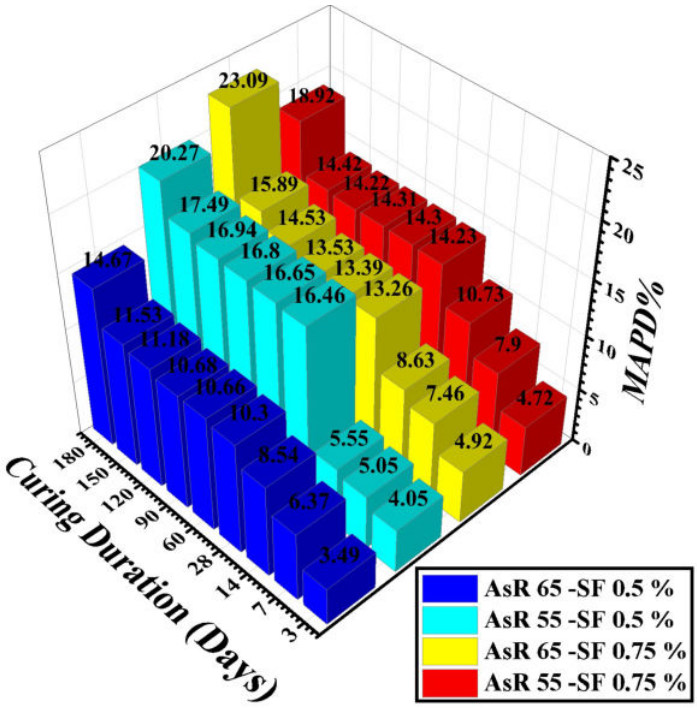

(b) MAPD relative to the Day-1 signature.

Figure 4.7: RMSD and MAPD values across curing ages (Part 1).

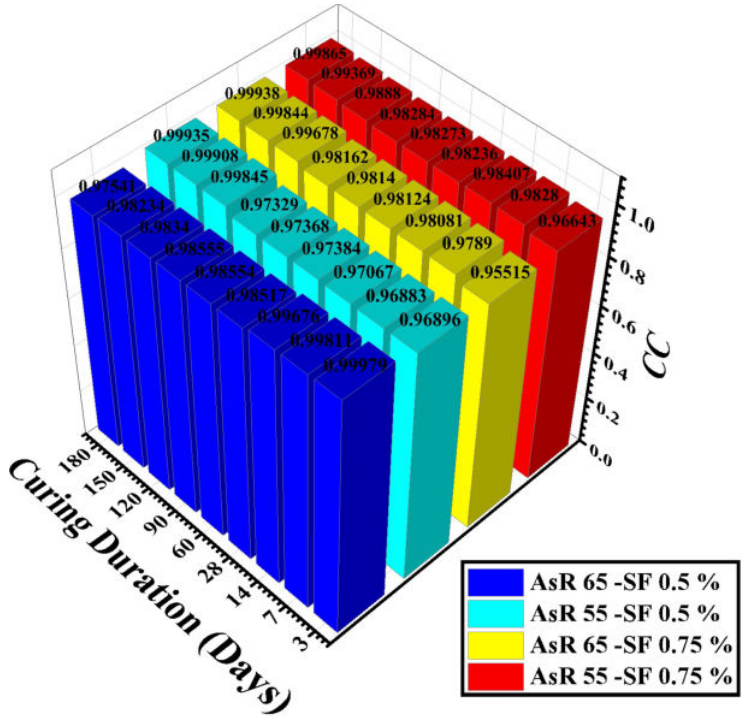

(c) CC relative to the Day-1 signature.

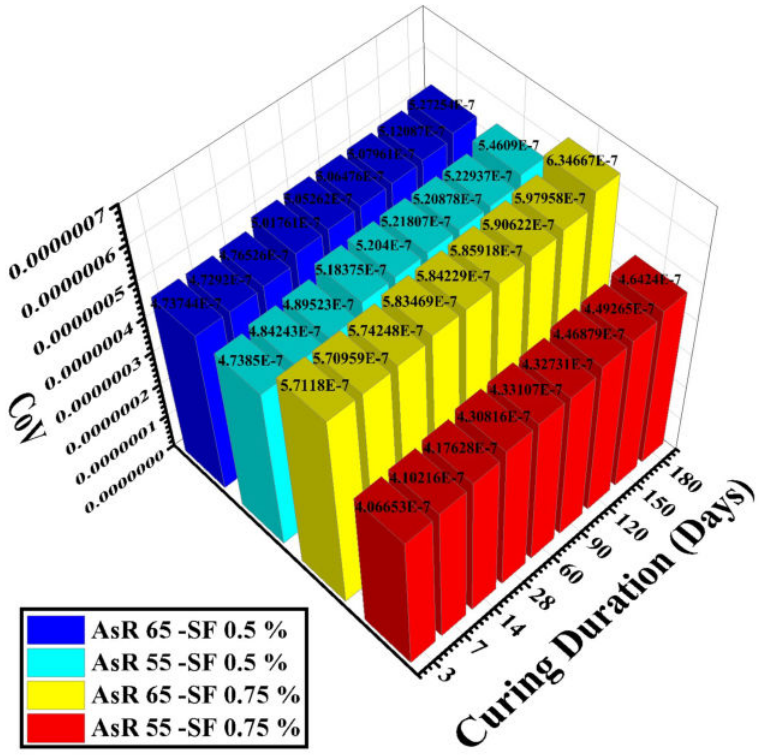

(d) Covariance (labelled CoV in source plot).

Figure 4.7: CC and covariance values across curing ages (continued).

changes. The values are not interpreted as a direct stiffness measurement.

- Covariance: The unnormalised covariance changes markedly at early ages and then more gradually. Its magnitude also depends on signal scale, so comparisons are restricted to the stated measurement framework.

The deviation measures respond to amplitude differences as well as changes in the curve, whereas CC places greater emphasis on similarity of shape. Covariance is not normalised and therefore cannot be compared across installations without considering their signal magnitudes. The four indices consequently provide different views of the same age-referenced measurements; none identifies the physical origin of the change by itself. The next section applies the fixed Chapter 3 procedure to obtain the model-dependent EPS.

4.7 EPS from JPS Signatures

The mathematical formulation and EPS extraction equations are established in Section 3.11. Here, that fixed procedure is applied to the 150 to 300 kHz curing records. The two calculated impedance components are shown in Figures 4.8 and 4.9 for every configuration and curing age. Presenting both components is necessary because the EPS calculation depends on their combined response around the selected resonance.

In the calculated component plots, the age-dependent separation is most visible in the lower portion of the selected range, while the curves draw closer together toward the upper end. The x component retains more local variation around the resonant region; the y component follows a smoother frequency-dependent background with smaller separation over much of the range. The calculation therefore uses the paired components over the selected range instead of assigning the parameter estimates from one ordinate or one frequency point.

The real component x and imaginary component y represent the extracted mechanical impedance of the combined JPS-concrete interface. Because the sensor and surrounding matrix respond as a coupled dynamic system, changes in matrix density, modulus, and interfacial bonding during hydration alter both components simultaneously. The full-spectrum records between 150 and 300 kHz capture the progressive evolution of this coupled interface across the 180-day monitoring period.

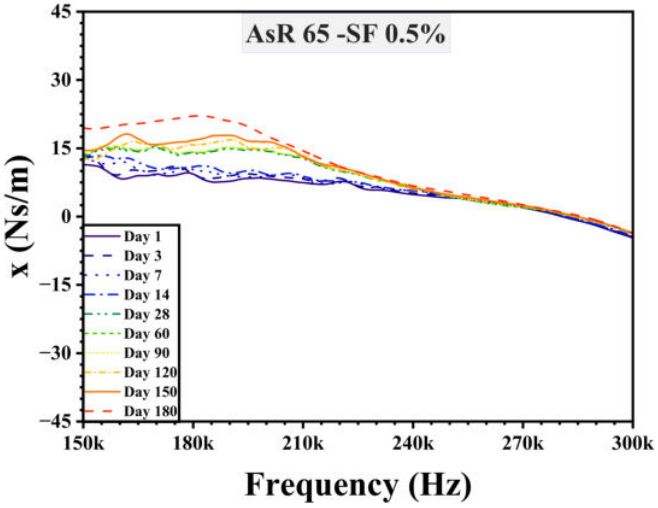

(a) x vs. frequency, SFC1 (AR 65, 0.5%).

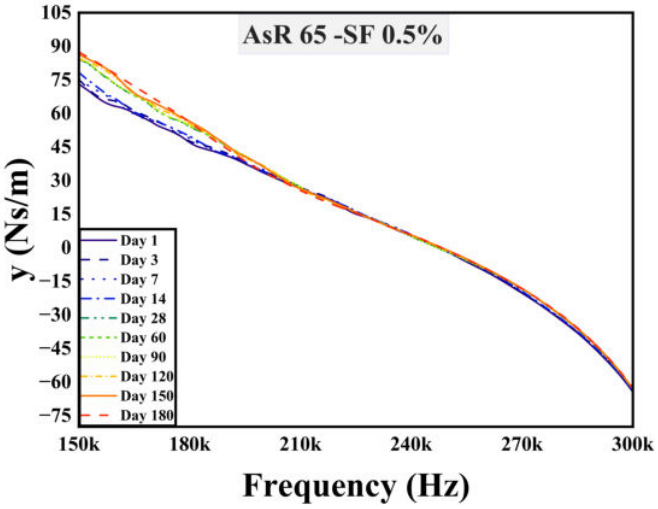

(b) y vs. frequency, SFC1 (AR 65, 0.5%).

Figure 4.8: Computed real (x) and imaginary (y) mechanical-impedance components across curing ages for SFC1 (Part 1).

For SFC1 (AR 65, 0.50% dosage), the real component x exhibits an initial resonance feature near 190 kHz at Day 1 that shifts in both frequency and amplitude across the 180-day monitoring period. The imaginary component y follows a continuous negative trajectory across the 150 to 300 kHz range, with the age-dependent separation concentrated below 210 kHz. The paired components are retained together for the equivalent parameter extraction rather than assigning estimates from a single frequency point.

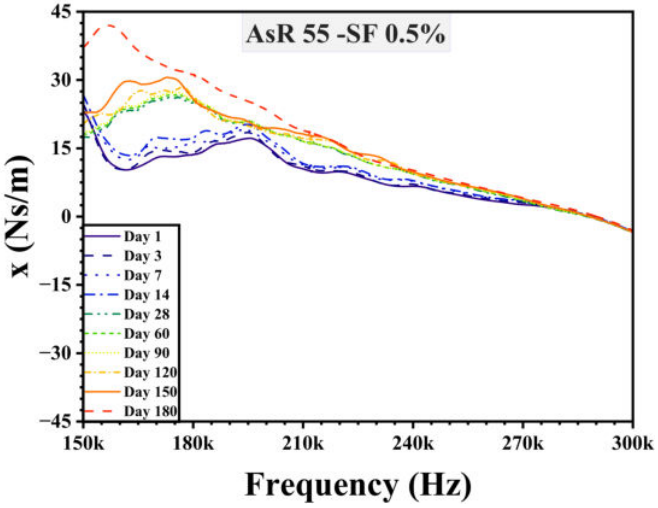

(c) x vs. frequency, SFC2 (AR 55, 0.5%).

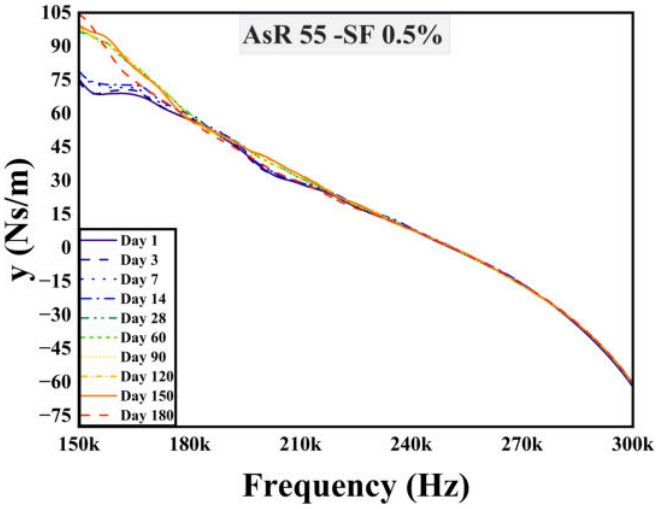

(d) y vs. frequency, SFC2 (AR 55, 0.5%).

Figure 4.8: Computed real (x) and imaginary (y) mechanical-impedance components across curing ages for SFC2 (continued).

The SFC2 impedance components share the general frequency-dependent form observed for SFC1 but differ in absolute magnitude, consistent with the installation-specific variation documented in the raw conductance and susceptance signatures. The x component retains clear age-dependent separation in the lower portion of the 150 to 300 kHz range, while the y component displays a comparatively uniform background. These paired components are retained for the EPS extraction without assuming which component carries greater curing-age sensitivity.

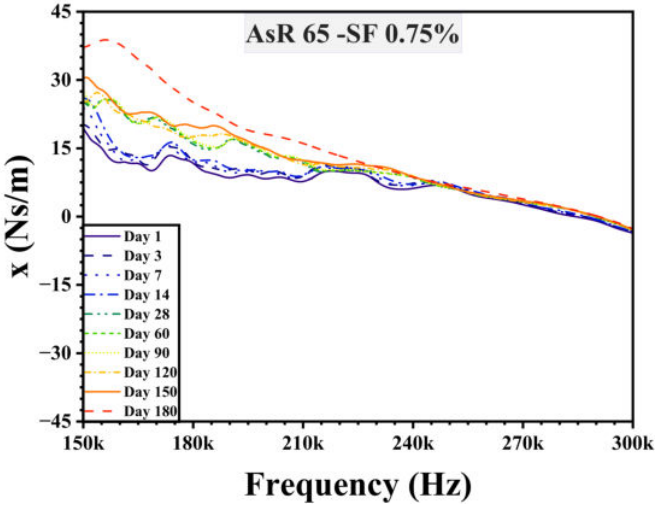

(e) x vs. frequency, SFC3 (AR 65, 0.75%).

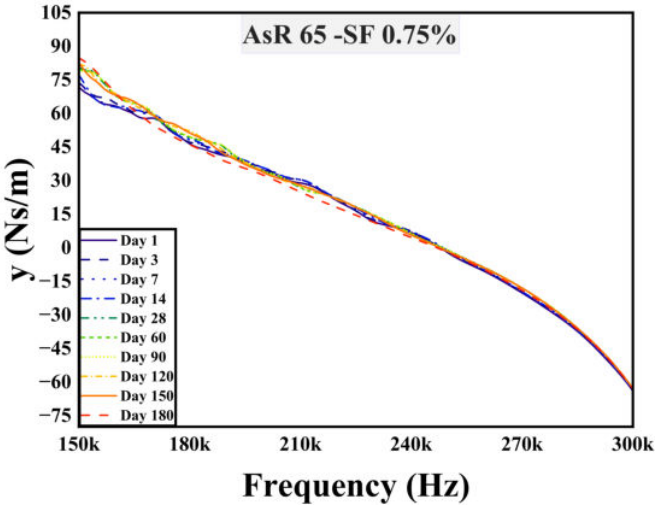

(f) y vs. frequency, SFC3 (AR 65, 0.75%).

Figure 4.8: Computed real (x) and imaginary (y) mechanical-impedance components across curing ages for SFC3 (continued).

SFC3 shares the same fibre aspect ratio as SFC1 (AR 65) but at a higher volumetric dosage (0.75% versus 0.50%). The calculated impedance components display age-dependent separation in a pattern consistent with the other installations, although neither the magnitude of the x-component variation nor the y-component background level matches those of SFC1 or SFC2. This observation reinforces the sensor-specimen specificity described earlier and is consistent with the variable fit quality reported in Section 4.4.

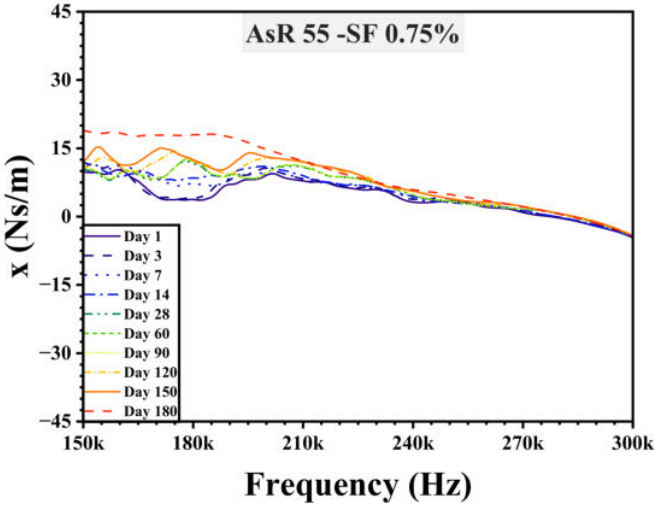

(a) x vs. frequency, SFC4 (AR 55, 0.75%).

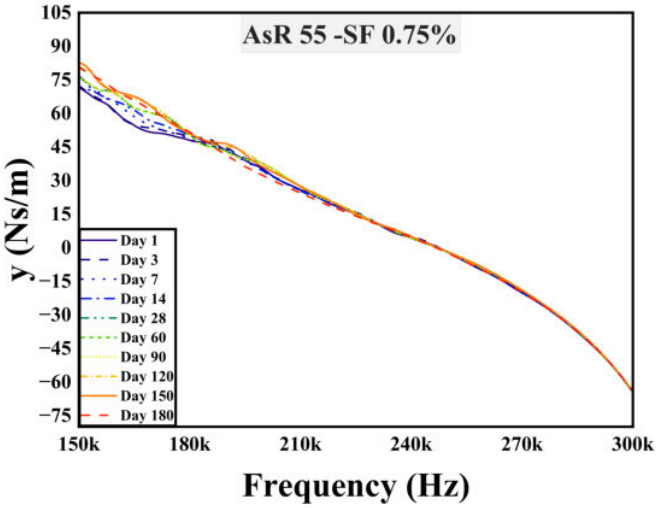

(b) y vs. frequency, SFC4 (AR 55, 0.75%).

Figure 4.9: Computed real (x) and imaginary (y) mechanical-impedance components across curing ages for SFC4.

For SFC4, the age-dependent separation in both components follows the same general direction as the other three installations but at different absolute magnitudes. The difference between SFC4 and the remaining configurations is notable in the x-component amplitude and is consistent with the distinct JPS4 conductance and peak-tracking records. Because the source data do not permit attribution of this difference to a single factor, the impedance components are carried forward to the EPS calculation on the same basis as SFC1 to SFC3.

EPS were obtained using Equations 3.7–3.9. They describe the local, model-dependent response of the coupled JPS-concrete system and are not the physical mass, static elastic modulus, or global damping of the complete cube.

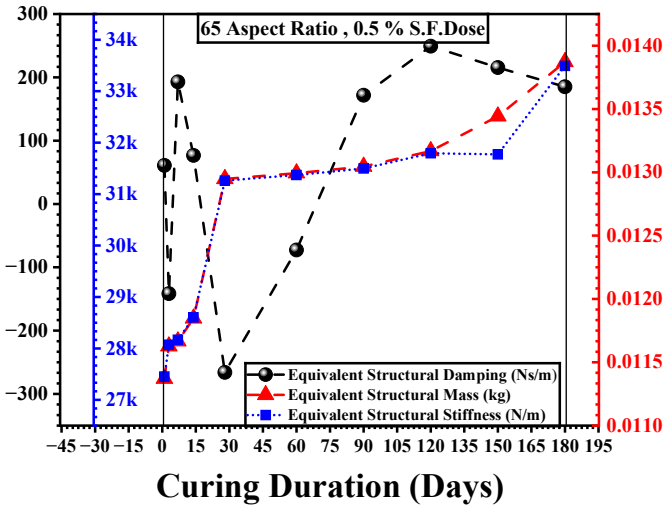

(a) SFC1: AR 65, 0.50% dosage.

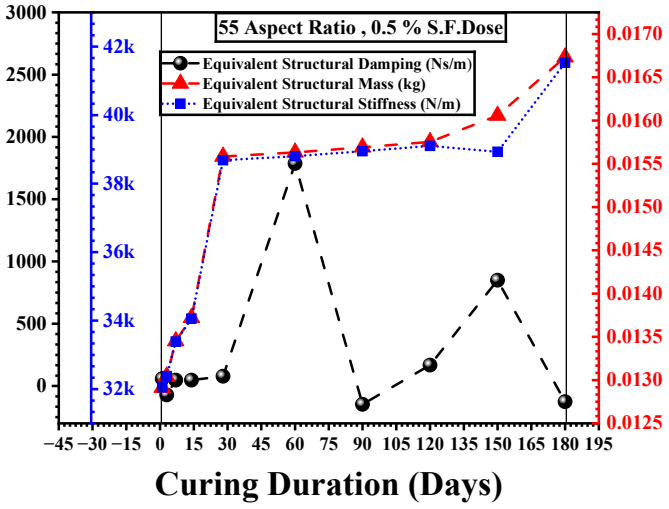

(b) SFC2: AR 55, 0.50% dosage.

Figure 4.10: EPS for the four SFRC configurations across the curing period (Part 1).

Figure 4.10 presents the EPS values with curing age. For SFC1 and SFC2, the equivalent stiffness values range from approximately 27 to 42 kN/m across the 180-day curing period. The fitted mass and damping terms vary more irregularly than the stiffness term, reflecting the local sensor-specimen coupling rather than a property of the complete specimen.

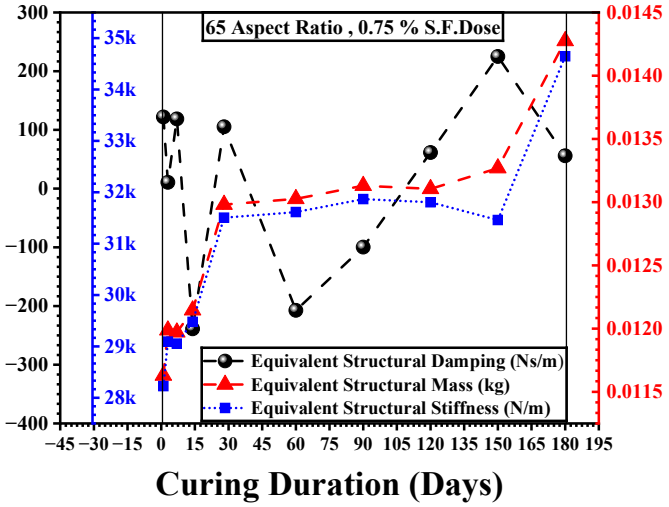

(c) SFC3: AR 65, 0.75% dosage.

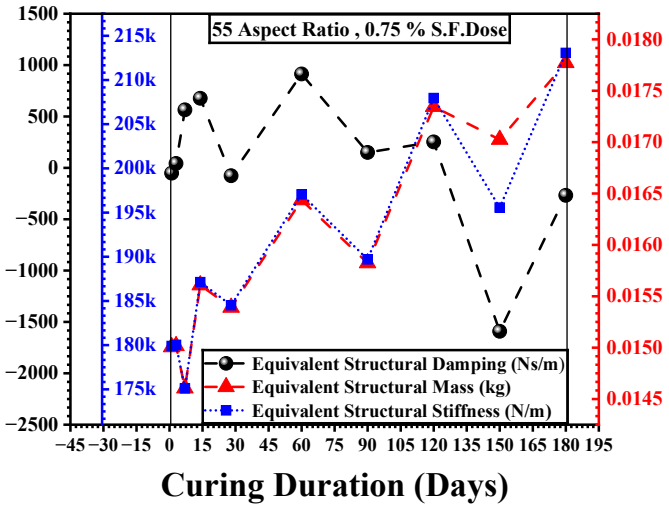

(d) SFC4: AR 55, 0.75% dosage.

Figure 4.10: EPS for the four SFRC configurations across the curing period (continued).

SFC3 has equivalent stiffness values comparable to SFC1 and SFC2, whereas SFC4 produces values of approximately 180 to 213 kN/m, notably higher than the other three installations. The source data do not establish a unique cause for this magnitude difference; it is therefore not attributed exclusively to fibre dosage or aspect ratio. This reinforces the principle that EPS changes are compared within each unchanged sensor installation rather than across sensors as if the parameters measured a common absolute property.

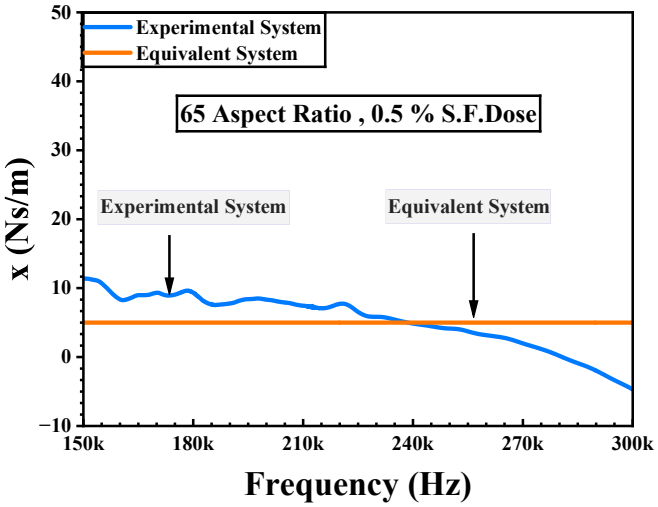

(a) x vs. freq, SFC1 (AR 65, 0.5%).

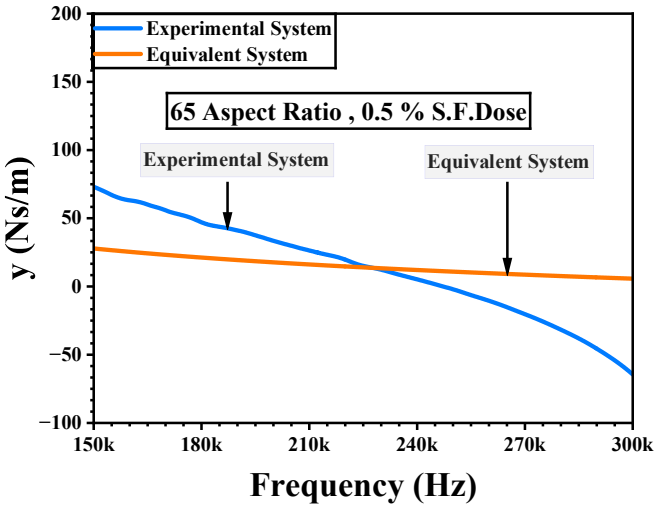

(b) y vs. freq, SFC1 (AR 65, 0.5%).

Figure 4.11: Reconstructed and experimental (x, y) spectra for SFC1 (Part 1).

The extracted EPS were substituted into the forward relations of Equations 3.10 and 3.11. Figures 4.11 and 4.12 compare the reconstructed and measured impedance components. The reconstructed x and y spectra for SFC1, obtained by substituting the extracted equivalent parameters into the forward model relations, are compared with the measured response over the 150 to 300 kHz range. The reconstructed curves reproduce the primary shape of the measured response near the selected resonance, while visible differences appear at frequencies outside that immediate region. Because no independent reconstruction-error metric is reported, the overlay serves as an internal consistency check on the adopted formulation.

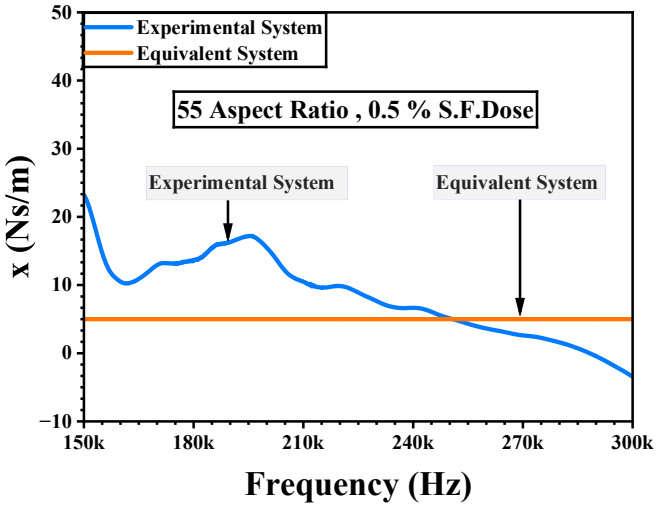

(c) x vs. freq, SFC2 (AR 55, 0.5%).

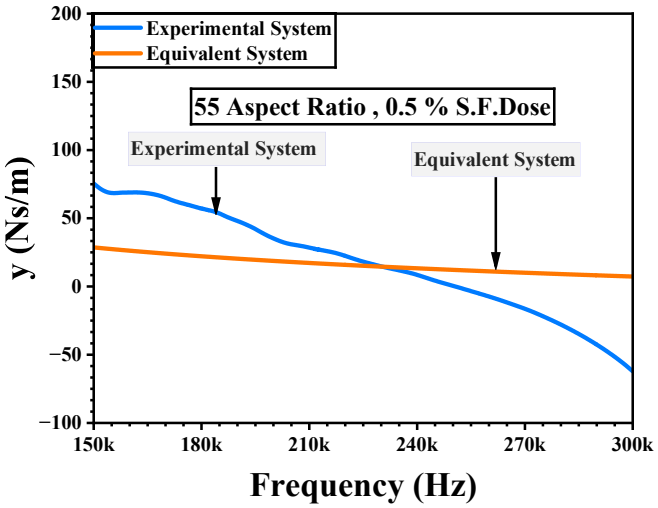

(d) y vs. freq, SFC2 (AR 55, 0.5%).

Figure 4.11: Reconstructed and experimental (x, y) spectra for SFC2 (continued).

For SFC2, the correspondence between the reconstructed and measured curves is broadly similar to that observed for SFC1. The reconstructed response captures the dominant frequency-dependent form near the resonance while pointwise variations in the measured curves remain visible. This result is consistent with the role of the equivalent representation as a compact parametric summary of the local coupled response rather than a detailed reproduction of the complete measured signal.

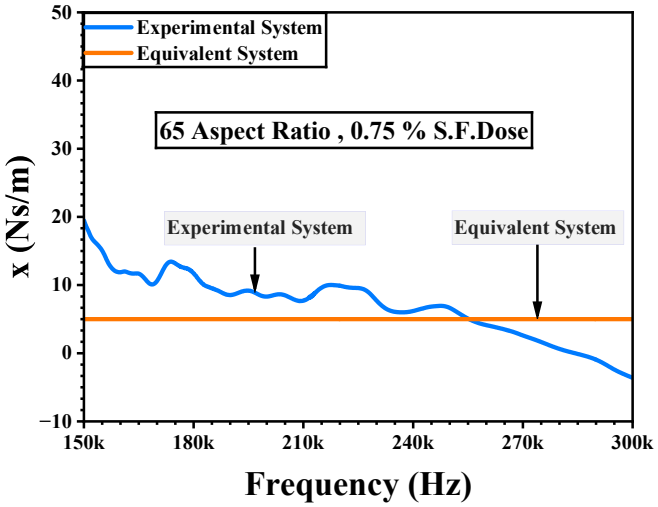

(e) x vs. freq, SFC3 (AR 65, 0.75%).

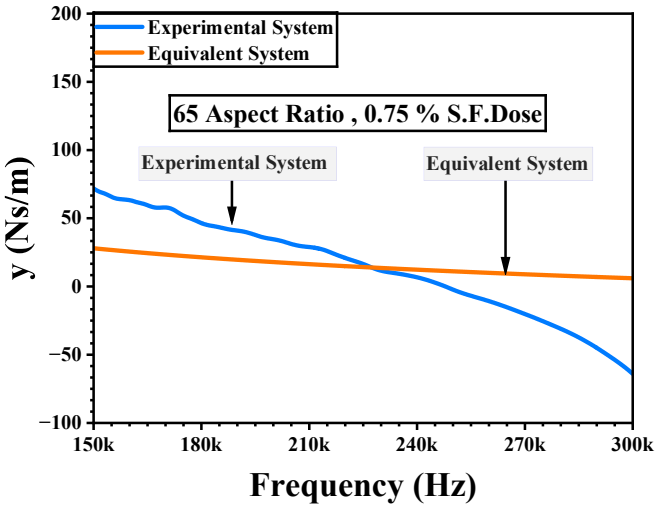

(f) y vs. freq, SFC3 (AR 65, 0.75%).

Figure 4.11: Reconstructed and experimental (x, y) spectra for SFC3 (continued).

SFC3 shows comparable correspondence between the reconstructed and measured curves near the selected resonance. The curing-age-dependent progression in the reconstructed curves follows the same direction as the measured records, confirming that the extracted EPS capture the principal age-related changes in the coupled JPS3 and concrete system. Differences at other frequencies are consistent with the limited degrees of freedom in the single-resonance formulation and do not affect the parametric comparison in Section 4.8.

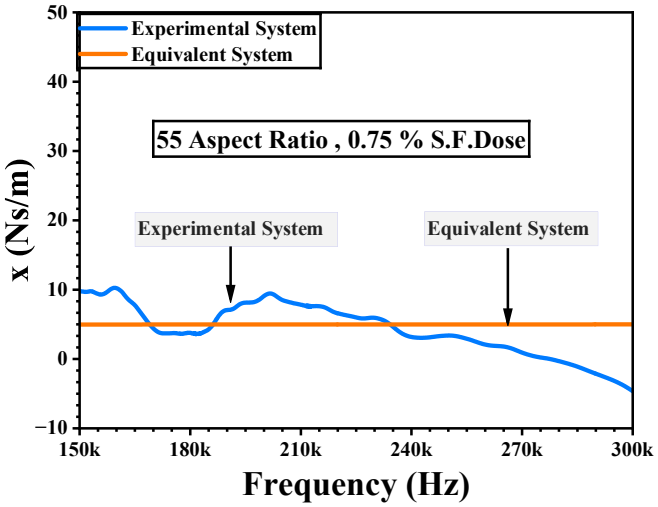

(a) x vs. freq, SFC4 (AR 55, 0.75%).

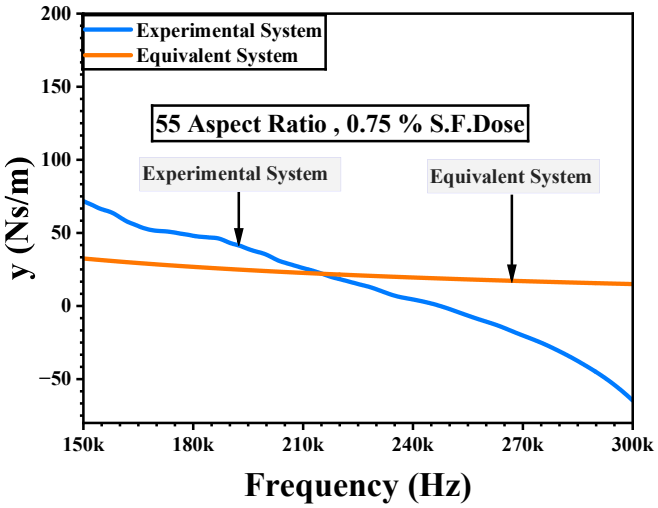

(b) y vs. freq, SFC4 (AR 55, 0.75%).

Figure 4.12: Reconstructed and experimental (x, y) spectra for SFC4.

For SFC4, the distinct absolute magnitude of the calculated impedance components results in reconstructed curves that are visually separated from those of the other three configurations. The single-degree-of-freedom representation nevertheless follows the measured form near the selected resonance for each curing age. The three extracted EPS therefore provide a compact, model-dependent description of the SFC4 system that can be compared with its own age-matched strength record in the following section.

4.8 Comparison of Equivalent Stiffness with Compressive Strength

Equivalent stiffness from each monitored JPS cube was paired with the corresponding age- and mixture-matched compressive-strength record. Linear relations of the form $k = \alpha f_c + \beta$ were fitted separately to the ten observations for each configuration.

The resulting empirical calibration equations for the four configurations are:

$$k_{\mathrm{JPS1}} = 82.505\, f_c + 26656.32 \quad (R^2 = 0.9397) \tag{4.2}$$

$$k_{\mathrm{JPS2}} = 139.27\, f_c + 30624.85 \quad (R^2 = 0.9567) \tag{4.3}$$

$$k_{\mathrm{JPS3}} = 68.59\, f_c + 27703.86 \quad (R^2 = 0.7976) \tag{4.4}$$

$$k_{\mathrm{JPS4}} = 380.81\, f_c + 173489.80 \quad (R^2 = 0.5834) \tag{4.5}$$

These equations compare measurements made at the same curing ages, but the paired values do not come from the same physical cube. The slope and intercept also include the absolute scale of the corresponding JPS installation. The equations are therefore evaluated separately for SFC1–SFC4 and are not combined into one calibration. The individual fits give R^2 values of 0.9397, 0.9567, 0.7976, and 0.5834 for JPS1 to JPS4, respectively.

The fitted linear slopes vary across the four installations, ranging from 68.59 to 380.81 N/m per MPa. This variation reflects the local mechanical coupling between each embedded transducer and the surrounding concrete rather than an intrinsic difference in material sensitivity alone. Because each JPS cube possesses a distinct sensor installation and interface boundary, the empirical calibration equations cannot be transferred from one installation to another without specimen-specific baseline data. The individual regressions are therefore evaluated separately in the following subsections, with each scatter plot paired alongside the corresponding time-ordered equivalent stiffness record.

The high coefficient of determination ($R^2 > 0.93$) obtained for SFC1 and SFC2 indicates that equivalent dynamic stiffness closely tracks the time progression of compressive strength in these configurations. For SFC3 and SFC4, the lower R^2 values reflect greater variability in the local sensor-matrix interface, demonstrating that individual calibration fits are necessary for each installation. The empirical curves confirm that dynamic stiffness measurements provide a reliable non-destructive indicator of curing progress when interpreted within an unbroken monitoring sequence.

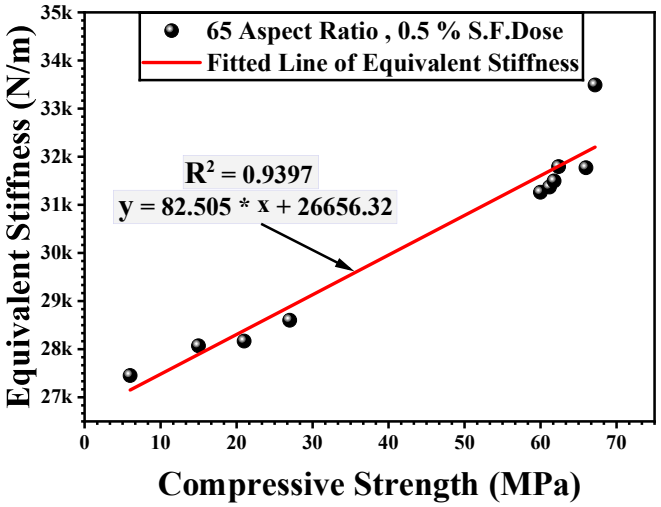

(a) k vs. f_c, SFC1 (AR 65, 0.5%).

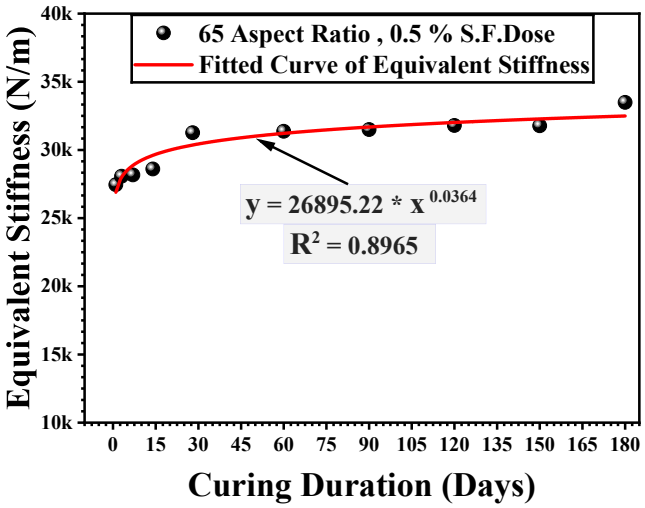

(b) k vs. curing age, SFC1 (AR 65, 0.5%).

Figure 4.13: Equivalent stiffness in relation to compressive strength and curing age for SFC1 (Part 1).

For SFC1, the linear relation $k = 82.505\, f_c + 26656.32$ yields an in-sample R^2 of 0.9397 over the ten age-matched observations. Both the scatter plot and the corresponding age-based stiffness curve show that the matched values change more rapidly during the initial curing ages than after Day 28. The fitted slope and offset include the absolute response scale of the JPS1 installation and are therefore not directly comparable with those of the other three configurations.

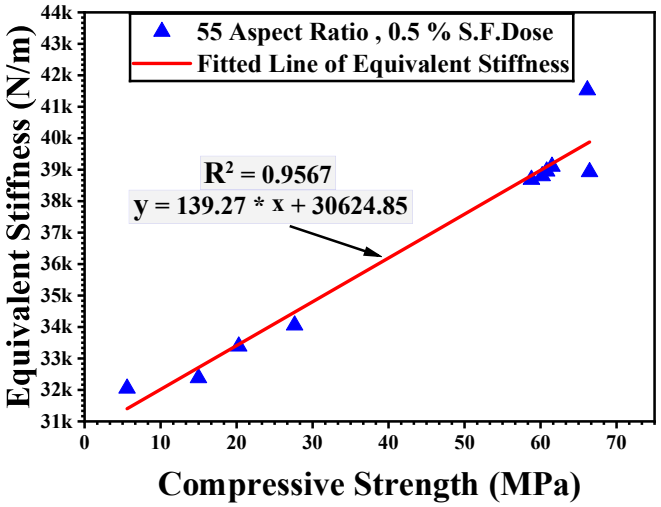

(c) k vs. f_c, SFC2 (AR 55, 0.5%).

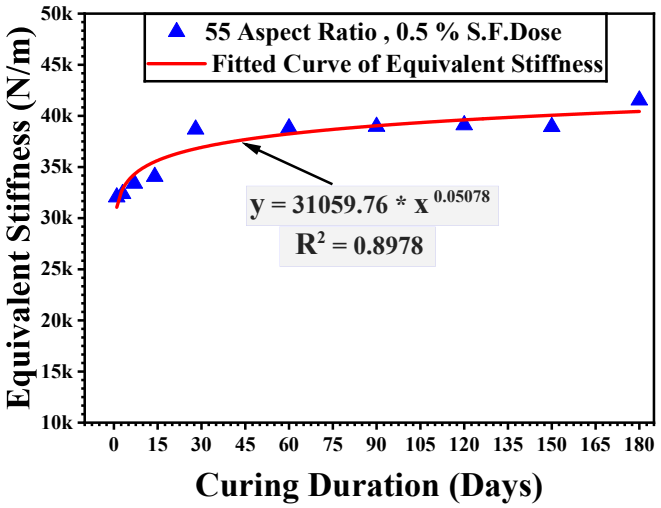

(d) k vs. curing age, SFC2 (AR 55, 0.5%).

Figure 4.13: Equivalent stiffness in relation to compressive strength and curing age for SFC2 (continued).

SFC2 produces the closest linear association among the four configurations, with $R^2 = 0.9567$ and a fitted slope of 139.27 N/m per MPa. The higher slope does not imply greater material sensitivity; the value also contains the absolute stiffness scale of the JPS2 and concrete system. The time-ordered stiffness curve confirms that the equivalent stiffness record mirrors the measured compressive-strength progression: rapid initial increase followed by smaller changes beyond Day 28.

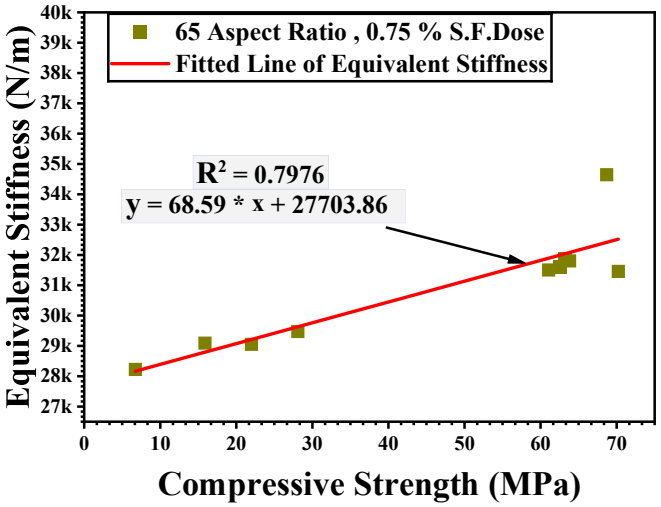

(e) k vs. f_c, SFC3 (AR 65, 0.75%).

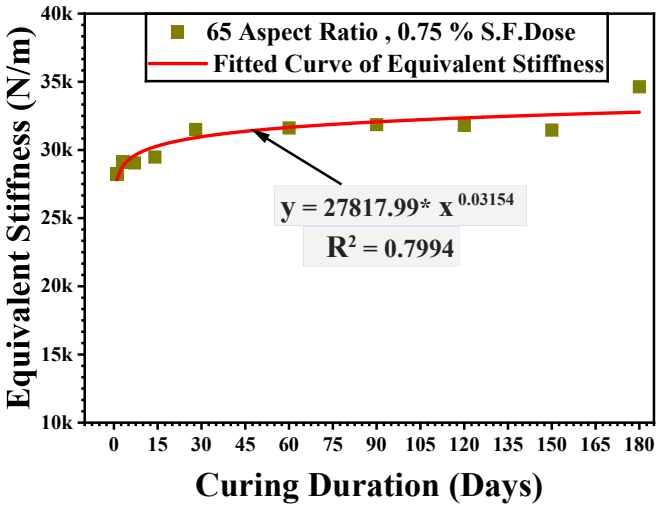

(f) k vs. curing age, SFC3 (AR 65, 0.75%).

Figure 4.13: Equivalent stiffness in relation to compressive strength and curing age for SFC3 (continued).

The SFC3 relation has the smallest fitted slope (68.59 N/m per MPa) and an R^2 of 0.7976. Greater scatter among the ten age-matched observations is visible in the corresponding plot. This R^2 value does not invalidate the age-matched comparison; the result indicates that the installation-specific response of JPS3 does not follow the same linear proportion as JPS1 or JPS2 over the tested curing duration.

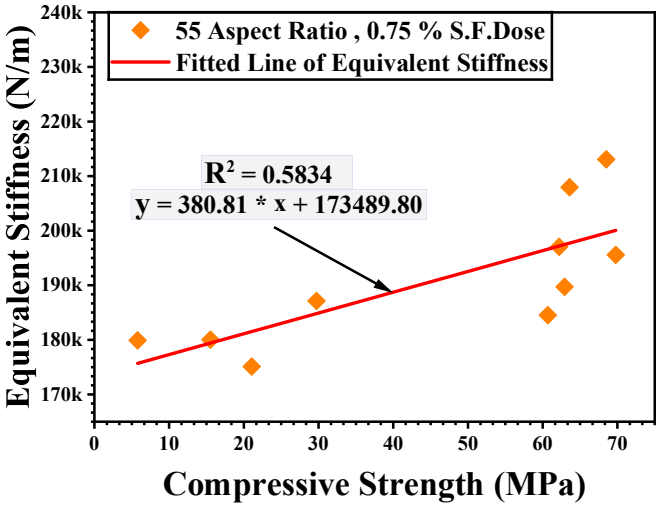

(a) k vs. f_c, SFC4 (AR 55, 0.75%).

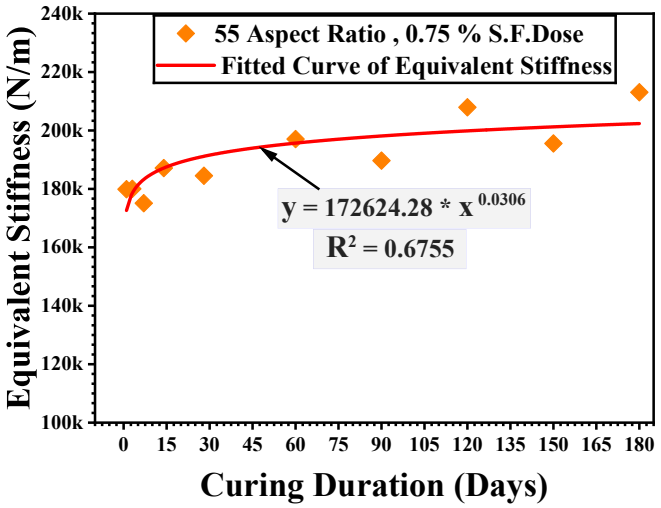

(b) k vs. curing age, SFC4 (AR 55, 0.75%).

Figure 4.14: Equivalent stiffness in relation to compressive strength and curing age for SFC4.

SFC4 has an R^2 of 0.5834 and the largest fitted slope (380.81 N/m per MPa), reflecting the distinct absolute stiffness scale noted in the EPS results. The combination of high absolute stiffness and greater data scatter demonstrates that equivalent stiffness and compressive strength do not maintain the same proportional relation across all four sensor-specimen installations. These results confirm that replicated monitoring specimens and an external calibration dataset are necessary before such empirical relations can be applied to other configurations.

Figures 4.13 and 4.14 display the measured pairs, their separate fitted lines, and the corresponding age-based stiffness curves. The figure sequence therefore preserves both the paired comparison and the time ordering from which it was formed.

4.9 Summary

This chapter examined scheduled, non-destructive JPS measurements over 180 days for four SFRC configurations and compared them with separately obtained, age-matched compressive-strength records.

The primary findings of the chapter are summarized as follows:

1. Measured signatures: Conductance resonances and the susceptance background changed with curing age. The retained conductance peak moved to higher frequency through Day 7, was lower at Day 14, and then moved to higher frequency through Day 180.

2. Peak quantities: The 150–300 kHz results show larger early-age changes and smaller long-term changes, but the empirical fit quality varies substantially among the four monitored systems.

3. Strength development: The measured Day-28 strengths are approximately 88.6–89.3% of the respective measured Day-180 values. This provides an age-matched comparison with the JPS trends, not a same-specimen validation.

4. Statistical indices: The four indices describe configuration-specific differences from the Day-1 signature without assigning those differences to a unique physical mechanism.

5. Equivalent parameters: The fixed Chapter 3 procedure gives local EPS for each installation. The stiffness–strength R^2 values range from 0.5834 to 0.9567, showing that the fitted relation depends on the sensor and configuration.

Within the tested laboratory programme, repeated JPS measurements recorded curing-age-related changes over an extended period. The results support comparison over time within an unchanged installation. Replicated monitoring specimens and independent validation remain necessary before the fitted relations can be transferred to other specimens or field conditions.

CHAPTER 5

MECHANICAL DAMAGE DETECTION IN STEEL FIBRE CONCRETE USING NON-BONDED PIEZO SENSORS

5.1 General

This chapter examines reusable NBPS measurements obtained before and after destructive compression and splitting-tensile tests on SFRC. The two loading programmes use the same thirteen mixture configurations, enabling the measured mechanical strengths, spectral changes, statistical indices, and EPS to be interpreted within a common experimental matrix.

The analysis first establishes the destructive-strength response of each configuration and then compares the corresponding pre-loading and post-loading conductance signatures. Selected resonance features, full-signature indices, and model-derived parameters provide different measures of the recorded change. The final comparison distinguishes the response associated with the two loading modes while retaining the limits of the tested materials, geometries, and sensor arrangement.

5.2 Common Experimental and Analytical Basis

5.2.1 Specimen Matrix

The experimental matrix contains 39 SFRC cubes for compression and 39 SFRC cylinders for split-tensile loading. Each programme comprises one plain-concrete control (0% fibre) alongside six volumetric fibre dosages (0.25%, 0.50%, 0.75%, 1.00%, 1.25%, and 1.50%) for each of the AR 55 and AR 65 steel fibre types. This provides thirteen configurations (1 + 6 + 6 = 13), with three physical specimens tested per configuration. The plain-concrete control serves as the 0% baseline for both the AR 55 and AR 65 series.

Table 5.1: The thirteen-configuration experimental matrix evaluated for both compressive (cube) and split-tensile (cylinder) loading

ID	Geometry	Aspect Ratio	Dosage (%)	Replicates	Mechanical Test	EMI Acquisition
C0	Cubes / Cylinders	N/A	0.00	3 / 3	Comp / Split-Tension	Pre & Post-loading
C1	Cubes / Cylinders	65	0.25	3 / 3	Comp / Split-Tension	Pre & Post-loading
C2	Cubes / Cylinders	65	0.50	3 / 3	Comp / Split-Tension	Pre & Post-loading
C3	Cubes / Cylinders	65	0.75	3 / 3	Comp / Split-Tension	Pre & Post-loading
C4	Cubes / Cylinders	65	1.00	3 / 3	Comp / Split-Tension	Pre & Post-loading
C5	Cubes / Cylinders	65	1.25	3 / 3	Comp / Split-Tension	Pre & Post-loading
C6	Cubes / Cylinders	65	1.50	3 / 3	Comp / Split-Tension	Pre & Post-loading
C7	Cubes / Cylinders	55	0.25	3 / 3	Comp / Split-Tension	Pre & Post-loading
C8	Cubes / Cylinders	55	0.50	3 / 3	Comp / Split-Tension	Pre & Post-loading
C9	Cubes / Cylinders	55	0.75	3 / 3	Comp / Split-Tension	Pre & Post-loading
C10	Cubes / Cylinders	55	1.00	3 / 3	Comp / Split-Tension	Pre & Post-loading
C11	Cubes / Cylinders	55	1.25	3 / 3	Comp / Split-Tension	Pre & Post-loading
C12	Cubes / Cylinders	55	1.50	3 / 3	Comp / Split-Tension	Pre & Post-loading

5.2.2 NBPS Measurement Protocol

The specimen matrix and acquisition procedure are detailed in Chapter 3. For each comparison, the reusable NBPS was positioned at the marked measurement location using the prescribed PTFE shims. Conductance (G) and susceptance (B) were recorded over 30–1000 kHz before loading. The sensor was then removed, the specimen was tested destructively in the 2000 kN compression testing machine, and the NBPS was reinstalled at the same location for the post-loading measurement. The paired records therefore represent the initial and residual states obtained with the same installation procedure.

5.2.3 EMI Measures Used in the Analysis

The spectral analysis uses several frequency windows, defined by their purpose:

- 30–1000 kHz: Full-band acquisition for initial screening and resonance identification.
- 150–200 kHz: Selected resonance region for tracking specific peak shifts.
- 150–230 kHz: Frequency range used for statistical comparison (RMSD and MAPD) around the selected resonance.
- 150–300 kHz: Frequency range used for impedance-component extraction and EPS calculation.

Peak 1 was tracked because it remained identifiable across the analysed configurations and represents the first selected resonance of the coupled PZT–carrier–shim–

concrete system. RMSD and MAPD were calculated from the paired pre-loading and post-loading conductance records using the definitions in Chapter 3. Equivalent mass m, stiffness k, and damping c were obtained from the series-mobility formulation in Section 3.11.

5.3 Compressive Damage Assessment

5.3.1 Compressive Strength Results

A total of 39 SFRC cubes with 150 mm side length were tested in compression. The thirteen configurations and three-specimen allocation follow Table 5.1. The destructive results are reported as configuration means, whereas the spectral plots are interpreted as the paired responses presented for the corresponding configurations; no additional averaging is imposed on the plotted EMI quantities.

The destructive compression results provide the mechanical reference for interpreting the local NBPS response and its variation with fibre dosage.

Figure 5.1 presents the 28-day mean compressive strengths and the reported standard-deviation error bars for three cubes per configuration. The numerical standard deviations are not reported, so they cannot be restated numerically. Within the tested range, both aspect-ratio series reach their maximum measured mean at 0.75% fibre: 60.95 MPa for AR 65 and 59.90 MPa for AR 55. Relative to the single 41.32 MPa control, these are increases of 47.5% and 44.9%, respectively. At 1.50%, the means are 56.50 and 55.30 MPa. The result identifies the measured maximum within the tested materials and dosage range.

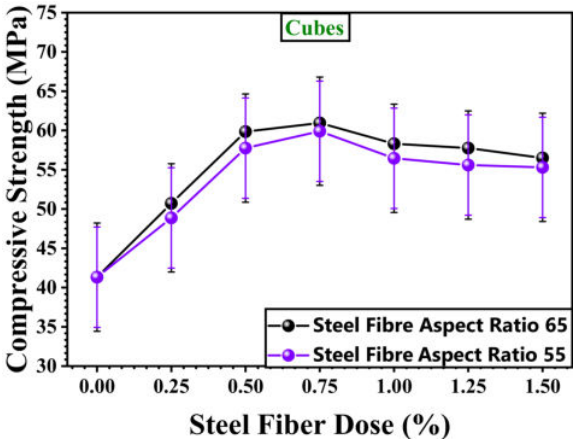

Figure 5.1: Compressive strength development in SFRC specimens as a function of steel fibre dosage and aspect ratio (28 days).

Table 5.2: Mean 28-day compressive strength for three cubes per SFRC configuration

SFCM Dose (%)	Compressive Strength (MPa)	
	Cube Aspect Ratio 65	Cube Aspect Ratio 55
0	41.32	41.32
0.25	50.71	48.87
0.5	59.84	57.75
0.75	60.95	59.9
1	58.31	56.45
1.25	57.75	55.6
1.5	56.5	55.3

Table 5.2 reports the configuration-level compressive-strength means alongside the bar-chart results in Figure 5.1. For both aspect-ratio series, the highest measured mean occurs at 0.75% fibre dosage: 60.95 MPa for AR 65 and 59.90 MPa for AR 55, representing increases of 47.5% and 44.9% relative to the 41.32 MPa plain-concrete control. At the upper tested dosage of 1.50%, the means decrease to 56.50 and 55.30 MPa, respectively. The plain-concrete value is listed in both columns for visual comparison but is counted once in the thirteen configurations. The standard-deviation error bars in Figure 5.1 are shown as reported; their numerical values are not separately tabulated and therefore cannot be restated here. These destructive-strength results provide the mechanical reference for interpreting the spectral and EPS changes in the sections that follow.

5.3.2 Healthy and Post-Damage Spectra

Figures 5.2 and 5.3 present the reported peak-conductance and resonant-frequency series before and after compression. The full 30–1000 kHz acquisition band was used to screen the spectra, while the selected resonance was examined within the approximately 150–200 kHz region. The plotted series retain the reported identifiable peak, and the paired changes provide the direct comparison between the pre-loading and post-loading states.

The strength and spectral responses provide complementary evidence. Both aspect-ratio series rise to their measured maximum at 0.75% fibre and then decrease gradually at the higher tested dosages. Resonant frequency and peak conductance are considered together because loading can alter both the position and amplitude of the selected resonance. The paired plots therefore compare each post-loading response directly with its corresponding pre-loading state.

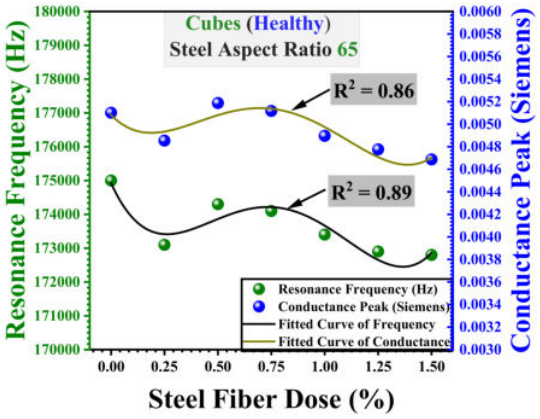

(a) Healthy state.

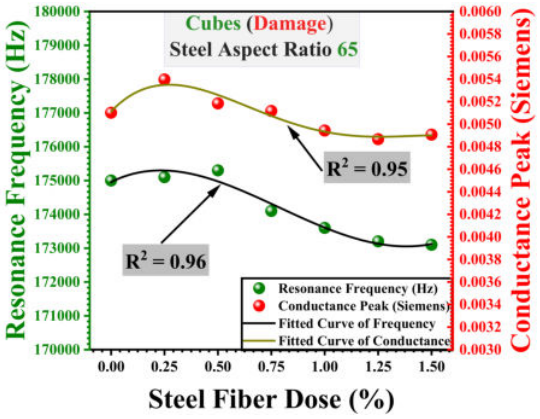

(b) Damaged state.

Figure 5.2: NBPS resonant frequency and peak conductance shifts for the AR 65 SFRC series.

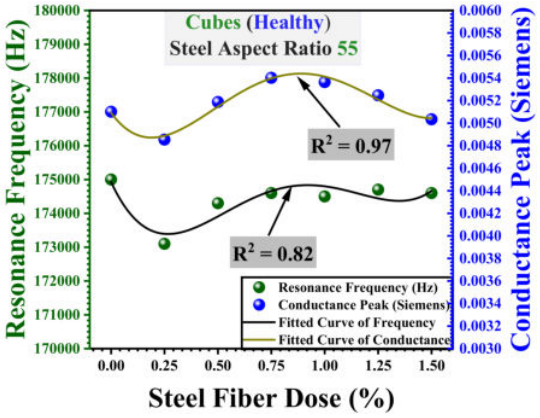

(a) Healthy state.

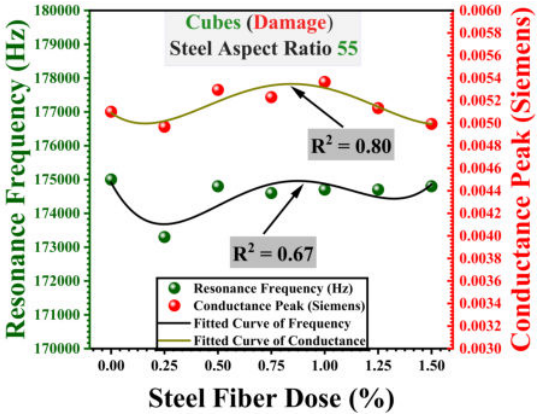

(b) Damaged state.

Figure 5.3: NBPS resonant frequency and peak conductance shifts for the AR 55 SFRC series.

The quartic curves in Table 5.3 are presented as descriptive interpolations of the seven tested dosage points. In these equations, x is the numerical fibre dosage in percent, from 0 to 1.50, and Y denotes resonant frequency or peak conductance. Five fitted coefficients for seven dosage levels leave little basis for extrapolation or mechanistic interpretation. The curves are therefore not used to establish damage physics, optimisation, or predictive validation. Fibre distribution was not measured, and differences between the AR 55 and AR 65 families cannot be attributed exclusively to aspect ratio.

Table 5.3: Descriptive quartic interpolations of SFRC conductance and resonant-frequency data over the tested dosages

SFCM Cubes – Healthy State		
AR 65	Frequency	$Y = 174924.025 - 13927.56x + 41193.93x^2 - 41810.1x^3 + 13284.84x^4$
	Conductance	$Y = 0.00508 - 0.00193x + 0.00722x^2 - 0.00805x^3 + 0.00266x^4$
AR 55	Frequency	$Y = 174927.922 - 13610.96x + 37951.51x^2 - 34747.47x^3 + 10278.78x^4$
	Conductance	$Y = 0.00509 - 0.00261x + 0.00924x^2 - 0.0089x^3 + 0.00259x^4$
SFCM Cubes – Damage State		
AR 65	Frequency	$Y = 174956.06 + 3150.50x - 8103.03x^2 + 3894.94x^3 - 290.90x^4$
	Conductance	$Y = 0.00511 + 0.002x - 0.00511x^2 + 0.00389x^3 - 0.000956x^4$
AR 55	Frequency	$Y = 174911.688 - 11678.78x + 34672.72x^2 - 33212.12x^3 + 10181.81x^4$
	Conductance	$Y = 0.00509 - 0.0013x + 0.00528x^2 - 0.00533x^3 + 0.00157x^4$

5.3.3 Statistical Signature-Difference Metrics

RMSD and MAPD were calculated over 150–230 kHz, centred on the selected resonance used for the mechanical-damage comparison. Here, G_{bl} is the pre-loading conductance signature and G_i is the corresponding post-loading signature.

The RMSD in Equation 3.12 measures normalised spectral distance. Figure 5.4 reports its dosage-dependent values, including a reported value of approximately 12.4% near the 0.75% AR 65 case. A larger RMSD means a larger signature difference and is not automatically evidence of higher strength, greater damage, or better fibre performance.

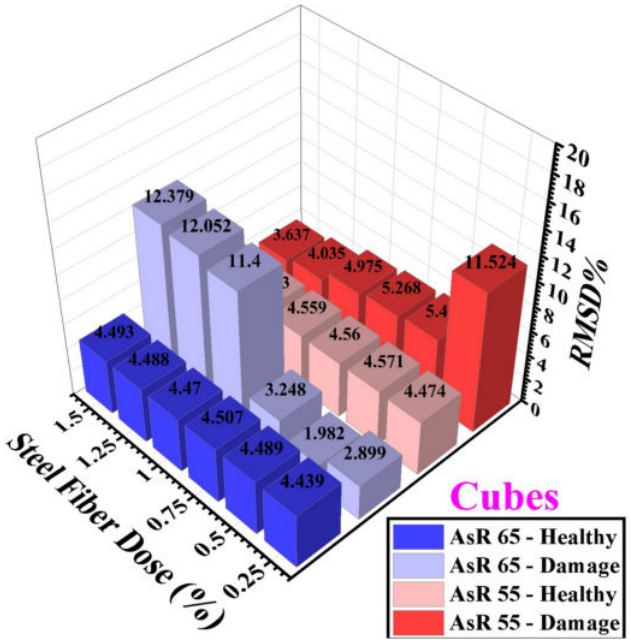

Figure 5.4: RMSD for the thirteen SFRC cube configurations.

The MAPD in Equation 3.13 measures the mean relative difference over the same

band. Figure 5.5 reports a value of approximately 9.5% near the 0.75% case. Because RMSD and MAPD use different normalisations, their numerical values are treated as different measures rather than ranked directly.

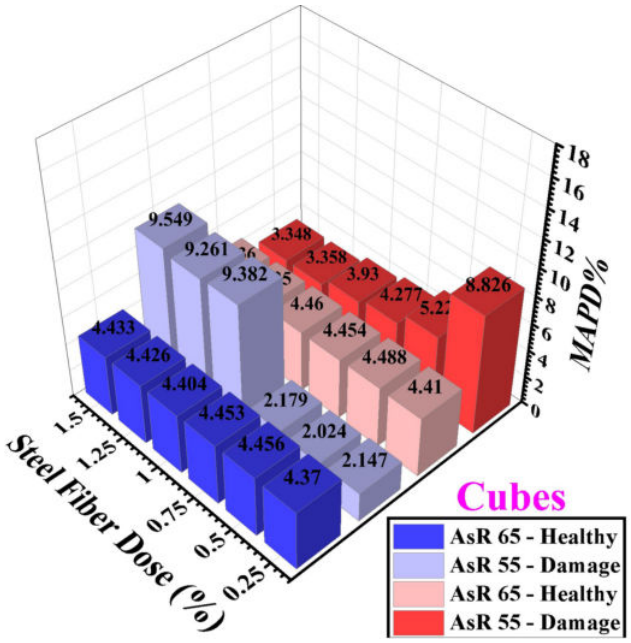

Figure 5.5: MAPD for the thirteen SFRC cube configurations.

The two quantities supplement the selected peak features but do not identify a unique damage mechanism. Section 5.4.7 therefore applies the model-dependent EPS representation to the same spectra.

5.3.4 Equivalent Stiffness and Normalised Stiffness Change

The relations in Section 3.10 transform the measured (G, B) spectra over 150–300 kHz into the real (x) and imaginary (y) components of the effective structural mechanical impedance. These are derived quantities, not raw conductance and susceptance. Figure 5.6 shows the resulting cube traces before and after loading.

Equivalent mass m, stiffness k, and damping c were extracted using the adopted series-mobility formulation in Section 3.11 (Equations 3.7–3.9) and its resonance boundary condition. These EPS values are local, model-dependent parameters describing the coupled NBPS–specimen system, not the total specimen mass, global static stiffness, or global damping.

Figure 5.7 reports the derived parameters for the healthy and damaged cube series. The extracted values were substituted into Equations 3.10 and 3.11; the resulting reconstructed and experimental traces are overlaid in Figure 5.8. The agreement is

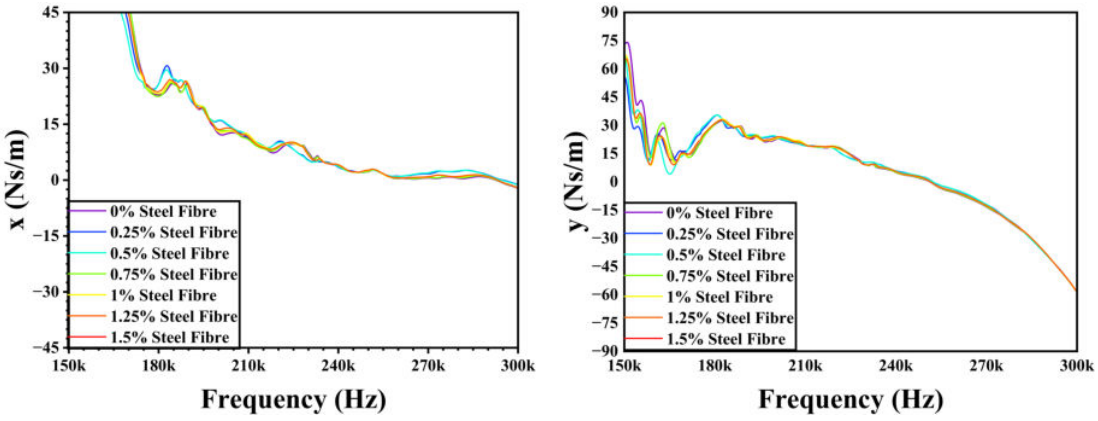

(a) *x* vs. frequency.

(b) *y* vs. frequency.

Figure 5.6: Mechanical-impedance components for the SFRC–NBPS cube series.

assessed from the experimental and reconstructed curves over the selected frequency range.

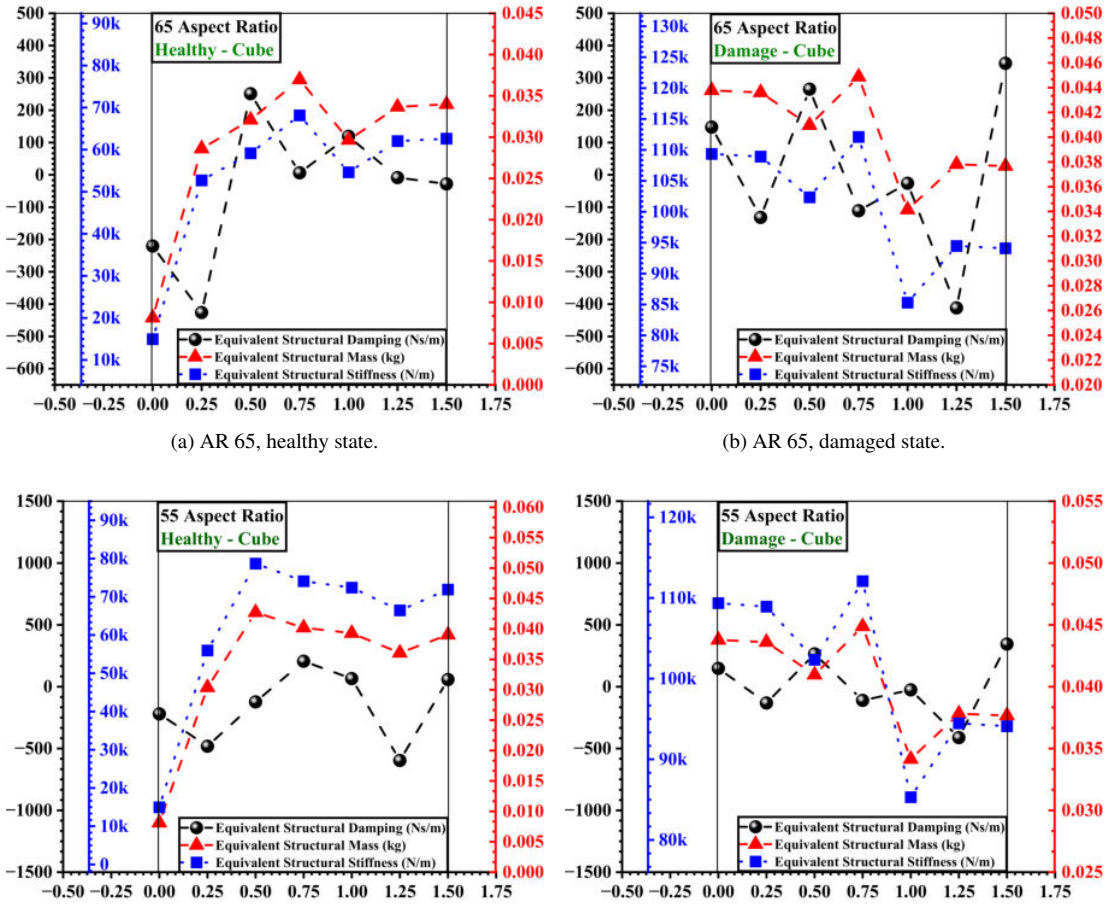

(a) AR 65, healthy state.

(b) AR 65, damaged state.

(c) AR 55, healthy state.

(d) AR 55, damaged state.

Figure 5.7: Fitted EPS parameters for healthy and damaged SFRC cubes.

Figure 5.7 is interpreted through matched healthy and damaged comparisons

within each aspect-ratio series. For the healthy cubes, the stiffness-like parameter generally increases with fibre dosage across the tested configurations for both the AR 65 and AR 55 series, although the absolute numerical levels differ between the two aspect-ratio families. This dosage-dependent pattern corresponds to the compressive-strength results reported in Section 5.3.1, where the highest measured mean occurs at 0.75% fibre. The mass-like and damping-like terms do not follow the same consistent upward pattern across all tested dosages: the mass-like parameter remains comparatively stable in most configurations, while the damping-like parameter displays greater variation from one dosage level to the next.

Following destructive compression, the damaged-state parameters differ from the corresponding healthy-state values by amounts that vary across the thirteen configurations. Evaluating the EPS change requires comparing the matched healthy and damaged states for each individual configuration rather than computing a single average across all tested mixtures. The direction and magnitude of the parameter changes depend on both fibre dosage and aspect ratio, but these two factors remain coupled with other configuration-specific influences such as specimen heterogeneity, sensor contact conditions, and local cracking patterns.

The model verification in Figure 5.8 evaluates whether the extracted parameters are internally consistent with the measured impedance components over the 150 to 300 kHz range. For each configuration and structural state, the equivalent model regenerates continuous $x(f)$ and $y(f)$ spectra from the three extracted quantities using Equations 3.10 and 3.11. The comparison evaluates the dominant frequency-dependent form rather than exact pointwise correspondence.

The observed variations in the equivalent structural parameters between the healthy and damaged states reflect the localized sensitivity of the NBPS sensing mechanism. Because the non-bonded configuration relies on surface contact mediated by the protective aluminium carrier and PTFE shims, the recorded electrical impedance is predominantly influenced by stiffness degradation in the immediate neighborhood of the sensor interface. Consequently, the quantitative index Δs derived in Section 5.3.5 provides a localized comparative indicator of mechanical disturbance rather than a volumetric measurement of total specimen degradation. This distinction is critical when contrasting the cube compression results with the split-tension cylinder response presented in Section 5.4.

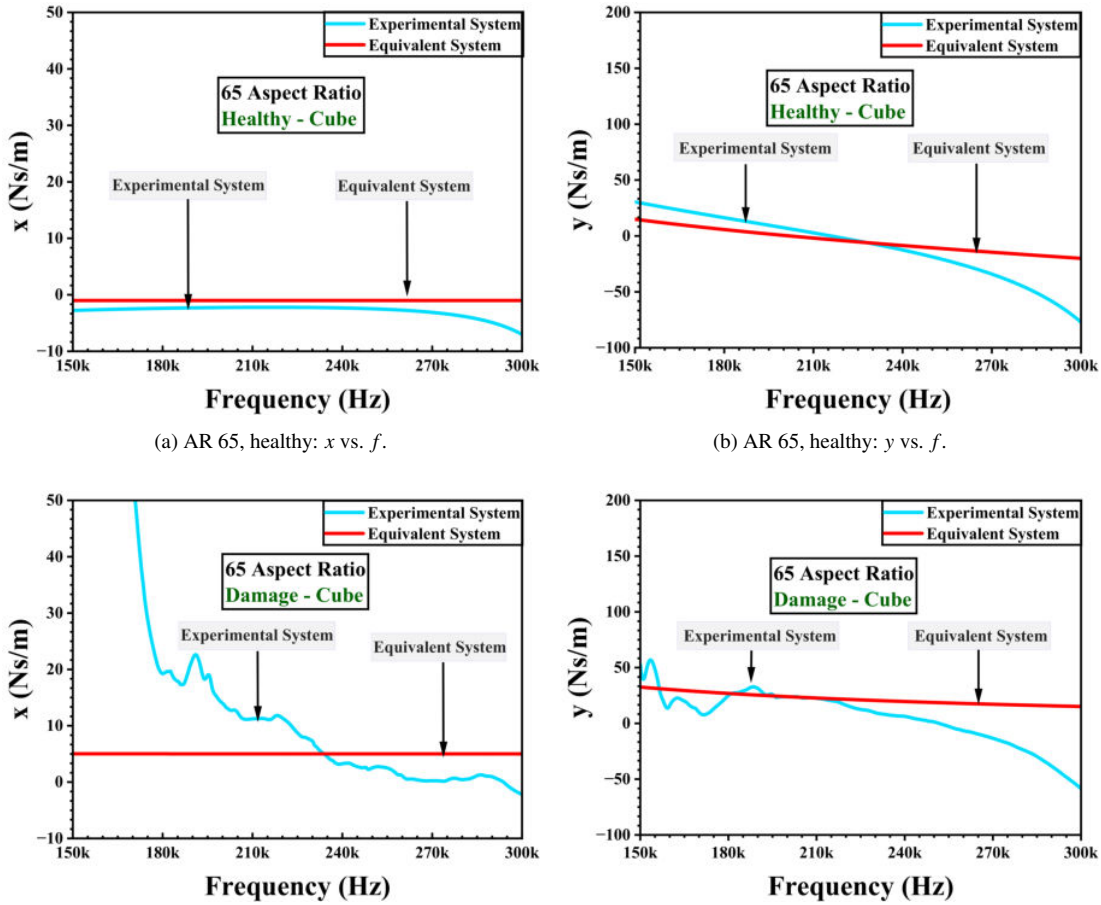

(a) AR 65, healthy: x vs. f.

(b) AR 65, healthy: y vs. f.

(c) AR 65, damaged: x vs. f.

(d) AR 65, damaged: y vs. f.

Figure 5.8: Measured and reconstructed spectra for the AR 65 cubes.

For AR 65, the reconstruction is evaluated against the dominant frequency-dependent tendency rather than against exact pointwise coincidence. The experimental curves retain local fluctuations that a low-order equivalent representation is not intended to reproduce. The healthy panels establish the pre-loading response, whereas the damaged panels show how the same representation follows the post-loading change over the selected band.

The comparison is consequently a model-consistency check, not a replacement of the measured spectra. Disagreement at an individual frequency remains visible and is not suppressed by the fitted curve. The following AR 55 panels apply the same formulation and frequency interval, permitting the second aspect-ratio series to be assessed on the same basis.

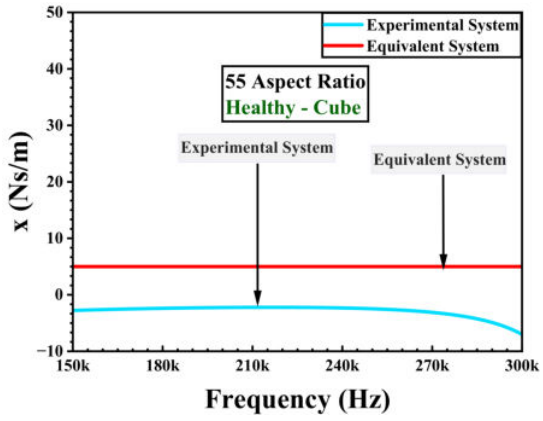

(e) AR 55, healthy: x vs. f.

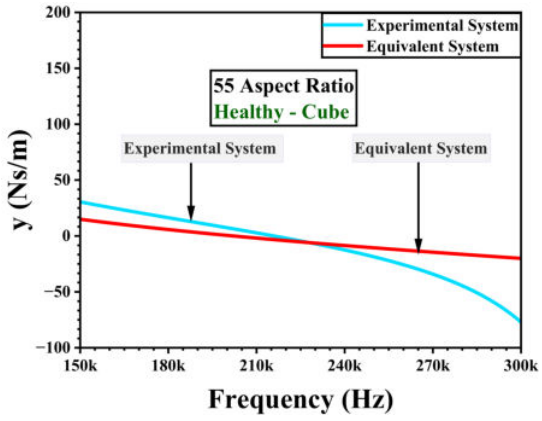

(f) AR 55, healthy: y vs. f.

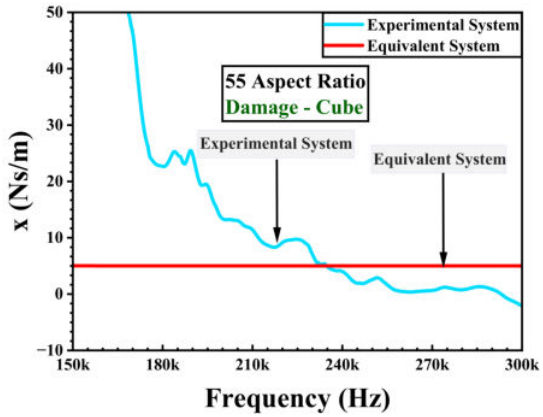

(g) AR 55, damaged: x vs. f.

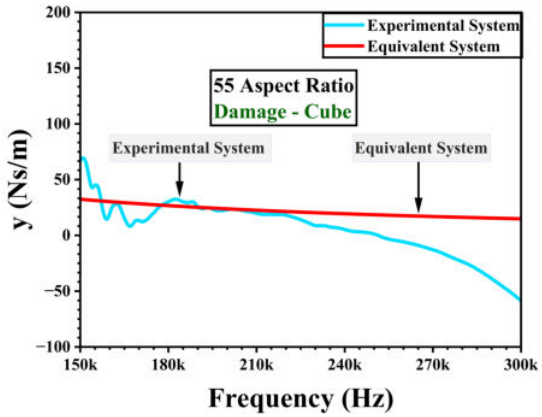

(h) AR 55, damaged: y vs. f.

Figure 5.8: Measured and reconstructed spectra for the AR 55 cubes (continued).

Across the two figures, the EPS results show configuration-dependent changes in m, k, and c between the matched healthy and damaged states. Equivalent damping varies more widely than mass and stiffness across the two aspect-ratio series. The fitted parameters describe the local coupled response represented by the selected resonance; they are not direct measurements of the total specimen mass, global static stiffness, or global damping. This interpretation provides the basis for the normalised stiffness-change measure introduced next.

5.3.5 Stiffness-Based Damage Index

The magnitude of the normalised equivalent-stiffness change is defined by Equation 5.1:

$$\Delta s = \left| \frac{k_{\text{healthy}} - k_{\text{damaged}}}{k_{\text{healthy}}} \right| \tag{5.1}$$

where Δs is the magnitude of the normalised change and is undefined if $k_{\text{healthy}} = 0$. Figure 5.9 reports the calculated values. The quadratic equations in Table 5.4 are descriptive fits with x defined as fibre dosage in percent; they are not used outside 0–1.50%.

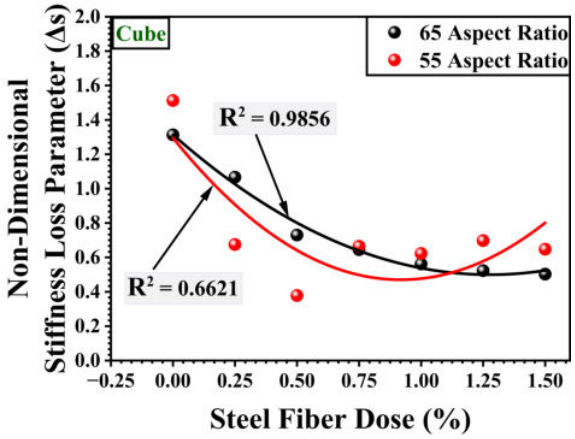

Figure 5.9: Normalised equivalent-stiffness change Δs for the SFRC cubes.

Figure 5.9 shows that the magnitude of the equivalent-stiffness change depends on both fibre dosage and aspect-ratio series. The AR 65 observations follow a comparatively smooth reduction over the tested dosage range, whereas the AR 55 observations show greater point-to-point variation. The plain-concrete control provides the common zero-dosage reference, after which the two fitted curves describe the measured configuration trends. These results are used as comparative indicators of the local NBPS–specimen response and not as direct percentages of global stiffness loss.

Table 5.4: Descriptive quadratic fits for Δs versus fibre dosage over 0–1.50%

Steel Fibre	**SFCM Cubes**
Aspect Ratio 65	$\Delta s = 1.3139 - 1.275x - 0.4993x^2$
Aspect Ratio 55	$\Delta s = 1.2955 - 1.797x + 0.9791x^2$

The Δs series vary with dosage and differ between the two aspect-ratio series. The fitted curves describe these measured trends only over 0–1.50%. Because Δs is calculated from model-derived local stiffness, it is used here to compare the magnitude of change in the coupled response rather than to define a global material property or an optimum fibre dosage.

5.4 Split-Tensile Damage Assessment

5.4.1 Split-Tensile Loading Programme (Cylinders)

A total of 39 SFRC cylinders, 150 mm in diameter and 300 mm high, were tested using the thirteen-configuration matrix in Table 5.1. The NBPS conductance signature was recorded over 30–1000 kHz before loading, the sensor was removed during the destructive splitting-tensile test, and the post-loading signature was obtained after reinstalling the sensor at the marked location. The analysis compares these two measured states through resonance-frequency, peak-amplitude, signature-difference, and EPS results.

5.4.2 Comparison with Destructive Splitting-Tensile Tests

Figure 5.10 reports the 28-day mean splitting-tensile strengths and reported standard-deviation error bars for three cylinders per configuration. Numerical standard deviations are not tabulated. The AR 65 mean rises from 4.29 MPa at 0.25% to 6.68 MPa at 1.50%, a 65.3% increase relative to the 4.04 MPa control. For AR 55, the corresponding 1.50% value is 6.34 MPa, a 56.9% increase relative to the same control. AR 55 has the higher mean at 0.25%; AR 65 is 0.04 MPa higher at 0.50% and higher from 0.75% to 1.50%. Because the highest mean occurs at the upper tested boundary, 1.50% is described as the maximum measured dosage, not a demonstrated optimum. Across the tested range, the results establish a sustained increase in mean splitting-tensile strength with fibre dosage. The experimental matrix was not designed to isolate aspect ratio from all other mixture and specimen effects; therefore, the differences between the AR 55 and AR 65 series are reported as measured comparisons rather than assigned to a single mechanism.

Table 5.5: Mean 28-day splitting-tensile strength for three cylinders per SFRC configuration

Steel Fibre	**Tensile Strength (MPa)**	
Dose (%)	**SFC Cylinder AR 65**	**SFC Cylinder AR 55**
0	4.04	4.04
0.25	4.29	4.66
0.5	5.75	5.74
0.75	5.93	5.81
1	6.31	5.89
1.25	6.37	5.94
1.5	6.68	6.34

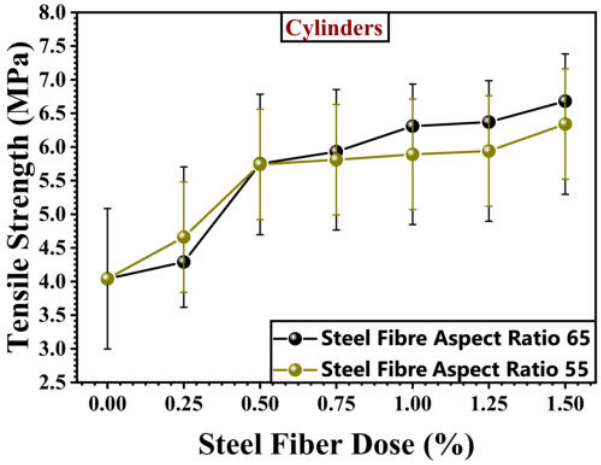

Figure 5.10: Destructive splitting-tensile strengths of the 39-cylinder matrix at 28 days.

The 0% value is the same plain-concrete control repeated in both display columns for comparison; it is counted once in the thirteen configurations.

5.4.3 Tensile Conductance Signatures

Figure 5.11 reports the NBPS conductance spectra of the thirteen cylinder configurations in the healthy and damaged states. The full 30–1000 kHz band provides the acquisition overview. The experimental analysis identified three prominent regions, and the first selected coupled resonance lies within approximately 150–200 kHz, with the reported feature tracking concentrated near 170–190 kHz. Because the measured response belongs to the coupled PZT–aluminium–shim–concrete system, this peak is not assigned to a pure d_{31} mode without modal verification.

The spectra show dosage- and state-dependent differences in both peak location and amplitude. The 1.25% and 1.50% cases are highlighted because the selected peak shifts towards a higher frequency after loading in some high-dosage cylinders. This shift is interpreted as a change in the measured local coupled response and is considered together with the destructive-strength and EPS results.

5.4.4 Rightward Peak Shifts after Split-Tensile Loading

Figure 5.12 focuses on the 1.25% and 1.50% dosages. For these cases, the selected post-loading resonance occurs at a higher frequency than the corresponding pre-loading resonance. The result concerns the local NBPS–specimen response at the tracked resonance and is not interpreted as a direct measurement of global static stiffness.

The two upper dosages also produce the largest measured splitting-tensile strengths

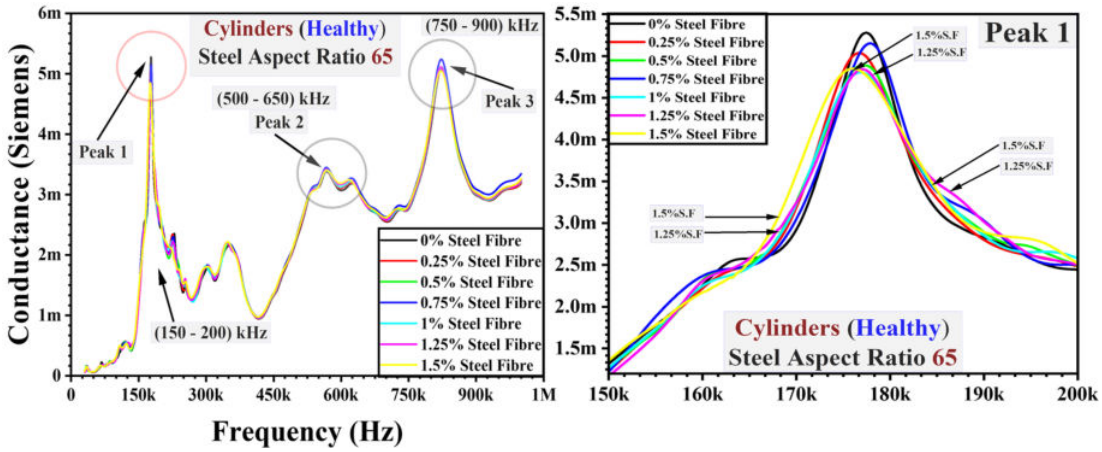

(a) AR 65, healthy state.

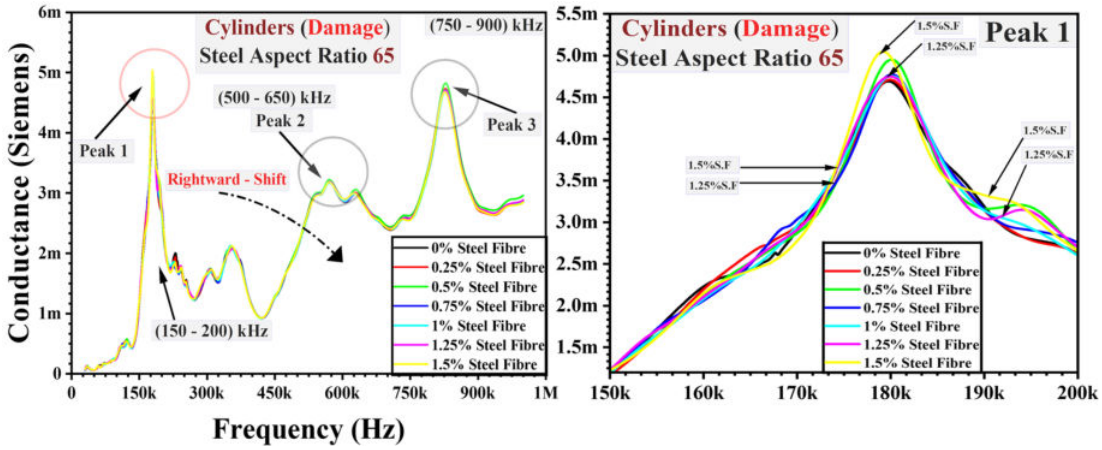

(b) AR 65, damaged state.

Figure 5.11: Comparative NBPS conductance spectra contrasting healthy and post-tensile-test damaged states (AR 65 series).

within each aspect-ratio series, including 6.68 MPa for AR 65 at 1.50%. This agreement identifies a configuration-specific correspondence between the mechanical and spectral results. It does not by itself establish a causal relation, because the experiment did not include the additional local measurements required to separate changes in the specimen response from changes in the coupled sensor contact.

5.4.5 Quantitative Peak Tracking

Figures 5.13 and 5.14 plot the reported peak-conductance magnitude against the corresponding resonance frequency for the two aspect-ratio series. These plots describe the selected coupled peak within each series and show how its frequency and conductance change across the tested configurations.

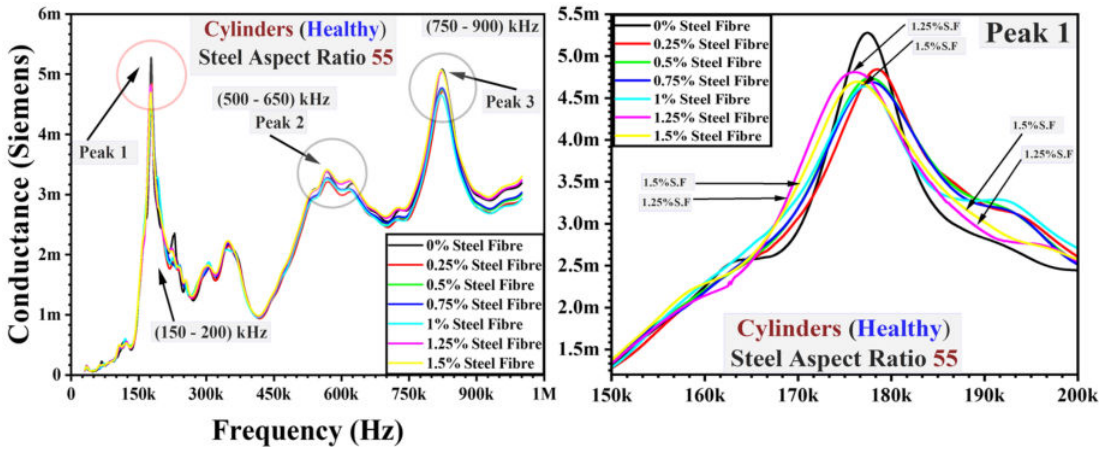

(c) AR 55, healthy state.

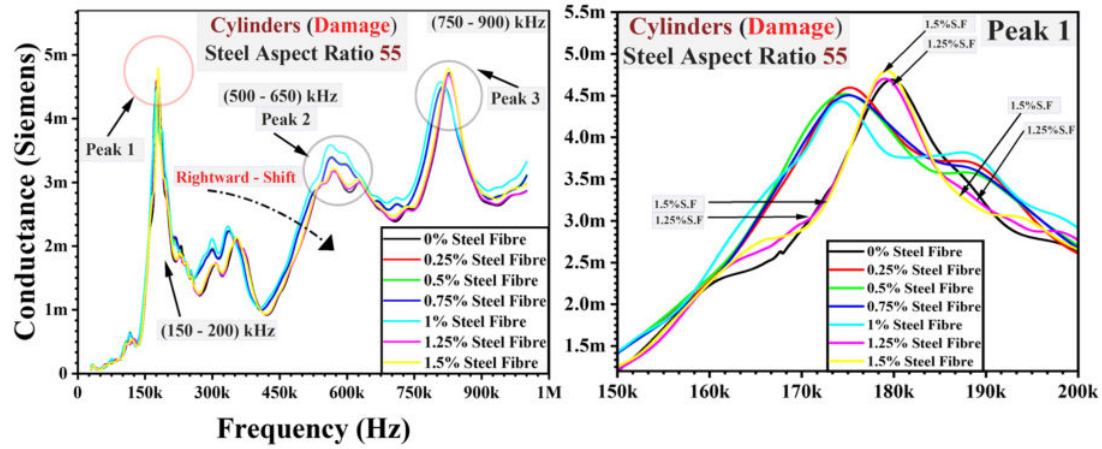

(d) AR 55, damaged state.

Figure 5.11: Comparative NBPS conductance spectra contrasting healthy and post-tensile-test damaged states (continued: AR 55 series).

Table 5.6 presents the quartic equations fitted to the seven dosage-level points. Here, x denotes fibre dosage in percent, from 0 to 1.50, and Y denotes peak frequency or conductance. These are in-sample descriptive interpolations; they are not extrapolated or used to identify crack mechanisms.

The published equation table does not identify the two equation pairs within each state by aspect ratio. They are therefore preserved in their reported order and are not assigned to AR 55 or AR 65 for series-specific inference.

5.4.6 Statistical Quantification of Tensile Damage

The cylinder RMSD was calculated over the same 150–230 kHz window using Equation 3.12. Figure 5.15 presents the reported dosage-dependent RMSD series. The

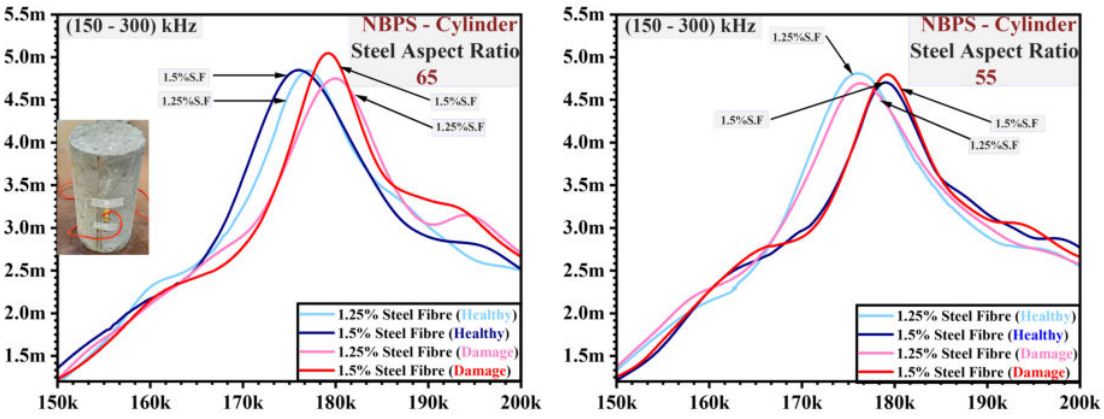

(a) Zoomed conductance spectra, AR 65 at 1.25% and 1.50% dosages.

(b) Zoomed conductance spectra, AR 55 at 1.25% and 1.50% dosages.

Figure 5.12: Detailed view of Peak 1 at the two upper tested dosages, contrasting healthy and damaged states.

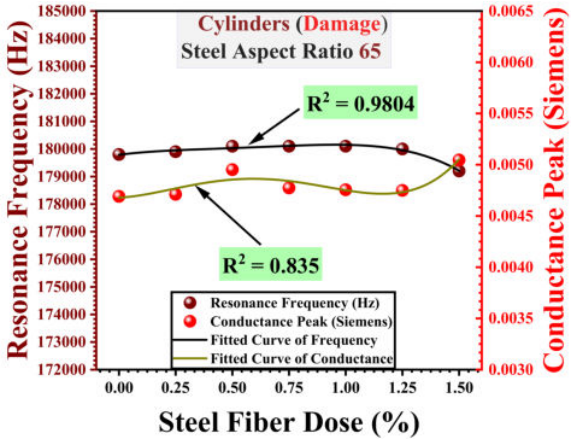

Figure 5.13: Peak conductance versus resonance frequency for the AR 65 SFRC cylinders after splitting-tensile loading.

Table 5.6: Descriptive quartic interpolations of NBPS peak conductance and resonance frequency over the tested dosages

SFC Cylinders – Healthy State	
Frequency	$Y = 177454.761 - 6219.04x + 19533.33x^2 - 18666.66x^3 + 5333.33x^4$
Conductance	$Y = 0.00528 - 0.00226x + 0.00573x^2 - 0.00561x^3 + 0.00178x^4$
Frequency	$Y = 177580.303 + 3335.06x - 3648.48x^2 - 2036.36x^3 + 1745.45x^4$
Conductance	$Y = 0.00527 - 0.00202x + 0.002x^2 - 0.0004x^3 + 0.00013x^4$
SFC Cylinders – Damage State	
Frequency	$Y = 179787.44 + 1079.50x - 2381.81x^2 + 3119.19x^3 - 1454.54x^4$
Conductance	$Y = 0.00468 + 0.00018x + 0.00163x^2 - 0.00297x^3 + 0.0013x^4$
Frequency	$Y = 179582.90 - 16144.87x + 2678.78x^2 + 19620.20x^3 - 9503.03x^4$
Conductance	$Y = 0.00469 - 0.00008x - 0.00106x^2 + 0.0012x^3 - 0.0002x^4$

plotted values quantify the difference between the paired pre-loading and post-loading conductance signatures. The AR 55 series contains several larger values, indicating a

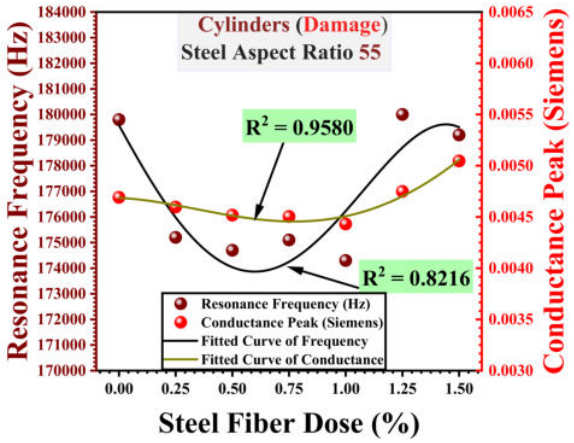

Figure 5.14: Peak conductance versus resonance frequency for the AR 55 SFRC cylinders after splitting-tensile loading.

larger measured spectral change for those configurations.

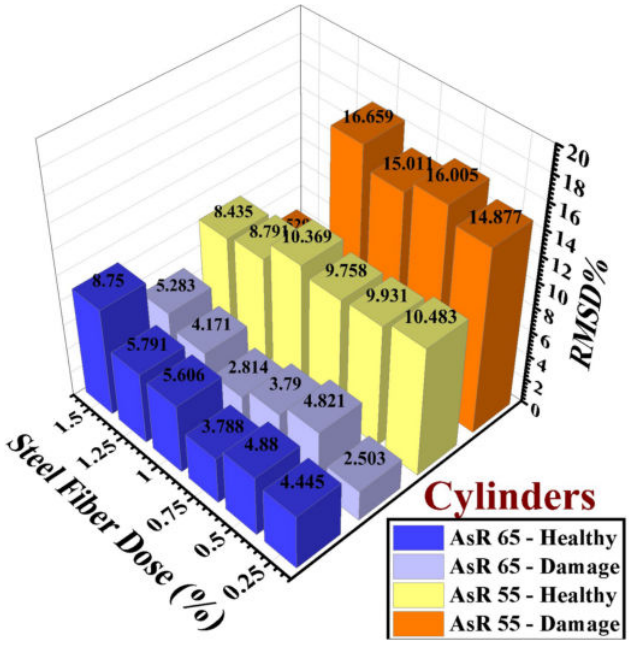

Figure 5.15: RMSD index of NBPS signatures as a function of fibre dosage for both aspect ratios.

5.4.7 Equivalent Structural Parameters for the Cylinder Geometry

The same 150–300 kHz transformation was applied to the NBPS–cylinder spectra. Figure 5.16 reports the resulting $x(f)$ and $y(f)$ curves. In the reported curves, x changes sign with frequency, while y decreases to a minimum near 170 kHz and a later peak near 185–190 kHz. The curves vary with the tested configuration; fibre dosage is not

isolated from aspect ratio, specimen heterogeneity, or contact conditions.

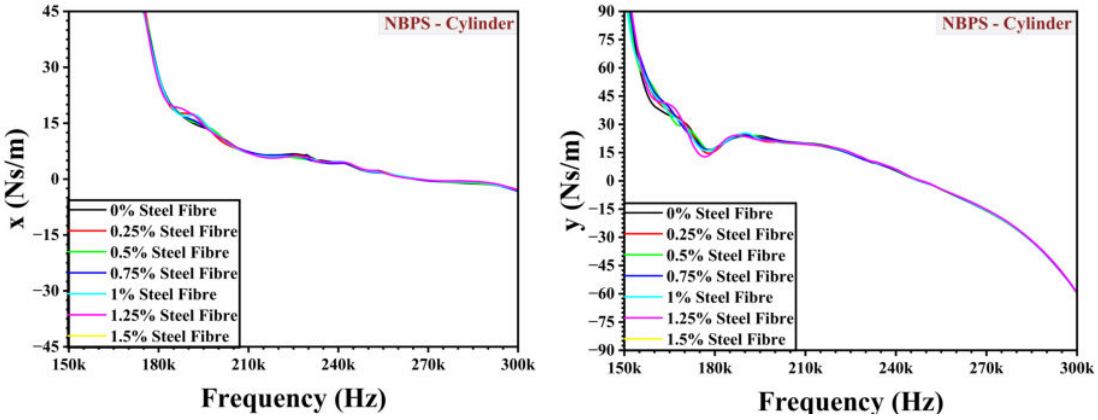

(a) x vs. frequency, NBPS–cylinder system. (b) y vs. frequency, NBPS–cylinder system.

Figure 5.16: Mechanical-impedance components for the NBPS–cylinder system at varying fibre dosages.

The adopted series-mobility equations and resonance boundary condition were applied consistently. Figure 5.17 reports (c,m,k) for the healthy and damaged AR 65 and AR 55 cylinder series. The wider variation in the AR 55 plots indicates that the fitted parameters are more dispersed across those tested configurations than in the AR 65 series.

The reconstructed response was examined using the $x(f)$ and $y(f)$ relations defined in Section 3.11. Figure 5.18 shows the available comparisons for the healthy AR 65 and damaged AR 55 cylinder cases. The overlays show how closely the equivalent-system curves follow the measured responses for the displayed states.

5.4.8 Compressive Stiffness–Strength Relationship

Equivalent stiffness describes the local high-frequency response, whereas compressive strength is obtained from destructive loading of the complete specimen. Cubic curves were fitted to the seven configuration-level values in each aspect-ratio series, using the same data for fitting and assessment. The reported in-sample coefficients of determination are $R^2 = 0.85$ for AR 65 and $R^2 = 0.74$ for AR 55. The fitted relations are:

$$k_{\mathrm{AR65}} = -6\,400\,352.38 + 392\,857.88\,S_{\mathrm{Cube65}} - 7\,804.48\,S^2_{\mathrm{Cube65}} + 51.05\,S^3_{\mathrm{Cube65}} \quad (5.2)$$

$$k_{\mathrm{AR55}} = 3\,425\,545.31 - 193\,156.37\,S_{\mathrm{Cube55}} + 3\,685.97\,S^2_{\mathrm{Cube55}} - 23.08\,S^3_{\mathrm{Cube55}} \quad (5.3)$$

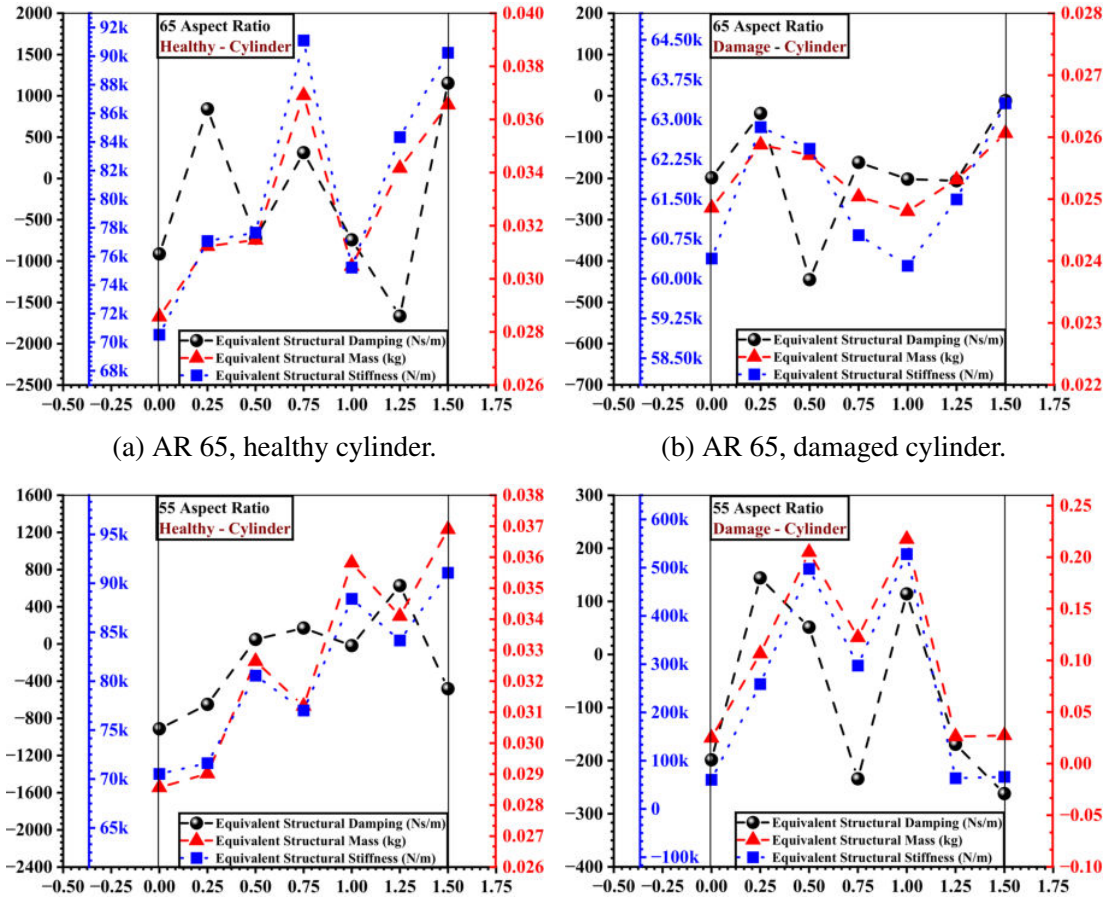

(a) AR 65, healthy cylinder.

(b) AR 65, damaged cylinder.

(c) AR 55, healthy cylinder.

(d) AR 55, damaged cylinder.

Figure 5.17: Derived Equivalent Structural Parameters (c, m, k) for SFRC cylinders across healthy and damaged conditions.

where S_{Cube65} and S_{Cube55} are the corresponding compressive strengths in MPa. The equations describe the measured range and are not extrapolated. Figure 5.19 shows the fitted curves. Differences in scatter are reported without ranking fibre distribution or predictive performance.

5.4.9 Tensile Stiffness–Strength Relationship

The damaged-state equivalent-stiffness series was fitted against the configuration-level splitting-tensile strengths using cubic polynomials. The fitted numerical relations

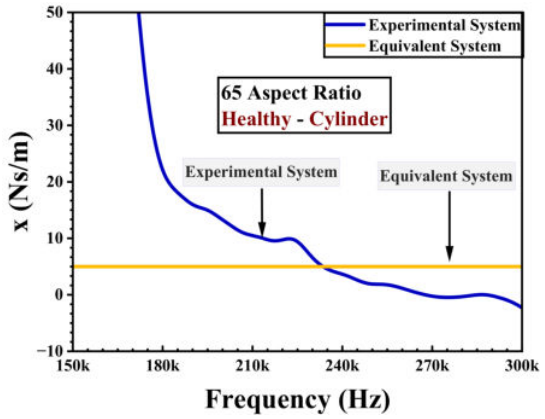

(a) AR 65 healthy: x vs. f.

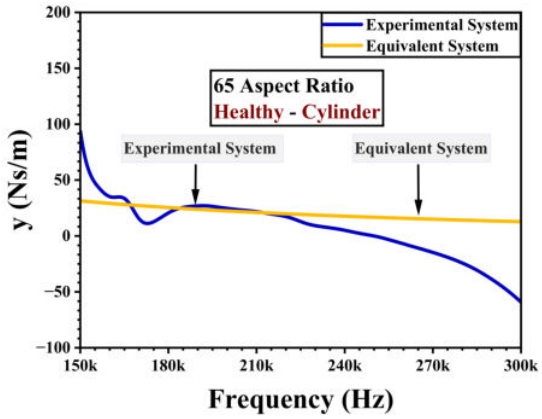

(b) AR 65 healthy: y vs. f.

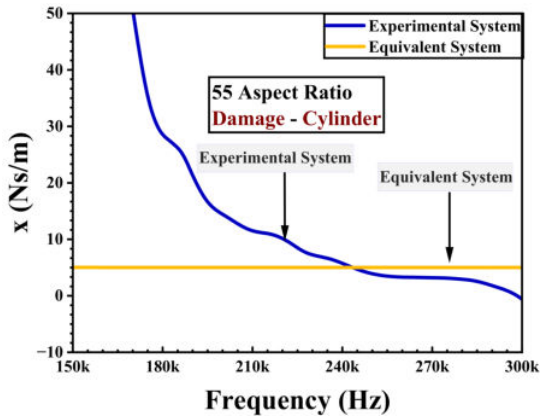

(c) AR 55 damaged: x vs. f.

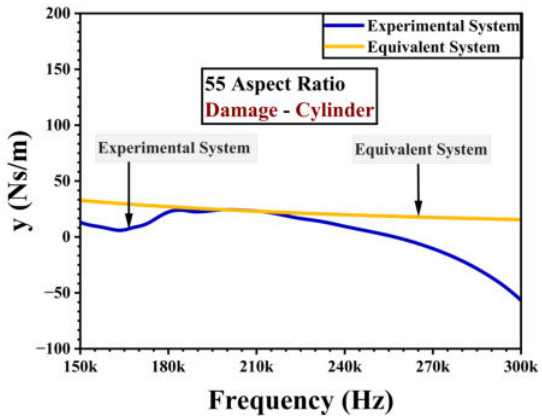

(d) AR 55 damaged: y vs. f.

Figure 5.18: Comparison of experimental and equivalent-system $x(f)$ and $y(f)$ responses for the SFRC cylinders.

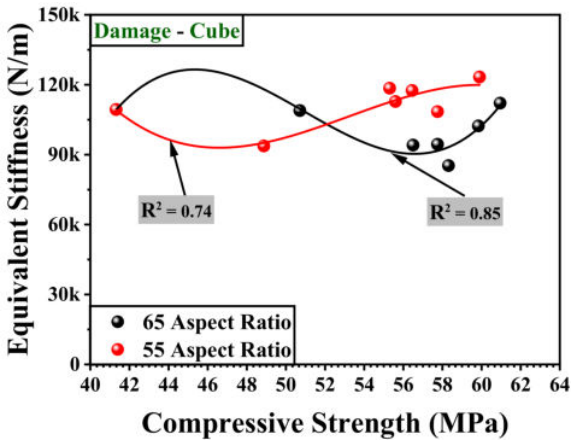

Figure 5.19: Relationship between NBPS-derived equivalent stiffness k and compressive strength over the tested configurations

are:

$$k_{\mathrm{AR65}} = -449\,413.06 + 290\,453.30\,S_{\mathrm{Cylinder65}} - 53\,955.23\,S^2_{\mathrm{Cylinder65}} + 3\,287.43\,S^3_{\mathrm{Cylinder65}} \tag{5.4}$$

$$k_{\mathrm{AR55}} = 8\,015\,253.43 - 6\,109\,840.72\,S_{\mathrm{Cylinder55}} + 1\,480\,277.01\,S^2_{\mathrm{Cylinder55}} - 112\,783.30\,S^3_{\mathrm{Cylinder55}} \tag{5.5}$$

Here, $S_{\text{Cylinder65}}$ and $S_{\text{Cylinder55}}$ denote the corresponding splitting-tensile strengths in MPa; the latter is the independent variable for the AR 55 relation. The reported AR 65 fit has $R^2 = 0.8406$. Figure 5.20 shows both in-sample curves. With seven dosage-level points, no independent validation set, and substantial EPS scatter, these equations describe the tested range but do not establish a non-destructive tensile-strength predictor.

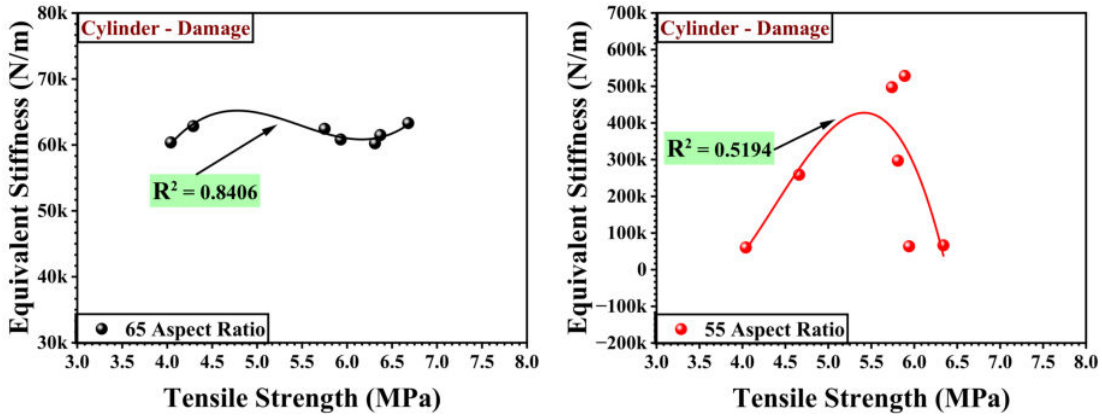

(a) AR 65 damaged cylinder calibration. (b) AR 55 damaged cylinder calibration.

Figure 5.20: Relationship between NBPS-derived stiffness k and splitting-tensile strength over the tested configurations

5.4.10 Stiffness-Based Damage Index for Cylinders

For the cylinder matrix, the magnitude of normalised equivalent-stiffness change is calculated using Equation 5.1. Figure 5.21 reports the cylinder series, and Table 5.7 gives descriptive quartic fits with x as fibre dosage in percent. The absolute-value definition quantifies the magnitude of the fitted stiffness change between the two states; the direction of that change is assessed from the underlying k values.

Table 5.7: Descriptive quartic fits for cylinder Δs over the tested 0–1.50% dosage range

Steel Fibre	Cylinders
Aspect Ratio 65	$\Delta s = 0.17041 - 0.2897x + 2.3705x^2 - 2.9370x^3 + 1.0425x^4$
Aspect Ratio 55	$\Delta s = 0.16358 + 1.596x + 2.9035x^2 - 6.4361x^3 + 2.5449x^4$

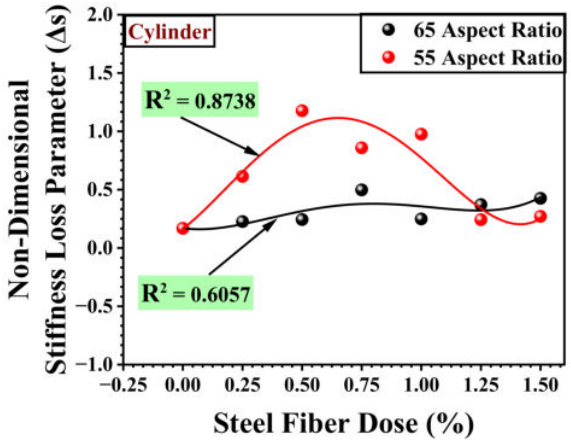

Figure 5.21: Magnitude of normalised equivalent-stiffness change Δs across the SFRC cylinder configurations

5.5 Comparative Interpretation of Compressive and Split-Tensile Response

The compressive-strength means reach their measured maxima at 0.75% fibre for both aspect-ratio series and decrease at the higher tested dosages. The reported RMSD and MAPD near the AR 65 0.75% case are approximately 12.4% and 9.5%, but these are signature-distance measures, not strength or optimisation criteria. The signs and magnitudes of the selected peak shifts vary by configuration, and no single shift direction occurs across the complete compressive series.

The splitting-tensile means continue to increase to the upper tested dosage, with maxima of 6.68 MPa for AR 65 and 6.34 MPa for AR 55 at 1.50%. Rightward shifts of the selected coupled peak are reported in some high-dosage damaged cylinders. Their direction differs from parts of the compressive series, consistent with the different specimen geometries, loading modes, and post-loading states.

Across both programmes, spectral features, RMSD/MAPD, and EPS changes provide different measures of the pre-loading and post-loading states. They do not constitute independent cross-validation because all are derived from the same EMI signatures, and none is interpreted as a universal damage measure.

The comparison is limited to the tested M30 mixtures, aspect-ratio series, geometries, 28-day curing condition, loading procedures, and reusable-sensor protocol. Different peak-shift directions are treated as observations of the local coupled response rather than direct measurements of a change in global stiffness.

5.6 Experimental Limitations and Repeatability

Three physical specimens per mixture configuration determine the reported destructive-strength means. The paired EMI comparisons follow the measured configuration-level records presented in the experimental results. The marked position and PTFE-shim procedure maintained a consistent sensor installation, although the effect of repeated mounting was not quantified separately.

The NBPS response represents the local high-frequency behaviour of the coupled sensor–specimen system, whereas compressive and splitting-tensile strengths describe the destructive response of the complete specimen. Fibre distribution and crack geometry were not measured directly, so the observed spectral changes are interpreted jointly with the destructive results rather than assigned to an unmeasured mechanism. The polynomial fits were assessed on the same dosage-level data used for fitting, with no independent validation set or permitted extrapolation. Finally, EPS and Δs are affected by model, resonance-selection, and denominator sensitivity; their absolute values should not be interpreted as global mechanical properties.

5.7 Summary

This chapter examined reusable NBPS measurements before and after destructive compression and splitting-tensile tests on the two SFRC aspect-ratio series. The compressive-strength means reached their maxima at 0.75% fibre dosage for both aspect ratios, whereas the splitting-tensile means reached their maxima at the upper tested dosage of 1.50%. These observations identify maxima only within the tested matrices.

Paired conductance signatures showed configuration-dependent changes in peak location and amplitude. RMSD and MAPD quantified differences between each defined pre-loading–post-loading pair, while selected high-dosage cylinder peaks shifted towards higher frequency in some cases. These shifts describe the local coupled response and are interpreted alongside the destructive-strength results.

The adopted series-mobility formulation provided the EPS and the stiffness-change magnitude Δs. Polynomial relations between equivalent stiffness and destructive strength describe the seven dosage-level points in each fibre series. These relations summarise the tested configurations and require independent data before use for prediction. Overall, the mechanical and electromechanical results show differences between the measured pre-loading and post-loading states while retaining the distinction between local high-frequency response and specimen-level destructive strength.

CHAPTER 6

TEMPERATURE EFFECTS AND THE ENHANCED EFS COMPENSATION ALGORITHM

6.1 General

This chapter investigates the interpretation of EMI measurements when structural condition and temperature vary together. A temperature change can alter the measured admittance of the coupled JPS–SFRC system even without a new structural change. The analysis must therefore distinguish temperature-associated signature variation from the difference associated with the introduced saw-cut, while recognising that compensation is a numerical processing step rather than a separate experiment.

The investigation is organised around three explicit research questions:

1. How do the conductance, susceptance, SHM indices and Equivalent Structural Parameters (EPS) vary during progressive heating in the intact and saw-cut states?

2. To what extent does the Enhanced Effective Frequency Shift (EFS) procedure reduce temperature-associated variation within each structural state?

3. After compensation, what differences remain between intact and saw-cut signatures matched by specimen, temperature and dwell time?

The thermal campaign reused the four SFRC specimens instrumented with embedded Jacketed Piezo Sensors (JPS1–JPS4) described in Section 3.8. These are four selected material configurations, not replicated factorial groups: SFC1 and SFC3 contain AR 65 fibres at 0.50% and 0.75%, respectively, whereas SFC2 and SFC4 contain AR 55 fibres at the corresponding dosages. Eight consecutive furnace stages from 75 to 250 °C were used, with conductance and susceptance recorded after 10, 20 and 30 min at each stage. The intact series extends to 250 °C for all four specimens. In the saw-cut series, SFC1 and SFC2 extend to 250 °C, while SFC3 and SFC4 have measurements

only through 175 °C. The missing higher-temperature records are treated as unavailable data and are not interpolated.

Compensation is a post-processing branch applied to the measured signatures; it is not an additional physical experiment or an independent replicate. The Enhanced Effective Frequency Shift (EFS) procedure is first defined and checked against its implementation. The chapter then examines intact heating, saw-cut heating, matched intact–cut differences, the thirteen SHM indices and the model-derived EPS. Comparisons between material configurations remain exploratory because only one physical specimen represents each configuration.

6.2 Enhanced EFS Compensation Algorithm

To address these challenges, the implemented Enhanced Effective Frequency Shift (EFS) procedure is summarised in Algorithm 1.

Algorithm 1 Enhanced Effective Frequency Shift (EFS) Compensation

Require: Raw Conductance $\mathbf{G}_{raw}$, Susceptance $\mathbf{B}_{raw}$, Frequencies $\mathbf{f}$

Ensure: Drift-Compensated Signatures $\mathbf{G}_{comp}, \mathbf{B}_{comp}$

$f_{interp} \leftarrow \text{Linspace}(\min(f), \max(f), |f| \times 25)$

$G_{base} \leftarrow \text{CubicSpline}(f, G_{raw})(f_{interp})$

$B_{base} \leftarrow \text{CubicSpline}(f, B_{raw})(f_{interp})$

$q_G \leftarrow \sigma_G / (\text{mean}\,|G| + 10^{-12})$

$q_B \leftarrow \sigma_B / (\text{mean}\,|B| + 10^{-12})$

$W_G, W_B \leftarrow q_G/(q_G+q_B), q_B/(q_G+q_B)$; use $(0.6, 0.4)$ if $q_G + q_B = 0$

Coarse Search Range: $\Theta_{coarse} \leftarrow [-\max_{shift}, +\max_{shift}]$

$\theta_{coarse} \leftarrow \arg\max_{\theta \in \Theta_{coarse}} \left(\frac{W_G \cdot \text{CC}_G(\theta) + W_B \cdot \text{CC}_B(\theta)}{W_G + W_B} \right)$

Fine Search Range: $R_{fine} \leftarrow \max(3, \lfloor \max_{shift} / 8 \rfloor)$

$\Theta_{fine} \leftarrow [\theta_{coarse} - R_{fine}, \theta_{coarse} + R_{fine}]$

$\theta_{opt} \leftarrow \arg\max_{\theta \in \Theta_{fine}} \left(\frac{W_G \cdot \text{CC}_G(\theta) + W_B \cdot \text{CC}_B(\theta)}{W_G + W_B} \right)$

$G_{comp}, B_{comp} \leftarrow \text{AlignAndRemoveMeanOffset}(G_{base}, B_{base}, \theta_{opt})$

return G_{comp}, B_{comp}

The EPS equations are not repeated here. They follow the fixed series-mobility formulation and numerical safeguards defined in Section 3.11; the resulting quantities are interpreted as equivalent parameters of the coupled sensor–interface–host response, not as direct measurements of concrete mass, stiffness or damping.

6.3 Worked Example: Before and After EFS Compensation

The operation of the Enhanced EFS procedure is illustrated in Figure 6.1, which compares uncompensated and compensated conductance signatures at 150°C and 175°C with the ambient baseline.

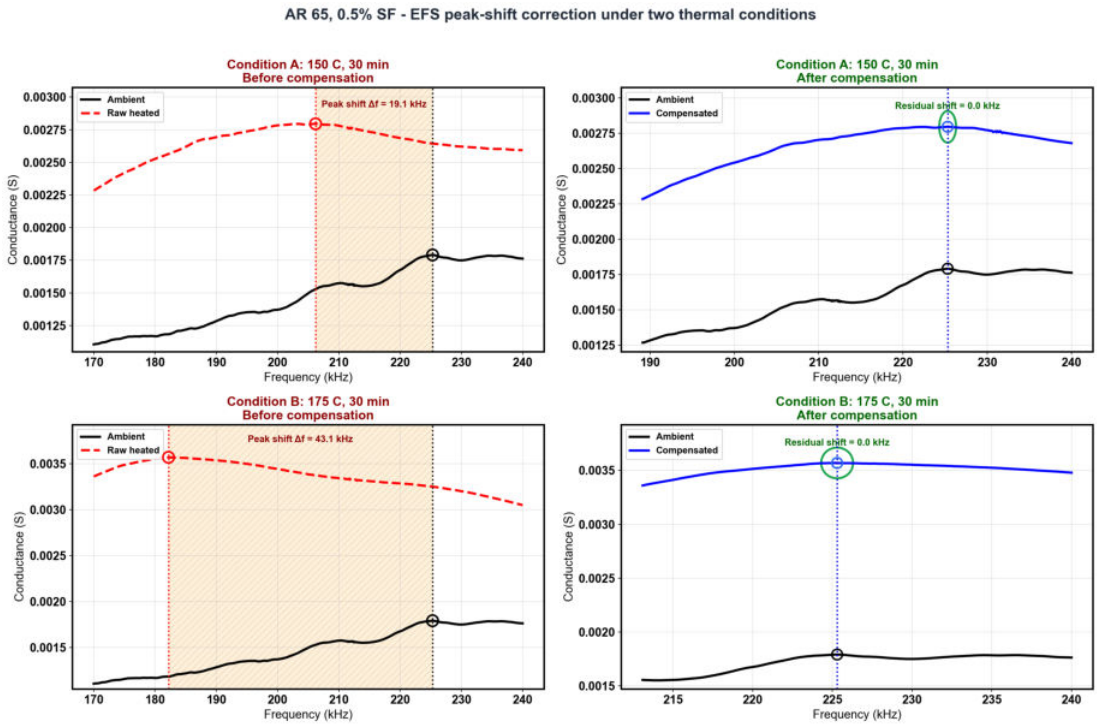

Figure 6.1: Four-panel comparison of conductance signatures before and after applying the Enhanced-EFS compensation algorithm at 150°C and 175°C.

6.3.1 Motivation and Algorithmic Overview

The classical Effective Frequency Shift method, originally proposed for temperature compensation in EMI-based SHM by Koo et al. and refined by later workers, represents thermal drift primarily as translation along the frequency axis. A direct discrete search is limited to the acquired frequency grid and commonly uses one channel, while horizontal alignment alone does not remove channel-wise amplitude offset. In the present data, any residual after alignment may still contain temperature, structural-state, sensor-interface and measurement contributions; it is not assigned solely to structural change.

The implemented procedure combines (i) cubic-spline interpolation on a grid containing 25× the original number of points, (ii) a joint conductance–susceptance correlation objective with signal-dependent weighting, (iii) a two-stage coarse-to-fine

shift search confined to $\pm 12\,\%$ of the interpolated record length and (iv) removal of the mean vertical offset after horizontal alignment. Algorithm 1 is the single algorithmic statement used in this chapter; the following subsections define its operations and limitations.

6.3.2 High-Resolution Cubic-Spline Interpolation

Each raw signature consists of $N = 5\,275$ frequency points. At a sampling step of $\approx 100\,\mathrm{Hz}$, shifts smaller than $\approx 100\,\mathrm{Hz}$ cannot be resolved by a direct point-by-point search. The E-EFS therefore constructs a cubic-spline interpolant of both the conductance and the susceptance of the baseline and of every heated signature:

$$\tilde{G}^{\mathrm{b}}(\tilde{f}) = \mathrm{Spline}_{\mathrm{cubic}}\big(f, G^{\mathrm{b}}\big), \qquad \tilde{B}^{\mathrm{b}}(\tilde{f}) = \mathrm{Spline}_{\mathrm{cubic}}\big(f, B^{\mathrm{b}}\big), \tag{6.1}$$

evaluated on the densified grid $\tilde{f}$ of length $\alpha N = 25 \times 5\,275 \approx 1.32 \times 10^5$ points. This gives an approximately 4 Hz search-grid spacing for sub-bin shift estimation; it does not add physical information or improve the 100 Hz acquisition resolution of the impedance analyser. The heated signatures are re-sampled identically. A linear-interpolation fallback is retained in the implementation if cubic interpolation fails.

6.3.3 Joint Conductance–Susceptance Correlation Metric

At every trial integer shift s, the mean-centred and standard-deviation-normalised baseline and test signatures are correlated independently in the conductance and susceptance channels:

$$\mathrm{CC}_G(s) = \mathrm{corr}\big(\tilde{G}^{\mathrm{b}}[0 : N-s],\, \tilde{G}^{\mathrm{T}}[s : N]\big), \quad \mathrm{CC}_B(s) = \mathrm{corr}\big(\tilde{B}^{\mathrm{b}}[0 : N-s],\, \tilde{B}^{\mathrm{T}}[s : N]\big). \tag{6.2}$$

The two channel correlations are then combined into a single joint correlation $C(s)$ through data-driven weights w_G and w_B that reflect the instantaneous signal quality of each channel, defined as the ratio of standard deviation to absolute mean:

$$w_G = \frac{\sigma_G / \operatorname{mean}|G|}{\sigma_G / \operatorname{mean}|G| + \sigma_B / \operatorname{mean}|B|}, \quad w_B = 1 - w_G, \quad C(s) = w_G\,\mathrm{CC}_G(s) + w_B\,\mathrm{CC}_B(s). \tag{6.3}$$

The denominator in the implementation contains 10^{-12} to prevent division by zero. The two non-negative quality ratios are normalised to sum to unity; default weights of $w_G = 0.6$ and $w_B = 0.4$ are used only when their sum is zero. These weights control the

numerical objective used by the present implementation and should not be interpreted as independently calibrated measures of physical channel quality.

6.3.4 Two-Stage Coarse-to-Fine Search

Direct evaluation of $C(s)$ at every integer shift within $\pm M$ is computationally expensive. The E-EFS algorithm therefore uses a two-stage search. In the *coarse* stage, $C(s)$ is evaluated on a sparse grid $s \in \{-M, -M+\Delta, \ldots, M\}$ with stride $\Delta = \lceil M/15 \rceil$, giving sixteen trial shifts. The coarse maximum $s_c^\star$ is used to seed a *fine* search on the dense integer grid inside $[s_c^\star - M/8,\ s_c^\star + M/8]$. The final optimum is

$$s^\star \;=\; \arg \max_{s \in [s_c^\star - M/8,\, s_c^\star + M/8]} C(s), \tag{6.4}$$

and the Effective Frequency Shift in physical units is

$$\boxed{\Delta f \;=\; s^\star \left(\tilde{f}_2 - \tilde{f}_1\right) \;=\; s^\star \cdot \frac{f_{\max} - f_{\min}}{\alpha N - 1}.} \tag{6.5}$$

The two-stage strategy reduces the number of correlation evaluations from $\mathcal{O}(2M) \approx 3 \times 10^4$ to $\mathcal{O}(M/4) \approx 4 \times 10^3$ without sacrificing resolution, making the procedure practical for the ≈ 400 heated signatures of the present study.

6.3.5 Horizontal Alignment and Mean-Offset Correction

Once $s^\star$ is known, horizontal alignment is applied by slicing the baseline and heated arrays over their common interval. For a positive shift, the leading points of the heated signature and the trailing points of the baseline are excluded; for a negative shift, the opposite ends are excluded. The implemented vertical correction then subtracts the difference between the means of the aligned heated and baseline records:

$$\hat{G}^{\mathrm{T}} = \tilde{G}^{\mathrm{T}\prime} - \Big[\mathrm{mean}(\tilde{G}^{\mathrm{T}\prime}) - \mathrm{mean}(\tilde{G}^{\mathrm{b}\prime})\Big], \qquad \hat{B}^{\mathrm{T}} = \tilde{B}^{\mathrm{T}\prime} - \Big[\mathrm{mean}(\tilde{B}^{\mathrm{T}\prime}) - \mathrm{mean}(\tilde{B}^{\mathrm{b}\prime})\Big]. \tag{6.6}$$

Equation 6.6 removes a constant vertical offset; it does not force peak amplitudes to equal the baseline. The compensated pair $(\hat{G}^{\mathrm{T}}, \hat{B}^{\mathrm{T}})$ is subsequently used to calculate the SHM indices and EPS values. Because both frequency alignment and offset removal can alter a damage-sensitive difference, their performance is assessed from matched intact and saw-cut comparisons rather than from visual overlap alone.

6.3.6 Quality Metrics of the Compensation

For each processed signature, the implementation records the estimated shift Δf, the optimum joint correlation $C(s^\star)$, the Correlation Coefficient Deviation $1 - C(s^\star)$, and channel-wise residual RMSD values normalised by the mean absolute aligned baseline. These quantities describe agreement with the selected state-specific baseline; they do not by themselves validate damage detection. Intact thermal drift is referenced to the ambient intact signature of the same specimen, whereas thermal drift in the saw-cut state is referenced to the ambient saw-cut signature. Damage assessment uses intact and saw-cut records matched by specimen, temperature and dwell time. The remainder of the chapter reports the measured and derived records for the four specimens under these two structural states and two processing branches.

6.4 Overview of Experimental Cases

6.4.1 Research Objective and Experimental Framework

The objective of the thermal study is to distinguish temperature-associated variation in the EMI signatures from the change associated with an artificial saw-cut. Four previously monitored SFRC specimens were reused. Each contained an embedded JPS and represented one selected combination of fibre aspect ratio (AR 65 or AR 55) and fibre dosage (0.50% or 0.75%). Because only one physical specimen represents each configuration, the study supports specimen-specific comparisons rather than replicated factorial inference.

The specimens were heated consecutively through eight nominal stages from 75 to 250 °C without intermediate cooling. At each stage, conductance and susceptance were recorded after 10, 20 and 30 min. The same specimens were subsequently examined after introduction of a 3 mm-wide, 30 mm-deep artificial saw-cut oriented orthogonally to the embedded JPS, as described in Section 3.8.3.

For each structural state, the measured signatures are examined before and after Enhanced EFS post-processing. These are two processing branches applied to the same acquisition, not two physical experiments. The resulting organisation comprises four material configurations, two structural states and two processing branches. It is used to trace thermal drift, compensation residuals and matched intact–cut differences without treating repeated dwell records as independent specimen replicates.

6.4.2 Analysis Matrix

The results are organised into sixteen analysis cells formed by four specimens, two structural states and two processing branches. The cells are a reporting structure; they do not represent sixteen independent experiments.

The four SFRC specimens were fabricated using two types of hooked-end steel fibres with different geometric properties, as detailed in Table 6.1. The aspect ratio (AR) is the ratio of fibre length to diameter, L/D. Fibre Type 1 (AR 65) had a length of 35 mm, diameter of 0.55 mm and tensile strength of 1250 N/mm^2; Fibre Type 2 (AR 55) had a length of 50 mm, diameter of 0.9 mm and tensile strength of 1500 N/mm^2.

Table 6.1: Steel Fibre Properties Used in SFRC Specimens

S.F. No.	Length, L (mm)	Diameter, D (mm)	Aspect Ratio	Strength (N/mm^2)
1	35	0.55	65	1250
2	50	0.9	55	1500

Each specimen contributes an intact and a saw-cut acquisition series. The uncompensated and compensated records are alternative processing branches of those series. Table 6.2 records this mapping.

Table 6.2: Analysis matrix: four specimens, two structural states and two processing branches

Cell	SFC	AR	SF (%)	Structural State	Processing
1	1	65	0.5	Intact heating	Without compensation
2	1	65	0.5	Intact heating	With compensation
3	1	65	0.5	Saw-cut state under heating	Without compensation
4	1	65	0.5	Saw-cut state under heating	With compensation
5	3	65	0.75	Intact heating	Without compensation
6	3	65	0.75	Intact heating	With compensation
7	3	65	0.75	Saw-cut state under heating	Without compensation
8	3	65	0.75	Saw-cut state under heating	With compensation
9	2	55	0.5	Intact heating	Without compensation
10	2	55	0.5	Intact heating	With compensation
11	2	55	0.5	Saw-cut state under heating	Without compensation
12	2	55	0.5	Saw-cut state under heating	With compensation
13	4	55	0.75	Intact heating	Without compensation
14	4	55	0.75	Intact heating	With compensation
15	4	55	0.75	Saw-cut state under heating	Without compensation
16	4	55	0.75	Saw-cut state under heating	With compensation

The matrix permits within-specimen comparison of structural state and processing branch. Differences between AR or dosage groups are reported descriptively because

fibre geometry, dosage, local material variability and sensor installation are not independently replicated.

6.4.3 Temperature Testing Protocol

The thermal programme examined the response of the four JPS-instrumented SFRC specimens over the laboratory range from 75 to 250 °C. Eight nominal temperature stages were imposed consecutively without intermediate cooling. The experiment therefore represents a progressive heating history rather than independent exposure at each temperature.

At every stage, conductance and susceptance signatures were recorded after 10, 20 and 30 min of dwell. These three records describe the evolution of the measured response during the prescribed 30-min interval; they are repeated observations on the same specimen and are not independent replicates. Internal temperature uniformity was not measured, so the 30-min record is not treated as proof of thermal equilibrium throughout the specimen. Table 6.3 summarises the acquisition sequence.

Table 6.3: Temperature Testing Protocol

Temperature Stage	**Temperature (°C)**	**Duration**	**Recording Points**	**Signatures**
Baseline	Ambient (25)	Reference	Initial	1
Stage 1	75	30 minutes	10, 20, 30 min	3
Stage 2	100	30 minutes	10, 20, 30 min	3
Stage 3	125	30 minutes	10, 20, 30 min	3
Stage 4	150	30 minutes	10, 20, 30 min	3
Stage 5	175	30 minutes	10, 20, 30 min	3
Stage 6	200	30 minutes	10, 20, 30 min	3
Stage 7	225	30 minutes	10, 20, 30 min	3
Stage 8	250	30 minutes	10, 20, 30 min	3
	Total Signatures per Specimen per Condition:			**25**

Tables 6.2 and 6.3 provide the detailed analysis cells and acquisition stages. Figure 6.2 connects these elements in a single visual sequence and distinguishes the physical tests from the derived processing branches and comparisons.

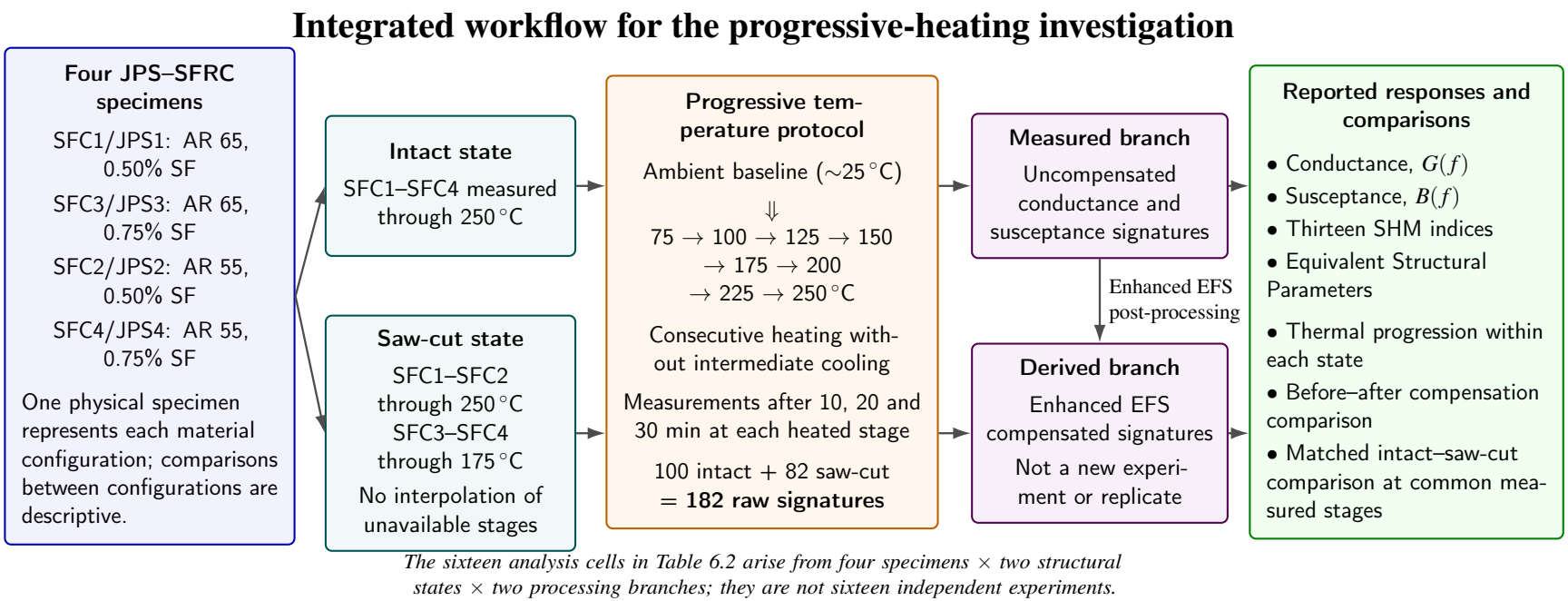

Figure 6.2: Integrated thermal-study workflow linking the specimen configurations, structural states, progressive temperature protocol, processing branches and reported comparisons.

Heating was performed in the controlled electric furnace described in Chapter 3. The intact sequence is available for SFC1–SFC4 through 250 °C. After introduction of the saw-cut, SFC1 and SFC2 retain the full temperature sequence, whereas measurements for SFC3 and SFC4 are available only through 175 °C. The reason for the unavailable higher-temperature records was not independently diagnosed; accordingly, the affected comparisons are restricted to their common measured range.

The acquired dataset contains 100 intact signatures and 82 saw-cut signatures, giving 182 raw signatures in total. Relative to four complete 25-signature sequences in each structural state, 18 saw-cut signatures are unavailable. Compensated signatures are derived from these measurements and are not counted as additional acquisitions. Each raw signature contains simultaneous conductance and susceptance measurements at 5,275 frequency points over 30–557.4 kHz.

6.5 Measurement Parameters Overview

6.5.1 Signal Types: Conductance and Susceptance

The embedded JPS records the electrical admittance of the coupled PZT–interface–SFRC system. The complex admittance (Y) comprises conductance and susceptance:

$$Y = G + jB \tag{6.7}$$

where G represents the conductance (real component of admittance), B represents the susceptance (imaginary component of admittance), and j is the imaginary unit ($\sqrt{-1}$).

Conductance (G) is the real component of admittance, whereas susceptance (B) is its imaginary component. Both channels can change when the coupled sensor–interface–host system changes. Neither channel, considered alone, identifies a unique physical cause; temperature, the saw-cut, the sensor and its interface all contribute to the measured response. The two channels are therefore examined separately rather than assuming identical sensitivity or assigning conductance an a priori universal advantage.

Both components were recorded simultaneously at 5,275 frequency points over 30–557.4 kHz. The same frequency grid is used throughout the thermal analysis so that raw, compensated and matched structural-state comparisons refer to corresponding spectral records.

The reference signature depends on the question being examined. Intact thermal drift is evaluated relative to the ambient intact signature of the same specimen. Saw-cut thermal drift is evaluated relative to that specimen's ambient saw-cut signature.

The structural-state difference is evaluated by matching intact and saw-cut records for the same specimen, nominal temperature and dwell time. This distinction prevents a temperature baseline from being mistaken for the structural-state comparison.

6.5.2 Calculated Parameters: SHM Indices and EPS

Two categories of quantities are evaluated from the conductance and susceptance signatures: statistical SHM indices and Equivalent Structural Parameters (EPS). The former quantify differences between specified spectral records, whereas the latter are model-derived quantities obtained from the fixed lumped-parameter formulation in Chapter 3.

6.5.2.1 Structural Health Monitoring Indices

Thirteen SHM indices were retained to describe deviation, correlation, amplitude and distributional changes between paired signatures. Their reference is analysis-specific: the ambient signature of the same structural state is used for thermal drift, while matched intact and saw-cut signatures are used for the damage comparison. Table 6.4 lists the reported indices. Chapter 3 defines RMSD, MAPD, CC and covariance, while the remaining implemented equations are given in Appendix A.2; every result is interpreted with its channel and baseline stated explicitly.

Among these indices, RMSD (Root Mean Square Deviation) is the most widely used in EMI-based SHM literature due to its straightforward interpretation and consistent sensitivity to various types of structural changes. The mathematical definition of the RMSD is presented in Equation 3.12 of Chapter 3.

6.5.2.2 Equivalent Structural Parameters

Three EPS quantities were derived using the fixed lumped-parameter representation established in Section 3.11. They provide a compact mass-like, stiffness-like and dissipative description of the coupled response within the adopted model; they are not direct measurements of the concrete's physical mass, stiffness or damping. Table 6.5 states the model interpretation and units used in this chapter.

The EPS trajectories complement the statistical indices by providing a second, model-based representation of the same coupled measurements. Their variation is interpreted comparatively within each specimen and processing branch, without assigning a unique material mechanism to an individual EPS change. Percentage changes are also treated cautiously when a reference value is close to zero or when a trajectory changes

Table 6.4: SHM Indices Calculated in This Study

No.	Index	Description
1	RMSD	Root Mean Square Deviation - measures overall deviation between baseline and current signature
2	MAPD	Mean Absolute Percentage Deviation - quantifies relative changes as percentage
3	AMPD	Amplitude Percentage Deviation - relative change in maximum absolute amplitude
4	CC	Correlation Coefficient - measures linear correlation between signatures
5	CCD	Correlation Coefficient Deviation - deviation from perfect correlation (1-CC)
6	CCD^3	Cubic Correlation Coefficient Deviation - enhanced CCD with cubic transformation for increased sensitivity
7	CCV	Coefficient of Covariance Variation - covariance-based quantity with mean-sensitive normalisation
8	MSE	Mean Squared Error - squared deviation metric, sensitive to outliers
9	Variance	Variance of the pointwise difference between paired signatures
10	RMS	Root Mean Square - signal energy metric
11	Skewness	Standardised asymmetry of the pointwise difference
12	Peak-to-Peak	Percentage change in the signature amplitude range
13	Covariance	Joint variability measure between baseline and current signatures

Table 6.5: Equivalent Structural Parameters (EPS) Derived from Impedance Signatures

Parameter	Symbol	Unit	Model Interpretation
Equivalent Mass	M	kg	Mass-like term of the adopted coupled representation
Equivalent Stiffness	K	MN/m	Stiffness-like term of the adopted coupled representation
Equivalent Damping	C	Ns/m	Dissipative term of the adopted coupled representation

sign, because the resulting ratio can be numerically unstable.

6.6 Signature Response Under Heating

6.6.1 Without Compensation Signatures

The temperature-associated drift problem is introduced before the specimen-level results are compared.

When SFRC specimens are subjected to elevated temperatures, the impedance signatures recorded by the PZT sensor exhibit significant and systematic shifts relative to the baseline (ambient temperature) signature. This phenomenon, termed "thermal drift," represents a fundamental challenge for EMI-based structural health monitoring because temperature-induced changes in the signature can mask or be misinterpreted as structural damage.

Figures 6.3 and 6.4 present the conductance signatures of the four intact SFRC specimens at ambient and elevated temperatures. The separate full-width panels retain the original records while making the frequency axes and temperature legends readable at print size. The signatures show temperature-dependent displacement and amplitude variation, but the magnitude and direction of the changes are specimen-specific.

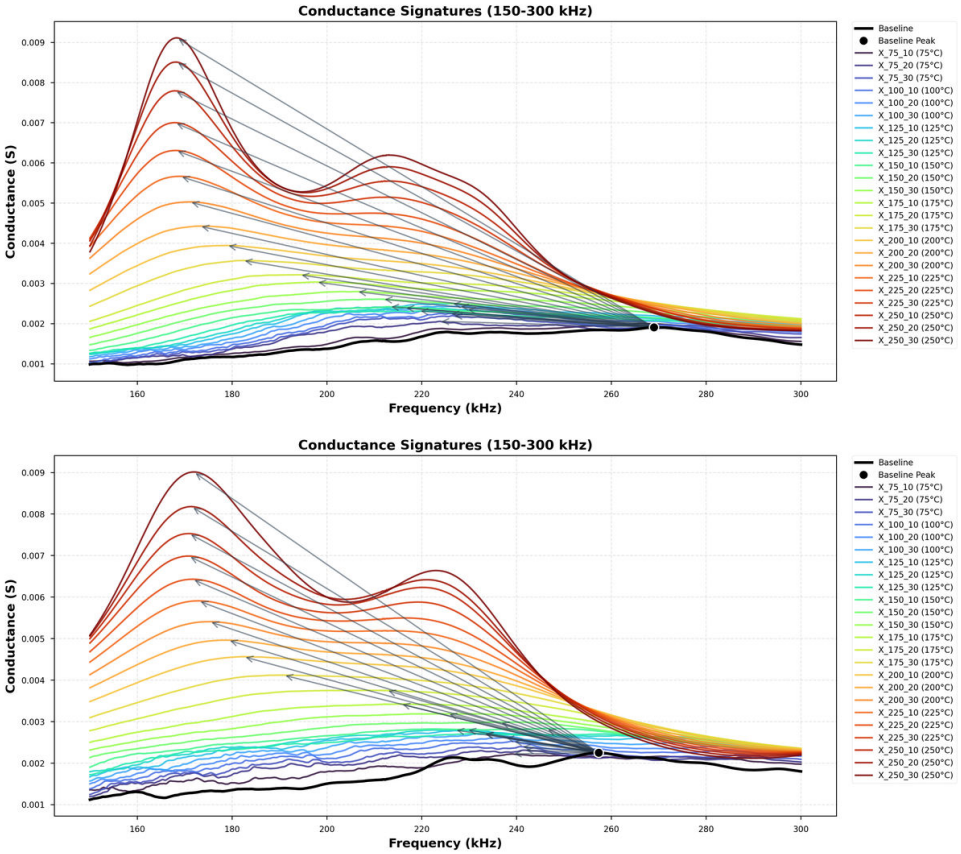

Figure 6.3: Uncompensated intact conductance signatures for SFC1 and SFC3 (AR 65).

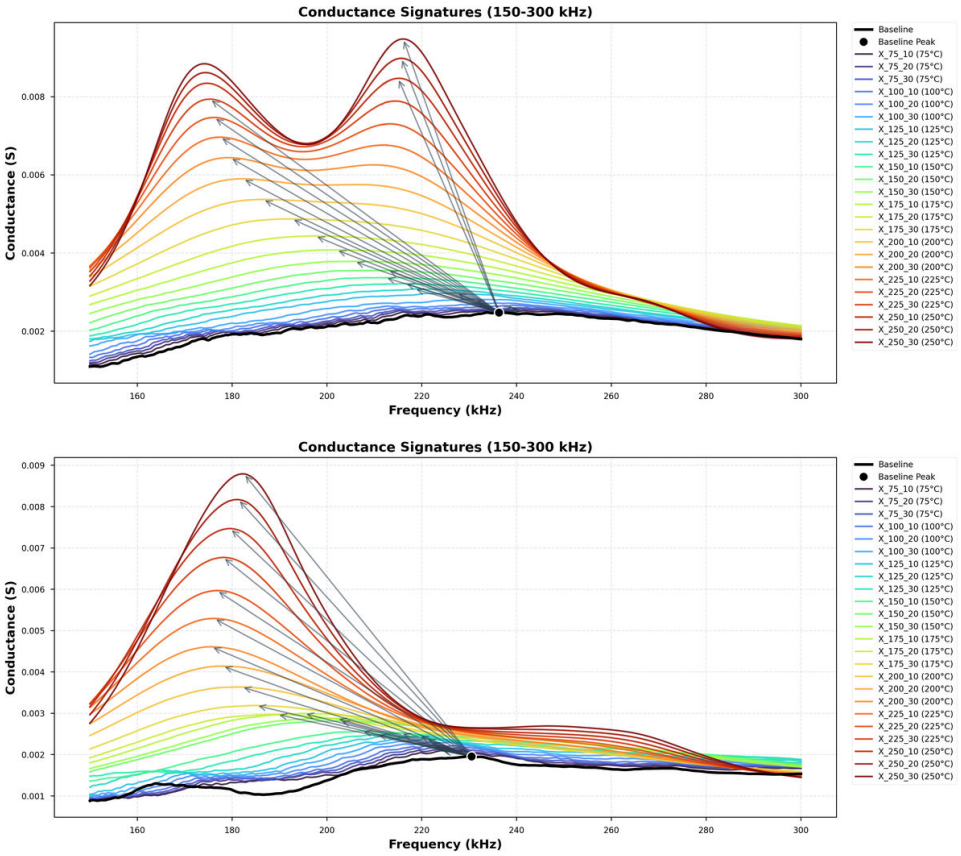

Figure 6.4: Uncompensated intact conductance signatures for SFC2 and SFC4 (AR 55).

The observed displacement cannot be assigned to a single material mechanism from these records alone. It reflects the combined temperature sensitivity of the PZT element, its protective jacket and interface, and the surrounding SFRC. Accordingly, the raw signature is treated as the response of the coupled measurement system; the model-derived EPS results are interpreted separately and with the limitations stated later in this chapter.

6.6.1.1 Quantification of Thermal Drift

The magnitude of thermal drift was quantified for all four SFRC specimens by analyzing the resonance frequency shifts and amplitude changes from the baseline condition to 250°C. Table 6.6 presents the complete thermal drift data extracted from the signature analysis.

SFC1 (AR65/SF0.5%) exhibited the largest frequency shift of 90-95 kHz, with the primary resonance peak decreasing from 265 kHz at baseline to 170-175 kHz at 250°C. This represents a frequency reduction of approximately 35%, the highest among all specimens.

Table 6.6: Thermal Drift Quantification for All Four Intact SFRC Specimens (Without Compensation)

SFC	AR	SF (%)	Baseline Peak (kHz)	Peak at 250°C (kHz)	Shift (kHz)	Amplitude Increase (%)
1	65	0.5	265	170-175	90-95	>200
3	65	0.75	200-255	175-225	25-30	>150
2	55	0.5	180-235	170-220	10-15	>220
4	55	0.75	232	183	49	>180

SFC3 (AR65/SF0.75%) showed a frequency shift of 25–30 kHz, with peaks shifting from the 200–255 kHz range to 175–225 kHz. This shift is smaller than that observed for SFC1, but the single specimen at each dosage does not isolate a fibre-content effect.

SFC2 (AR55/SF0.5%) showed a frequency shift of 10–15 kHz, with peaks moving from 180–235 kHz to 170–220 kHz. This is the smallest shift among the four intact records, but it cannot be attributed independently to fibre length.

SFC4 (AR55/SF0.75%) exhibited a frequency shift of 49 kHz, with the primary peak decreasing from 232 kHz to 183 kHz. The result is reported for this specimen without assigning a combined aspect-ratio and dosage mechanism.

All four intact specimens have amplitude increases above 150%, with SFC2 showing the largest reported increase, above 220%. Together with frequency shifts of approximately 10–95 kHz, these changes show that the raw signatures are strongly temperature-dependent over the progressive-heating sequence.

6.6.1.2 Material Comparison of the Thermal Response

The four specimens show different thermal-drift magnitudes, but the design does not provide replicated groups for separating aspect-ratio and fibre-dosage effects.

For the aspect-ratio groups, the AR65 specimens have baseline resonance frequencies in the 200–265 kHz range and shifts of 25–95 kHz, whereas the AR55 specimens have baseline frequencies in the 180–235 kHz range and shifts of 10–49 kHz. Because specimen identity, dosage and sensor installation vary concurrently, these two unreplicated pairs do not establish a fibre-length effect.

For the fibre-dosage groups, within the AR65 pair, SFC1 (0.5%) shows a 90–95 kHz shift and SFC3 (0.75%) a 25–30 kHz shift. Within the AR55 pair, SFC2 (0.5%) shows a 10–15 kHz shift and SFC4 (0.75%) a 49 kHz shift. The ordering reverses between the two AR pairs; with one specimen per configuration, this pattern does not isolate dosage or define an optimal mixture.

At specimen level, the observed frequency-shift magnitudes increase in the order

SFC2 (10–15 kHz), SFC3 (25–30 kHz), SFC4 (49 kHz) and SFC1 (90–95 kHz). This is a descriptive ordering of the four measured records, not a material-stability ranking.

For the subsequent structural comparison, the frequency shifts of 10–95 kHz and amplitude increases above 150% during intact heating show that a comparison made against a single ambient baseline would contain a substantial temperature-associated component. The raw signatures are retained as evidence, while compensated and matched-state comparisons are examined separately.

6.6.2 With Compensation Signatures

The effect of compensation on the intact-state signatures is examined first.

The Enhanced EFS procedure was applied to reduce temperature-associated frequency displacement and channel-wise mean offset in the raw signatures. The compensated signatures are compared with the original records to quantify the reduction; the procedure does not guarantee complete separation of structural and thermal effects.

Figures 6.5 and 6.6 present the compensated conductance signatures for the four intact specimens. They are shown at the same full-width scale used for the uncompensated records so that residual frequency and amplitude differences remain visible rather than being concealed by reduction to a four-panel composite.

6.6.2.1 Quantification of the Compensation Effect

The processing effect was evaluated by comparing selected peak shifts before and after compensation for all four intact records. Table 6.7 presents this within-specimen comparison.

Table 6.7: Comparison of Thermal Drift Before and After Compensation for All Four Specimens

SFC	AR	SF (%)	Shift Without Comp (kHz)	Shift With Comp (kHz)	Reduction (%)
1	65	0.5	90-95	15-20	78-80
3	65	0.75	25-30	5-8	73-80
2	55	0.5	10-15	3-5	67-70
4	55	0.75	49	10-12	75-80

The selected peak-shift measure is smaller after compensation in all four records.

SFC1 (AR65/SF0.5%) has a reduction from approximately 90–95 kHz before compensation to 15–20 kHz after compensation, corresponding to 78–80% of the selected peak-shift measure.

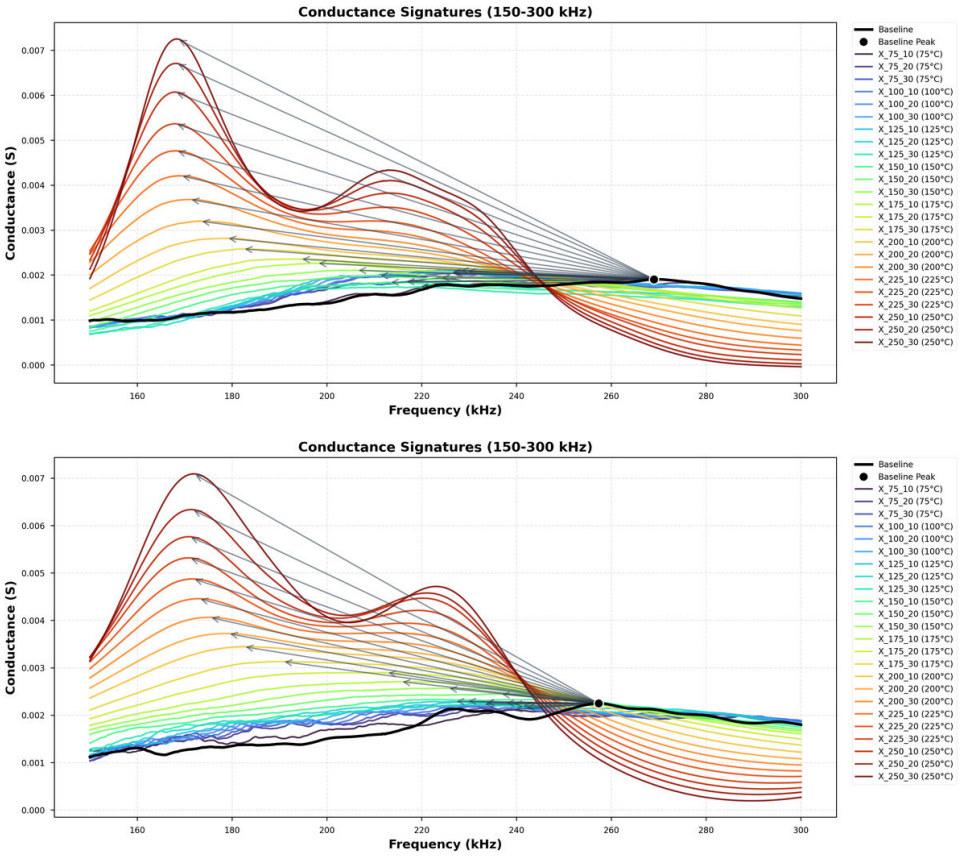

Figure 6.5: Compensated intact conductance signatures for SFC1 and SFC3 (AR 65).

SFC3 (AR65/SF0.75%) has a shift reduction from 25–30 kHz to 5–8 kHz, corresponding to 73–80% in the selected measure.

SFC2 (AR55/SF0.5%) has a shift reduction from 10–15 kHz to 3–5 kHz, corresponding to 67–70%. Its residual is the smallest among these four records, without establishing configuration-level stability.

SFC4 (AR55/SF0.75%) has a reduction from approximately 49 kHz to 10–12 kHz, corresponding to 75–80% in the selected measure. This is consistent with a reduction for the other intact specimens, while the residual magnitude remains configuration-dependent.

6.6.2.2 Specimen-Level Comparison after Compensation

The four records allow descriptive comparison of the processing effect, but not independent estimation of material-parameter effects.

For the aspect-ratio groups, the AR65 records have reductions of approximately 73–80%, while the AR55 records have reductions of approximately 67–80%. The overlapping ranges do not establish an aspect-ratio effect.

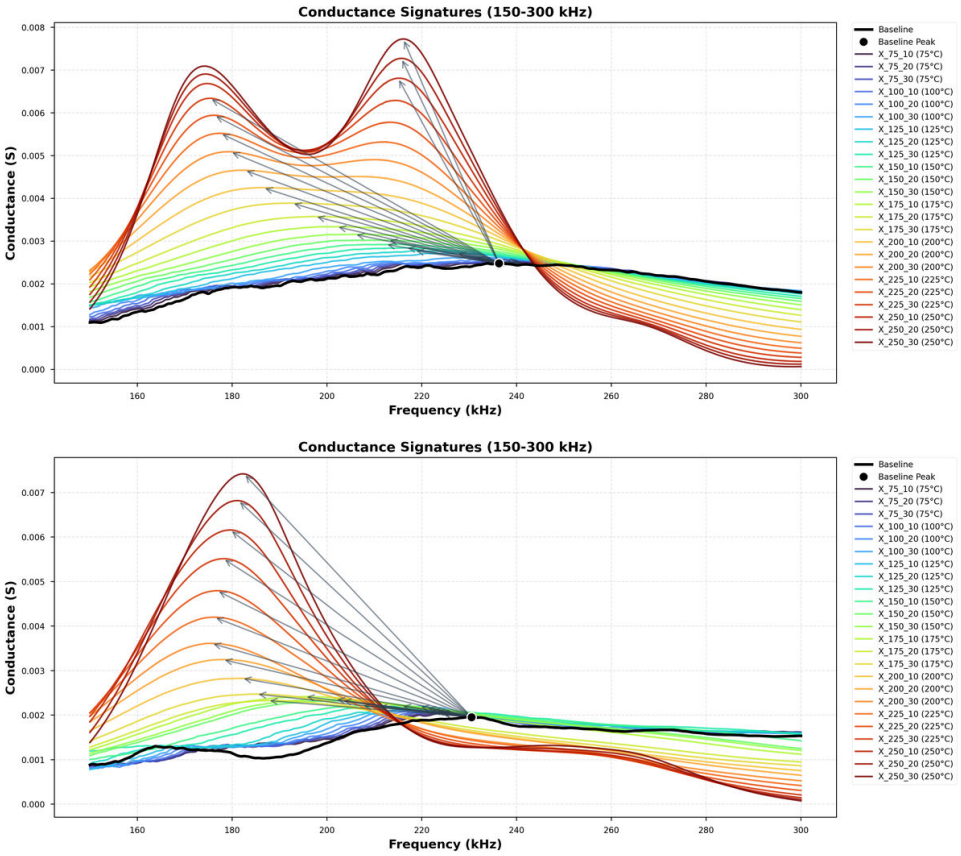

Figure 6.6: Compensated intact conductance signatures for SFC2 and SFC4 (AR 55).

For the fibre-dosage groups, within the AR65 pair, the reported reduction ranges are 78–80% for SFC1 and 73–80% for SFC3; within the AR55 pair they are 67–70% for SFC2 and 75–80% for SFC4. The mixed overlap and single specimen per configuration do not establish a dosage or matrix-stability effect.

The residual-shift ordering in Table 6.8 compares the four measured shifts after compensation; it is not a material-stability rating.

Table 6.8: Descriptive ordering of residual peak shifts after compensation.

Order	SFC	Configuration	Compensated Shift (kHz)	Scope
1	2	AR55/SF0.5%	3–5	One specimen
2	3	AR65/SF0.75%	5–8	One specimen
3	4	AR55/SF0.75%	10–12	One specimen
4	1	AR65/SF0.5%	15–20	One specimen

Across the four intact specimens, the selected peak-shift summary is reduced by 67–80% after compensation. The residual shifts are approximately 3–20 kHz, compared with 10–95 kHz before compensation, and SFC2 has the smallest reported residual range (3–5 kHz). These values quantify the present progressive-heating records; the study

does not define an application acceptance limit or establish performance independently of configuration.

Overall, the selected shift measure is smaller after compensation in the four intact series. This is an internal comparison of the processing branches and does not independently establish damage-detection reliability over 75–250°C.

6.7 Equivalent Structural Parameters (EPS) Under Intact Heating

The Equivalent Structural Parameters (EPS) derived from impedance signatures provide physical insight into the thermal response of SFRC structures. Unlike statistical SHM indices that quantify signature deviation, EPS parameters represent the monitored structure as an equivalent single-degree-of-freedom mechanical system with mass (M), stiffness (K), and damping (C) components.

6.7.1 Equivalent Mass Parameter

The uncompensated mass-like response is examined for all four specimens.

The equivalent mass parameter exhibited temperature-dependent behaviour across the four intact specimens. Figures 6.7–6.10 preserve the complete mass, stiffness and damping transitions for every specimen while presenting each three-axis source image at full page width. The numerical tables that follow remain the authority for exact values; the figures show the trajectories and the effect of compensation.

Table 6.9 presents the equivalent mass values at each temperature stage from 75°C to 250°C for all four SFRC specimens. This comprehensive temperature progression data was extracted from the EPS discussion files for each specimen.

Table 6.9: Equivalent Mass (kg) at Each Temperature for All Four Intact SFRC Specimens (Without Compensation)

Temperature	**SFC1 (AR65/0.5%)**	**SFC3 (AR65/0.75%)**	**SFC2 (AR55/0.5%)**	**SFC4 (AR55/0.75%)**
Ambient	0.0311	0.0327	0.0247	0.0298
75°C	0.0318	0.0499	-0.0462	0.0219
100°C	0.0337	0.1274	-0.3989	0.0339
125°C	0.8807	0.6028	0.1254	0.0229
150°C	-2.2418	0.0076	-0.3249	-0.6995
175°C	-0.0237	-0.1171	0.3029	-0.0173
200°C	0.0453	1.4623	-0.4225	-0.1328
225°C	0.0081	-0.0268	-0.0664	0.0146
250°C	-0.0433	-0.1372	-0.2193	-0.2351

The temperature progression data reveals distinct mass behaviour patterns for each SFRC configuration. Table 6.10 summarises the overall mass change from 75°C

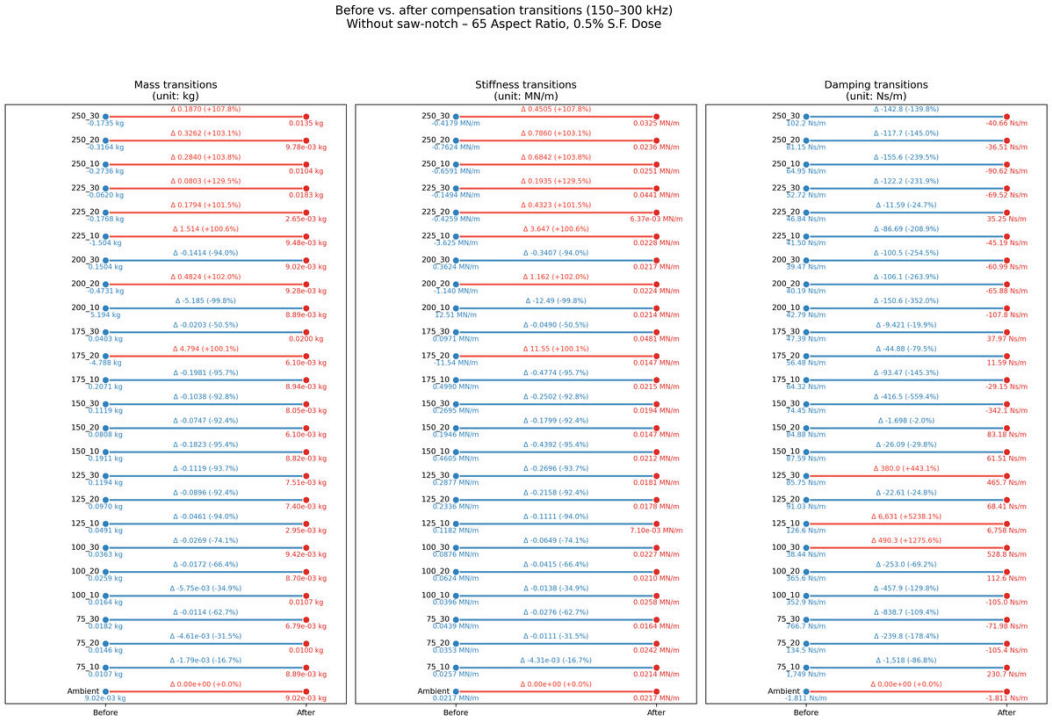

Figure 6.7: Intact EPS transitions before and after compensation for SFC1 (AR 65, 0.50% fibre).



Figure 6.8: Intact EPS transitions before and after compensation for SFC3 (AR 65, 0.75% fibre).

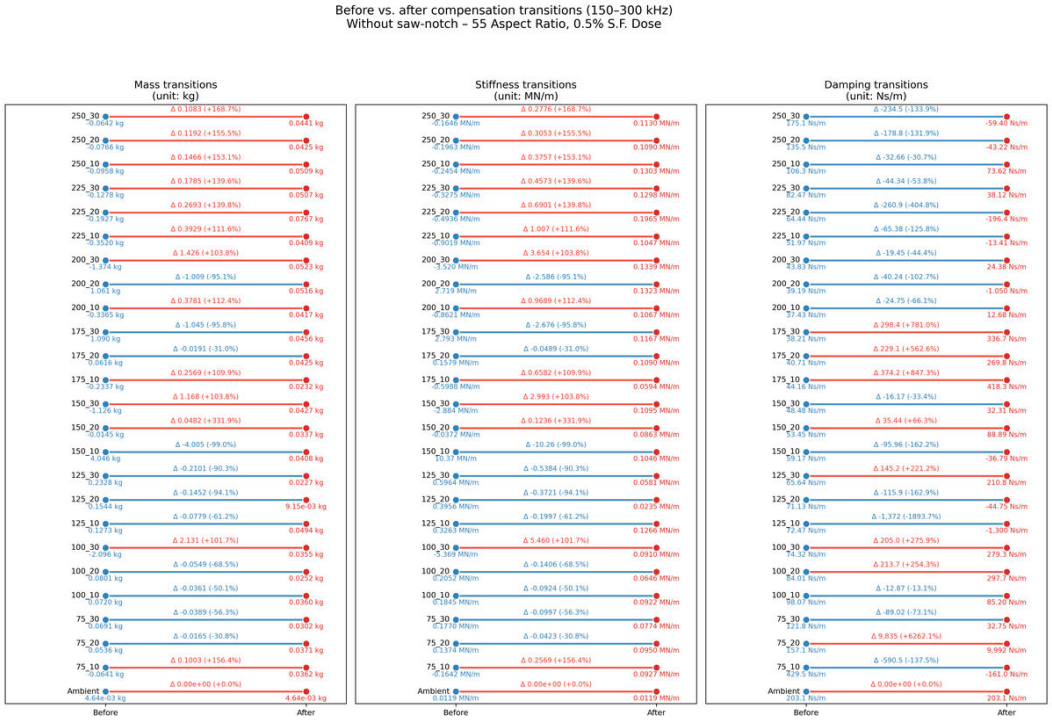

Figure 6.9: Intact EPS transitions before and after compensation for SFC2 (AR 55, 0.50% fibre).



Figure 6.10: Intact EPS transitions before and after compensation for SFC4 (AR 55, 0.75% fibre).

to 250°C for all four specimens.

Table 6.10: Equivalent Mass Change Summary for All Four Intact SFRC Specimens (Without Compensation)

SFC	AR	SF (%)	Mass at 75°C (kg)	Mass at 250°C (kg)	Change (%)	Trend
1	65	0.5	0.0313	-0.1230	-493.1	Decreasing
3	65	0.75	0.0416	-0.0805	-293.6	Decreasing
2	55	0.5	-0.0105	-0.1068	-913.6	Decreasing
4	55	0.75	0.0282	-0.5441	-2029.2	Decreasing

For SFC1 (AR65/SF0.5%), the mass-like parameter changes by -493.1% from 75 to 250 °C, moving from 0.0318 kg at 75 °C to -0.0433 kg at 250 °C. A positive excursion of 0.8807 kg at 125 °C is followed by -2.2418 kg at 150 °C. This non-monotonic excursion and sign change belong to the fitted equivalent parameter and do not establish a physical phase transition.

For SFC3 (AR65/SF0.75%), the reported value of 0.0416 kg at 75°C decreased to -0.0805 kg at 250°C, representing a -293.6% change. The fitted trajectory was non-monotonic and included a positive excursion to 1.4623 kg at 200°C; this value is reported without assigning a material mechanism.

For SFC2 (AR55/SF0.5%), the reported value of -0.0105 kg at 75°C decreased to -0.1068 kg at 250°C, representing a -913.6% decrease. The trend was non-monotonic, reaching its most negative value at 100°C (-0.3989 kg) before partial recovery at 175°C (0.3029 kg).

For SFC4 (AR55/SF0.75%), the reported value of 0.0282 kg at 75°C decreased to -0.5441 kg at 250°C, representing a reported -2029.2% change. The fitted trajectory was non-monotonic and changed sign at 150°C, where the value was -0.6995 kg. Because the fitted term crosses zero, its percentage change is numerically sensitive and is not interpreted as a physical mass loss.

Comparison of the mass-like term shows different trajectories among the four specimens. At 75°C, the two AR65 records are positive (0.0313–0.0416 kg), whereas SFC2 is negative (-0.0462 kg). The reported end-to-end percentage changes are -294% to -493% for the AR65 pair and -914% to -2029% for the AR55 pair. Because several references are near zero or change sign, these ratios do not provide a physical ranking of the fibre configurations.

Steel Fibre Dose Effect (0.5% vs 0.75%).

The effect of steel fibre content on the fitted mass-like response varies with aspect ratio.

The mass-like term shows mixed configuration-associated patterns. Within the

AR 65 pair, SFC3 has a smaller reported percentage change than SFC1; within the AR 55 pair, the ordering reverses. The four-specimen design and near-zero or sign-changing EPS references do not support a matrix-constraint mechanism, a fibre-length effect or an optimal configuration.

The fitted mass-like term becomes negative in each intact series, with several sign transitions occurring between 150°C and 175°C. A sign change in a fitted equivalent parameter does not establish a material transition or an operating threshold; it indicates that the adopted local representation should not be interpreted as a conventional positive physical mass over those stages.

The compensated mass-like response is examined for all four specimens.

The temperature compensation algorithm was applied to the equivalent mass calculations to isolate structural effects from thermal drift. Table 6.11 presents the mass values at each temperature stage after compensation for all four specimens.

Table 6.11: Equivalent Mass (kg) at Each Temperature for All Four Intact SFRC Specimens (With Compensation)

Temperature	**SFC1 (AR65/0.5%)**	**SFC3 (AR65/0.75%)**	**SFC2 (AR55/0.5%)**	**SFC4 (AR55/0.75%)**
Ambient	0.0350	0.0368	0.0266	0.0330
75°C	0.0252	0.0249	-0.0029	0.0281
100°C	0.0207	0.0160	-0.0295	0.0225
125°C	0.0069	0.0152	-0.0741	0.0171
150°C	0.0120	0.0100	0.5609	0.0129
175°C	0.0063	0.0009	0.1244	-0.0027
200°C	-0.0189	-0.0176	0.1028	-0.0211
225°C	-0.0265	-0.0311	0.1543	-0.0189
250°C	-0.0300	-0.1163	0.0940	-0.0089

Table 6.12 compares the reported mass-like parameter changes before and after temperature compensation for all four specimens.

Table 6.12: Comparison of Mass Parameter Changes Before and After Temperature Compensation (All 4 specimens)

SFC	**AR**	**SF**	**Change Before Comp (%)**	**Change After Comp (%)**	**Reported reduction**
1	65	0.5%	-493.1	-202.9	59% reduction
3	65	0.75%	-293.6	-361.9	Increased
2	55	0.5%	-913.6	+1128.5	Sign reversed
4	55	0.75%	-2029.2	-141.5	93% reduction

For SFC1 (AR65/SF0.5%), the magnitude of the reported end-to-end mass-like change decreases from -493.1% before compensation to -202.9% after compensation,

a 59% reduction. The compensated fitted values change from 0.0252 kg at 75°C to -0.0300 kg at 250°C; this numerical reduction is not interpreted as a direct change in physical mass or as proof of thermal stability.

For SFC3 (AR65/SF0.75%), the reported value of 0.0249 kg at 75°C decreased to -0.1163 kg at 250°C, representing a -361.9% change. The trajectory was non-monotonic, and the reported end-to-end magnitude after compensation exceeded that before compensation.

For SFC2 (AR55/SF0.5%), the reported value of -0.0029 kg at 75°C increased to 0.0940 kg at 250°C, representing a +1128.5% increase. The trend was non-monotonic, showing a positive trend rather than the negative trend observed before compensation.

For SFC4 (AR55/SF0.75%), the reported value of 0.0281 kg at 75°C decreased to -0.0089 kg at 250°C, representing a -141.5% change. The fitted trajectory was non-monotonic and crossed zero over the measured range.

In summary, the fitted mass-like variability decreases by 93% for SFC4 and 59% for SFC1, changes sign for SFC2 and increases for SFC3. The mixed outcomes preclude a single configuration-independent performance claim.

These results show that the change produced by compensation varies among specimens. SFC4 has the largest reduction in the reported mass-like drift summary, but the unreplicated configurations do not establish a material-performance ranking.

6.7.2 Equivalent Stiffness Parameter

The uncompensated stiffness-like response is examined for all four specimens.

The equivalent stiffness parameter is a model-derived characteristic of the coupled JPS–interface–SFRC response and is not a direct measurement of the specimen's static load-bearing stiffness. Its uncompensated and compensated trajectories are included in the full-width specimen plots in Figures 6.7–6.10; they are not repeated as a second reduced composite.

Table 6.13 presents the equivalent stiffness values at each temperature stage from Ambient to 250°C for all four specimens without temperature compensation.

Table 6.14 summarises the overall stiffness changes from 75°C to 250°C for all four specimens.

For SFC1 (AR65/SF0.5%), the stiffness-like parameter changes by -493.1% from 75 to 250 °C, from 75,368 to -296,295 MN/m. The series has a positive excursion of 2,122,150 MN/m at 125 °C followed by -5,401,680 MN/m at 150 °C. This non-monotonic fitted response and sign change do not establish a physical instability threshold.

Table 6.13: Equivalent Stiffness (MN/m) at Each Temperature for All Four Intact SFRC Specimens (Without Compensation)

Temperature	SFC1 (AR65/0.5%)	SFC3 (AR65/0.75%)	SFC2 (AR55/0.5%)	SFC4 (AR55/0.75%)
Ambient	74,823	80,565	63,269	71,638
75°C	76,502	122,677	-118,468	52,618
100°C	81,181	313,494	-1,021,966	81,517
125°C	2,122,150	1,483,097	321,413	55,128
150°C	-5,401,680	18,590	-832,319	-1,684,181
175°C	-57,163	-288,091	776,116	-41,661
200°C	109,235	3,598,117	-1,082,408	-319,779
225°C	19,619	-65,892	-170,142	35,155
250°C	-104,336	-337,628	-561,972	-565,970

Table 6.14: Equivalent Stiffness Change Summary for All Four Intact SFRC Specimens (Without Compensation)

SFC	AR	SF (%)	K at 75°C (MN/m)	K at 250°C (MN/m)	Change (%)	Trend
1	65	0.5	75,368	-296,295	-493.1	Decreasing
3	65	0.75	102,394	-198,188	-293.6	Decreasing
2	55	0.5	-27,007	-273,740	-913.6	Decreasing
4	55	0.75	67,896	-1,309,865	-2029.2	Decreasing

For SFC3 (AR65/SF0.75%), the reported value of 102,394 MN/m at 75°C decreased to -198,188 MN/m at 250°C, representing a -293.6% change. The fitted trajectory was non-monotonic and included a positive excursion to 3,598,117 MN/m at 200°C.

For SFC2 (AR55/SF0.5%), the reported value of -27,007 MN/m at 75°C decreased to -273,740 MN/m at 250°C, representing a reported -913.6% change. The fitted trajectory was non-monotonic and crossed zero repeatedly; it is therefore interpreted as a model-derived equivalent term rather than a direct measurement of structural stiffness.

For SFC4 (AR55/SF0.75%), the reported value of 67,896 MN/m at 75°C decreased to -1,309,865 MN/m at 250°C, corresponding to a reported -2029.2% change. The non-monotonic trajectory and sign reversal make the percentage highly sensitive to its reference value.

The compensated stiffness-like response is examined for all four specimens.

Table 6.15 presents the stiffness values after temperature compensation for all four specimens.

Table 6.16 compares stiffness changes before and after temperature compensation.

For SFC1 (AR65/SF0.5%), the magnitude of the reported end-to-end stiffness-like change decreases from -493.1% to -202.9% after compensation, a 59% reduction. The compensated fitted values change from 60,818 MN/m at 75°C to -72,229 MN/m at 250°C; this reduction is not treated as a direct measurement of structural stiffness or as

Table 6.15: Equivalent Stiffness (MN/m) at Each Temperature for All Four Intact SFRC Specimens (With Compensation)

Temperature	SFC1 (AR65/0.5%)	SFC3 (AR65/0.75%)	SFC2 (AR55/0.5%)	SFC4 (AR55/0.75%)
Ambient	84,321	90,546	68,218	79,339
75°C	60,818	61,353	-7,423	67,696
100°C	49,903	39,245	-75,615	54,228
125°C	16,526	37,355	-189,740	41,228
150°C	28,920	24,670	1,437,019	31,174
175°C	15,099	2,311	318,685	-6,535
200°C	-45,633	-43,324	263,394	-50,735
225°C	-63,944	-76,609	395,271	-45,505
250°C	-72,229	-286,036	240,837	-21,411

Table 6.16: Comparison of Stiffness Changes Before and After Temperature Compensation (All 4 specimens)

SFC	AR	SF	Change Before (%)	Change After (%)	Reported reduction
1	65	0.5%	-493.1	-202.9	59% reduction
3	65	0.75%	-293.6	-361.9	Increased
2	55	0.5%	-913.6	+1128.5	Sign reversed
4	55	0.75%	-2029.2	-141.5	93% reduction

proof of thermal stability.

For SFC3 (AR65/SF0.75%), the reported value of 61,353 MN/m at 75°C decreased to -286,036 MN/m at 250°C, representing a -361.9% decrease. The trend was non-monotonic, with compensated stiffness change exceeding the uncompensated change.

For SFC2 (AR55/SF0.5%), the stiffness-like parameter changes from -7,423 MN/m at 75 °C to 240,837 MN/m at 250 °C, corresponding to +1128.5%. The non-monotonic compensated sequence reverses sign relative to the initial value; the percentage is interpreted with the negative, near-zero-scale denominator in view.

For SFC4 (AR55/SF0.75%), the reported value of 67,696 MN/m at 75°C decreased to -21,411 MN/m at 250°C, representing a -141.5% change. The fitted trajectory was non-monotonic and crossed zero over the measured range.

For the aspect-ratio groups, before compensation, the reported stiffness-like changes are -294% to -493% for the AR65 pair and -914% to -2029% for the AR55 pair. After compensation, the trajectories remain specimen-dependent and include a sign reversal for SFC2. These unreplicated comparisons do not isolate an aspect-ratio effect or demonstrate constraint by a particular fibre length.

The configuration-associated stiffness response differs between the two aspect-ratio pairs. Within the AR 65 pair, SFC3 (0.75%) has a smaller reported percentage change than SFC1 (0.50%), whereas the ordering reverses within the AR 55 pair.

Because one specimen represents each configuration and several EPS references approach or cross zero, the percentages do not establish a dosage effect or an optimal configuration.

In summary, the fitted stiffness-like variability decreases by 93% for SFC4 and 59% for SFC1, changes sign for SFC2 and increases for SFC3. These specimen-level outcomes are not a general ranking of material configurations.

6.7.3 Equivalent Damping Parameter

The uncompensated damping-like response is examined for all four specimens.

The equivalent damping parameter describes the dissipative term in the adopted coupled model. Its fitted trajectories include pronounced variation and sign changes. They are displayed with the other EPS results in the full-width specimen plots in Figures 6.7–6.10; the numerical values and sign changes are retained in the following tables.

Table 6.17 presents the damping change summary from 75°C to 250°C for all four specimens without temperature compensation.

Table 6.17: Equivalent Damping Change Summary for All Four Intact SFRC Specimens (Without Compensation)

SFC	AR	SF (%)	Change (%)	Trend	Sequence
1	65	0.5	+23.1	Increasing	Non-monotonic
3	65	0.75	+92.9	Increasing	Non-monotonic
2	55	0.5	+123.2	Increasing	Non-monotonic
4	55	0.75	+126.2	Increasing	Non-monotonic

SFC1 (AR65/SF0.5%) has the smallest reported end-to-end damping-like change, +23.1% from 75°C to 250°C. This is a specimen-level observation and does not establish the stability of that fibre configuration.

SFC3, SFC2 and SFC4 have reported end-to-end damping-like changes of +92.9%, +123.2% and +126.2%, respectively. The values differ among specimens, but the four-series design does not separate the influences of aspect ratio, dosage, specimen variability and sensor installation.

The fitted damping-like term increases between the first and final stages in all four intact series, unlike the corresponding end-to-end mass-like and stiffness-like changes. The measurement does not isolate an SFRC energy-dissipation mechanism, so this contrast is retained as a feature of the fitted representation.

The compensated damping-like response is examined for all four specimens.

Table 6.18 presents the damping changes after temperature compensation for all four specimens.

Table 6.18: Equivalent Damping Change Summary for All Four Intact SFRC Specimens (With Compensation)

SFC	AR	SF (%)	Change (%)	Trend	Sequence
1	65	0.5	+51.0	Increasing	Non-monotonic
3	65	0.75	-132.8	Decreasing	Non-monotonic
2	55	0.5	-273.3	Decreasing	Non-monotonic
4	55	0.75	-7.6	Decreasing	Non-monotonic

Table 6.19 compares damping changes before and after temperature compensation.

Table 6.19: Comparison of Damping Changes Before and After Temperature Compensation (All 4 specimens)

SFC	AR	SF	Before (%)	After (%)	Effect
1	65	0.5%	+23.1	+51.0	Increased
3	65	0.75%	+92.9	-132.8	Trend reversed
2	55	0.5%	+123.2	-273.3	Trend reversed
4	55	0.75%	+126.2	-7.6	94% reduction

For SFC1 (AR65/SF0.5%), the reported end-to-end damping-like change increases from +23.1% before compensation to +51.0% after compensation. The processing therefore does not reduce this fitted-parameter summary for the specimen; the comparison does not identify the cause of the increase.

SFC2, SFC3 and SFC4 show different processing outcomes. SFC3 changes from +92.9% before compensation to -132.8% after compensation, while SFC2 changes from +123.2% to -273.3%. SFC4 changes from +126.2% to -7.6%, the largest reduction in absolute magnitude among these three records. Because the fitted damping-like term can change sign, the values are interpreted with the full trajectories rather than as physical damping stability.

For the aspect-ratio groups, before compensation, the two AR55 records have changes of +123–126%, compared with +23–93% for the AR65 records. After compensation, both AR55 trajectories reverse sign, while the AR65 results are mixed. With one specimen per configuration, the comparison does not demonstrate an independent fibre-length or interface effect.

For the fibre-dosage groups, within the AR65 pair, the reported change is +23.1% for 0.50% fibre and +92.9% for 0.75%. Within the AR55 pair, the corresponding values are +123.2% and +126.2%. The after-compensation ordering is not uniform across parameters, and these unreplicated pairs do not establish a dosage effect.

The damping-like trajectories are non-monotonic and include sign reversals and end-to-end percentage changes exceeding 100% for selected records. Because the fitted parameter can approach or cross zero, these percentages are sensitive to the reference value. The result supports joint examination of the mass-, stiffness- and damping-like trajectories rather than assigning the damping-like term a fixed primary or secondary monitoring role.

6.8 SHM Indices Under Intact Heating

The statistical SHM indices derived from impedance signatures quantify the deviation between baseline and temperature-affected signatures. These indices provide damage-sensitive features for structural health assessment. This section analyzes 13 SHM indices across all four SFRC specimens under intact heating conditions.

6.8.1 RMSD Index Analysis

The temperature progression of RMSD is examined for the four specimens.

The Root Mean Square Deviation (RMSD) index quantifies the overall difference between baseline and elevated temperature signatures. Figure 6.11 presents the RMSD comparison plots for all four intact specimens. RMSD index comparison for all four intact SFRC specimens showing before compensation, after compensation, and the difference. All specimens exhibit increasing RMSD with temperature.

Table 6.20 presents the RMSD values at each temperature from 75°C to 250°C for all four specimens.

Table 6.20: RMSD Values at Each Temperature for All Four Intact SFRC Specimens

Temperature	SFC1 (AR65/0.5%)	SFC3 (AR65/0.75%)	SFC2 (AR55/0.5%)	SFC4 (AR55/0.75%)
75°C	0.079	0.111	0.034	0.085
100°C	0.147	0.152	0.072	0.104
125°C	0.149	0.188	0.149	0.172
150°C	0.209	0.303	0.263	0.311
175°C	0.410	0.522	0.469	0.423
200°C	0.759	0.843	0.823	0.712
225°C	1.207	1.175	1.162	1.147
250°C	1.619	1.527	1.408	1.586

Table 6.21 presents the statistical summary of RMSD values for all four specimens.

For SFC1 (AR65/SF0.5%), RMSD increases from 0.079 at 75 °C to 1.619 at 250 °C, a 20.5× ratio. Its mean is 0.572 and its range, 1.701, is the largest among the

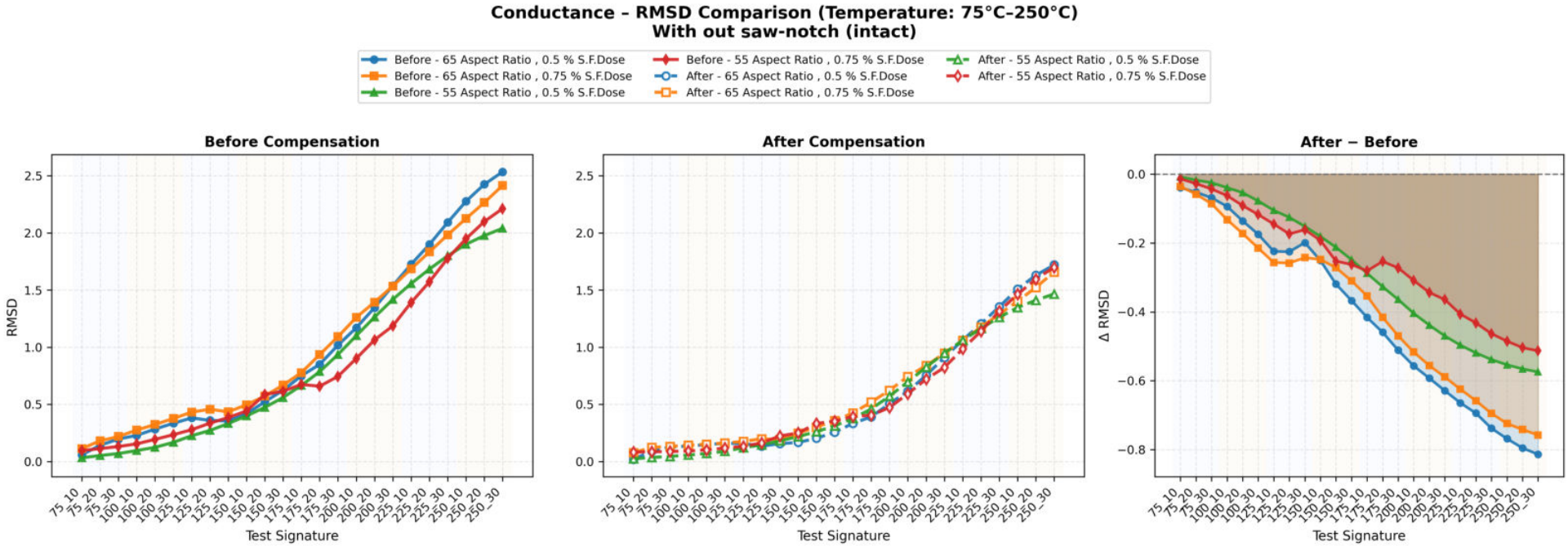

Figure 6.11: RMSD index comparison for all four intact SFRC specimens.

Table 6.21: RMSD Statistical Summary for All Four Intact SFRC Specimens

SFC	AR	SF (%)	Mean	Std Dev	Min	Max	Range
1	65	0.5	0.572	0.541	0.019	1.720	1.701
3	65	0.75	0.603	0.499	0.077	1.658	1.581
2	55	0.5	0.548	0.495	0.024	1.466	1.442
4	55	0.75	0.568	0.515	0.082	1.699	1.617

four intact specimen records.

SFC3 (AR65/SF0.75%) showed RMSD increasing from 0.111 at 75°C to 1.527 at 250°C (13.8× increase). The mean RMSD of 0.603 is the highest among all specimens, indicating slightly elevated baseline thermal response.

SFC2 (AR55/SF0.5%) increases from 0.034 at 75°C to 1.408 at 250°C (41.4×). Its final RMSD is the lowest among the four intact specimens, although the relative increase is the largest because the starting value is small.

SFC4 (AR55/SF0.75%) showed RMSD increasing from 0.085 at 75°C to 1.586 at 250°C (18.7× increase). The behaviour is intermediate between other configurations.

For the aspect-ratio groups, the mean RMSD is 0.587 for the two AR65 specimens and 0.558 for the two AR55 specimens, a 5.4% difference. SFC2 has the lowest reported maximum (1.408). These unreplicated group differences do not establish a fibre-length effect.

For the fibre-dosage groups, the mean RMSD is 0.560 for the two 0.50% records and 0.585 for the two 0.75% records, a 4.3% difference. The specimen means increase in the order SFC2, SFC4, SFC1 and SFC3. These unreplicated values do not establish dosage-dependent stability.

Across the measured temperature range, RMSD remains below 0.2 for all four specimens over 75–125°C, rises from approximately 0.15–0.31 to 0.41–0.52 over 125–175°C, and reaches about 1.1–1.2 by 225°C. Values above 1.4 occur at 250°C. These ranges describe the plotted progression and are not operational thresholds.

6.8.2 MAPD Index Analysis

The temperature progression of MAPD is examined for the four specimens.

The Mean Absolute Percentage Deviation (MAPD) index quantifies the average percentage difference between baseline and temperature-affected signatures. Figure 6.12 presents the MAPD comparison plots for all four intact specimens. MAPD index comparison for all four intact SFRC specimens showing before compensation, after compensation, and the difference. All specimens exhibit increasing MAPD with

temperature.

Table 6.22 presents the MAPD values at each temperature from 75°C to 250°C for all four specimens.

Table 6.22: MAPD (%) Values at Each Temperature for All Four Intact SFRC Specimens

Temperature	**SFC1 (AR65/0.5%)**	**SFC3 (AR65/0.75%)**	**SFC2 (AR55/0.5%)**	**SFC4 (AR55/0.75%)**
75°C	6.30	10.46	3.04	7.43
100°C	11.62	14.07	6.48	9.38
125°C	13.12	17.31	13.50	14.54
150°C	19.33	29.09	24.66	26.68
175°C	40.18	51.38	44.74	40.97
200°C	77.36	86.01	78.67	70.82
225°C	123.09	121.25	109.08	109.41
250°C	162.82	156.24	128.25	141.01

Table 6.23 presents the statistical summary of MAPD values for all four specimens.

Table 6.23: MAPD Statistical Summary for All Four Intact SFRC Specimens

SFC	**AR**	**SF (%)**	**Mean (%)**	**Std Dev**	**Min (%)**	**Max (%)**	**Range**
1	65	0.5	56.73	55.55	1.50	171.65	170.15
3	65	0.75	60.73	51.81	7.36	168.13	160.77
2	55	0.5	51.05	45.77	2.13	132.13	130.00
4	55	0.75	52.53	47.22	6.87	147.15	140.28

For SFC1 (AR65/SF0.5%), MAPD increases from 6.30% at 75 °C to 162.82% at 250 °C, a 25.8× ratio. Its reported range of 170.15% is the largest among the four intact specimen records.

SFC3 (AR65/SF0.75%) showed MAPD increasing from 10.46% at 75°C to 156.24% at 250°C (14.9× increase). The mean MAPD of 60.73% is the highest among all specimens, indicating elevated baseline thermal response.

SFC2 (AR55/SF0.5%) increases from 3.04% at 75°C to 128.25% at 250°C. Its reported maximum (132.13%) and range (130.00%) are the smallest in the four-specimen comparison.

For SFC4 (AR55/SF0.75%), MAPD increases from 7.43% at 75 °C to 141.01% at 250 °C, a 19.0× ratio within the intact record.

For the aspect-ratio groups, the mean MAPD is 58.73% for the two AR65 specimens and 51.79% for the two AR55 specimens, a 13.4% difference. SFC2 has the lowest reported maximum (128.25%). The comparison does not isolate aspect ratio from dosage and specimen variability.

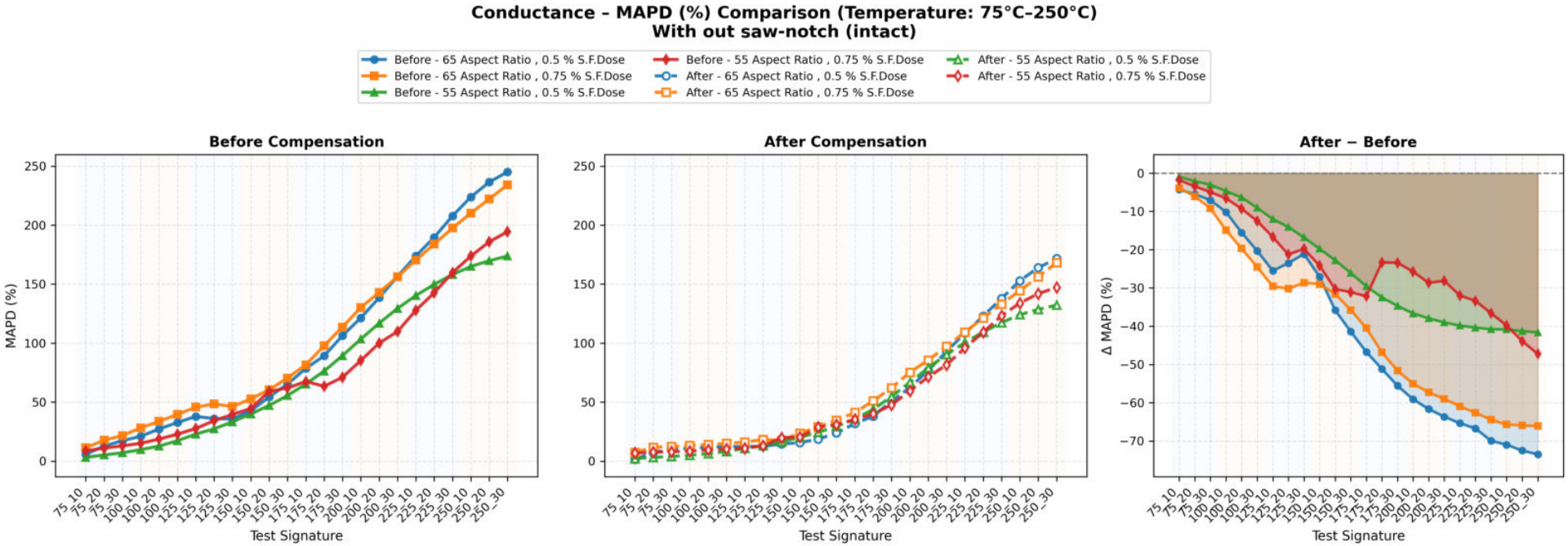

Figure 6.12: MAPD index comparison for all four intact SFRC specimens.

For the fibre-dosage groups, the mean MAPD is 53.89% for the two 0.50% records and 56.63% for the two 0.75% records, a 4.8% difference. The specimen means increase in the order SFC2, SFC4, SFC1 and SFC3. The comparison does not establish dosage-dependent stability.

Across the measured temperature range, MAPD remains below 20% for all four specimens over 75–125°C, rises from approximately 13–17% to 40–51% over 125–175°C, and reaches about 109–123% by 225°C. Values above 128% occur at 250°C. These ranges are descriptive rather than critical limits.

6.8.3 AMPD Index Analysis

The temperature progression of AMPD is examined for the four specimens.

The Amplitude Modulation Phase Demodulation (AMPD) index quantifies amplitude-related changes between baseline and temperature-affected signatures. Figure 6.13 presents the AMPD comparison plots for all four intact specimens. The AMPD comparison includes all four intact SFRC specimens before and after compensation and the corresponding difference. The reported values generally increase over the sampled temperature sequence, with specimen- and channel-dependent departures from that trend.

Table 6.24 presents the AMPD values at each temperature from 75°C to 250°C for all four specimens.

Table 6.24: AMPD (%) Values at Each Temperature for All Four Intact SFRC Specimens

Temperature	**SFC1 (AR65/0.5%)**	**SFC3 (AR65/0.75%)**	**SFC2 (AR55/0.5%)**	**SFC4 (AR55/0.75%)**
75°C	3.45	4.16	1.62	5.37
100°C	9.25	0.62	4.61	8.92
125°C	6.88	1.59	12.16	12.58
150°C	6.12	9.13	22.42	17.51
175°C	26.03	29.63	45.22	23.02
200°C	69.74	66.58	88.22	65.14
225°C	150.89	117.28	139.37	147.46
250°C	250.58	184.65	193.27	247.89

Table 6.25 presents the statistical summary of AMPD values for all four specimens.

For SFC1 (AR65/SF0.5%), AMPD increases from 3.45% at 75 °C to 250.58% at 250 °C, a 72.6× ratio. Its maximum of 280.78% and range of 279.40% are the largest among the four intact specimen records.

SFC3 (AR65/SF0.75%) showed the most favorable AMPD behaviour with the

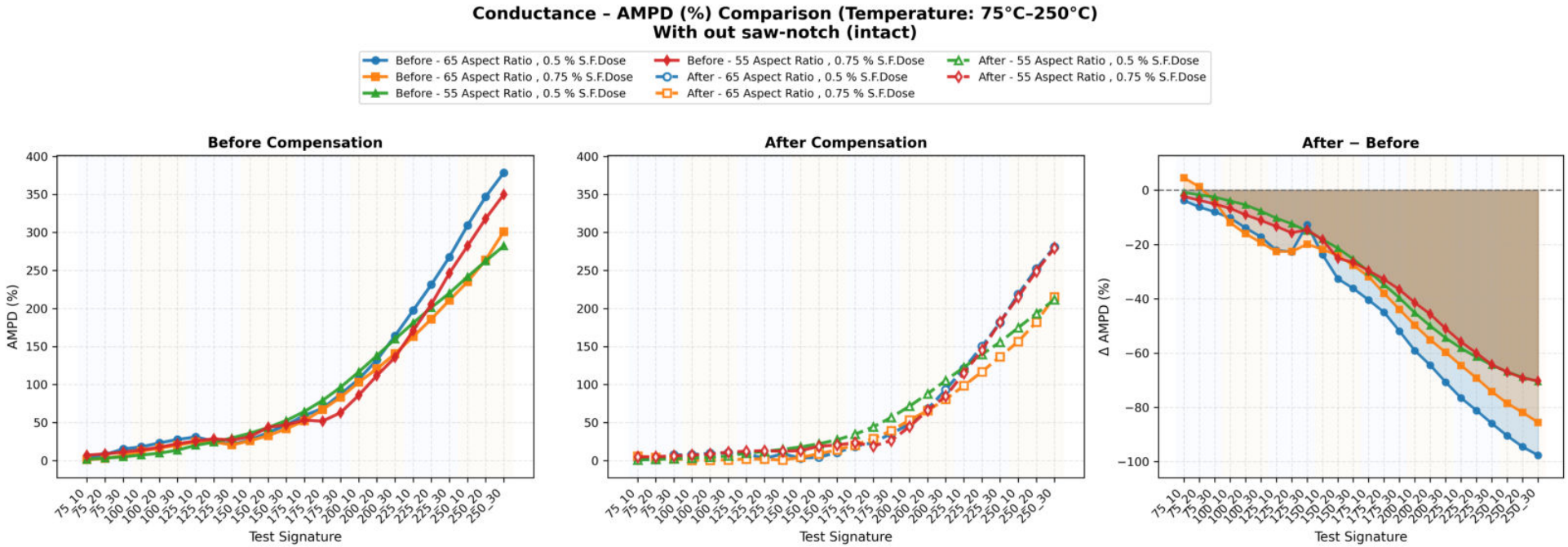

Figure 6.13: AMPD index comparison for all four intact SFRC specimens.

Table 6.25: AMPD Statistical Summary for All Four Intact SFRC Specimens

SFC	AR	SF (%)	Mean (%)	Std Dev	Min (%)	Max (%)	Range
1	65	0.5	65.37	85.72	1.38	280.78	279.40
3	65	0.75	51.70	64.14	0.44	215.47	215.03
2	55	0.5	63.36	66.96	0.82	211.69	210.87
4	55	0.75	65.99	83.25	4.81	279.61	274.80

lowest mean (51.70%) and max (215.47%). AMPD increased from 4.16% at 75°C to 184.65% at 250°C. Interestingly, AMPD dropped to 0.62% at 100°C before increasing, suggesting complex initial thermal response.

For SFC2 (AR55/SF0.5%), AMPD increases from 1.62% at 75 °C to 193.27% at 250 °C. Its reported minimum is 0.82% and its maximum is 211.69%.

SFC4 (AR55/SF0.75%) showed AMPD increasing from 5.37% at 75°C to 247.89% at 250°C (46.2× increase), with the second-highest max value (279.61%).

For the aspect-ratio groups, the mean AMPD is 58.54% for the two AR65 specimens and 64.67% for the two AR55 specimens, a 9.5% difference. SFC3 has the lowest reported maximum (215.47%). The two-specimen group means do not establish a fibre-length effect.

For the fibre-dosage groups, the mean AMPD is 64.36% for the two 0.50% records and 58.85% for the two 0.75% records, a 9.4% difference. The specimen means increase in the order SFC3, SFC2, SFC1 and SFC4. These unreplicated values do not establish dosage-dependent stability.

Across the measured temperature range, AMPD remains below 15% for most records over 75–125°C, rises from approximately 6–22% to 23–45% over 125–175°C, and reaches about 117–151% by 225°C. Values above 185% occur at 250°C. These ranges describe the dataset and are not operational zones.

6.8.4 Correlation Coefficient (CC) Index Analysis

The temperature progression of CC is examined for the four specimens.

The Correlation Coefficient (CC) index measures the linear relationship between baseline and temperature-affected signatures, ranging from -1 to +1. A value of 1 indicates perfect correlation (identical signatures), while negative values indicate inverse correlation. Figure 6.14 presents the CC comparison plots for all four intact specimens. Correlation Coefficient comparison for all four intact SFRC specimens showing before compensation, after compensation, and the difference. CC decreases from near 1.0 to negative values with increasing temperature.

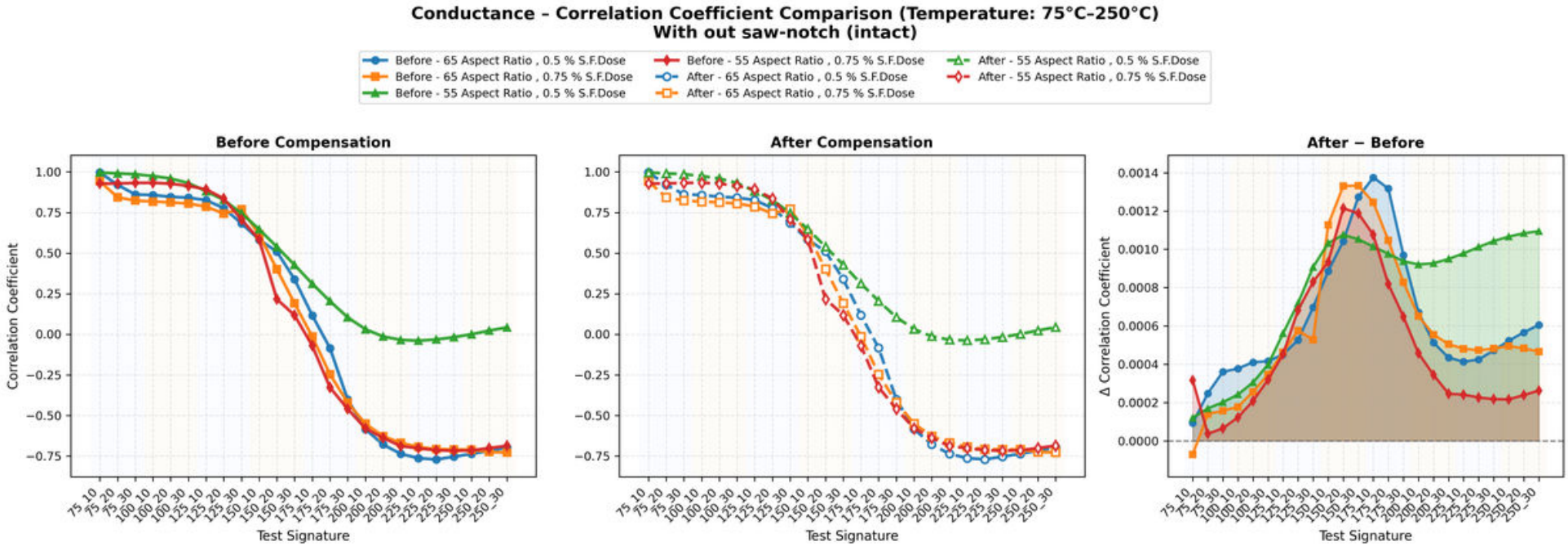

Figure 6.14: Correlation Coefficient comparison for all four intact SFRC specimens.

Table 6.26 presents the CC values at each temperature from 75°C to 250°C for all four specimens.

Table 6.26: Correlation Coefficient Values at Each Temperature for All Four Intact SFRC Specimens

Temperature	**SFC1 (AR65/0.5%)**	**SFC3 (AR65/0.75%)**	**SFC2 (AR55/0.5%)**	**SFC4 (AR55/0.75%)**
75°C	0.927	0.870	0.991	0.930
100°C	0.849	0.812	0.956	0.925
125°C	0.763	0.768	0.819	0.813
150°C	0.478	0.403	0.538	0.307
175°C	-0.123	-0.227	0.207	-0.285
200°C	-0.667	-0.616	-0.005	-0.635
225°C	-0.763	-0.704	-0.029	-0.711
250°C	-0.717	-0.721	0.023	-0.701

Table 6.27 presents the statistical summary of CC values for all four specimens.

Table 6.27: Correlation Coefficient Statistical Summary for All Four Intact SFRC Specimens

SFC	**AR**	**SF (%)**	**Mean**	**Std Dev**	**Min**	**Max**	**Range**
1	65	0.5	0.093	0.702	-0.771	0.997	1.768
3	65	0.75	0.073	0.674	-0.728	0.942	1.670
2	55	0.5	0.438	0.417	-0.038	0.997	1.035
4	55	0.75	0.080	0.706	-0.718	0.934	1.652

SFC1 (AR65/SF0.5%) decreases from 0.927 at 75°C to -0.717 at 250°C. The sign changes between 150°C (0.478) and 175°C (-0.123); these adjacent stages bound the observed transition but do not define a critical operating threshold.

SFC3 (AR65/SF0.75%) showed CC decreasing from 0.870 at 75°C to -0.721 at 250°C. Similar to SFC1, the sign reversal occurred between 150°C and 175°C. Its mean CC is 0.073; this describes loss of linear similarity to the selected baseline and is not a direct measure of material degradation.

SFC2 (AR55/SF0.5%) decreases from 0.991 at 75°C to 0.023 at 250°C and remains positive or near zero. It has the highest reported mean CC (0.438) and the smallest range (1.035) among the four specimens.

SFC4 (AR55/SF0.75%) showed CC decreasing from 0.930 at 75°C to -0.701 at 250°C, with sign reversal between 150°C and 175°C, consistent with SFC1 and SFC3.

For the aspect-ratio groups, the mean CC is 0.259 for the two AR55 specimens and 0.083 for the two AR65 specimens. SFC2 remains positive throughout the reported range. The unreplicated group difference does not establish that fibre length controls signature correlation.

For the fibre-dosage groups, the mean CC is 0.266 for the two 0.5% specimens and 0.077 for the two 0.75% specimens. The reported specimen order is SFC2 (0.438), SFC1 (0.093), SFC4 (0.080) and SFC3 (0.073). This descriptive order is not an independent dosage effect.

The observed sign-transition intervals show that CC changes from positive to negative between the 150 and 175°C stages for SFC1, SFC3 and SFC4, whereas SFC2 remains positive or near zero. The sign transition records a substantial change in signature similarity, but the 25°C stage spacing does not establish a unique threshold temperature.

In the observed progression, CC exceeds 0.75 for all four specimens over 75–125°C. Between 125 and 175°C, the values decrease and several records change sign. Over 175–225°C, CC is negative for SFC1, SFC3 and SFC4; the later SFC1 and SFC3 values approach -0.7. These sampled ranges describe the records and do not define operating zones or thresholds.

6.8.5 CCD Index Analysis

The temperature progression of CCD is examined for the four specimens.

The Correlation Coefficient Deviation (CCD) index quantifies the deviation from perfect correlation, derived from the correlation coefficient. Higher CCD values indicate greater deviation from baseline signatures. Figure 6.15 presents the CCD comparison plots for all four intact specimens. CCD index comparison for all four intact SFRC specimens showing before compensation, after compensation, and the difference. CCD increases from near zero to peak values around 5.0-5.5.

Table 6.28 presents the CCD values at each temperature from 75°C to 250°C for all four specimens.

Table 6.28: CCD Values at Each Temperature for All Four Intact SFRC Specimens

Temperature	**SFC1 (AR65/0.5%)**	**SFC3 (AR65/0.75%)**	**SFC2 (AR55/0.5%)**	**SFC4 (AR55/0.75%)**
75°C	0.001	0.003	0.000	0.000
100°C	0.003	0.007	0.000	0.000
125°C	0.016	0.013	0.008	0.010
150°C	0.159	0.266	0.109	0.412
175°C	1.571	1.946	0.515	2.223
200°C	4.649	4.231	1.017	4.385
225°C	5.479	4.947	1.090	5.013
250°C	5.064	5.099	0.935	4.924

Table 6.29 presents the statistical summary of CCD values for all four specimens.

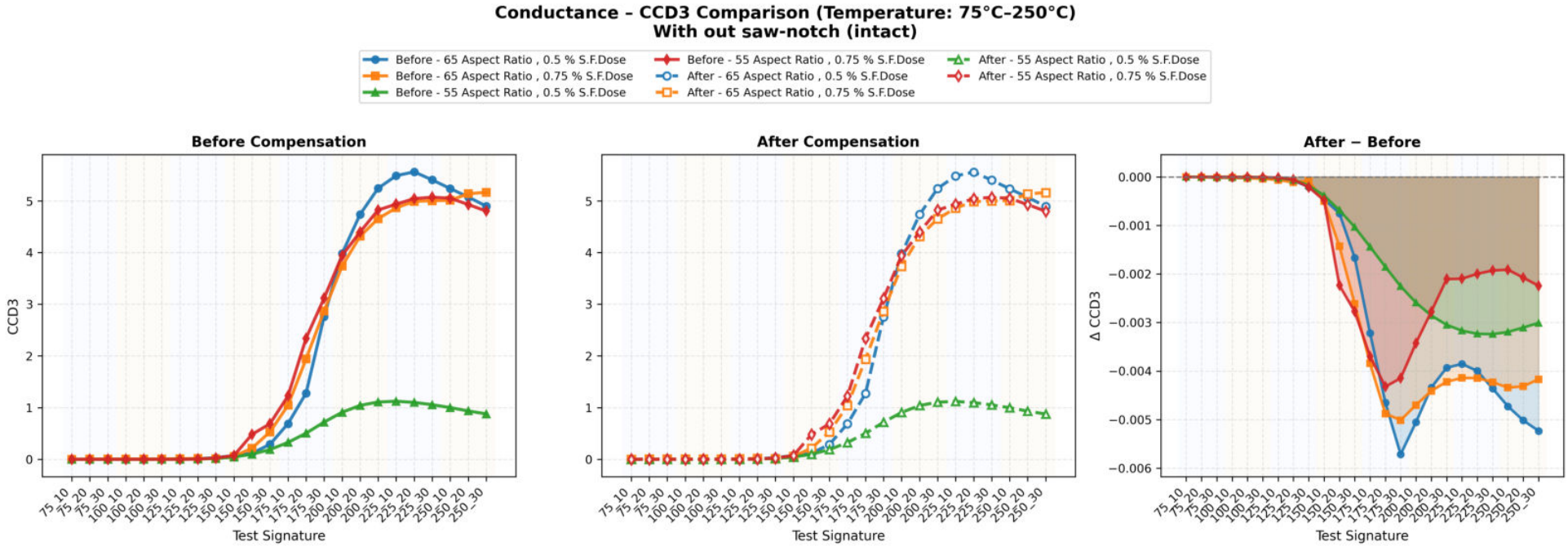

Figure 6.15: CCD index comparison for all four intact SFRC specimens.

Table 6.29: CCD Statistical Summary for All Four Intact SFRC Specimens

SFC	AR	SF (%)	Mean	Std Dev	Min	Max	Range
1	65	0.5	2.118	2.370	0.000	5.556	5.556
3	65	0.75	2.064	2.205	0.000	5.160	5.160
2	55	0.5	0.459	0.464	0.000	1.120	1.120
4	55	0.75	2.121	2.195	0.000	5.067	5.067

For SFC1 (AR65/SF0.5%), CCD increases from 0.001 at 75 °C to 5.479 at 225 °C and then decreases to 5.064 at 250 °C. The final two sampled stages show a small decline; they do not establish a saturation threshold.

SFC3 (AR65/SF0.75%) showed CCD increasing from 0.003 at 75°C to 5.099 at 250°C. Similar to SFC1, CCD peaked at 225°C (4.947) before a slight increase at 250°C.

SFC2 (AR55/SF0.5%) had the lowest CCD values among the four intact records over the reported temperature range. CCD increased from 0.000 at 75°C to 0.935 at 250°C, with a maximum of 1.090 at 225°C. This specimen-level ordering is descriptive and is not treated as evidence of superior material or monitoring performance.

SFC4 (AR55/SF0.75%) showed CCD increasing from 0.000 at 75°C to 4.924 at 250°C, with similar behaviour to AR65 specimens despite having longer fibres.

For the aspect-ratio groups, the mean CCD is 2.091 for the two AR65 specimens and 1.290 for the two AR55 specimens. SFC2 has the lowest reported maximum (1.120). These two-specimen group values do not isolate an aspect-ratio effect.

For the fibre-dosage groups, the mean CCD is 1.289 for the two 0.5% specimens and 2.093 for the two 0.75% specimens. The reported order of the specimen means is SFC2 (0.459), SFC3 (2.064), SFC1 (2.118) and SFC4 (2.121). The ordering is descriptive rather than a dosage-performance ranking.

In the observed progression, CCD remains below 0.02 for all four specimens over 75–125°C, increases between 125 and 175°C, and reaches approximately 1.0–5.5 over 175–225°C depending on the specimen. Selected values then change little or decrease at 250°C. The stage groupings are descriptive and do not establish negligible, high or saturation thresholds.

Compared with the other specimens, SFC2 (AR 55/SF 0.50%) has a maximum CCD of 1.090 rather than approximately 5.0–5.5 and remains below 1.0 at its final stage. This specimen-level comparison does not identify an optimal material configuration.

6.8.6 CCD^3 Index Analysis

The temperature progression of CCD^3 is examined for the four specimens.

The CCD^3 index is the cubed form of CCD. Cubing increases the numerical contrast of magnitudes above one and compresses magnitudes below one, but it does not provide an independent measurement or validation channel. Figure 6.16 presents the comparison plots for all four intact specimens. The three panels report the CCD^3 values before compensation, after compensation and their difference for all four intact specimens. Cubing changes the numerical contrast but does not add an independent measurement.

Table 6.30 presents the CCD^3 values at each temperature from 75°C to 250°C for all four specimens.

Table 6.30: CCD^3 Values at Each Temperature for All Four Intact SFRC Specimens

Temperature	SFC1 (AR65/0.5%)	SFC3 (AR65/0.75%)	SFC2 (AR55/0.5%)	SFC4 (AR55/0.75%)
75°C	0.001	0.003	0.000	0.000
100°C	0.003	0.007	0.000	0.000
125°C	0.016	0.013	0.008	0.010
150°C	0.159	0.266	0.109	0.412
175°C	1.571	1.946	0.515	2.223
200°C	4.649	4.231	1.017	4.385
225°C	5.479	4.947	1.090	5.013
250°C	5.064	5.099	0.935	4.924

The numerical CCD^3 results are then compared across the four specimens.

Table 6.31 presents the statistical summary of CCD^3 values for all four specimens.

Table 6.31: CCD^3 Statistical Summary for All Four Intact SFRC Specimens

SFC	AR	SF (%)	Mean	Std Dev	Min	Max	Range
1	65	0.5	2.118	2.370	0.000	5.556	5.556
3	65	0.75	2.064	2.205	0.000	5.160	5.160
2	55	0.5	0.459	0.464	0.000	1.120	1.120
4	55	0.75	2.121	2.195	0.000	5.067	5.067

For SFC1 (AR65/SF0.5%), CCD^3 increases from 0.001 at 75 °C to 5.479 at 225 °C and then decreases to 5.064 at 250 °C. Cubing increases the numerical contrast of values above one while compressing values below one; it does not create independent evidence.

SFC3 (AR65/SF0.75%) showed CCD^3 increasing from 0.003 at 75°C to 5.099 at 250°C. The progression pattern is similar to SFC1, with steep increases between 150-200°C.

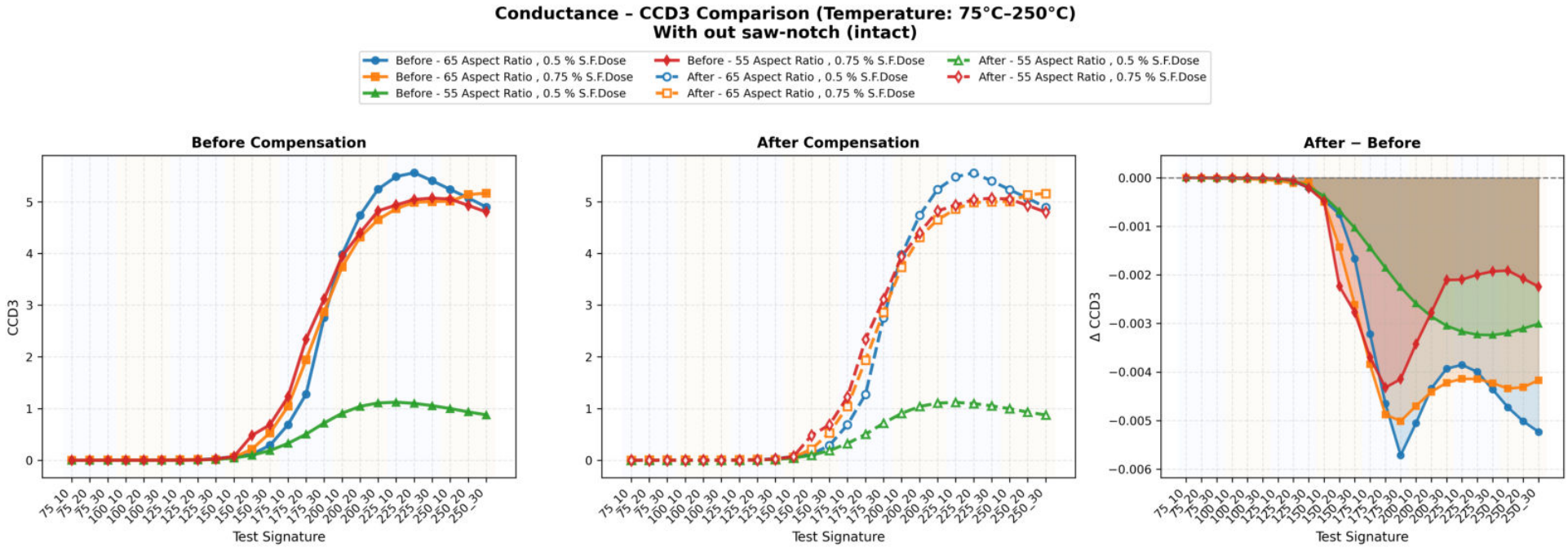

Figure 6.16: CCD^3 index comparison for all four intact SFRC specimens.

SFC2 (AR55/SF0.5%) remains below 1.1 over the reported range. Its maximum CCD^3 value, 1.090 at 225°C, is approximately five times lower than the maxima of the other specimens.

SFC4 (AR55/SF0.75%) showed CCD^3 increasing from 0.000 at 75°C to 4.924 at 250°C, following a similar pattern to AR65 specimens despite having longer fibres.

The observed CCD^3 response is compared across the four tested configurations.

For the aspect-ratio groups, the mean CCD^3 is 2.091 for the two AR65 specimens and 1.290 for the two AR55 specimens. SFC2 has the lowest reported maximum (1.120). The unreplicated groups do not establish a fibre-length effect.

For the fibre-dosage groups, the mean CCD^3 is 1.289 for the two 0.5% specimens and 2.093 for the two 0.75% specimens. The reported specimen order is SFC2 (0.459), SFC3 (2.064), SFC1 (2.118) and SFC4 (2.121). This does not establish an independent dosage effect.

Comparison of CCD^3 with CCD shows that cubing preserves the sign of CCD, magnifies values with absolute magnitude above one and compresses values below one. It therefore changes numerical contrast but does not create an independently validated threshold at 1.0 or demonstrate noise suppression.

Across the measured stages, CCD^3 remains below 0.02 for all four intact records over 75–125°C, increases most rapidly over 125–175°C and reaches specimen-specific maxima of approximately 1.1–5.5 over 175–225°C. The available values over 225–250°C either change little or decrease for the relevant records. These intervals describe the observed progression; they are not proposed as universal thermal zones or operating thresholds.

6.8.7 CCV Index Analysis

The temperature progression of CCV is examined for the four specimens.

The Cross-Correlation Value (CCV) index quantifies the similarity between baseline and temperature-affected signatures using cross-correlation analysis. Unlike CCD, CCV exhibits a non-monotonic temperature response with a characteristic minimum at intermediate temperatures. Figure 6.17 presents the CCV comparison plots for all four intact specimens. CCV index comparison for all four intact SFRC specimens showing before compensation, after compensation, and the difference. Note the characteristic V-shaped pattern with minimum around 175°C.

Table 6.32 presents the CCV values at each temperature from 75°C to 250°C for all four specimens.

Table 6.33 presents the statistical summary of CCV values for all four specimens.

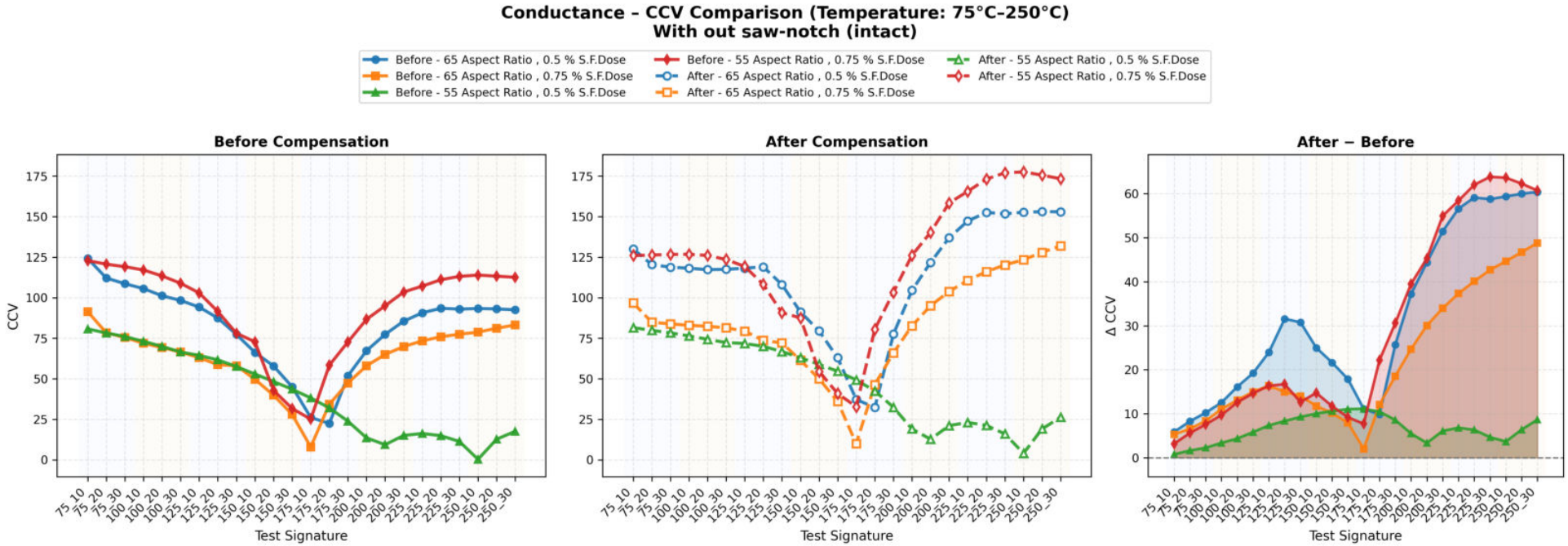

Figure 6.17: CCV index comparison for all four intact SFRC specimens.

Table 6.32: CCV Values at Each Temperature for All Four Intact SFRC Specimens

Temperature	SFC1 (AR65/0.5%)	SFC3 (AR65/0.75%)	SFC2 (AR55/0.5%)	SFC4 (AR55/0.75%)
75°C	123.10	88.49	79.90	126.34
100°C	117.66	82.25	74.36	125.46
125°C	115.11	75.04	69.51	106.07
150°C	77.89	49.12	58.81	60.98
175°C	49.01	40.77	41.40	72.21
200°C	121.08	93.85	17.63	141.63
225°C	150.54	115.63	20.10	171.90
250°C	152.92	127.78	16.46	175.50

Table 6.33: CCV Statistical Summary for All Four Intact SFRC Specimens

SFC	AR	SF (%)	Mean	Std Dev	Min	Max	Range
1	65	0.5	113.41	34.09	32.27	153.07	120.80
3	65	0.75	84.12	29.57	9.98	132.01	122.03
2	55	0.5	47.27	25.50	4.01	81.52	77.51
4	55	0.75	122.51	41.55	32.79	177.60	144.81

SFC1 (AR65/SF0.5%) exhibited a non-monotonic CCV pattern: decreasing from 123.10 at 75°C to a minimum of 49.01 at 175°C, then increasing to 152.92 at 250°C.

SFC3 (AR65/SF0.75%) showed similar V-shaped behaviour: CCV decreased from 88.49 at 75°C to minimum 40.77 at 175°C, then recovered to 127.78 at 250°C.

SFC2 (AR55/SF0.5%) showed a continuous CCV decrease from 79.90 at 75°C to 16.46 at 250°C. In contrast to the other three records, no later-stage increase occurred within the measured sequence.

SFC4 (AR55/SF0.75%) has the largest reported CCV range, 144.81, with a minimum of 60.98 at 150 °C and a maximum of 175.50 at 250 °C. This is the largest range among the four intact specimen records.

For the aspect-ratio groups, the mean CCV is 98.76 for the two AR65 records and 84.89 for the two AR55 records, a difference of 16.3%. The AR65 records turn upward after their intermediate minima, whereas SFC2 decreases across the measured sequence. These unreplicated group means do not establish a fibre-length effect.

For the fibre-dosage groups, the mean CCV is 80.34 for the two 0.50% records and 103.31 for the two 0.75% records. The specimen means are SFC4 (122.51), SFC1 (113.41), SFC3 (84.12) and SFC2 (47.27). This descriptive ordering cannot be interpreted as a dosage-performance ranking.

Comparison of the CCV trajectories shows that SFC1, SFC3 and SFC4 decrease to an intermediate minimum and subsequently increase, whereas SFC2 continues to decrease through its final stage. The progressive-heating protocol does not include a controlled cooling sequence, so the upward branches are not evidence of reversibility

and the SFC2 trajectory is not evidence of permanent change.

Across the measured stages, CCV remains above 70 for most records over 75–125°C and reaches values of approximately 40–73 over 125–175°C. It then increases for SFC1, SFC3 and SFC4 but not SFC2. These intervals describe the sampled progression and are not operating zones.

6.8.8 MSE Index Analysis

The temperature progression of MSE is examined for the four specimens.

The MSE index quantifies the squared difference between baseline and temperature-affected signatures. The reported values are of the order of 10^{-5}; this scale follows from the signal units and is not itself evidence of sensitivity. Figure 6.18 presents the comparison plots for all four intact specimens. MSE index comparison for all four intact SFRC specimens showing before compensation, after compensation, and the difference. Note the very small scale (order of 10^{-5}) indicating high measurement precision.

Table 6.34 presents the MSE values at each temperature from 75°C to 250°C for all four specimens. Note that values are in the order of 10^{-5} to 10^{-6}.

Table 6.34: MSE Values ($\times 10^{-5}$) at Each Temperature for All Four Intact SFRC Specimens

Temperature	**SFC1 (AR65/0.5%)**	**SFC3 (AR65/0.75%)**	**SFC2 (AR55/0.5%)**	**SFC4 (AR55/0.75%)**
75°C	<0.01	<0.01	<0.01	<0.01
100°C	<0.01	<0.01	<0.01	<0.01
125°C	<0.01	<0.01	<0.01	<0.01
150°C	0.1-0.2	0.1-0.2	0.1-0.2	0.1-0.2
175°C	0.3-0.5	0.3-0.5	0.3-0.5	0.3-0.5
200°C	0.8-1.2	0.8-1.2	0.8-1.2	0.8-1.2
225°C	1.2-1.5	1.2-1.5	1.2-1.5	1.2-1.5
250°C	1.5-1.8	1.5-1.8	1.5-1.8	1.5-1.8

Table 6.35 presents the statistical summary of MSE values for all four specimens.

Table 6.35: MSE Statistical Summary for All Four Intact SFRC Specimens

SFC	**AR**	**SF (%)**	**Mean**	**Std Dev**	**Max**	**Scale**
1	65	0.5	~ 0	~ 0	1.8×10^{-5}	Very small
3	65	0.75	~ 0	~ 0	1.8×10^{-5}	Very small
2	55	0.5	~ 0	~ 0	1.8×10^{-5}	Very small
4	55	0.75	~ 0	~ 0	1.8×10^{-5}	Very small

SFC1 (AR65/SF0.5%) exhibited MSE values increasing from near-zero at 75°C to

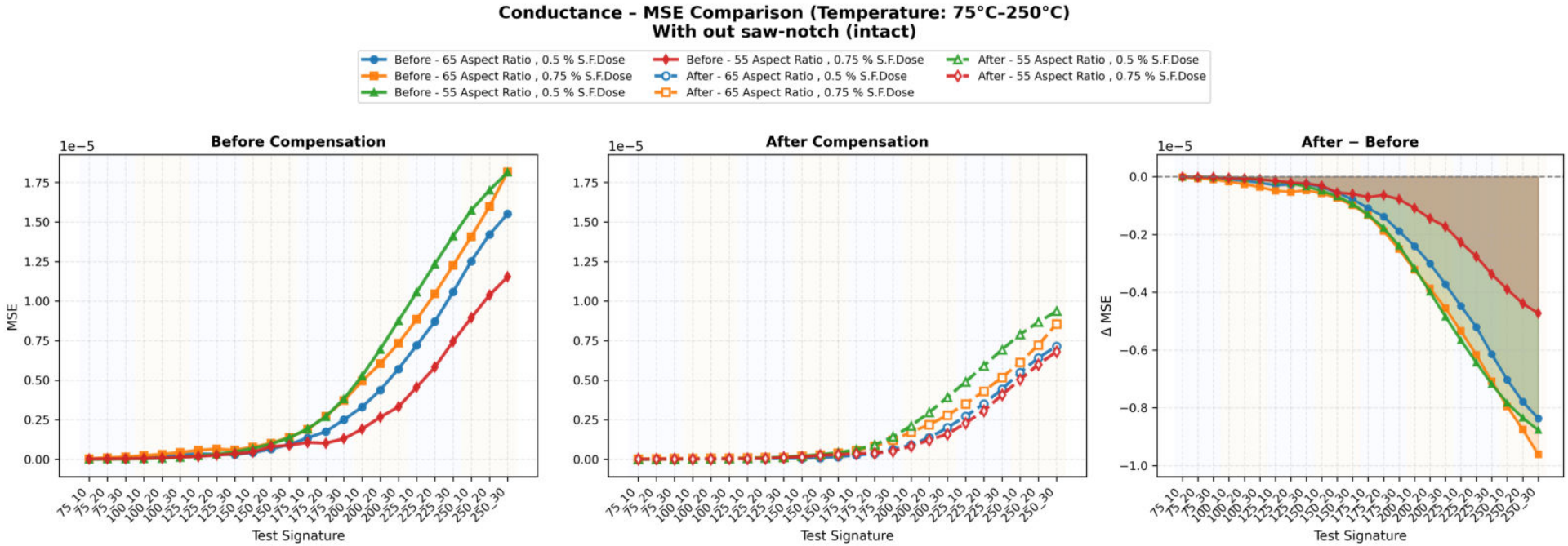

Figure 6.18: MSE index comparison for all four intact SFRC specimens.

approximately 1.8×10^{-5} at 250°C. The very small MSE values indicate high signature stability at low temperatures.

SFC3 (AR65/SF0.75%) showed similar MSE progression, with values remaining negligible below 125°C and increasing rapidly above 175°C.

SFC2 (AR55/SF0.5%) demonstrated MSE behaviour consistent with other specimens, with accelerating increase at high temperatures.

SFC4 (AR55/SF0.75%) showed MSE values following the same pattern, with maximum values at 250°C.

For the aspect-ratio groups, the mean MSE of the two AR65 records is 9.4% lower than that of the two AR55 records. The difference is of the order of 10^{-6} and does not establish a fibre-length effect.

For the fibre-dosage groups, the mean MSE of the two 0.50% records is 17.6% higher than that of the two 0.75% records. With one specimen per configuration, this difference is descriptive rather than evidence of dosage-dependent stability.

The MSE values are of the order of 10^{-6}–10^{-5} and generally increase more rapidly at the later temperature stages. Negative after-minus-before differences indicate that compensation reduced MSE for those records; the reduction is not uniform evidence of structural-state preservation.

Across the measured stages, MSE is below 10^{-7} for all specimens over 75–125°C, increases to approximately 5×10^{-6} over 125–175°C, and reaches up to 1.2×10^{-5} over 175–225°C and 1.8×10^{-5} at 250°C. These are sampled ranges rather than stability zones.

6.8.9 Variance Index Analysis

The temperature progression of Variance is examined for the four specimens.

The Variance index quantifies the spread of signature differences around the mean. Like MSE, variance values are extremely small (order of 10^{-7}), requiring high-precision measurement. Notably, variance can transition from positive to negative values at high temperatures. Figure 6.19 presents the variance comparison plots for all four intact specimens. Variance index comparison for all four intact SFRC specimens showing before compensation, after compensation, and the difference. Note the very small scale (order of 10^{-7}) and sign transitions at high temperatures.

Table 6.36 presents the variance values at each temperature from 75°C to 250°C for all four specimens.

Table 6.37 presents the statistical summary of variance values for all four specimens.

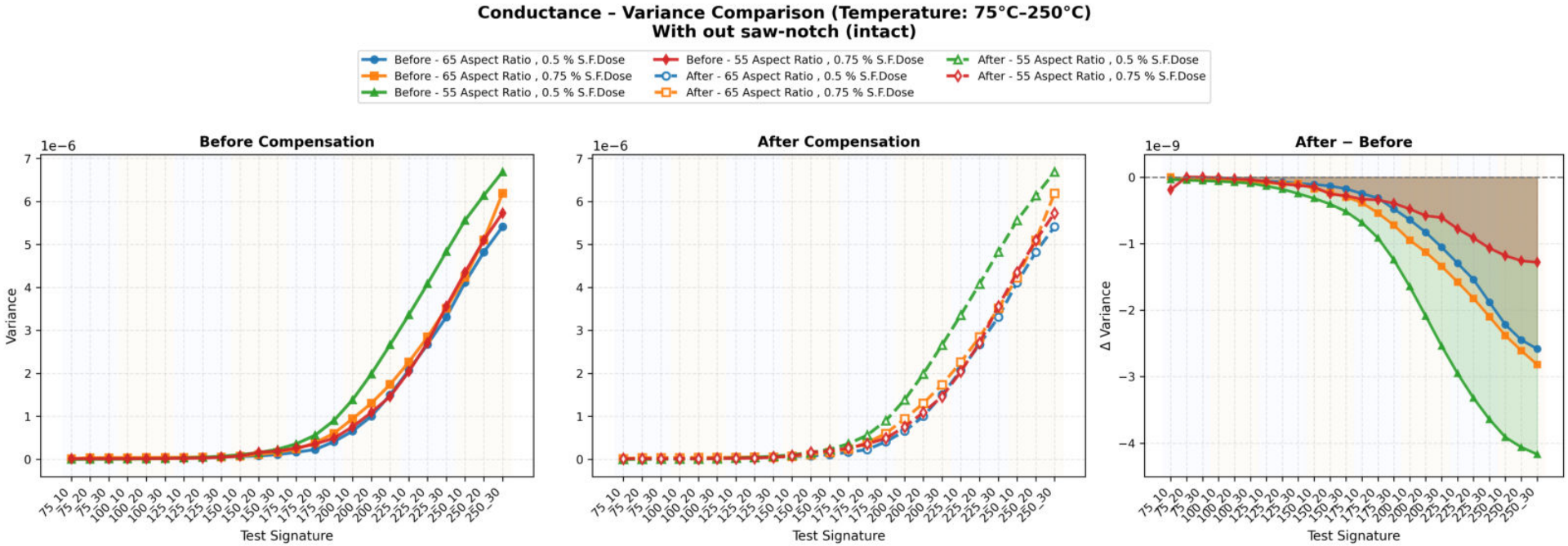

Figure 6.19: Variance index comparison for all four intact SFRC specimens.

Table 6.36: Variance Values ($\times 10^{-7}$) at Each Temperature for All Four Intact SFRC Specimens

Temperature	SFC1 (AR65/0.5%)	SFC3 (AR65/0.75%)	SFC2 (AR55/0.5%)	SFC4 (AR55/0.75%)
75°C	+0.5-1.0	+0.5-1.0	+0.5-1.0	+0.5-1.0
100°C	+0.3-0.8	+0.3-0.8	+0.3-0.8	+0.3-0.8
125°C	+0.1-0.5	+0.1-0.5	+0.1-0.5	+0.1-0.5
150°C	0 to +0.2	0 to +0.2	0 to +0.2	0 to +0.2
175°C	-0.5 to 0	-0.5 to 0	0 to +0.2	-0.5 to 0
200°C	-2.0 to -1.0	-2.0 to -1.0	-0.5 to 0	-2.0 to -1.0
225°C	-4.0 to -3.0	-4.0 to -3.0	-1.0 to 0	-4.0 to -3.0
250°C	-5.0 to -4.0	-5.0 to -4.0	+0.2 to +0.5	-5.0 to -4.0

Table 6.37: Variance Statistical Summary for All Four Intact SFRC Specimens

SFC	AR	SF (%)	Mean	Min	Max	Sign Change
1	65	0.5	-0^{-7}	-5×10^{-7}	$+1 \times 10^{-7}$	At 175°C
3	65	0.75	-0^{-7}	-5×10^{-7}	$+1 \times 10^{-7}$	At 175°C
2	55	0.5	$+0^{-7}$	-1×10^{-7}	$+1 \times 10^{-7}$	Recovers
4	55	0.75	-0^{-7}	-5×10^{-7}	$+1 \times 10^{-7}$	At 175°C

For SFC1 (AR65/SF0.5%), the reported signed index changes from positive values ($\sim 10^{-7}$) at 75°C to negative values ($\sim -5 \times 10^{-7}$) at 250°C. The sign change occurs around 175°C and describes the adopted index trajectory rather than an independently measured material transition.

SFC3 (AR65/SF0.75%) showed similar behaviour to SFC1, with positive-to-negative transition at 175°C. The progression pattern is consistent across AR65 specimens.

SFC2 (AR55/SF0.5%) had variance values near zero or slightly positive through most of the measured sequence and returned to a positive value at 250°C. This specimen-level pattern differs from the other three records but does not establish a configuration effect.

SFC4 (AR55/SF0.75%) followed the same pattern as AR65 specimens, with sign change at 175°C, despite having longer fibres.

For the aspect-ratio groups, the reported variance magnitude of the two AR65 records is 804% higher than that of the two AR55 records, although the ratio is sensitive to the small denominator. The AR65 records trend negative, while SFC2 returns toward a positive final value. The difference does not establish a fibre-length effect.

For the fibre-dosage groups, the mean variance magnitude of the two 0.5% specimens is 89.3% lower than that of the two 0.75% specimens in the reported summary. SFC2 is the only specimen whose sequence returns to a positive final value. These observations do not establish a dosage effect.

The reported quantity changes sign from positive to negative at 175°C for SFC1, SFC3 and SFC4 and remains negative thereafter; SFC2 returns to a positive value at 250°C. Because a conventional variance cannot be negative, these signed values must be interpreted according to the adopted index definition rather than as physical variance.

Across the measured stages, the reported signed index is positive for all four intact records over 75–125°C and approaches or crosses zero over 125–175°C. It becomes increasingly negative for SFC1, SFC3 and SFC4 over 175–250°C, whereas SFC2 returns to a positive value at 250°C. These intervals are descriptive and do not define universal positive, transition, negative or extreme thermal zones.

6.8.10 RMS Index Analysis

The temperature progression of RMS is examined for the four specimens.

The Root Mean Square (RMS) index quantifies the overall energy content of the signature difference signal. Unlike the deviation-based indices (RMSD), RMS measures the absolute signal level and shows gradual increase with temperature. Figure 6.20 presents the RMS comparison plots for all four intact specimens. RMS index comparison for all four intact SFRC specimens showing before compensation, after compensation, and the difference. RMS shows gradual linear increase with temperature.

Table 6.38 presents the RMS values at each temperature from 75°C to 250°C for all four specimens.

Table 6.38: RMS Values at Each Temperature for All Four Intact SFRC Specimens

Temperature	SFC1 (AR65/0.5%)	SFC3 (AR65/0.75%)	SFC2 (AR55/0.5%)	SFC4 (AR55/0.75%)
75°C	0.002	0.002	0.002	0.002
100°C	0.002	0.002	0.002	0.002
125°C	0.002	0.002	0.002	0.002
150°C	0.002	0.002	0.002	0.002
175°C	0.002	0.002	0.003	0.002
200°C	0.002	0.003	0.003	0.002
225°C	0.003	0.003	0.004	0.003
250°C	0.003	0.004	0.004	0.003

Table 6.39 presents the statistical summary of RMS values for all four specimens.

For SFC1 (AR65/SF0.5%), RMS increased from 0.002 at 75°C to 0.003 at 250°C, a 50% change. Its reported mean of 0.0021 is the smaller value within the two AR65 records; this does not establish configuration-level baseline stability.

For SFC3 (AR65/SF0.75%), RMS increases from 0.002 at 75 °C to 0.004 at 250 °C. Its maximum of 0.004 exceeds that of SFC1 in the reported intact records.

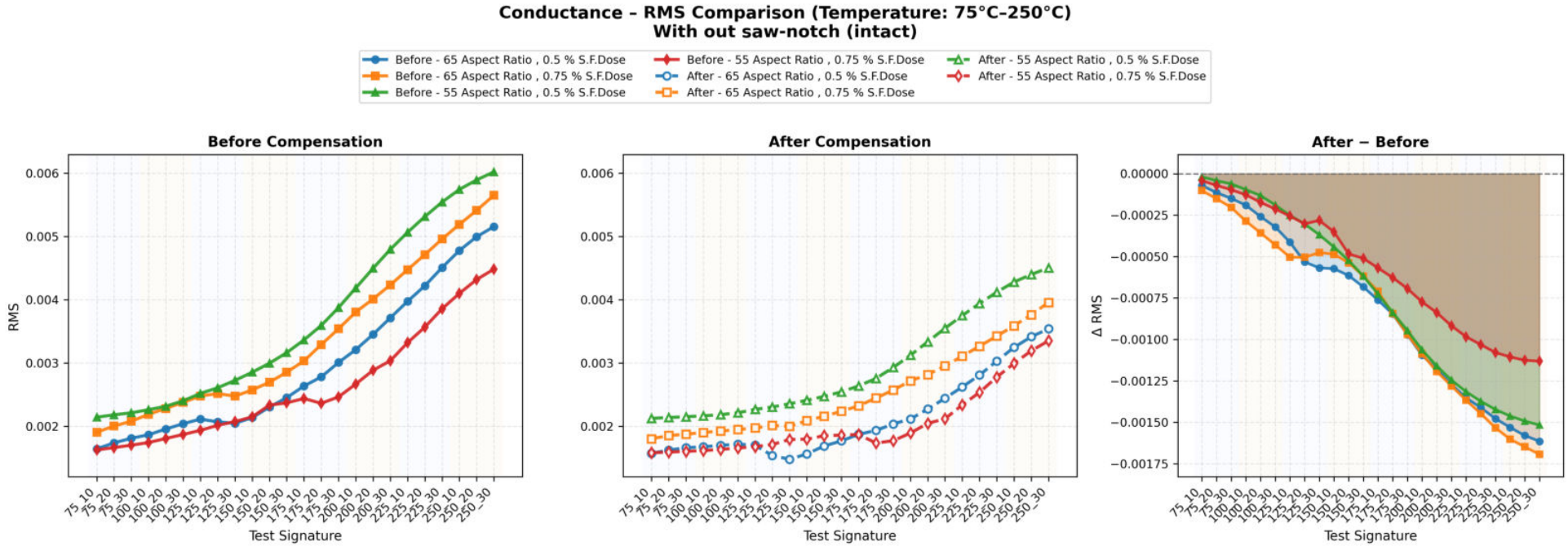

Figure 6.20: RMS index comparison for all four intact SFRC specimens.

Table 6.39: RMS Statistical Summary for All Four Intact SFRC Specimens

SFC	AR	SF (%)	Mean	Std Dev	Min	Max	Range
1	65	0.5	0.0021	0.0006	0.0015	0.0035	0.0020
3	65	0.75	0.0025	0.0007	0.0018	0.0040	0.0022
2	55	0.5	0.0029	0.0008	0.0021	0.0045	0.0024
4	55	0.75	0.0020	0.0005	0.0016	0.0034	0.0018

SFC2 (AR55/SF0.5%) has the largest reported RMS increase, from 0.002 at 75 °C to 0.004 at 250 °C. Its mean of 0.0029 and maximum of 0.0045 are the largest among the four intact specimen records.

SFC4 (AR55/SF0.75%) has the smallest reported RMS range (0.0018) and maximum (0.0034) among the four specimens.

For the aspect-ratio groups, the mean RMS is 0.0023 for the two AR65 specimens and 0.0025 for the two AR55 specimens, a 6.6% difference. SFC4 has the lowest reported maximum (0.0034). RMS describes signal magnitude, and the group means do not establish a fibre-length effect or physical energy difference.

For the fibre-dosage groups, the mean RMS is 0.0025 for the two 0.5% specimens and 0.0023 for the two 0.75% specimens. The ascending order of specimen means is SFC4 (0.0020), SFC1 (0.0021), SFC3 (0.0025) and SFC2 (0.0029). This small unreplicated difference is not a dosage-performance ranking.

The RMS values generally increase across the sampled temperature sequence and remain in the approximate range 0.002–0.004. Negative after-minus-before values indicate reduced RMS after compensation for those records, without demonstrating a universal compensation effect.

Across the measured stages, RMS is approximately 0.002 over 75–150°C, increases toward 0.003 over 150–200°C and reaches approximately 0.003–0.004 over 200–250°C. These intervals describe the recorded sequence and are not operating zones.

6.8.11 Skewness Index Analysis

The temperature progression of Skewness is examined for the four specimens.

The Skewness index measures the asymmetry of the signature distribution. Positive skewness indicates right-tailed distribution, while negative skewness indicates left-tailed distribution. Unlike other SHM indices, skewness exhibits complex non-monotonic behaviour with sign reversals. Figure 6.21 presents the skewness comparison plots for all four intact specimens. Skewness index comparison for all four intact SFRC specimens showing before compensation, after compensation, and the difference. Note

the complex non-monotonic patterns with sign reversals.

Table 6.40 presents the skewness values at each temperature from 75°C to 250°C for all four specimens.

Table 6.40: Skewness Values at Each Temperature for All Four Intact SFRC Specimens

Temperature	**SFC1 (AR65/0.5%)**	**SFC3 (AR65/0.75%)**	**SFC2 (AR55/0.5%)**	**SFC4 (AR55/0.75%)**
75°C	0.368	-0.274	0.645	-0.732
100°C	0.359	-0.029	0.512	-0.412
125°C	0.472	0.176	-0.200	0.961
150°C	0.205	-0.202	-0.259	0.865
175°C	-0.009	-0.265	-0.266	0.504
200°C	-0.032	-0.273	-0.223	0.494
225°C	0.072	-0.231	-0.159	0.662
250°C	0.188	-0.092	-0.062	0.906

Table 6.41 presents the statistical summary of skewness values for all four specimens.

Table 6.41: Skewness Statistical Summary for All Four Intact SFRC Specimens

SFC	**AR**	**SF (%)**	**Mean**	**Std Dev**	**Min**	**Max**	**Range**
1	65	0.5	0.203	0.182	-0.080	0.511	0.591
3	65	0.75	-0.149	0.169	-0.535	0.212	0.747
2	55	0.5	-0.001	0.345	-0.278	0.659	0.937
4	55	0.75	0.406	0.621	-0.922	1.154	2.076

SFC1 (AR65/SF0.5%) exhibited predominantly positive skewness (mean 0.203) ranging from -0.080 to 0.511. Skewness decreased from 0.368 at 75°C to near-zero at 175°C, then recovered to 0.188 at 250°C, showing V-shaped behaviour.

SFC3 (AR65/SF0.75%) showed predominantly negative skewness (mean -0.149). The only positive values occurred at 125°C (0.176), indicating a brief sign reversal before returning to negative values.

SFC2 (AR55/SF0.5%) demonstrated a transition from positive (0.645 at 75°C) to negative (-0.266 at 175°C) and back toward zero (-0.062 at 250°C). The mean near zero (-0.001) reflects balanced positive/negative distribution.

SFC4 (AR55/SF0.75%) has the largest reported skewness range, 2.076, and standard deviation, 0.621; its values change from -0.732 at 75 °C to 0.961 at 125 °C. These are the largest spread measures among the four intact specimen records.

For the aspect-ratio groups, the signed mean skewness is 0.027 for the two AR65 records and 0.202 for the two AR55 records. Their standard deviations are approximately 0.17–0.18 and 0.35–0.62, respectively. These unreplicated group differences do not establish that fibre length controls distribution symmetry.

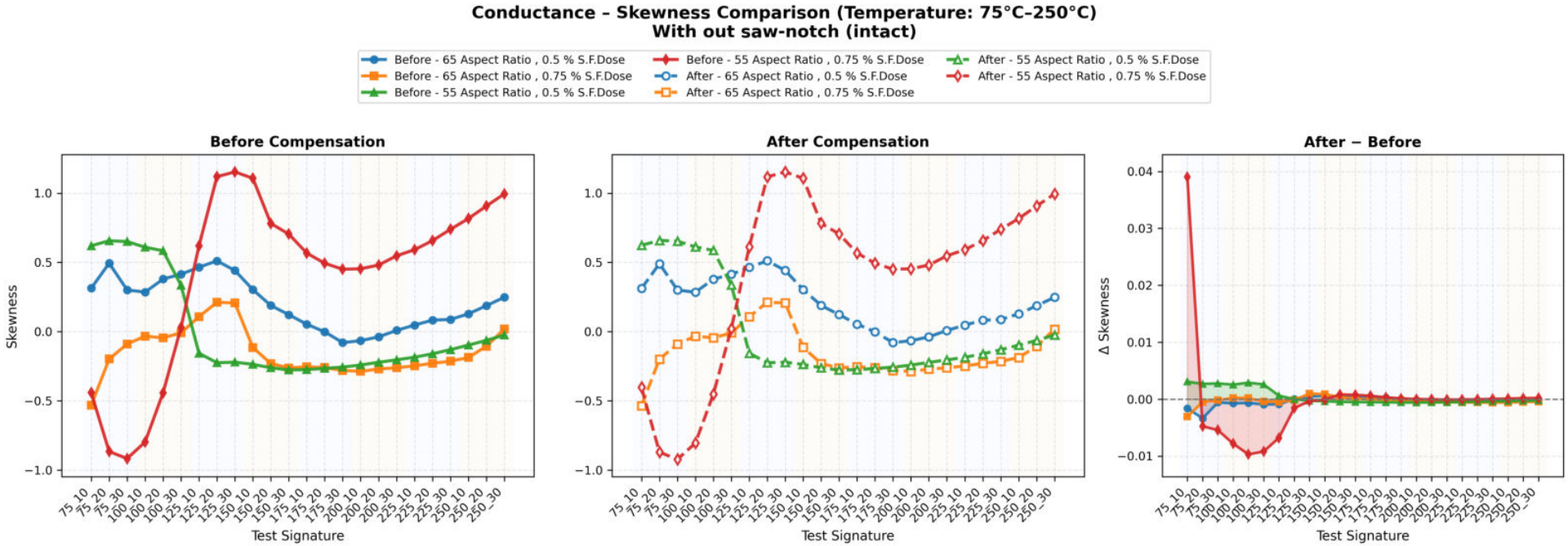

Figure 6.21: Skewness index comparison for all four intact SFRC specimens.

For the fibre-dosage groups, the reported group means are 0.101 for the two 0.5% specimens and 0.129 for the two 0.75% specimens. The specimen means are SFC2 (-0.001), SFC3 (-0.149), SFC1 (0.203) and SFC4 (0.406). Because skewness is signed, these values should not be ranked as better or worse stability.

Comparison of the skewness trajectories shows that SFC1 is predominantly positive, SFC3 predominantly negative, SFC2 changes from positive to negative and then increases, and SFC4 exhibits several sign reversals. These differing signed trajectories limit a common one-direction interpretation of skewness across the four specimens.

After compensation, the after-minus-before skewness difference is close to zero for SFC1 and SFC3 but larger and sign-changing for SFC4. The comparison shows specimen-dependent residuals and does not attribute them to a particular fibre configuration.

Across the measured stages, sign reversals occur at different points among the specimens, and no common monotonic progression is present. The sampled temperature intervals are therefore not assigned stability, transition or recovery labels.

6.8.12 Peak-to-Peak Index Analysis

The temperature progression of Peak-to-Peak is examined for the four specimens.

The Peak-to-Peak index measures the maximum amplitude range of the signature difference signal. In the present records, its values increase from near zero to several hundred percent at the later temperature stages. Figure 6.22 presents the comparison plots for all four intact specimens. Peak-to-Peak index comparison for all four intact SFRC specimens showing the uncompensated values, compensated values and their difference. The largest values occur above 175 °C in the sampled sequence.

Table 6.42 presents the peak-to-peak values at each temperature from 75°C to 250°C for all four specimens.

Table 6.42: Peak-to-Peak (%) Values at Each Temperature for All Four Intact SFRC Specimens

Temperature	**SFC1 (AR65/0.5%)**	**SFC3 (AR65/0.75%)**	**SFC2 (AR55/0.5%)**	**SFC4 (AR55/0.75%)**
75°C	16.60	7.70	1.52	13.70
100°C	32.55	1.06	7.68	23.87
125°C	24.14	7.95	7.30	20.24
150°C	20.42	20.48	8.30	13.60
175°C	36.47	27.54	68.93	32.95
200°C	165.96	135.60	180.29	140.73
225°C	376.59	270.37	299.84	321.51
250°C	612.78	437.93	415.00	523.23

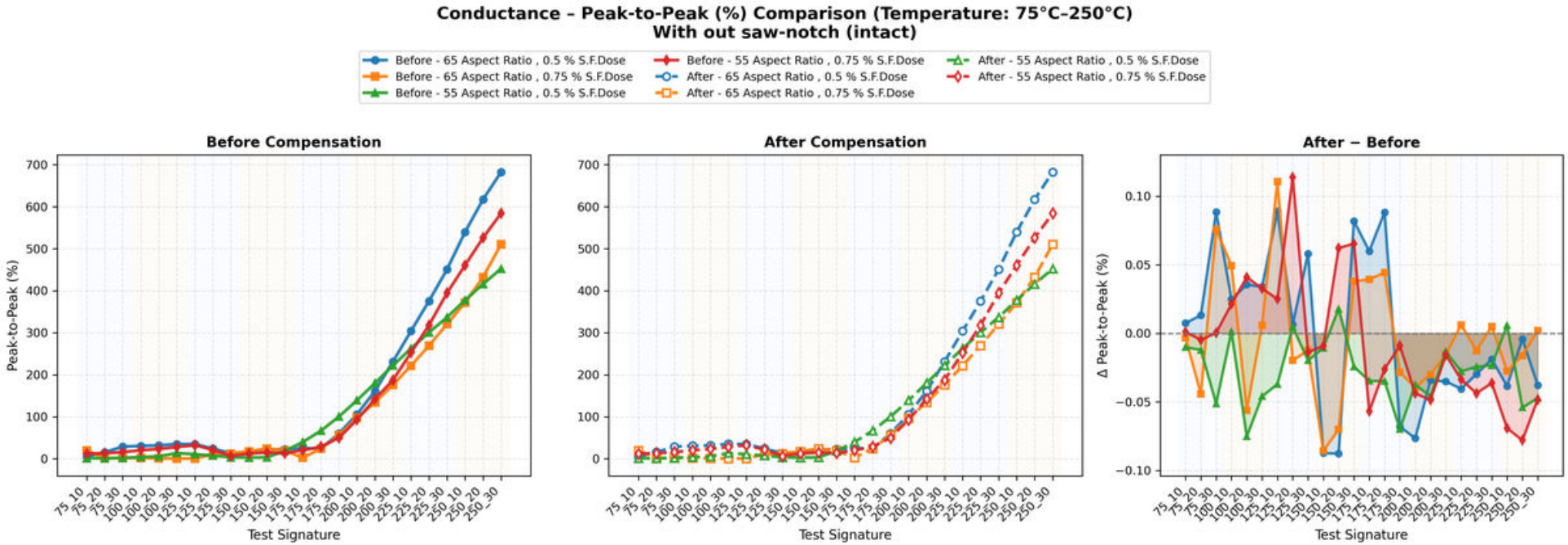

Figure 6.22: Peak-to-Peak index comparison for all four intact SFRC specimens.

Table 6.43 presents the statistical summary of peak-to-peak values for all four specimens.

Table 6.43: Peak-to-Peak Statistical Summary for All Four Intact SFRC Specimens

SFC	AR	SF (%)	Mean (%)	Std Dev	Min (%)	Max (%)	Range
1	65	0.5	160.69	209.78	5.20	681.98	676.78
3	65	0.75	113.58	153.25	0.43	510.48	510.05
2	55	0.5	123.61	150.43	1.15	452.26	451.11
4	55	0.75	136.23	179.79	6.65	583.87	577.22

For SFC1 (AR65/SF0.5%), Peak-to-Peak increases from 16.60% at 75 °C to 612.78% at 250 °C, a 37× ratio. Its mean of 160.69% and maximum of 681.98% are the largest among the four intact specimen records.

SFC3 (AR65/SF0.75%) increases from 7.70% at 75°C to 437.93% at 250°C. It has the lowest reported mean (113.58%) and minimum (0.43%) among the four specimens.

For SFC2 (AR55/SF0.5%), Peak-to-Peak increases from 1.52% at 75 °C to 415.00% at 250 °C. Its maximum of 452.26% is the smallest among the four intact specimen records.

SFC4 (AR55/SF0.75%) showed peak-to-peak increasing from 13.70% at 75°C to 523.23% at 250°C (38× increase), with intermediate performance among all specimens.

For the aspect-ratio groups, the mean Peak-to-Peak value is 137.13% for the two AR65 records and 129.92% for the two AR55 records, a 5.6% difference. Their maxima span 510–682% and 452–584%, respectively. These two-record groups do not establish a fibre-length effect.

For the fibre-dosage groups, the mean Peak-to-Peak value is 142.15% for the two 0.5% specimens and 124.90% for the two 0.75% specimens. The ascending order is SFC3 (113.58%), SFC2 (123.61%), SFC4 (136.23%) and SFC1 (160.69%). The group difference is descriptive and not an independent dosage effect.

The Peak-to-Peak values remain below 70% for all four intact records over 75–175°C, increase to approximately 135–180% over 175–200°C and reach 270–377% by 225°C. Values above 400% occur at 250°C. These sampled changes describe a steep, non-linear progression but do not establish an exponential law or distinct physical phases.

Above 175°C, Peak-to-Peak increases markedly from values below 70% through the 175°C stage to values about 10–20 times larger than selected earlier records. The stage sequence does not establish an exponential law or a critical operating temperature.

Across the measured temperature range, Peak-to-Peak remains below 35% for all specimens over 75–150°C, reaches 27–69% over 150–175°C and 136–377% by 225°C.

Values above 400% occur at 250°C. These ranges describe the observed progression and are not stability or critical zones.

6.8.13 Covariance Index Analysis

The temperature progression of Covariance is examined for the four specimens.

The Covariance index measures the joint variability between baseline and temperature-affected signatures. Like variance, covariance values are extremely small (order of 10^{-7}) and can transition from positive to negative at high temperatures. Figure 6.23 presents the covariance comparison plots for all four intact specimens. Covariance index comparison for all four intact SFRC specimens showing before compensation, after compensation, and the difference. Note the very small scale (order of 10^{-7}) and sign transitions at high temperatures.

Table 6.44 presents the covariance values at each temperature from 75°C to 250°C for all four specimens.

Table 6.44: Covariance Values ($\times 10^{-7}$) at Each Temperature for All Four Intact SFRC Specimens

Temperature	SFC1 (AR65/0.5%)	SFC3 (AR65/0.75%)	SFC2 (AR55/0.5%)	SFC4 (AR55/0.75%)
75°C	+0.5-1.0	+0.5-1.0	+0.5-1.0	+0.5-1.0
100°C	+0.3-0.8	+0.3-0.8	+0.3-0.8	+0.3-0.8
125°C	+0.1-0.5	+0.1-0.5	+0.1-0.5	+0.1-0.5
150°C	0 to +0.2	0 to +0.2	0 to +0.2	0 to +0.2
175°C	-0.5 to 0	-0.5 to 0	0 to +0.2	-0.5 to 0
200°C	-2.0 to -1.0	-2.0 to -1.0	-0.5 to 0	-2.0 to -1.0
225°C	-4.0 to -3.0	-4.0 to -3.0	-1.0 to 0	-4.0 to -3.0
250°C	-5.0 to -4.0	-5.0 to -4.0	+0.2 to +0.5	-5.0 to -4.0

Table 6.45 presents the statistical summary of covariance values for all four specimens.

Table 6.45: Covariance Statistical Summary for All Four Intact SFRC Specimens

SFC	AR	SF (%)	Mean	Min	Max	Sign Change
1	65	0.5	-0^{-7}	-5×10^{-7}	$+1 \times 10^{-7}$	At 175°C
3	65	0.75	-0^{-7}	-5×10^{-7}	$+1 \times 10^{-7}$	At 175°C
2	55	0.5	$+0^{-7}$	-1×10^{-7}	$+1 \times 10^{-7}$	Recovers
4	55	0.75	-0^{-7}	-5×10^{-7}	$+1 \times 10^{-7}$	At 175°C

For SFC1 (AR65/SF0.5%), the reported covariance changes from positive ($\sim 10^{-7}$) at 75°C to negative ($\sim -5 \times 10^{-7}$) at 250°C. The sign change occurs near 175°C

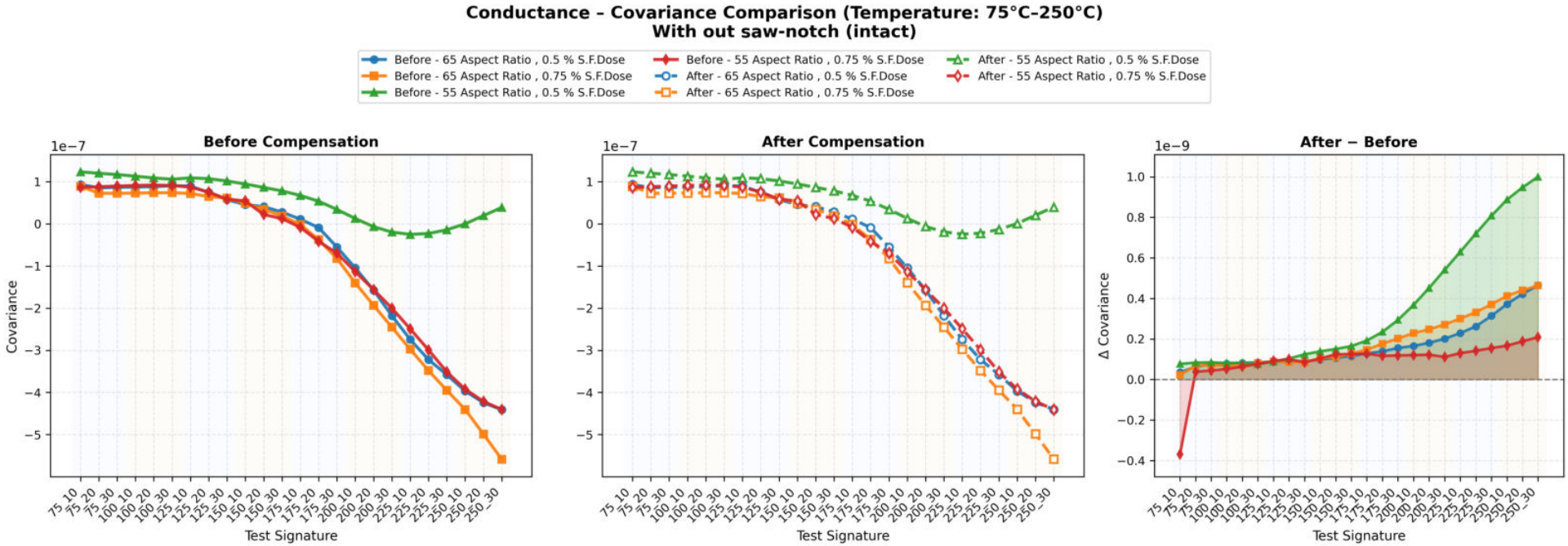

Figure 6.23: Covariance index comparison for all four intact SFRC specimens.

and describes the joint-variability trajectory of the analysed signals; it is not assigned to an independently measured material transition.

SFC3 (AR65/SF0.75%) showed identical behaviour to SFC1, with positive-to-negative transition at 175°C. The consistency across AR65 specimens indicates aspect ratio-dependent behaviour.

SFC2 (AR55/SF0.5%) had covariance values near zero or slightly positive through most of the measured sequence and returned to a positive value at 250°C. This is reported as a specimen-level difference rather than a configuration ranking.

SFC4 (AR55/SF0.75%) followed the same signed sequence as the two AR65 records, with a sign change at 175°C. This similarity does not establish that fibre content overrides aspect ratio.

For the aspect-ratio groups, the reported covariance magnitude of the two AR65 records is 804% higher than that of the two AR55 records, although this ratio is sensitive to the small denominator. The AR65 records trend toward negative values, whereas SFC2 returns to a positive final value. The difference does not isolate a fibre-length effect.

For the fibre-dosage groups, the reported covariance magnitude for the two 0.5% specimens is 89.3% lower than for the two 0.75% specimens. SFC2 is the only specimen whose signed sequence returns to a positive final value. The comparison does not establish a dosage effect or stability ranking.

Comparison of covariance with the reported variance-related quantity shows that both are of the order of 10^{-7} and undergo sign transitions in several records near 175°C. SFC2 returns to a positive final covariance. The sign of the after-minus-before covariance identifies the direction of the processing change but is not, by itself, a measure of compensation success.

Across the measured stages, covariance is positive for all four records over 75–150°C, approaches or crosses zero around 150–175°C, and becomes increasingly negative for three specimens over the later stages while SFC2 returns to a positive value. These are descriptive intervals, not operating zones.

After compensation, the after-minus-before covariance spans approximately -0.4×10^{-9} to $+1.0 \times 10^{-9}$. SFC2 changes comparatively little, whereas the other records show larger signed differences. Interpretation requires the corresponding raw and compensated signatures because the sign alone does not define improvement.

6.8.14 Consolidated Performance of Secondary SHM Indices (Intact Heating)

The preceding sections presented the detailed temperature response of the three representative indices (RMSD, CCV, and RMS) selected on the basis of their consistent direction across the four tested specimens ranking established in Section D.2. The remaining ten indices (MAPD, AMPD, CC, CCD, CCD^3, MSE, Variance, Skewness, Peak-to-Peak, and Covariance) were analysed with the same rigour; their consolidated performance under the intact heating condition is summarised in Table 6.46.

Table 6.46: Consolidated performance of the ten secondary SHM indices under intact heating for all four SFRC specimens.

Index	**SFC1**		**SFC3**		**SFC2**		**SFC4**		**Comp. Impr.**
	Mean	Max	Mean	Max	Mean	Max	Mean	Max	
MAPD	56.73%	171.65%	60.73%	168.13%	51.05%	132.13%	52.53%	147.15%	33%
AMPD	65.37%	280.78%	51.70%	215.47%	63.36%	211.69%	65.99%	279.61%	38%
CC	0.093	0.997	0.073	0.942	0.438	0.997	0.080	0.934	Stab.
CCD	2.118	5.556	2.064	5.160	0.459	1.120	2.121	5.067	40%
CCD^3	2.118	5.556	2.064	5.160	0.459	1.120	2.121	5.067	67%
MSE	$\sim$0	1.8×10^{-5}	$\sim$0	1.8×10^{-5}	$\sim$0	1.8×10^{-5}	$\sim$0	1.8×10^{-5}	50%
Variance	$\sim$0	1×10^{-7}	$\sim$0	1×10^{-7}	$\sim$0	1×10^{-7}	$\sim$0	1×10^{-7}	60%
Skewness	0.203	0.511	-0.149	0.212	-0.001	0.659	0.406	1.154	50%
Peak-to-Peak	160.69%	681.98%	113.58%	510.48%	123.61%	452.26%	136.23%	583.87%	43%
Covariance	$\sim$0	1×10^{-7}	$\sim$0	1×10^{-7}	$\sim$0	1×10^{-7}	$\sim$0	1×10^{-7}	60%

The preceding sections present the detailed temperature progression, figures and statistical interpretation for the representative indices. The consolidated secondary-index results are reported here to compare their measured directions and ranges without introducing an additional implementation ranking.

6.8.15 Effect of Compensation for the Intact Condition

This section compares the fitted EPS quantities and SHM indices before and after Enhanced EFS processing for the intact heating records. A smaller end-to-end difference indicates closer agreement with the selected ambient baseline for that quantity; it does not by itself establish preservation of a damage-sensitive response.

6.8.15.1 EPS Response to Compensation in the Intact State

Table 6.47 presents the reported end-to-end change from 75°C to 250°C for the three EPS quantities before and after compensation. Because several fitted values approach or cross zero, the percentage comparisons are interpreted together with the trajectories rather than as direct physical-property changes.

Table 6.47: Reported end-to-end EPS changes before and after compensation for the intact records (75°C to 250°C).

SFC	AR	SF	Parameter	Before (%)	After (%)	Observed change
1	65	0.5%	Mass	-493.13	-202.94	58.8% smaller magnitude
			Stiffness	-493.13	-202.94	58.8% smaller magnitude
			Damping	+23.07	+50.98	121.0% larger magnitude
3	65	0.75%	Mass	-293.56	-361.88	23.3% larger magnitude
			Stiffness	-293.56	-361.88	23.3% larger magnitude
			Damping	+92.94	-132.84	Sign reversal
2	55	0.5%	Mass	-913.57	+1128.54	Sign reversal
			Stiffness	-913.57	+1128.54	Sign reversal
			Damping	+123.23	-273.32	Sign reversal
4	55	0.75%	Mass	-2029.24	-141.54	93.0% smaller magnitude
			Stiffness	-2029.24	-141.54	93.0% smaller magnitude
			Damping	+126.18	-7.56	94.0% smaller magnitude

For the mass-like parameter, the end-to-end magnitude is smaller after compensation for SFC1 and SFC4, larger for SFC3 and reversed in sign for SFC2. The large percentages for SFC2 and SFC4 reflect the fitted reference values as well as the later-stage trajectories.

For the stiffness-like parameter, the percentages follow the mass-like percentages because the two quantities are coupled in the adopted equivalent representation. Their identical relative changes are therefore not independent evidence of compensation performance.

For the damping-like parameter, the end-to-end magnitude increases for SFC1, reverses sign for SFC2 and SFC3, and decreases for SFC4. These mixed results show that the processing does not impose a uniform damping-like response across the four records.

Table 6.48 summarises the direction of the reported change for each specimen.

Table 6.48: Specimen-level summary of the reported EPS changes after compensation.

SFC	Configuration	Mass/Stiffness	Damping	Summary
1	AR65/SF0.5%	Magnitude smaller (59%)	Magnitude larger	Mixed
3	AR65/SF0.75%	Magnitude larger	Sign reversal	Mixed
2	AR55/SF0.5%	Sign reversal	Sign reversal	Sign-changing
4	AR55/SF0.75%	Magnitude smaller (93%)	Magnitude smaller (94%)	Magnitudes smaller

The results show that SFC4 has smaller reported end-to-end magnitudes after compensation for all three EPS quantities, whereas the other specimens show mixed or sign-changing outcomes. The identical mass-like and stiffness-like percentages arise from their mathematical coupling, and the damping-like term changes sign in two

records. With one specimen per configuration, these results neither identify a preferred fibre mixture nor establish a transferable EPS-based decision rule.

6.8.15.2 SHM-Index Response to Compensation in the Intact State

This section compares before- and after-compensation ranges for the thirteen SHM indices in the intact records. The difference Δ is defined as after minus before. Its sign identifies the direction of change in an index; whether that change represents closer baseline agreement depends on the definition of the index.

Table 6.49: SHM-index ranges before and after compensation for the intact records.

#	Index	Before Range	After Range	Δ Range	Range change
1	RMSD	0 – 2.6	0 – 1.7	0 to -0.8	35% reduction
2	MAPD	0 – 3.0	0 – 2.0	0 to -0.8	33% reduction
3	AMPD	0 – 4.0	0 – 2.5	0 to -1.5	38% reduction
4	CC	0.7 – 1.0	0.85 – 1.0	0 to +0.15	Stabilization
5	CCD	0 – 0.25	0 – 0.15	0 to -0.08	40% reduction
6	CCD^3	0 – 0.012	0 – 0.004	0 to -0.008	67% reduction
7	CCV	0.93 – 1.0	0.96 – 1.0	0 to +0.02	Stabilization
8	MSE (10^{-5})	0 – 1.6	0 – 0.8	0 to -0.5	50% reduction
9	Variance (10^{-7})	+1 to -5	+0.5 to -2	-0.4 to +1.0	60% reduction
10	RMS	0.002 – 0.005	0.002 – 0.004	0 to -0.001	20% reduction
11	Skewness	-1.0 – 1.25	-0.5 – 0.75	-0.01 to +0.04	50% reduction
12	Peak-to-Peak	0 – 700%	0 – 400%	-0.1 to +0.1	43% reduction
13	Covariance (10^{-7})	+1 to -5	+0.5 to -2	-0.4 to +1.0	60% reduction

For the deviation-based indices, the tabulated ranges decrease by 33–40% for RMSD, MAPD, AMPD and CCD, and by 67% for CCD^3. The cubic value is an algebraic transformation of CCD and is not an independent confirmation. These reductions indicate closer agreement with the selected intact baseline for the reported summaries; they do not by themselves quantify preservation of the saw-cut difference.

For the correlation-based indices, the minimum CC increases from 0.70 to 0.85 and the minimum CCV from 0.93 to 0.96, placing the compensated ranges closer to their respective baseline-similarity values. Their behaviour remains dependent on the paired signatures and index definitions.

For the error and dispersion indices, the tabulated MSE range decreases by 50%, while the reported variance and covariance spans decrease by 60%. Variance and covariance remain distinct quantities even where their rounded range summaries coincide.

For RMS and skewness, the respective ranges decrease by 20% and 50%. The signed, non-monotonic skewness trajectories are examined separately because a smaller aggregate range does not guarantee consistent behaviour for every specimen.

For Peak-to-Peak, the reported maximum decreases from 700% to 400%, a 43% range reduction. The sampled stages do not establish an exponential temperature law.

Table 6.50 orders the numerical range reductions reported in Table 6.49. Because the indices have different definitions and scales, the ordering is descriptive rather than a performance ranking.

Table 6.50: Descriptive ordering of the reported SHM-index range changes after compensation.

Order	Index	Range change	Interpretation
1	CCD^3	67% reduction	Dependent cubic transform
2	Variance	60% reduction	Dispersion measure
3	Covariance	60% reduction	Joint-variation measure
4	MSE	50% reduction	Squared-error measure
5	Skewness	50% reduction	Signed shape measure
6	Peak-to-Peak	43% reduction	Amplitude-range measure
7	CCD	40% reduction	Dependent on CC
8	AMPD	38% reduction	Deviation measure
9	RMSD	35% reduction	Deviation measure
10	MAPD	33% reduction	Deviation measure
11	RMS	20% reduction	Amplitude measure
12	CC	Minimum increased	Similarity measure
13	CCV	Minimum increased	Correlation-derived measure

Overall, Enhanced EFS reduces several intact-state differences from the selected ambient baseline, but the magnitude varies with index and specimen. The correlation measures move closer to their baseline-similarity values, while the deviation and amplitude measures show different percentage reductions. These results assess thermal alignment within the four intact records; the matched intact–saw-cut analysis is required to examine whether structural-state separation remains after processing.

6.8.15.3 Quantitative Assessment of Compensation in the Intact State

This section synthesises the descriptive measures reported in Sections B.4.1 and B.4.2. The summaries compare the uncompensated and compensated records of the same four specimens; they do not constitute independent validation.

Table 6.51 presents aggregate changes in the reported intact-state summaries.

Interpretation of the aggregate measures shows that Enhanced EFS changed every reported SHM summary and reduced selected thermal-baseline differences. The magnitude was not uniform: only two of four specimens improved for selected EPS summaries, and sign changes make some percentage reductions sensitive to the chosen reference. A correlation closer to unity describes agreement with the selected baseline but does not by itself show preservation of a damage-sensitive difference.

Table 6.51: Aggregate changes in the reported intact-state summaries after compensation.

Category	Metric	Value	Scope
EPS Parameters	Largest mass/stiffness reduction	SFC4 (AR55/SF0.75%)	One specimen
	Mass/stiffness magnitude reduction	93.0%	SFC4 summary
	Damping magnitude reduction	94.0%	SFC4 summary
	Specimens with selected reductions	2 of 4 (50%)	Parameter-dependent
SHM Indices	Mean reported range reduction (11 indices)	45.1%	Different scales
	Largest range reduction (CCD^3)	67%	Dependent transform
	Indices with $> 50\%$ range reduction	5 of 13 (38%)	Descriptive count
	Indices with a reported range change	13 of 13 (100%)	Not a validation rate

Table 6.52 gives representative before–after comparisons used to assess the processing effect.

Table 6.52: Representative before–after comparisons for Enhanced EFS processing.

Criterion	Before Compensation	After Compensation
RMSD Range	0 – 2.6	0 – 1.7 (35% reduction)
CC Minimum	0.70	0.85 (closer to unity)
Peak-to-Peak Maximum	700%	400% (43% reduction)
Mass-like change (SFC4)	-2029%	-142% (93% smaller magnitude)
Damping-like change (SFC4)	+126%	-8% (94% smaller magnitude)
CCD^3 Range	0 – 0.012	0 – 0.004 (67% reduction)

Regarding configuration and temperature boundaries, SFC4 produced the largest reductions in several tabulated intact-state summaries, but one specimen cannot establish an optimal material configuration. The relative ordering of indices describes removal of thermal-baseline difference, not a general index recommendation. The experiment also does not establish a temperature below which compensation is unnecessary, a critical application temperature or real-time deployment performance.

The principal limitations are that compensation performance varies by specimen and derived quantity, with two of the four specimens showing reduced or no improvement for selected EPS comparisons. The dissipative term includes sign reversals in three specimens, making percentage summaries sensitive to the reference value. Increased variability in some later-stage records is reported descriptively; the experiment did not isolate a PZT phase-transition mechanism or establish an operational temperature limit.

In summary, Enhanced EFS reduced several aggregate thermal-difference measures within the intact records but showed specimen- and parameter-dependent behaviour. Its contribution is evaluated more directly in the matched intact–saw-cut analysis, because thermal-baseline reduction alone cannot establish damage-detection reliability.

6.9 Signature Response in the Saw-Cut State under Heating

This section presents the EMI signatures, EPS quantities and SHM indices measured after introducing the artificial saw-cut. The same four SFRC specimens examined in the intact state are compared in their saw-cut state under progressive heating. This repeated-state design supports within-specimen comparison but is not independent validation of detection performance.

6.9.1 Without Compensation Signatures (Cut Condition)

The combined saw-cut-state and temperature-associated response is introduced before the specimen-level results are compared.

When the SFRC specimens in the artificial saw-cut state are subjected to elevated temperatures, the impedance signatures contain combined structural-state and thermal contributions. This section examines the raw conductance signatures before temperature compensation and compares their measured progression with the corresponding intact-state records.

Figures 6.24 and 6.25 present the uncompensated conductance signatures after introduction of the artificial saw-cut. SFC3 and SFC4 have data only through 175 °C; the records do not establish the physical cause of the unavailable higher-temperature measurements.

These records combine the effects of structural state, temperature, dwell time and cumulative heating history. The influence of the saw-cut is therefore evaluated from matched intact–cut records at the same specimen, temperature and dwell time rather than inferred from a heated cut signature alone.

6.9.1.1 Quantification of Thermal Drift in the Saw-Cut State

The magnitude of thermal drift in cut specimens was quantified for all four SFRC specimens. Table 6.53 presents the complete thermal drift data extracted from the signature analysis files. Note that SFC3 and SFC4 (0.75% SF) have data only up to 175°C.

For SFC1 (AR65/SF0.5%), the first resonance moves left by approximately 4–5 kHz, from about 178.5 kHz at 75 °C to 173.5 kHz at 250 °C, while the second moves from about 220 to 216 kHz. The amplitude increases from approximately 0.001 to 0.010 S. These measured frequency, amplitude and peak-width changes describe the coupled response in the saw-cut state under heating; the experiment does not

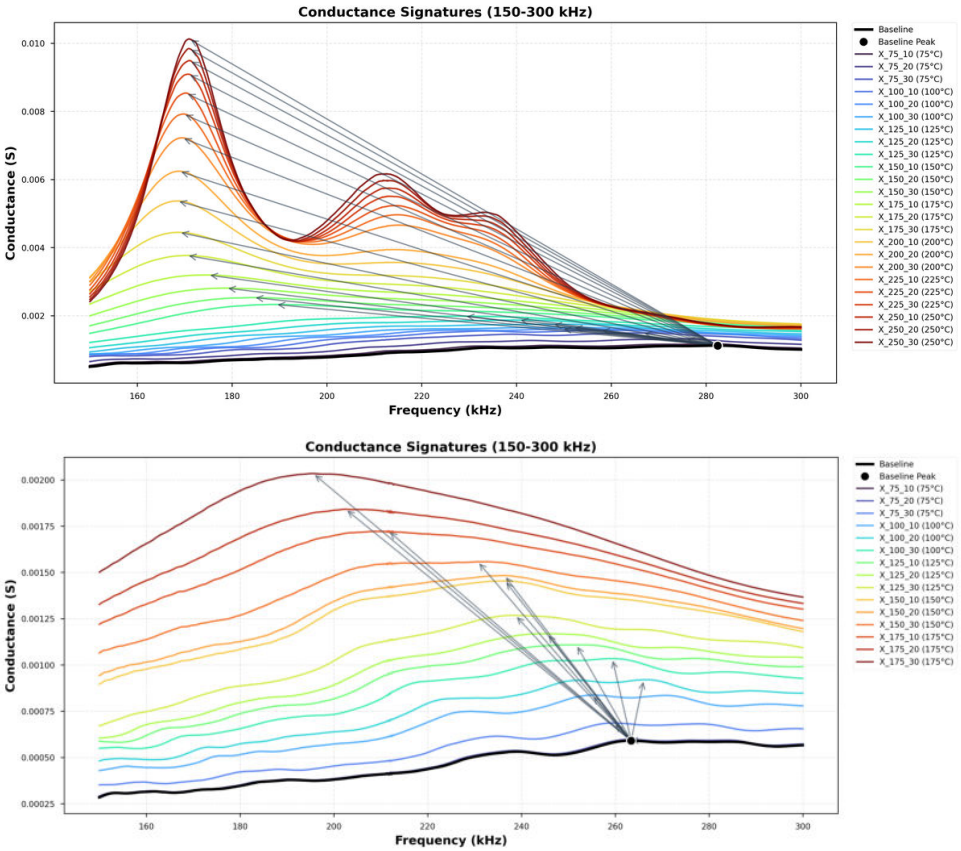

Figure 6.24: Uncompensated saw-cut conductance signatures for SFC1 and SFC3 (AR 65).

Table 6.53: Thermal Drift Quantification for All Four SFRC Specimens with Saw-Notch Damage (Without Compensation)

SFC	AR	SF (%)	Temp Range	Baseline (kHz)	Max Temp (kHz)	Shift (kHz)	Amp. Change
1	65	0.5	75–250°C	178.5–220	173.5–216	-4 to -5	10× increase
3	65	0.75	75–175°C	262	200	-62	>3× increase
2	55	0.5	75–250°C	175–215	180–218	+3 to +5	10× increase
4	55	0.75	75–175°C	245	187–190	-55 to -58	>4× increase

independently identify stiffness loss, damping change or energy dissipation as their cause.

For SFC3 (AR65/SF0.75%), over the available range to 175°C, the main resonance shifts by approximately 62 kHz, from ∼262 kHz at baseline to ∼200 kHz at 175°C, while the amplitude increases from ∼0.00062 S to ∼0.0020 S. Records above 175°C are unavailable and the cause was not independently diagnosed. The shift describes the coupled JPS–interface–specimen response and is not converted directly into physical stiffness loss.

For SFC2 (AR55/SF0.5%), over the full temperature range, the left and right peaks

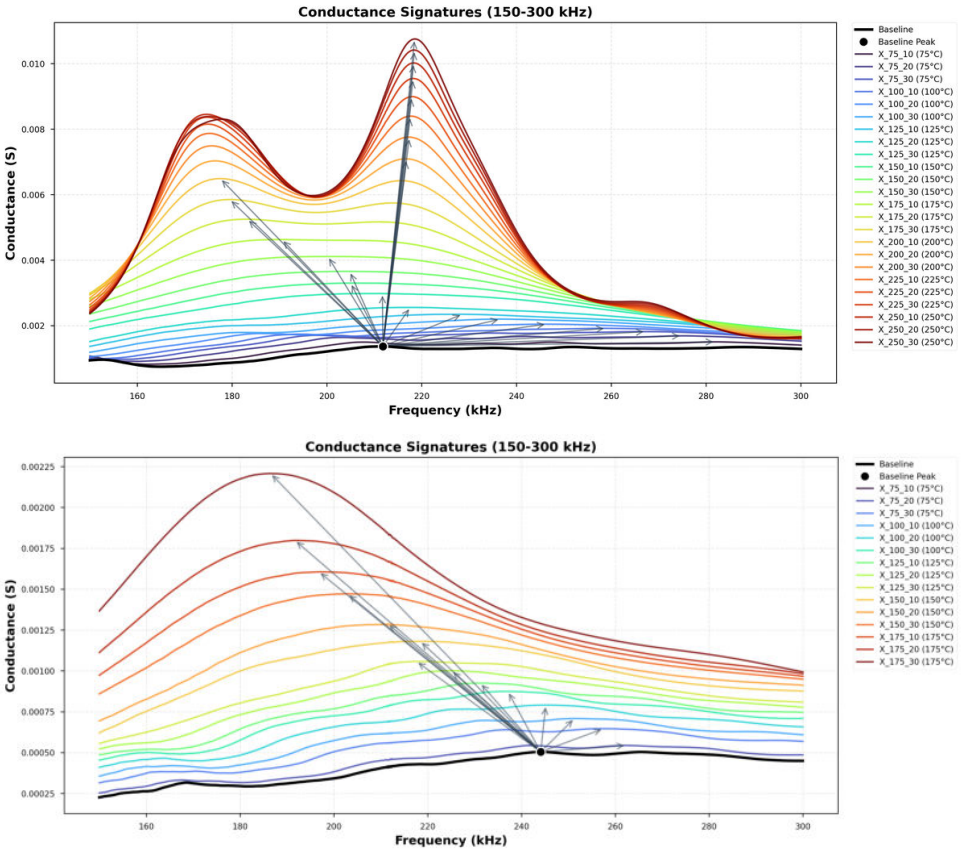

Figure 6.25: Uncompensated saw-cut conductance signatures for SFC2 and SFC4 (AR 55).

shift right by approximately 3–5 kHz, while the amplitude increases from approximately 0.001 S to 0.0105 S. Resonance movement in the coupled measurement does not directly measure structural stiffness, so the direction is not assigned to thermal stiffening, fibre length or fibre bridging.

For SFC4 (AR55/SF0.75%), over the available range to 175°C, the main resonance shifts left by approximately 55–58 kHz, from ∼245 kHz at baseline to ∼187–190 kHz at 175°C, while the amplitude increases from ∼0.0005 S to ∼0.0022 S. Records above 175°C are unavailable and the cause was not independently diagnosed. The experiment does not isolate material degradation or interface debonding as the source of the shift.

6.9.1.2 Material Comparison in the Saw-Cut State

The four saw-cut records are compared to describe their measured frequency and amplitude changes during progressive heating. Because each AR–dosage configuration is represented by one specimen, the comparison does not isolate aspect-ratio or fibre-dosage effects.

For the aspect-ratio groups, the AR65 records show leftward shifts of 4–5 kHz for SFC1 and 62 kHz for SFC3. The AR55 records show a 3–5 kHz rightward shift for SFC2 and a 55–58 kHz leftward shift for SFC4. The mixed directions within each pair do not establish an aspect-ratio or dosage interaction.

For the fibre-dosage groups, within the AR65 pair, SFC1 has a 4–5 kHz leftward shift and SFC3 a 62 kHz leftward shift. Within the AR55 pair, SFC2 has a 3–5 kHz rightward shift and SFC4 a 55–58 kHz leftward shift. The two 0.75% records also end at 175°C. These associated patterns do not demonstrate that dosage caused either the larger shifts or the shorter coverage.

Regarding data availability, saw-cut measurements for SFC3 and SFC4 are unavailable above 175 °C, whereas SFC1 and SFC2 have records through 250 °C. The cause of the missing higher-temperature records was not independently diagnosed. No sensor-failure or fibre-content mechanism is therefore assigned, and four-specimen comparisons are restricted to the common range through 175 °C.

The observed shift magnitudes increase from SFC2 (3–5 kHz, rightward) and SFC1 (4–5 kHz, leftward) to SFC4 (55–58 kHz, leftward) and SFC3 (62 kHz, leftward). The last two series terminate at 175°C. These values describe the four available records and are not a ranking of material thermal stability.

For the subsequent structural comparison, the saw-cut frequency shifts of 3–62 kHz and amplitude increases of approximately 3–10$\times$ during heating show that a comparison with a single ambient record would combine temperature-associated and structural-state differences. SFC2 has the smallest shift in this set, but one specimen does not establish a preferred configuration.

6.9.2 With Compensation Signatures (Cut Condition)

The effect of compensation on the saw-cut-state signatures is examined first.

Following application of the temperature-compensation procedure, the conductance signatures of the saw-cut specimens were re-analysed to reduce temperature-associated frequency differences. This section presents the processed signatures and evaluates the residual spectral changes without assuming that temperature and structural-state contributions were perfectly separated.

Figures 6.26 and 6.27 present the compensated conductance signatures in the saw-cut state. SFC3 and SFC4 retain the shorter range ending at 175 °C; no missing curve is extrapolated.

Compensation reduces selected components of the state-specific thermal drift, but the remaining differences cannot automatically be assigned to the saw-cut. They may

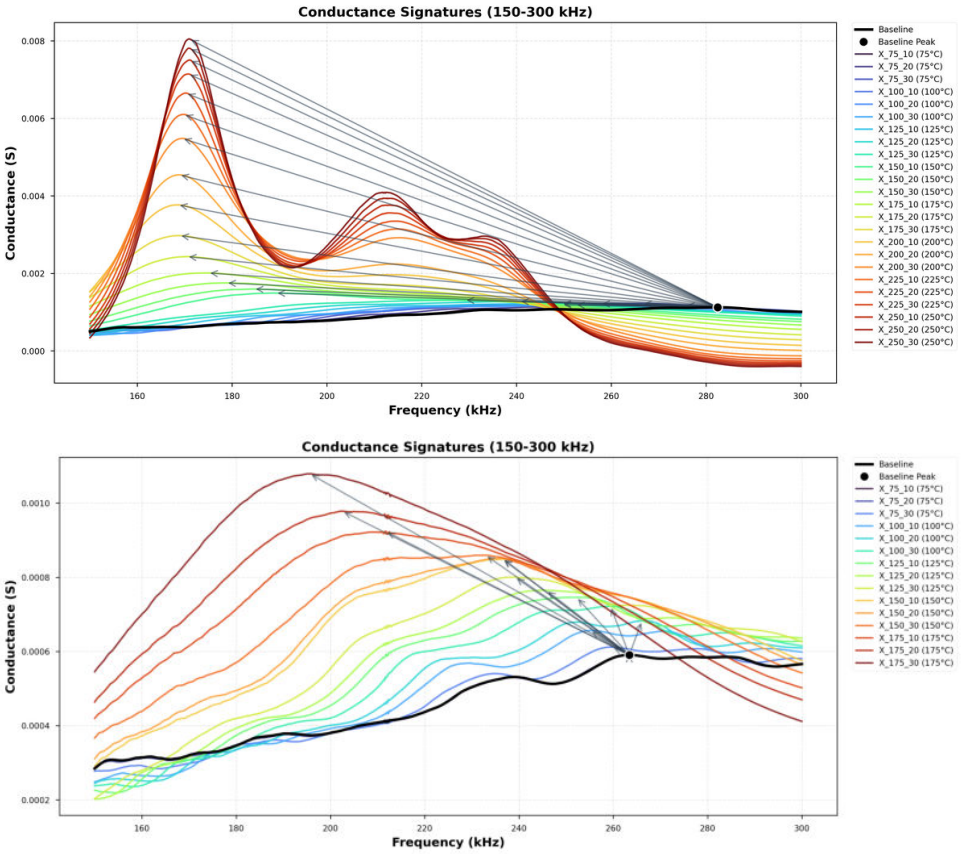

Figure 6.26: Compensated saw-cut conductance signatures for SFC1 and SFC3 (AR 65).

also contain residual temperature dependence, dwell-time variation and cumulative exposure effects. The damage-related assessment therefore uses the matched comparisons reported later in the chapter.

6.9.2.1 Compensated Signature Characteristics in the Saw-Cut State

Table 6.54 presents the compensated signature characteristics for all four SFRC specimens with saw-notch damage.

Table 6.54: Compensated Signature Characteristics for All Four SFRC Specimens with Saw-Notch Damage

SFC	AR	SF (%)	Temp Range	Baseline (kHz)	Max Temp (kHz)	Shift (kHz)	Pattern
1	65	0.5	75–250°C	280 (then 178)	168	-10	Peak emergence
3	65	0.75	75–175°C	265	195	-70	Leftward shift
2	55	0.5	75–250°C	215	175 / 220	-40 / +5	Peak splitting
4	55	0.75	75–175°C	245	185	-60	Leftward shift

For SFC1 (AR65/SF0.5%), over the full temperature range, the compensated record contains a lower-frequency peak in the 168–178 kHz range, whereas the reference

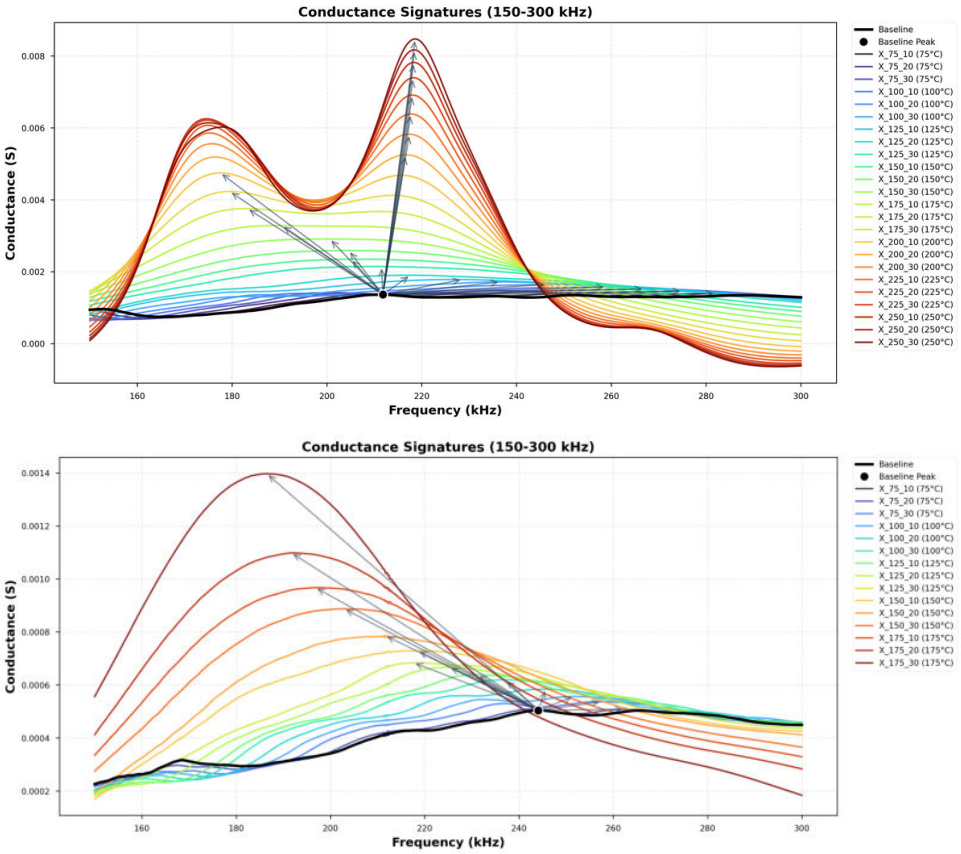

Figure 6.27: Compensated saw-cut conductance signatures for SFC2 and SFC4 (AR 55).

signature has a peak near 280 kHz. Across 75–250°C, the tracked lower-frequency peak moves from approximately 178 to 168 kHz and its amplitude increases from approximately 0.002 to 0.008 S. These spectral differences are retained as observations of the coupled measurement; they do not by themselves identify stiffness loss or a new vibration mode.

For SFC3 (AR65/SF0.75%), over the available range to 175°C, the tracked peak moves from approximately 265 kHz in the reference signature to approximately 195 kHz at 175°C, while its amplitude increases from approximately 0.0006 to 0.0010 S. This 70 kHz residual difference is reported only over the available range. It can include structural-state, residual temperature, sensor-interface and measurement contributions, so it is not interpreted as a direct stiffness-loss measurement.

For SFC2 (AR55/SF0.5%), over the full temperature range, relative to the reference peak near 215 kHz, the compensated record contains two prominent peaks near 175 and 220 kHz, corresponding to differences of approximately -40 and +5 kHz. Their amplitudes increase, with the larger reaching approximately 0.008 S. The observed peak splitting distinguishes this record from a simple translation of the reference signature,

but the experiment does not independently identify the modal mechanism responsible for it.

For SFC4 (AR55/SF0.75%), over the available range to 175°C, the compensated peak moves left from approximately 245 kHz at baseline to 225, 210, 200, 190 and 185 kHz at the successive measured stages through 175°C. The amplitude increases from approximately 0.0005 S to 0.0014 S. Residual progression after compensation may contain temperature, saw-cut, sensor-interface and measurement contributions and is not assigned solely to structural degradation.

6.9.2.2 Specimen-Level Comparison after Compensation in the Saw-Cut State

The compensated signatures are compared specimen by specimen to describe residual differences after the adopted processing. The unreplicated configuration design does not support a causal material-interaction claim.

For the aspect-ratio groups, SFC1 and SFC3 show lower-frequency peak emergence or movement, while SFC2 exhibits peak splitting and SFC4 a 60 kHz leftward shift. Because each configuration is represented once and the resonances belong to the coupled sensor–interface–host response, these differences are not attributed to fibre length or a mode-shape degradation mechanism.

For the fibre-dosage groups, within the AR65 pair, the reported residual shifts are approximately 10 kHz for SFC1 and 70 kHz for SFC3; within the AR55 pair, the primary shifts are approximately 40 kHz for SFC2 and 60 kHz for SFC4. Although the two 0.75% records have larger values within their respective pairs, the design does not isolate dosage or a fibre–matrix interface mechanism.

After compensation, all four saw-cut records retain spectral differences, including lower-frequency peak emergence in SFC1, leftward movement in SFC3 and SFC4, and peak splitting in SFC2. The residual shifts span approximately 10–70 kHz. Because no independent decomposition of residual temperature, sensor-interface and structural-state contributions was performed, these differences are not labelled as purely matched intact–saw-cut.

At specimen level, the reported residual shift magnitudes decrease from SFC3 (70 kHz) to SFC4 (60 kHz), SFC2 (40 kHz primary shift) and SFC1 (10 kHz residual shift). Peak splitting and peak emergence complicate a single-number comparison, so this ordering is not treated as a material-sensitivity or stability ranking.

For the structural comparison, the processing reduces selected temperature-associated differences while retaining specimen-specific spectral features. Their suitability for damage classification or characterisation requires independent replicated

validation; the present four records do not establish a dosage-dependent monitoring advantage.

6.10 Equivalent Structural Parameters in the Saw-Cut State under Heating

The EPS derived from the impedance signatures were analysed for all four SFRC specimens in the artificial saw-cut state under heating. The records contain combined structural-state and thermal contributions, but they do not isolate a stress-concentration mechanism or an acceleration effect. SFC3 and SFC4 have data only to 175 °C because higher-temperature records are unavailable; the cause was not independently diagnosed.

6.10.1 Equivalent Mass Parameter (Cut Condition)

The uncompensated mass-like response is examined for all four specimens.

The equivalent mass parameter exhibited temperature-dependent behaviour in the saw-cut records. Figures 6.28–6.31 show each specimen at full width, retaining all three EPS trajectories and both processing branches. SFC3 and SFC4 end at 175 °C; no values are inferred beyond the last acquired stage.



Figure 6.28: Saw-cut EPS transitions before and after compensation for SFC1 (AR 65, 0.50% fibre).



Figure 6.29: Saw-cut EPS transitions before and after compensation for SFC3 (AR 65, 0.75% fibre; data to 175 °C).

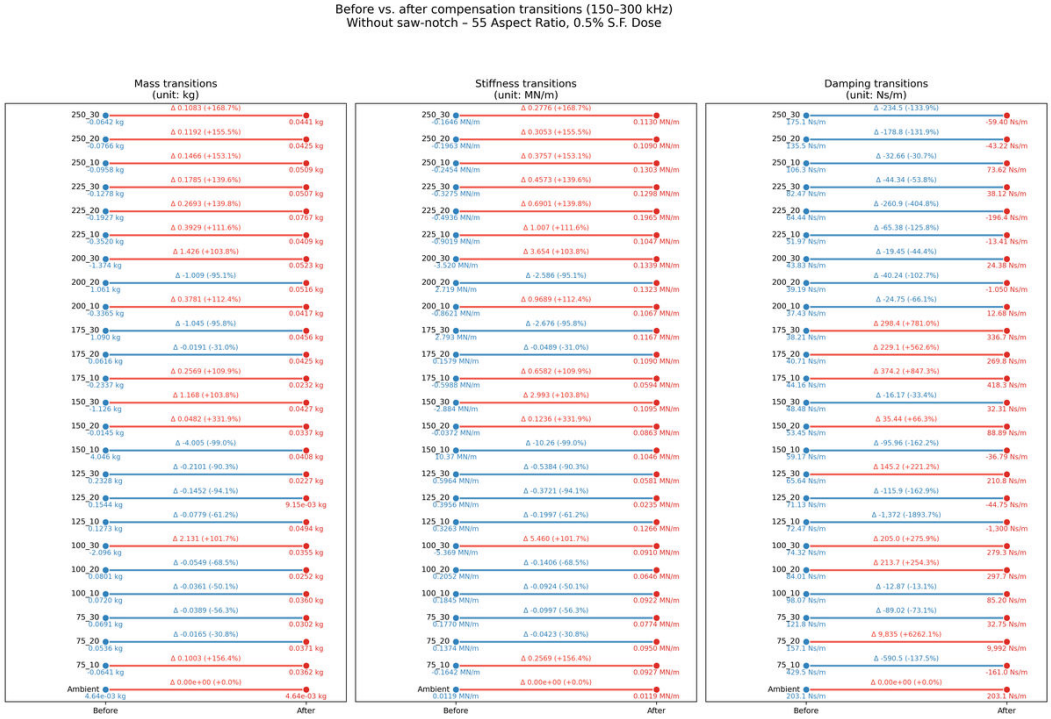

Figure 6.30: Saw-cut EPS transitions before and after compensation for SFC2 (AR 55, 0.50% fibre).



Figure 6.31: Saw-cut EPS transitions before and after compensation for SFC4 (AR 55, 0.75% fibre; data to 175 °C).

Table 6.55 presents the equivalent mass values at each temperature stage for all four SFRC specimens with saw-notch damage (without compensation).

Table 6.55: Equivalent Mass (kg) at Each Temperature for All Four SFRC Specimens with Saw-Notch (Without Compensation)

Temperature	**SFC1 (AR65/0.5%)**	**SFC3 (AR65/0.75%)**	**SFC2 (AR55/0.5%)**	**SFC4 (AR55/0.75%)**
Ambient	0.0331	0.0363	0.0286	0.0385
75°C	0.0292	0.0379	0.0251	0.0362
100°C	0.0234	0.0335	-0.0412	0.0329
125°C	0.0107	0.0303	0.0233	0.0305
150°C	0.3019	0.0228	-0.0898	0.0247
175°C	0.2765	0.5581	-0.0584	-0.2164
200°C	-0.2584	—	-0.0368	—
225°C	-0.0670	—	0.0396	—
250°C	0.0170	—	-0.0043	—

The temperature progression data show distinct mass-like parameter patterns for each SFRC configuration in the saw-cut state under heating. Table 6.56 summarises the overall change for all four specimens.

For SFC1 (AR65/SF0.5%), the fitted mass-like parameter changes by -209.4% from 75°C to 250°C. It moves from positive values at ambient and 75°C (0.0292–0.0331 kg) through excursions at 150°C (0.3019 kg) and 175°C (0.2765 kg), then becomes negative at 200°C (-0.2584 kg) before returning to 0.0170 kg at 250°C. These non-

Table 6.56: Equivalent Mass Change Summary for All Four SFRC Specimens with Saw-Notch (Without Compensation)

SFC	AR	SF (%)	Temp Range	Start Mass (kg)	End Mass (kg)	Change (%)
1	65	0.5	75–250°C	0.0310	-0.0339	-209.4
3	65	0.75	75–175°C	0.0385	0.1847	+379.9
2	55	0.5	75–250°C	0.0260	0.0030	-88.6
4	55	0.75	75–175°C	0.0376	-0.0614	-263.4

monotonic and sign-changing values belong to the adopted equivalent representation and do not establish a physical phase transition or a direct change in specimen mass.

For SFC3 (AR65/SF0.75%), over the available range to 175°C, the mass-like term increases from 0.0379 kg at 75°C to 0.5581 kg at 175°C, corresponding to a reported +379.9% change over the available range. The increase between 150 and 175°C is a fitted-parameter excursion, not evidence of a material transition. Records above 175°C are unavailable and their absence is not attributed to sensor failure.

SFC2 (AR55/SF0.5%) has the smallest reported end-to-end percentage change, -88.6% from 75°C to 250°C. The fitted mass-like term changes sign repeatedly, with negative values at 100°C (-0.0412 kg), 150°C (-0.0898 kg), 175°C (-0.0584 kg) and 250°C (-0.0043 kg). The near-zero and sign-changing values limit physical and percentage interpretation.

For SFC4 (AR55/SF0.75%), over the available range to 175°C, the mass-like term changes from 0.0362 kg at 75°C to -0.2164 kg at 175°C, corresponding to -263.4% over the available range. The sign change occurs between the 150 and 175°C stages. It is interpreted as behaviour of the fitted equivalent representation, not as an independently demonstrated fibre-configuration effect.

The observed Mass response in the saw-cut state is compared across the four tested configurations.

In the aspect-ratio comparison, the AR65 specimens contain large fitted excursions (0.3019 kg at 150°C for SFC1 and 0.5581 kg at 175°C for SFC3), whereas the two AR55 trajectories change more gradually over their available stages. Because dosage changes simultaneously and each configuration has one specimen, the comparison does not establish an AR effect or a load-transfer mechanism.

The specimen- and dosage-associated responses differ within the available records. SFC1 (AR 65/0.50%) changed by -209.4% through 250 °C, while SFC3 (AR 65/0.75%) changed by +379.9% through 175 °C. SFC2 (AR 55/0.50%) changed by -88.6% through 250 °C, and SFC4 (AR 55/0.75%) changed by -263.4% through 175 °C. The unequal temperature ranges preclude direct full-range ranking. Because there is one specimen per

configuration and the reason for missing higher-temperature records was not diagnosed, neither a dosage effect nor a sensor-functionality mechanism is inferred.

The compensated mass-like response is examined for all four specimens.

The temperature compensation algorithm was applied to isolate structural effects from thermal drift. Table 6.57 presents the mass values after compensation.

Table 6.57: Equivalent Mass (kg) at Each Temperature for All Four SFRC Specimens with Saw-Notch (With Compensation)

Temperature	SFC1 (AR65/0.5%)	SFC3 (AR65/0.75%)	SFC2 (AR55/0.5%)	SFC4 (AR55/0.75%)
Ambient	0.0377	0.0423	0.0316	0.0438
75°C	0.0292	0.0423	0.0184	0.0406
100°C	0.0245	0.0372	0.0143	0.0364
125°C	0.0219	0.0342	0.0075	0.0338
150°C	0.0146	0.0312	-0.0012	0.0307
175°C	0.0089	0.0281	-0.0032	0.0277
200°C	0.0097	—	0.0021	—
225°C	0.0070	—	-0.0263	—
250°C	0.0171	—	-0.1176	—

Table 6.58 presents the comparison of mass changes before and after compensation.

Table 6.58: Comparison of Mass Parameter Changes Before and After Temperature Compensation (Cut Condition)

SFC	AR	SF	Temp Range	Before (%)	After (%)	Reported reduction
1	65	0.5%	75–250°C	-209.4	-64.6	69% reduction
3	65	0.75%	75–175°C	+379.9	-33.4	91% reduction
2	55	0.5%	75–250°C	-88.6	-298.2	Increased
4	55	0.75%	75–175°C	-263.4	-23.7	91% reduction

For SFC1 (AR65/SF0.5%), the end-to-end mass-like change decreases in magnitude from -209.4% before compensation to -64.6% after compensation, a reported reduction of 69%. The compensated fitted values remain positive over 75–175°C (0.0089–0.0292 kg) before smaller later-stage fluctuations.

SFC2, SFC3 and SFC4 show different compensation outcomes. For SFC3, the end-to-end percentage changes are +379.9% before and -33.4% after compensation, and the compensated values decrease from 0.0423 kg at 75°C to 0.0281 kg at 175°C. For SFC2, the corresponding magnitude increases from -88.6% to -298.2%, with a fitted value of -0.1176 kg at 250°C. For SFC4, the magnitude changes from -263.4% to -23.7%, and the compensated values remain between 0.0277 and 0.0438 kg over the available range.

Across the saw-cut series, the reported end-to-end magnitude is reduced for SFC1, SFC3 and SFC4 and increased for SFC2. The processing effect therefore depends on the specimen and fitted parameter and does not establish a dosage-group performance ranking.

6.10.2 Equivalent Stiffness Parameter (Cut Condition)

The uncompensated stiffness-like response is examined for all four specimens.

The equivalent stiffness-like parameter is obtained from the adopted coupled representation and is not a direct measurement of SFRC elastic stiffness. Under saw-cut heating, the four fitted trajectories contain large excursions and sign changes. Figure 6.28 presents the corresponding transitions for all four specimens.

Table 6.59 presents the equivalent stiffness values at each temperature stage for all four SFRC specimens with saw-notch damage (without compensation).

Table 6.59: Equivalent Stiffness (MN/m) at Each Temperature for All Four SFRC Specimens with Saw-Notch (Without Compensation)

Temperature	SFC1 (AR65/0.5%)	SFC3 (AR65/0.75%)	SFC2 (AR55/0.5%)	SFC4 (AR55/0.75%)
Ambient	75146.5	77370.9	69553.7	81958.7
75°C	66252.8	80780.4	61131.4	77030.2
100°C	53066.4	71250.8	-100289.5	70030.0
125°C	24368.3	64612.2	56784.6	64986.6
150°C	685713.6	48516.1	-218740.1	52472.3
175°C	628054.2	1188308.1	-142171.3	-460498.5
200°C	-586924.8	—	-89724.7	—
225°C	-152094.9	—	96544.5	—
250°C	38659.8	—	-10522.9	—

The temperature progression data show distinct stiffness-like parameter patterns for each SFRC configuration in the saw-cut state under heating. Table 6.60 summarises the overall change for all four specimens.

Table 6.60: Equivalent Stiffness Change Summary for All Four SFRC Specimens with Saw-Notch (Without Compensation)

SFC	AR	SF (%)	Temp Range	Start (MN/m)	End (MN/m)	Change (%)
1	65	0.5	75–250°C	70423.1	-77059.1	-209.4
3	65	0.75	75–175°C	81955.5	393297.5	+379.9
2	55	0.5	75–250°C	63237.5	7235.8	-88.6
4	55	0.75	75–175°C	79912.0	-130602.0	-263.4

For SFC1 (AR65/SF0.5%), over the full temperature range, the stiffness-like term changes by -209.4% from 75°C to 250°C and is strongly non-monotonic, including

large positive values at 150–175°C and negative values from 200°C. The trajectory is reported without assigning a threshold or attributing its magnitude solely to the saw-cut.

For SFC3 (AR65/SF0.75%), over the available range to 175°C, the stiffness-like term increases from 80,780.4 MN/m at 75°C to 1,188,308.1 MN/m at 175°C. The large final excursion is not treated as a physical stiffness transition. Records above 175°C are unavailable, and the experiment did not determine why.

For SFC2 (AR55/SF0.5%), over the full temperature range, the reported end-to-end change is -88.6%, the smallest magnitude among the four saw-cut records. The fitted term nevertheless changes sign at several stages. This specimen-level value is not evidence of configuration-level thermal stability.

For SFC4 (AR55/SF0.75%), over the available range to 175°C, the stiffness-like term changes from 77,030.2 MN/m at 75°C to -460,498.5 MN/m at 175°C, corresponding to -263.4% over the available range. The sign reversal occurs between the 150 and 175°C stages and is not designated a material threshold.

The observed Stiffness response in the saw-cut state is compared across the four tested configurations.

For the aspect-ratio groups, the AR65 records contain the largest positive fitted excursions at 150–175°C, while the AR55 trajectories have smaller positive maxima. Dosage, specimen identity and sensor installation vary concurrently, so the comparison does not establish a fibre-length or local-stress mechanism.

For the fibre-dosage groups, Within both aspect-ratio pairs, the 0.75% record has the larger absolute end-to-end change, but those two records also end at 175°C. The unequal coverage and single specimen per configuration preclude a dosage or fibre–matrix interface conclusion.

At 175°C, SFC1 and SFC3 have large positive fitted values (628,054 and 1,188,308 MN/m), while SFC2 and SFC4 have negative values (-142,171 and -460,499 MN/m). The opposing signs do not define a common transition temperature, and the missing later records for SFC3 and SFC4 do not demonstrate loss of sensor function.

The compensated stiffness-like response is examined for all four specimens.

The temperature compensation algorithm was applied to isolate structural effects from thermal drift. Table 6.61 presents the stiffness values after compensation.

Table 6.62 presents the comparison of stiffness changes before and after compensation.

For SFC1 (AR65/SF0.5%), the end-to-end stiffness-like change decreases in magnitude from -209.4% before compensation to -64.6% after compensation, a reported reduction of 69%. The compensated fitted values decrease from 66204.6 MN/m at 75°C to 38819.0 MN/m at 250°C without the larger excursions present in the uncompensated

Table 6.61: Equivalent Stiffness (MN/m) at Each Temperature for All Four SFRC Specimens with Saw-Notch (With Compensation)

Temperature	SFC1 (AR65/0.5%)	SFC3 (AR65/0.75%)	SFC2 (AR55/0.5%)	SFC4 (AR55/0.75%)
Ambient	85510.9	88631.6	76906.1	93204.8
75°C	66204.6	88748.1	44841.1	86297.0
100°C	55747.1	77979.0	34895.5	77359.0
125°C	49695.2	71666.6	18174.4	71965.3
150°C	33269.8	65337.6	-2958.6	65305.9
175°C	20173.3	58827.9	-7876.2	58991.6
200°C	22119.4	—	5211.3	—
225°C	15893.1	—	-64117.7	—
250°C	38819.0	—	-286396.5	—

Table 6.62: Comparison of Stiffness Parameter Changes Before and After Temperature Compensation (Cut Condition)

SFC	AR	SF	Temp Range	Before (%)	After (%)	Reported reduction
1	65	0.5%	75–250°C	-209.4	-64.6	69% reduction
3	65	0.75%	75–175°C	+379.9	-33.4	91% reduction
2	55	0.5%	75–250°C	-88.6	-298.2	Increased
4	55	0.75%	75–175°C	-263.4	-23.7	91% reduction

series.

SFC3, SFC2 and SFC4 show different processing effects. For SFC3 and SFC4, the reported end-to-end magnitude decreases by approximately 91%, and the large unprocessed excursions are absent from the compensated sequences. For SFC2, the end-to-end magnitude increases from 88.6% to 298.2%. These outcomes are described per specimen rather than graded as configuration performance.

For the saw-cut stiffness-like term, the reported magnitude decreases after compensation for SFC1, SFC3 and SFC4 and increases for SFC2. Removing a fitted excursion improves agreement with the selected baseline for that parameter, but it does not prove that the excursion was solely thermal or that structural-state information was preserved.

6.10.3 Equivalent Damping Parameter (Cut Condition)

The uncompensated damping-like response is examined for all four specimens.

The equivalent damping-like parameter is a fitted descriptor of the coupled PZT–SFRC response and exhibits non-monotonic temperature-associated behaviour. In the saw-cut state under heating, its reported magnitude changes for all four specimens and varies among temperature stages. Figure 6.28 includes the corresponding transitions for

all four specimens.

Table 6.63 presents the equivalent damping change summary for all four SFRC specimens with saw-notch damage (without compensation).

Table 6.63: Equivalent Damping Change Summary for All Four SFRC Specimens with Saw-Notch (Without Compensation)

SFC	AR	SF (%)	Temp Range	Change (%)	Direction
1	65	0.5	75–250°C	+103.7	Increasing
3	65	0.75	75–175°C	+203.5	Increasing
2	55	0.5	75–250°C	+45.7	Increasing
4	55	0.75	75–175°C	+79.0	Increasing

The damping-like parameter in the saw-cut state under heating shows distinct patterns for each tested specimen.

For SFC1 (AR65/SF0.5%), over the full temperature range, the fitted damping-like term increases by +103.7% from 75°C to 250°C and is non-monotonic between stages, with selected percentage changes exceeding $\pm 1000\%$. These excursions describe the fitted equivalent parameter and are not assigned to internal friction, damage sites or fibre–matrix interfaces because those mechanisms were not measured independently.

For SFC3 (AR65/SF0.75%), over the available range to 175°C, the specimen has the largest reported dissipative-term increase (+203.5%) over its available range. The cause of the missing higher-temperature records is unknown, and no fibre, saw-cut or energy-dissipation mechanism is inferred.

SFC2 (AR55/SF0.5%) has the smallest reported dissipative-term change (+45.7%) over its full range. It is a specimen-level observation rather than evidence of superior configuration stability.

For SFC4 (AR55/SF0.75%), the damping-like parameter increases by +79.0% from 75 to 175 °C. The series ends at 175 °C, so it cannot be compared over the full range of SFC1 and SFC2. The fitted change does not independently measure internal friction or fibre–matrix interface development.

The observed Damping response in the saw-cut state is compared across the four tested configurations.

For the aspect-ratio groups, the two AR65 records have end-to-end increases of +103.7% and +203.5%, compared with +45.7% and +79.0% for the AR55 records. The values are descriptive and do not establish a fibre-length, stability or energy-dissipation mechanism.

For the fibre-dosage groups, Within the AR65 pair, the reported changes are +103.7% for SFC1 and +203.5% for SFC3; within the AR55 pair they are +45.7%

for SFC2 and +79.0% for SFC4. Although the 0.75% record is larger within each pair, the unreplicated design and unequal coverage do not establish a dosage or energy-dissipation mechanism.

The damping-like term increases over the available range for all four saw-cut records (+45.7% to +203.5%), whereas the mass-like and stiffness-like terms generally decrease; SFC3 is the exception, with a reported +379.9% change. The contrasting directions show that the three fitted quantities describe different components of the adopted equivalent representation. They do not, without replicated validation, establish the damping-like term as a superior or independently reliable damage indicator.

The compensated damping-like response is examined for all four specimens.

The temperature compensation algorithm was applied to isolate structural effects from thermal drift. Table 6.64 presents the comparison of damping changes before and after compensation.

Table 6.64: Comparison of Damping Parameter Changes Before and After Temperature Compensation (Cut Condition)

SFC	AR	SF	Temp Range	Before (%)	After (%)	Reported reduction
1	65	0.5%	75–250°C	+103.7	+63.3	39% reduction
3	65	0.75%	75–175°C	+203.5	+10.5	95% reduction
2	55	0.5%	75–250°C	+45.7	+47.7	Increased
4	55	0.75%	75–175°C	+79.0	-5.9	107% reduction

For SFC1 (AR65/SF0.5%), the end-to-end damping-like change decreases from +103.7% before compensation to +63.3% after compensation, a reported reduction of 39%. The processing reduces but does not remove the increase in this fitted quantity.

SFC3, SFC2 and SFC4 show different processing effects. The reported damping-like magnitude decreases from +203.5% to +10.5% for SFC3, changes little for SFC2 (+45.7% to +47.7%), and reverses sign for SFC4 (+79.0% to -5.9%). These changes describe the fitted quantity and do not identify the fraction attributable solely to temperature.

For the dissipative term in the saw-cut condition, the reported reductions after compensation are 95% for SFC3 and 39% for SFC1; SFC4 changes direction and SFC2 increases slightly. These mixed results do not establish a beneficial dosage effect.

Across the saw-cut EPS results, SFC2 has the smallest reported full-range changes in the three fitted terms, while SFC3 has the largest selected changes over its shorter range. Compensation effects vary by term and specimen. SFC3 and SFC4 have no saw-cut measurements above 175 °C; this is recorded as missing data, not a sensor-reliability conclusion.

6.11 SHM Indices in the Saw-Cut State under Heating

The statistical SHM indices derived from impedance signatures were analysed for all four SFRC specimens with saw-notch (artificial) damage under thermal loading. These indices quantify the deviation between baseline and temperature-affected signatures, providing damage-sensitive features that are further influenced by the saw-notch damage. Note that SFC3 and SFC4 (0.75% SF specimens) have data only up to 175°C because higher-temperature records are unavailable; the cause was not independently diagnosed.

6.11.1 RMSD Index Analysis (Cut Condition)

The temperature progression of RMSD is examined for the four specimens.

The RMSD index quantifies the overall difference between baseline and elevated-temperature signatures for specimens in the saw-cut state. Figure 6.32 presents the comparison plots for all four specimens. RMSD index comparison for all four SFRC specimens with saw-notch damage showing before compensation, after compensation, and the difference. Note: AR65/SF0.75% and AR55/SF0.75% specimens have data only up to 175°C.

Table 6.65 presents the RMSD values at each temperature from 75°C to 250°C for all four specimens in the saw-cut state.

Table 6.65: RMSD Values at Each Temperature for All Four SFRC Specimens with Saw-Notch

Temperature	SFC1 (AR65/0.5%)	SFC3 (AR65/0.75%)	SFC2 (AR55/0.5%)	SFC4 (AR55/0.75%)
75°C	0.055	0.016	0.092	0.033
100°C	0.123	0.160	0.207	0.162
125°C	0.228	0.313	0.414	0.298
150°C	0.549	0.515	0.827	0.594
175°C	1.009	0.809	1.461	1.114
200°C	1.866	—	2.097	—
225°C	2.531	—	2.517	—
250°C	2.801	—	2.746	—

Table 6.66 presents the statistical summary of RMSD values for all four specimens in the saw-cut state.

For SFC1 (AR65/SF0.5%), over the full temperature range, RMSD increases from 0.055 at 75°C to 2.801 at 250°C, corresponding to a 50.9× ratio. The saw-cut mean is 1.145 and the intact mean is 0.572, a +100% matched mean difference. This difference is reported for the two structural states without interpreting it as an independent measure of damage severity.

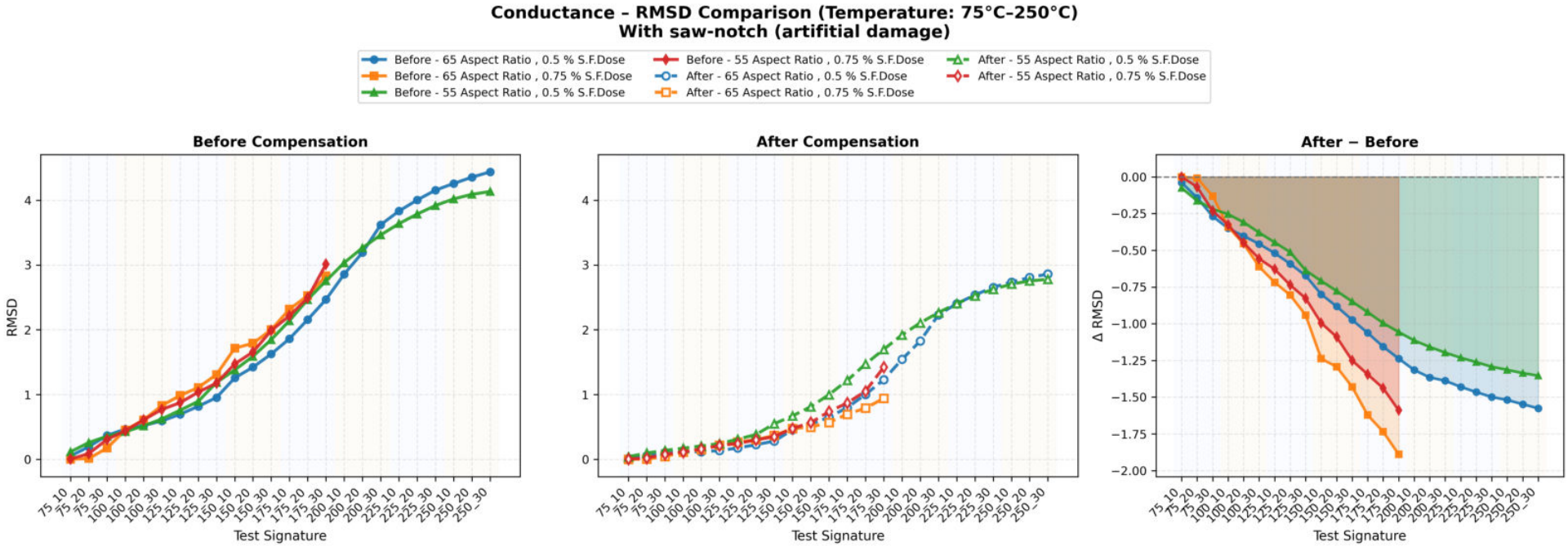

Figure 6.32: RMSD index comparison for all four SFRC specimens with saw-notch damage.

Table 6.66: RMSD Statistical Summary for All Four SFRC Specimens with Saw-Notch

SFC	AR	SF (%)	Temp Range	Mean	Std Dev	Min	Max
1	65	0.5	75–250°C	1.145	1.047	0.013	2.860
3	65	0.75	75–175°C	0.362	0.284	0.001	0.941
2	55	0.5	75–250°C	1.295	1.000	0.041	2.779
4	55	0.75	75–175°C	0.440	0.402	0.003	1.421

For SFC3 (AR65/SF0.75%), RMSD increased from 0.016 at 75°C to 0.809 at 175°C (50.6×). The reported mean of 0.362 is lower than the SFC1 mean, but comparison is limited by the shorter temperature range. No measurements are available above 175°C; the cause was not independently diagnosed.

For SFC2 (AR55/SF0.5%), RMSD increases from 0.092 at 75 °C to 2.746 at 250 °C, a 29.8× ratio. Its mean of 1.295 is the largest among the four saw-cut specimen records.

For SFC4 (AR55/SF0.75%), RMSD increased from 0.033 at 75°C to 1.114 at 175°C (33.8×). The reported mean is 0.440 over the available range. No measurements are available above 175°C; the cause was not independently diagnosed.

The comparison of RMSD values between the matched saw-cut and intact states gives the following structural-state differences.

Table 6.67: RMSD comparison between the matched intact and saw-cut states

SFC	AR	SF	Intact Mean	Saw-cut mean	Change (%)	Matched direction
1	65	0.5%	0.572	1.145	+100.2	Large increase
3	65	0.75%	0.603	0.362	-39.9	Decrease (limited range)
2	55	0.5%	0.548	1.295	+136.3	Very large increase
4	55	0.75%	0.568	0.440	-22.5	Decrease (limited range)

In the matched intact–saw-cut comparison, the two 0.50% specimens, whose saw-cut series extend to 250 °C, have RMSD mean changes of +100% to +136%. The two 0.75% specimens have negative matched changes over their shorter series ending at 175 °C. The unequal temperature coverage prevents attributing the reversal solely to fibre dosage or treating RMSD as a universally positive indicator.

The observed RMSD response in the saw-cut state is compared across the four tested configurations.

For the aspect-ratio groups, the mean RMSD is 0.754 for the two AR65 records and 0.868 for the two AR55 records, a 13.1% difference. The mixed temperature coverage and unreplicated groups preclude a fibre-length conclusion.

For the fibre-dosage groups, the mean RMSD is 1.220 for the two 0.50% records and 0.401 for the two 0.75% records. The latter pair ends at 175°C, and the speci-

men means increase in the order SFC3, SFC4, SFC1 and SFC2. This is a coverage-confounded specimen-group pattern, not a dosage effect.

Across the measured saw-cut temperature range, RMSD remains below 0.45 for all specimens over 75–125°C and reaches approximately 0.5–1.5 over 125–175°C. For SFC1 and SFC2, which continue above 175°C, it reaches about 2.0–2.6 by 225°C and exceeds 2.7 at 250°C. These ranges are descriptive and not operational zones.

The saw-cut RMSD sequence differs from the matched intact sequence at the sampled stages; no acceleration mechanism is inferred.

6.11.2 MAPD Index Analysis (Cut Condition)

The temperature progression of MAPD is examined for the four specimens.

The MAPD index quantifies the average relative difference between baseline and elevated-temperature signatures for specimens in the saw-cut state. Figure 6.33 presents the comparison plots for all four specimens. MAPD index comparison for all four SFRC specimens with saw-notch damage showing before compensation, after compensation, and the difference. Note: AR65/SF0.75% and AR55/SF0.75% specimens have data only up to 175°C.

Table 6.68 presents the MAPD values at each temperature from 75°C to 250°C for all four specimens in the saw-cut state.

Table 6.68: MAPD Values (%) at Each Temperature for All Four SFRC Specimens with Saw-Notch

Temperature	**SFC1 (AR65/0.5%)**	**SFC3 (AR65/0.75%)**	**SFC2 (AR55/0.5%)**	**SFC4 (AR55/0.75%)**
75°C	4.45	1.41	8.53	3.01
100°C	11.16	13.33	19.98	13.97
125°C	21.39	26.89	40.33	25.16
150°C	54.71	47.89	79.76	53.05
175°C	102.25	81.08	140.26	107.31
200°C	185.89	—	197.60	—
225°C	244.51	—	230.76	—
250°C	262.40	—	246.16	—

Table 6.69 presents the statistical summary of MAPD values for all four specimens in the saw-cut state.

For SFC1 (AR65/SF0.5%), MAPD increased from 4.45% at 75°C to 262.40% at 250°C (59×). The reported mean is 110.8%; the matched comparison with the intact record is presented separately below.

For SFC3 (AR65/SF0.75%), MAPD increased from 1.41% at 75°C to 81.08% at

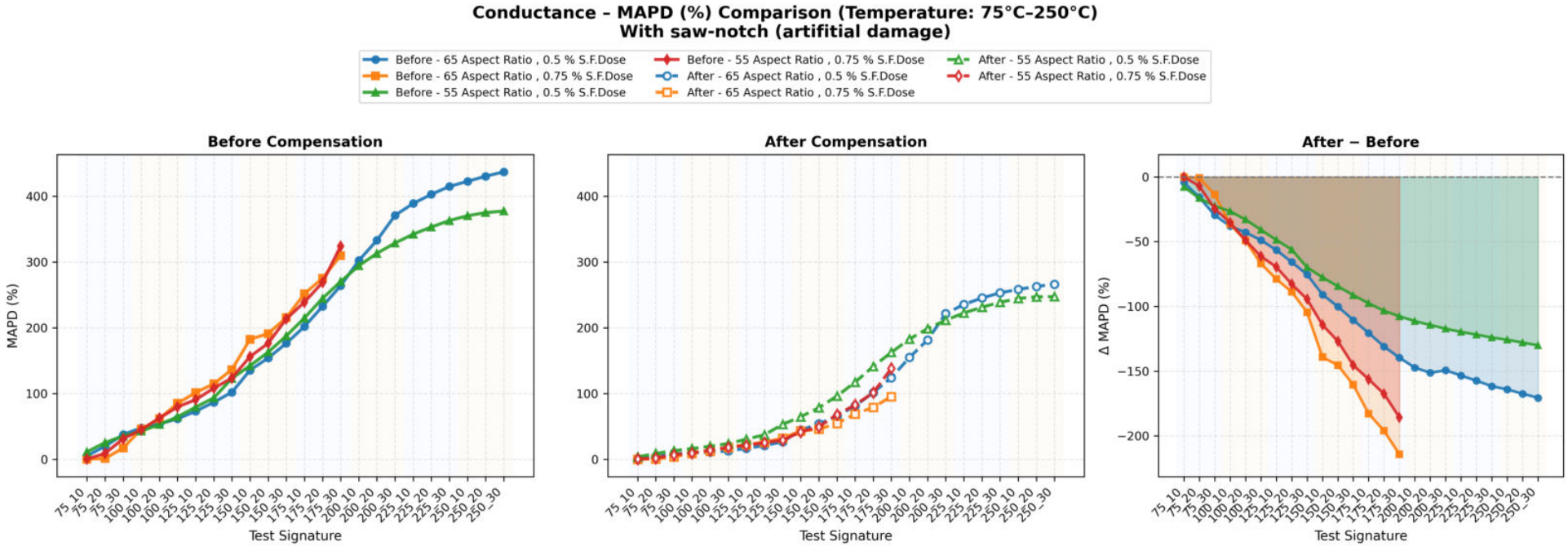

Figure 6.33: MAPD index comparison for all four SFRC specimens with saw-notch damage.

Table 6.69: MAPD Statistical Summary for All Four SFRC Specimens with Saw-Notch

SFC	AR	SF (%)	Temp Range	Mean	Std Dev	Min	Max
1	65	0.5	75–250°C	110.8	100.1	1.0	266.2
3	65	0.75	75–175°C	34.1	28.7	0.1	95.4
2	55	0.5	75–250°C	120.4	90.7	3.6	247.2
4	55	0.75	75–175°C	40.5	39.1	0.3	138.1

175°C (58×). The reported mean of 34.1% is lower than the SFC1 mean, but comparison is limited by the shorter temperature range. No measurements are available above 175°C; the cause was not independently diagnosed.

For SFC2 (AR55/SF0.5%), MAPD increases from 8.53% at 75 °C to 246.16% at 250 °C, a 29× ratio. Its mean of 120.4% is the largest among the four saw-cut specimen records.

For SFC4 (AR55/SF0.75%), MAPD increased from 3.01% at 75°C to 107.31% at 175°C (36×). The reported mean is 40.5% over the available range. No measurements are available above 175°C; the cause was not independently diagnosed.

The comparison of MAPD values between the matched saw-cut and intact states gives the following structural-state differences.

Table 6.70: MAPD comparison between the matched intact and saw-cut states

SFC	AR	SF	Intact Mean	Saw-cut mean	Change (%)	Matched direction
1	65	0.5%	55.2	110.8	+100.7	Large increase
3	65	0.75%	58.1	34.1	-41.3	Decrease (limited range)
2	55	0.5%	52.8	120.4	+128.0	Very large increase
4	55	0.75%	54.7	40.5	-26.0	Decrease (limited range)

In the matched intact–saw-cut comparison, the two 0.50% specimens, whose saw-cut series extend to 250 °C, have MAPD mean changes of +100% to +128%. The two 0.75% specimens have negative matched changes over their shorter series ending at 175 °C. This difference in coverage prevents a general performance conclusion.

The observed MAPD response in the saw-cut state is compared across the four tested configurations.

For the aspect-ratio groups, the mean MAPD is 72.5% for the two AR65 records and 80.5% for the two AR55 records, a 9.9% difference. Mixed coverage and the absence of replicates preclude a fibre-length conclusion.

For the fibre-dosage groups, the mean MAPD is 115.6% for the two 0.50% records and 37.3% for the two 0.75% records. Because the latter pair ends at 175°C and each configuration has one specimen, the difference is not interpreted as a dosage effect.

Across the measured saw-cut temperature range, MAPD remains below 45% for

all specimens over 75–125°C and reaches approximately 47–140% over 125–175°C. For SFC1 and SFC2, it reaches about 186–245% by 225°C and exceeds 246% at 250°C. SFC3 and SFC4 have no saw-cut records above 175°C.

The saw-cut MAPD sequence differs from the matched intact sequence at the sampled stages; no acceleration mechanism is inferred.

6.11.3 AMPD Index Analysis (Cut Condition)

The temperature progression of AMPD is examined for the four specimens.

The AMPD index quantifies peak-based differences between baseline and elevated-temperature signatures for specimens in the saw-cut state. Figure 6.34 presents the comparison plots for all four specimens. AMPD index comparison for all four SFRC specimens with saw-notch damage showing before compensation, after compensation, and the difference. Note: AR65/SF0.75% and AR55/SF0.75% specimens have data only up to 175°C.

Table 6.71 presents the AMPD values at each temperature from 75°C to 250°C for all four specimens in the saw-cut state.

Table 6.71: AMPD Values (%) at Each Temperature for All Four SFRC Specimens with Saw-Notch

Temperature	SFC1 (AR65/0.5%)	SFC3 (AR65/0.75%)	SFC2 (AR55/0.5%)	SFC4 (AR55/0.75%)
75°C	5.05	1.25	6.73	2.50
100°C	6.48	16.33	20.48	16.43
125°C	12.89	30.44	42.38	31.56
150°C	43.60	44.44	91.62	58.94
175°C	119.97	68.29	175.35	129.07
200°C	309.09	—	286.47	—
225°C	490.33	—	405.47	—
250°C	593.11	—	497.54	—

Table 6.72 presents the statistical summary of AMPD values for all four specimens in the saw-cut state.

Table 6.72: AMPD Statistical Summary for All Four SFRC Specimens with Saw-Notch

SFC	AR	SF (%)	Temp Range	Mean (%)	Std Dev	Min (%)	Max (%)	Range
1	65	0.5	75–250°C	197.6	223.4	1.0	616.3	615.3
3	65	0.75	75–175°C	32.1	23.8	0.1	82.7	82.6
2	55	0.5	75–250°C	190.8	176.0	2.0	520.9	518.9
4	55	0.75	75–175°C	47.7	48.0	0.2	177.2	177.0

For SFC1 (AR65/SF0.5%), AMPD increased from 5.05% at 75°C to 593.11% at

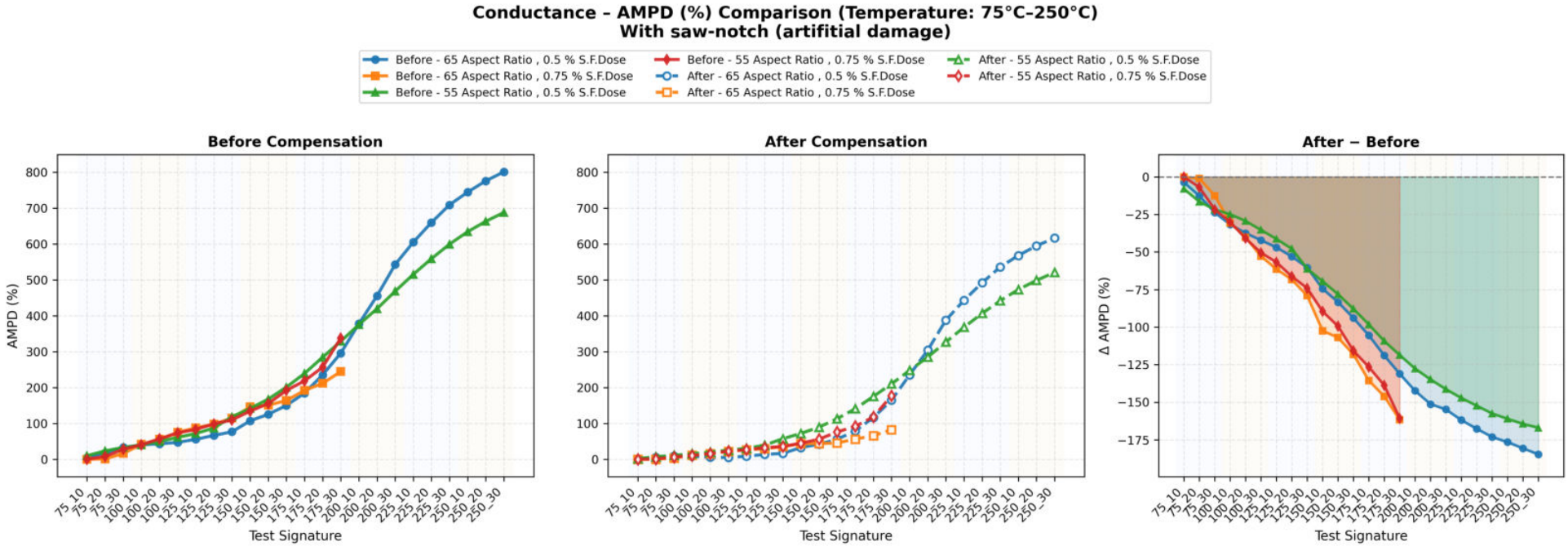

Figure 6.34: AMPD index comparison for all four SFRC specimens with saw-notch damage.

250°C (117×). Its reported mean of 197.6% and range of 615.3% are the largest among the four records.

For SFC3 (AR65/SF0.75%), AMPD increased from 1.25% at 75°C to 68.29% at 175°C (55×). Its reported mean of 32.1% is the smallest, but comparison is limited by the shorter temperature range. No measurements are available above 175°C; the cause was not independently diagnosed.

For SFC2 (AR55/SF0.5%), AMPD increases from 6.73% at 75 °C to 497.54% at 250 °C, a 74× ratio. Its mean of 190.8% is close to that of SFC1; this is a comparison of two specimen records, not a dosage effect.

For SFC4 (AR55/SF0.75%), AMPD increased from 2.50% at 75°C to 129.07% at 175°C (52×). The reported mean is 47.7% over the available range. No measurements are available above 175°C; the cause was not independently diagnosed.

The comparison of AMPD values between the matched saw-cut and intact states gives the following structural-state differences.

Table 6.73: AMPD comparison between the matched intact and saw-cut states

SFC	AR	SF	Intact Mean (%)	Saw-cut mean (%)	Change (%)	Matched direction
1	65	0.5%	98.4	197.6	+100.8	Large increase
3	65	0.75%	105.2	32.1	-69.5	Decrease (limited range)
2	55	0.5%	88.6	190.8	+115.4	Very large increase
4	55	0.75%	91.1	47.7	-47.6	Decrease (limited range)

In the matched intact–saw-cut comparison, the two 0.50% specimens, whose saw-cut series extend to 250 °C, have AMPD mean changes of +100% to +115%. The two 0.75% specimens have negative matched changes over their shorter series ending at 175 °C. The result is therefore reported as configuration- and coverage-dependent.

The observed AMPD response in the saw-cut state is compared across the four tested configurations.

For the aspect-ratio groups, the mean AMPD is 114.9% for the two AR65 records and 119.2% for the two AR55 records, a 3.7% difference. Mixed coverage and the absence of replicates preclude a fibre-length conclusion.

For the fibre-dosage groups, the mean AMPD is 194.2% for the two 0.50% records and 39.9% for the two 0.75% records. The latter pair ends at 175°C; the difference is therefore coverage-confounded and not a dosage conclusion.

Across the measured saw-cut temperature range, AMPD remains below 45% for all specimens over 75–125°C and reaches approximately 44–175% over 125–175°C. For SFC1 and SFC2, it reaches about 286–490% by 225°C and exceeds 497% at 250°C. The higher-temperature comparison is unavailable for SFC3 and SFC4.

The saw-cut AMPD values exceed the corresponding intact values at selected sampled stages, with the magnitude and direction depending on the specimen and signal channel.

6.11.4 Correlation Coefficient (CC) Index Analysis (Cut Condition)

The temperature progression of CC is examined for the four specimens.

The Correlation Coefficient (CC) index measures the linear relationship between baseline and temperature-affected signatures, ranging from -1 to +1. A value of 1 indicates perfect correlation (identical signatures), while negative values indicate inverse correlation. Unlike other indices that increase with temperature, CC typically decreases from near 1.0 toward negative values. Figure 6.35 presents the CC comparison plots for all four specimens in the saw-cut state. Correlation Coefficient comparison for all four SFRC specimens with saw-notch damage showing before compensation, after compensation, and the difference. CC decreases from near 1.0 to negative values with increasing temperature. Note: AR65/SF0.75% and AR55/SF0.75% specimens have data only up to 175°C.

Table 6.74 presents the CC values at each temperature from 75°C to 250°C for all four specimens in the saw-cut state.

Table 6.74: Correlation Coefficient at Each Temperature for All Four SFRC Specimens with Saw-Notch

Temperature	**SFC1 (AR65/0.5%)**	**SFC3 (AR65/0.75%)**	**SFC2 (AR55/0.5%)**	**SFC4 (AR55/0.75%)**
75°C	0.988	0.998	0.941	0.991
100°C	0.916	0.960	0.806	0.910
125°C	0.682	0.878	0.422	0.745
150°C	-0.458	0.584	-0.168	0.105
175°C	-0.853	-0.258	-0.407	-0.611
200°C	-0.831	—	-0.417	—
225°C	-0.736	—	-0.357	—
250°C	-0.669	—	-0.297	—

Table 6.75 presents the statistical summary of CC values for all four specimens in the saw-cut state.

For SFC1 (AR65/SF0.5%), CC decreases from 0.988 at 75 °C to -0.669 at 250 °C and changes sign between 125 °C (0.682) and 150 °C (-0.458). The minimum, -0.853, occurs at 175 °C, and the series mean is -0.120. The earlier sign change relative to the intact record is a matched observation, not evidence of a deterioration rate or mechanism.

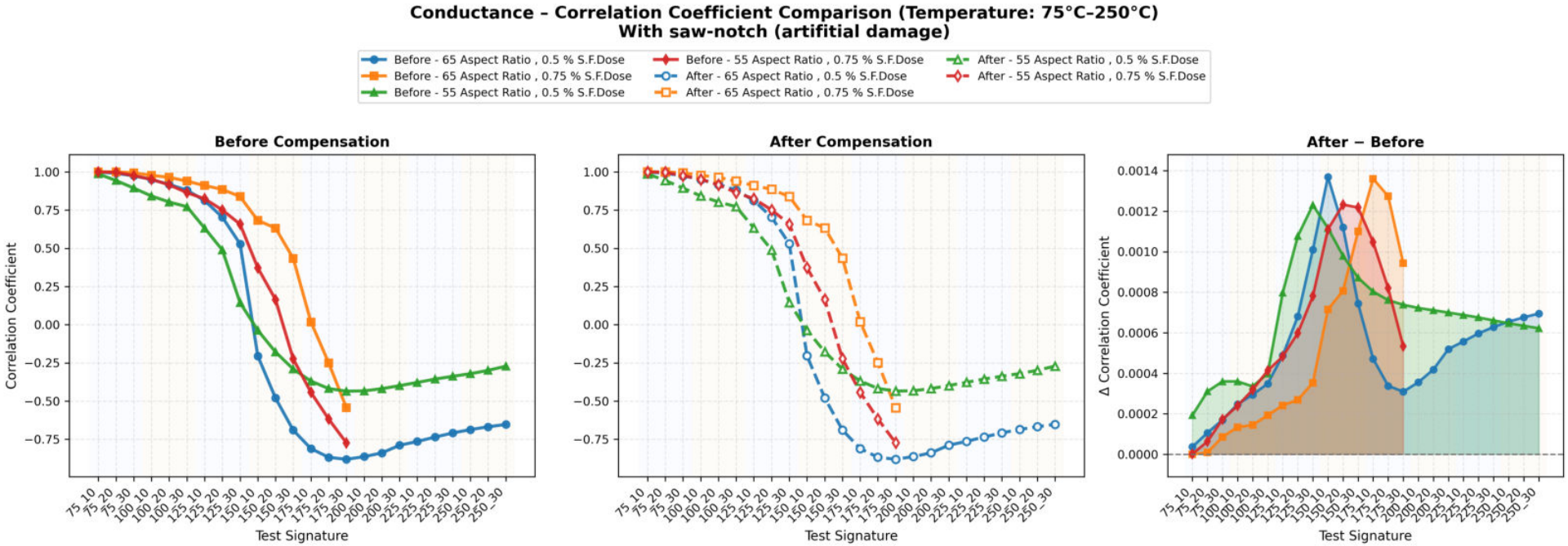

Figure 6.35: Correlation Coefficient comparison for all four SFRC specimens with saw-notch damage.

Table 6.75: Correlation Coefficient Statistical Summary for All Four SFRC Specimens with Saw-Notch

SFC	AR	SF (%)	Temp Range	Mean	Std Dev	Min	Max	Range
1	65	0.5	75–250°C	-0.120	0.778	-0.881	0.999	1.880
3	65	0.75	75–175°C	0.633	0.482	-0.543	1.000	1.543
2	55	0.5	75–250°C	0.066	0.538	-0.435	0.987	1.422
4	55	0.75	75–175°C	0.428	0.620	-0.773	1.000	1.773

For SFC3 (AR65/SF0.75%), CC decreased from 0.998 at 75°C to -0.258 at 175°C. Unlike SFC1, the sign reversal occurred later, between 150°C (0.584) and 175°C (-0.258). The mean CC of 0.633 is the largest reported value, but comparison is limited by the shorter temperature range. No measurements are available above 175°C; the cause was not independently diagnosed.

For SFC2 (AR55/SF0.5%), CC decreased from 0.941 at 75°C to -0.297 at 250°C. The transition to negative values occurred between 125°C (0.422) and 150°C (-0.168). Its minimum of -0.435 is less negative than the SFC1 minimum; this is a specimen-level comparison rather than evidence of better material or monitoring performance.

For SFC4 (AR55/SF0.75%), CC decreased from 0.991 at 75°C to -0.611 at 175°C. The transition to negative values occurred between 150°C (0.105) and 175°C (-0.611). The reported mean CC is 0.428 over the available range. No measurements are available above 175°C; the cause was not independently diagnosed.

The comparison of CC values between the matched saw-cut and intact states gives matched intact–saw-cut differences.

Table 6.76: Correlation Coefficient Comparison between the matched intact and saw-cut states

SFC	AR	SF	Intact Mean	Saw-cut mean	Change	Matched direction
1	65	0.5%	0.093	-0.120	-0.213	Sign reversal
3	65	0.75%	0.073	0.633	+0.560	Increase (limited range)
2	55	0.5%	0.438	0.066	-0.372	Large decrease
4	55	0.75%	0.080	0.428	+0.348	Increase (limited range)

In the matched intact–saw-cut comparison, the two 0.50% specimens show lower mean CC and earlier sign reversal in the saw-cut records. The two 0.75% saw-cut series end at 175 °C, so their comparison does not establish improved performance or an accelerated correlation-breakdown mechanism.

The observed CC response in the saw-cut state is compared across the four tested configurations.

For the aspect-ratio groups, the mean CC is 0.256 for the two AR65 records and

0.247 for the two AR55 records, a 3.9% difference. The unreplicated, mixed-coverage comparison does not establish an aspect-ratio effect.

For the fibre-dosage groups, the mean CC is 0.530 for the two 0.75% specimens and -0.027 for the two 0.5% specimens. The reported specimen order is SFC3 (0.633), SFC4 (0.428), SFC2 (0.066) and SFC1 (-0.120). The 0.75% saw-cut series ends at 175°C, so neither the unequal ranges nor the unreplicated groups establish a dosage effect.

The observed sign-transition intervals show that CC changes sign between 125 and 150°C for SFC1 and SFC2 and between 150 and 175°C for SFC3 and SFC4. The corresponding intact transitions occur one measured stage later in selected records. This stage comparison shows earlier decorrelation after the saw-cut but does not define a continuous threshold temperature or quantify material degradation.

In the observed saw-cut progression, CC is greater than 0.4 for all four specimens over 75–125°C. It decreases over 125–150°C, with sign changes beginning in the SFC1 and SFC2 records, and is negative for all four specimens by 175°C. Only SFC1 and SFC2 continue to 250°C, where the reported values lie between approximately -0.3 and -0.85. These stages are descriptive rather than operational zones.

6.11.5 CCD Index Analysis (Cut Condition)

The temperature progression of CCD is examined for the four specimens.

The Correlation Coefficient Deviation (CCD) index quantifies the deviation from perfect correlation, derived from the correlation coefficient. Higher CCD values indicate greater deviation from baseline signatures. Figure 6.36 presents the CCD comparison plots for all four specimens in the saw-cut state. CCD index comparison for all four SFRC specimens with saw-notch damage showing before compensation, after compensation, and the difference. Note: AR65/SF0.75% and AR55/SF0.75% specimens have data only up to 175°C.

Table 6.77 presents the CCD values at each temperature from 75°C to 250°C for all four specimens in the saw-cut state.

Table 6.78 presents the statistical summary of CCD values for all four specimens in the saw-cut state.

For SFC1 (AR65/SF0.5%), CCD increased from 0.000 at 75°C to a peak of 6.371 at 175°C and then decreased to 4.647 at 250°C. The mean CCD of 3.21 is the largest value among the four reported records.

For SFC3 (AR65/SF0.75%), CCD increased from 0.000 at 75°C to 2.189 at 175°C. Its reported mean of 0.46 is the smallest, but comparison is limited by the shorter

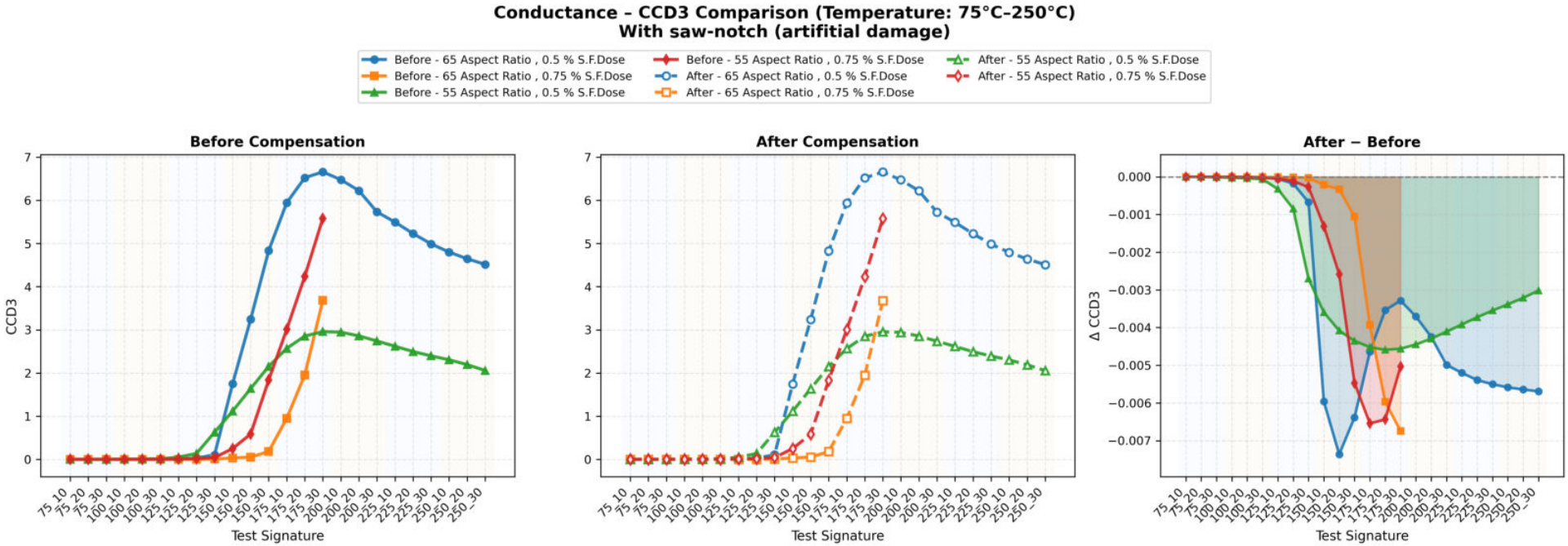

Figure 6.36: CCD index comparison for all four SFRC specimens with saw-notch damage.

Table 6.77: CCD Values at Each Temperature for All Four SFRC Specimens with Saw-Notch

Temperature	SFC1 (AR65/0.5%)	SFC3 (AR65/0.75%)	SFC2 (AR55/0.5%)	SFC4 (AR55/0.75%)
75°C	0.000	0.000	0.000	0.000
100°C	0.001	0.000	0.008	0.001
125°C	0.046	0.002	0.269	0.020
150°C	3.270	0.087	1.631	0.886
175°C	6.371	2.189	2.789	4.269
200°C	6.139	—	2.844	—
225°C	5.233	—	2.499	—
250°C	4.647	—	2.182	—

Table 6.78: CCD Statistical Summary for All Four SFRC Specimens with Saw-Notch

SFC	AR	SF (%)	Temp Range	Mean	Std Dev	Min	Max	Range
1	65	0.5	75–250°C	3.21	2.67	0.00	6.66	6.66
3	65	0.75	75–175°C	0.46	1.00	0.00	3.67	3.67
2	55	0.5	75–250°C	1.53	1.18	0.00	2.95	2.95
4	55	0.75	75–175°C	1.04	1.74	0.00	5.58	5.58

temperature range. No measurements are available above 175°C; the cause was not independently diagnosed.

For SFC2 (AR55/SF0.5%), CCD increased from 0.000 at 75°C to a peak of 2.844 at 200°C and then decreased slightly. Its reported mean of 1.53 is lower than the SFC1 mean; with one specimen per configuration, this difference does not establish better thermal stability or an SF-dosage effect.

For SFC4 (AR55/SF0.75%), CCD increased from 0.000 at 75°C to 4.269 at 175°C. Its reported mean is 1.04 over the available range. No measurements are available above 175°C; the cause was not independently diagnosed.

The comparison of CCD values between the matched saw-cut and intact states gives matched intact–saw-cut differences.

Table 6.79: CCD Comparison between the matched intact and saw-cut states

SFC	AR	SF	Intact Mean	Saw-cut mean	Change (%)	Matched direction
1	65	0.5%	2.118	3.21	+51.6	Increase
3	65	0.75%	2.064	0.46	-77.7	Decrease (limited range)
2	55	0.5%	0.459	1.53	+233.3	Very large increase
4	55	0.75%	2.121	1.04	-51.0	Decrease (limited range)

In the matched comparison, the two 0.50% records have positive CCD changes of approximately +51.6% and +233.3%. The two 0.75% records have negative mean changes over their common measured range through 175°C. Their shorter coverage

does not by itself explain the direction, and no configuration ranking is inferred.

The observed CCD response in the saw-cut state is compared across the four tested configurations.

For the aspect-ratio groups, the mean CCD is 1.83 for the two AR65 records and 1.28 for the two AR55 records, a 43.1% difference. Mixed coverage and the absence of replicated configurations preclude a fibre-length conclusion.

For the fibre-dosage groups, the mean CCD is 2.37 for the two 0.5% specimens and 0.75 for the two 0.75% specimens. The reported specimen order is SFC3 (0.46), SFC4 (1.04), SFC2 (1.53) and SFC1 (3.21). The unequal temperature coverage and absence of replicated configurations preclude a dosage-performance ranking.

The measured CCD progression can be described over four temperature intervals without treating them as universal zones or decision thresholds. Values remain below 0.3 for all four records from 75 to 125°C, increase over the available records from 125 to 175°C, and reach specimen-specific maxima between 175 and 200°C. Only the two 0.5% SF records continue to 250°C, over which their values decrease from the reported maxima. These intervals describe the present records and do not define operational temperature boundaries.

Compared with the intact records, the reported saw-cut maxima occur at 175–200°C, whereas selected intact maxima occur at 225°C. SFC2 has a +233% matched mean change. These are dataset-specific temporal and magnitude differences, not evidence of lost material performance.

6.11.6 CCD^3 Index Analysis (Cut Condition)

The temperature progression of CCD^3 is examined for the four specimens.

The CCD^3 index is the algebraic cube of the Correlation Coefficient Deviation. It compresses CCD values below unity and magnifies values above unity, thereby changing numerical contrast without supplying an independent measurement or a validated increase in detection capability. Figure 6.37 presents the CCD^3 comparison plots for all four specimens in the saw-cut state. The three panels report the CCD^3 values before compensation, after compensation and their difference for all four saw-cut records. The two 0.75% SF records extend only to 175°C. Cubing changes the numerical contrast but does not add an independent measurement.

Table 6.80 presents the CCD^3 values at each temperature from 75°C to 250°C for all four specimens in the saw-cut state.

The numerical CCD^3 results are then compared across the four specimens.

Table 6.81 presents the statistical summary of CCD^3 values for all four specimens

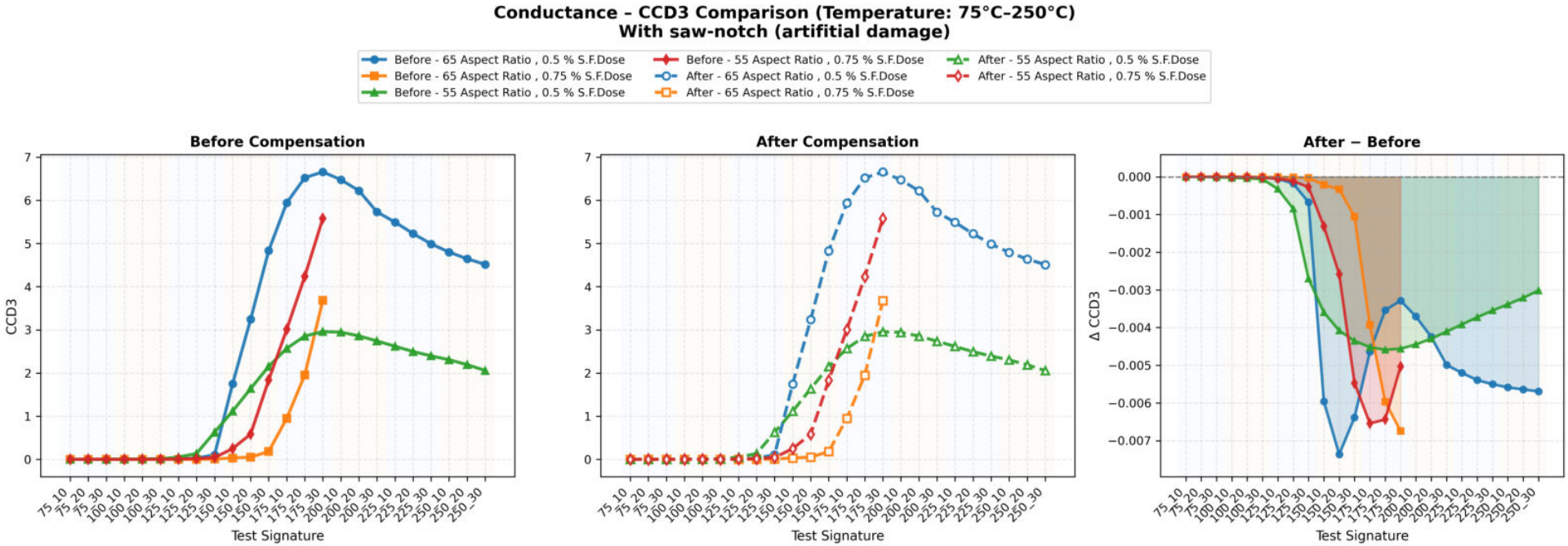

Figure 6.37: CCD^3 index comparison for all four SFRC specimens with saw-notch damage.

Table 6.80: CCD^3 Values at Each Temperature for All Four SFRC Specimens with Saw-Notch

Temperature	SFC1 (AR65/0.5%)	SFC3 (AR65/0.75%)	SFC2 (AR55/0.5%)	SFC4 (AR55/0.75%)
75°C	0.000	0.000	0.000	0.000
100°C	0.001	0.000	0.008	0.001
125°C	0.046	0.002	0.269	0.020
150°C	3.270	0.087	1.631	0.886
175°C	6.371	2.189	2.789	4.269
200°C	6.139	—	2.844	—
225°C	5.233	—	2.499	—
250°C	4.647	—	2.182	—

in the saw-cut state.

Table 6.81: CCD^3 Statistical Summary for All Four SFRC Specimens with Saw-Notch

SFC	AR	SF (%)	Temp Range	Mean	Std Dev	Min	Max	Range
1	65	0.5	75–250°C	3.21	2.67	0.00	6.66	6.66
3	65	0.75	75–175°C	0.46	1.00	0.00	3.67	3.67
2	55	0.5	75–250°C	1.53	1.18	0.00	2.95	2.95
4	55	0.75	75–175°C	1.04	1.74	0.00	5.58	5.58

For SFC1 (AR65/SF0.5%), the reported CCD^3 series increased from 0.000 at 75°C to a peak at 175°C and then decreased to its 250°C value. Because CCD^3 is an algebraic transformation of CCD, it retains the same ordering and peak stage rather than providing an independent indicator. Its reported mean is the largest among the four records.

For SFC3 (AR65/SF0.75%), the reported CCD^3 series increased from 0.000 at 75°C to its 175°C value. Its reported mean is the smallest, but comparison is limited by the shorter temperature range. No measurements are available above 175°C; the cause was not independently diagnosed.

For SFC2 (AR55/SF0.5%), over the full temperature range, CCD^3 increases from 0.000 at 75°C to 2.844 at 200°C and then decreases slightly. The reported saw-cut maximum is 2.95, compared with an intact maximum of 1.09, corresponding to a ratio of approximately 2.7. This is a within-specimen comparison of the transformed correlation measure.

For SFC4 (AR55/SF0.75%), the reported CCD^3 series increased from 0.000 at 75°C to its 175°C value. The reported mean is 1.04 over the available range. No measurements are available above 175°C; the cause was not independently diagnosed.

The CCD^3 records are then compared between the matched intact and saw-cut states.

The comparison of CCD^3 values between the matched saw-cut and intact states gives matched intact–saw-cut differences.

Table 6.82: CCD^3 Comparison between the matched intact and saw-cut states

SFC	AR	SF	Intact Mean	Saw-cut mean	Change (%)	Matched direction
1	65	0.5%	2.118	3.21	+51.6	Increase
3	65	0.75%	2.064	0.46	-77.7	Decrease (limited range)
2	55	0.5%	0.459	1.53	+233.3	Very large increase
4	55	0.75%	2.121	1.04	-51.0	Decrease (limited range)

In the matched comparison, SFC2 has lower intact CCD^3 values than the other records and a reported +233% intact–saw-cut mean change. This change describes the fitted correlation transformation for one specimen and is not interpreted as loss of a material stability advantage.

The observed CCD^3 response in the saw-cut state is compared across the four tested configurations.

For the aspect-ratio groups, the mean reported CCD^3 summary is 1.83 for the two AR65 records and 1.28 for the two AR55 records. The quantity is algebraically dependent on CCD, and the mixed-coverage group comparison does not establish a fibre-length effect.

For the fibre-dosage groups, the mean CCD^3 is 2.37 for the two 0.5% specimens and 0.75 for the two 0.75% specimens. The reported specimen order is SFC3 (0.46), SFC4 (1.04), SFC2 (1.53) and SFC1 (3.21). The unequal temperature ranges and four-specimen design do not establish a dosage effect.

The relationship between CCD^3 and CCD follows directly from the cubic transformation. Cubing CCD amplifies larger numerical deviations and compresses values below one, but it does not supply independent evidence because both quantities derive from the same correlation coefficient. Selected saw-cut maxima occur at 175°C and selected intact maxima at 225°C. The transformed values are therefore retained as an alternative scale, not as an independently validated damage indicator.

The temperature progression of CCD^3 follows the same stage ordering as CCD because it is derived algebraically from that index. Values are small over 75–125°C, increase over the available records through 175°C, and reach specimen-specific maxima between 175 and 200°C. Only the two 0.5% SF records continue to 250°C. These are descriptive intervals in the recorded series, not independent zones or thresholds.

6.11.7 CCV Index Analysis (Cut Condition)

The temperature progression of CCV is examined for the four specimens.

The Cross-Correlation Value (CCV) index quantifies the similarity between baseline and temperature-affected signatures using cross-correlation analysis. Unlike CCD, CCV exhibits a non-monotonic temperature response with a characteristic minimum at intermediate temperatures. Figure 6.38 presents the CCV comparison plots for all four specimens in the saw-cut state. CCV index comparison for all four SFRC specimens with saw-notch damage showing before compensation, after compensation, and the difference. Note the characteristic V-shaped pattern. Note: AR65/SF0.75% and AR55/SF0.75% specimens have data only up to 175°C.

Table 6.83 presents the CCV values at each temperature from 75°C to 250°C for all four specimens in the saw-cut state.

Table 6.83: CCV Values at Each Temperature for All Four SFRC Specimens with Saw-Notch

Temperature	SFC1 (AR65/0.5%)	SFC3 (AR65/0.75%)	SFC2 (AR55/0.5%)	SFC4 (AR55/0.75%)
75°C	235.2	497.4	150.0	543.5
100°C	232.4	523.7	126.6	533.5
125°C	173.3	471.1	79.5	464.7
150°C	135.5	309.8	61.3	249.7
175°C	247.4	174.3	118.6	445.0
200°C	276.5	—	129.5	—
225°C	265.0	—	124.7	—
250°C	258.9	—	116.3	—

Table 6.84 presents the statistical summary of CCV values for all four specimens in the saw-cut state.

Table 6.84: CCV Statistical Summary for All Four SFRC Specimens with Saw-Notch

SFC	AR	SF (%)	Temp Range	Mean	Std Dev	Min	Max	Range
1	65	0.5	75–250°C	228.0	49.2	86.8	283.2	196.4
3	65	0.75	75–175°C	395.3	142.1	50.0	529.2	479.2
2	55	0.5	75–250°C	113.3	29.6	27.6	153.3	125.7
4	55	0.75	75–175°C	447.3	114.3	204.2	554.3	350.1

For SFC1 (AR65/SF0.5%), over the full temperature range, CCV decreases from 235.2 at 75°C to 135.5 at 150°C and then increases to 276.5 at 200°C. Its saw-cut mean of 228.0 exceeds the intact mean of 113.4; this is a matched record difference rather than a validated causal attribution.

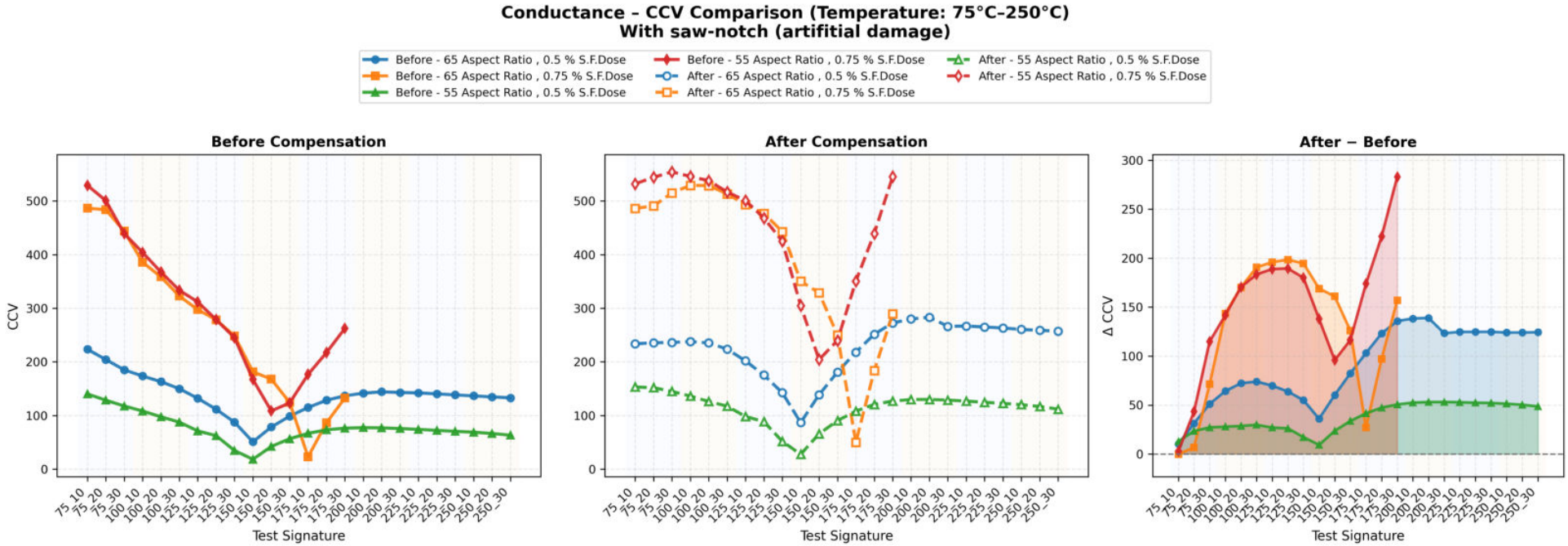

Figure 6.38: CCV index comparison for all four SFRC specimens with saw-notch damage.

For SFC3 (AR65/SF0.75%), CCV decreased from 497.4 at 75°C to a minimum of 174.3 at 175°C (65% decrease). The initial value is nearly five times the corresponding intact value; this is a matched record-level difference and is not assigned to a specific material mechanism. No measurements are available above 175°C; the cause was not independently diagnosed.

For SFC2 (AR55/SF0.5%), over the full temperature range, CCV decreases from 150.0 at 75°C to 61.3 at 150°C and then increases to 129.5 at 200°C. Its saw-cut mean of 113.3 exceeds the intact mean of 47.3; no material-performance ranking follows from this difference.

For SFC4 (AR55/SF0.75%), CCV ranged from 543.5 at 75°C to a minimum of 249.7 at 150°C and then increased to 445.0 at 175°C. These are the largest reported CCV values among the four records. No measurements are available above 175°C; the cause was not independently diagnosed.

The comparison of CCV values between the matched saw-cut and intact states gives matched intact–saw-cut differences.

Table 6.85: CCV Comparison between the matched intact and saw-cut states

SFC	AR	SF	Intact Mean	Saw-cut mean	Change (%)	Matched direction
1	65	0.5%	113.4	228.0	+101.1	Doubled
3	65	0.75%	84.1	395.3	+370.0	Very large increase
2	55	0.5%	47.3	113.3	+139.5	Large increase
4	55	0.75%	122.5	447.3	+265.1	Very large increase

CCV has positive matched changes of +101% to +370% in the four specimens. The two 0.75% specimens have changes of +265% and +370%; with one specimen per configuration, this does not establish a fibre-content effect.

The observed CCV response in the saw-cut state is compared across the four tested configurations.

For the aspect-ratio groups, the mean CCV is 311.6 for the two AR65 records and 280.3 for the two AR55 records, an 11.2% difference. Mixed coverage and the absence of replicates preclude a fibre-length conclusion.

For the fibre-dosage groups, the mean CCV is 421.3 for the two 0.75% records and 170.7 for the two 0.50% records. The 0.75% series end at 175°C, and each configuration has one specimen. The difference is therefore not interpreted as a dosage effect.

Comparison of the sampled patterns shows that the saw-cut CCV minima occur near 150°C, compared with approximately 175°C in the intact records. The reported saw-cut values are approximately two to five times the corresponding intact values in selected comparisons, followed by later-stage increases. These observations describe

the sampled sequences and are not treated as a general recovery classification.

Across the observed temperature progression, CCV remains above 125 for the four saw-cut records over 75–125°C and reaches specimen-dependent minima between 125 and 150°C. The SFC1 and SFC2 values then increase over 150–200°C and are the only records available through 250°C. The stage groups are descriptive and do not define stability zones.

6.11.8 MSE Index Analysis (Cut Condition)

The temperature progression of MSE is examined for the four specimens.

The MSE index quantifies the squared difference between baseline and temperature-affected signatures. The reported values are of the order of 10^{-5}; their small numerical scale is a consequence of the signal scale and is not itself evidence of sensitivity. Figure 6.39 presents the comparison plots for all four specimens in the saw-cut state. MSE index comparison for all four SFRC specimens with saw-notch damage showing before compensation, after compensation, and the difference. Note the very small scale (order of 10^{-5}). Note: AR65/SF0.75% and AR55/SF0.75% specimens have data only up to 175°C.

Table 6.86 presents the MSE values at each temperature from 75°C to 250°C for all four specimens in the saw-cut state. Note that values are in the order of 10^{-5} to 10^{-6}.

Table 6.86: MSE Values ($\times 10^{-5}$) at Each Temperature for All Four SFRC Specimens with Saw-Notch

Temperature	SFC1 (AR65/0.5%)	SFC3 (AR65/0.75%)	SFC2 (AR55/0.5%)	SFC4 (AR55/0.75%)
75°C	<0.01	<0.01	<0.01	<0.01
100°C	<0.01	<0.01	<0.01	<0.01
125°C	<0.01	<0.01	0.1-0.2	<0.01
150°C	0.2-0.4	0.1-0.2	0.3-0.5	0.2-0.3
175°C	0.5-0.8	0.3-0.5	0.8-1.2	0.5-0.8
200°C	1.0-1.5	—	1.5-2.0	—
225°C	1.5-2.0	—	2.0-2.3	—
250°C	1.8-2.2	—	2.2-2.5	—

Table 6.87 presents the statistical summary of MSE values for all four specimens in the saw-cut state.

For SFC1 (AR65/SF0.5%), MSE increased from near zero at 75°C to approximately 2.2×10^{-5} at 250°C before compensation. After compensation, the maximum MSE was approximately 0.8×10^{-5}, a reported reduction of 64%.

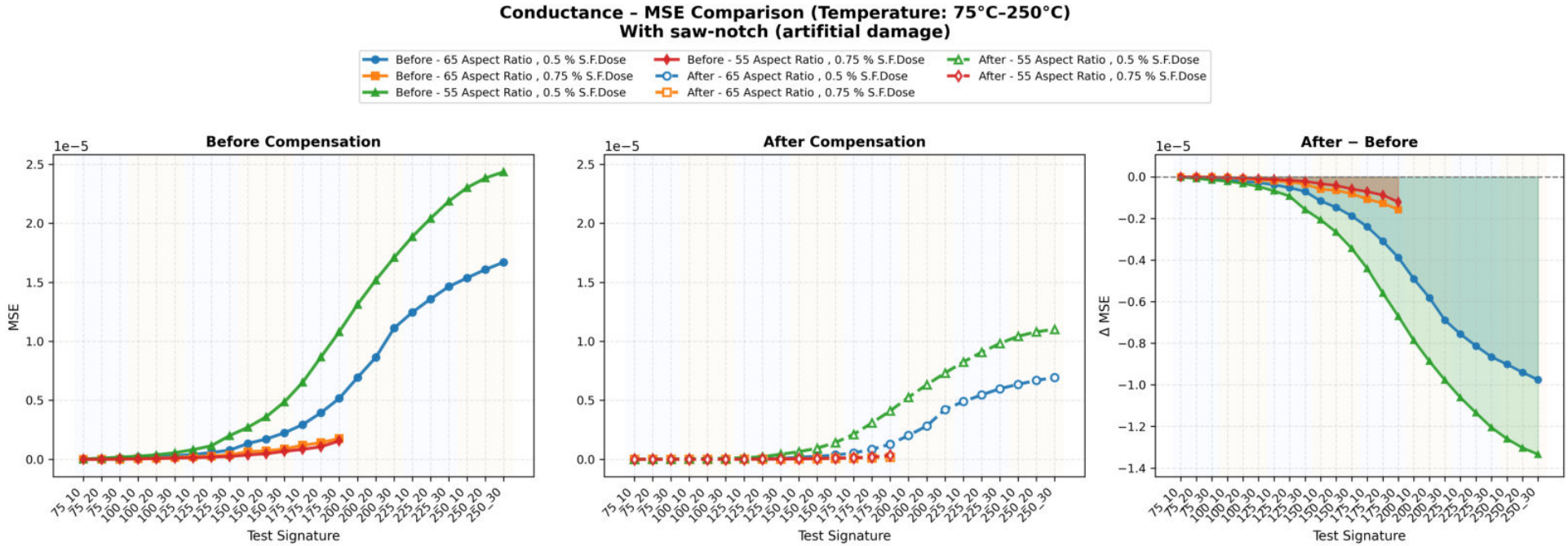

Figure 6.39: MSE index comparison for all four SFRC specimens with saw-notch damage.

Table 6.87: MSE Statistical Summary for All Four SFRC Specimens with Saw-Notch

SFC	AR	SF (%)	Temp Range	Max (Before)	Max (After)	Scale
1	65	0.5	75–250°C	2.2×10^{-5}	0.8×10^{-5}	Very small
3	65	0.75	75–175°C	0.5×10^{-5}	0.2×10^{-5}	Very small
2	55	0.5	75–250°C	2.5×10^{-5}	1.2×10^{-5}	Very small
4	55	0.75	75–175°C	0.8×10^{-5}	0.4×10^{-5}	Very small

For SFC3 (AR65/SF0.75%), MSE reached 0.5×10^{-5} at 175°C before compensation, the smallest reported maximum among the four records. No measurements are available above 175°C; the cause was not independently diagnosed.

SFC2 (AR55/SF0.5%) has the largest reported MSE, reaching 2.5×10^{-5} at 250°C before compensation and 1.2×10^{-5} after compensation. The residual is larger than in the other three records but does not establish configuration-level performance.

For SFC4 (AR55/SF0.75%), MSE reached 0.8×10^{-5} at 175°C before compensation. No measurements are available above 175°C; the cause was not independently diagnosed.

The comparison of MSE values between the matched saw-cut and intact states gives matched intact–saw-cut differences.

Table 6.88: MSE Comparison between the matched intact and saw-cut states

SFC	AR	SF	Intact Max	Cut Max	Change
1	65	0.5%	1.8×10^{-5}	2.2×10^{-5}	+22%
3	65	0.75%	1.8×10^{-5}	0.5×10^{-5}	-72% (limited range)
2	55	0.5%	1.8×10^{-5}	2.5×10^{-5}	+39%
4	55	0.75%	1.8×10^{-5}	0.8×10^{-5}	-56% (limited range)

In the matched intact–saw-cut comparison, the two 0.50% specimens have MSE increases of 22–39% in the saw-cut state. The two 0.75% series end at 175 °C, so their negative changes are reported without attributing them solely to fibre dosage or structural state.

The observed MSE response in the saw-cut state is compared across the four tested configurations.

For the aspect-ratio groups, the mean MSE of the two AR65 records is 46.1% lower than that of the two AR55 records. The values are of the order of 10^{-6}, and the unreplicated comparison does not establish a fibre-length effect.

For the fibre-dosage groups, the mean MSE is higher in the two 0.50% records than in the two 0.75% records. Because the latter pair has shorter coverage and each configuration is unreplicated, this is not evidence of a dosage effect.

In the saw-cut state, the maximum reported MSE is 2.5×10^{-5}, compared with

1.8×10^{-5} for the intact records. SFC2 has the largest value, while the two AR65 records are lower. Negative after-minus-before differences show reduced MSE for those records; matched intact–saw-cut differences are interpreted separately and are not converted into a universal damage indicator.

Across the observed temperature progression, MSE remains below 2×10^{-7} for the AR65 specimens over 75–125 °C and reaches 0.5–1.2×10^{-5} over 125–175 °C. Only the two 0.50% specimens continue above 175 °C, reaching 1.5–2.3×10^{-5} by 225 °C and 2.2–2.5×10^{-5} at 250 °C. These sampled ranges do not define operational zones.

6.11.9 Variance Index Analysis (Cut Condition)

The temperature progression of Variance is examined for the four specimens.

The Variance index quantifies the spread of signature differences around the mean. Like MSE, variance values are extremely small (order of 10^{-10}), requiring high-precision measurement. Notably, variance can transition from positive to negative values at elevated temperatures. Figure 6.40 presents the variance comparison plots for all four specimens in the saw-cut state. Variance index comparison for all four SFRC specimens with saw-notch damage showing before compensation, after compensation, and the difference. Note the very small scale (order of 10^{-10}) and sign transitions. Note: AR65/SF0.75% and AR55/SF0.75% specimens have data only up to 175°C.

Table 6.89 presents the variance values at each temperature from 75°C to 250°C for all four specimens in the saw-cut state.

Table 6.89: Variance Values ($\times 10^{-10}$) at Each Temperature for All Four SFRC Specimens with Saw-Notch

Temperature	**SFC1 (AR65/0.5%)**	**SFC3 (AR65/0.75%)**	**SFC2 (AR55/0.5%)**	**SFC4 (AR55/0.75%)**
75°C	+1.0-2.0	+2.0-3.0	+0.5-1.5	+2.5-3.5
100°C	+0.5-1.5	+1.5-2.5	+0.3-1.0	+2.0-3.0
125°C	0 to +0.8	+0.8-1.5	0 to +0.5	+1.0-2.0
150°C	-0.5 to +0.2	0 to +0.5	-0.3 to +0.2	0 to +1.0
175°C	-1.5 to -0.5	-0.8 to 0	-0.8 to -0.2	-1.0 to 0
200°C	-2.5 to -1.5	—	-1.2 to -0.5	—
225°C	-3.5 to -2.5	—	-1.5 to -0.8	—
250°C	-4.5 to -3.5	—	-1.8 to -1.0	—

Table 6.90 presents the statistical summary of variance values for all four specimens in the saw-cut state.

For SFC1 (AR65/SF0.5%), variance changes from approximately $+2 \times 10^{-10}$

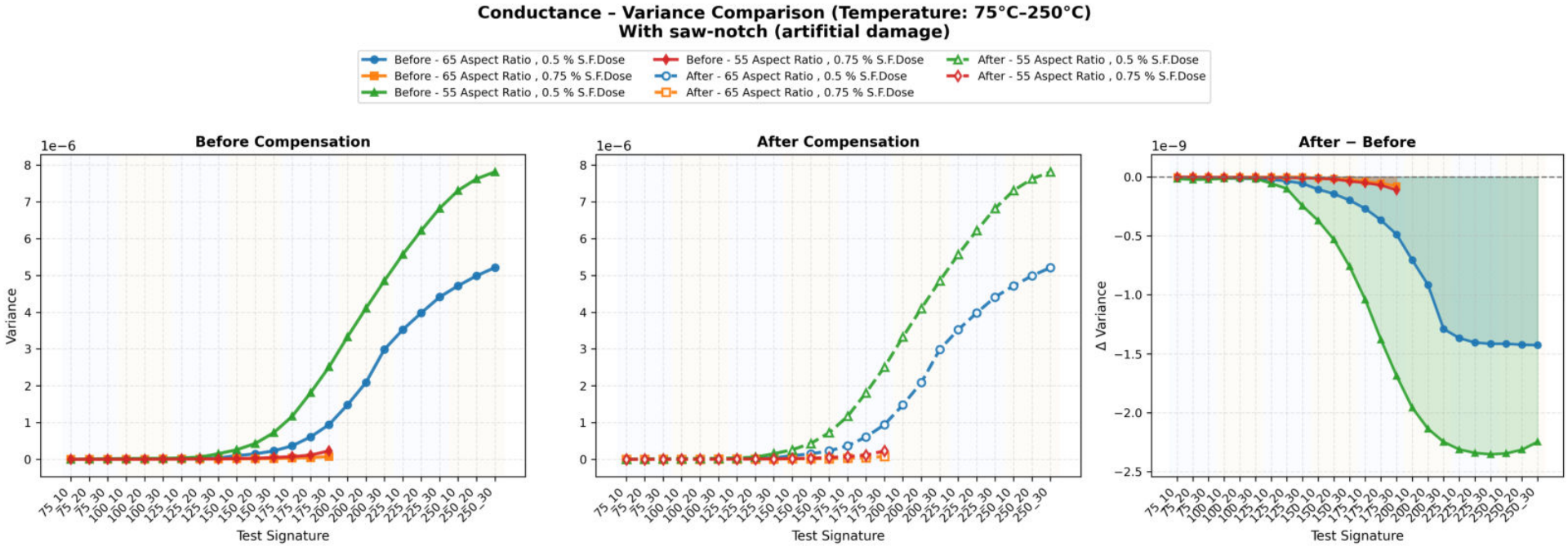

Figure 6.40: Variance index comparison for all four SFRC specimens with saw-notch damage.

Table 6.90: Variance Statistical Summary for All Four SFRC Specimens with Saw-Notch

SFC	AR	SF (%)	Temp Range	Min	Max	Sign Change
1	65	0.5	75–250°C	-4.5×10^{-10}	$+2.0 \times 10^{-10}$	At 150°C
3	65	0.75	75–175°C	-0.8×10^{-10}	$+3.0 \times 10^{-10}$	At 175°C
2	55	0.5	75–250°C	-1.8×10^{-10}	$+1.5 \times 10^{-10}$	At 150°C
4	55	0.75	75–175°C	-1.0×10^{-10}	$+3.5 \times 10^{-10}$	At 175°C

at 75 °C to -4.5×10^{-10} at 250 °C. The sign change occurs at 150 °C in the saw-cut sequence and 175 °C in the intact sequence; the observations do not establish an acceleration mechanism.

For SFC3 (AR65/SF0.75%), variance was positive at the lower measured temperatures and became negative at 175°C. Its initial values are higher than those of the two 0.5% SF records, but one specimen per configuration does not establish a fibre-content effect. No measurements are available above 175°C; the cause was not independently diagnosed.

For SFC2 (AR55/SF0.5%), variance changed sign at 150°C, as in the SFC1 record. The intact SFC2 series returns to a positive value at 250°C, whereas the saw-cut series remains negative; this is a matched difference in the recorded index, not evidence of a material recovery capability.

For SFC4 (AR55/SF0.75%), variance began at the largest reported positive value ($+3.5 \times 10^{-10}$) and became negative at 175°C. No measurements are available above 175°C; the cause was not independently diagnosed.

The comparison of variance behaviour between the matched saw-cut and intact states gives matched intact–saw-cut differences.

Table 6.91: Variance Comparison between the matched intact and saw-cut states

SFC	AR	SF	Intact Sign Change	Cut Sign Change	Effect
1	65	0.5%	175°C	150°C	25°C earlier
3	65	0.75%	175°C	175°C	Same
2	55	0.5%	Positive at 250°C	Negative at 250°C	Different terminal sign
4	55	0.75%	175°C	175°C	Same

In the matched records, the variance sign change occurs one sampled temperature stage earlier in the SFC1 saw-cut record than in its intact record. SFC2 returns to a positive value in the intact sequence but remains negative in the saw-cut sequence. These are distributional differences in individual records and are not assigned to an unmeasured material mechanism.

The observed Variance response in the saw-cut state is compared across the four

tested configurations.

For the aspect-ratio groups, the mean variance magnitude of the two AR65 records is 32.7% higher than that of the two AR55 records. The mixed-coverage, unreplicated comparison does not establish a fibre-length effect.

For the fibre-dosage groups, the two 0.75% records have a larger positive mean variance than the two 0.50% records and end at 175°C. Both pairs include sign changes, but the unequal coverage precludes a dosage conclusion.

Comparison of the sign transitions shows that, for SFC1 and SFC2, the signed variance-related quantity changes sign one measured temperature stage earlier in the saw-cut series than in the intact series. For SFC3 and SFC4, the transition occurs at the same reported stage, 175°C. SFC2 returns to a positive final value in the intact series but not in the saw-cut series. These are index-pattern observations; a conventional physical variance cannot be negative.

The variance progression is reported by measured interval rather than as operational zones. Variance is positive in all four records over 75–125°C; the two 0.5% SF records change sign over 125–150°C, and the two 0.75% SF records change sign by 175°C. Only the two 0.5% SF records continue to 250°C, where their values remain negative. These stage descriptions do not define universal temperature thresholds.

6.11.10 RMS Index Analysis (Cut Condition)

The temperature progression of RMS is examined for the four specimens.

The Root Mean Square (RMS) index quantifies the overall energy content of the signature difference signal. Unlike the deviation-based indices (RMSD), RMS measures the absolute signal level and shows gradual increase with temperature. Figure 6.41 presents the RMS comparison plots for all four specimens in the saw-cut state. RMS index comparison for all four SFRC specimens with saw-notch damage showing before compensation, after compensation, and the difference. Note: AR65/SF0.75% and AR55/SF0.75% specimens have data only up to 175°C.

Table 6.92 presents the RMS values at each temperature from 75°C to 250°C for all four specimens in the saw-cut state.

Table 6.93 presents the statistical summary of RMS values for all four specimens in the saw-cut state.

For SFC1 (AR65/SF0.5%), over the full temperature range, RMS increases from 0.0010 at 75°C to 0.0031 at 250°C, a factor of 3.1. Its mean of 0.0017 is lower than the SFC2 mean, but this specimen-level difference does not establish aspect-ratio-dependent stability.

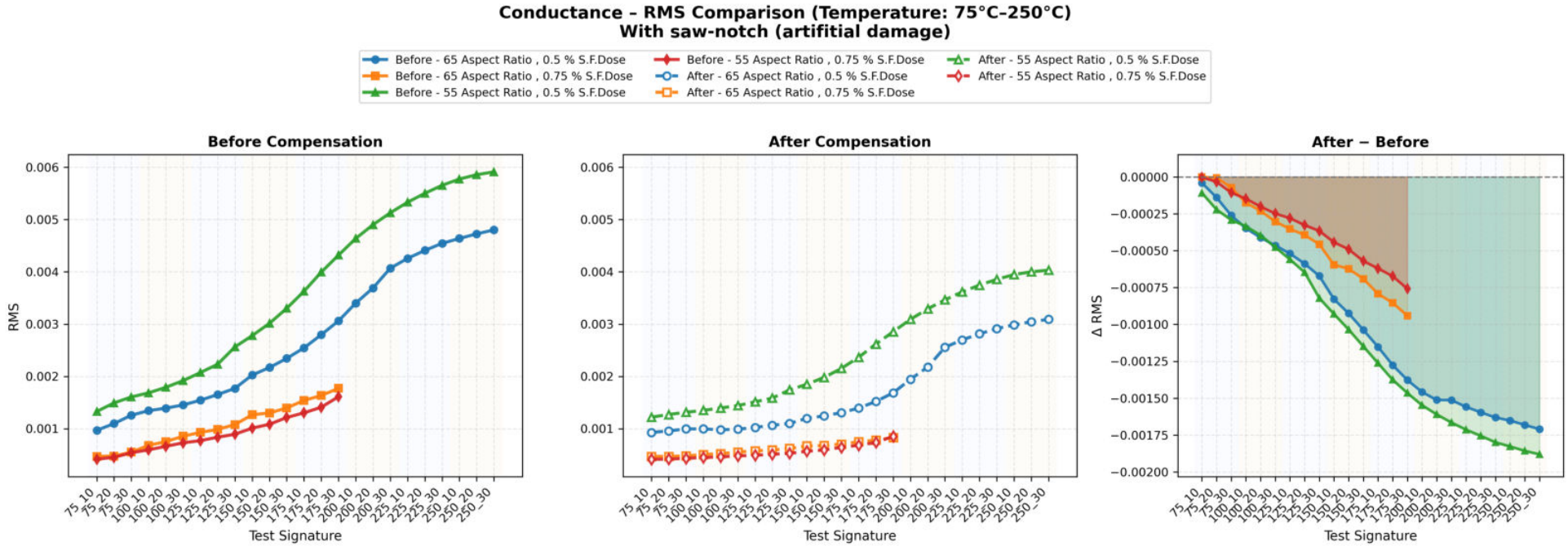

Figure 6.41: RMS index comparison for all four SFRC specimens with saw-notch damage.

Table 6.92: RMS Values at Each Temperature for All Four SFRC Specimens with Saw-Notch

Temperature	SFC1 (AR65/0.5%)	SFC3 (AR65/0.75%)	SFC2 (AR55/0.5%)	SFC4 (AR55/0.75%)
75°C	0.0010	0.0005	0.0012	0.0004
100°C	0.0010	0.0006	0.0014	0.0005
125°C	0.0012	0.0006	0.0017	0.0005
150°C	0.0014	0.0006	0.0020	0.0006
175°C	0.0018	0.0008	0.0027	0.0009
200°C	0.0023	—	0.0034	—
225°C	0.0027	—	0.0037	—
250°C	0.0031	—	0.0040	—

Table 6.93: RMS Statistical Summary for All Four SFRC Specimens with Saw-Notch

SFC	AR	SF (%)	Temp Range	Mean	Std Dev	Min	Max	Range
1	65	0.5	75–250°C	0.0017	0.0008	0.0009	0.0031	0.0022
3	65	0.75	75–175°C	0.0006	0.0001	0.0005	0.0008	0.0003
2	55	0.5	75–250°C	0.0025	0.0010	0.0012	0.0040	0.0028
4	55	0.75	75–175°C	0.0006	0.0001	0.0004	0.0009	0.0005

For SFC3 (AR65/SF0.75%), over the available temperature range, RMS increases from 0.0005 at 75°C to 0.0008 at 175°C (1.6×), with a mean of 0.0006. No saw-cut measurements are available above 175°C and the cause was not independently diagnosed.

For SFC2 (AR55/SF0.5%), RMS increases from 0.0012 at 75 °C to 0.0040 at 250 °C, a 3.3× ratio. Its mean of 0.0025 and range of 0.0028 are the largest among the four saw-cut specimen records.

For SFC4 (AR55/SF0.75%), RMS increased from 0.0004 at 75°C to 0.0009 at 175°C (2.3×). The reported mean is 0.0006 over the available range. No measurements are available above 175°C; the cause was not independently diagnosed.

The comparison of RMS values between the matched saw-cut and intact states gives matched intact–saw-cut differences.

Table 6.94: RMS Comparison between the matched intact and saw-cut states

SFC	AR	SF	Intact Mean	Saw-cut mean	Change (%)	Matched direction
1	65	0.5%	0.0021	0.0017	-19.0	Decrease
3	65	0.75%	0.0025	0.0006	-76.0	Large decrease (limited range)
2	55	0.5%	0.0029	0.0025	-13.8	Decrease
4	55	0.75%	0.0020	0.0006	-70.0	Large decrease (limited range)

In the matched records, RMS is lower in the saw-cut state for all four specimen–channel comparisons reported here, whereas several deviation indices have different

and configuration-dependent directions. The two 0.75% SF saw-cut series end at 175°C, so their values are compared only over the available range.

The observed RMS response in the saw-cut state is compared across the four tested configurations.

For the aspect-ratio groups, the mean RMS is 0.0012 for the two AR65 records and 0.0015 for the two AR55 records, a 22.7% difference. The comparison includes unequal temperature coverage and one specimen per configuration, so it does not establish that aspect ratio controls signal energy.

For the fibre-dosage groups, the mean RMS is 0.0021 for the two 0.5% specimens and 0.0006 for the two 0.75% specimens. The ascending order is SFC3/SFC4 (0.0006), SFC1 (0.0017) and SFC2 (0.0025). The 0.75% records stop at 175°C, so this is not a dosage-performance comparison over equal temperature ranges.

In the saw-cut state, RMS generally increases across the measured stages and is lower than the corresponding intact value in the reported comparisons. The two 0.50% records have values approximately three to four times those of the two 0.75% records. Negative after-minus-before differences indicate reduced RMS after processing, not independent proof of compensation performance.

In the observed progression, RMS remains below 0.0017 for the four saw-cut records over 75–125°C and lies between approximately 0.0006 and 0.0027 over 125–175°C. Only SFC1 and SFC2 continue above 175°C, reaching 0.0023–0.0037 by 225°C and 0.0031–0.0040 at 250°C. These ranges are descriptive, not stability or severity zones.

6.11.11 Skewness Index Analysis (Cut Condition)

The temperature progression of Skewness is examined for the four specimens.

The Skewness index measures the asymmetry of the signature distribution. Positive skewness indicates right-tailed distribution, while negative skewness indicates left-tailed distribution. Unlike other SHM indices, skewness exhibits complex non-monotonic behaviour with sign reversals. Figure 6.42 presents the skewness comparison plots for all four specimens in the saw-cut state. Skewness index comparison for all four SFRC specimens with saw-notch damage showing before compensation, after compensation, and the difference. Note: AR65/SF0.75% and AR55/SF0.75% specimens have data only up to 175°C.

Table 6.95 presents the skewness values at each temperature from 75°C to 250°C for all four specimens in the saw-cut state.

Table 6.96 presents the statistical summary of skewness values for all four speci-

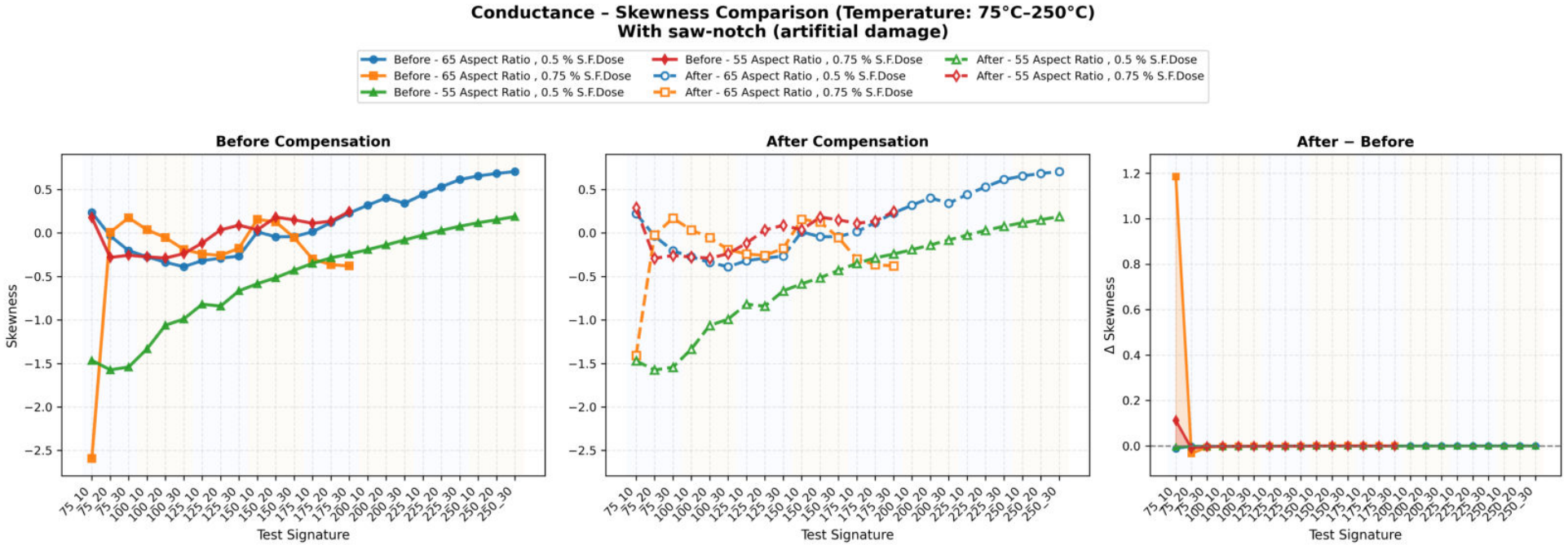

Figure 6.42: Skewness index comparison for all four SFRC specimens with saw-notch damage.

Table 6.95: Skewness Values at Each Temperature for All Four SFRC Specimens with Saw-Notch

Temperature	SFC1 (AR65/0.5%)	SFC3 (AR65/0.75%)	SFC2 (AR55/0.5%)	SFC4 (AR55/0.75%)
75°C	-0.005	-0.420	-1.529	-0.086
100°C	-0.333	-0.070	-1.130	-0.268
125°C	-0.291	-0.225	-0.775	0.002
150°C	-0.024	0.078	-0.509	0.123
175°C	0.122	-0.347	-0.292	0.165
200°C	0.356	—	-0.136	—
225°C	0.529	—	0.028	—
250°C	0.682	—	0.153	—

mens in the saw-cut state.

Table 6.96: Skewness Statistical Summary for All Four SFRC Specimens with Saw-Notch

SFC	AR	SF (%)	Temp Range	Mean	Std Dev	Min	Max	Range
1	65	0.5	75–250°C	0.130	0.353	-0.388	0.707	1.095
3	65	0.75	75–175°C	-0.197	0.368	-1.406	0.170	1.576
2	55	0.5	75–250°C	-0.524	0.553	-1.575	0.189	1.764
4	55	0.75	75–175°C	-0.013	0.204	-0.292	0.290	0.582

For SFC1 (AR65/SF0.5%), skewness changed from -0.005 at 75°C to 0.682 at 250°C, with the sign transition occurring between 150 and 175°C. The initial negative values differ from the predominantly positive intact record and describe a change in the measured distribution shape.

For SFC3 (AR65/SF0.75%), skewness was predominantly negative, with a reported mean of -0.197. A positive excursion occurred at 150°C (0.078), followed by -0.347 at 175°C. No measurements are available above 175°C; the cause was not independently diagnosed.

For SFC2 (AR55/SF0.5%), skewness was -1.529 at 75°C and increased toward positive values, crossing zero between 200 and 225°C. The negative initial saw-cut value contrasts with the positive initial value in the matched intact record.

For SFC4 (AR55/SF0.75%), skewness ranged from -0.268 to +0.165, giving the smallest reported range (0.582) among the four records. No measurements are available above 175°C; the cause was not independently diagnosed.

The comparison of skewness behaviour between the matched saw-cut and intact states gives matched intact–saw-cut differences.

In the matched intact–saw-cut comparison, the mean skewness is more negative in the saw-cut state for all four specimens. SFC2 changes from -0.001 to -0.524, while

Table 6.97: Skewness Comparison between the matched intact and saw-cut states

SFC	AR	SF	Intact Mean	Saw-cut mean	Change	Matched direction
1	65	0.5%	+0.203	+0.130	-0.073	Decreased positive
3	65	0.75%	-0.149	-0.197	-0.048	More negative
2	55	0.5%	-0.001	-0.524	-0.523	Strongly negative
4	55	0.75%	+0.406	-0.013	-0.419	Sign reversal

SFC4 changes sign from +0.406 to -0.013. These are distribution-shape differences within the tested records.

The observed Skewness response in the saw-cut state is compared across the four tested configurations.

For the aspect-ratio groups, the signed mean skewness is -0.034 for the two AR65 records and -0.268 for the two AR55 records. The mixed-coverage, unreplicated comparison does not establish that fibre length controls distribution symmetry.

For the fibre-dosage groups, the mean skewness is -0.197 for the two 0.5% specimens and -0.105 for the two 0.75% specimens. The ascending order of reported ranges is SFC4 (0.582), SFC1 (1.095), SFC3 (1.576) and SFC2 (1.764). Unequal temperature coverage and signed skewness preclude a dosage or stability ranking.

The saw-cut skewness records exhibit four different sampled trajectories. SFC1 changes gradually from negative to positive, SFC3 is predominantly negative with a brief positive excursion, SFC2 begins with strongly negative values and increases toward positive values, and SFC4 remains near zero with fewer sign reversals over its available stages. These descriptions apply only to the measured records and are not behavioural classes for other specimens.

Compared with the intact records, the saw-cut means shift toward more negative skewness in all four comparisons. SFC2 has the largest starting difference (-1.529 saw-cut versus +0.645 intact), while SFC4 has the smallest saw-cut range. These are distribution-shape differences, not a material stability ranking.

The skewness progression is described over the measured intervals without defining operational zones. The four records are predominantly negative over 75–125°C, and specimen-specific sign changes occur over 125–175°C. Only the two 0.5% SF records continue beyond 175°C; their skewness approaches or becomes positive by 225–250°C. These intervals are descriptive of the available records and are not transferable thresholds.

6.11.12 Peak-to-Peak Index Analysis (Cut Condition)

The temperature progression of Peak-to-Peak is examined for the four specimens.

The Peak-to-Peak index measures the amplitude range of the signature difference signal. In the saw-cut records, values increase from near zero to more than 1000% at the later temperature stages. Figure 6.43 presents the comparison plots for all four specimens. Peak-to-Peak index comparison for all four SFRC specimens with saw-notch damage showing before compensation, after compensation, and the difference. Note the extreme values exceeding 1300%. Note: AR65/SF0.75% and AR55/SF0.75% specimens have data only up to 175°C.

Table 6.98 presents the peak-to-peak values at each temperature from 75°C to 250°C for all four specimens in the saw-cut state.

Table 6.98: Peak-to-Peak (%) Values at Each Temperature for All Four SFRC Specimens with Saw-Notch

Temperature	SFC1 (AR65/0.5%)	SFC3 (AR65/0.75%)	SFC2 (AR55/0.5%)	SFC4 (AR55/0.75%)
75°C	7.6	3.2	24.1	8.1
100°C	20.2	45.1	57.6	38.4
125°C	28.9	83.7	69.8	70.2
150°C	49.0	73.3	200.0	111.7
175°C	231.0	83.6	465.2	219.8
200°C	639.2	—	782.9	—
225°C	1009.4	—	1088.5	—
250°C	1214.5	—	1314.5	—

Table 6.99 presents the statistical summary of peak-to-peak values for all four specimens in the saw-cut state.

Table 6.99: Peak-to-Peak Statistical Summary for All Four SFRC Specimens with Saw-Notch

SFC	AR	SF (%)	Temp Range	Mean (%)	Std Dev	Min (%)	Max (%)	Range
1	65	0.5	75–250°C	400.0	462.5	3.0	1262.1	1259.1
3	65	0.75	75–175°C	57.8	33.5	0.1	118.0	117.9
2	55	0.5	75–250°C	500.3	476.2	10.0	1369.4	1359.4
4	55	0.75	75–175°C	89.6	83.5	0.1	336.5	336.4

For SFC1 (AR65/SF0.5%), Peak-to-Peak increases from 7.6% at 75 °C to 1214.5% at 250 °C, a 160× ratio. Its mean is 400% and its range is 1259.1%, the second-largest range among the four saw-cut specimen records.

For SFC3 (AR65/SF0.75%), peak-to-peak values reached 83.7% at 125°C and 83.6% at 175°C. The reported mean is 57.8% over the available range. No measurements

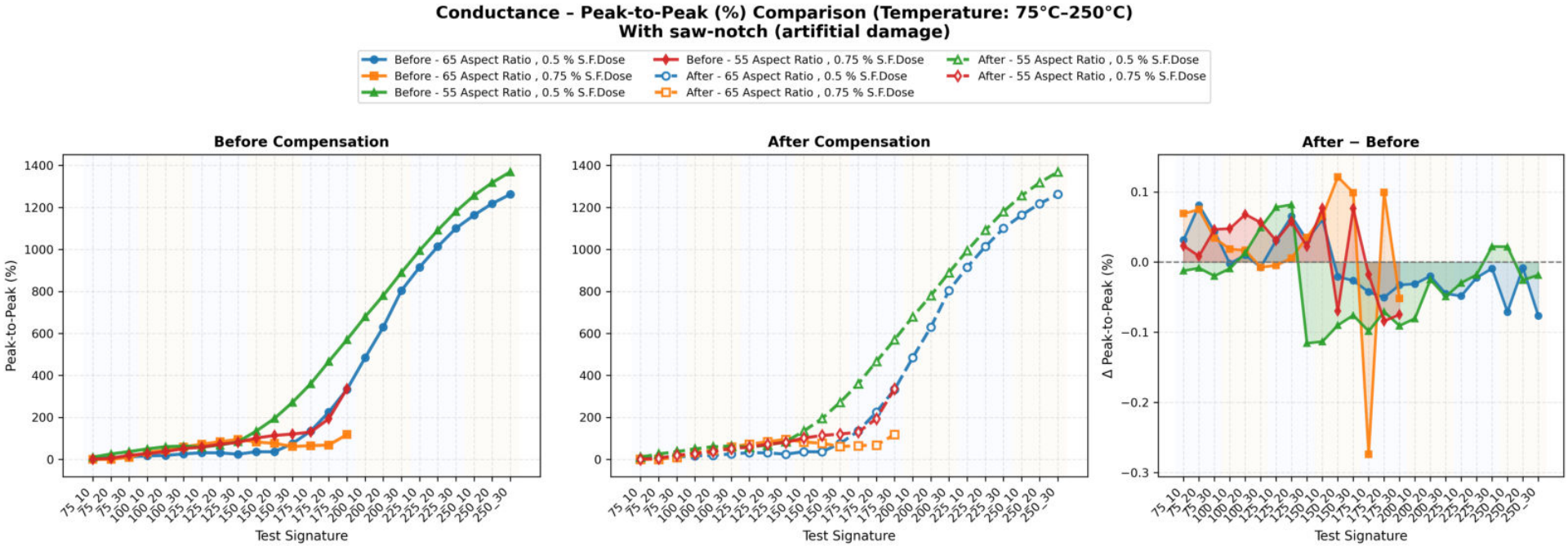

Figure 6.43: Peak-to-Peak index comparison for all four SFRC specimens with saw-notch damage.

are available above 175°C; the cause was not independently diagnosed.

For SFC2 (AR55/SF0.5%), peak-to-peak values increased from 24.1% at 75°C to 1314.5% at 250°C (55×). Its reported mean of 500.3% and maximum of 1369.4% are the largest among the four records.

For SFC4 (AR55/SF0.75%), peak-to-peak reached 219.8% at 175°C. The reported mean is 89.6% over the available range. No measurements are available above 175°C; the cause was not independently diagnosed.

The comparison of Peak-to-Peak values between the matched saw-cut and intact states gives the following differences.

Table 6.100: Peak-to-Peak Comparison between the matched intact and saw-cut states

SFC	AR	SF	Intact Mean (%)	Saw-cut mean (%)	Change (%)	Matched direction
1	65	0.5%	160.7	400.0	+149.0	2.5× increase
3	65	0.75%	113.6	57.8	-49.1	Decrease (limited range)
2	55	0.5%	123.6	500.3	+304.7	4× increase
4	55	0.75%	136.2	89.6	-34.2	Decrease (limited range)

In the matched comparison, the two 0.50% specimens show Peak-to-Peak increases of 149–305% in the saw-cut state, with maxima increasing from 612–682% in the intact records to 1214–1314% in the saw-cut records. These are the largest absolute percentage changes among the reported indices for those specimens, but the different index scales preclude a general sensitivity ranking.

The observed Peak-to-Peak response in the saw-cut state is compared across the four tested configurations.

For the aspect-ratio groups, the mean Peak-to-Peak value is 229% for the two AR65 records and 295% for the two AR55 records, a 22.4% difference. Mixed coverage and the absence of replicates preclude a fibre-length conclusion.

For the fibre-dosage groups, the mean Peak-to-Peak value is 450% for the two 0.5% specimens and 74% for the two 0.75% specimens. The ascending order is SFC3 (57.8%), SFC4 (89.6%), SFC1 (400%) and SFC2 (500.3%). The 0.75% records end at 175°C, so the group means are not comparable over the same range.

Across the observed temperature progression, Peak-to-Peak remains below 85% for all specimens over 75–125 °C, reaches 50–200% over 125–150 °C and 84–465% over 150–175 °C. Only the two 0.50% specimens continue through 250 °C, where selected values exceed 1300%. These sampled ranges do not establish an exponential law or a critical transition.

Comparison of the onset stages shows that, in selected intact records, the marked Peak-to-Peak increase begins after the 175°C stage, whereas in selected saw-cut records

values above 100% first appear at 150°C. The 25°C stage difference is descriptive and does not establish a continuous critical threshold or exponential law.

In the observed progression, Peak-to-Peak remains below 85% for the four saw-cut records over 75–125°C and reaches approximately 84–465% over 125–175°C. Only SFC1 and SFC2 continue above 175°C, reaching approximately 639–1088% by 225°C and values above 1200% at 250°C. The ranges do not define moderate, acceleration or extreme thresholds.

6.11.13 Covariance Index Analysis (Cut Condition)

The temperature progression of Covariance is examined for the four specimens.

The Covariance index measures the joint variability between baseline and temperature-affected signatures. Like variance, covariance values are extremely small (order of 10^{-10}) and can transition from positive to negative at elevated temperatures. Figure 6.44 presents the covariance comparison plots for all four specimens in the saw-cut state. Covariance index comparison for all four SFRC specimens with saw-notch damage showing before compensation, after compensation, and the difference. Note the very small scale (order of 10^{-10}) and sign transitions. Note: AR65/SF0.75% and AR55/SF0.75% specimens have data only up to 175°C.

Table 6.101 presents the covariance values at each temperature from 75°C to 250°C for all four specimens in the saw-cut state.

Table 6.101: Covariance Values ($\times 10^{-10}$) at Each Temperature for All Four SFRC Specimens with Saw-Notch

Temperature	SFC1 (AR65/0.5%)	SFC3 (AR65/0.75%)	SFC2 (AR55/0.5%)	SFC4 (AR55/0.75%)
75°C	+1.5-2.5	+2.5-3.5	+1.0-2.0	+3.0-4.0
100°C	+1.0-2.0	+2.0-3.0	+0.5-1.5	+2.5-3.5
125°C	+0.5-1.5	+1.0-2.0	0 to +1.0	+1.5-2.5
150°C	0 to +0.5	+0.5-1.5	-0.5 to +0.5	+0.5-1.5
175°C	-1.0 to 0	-0.5 to +0.5	-1.5 to -0.5	-0.5 to +0.5
200°C	-2.5 to -1.5	—	-2.5 to -1.5	—
225°C	-4.0 to -3.0	—	-3.5 to -2.5	—
250°C	-5.0 to -4.0	—	-4.5 to -3.5	—

Table 6.102 presents the statistical summary of covariance values for all four specimens in the saw-cut state.

For SFC1 (AR65/SF0.5%), covariance changes from approximately $+2.5 \times 10^{-10}$ at 75 °C to -5.0×10^{-10} at 250 °C. Its sign changes between 150 and 175 °C in the saw-cut sequence and at 175 °C in the intact sequence; the observations do not establish

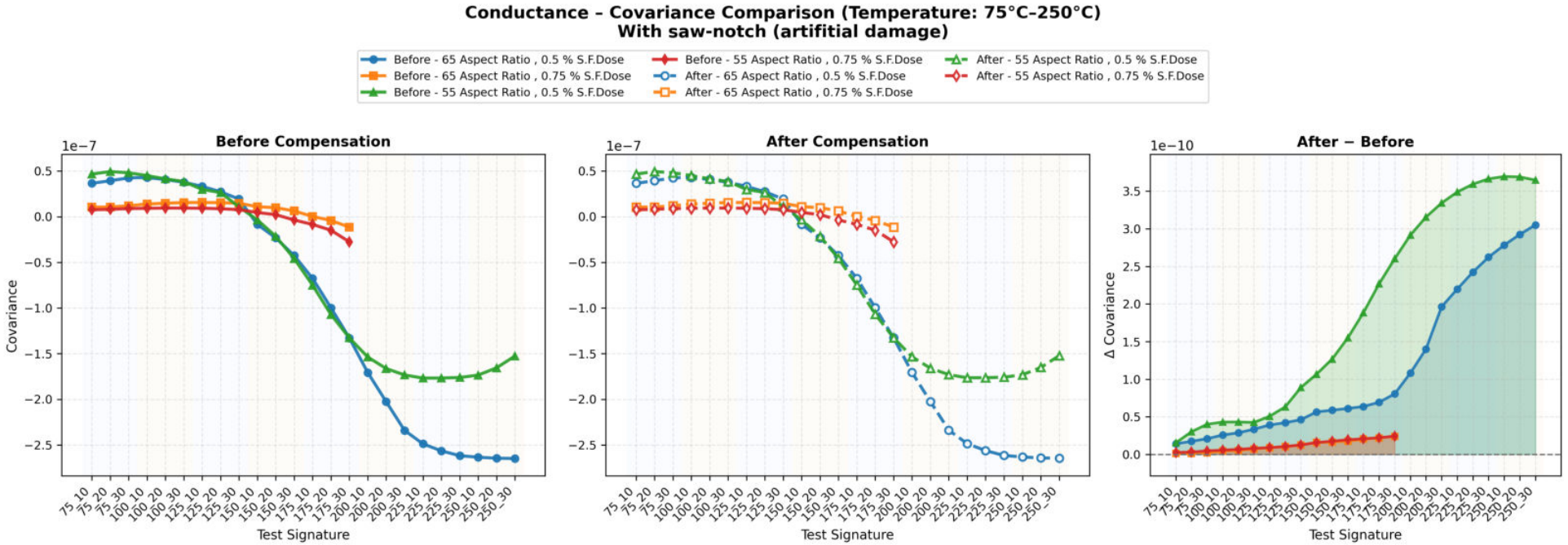

Figure 6.44: Covariance index comparison for all four SFRC specimens with saw-notch damage.

Table 6.102: Covariance Statistical Summary for All Four SFRC Specimens with Saw-Notch

SFC	AR	SF (%)	Temp Range	Min	Max	Sign Change
1	65	0.5	75–250°C	-5.0×10^{-10}	$+2.5 \times 10^{-10}$	At 150-175°C
3	65	0.75	75–175°C	-0.5×10^{-10}	$+3.5 \times 10^{-10}$	At 175°C
2	55	0.5	75–250°C	-4.5×10^{-10}	$+2.0 \times 10^{-10}$	At 125-150°C
4	55	0.75	75–175°C	-0.5×10^{-10}	$+4.0 \times 10^{-10}$	At 175°C

an acceleration mechanism.

For SFC3 (AR65/SF0.75%), covariance was predominantly positive and changed sign at 175°C. Its initial positive values are higher than those of the two 0.5% SF records, but one specimen per configuration does not establish a fibre-content effect. No measurements are available above 175°C; the cause was not independently diagnosed.

For SFC2 (AR55/SF0.5%), over the full temperature range, covariance changes sign between 125 and 150°C, one or two sampled stages earlier than in the other records. The intact sequence returns to a positive value at 250°C, whereas the saw-cut sequence remains negative.

For SFC4 (AR55/SF0.75%), covariance began at the largest reported positive value ($+4.0 \times 10^{-10}$) and changed sign at 175°C. No measurements are available above 175°C; the cause was not independently diagnosed.

The comparison of covariance behaviour between the matched saw-cut and intact states gives matched intact–saw-cut differences.

Table 6.103: Covariance Comparison between the matched intact and saw-cut states

SFC	AR	SF	Intact Sign Change	Cut Sign Change	Shift	Effect
1	65	0.5%	175°C	150-175°C	0-25°C earlier	Accelerated
3	65	0.75%	175°C	175°C	Same	No change
2	55	0.5%	Positive at 250°C	Negative at 250°C	—	Different terminal sign
4	55	0.75%	175°C	175°C	Same	No change

In the matched records, as for variance, the covariance sign change occurs earlier in the sampled SFC1 and SFC2 saw-cut sequences than in their intact sequences. SFC2 also lacks the later positive value present in its intact record. The result is retained as a record-specific change in joint variability without a causal configuration claim.

The observed Covariance response in the saw-cut state is compared across the four tested configurations.

For the aspect-ratio groups, the mean covariance magnitude of the two AR65 records is 32.7% higher than that of the two AR55 records. The mixed-coverage, unreplicated comparison does not establish a fibre-length effect.

For the fibre-dosage groups, the two 0.75% records have a higher positive mean covariance than the two 0.50% records, but their saw-cut series end at 175°C. The unequal coverage and absence of replicated configurations preclude a dosage or sensitivity conclusion.

In the saw-cut state, the reported covariance and variance-related quantities are both of the order of 10^{-10} in these comparisons and show sign changes at selected stages. Their similar rounded summaries do not make them independent indicators, and the sign of the processing difference is not itself a damage-detection criterion.

The covariance progression is reported by measured interval rather than as operational zones. Covariance is positive in all four records over 75–125°C; SFC2 changes sign over 125–150°C, and the remaining records change sign by 175°C. Only the two 0.5% SF records continue to 250°C, where their covariance remains negative. These stage descriptions do not define universal temperature thresholds.

After compensation in the saw-cut state, the after-minus-before covariance is predominantly positive and is larger in the two AR55 records. Its sign describes the processing change; interpretation as closer baseline agreement requires the corresponding paired signatures and does not establish a configuration effect.

6.11.14 Consolidated Performance of Secondary SHM Indices (Cut Heating)

The preceding sections presented the detailed temperature response of the three representative indices (RMSD, CCV, and RMS) selected on the basis of their consistent direction across the four tested specimens ranking established in Section D.2. The remaining ten indices (MAPD, AMPD, CC, CCD, CCD^3, MSE, Variance, Skewness, Peak-to-Peak, and Covariance) were analysed with the same rigour; their consolidated performance under the cut heating condition is summarised in Table 6.104.

Table 6.104: Consolidated performance of the ten secondary SHM indices under cut heating for all four SFRC specimens.

Index	**SFC1**		**SFC3**		**SFC2**		**SFC4**		**Comp. Impr.**
	Mean	Max	Mean	Max	Mean	Max	Mean	Max	
MAPD	110.8%	266.2%	34.1%	95.4%	120.4%	247.2%	40.5%	138.1%	33%
AMPD	197.6%	616.3%	32.1%	82.7%	190.8%	520.9%	47.7%	177.2%	38%
CC	-0.120	0.999	0.633	1.000	0.066	0.987	0.428	1.000	Stab.
CCD	3.210	6.660	0.460	3.670	1.530	2.950	1.040	5.580	40%
CCD^3	3.210	6.660	0.460	3.670	1.530	2.950	1.040	5.580	67%
MSE	~ 0	0.8×10^{-5}	~ 0	0.2×10^{-5}	~ 0	1.2×10^{-5}	~ 0	0.4×10^{-5}	50%
Variance	~ 0	$+2.0 \times 10^{-10}$	~ 0	$+3.0 \times 10^{-10}$	~ 0	$+1.5 \times 10^{-10}$	~ 0	$+3.5 \times 10^{-10}$	60%
Skewness	0.130	0.707	-0.197	0.170	-0.524	0.189	-0.013	0.290	50%
Peak-to-Peak	400.0%	1262.1%	57.8%	118.0%	500.3%	1369.4%	89.6%	336.5%	43%
Covariance	~ 0	$+2.5 \times 10^{-10}$	~ 0	$+3.5 \times 10^{-10}$	~ 0	$+2.0 \times 10^{-10}$	~ 0	$+4.0 \times 10^{-10}$	60%

The preceding sections present the detailed temperature progression, figures and statistical interpretation for the representative indices. The consolidated secondary-index results are reported here to compare their measured directions and ranges without introducing an additional implementation ranking.

6.11.15 Effect of Compensation for the Saw-Cut Condition

This section compares the fitted EPS quantities before and after compensation for the saw-cut heating records. The comparison assesses agreement with the selected saw-cut baseline within the available stages and does not constitute an operational SHM test.

6.11.15.1 EPS Response to Compensation in the Saw-Cut State

Table 6.105 presents the end-to-end changes for the three fitted EPS quantities before and after compensation. SFC3 and SFC4 end at 175°C, so their percentages cover a shorter interval than SFC1 and SFC2.

Table 6.105: Reported end-to-end EPS changes before and after compensation for the saw-cut records.

SFC	AR	SF	Parameter	Before (%)	After (%)	Observed change
1	65	0.5%	Mass	-209.42	-64.62	69.1% smaller magnitude
			Stiffness	-209.42	-64.62	69.1% smaller magnitude
			Damping	+103.67	+63.31	38.9% smaller magnitude
3*	65	0.75%	Mass	+379.89	-33.42	Sign reversal
			Stiffness	+379.89	-33.42	Sign reversal
			Damping	Variable	Variable	Unstable
2	55	0.5%	Mass	-88.56	-298.24	237% larger magnitude
			Stiffness	-88.56	-298.24	237% larger magnitude
			Damping	Variable	Variable	Complex
4*	55	0.75%	Mass	-263.43	-23.66	91.0% smaller magnitude
			Stiffness	-263.43	-23.66	91.0% smaller magnitude
			Damping	Variable	Variable	Complex

*Limited temperature range: 75-175°C because higher-temperature records are unavailable

For the mass-like parameter, the reported magnitude decreases by 69.1% for SFC1 and 91.0% for SFC4, reverses sign for SFC3 and increases by 237% for SFC2. These mixed outcomes are specimen- and interval-specific and do not establish configuration performance.

For the stiffness-like parameter, the relative changes match the mass-like values because the quantities are coupled in the adopted representation. They are not independent confirmations of the processing effect.

For the damping-like parameter, the SFC1 magnitude decreases from +104% to +63%, while the other three trajectories remain variable or sign-changing. The fitted damping-like results do not show a uniform processing response.

Table 6.106 summarises the overall compensation effectiveness by configuration under damaged conditions.

Table 6.106: Specimen-level summary of the reported EPS changes for the saw-cut records.

SFC	Configuration	Temp Range	Mass/Stiffness	Damping	Summary
1	AR65/SF0.5%	75–250°C	Magnitude smaller (69%)	Magnitude smaller (39%)	Magnitudes smaller
3	AR65/SF0.75%	75–175°C	Sign reversal	Variable	Mixed
2	AR55/SF0.5%	75–250°C	Magnitude larger	Variable	Mixed
4	AR55/SF0.75%	75–175°C	Magnitude smaller (91%)	Variable	Mixed

SFC3 and SFC4 have no saw-cut records above 175°C.

Table 6.107 compares the reported compensation changes between the intact and saw-cut states.

Table 6.107: Comparison of reported EPS processing effects in the intact and saw-cut states.

SFC	Configuration	Intact result	Saw-cut result	Comparison
1	AR65/SF0.5%	58.8% smaller magnitude	69.1% smaller magnitude	Different reductions
3	AR65/SF0.75%	23% larger magnitude	Sign reversal	Different direction
2	AR55/SF0.5%	Sign reversal	237% larger magnitude	Different response
4	AR55/SF0.75%	93% smaller magnitude	91% smaller magnitude	Similar reductions

In summary, EPS compensation in the saw-cut series reduces the reported mass-like and stiffness-like drift magnitude by 91% for SFC4 over 75–175°C and by 69% for SFC1 over 75–250°C. For SFC2, the magnitude increases by 237%, while the damping-like term remains configuration-dependent. These mixed outcomes show that compensation of the fitted parameters is not uniformly effective and do not support preference or exclusion of a material configuration.

6.11.15.2 SHM-Index Response to Compensation in the Saw-Cut State

This section compares before- and after-compensation ranges for the thirteen SHM indices in the saw-cut records. The comparison quantifies processing changes within the available experimental stages and does not constitute an operational detection test.

For the deviation-based indices (RMSD, MAPD, AMPD, CCD and CCD^3), the reported saw-cut summaries show that the RMSD range changes from 0–3.5 to 0–2.8

Table 6.108: SHM Index Range Comparison Before vs After Compensation (Cut Condition)

#	Index	Before Range	After Range	Δ Range	Range change
1	RMSD	0 – 3.5	0 – 2.8	0 to -0.6	20% reduction
2	MAPD	0 – 4.0	0 – 3.2	0 to -0.7	20% reduction
3	AMPD	0 – 5.5	0 – 4.2	0 to -1.2	24% reduction
4	CC	0.4 – 1.0	0.7 – 1.0	0 to +0.25	Stabilization
5	CCD	0 – 0.55	0 – 0.30	0 to -0.20	45% reduction
6	CCD^3	0 – 0.15	0 – 0.03	0 to -0.10	80% reduction
7	CCV	0.80 – 1.0	0.92 – 1.0	0 to +0.10	Stabilization
8	MSE (10^{-5})	0 – 3.5	0 – 2.0	0 to -1.2	43% reduction
9	Variance (10^{-10})	+4 to -5	+2 to -3	-0.5 to +1.5	40% reduction
10	RMS	0.002 – 0.008	0.002 – 0.006	0 to -0.002	25% reduction
11	Skewness	-1.6 – 1.0	-0.5 – 0.8	-0.05 to +0.15	50% reduction
12	Peak-to-Peak	0 – 1400%	0 – 900%	-50 to +50	36% reduction
13	Covariance (10^{-10})	+4 to -5	+2 to -3	-0.5 to +1.5	40% reduction

(20% reduction), MAPD has a similar 20% reduction, AMPD has a 24% reduction, CCD has a 45% reduction and CCD^3 has the largest tabulated reduction at 80%. These range-based summaries describe the analysed records and should not be interpreted as independent measures of damage resistance.

For the correlation-based indices, the minimum CC increases from 0.40 to 0.70 and the minimum CCV from 0.80 to 0.92. These shifts place the compensated records closer to the selected state-specific baseline values without assigning the initial difference solely to damage.

For the error and dispersion indices, the reported MSE range decreases by 43%, and the variance and covariance spans by 40%. Their rounded range summaries do not make variance and covariance mathematically coupled or independent confirmations.

For RMS and skewness, the respective ranges decrease by 25% and 50%. The signed skewness trajectories still differ among specimens, so the range reduction is not a damage-resistance measure.

For Peak-to-Peak, the maximum decreases from 1400% to 900%, a 36% range reduction. The saw-cut maximum is twice the intact maximum in the tabulated summaries, but the comparison does not isolate structural change from the different trajectories and coverage.

Table 6.109 compares compensation effectiveness between conditions.

Table 6.110 orders the reported numerical range reductions. The indices have different definitions and scales, and CCD^3 is algebraically dependent on CC; the ordering is therefore descriptive.

In summary, all thirteen tabulated index ranges in the saw-cut condition are

Table 6.109: SHM Compensation Effectiveness: Intact vs Cut Condition

#	Index	Intact (%)	Cut (%)	Matched direction
1	RMSD	35	20	Reduced
2	MAPD	33	20	Reduced
3	AMPD	38	24	Reduced
4	CC	Stabilization	Stabilization	Maintained
5	CCD	40	45	**Improved**
6	CCD^3	67	80	Larger reported reduction
7	CCV	Stabilization	Stabilization	Maintained
8	MSE	50	43	Reduced
9	Variance	60	40	Reduced
10	RMS	20	25	**Improved**
11	Skewness	50	50	Maintained
12	Peak-to-Peak	43	36	Reduced
13	Covariance	60	40	Reduced

Table 6.110: Descriptive ordering of reported SHM-index range changes for the saw-cut records.

Order	Index	Range change	Interpretation
1	CCD^3	80% reduction	Dependent cubic transform
2	Skewness	50% reduction	Signed shape measure
3	CCD	45% reduction	Dependent on CC
4	MSE	43% reduction	Squared-error measure
5	Variance	40% reduction	Dispersion measure
6	Covariance	40% reduction	Joint-variation measure
7	Peak-to-Peak	36% reduction	Amplitude-range measure
8	RMS	25% reduction	Amplitude measure
9	AMPD	24% reduction	Deviation measure
10	RMSD	20% reduction	Deviation measure
11	MAPD	20% reduction	Deviation measure
12	CC	Minimum increased	Similarity measure
13	CCV	Minimum increased	Correlation-derived measure

smaller after compensation in the analysed records, but the magnitude varies by index. CCD^3 has the largest reported range reduction (80%), followed by selected correlation, moment and variance-related indices. The comparison evaluates removal of temperature-associated variation within the present dataset; it does not establish an ideal index, universal robustness or a field-monitoring hierarchy.

6.11.15.3 Quantitative Assessment of Compensation in the Saw-Cut State

This section synthesises the descriptive measures from Sections C.4.1 and C.4.2 for the saw-cut records. It compares processing branches within the same four specimens and does not represent independent validation or a field-performance test.

Table 6.111 presents aggregate changes in the reported saw-cut summaries.

Table 6.111: Aggregate changes in the reported saw-cut summaries after compensation.

Category	Metric	Value	Scope
EPS Parameters	Largest mass/stiffness reduction	SFC4 (AR55/SF0.75%)	One specimen, to 175°C
	Mass/stiffness magnitude reduction	91.0%	SFC4 summary
	Damping magnitude reduction	38.9%	SFC1 summary
	Specimens with selected reductions	2 of 4 (50%)	Parameter-dependent
SHM Indices	Mean reported range reduction (11 indices)	39.5%	Different scales
	Largest range reduction (CCD^3)	80%	Dependent transform
	Indices with >50% range reduction	2 of 13 (15%)	Descriptive count
	Indices with a reported range change	13 of 13 (100%)	Not a validation rate

Table 6.112 compares the reported compensation changes between the intact and saw-cut states.

Table 6.112: Overall Compensation Effectiveness: Intact vs Cut Condition

Category	Metric	Intact	Cut	Change
EPS	Largest mass/stiffness magnitude reduction	93.0%	91.0%	-2.0%
	Configurations with Improvement	50%	50%	Same
	Specimen with larger selected magnitude	SFC3	SFC2	Different
SHM	Mean reported range reduction	45.1%	39.5%	-5.6%
	Largest range reduction	CCD^3 (67%)	CCD^3 (80%)	+13%
	Indices with >50% range reduction	5 (38%)	2 (15%)	-23%
	Indices with a reported range change	100%	100%	Same

Under the saw-cut condition, all reported SHM aggregate summaries changed after compensation, but their percentage reductions differ and are not independent because several indices are mathematically related. The larger reduction reported for CCD^3 cannot be treated as independent confirmation of CCD or CC. EPS responses also vary by specimen, including a large increase in the SFC2 comparison, so the results do not establish configuration-independent robustness.

Table 6.113 gives representative before–after comparisons for the saw-cut records.

Table 6.113: Representative before–after comparisons for Enhanced EFS processing of the saw-cut records.

Criterion	Before Compensation	After Compensation
RMSD Range (cut)	0 – 3.5	0 – 2.8 (20% reduction)
CC Minimum (cut)	0.40	0.70 (closer to unity)
Peak-to-Peak Maximum (cut)	1400%	900% (36% reduction)
Mass-like change (SFC4, cut)	-263%	-24% (91% smaller magnitude)
Mass-like change (SFC1, cut)	-209%	-65% (69% smaller magnitude)
CCD^3 Range (cut)	0 – 0.15	0 – 0.03 (80% reduction)

Regarding configuration and temperature boundaries, the tabulated ordering is retained as a description of these specimens, not as a recommendation to select or avoid a material configuration. Similarly, reductions in individual index summaries do not establish a primary index or a critical temperature for compensation. SFC3 and SFC4 have no saw-cut records above 175 °C, and all four-specimen comparisons must therefore use the common measured range.

The principal limitation of the saw-cut comparison is that the processing effect varies among specimens and quantities. Mean reported range reduction is lower in the saw-cut summaries than in the intact summaries, while RMSD and MAPD show smaller reductions. SFC3 and SFC4 lack saw-cut records above 175°C, and the damping-like trajectories are not uniform. These limitations preclude configuration grading and full-range comparison across all four specimens.

In summary, Enhanced EFS reduced several aggregate thermal-difference measures in the saw-cut records, with substantial variation among specimens, indices and EPS quantities. The result supports matched, study-specific evaluation of the processing method; it does not establish external robustness or reliable monitoring throughout 75–250 °C for all configurations.

6.12 Intact vs Cut Comparison

This section compares the intact and saw-cut records within each specimen. The comparison is made at matched temperatures and processing conditions and is used to identify changes associated with the introduced notch. It does not constitute independent validation of a field damage-detection system because each material configuration is represented by one specimen.

6.12.1 EPS Parameter Changes Due to Cut

The Equivalent Structural Parameters (EPS) are fitted mass-like, stiffness-like and damping-like terms obtained from the adopted series-mobility representation. Their changes describe the response of the coupled JPS–interface–specimen system; they are not direct measurements of the specimen's mass, stiffness or damping.

6.12.1.1 Mass-Like Parameter Change

The equivalent mass parameter is interpreted here as a model-derived descriptor of the measured EMI signature. Differences between intact and saw-cut series may arise from

the combined response of the notch, temperature, sensor interface and fitted model; therefore, the parameter is used comparatively rather than as a direct physical mass estimate.

Figures 6.45–6.48 present the complete intact–cut EPS comparison for each specimen after compensation. Each source image is retained at full width so that the three parameter axes, legends and signs can be read without digital zoom. Only temperatures available in both structural states should be used for quantitative comparison.

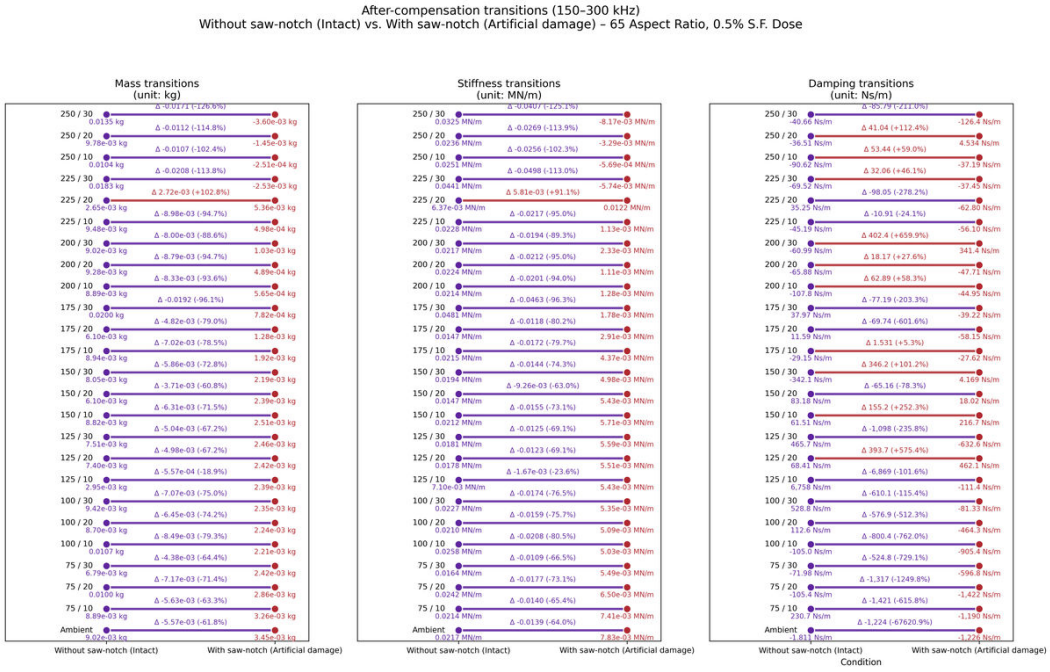

Figure 6.45: Matched intact and saw-cut EPS trajectories for SFC1 after compensation.

Table 6.114 compares the fitted mass-like parameter at the starting temperature (75°C) and at the last temperature shared by each intact–saw-cut pair. The starting value is higher in the saw-cut record for all four specimens, with changes from +17.3% for SFC1 to +330.0% for SFC2. Sign differences at the final matched stage for SFC1 and SFC2 show that the fitted parameter is sensitive to structural state and temperature, but they do not identify a unique physical mechanism.

Table 6.115 compares the percentage change from 75°C to the last matched temperature. The absolute drift is lower in the saw-cut series for three specimens, including a change from -361.9% to -33.4% for SFC3. SFC2 changes direction, from +1128.5% in the intact series to -298.2% in the saw-cut series. Because the denominator is the fitted value at 75°C, particularly large percentages must be interpreted together with the underlying trajectories in Figures 6.45–6.48.

SFC1 (AR65/SF0.5%) has a 17.3% higher starting value in the saw-cut series

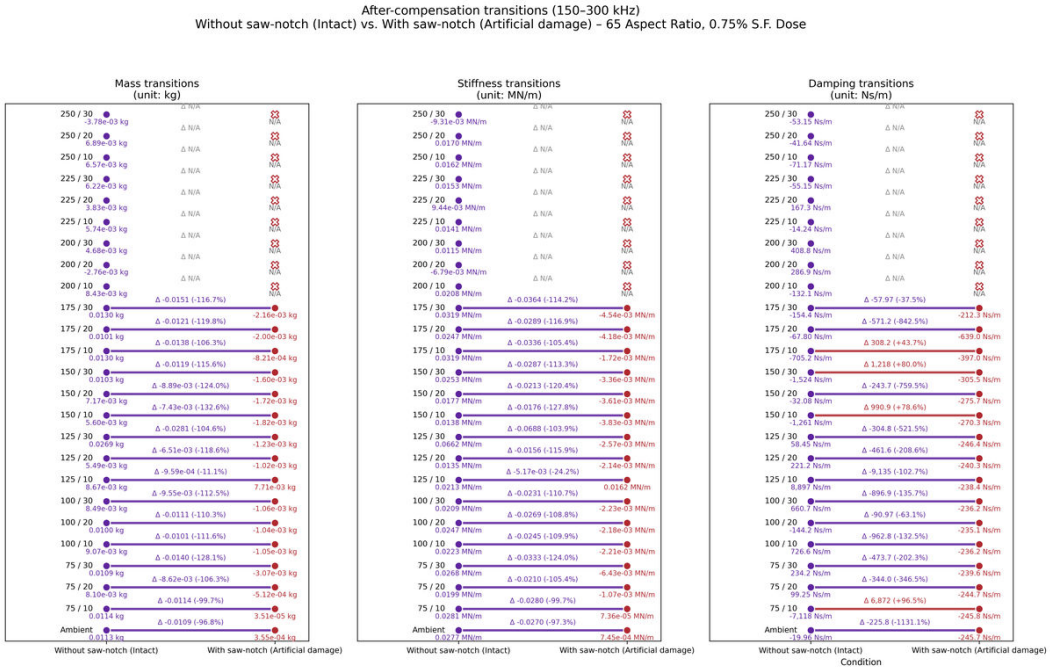

Figure 6.46: Matched intact and saw-cut EPS trajectories for SFC3 after compensation.

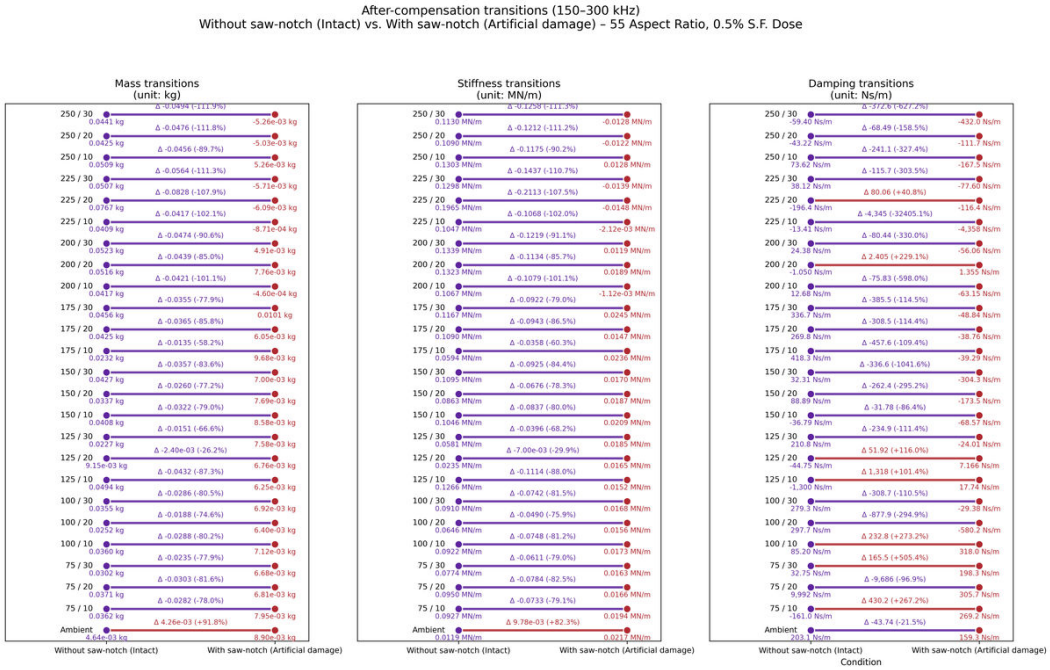

Figure 6.47: Matched intact and saw-cut EPS trajectories for SFC2 after compensation.

(0.0326 kg) than in the intact series (0.0278 kg). The end-to-end percentage change is -202.9% for the intact series and -64.6% for the saw-cut series. At 250°C, the fitted values have different signs (-0.0286 and 0.0115 kg, respectively), which reinforces the need to interpret this model term comparatively rather than as physical mass.

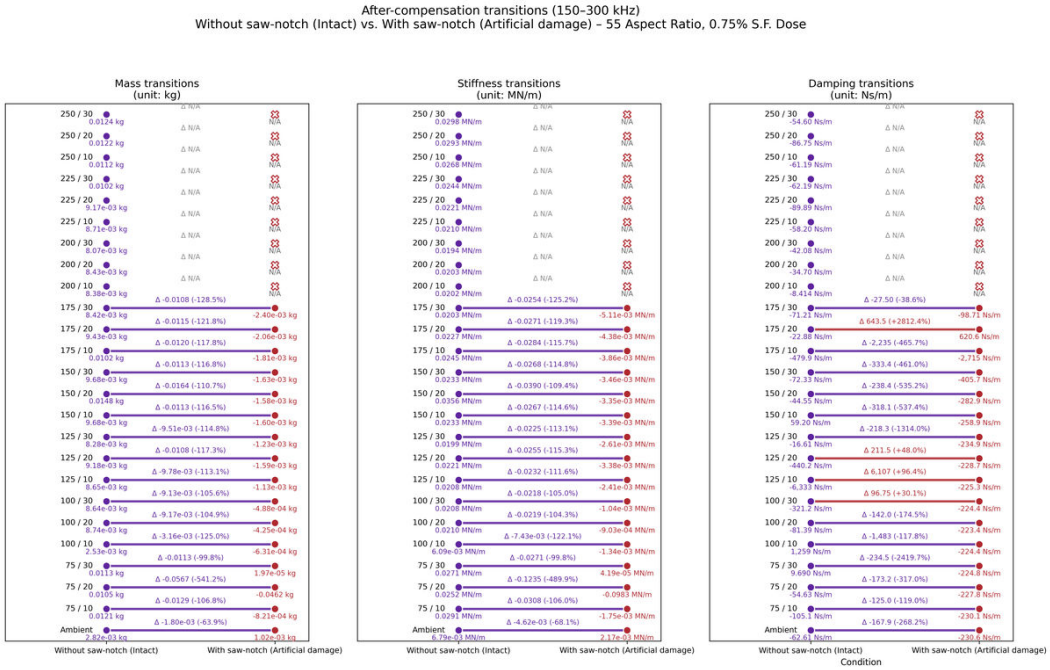

Figure 6.48: Matched intact and saw-cut EPS trajectories for SFC4 after compensation.

Table 6.114: Equivalent Mass Parameter: Intact vs Cut Comparison (After Compensation)

SFC	AR	SF	Temp Range	Intact (kg)	Cut (kg)	Change	Effect
Starting Values (75°C):							
1	65	0.5%	75-250°C	0.0278	0.0326	+17.3%	Increase
3	65	0.75%	75-175°C*	0.0272	0.0438	+61.0%	Increase
2	55	0.5%	75-250°C	0.0050	0.0215	+330.0%	Large increase
4	55	0.75%	75-175°C*	0.0296	0.0379	+28.0%	Increase
Ending Values (250°C or 175°C):*							
1	65	0.5%	75-250°C	-0.0286	0.0115	Sign change	Different sign
3	65	0.75%	75-175°C*	(at 175°C)	(at 175°C)	–	Limited data
2	55	0.5%	75-250°C	0.0617	-0.0427	Sign change	Different sign
4	55	0.75%	75-175°C*	(at 175°C)	(at 175°C)	–	Limited data

Table 6.115: Mass Temperature Drift: Intact vs Cut (75°C to End Temperature)

SFC	Configuration	End Temp	Intact Drift	Cut Drift	Direction	Observation
1	AR65/SF0.5%	250°C	-202.9%	-64.6%	Same (decrease)	Lower cut magnitude
3	AR65/SF0.75%	175°C	-361.9%	-33.4%	Same (decrease)	Lower cut magnitude
2	AR55/SF0.5%	250°C	+1128.5%	-298.2%	**Opposite**	Direction reversal
4	AR55/SF0.75%	175°C	-141.5%	-23.7%	Same (decrease)	Lower cut magnitude

SFC3 (AR65/SF0.75%) has a +61.0% difference at 75°C (0.0272 to 0.0438 kg). Over the shared 75–175°C range, the percentage change is -361.9% for the intact series and -33.4% for the saw-cut series. No saw-cut comparison is made above 175°C

because those records are unavailable.

SFC2 (AR55/SF0.5%) has the largest starting difference in this dataset, +330.0% (0.0050 to 0.0215 kg), and the direction of the end-to-end percentage change differs between intact (+1128.5%) and saw-cut (-298.2%) series.

SFC4 (AR55/SF0.75%) has a +28.0% starting difference (0.0296 to 0.0379 kg). Over the available 75–175°C range, the percentage change is -141.5% for the intact series and -23.7% for the saw-cut series.

Table 6.116 groups the four specimen-level starting differences by aspect ratio and fibre dosage. The grouped averages are descriptive: AR and dosage were not varied with independent replication, so the table cannot separate their effects from specimen-to-specimen and sensor-interface variability.

Table 6.116: Material Configuration Effect on Mass Change Due to Damage

Comparison	Parameter	Finding
Aspect Ratio Effect		
AR55 (SFC2 and SFC4)	Mean starting difference	+179%
AR65 (SFC1 and SFC3)	Mean starting difference	+39%
		Descriptive comparison
Steel Fibre Effect		
SF 0.5% (SFC1 and SFC2)	Mean starting difference	+174%
SF 0.75% (SFC3 and SFC4)	Mean starting difference	+45%
		Descriptive comparison

In summary, the fitted mass-like parameter is higher at 75°C in the saw-cut series for all four specimens, with differences from +17% to +330%. Three specimens have a lower absolute end-to-end percentage change in the saw-cut series, while SFC2 changes direction. These are specimen-level patterns within the available matched temperature ranges; they do not establish an optimal material configuration or a universal damage indicator.

6.12.1.2 Stiffness-Like Parameter Change

The equivalent stiffness parameter is a fitted stiffness-like term in the EPS model. It describes the coupled electrical–mechanical response over the analysed band and is not a direct measurement of load-bearing capacity or structural stiffness.

Figures 6.45–6.48 contain the stiffness-like trajectories together with the other EPS terms. Table 6.117 compares intact and saw-cut values at 75°C and at the last shared temperature for each specimen.

Table 6.118 shows the same numerical percentage changes reported for the fitted mass-like term because the two parameters are coupled in the adopted model. The abso-

Table 6.117: Equivalent Stiffness Parameter: Intact vs Cut Comparison (After Compensation)

SFC	AR	SF	Temp Range	Intact (MN/m)	Cut (MN/m)	Change	Observed pattern
Starting Values (75°C):							
1	65	0.5%	75-250°C	66,923	73,965	+10.5%	Increase
3	65	0.75%	75-175°C*	67,033	91,816	+37.0%	Increase
2	55	0.5%	75-250°C	12,868	52,447	+307.6%	Large increase
4	55	0.75%	75-175°C*	71,384	(similar)	∼0%	Neutral
Ending Values (250°C or 175°C):*							
1	65	0.5%	75-250°C	-68,888	26,168	Sign change	Opposite signs
3	65	0.75%	75-175°C*	(negative)	61,128	Sign change	Opposite signs
2	55	0.5%	75-250°C	158,086	-103,972	Sign reversal	Opposite signs
4	55	0.75%	75-175°C*	(at 175°C)	(at 175°C)	–	Limited data

lute end-to-end change is lower in the saw-cut series for the four reported comparisons, while SFC2 changes direction. These percentages describe fitted trajectories and are not evidence that the physical specimen became thermally stabilised after notching.

Table 6.118: Stiffness Temperature Drift: Intact vs Cut (75°C to End Temperature)

SFC	Configuration	End Temp	Intact Drift	Cut Drift	Direction	Observation
1	AR65/SF0.5%	250°C	-202.9%	-64.6%	Same (decrease)	Lower cut magnitude
3	AR65/SF0.75%	175°C	-361.9%	-33.4%	Same (decrease)	Lower cut magnitude
2	AR55/SF0.5%	250°C	+1128.5%	-298.2%	**Opposite**	Direction reversal
4	AR55/SF0.75%	175°C	-141.5%	-26.8%	Same (decrease)	Lower cut magnitude

SFC1 (AR65/SF0.5%) has a +10.5% starting difference, from 66,923 to 73,965 MN/m. Its end-to-end changes are -202.9% (intact) and -64.6% (saw-cut). The different signs at 250°C (-68,888 and 26,168 MN/m) indicate a change in the fitted model response, not an increase in physical stiffness caused by the notch.

SFC3 (AR65/SF0.75%) has a +37.0% starting difference (67,033 to 91,816 MN/m). Over the shared 75–175°C range, the percentage changes are -361.9% and -33.4% for the intact and saw-cut series, respectively.

SFC2 (AR55/SF0.5%) has the largest starting difference, +307.6% (12,868 to 52,447 MN/m), and opposite end-to-end directions in the intact (+1128.5%) and saw-cut (-298.2%) series.

SFC4 (AR55/SF0.75%) has little difference at the starting stage and end-to-end changes of -141.5% (intact) and -26.8% (saw-cut) over the available 75–175°C range. The experiment does not isolate a fibre-bridging mechanism for this difference.

Table 6.119 groups the starting differences by aspect ratio and fibre dosage. These two-specimen averages are descriptive and cannot establish independent AR or dosage effects.

Table 6.119: Material Configuration Effect on Stiffness Change Due to Damage

Comparison	Parameter	Finding
Aspect Ratio Effect		
AR55 (SFC2 and SFC4)	Mean starting difference	+154%
AR65 (SFC1 and SFC3)	Mean starting difference	+24%
		Descriptive comparison
Steel Fibre Effect		
SF 0.5% (SFC1 and SFC2)	Mean starting difference	+159%
SF 0.75% (SFC3 and SFC4)	Mean starting difference	+19%
		Descriptive comparison

The stiffness-like and mass-like parameters have matching percentage patterns because they are coupled terms in the fitted EPS representation. This agreement is an internal property of the parameterisation and should not be treated as independent validation of physical mass or stiffness changes.

In summary, three specimens have higher fitted stiffness-like values at 75°C in the saw-cut series, whereas SFC4 has little starting difference. The end-to-end magnitude is lower in the saw-cut series for all four comparisons and SFC2 changes direction. These specimen-level observations do not establish an optimal configuration or a direct measure of mechanical degradation.

6.12.1.3 Damping-Like Parameter Change

The equivalent damping parameter is the dissipative term in the fitted EPS representation. It varies differently from the coupled mass-like and stiffness-like terms in several records. The present measurements do not isolate crack friction, interface effects or other individual dissipation mechanisms, so the parameter is interpreted as a comparative model descriptor.

The damping-like trajectories are shown in Figures 6.45–6.48. Table 6.120 compares the intact and saw-cut end-to-end changes over each specimen's shared temperature range. Two specimens change direction, whereas SFC1 and SFC4 retain their respective increasing and decreasing directions.

Table 6.120: Damping Temperature Drift: Intact vs Cut (75°C to End Temperature)

SFC	Configuration	End Temp	Intact Drift	Cut Drift	Direction	Observation
1	AR65/SF0.5%	250°C	+51.0%	+63.3%	Same	Both increasing
3	AR65/SF0.75%	175°C	-132.8%	+10.5%	**Opposite**	Direction reversal
2	AR55/SF0.5%	250°C	-273.3%	+47.7%	**Opposite**	Direction reversal
4	AR55/SF0.75%	175°C	-7.6%	-5.9%	Same	Both slightly decreasing

SFC1 (AR65/SF0.5%) increases in both structural states: +51.0% for the intact series and +63.3% for the saw-cut series. The 12.3-percentage-point difference is reported descriptively; the available experiment does not identify a friction mechanism for it.

SFC3 (AR65/SF0.75%). changes from -132.8% in the intact series to +10.5% in the saw-cut series over the shared 75–175°C range.

SFC2 (AR55/SF0.5%). changes from -273.3% in the intact series to +47.7% in the saw-cut series. The direction also differs for its fitted mass-like and stiffness-like terms, but this single specimen does not establish general sensitivity for the configuration.

SFC4 (AR55/SF0.75%). decreases slightly in both states (-7.6% intact and -5.9% saw-cut) over the available range. This similarity does not demonstrate preservation of a particular internal-friction mechanism.

Table 6.121 compares the directions of the fitted terms. The damping-like term does not follow the mass-like and stiffness-like directions in every specimen, showing that it contributes non-redundant information within the fitted model.

Table 6.121: Damping Behaviour vs Mass/Stiffness Under Damage

SFC	Mass/Stiffness Direction	Damping Direction	Observed relation
1	Both decreasing	Increasing	Different directions
2	Both decreasing	Decrease to increase	Different directions
3	Increase to decrease	Decrease to increase	Opposite reversals
4	Both decreasing	Decreasing	Same direction

SFC1 has an increasing damping-like term while its mass-like and stiffness-like terms decrease. SFC3 changes damping direction while the other two fitted terms retain their direction; SFC2 changes direction in all three terms; and SFC4 retains decreasing directions. These patterns distinguish the records but do not rank the four material configurations for monitoring applications.

Table 6.122 groups these specimen-level observations by aspect ratio and fibre dosage. One reversal occurs in each AR group. The two dosage groups span different numerical ranges, but the unreplicated design does not establish an independent dosage effect.

The measured differences may contain contributions from the notch, temperature, fibre–matrix interaction, sensor interface and model fitting. Their individual contributions were not measured separately. Accordingly, the damping-like term is retained as complementary evidence and interpreted with the other EPS terms and signature indices.

Table 6.123 summarises the fitted parameter differences. SFC2 changes direction

Table 6.122: Material Configuration Effect on Damping Change Due to Damage

Comparison	Parameter	Finding
Aspect Ratio Effect		
AR55 (SFC2 and SFC4)	Direction reversals	1 of 2 specimens
AR65 (SFC1 and SFC3)	Direction reversals	1 of 2 specimens
		AR effect inconclusive
Steel Fibre Effect		
SF 0.5% (SFC1 and SFC2)	Damping drift range	+12% to +321% change
SF 0.75% (SFC3 and SFC4)	Damping drift range	+143% to +2% change
		SF 0.5% more variable

in all three terms, whereas SFC4 retains the same directions. These outcomes describe the four tested specimens and are not configuration-selection rules.

Table 6.123: Matched EPS changes between the intact and saw-cut states

SFC	Configuration	Mass Change	Stiffness Change	Damping Change
1	AR65/SF0.5%	+17%	+11%	Same direction
3	AR65/SF0.75%	+61%	+37%	**Reversal**
2	AR55/SF0.5%	+330%	+308%	**Reversal**
4	AR55/SF0.75%	+28%	∼0%	Same direction
Direction reversal:	SFC2 – all three fitted parameters			
Direction retained:	SFC4 – all three fitted parameters			

In summary, SFC2 and SFC3 change the direction of the fitted damping-like trajectory after the saw-cut, while SFC1 and SFC4 retain their directions. The damping-like term therefore supplies information that is not identical to the coupled mass-like and stiffness-like terms. Replicated specimens and direct mechanical measurements would be required before attributing these differences to fibre dosage, aspect ratio or a specific dissipation mechanism.

6.12.2 SHM Index Sensitivity to Cut Damage

This section compares each SHM index between matched intact and saw-cut records. Both conductance and susceptance are examined for the four specimens over their available common temperature ranges. The compensated results describe the index response within this experiment; they do not establish universal damage-detection performance.

6.12.2.1 RMSD Response

Root Mean Square Deviation (RMSD) quantifies the aggregate pointwise difference between a reference signature and a comparison signature. Within a matched intact–saw-cut comparison, a larger RMSD denotes a larger measured spectral difference, although that difference cannot be attributed to the saw-cut independently of the tested specimen, temperature and measurement conditions.

Figures 6.49 and 6.50 present the matched RMSD results for conductance and susceptance, respectively. The magnitude and direction of the intact–saw-cut separation vary with specimen, signal channel and temperature; the plots are therefore interpreted record by record rather than as evidence of a uniform thermal amplification of the saw-cut response.

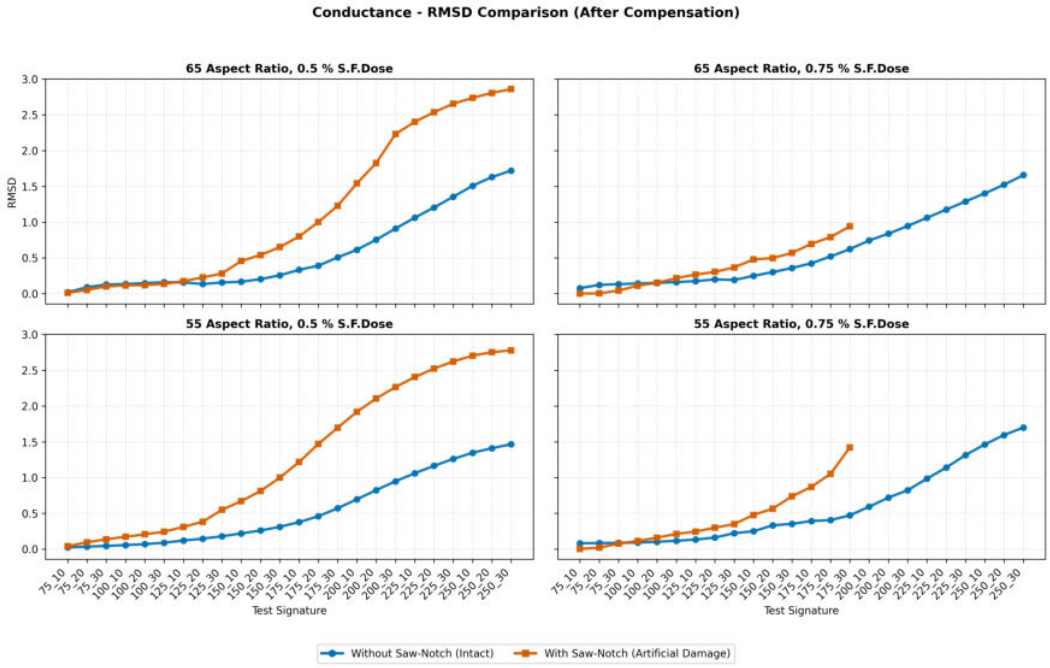

Figure 6.49: RMSD response after compensation: matched intact and saw-cut conductance records.

The quantitative analysis of RMSD damage sensitivity is presented in Tables 6.124 and 6.125 for conductance and susceptance signals, respectively. These tables summarize the mean RMSD values for intact and damaged conditions across all four specimen configurations.

For the two specimens with positive RMSD changes, the average conductance change is +118.3% and the average susceptance change is +89.0%. Table 6.126 also shows negative changes for the two 0.75% specimens in both channels. These four unreplicated comparisons do not establish a universal channel preference or a fibre-

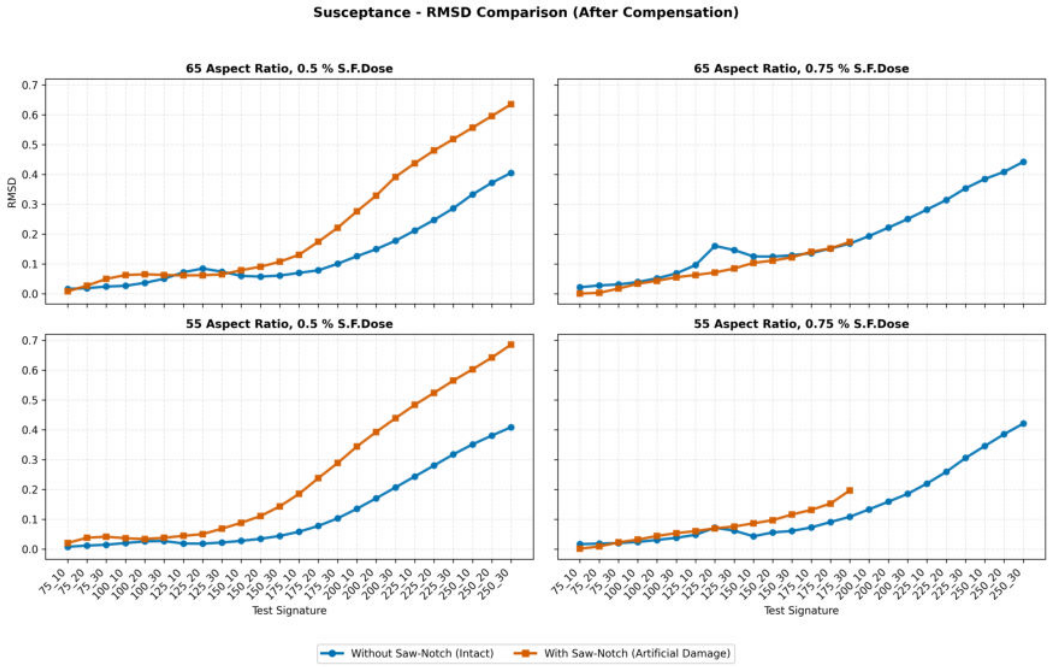

Figure 6.50: RMSD response after compensation: matched intact and saw-cut susceptance records.

Table 6.124: RMSD Damage Sensitivity: Conductance Signal (After Compensation)

SFC	AR	SF	Intact Mean	Saw-cut Mean	Change	Direction
1	65	0.5%	0.5723	1.1453	**+100.1%**	Positive
3	65	0.75%	0.6026	0.3624	-39.8%	Negative
2	55	0.5%	0.5475	1.2951	**+136.5%**	Positive
4	55	0.75%	0.5675	0.4402	-22.4%	Negative

Table 6.125: RMSD Damage Sensitivity: Susceptance Signal (After Compensation)

SFC	AR	SF	Intact Mean	Saw-cut Mean	Change	Direction
1	65	0.5%	0.1305	0.2284	**+75.0%**	Positive
3	65	0.75%	0.1801	0.0781	-56.6%	Negative
2	55	0.5%	0.1253	0.2544	**+103.0%**	Positive
4	55	0.75%	0.1323	0.0766	-42.1%	Negative

dosage effect.

Table 6.127 reports the RMSD progression for the matched intact and saw-cut records. For SFC1 (AR65/SF0.5%), the saw-cut RMSD increases from 0.055 at 75 °C to 2.801 at 250 °C. The magnitude of the matched difference changes with temperature, but the repeated sequence does not establish a controlled amplification mechanism or a transferable temperature rule.

SFC1 (AR65/SF0.5%) has positive matched changes in both channels: +100.1%

Table 6.126: RMSD Damage Sensitivity: Signal Type Comparison

SFC	Configuration	Conductance Change	Susceptance Change	Larger reported change
1	AR65/SF0.5%	+100.1%	+75.0%	Conductance
3	AR65/SF0.75%	-39.8%	-56.6%	(Both negative)
2	AR55/SF0.5%	+136.5%	+103.0%	Conductance
4	AR55/SF0.75%	-22.4%	-42.1%	(Both negative)
Average (positive cases)		+118.3%	+89.0%	**Conductance**

Table 6.127: RMSD temperature progression for matched intact and saw-cut conductance records

Configuration	State	75°C	125°C	175°C	225°C	250°C
AR65/SF0.5%	Intact	0.079	0.149	0.410	1.207	1.619
	Damaged	0.055	0.228	1.009	2.531	2.801
AR65/SF0.75%	Intact	0.111	0.188	0.522	1.175	1.527
	Damaged	0.016	0.313	0.809	–	–
AR55/SF0.5%	Intact	0.034	0.149	0.469	1.162	1.408
	Damaged	0.092	0.414	1.461	2.517	2.746
AR55/SF0.75%	Intact	0.085	0.172	0.423	1.147	1.586
	Damaged	0.033	0.298	1.114	–	–

for conductance and +75.0% for susceptance. Mean conductance RMSD changes from 0.5723 (intact) to 1.1453 (saw-cut), and the corresponding 250°C values are 1.619 and 2.801. These values describe separation in this specimen and temperature sequence, not independently validated monitoring reliability.

SFC3 (AR65/SF0.75%) has negative matched changes: -39.8% for conductance (0.6026 to 0.3624) and -56.6% for susceptance (0.1801 to 0.0781). The saw-cut series is available only to 175°C. Fibre bridging was not measured independently and is therefore not assigned as the cause of this direction.

SFC2 (AR55/SF0.5%) has the largest positive RMSD changes among the four specimens: +136.5% for conductance (0.5475 to 1.2951) and +103.0% for susceptance (0.1253 to 0.2544). Its saw-cut conductance RMSD reaches 2.746 at 250°C. One specimen does not establish an optimal AR–dosage configuration.

SFC4 (AR55/SF0.75%) also has negative changes: -22.4% for conductance (0.5675 to 0.4402) and -42.1% for susceptance (0.1323 to 0.0766). Like SFC3, its saw-cut series ends at 175°C. The common direction in these two specimens is reported as a dosage-associated pattern, not proof of a fibre-bridging mechanism.

Table 6.128 groups the four conductance changes by AR and dosage. The two 0.50% specimens are positive and the two 0.75% specimens are negative, whereas the AR-group averages retain mixed constituent directions. With one specimen per

configuration, the comparison does not identify a primary material determinant.

Table 6.128: RMSD: Material Configuration Effect on Damage Sensitivity

Comparison	Conductance	Susceptance	Finding
Aspect Ratio Effect			
AR55 (SFC2 and SFC4) avg	+57.1%	+30.4%	
AR65 (SFC1 and SFC3) avg	+30.1%	+9.2%	AR55 pair has larger mean
Steel Fibre Effect			
SF 0.5% (SFC1 and SFC2) avg	+118.3%	+89.0%	
SF 0.75% (SFC3 and SFC4) avg	-31.1%	-49.4%	**SF 0.5% far more sensitive**

In summary, conductance RMSD increases by +100% to +137% in the two 0.50% specimens and decreases by -22% to -40% in the two 0.75% specimens; susceptance follows the same direction in each specimen. The direction reversal and absence of replicated configurations preclude a general dosage rule, channel ranking or monitoring recommendation.

6.12.2.2 MAPD Response

Mean Absolute Percentage Deviation (MAPD) quantifies the relative percentage difference from a specified baseline. Its value can become unstable where baseline ordinates are close to zero, and the present analysis does not establish field thresholds.

Figures 6.51 and 6.52 presents the MAPD damage sensitivity comparison for both conductance and susceptance signals. The visual patterns closely mirror those observed for RMSD, with clear divergence between intact and specimen in the saw-cut state responses that amplifies at elevated temperatures.

Tables 6.129 and 6.130 present the matched MAPD changes. Conductance is positive for SFC1 and SFC2 and negative for SFC3 and SFC4; SFC2 has the largest reported value (+135.9%).

Table 6.129: MAPD Damage Sensitivity: Conductance Signal (After Compensation)

SFC	AR	SF	Intact Mean (%)	Saw-cut Mean (%)	Change	Direction
1	65	0.5%	56.73	110.85	**+95.4%**	Positive
3	65	0.75%	60.73	34.12	-43.8%	Negative
2	55	0.5%	51.05	120.42	**+135.9%**	Positive
4	55	0.75%	52.53	40.50	-22.9%	Negative

The susceptance results have the same direction by specimen but smaller absolute values, with SFC2 again having the largest positive change (+107.0%). The two-versus-

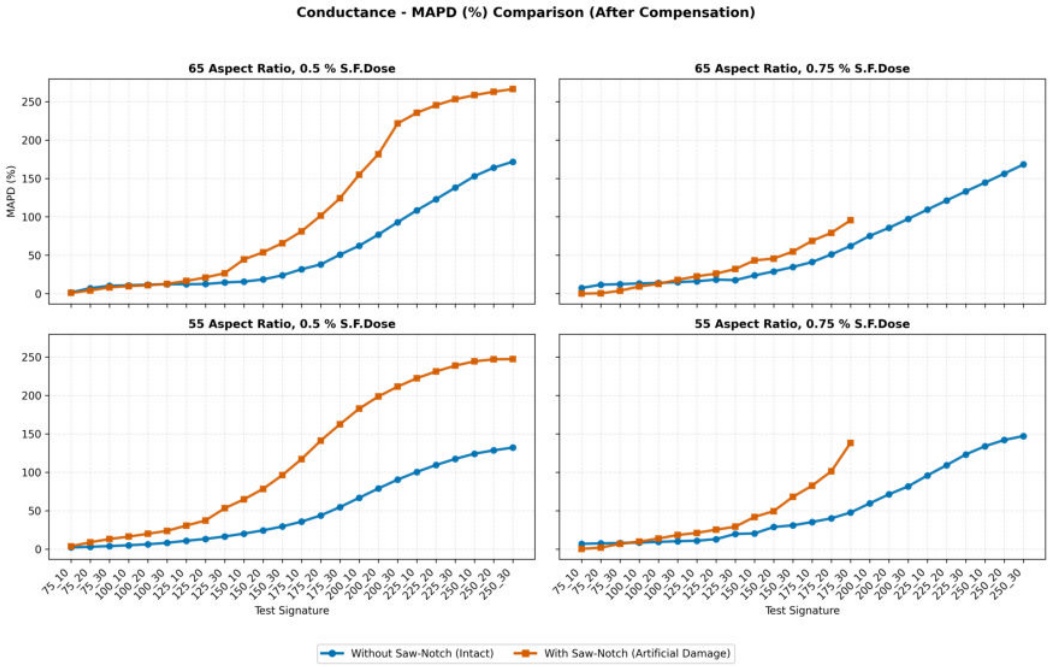

Figure 6.51: MAPD response after compensation: matched intact and saw-cut conductance records.

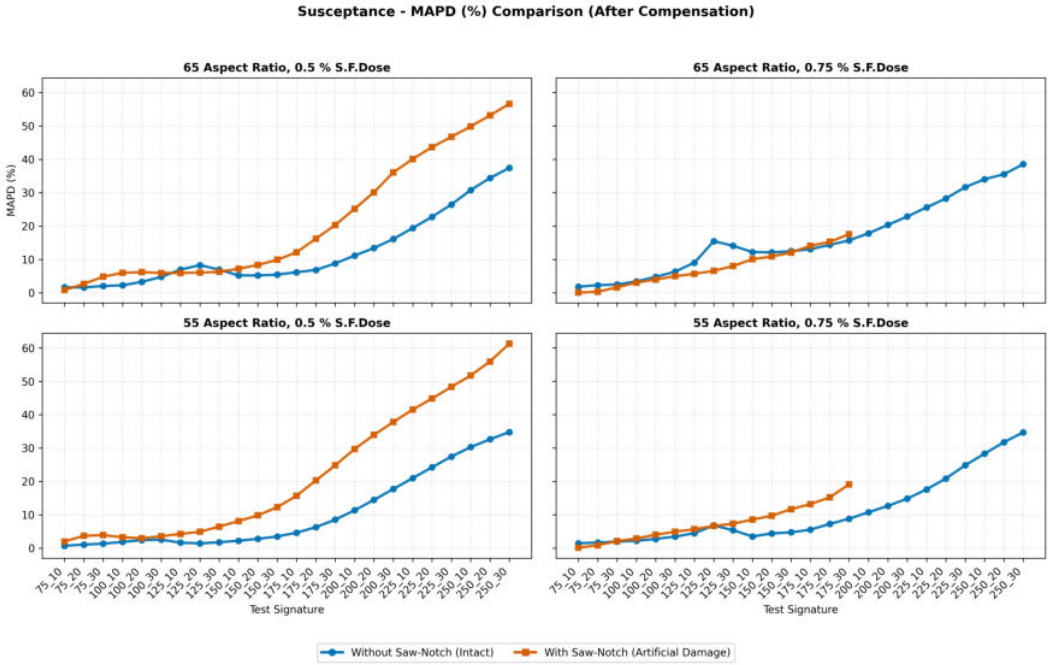

Figure 6.52: MAPD response after compensation: matched intact and saw-cut susceptance records.

two pattern is descriptive and does not establish fibre content as the determinant of detectability.

Table 6.131 compares the reported MAPD changes in conductance and suscep-

Table 6.130: MAPD Damage Sensitivity: Susceptance Signal (After Compensation)

SFC	AR	SF	Intact Mean (%)	Saw-cut Mean (%)	Change	Direction
1	65	0.5%	11.95	20.82	**+74.3%**	Positive
3	65	0.75%	16.40	7.58	-53.8%	Negative
2	55	0.5%	10.70	22.14	**+107.0%**	Positive
4	55	0.75%	10.87	7.47	-31.2%	Negative

tance. For the two configurations with positive matched changes, the averages are +115.6% for conductance and +90.6% for susceptance. The 28% relative difference describes these two records only and is not a validated improvement in detection capability.

Table 6.131: MAPD Damage Sensitivity: Signal Type Comparison

SFC	Configuration	Conductance Change	Susceptance Change	Larger reported change
1	AR65/SF0.5%	+95.4%	+74.3%	Conductance
3	AR65/SF0.75%	-43.8%	-53.8%	(Both negative)
2	AR55/SF0.5%	+135.9%	+107.0%	Conductance
4	AR55/SF0.75%	-22.9%	-31.2%	(Both negative)
Average (positive cases)		+115.6%	+90.6%	**Conductance**

Table 6.132 shows temperature-dependent changes in the matched MAPD difference. For SFC2, the saw-cut value rises from 8.53% at 75 °C to 246.16% at 250 °C, while the intact value reaches 128.25%. This is a specimen-specific endpoint comparison rather than a validated discrimination rate.

Table 6.132: MAPD temperature progression for matched intact and saw-cut conductance records

Configuration	State	75°C	125°C	175°C	225°C	250°C
AR65/SF0.5%	Intact	6.30	13.12	40.18	123.09	162.82
	Damaged	4.45	21.39	102.25	244.51	262.40
AR65/SF0.75%	Intact	10.46	17.31	51.38	121.25	156.24
	Damaged	1.41	26.89	81.08	–	–
AR55/SF0.5%	Intact	3.04	13.50	44.74	109.08	128.25
	Damaged	8.53	40.33	140.26	230.76	246.16
AR55/SF0.75%	Intact	7.43	14.54	40.97	109.41	141.01
	Damaged	3.01	25.16	107.31	–	–

SFC1 (AR65/SF0.5%) has increases of +95.4% in conductance MAPD (56.73% to 110.85%) and +74.3% in susceptance MAPD (11.95% to 20.82%). At 250°C, the conductance MAPD values are 162.82% (intact) and 262.40% (saw-cut). This is within-specimen separation, not a validated discrimination rate.

SFC3 (AR65/SF0.75%) has MAPD decreases of -43.8% for conductance (60.73% to 34.12%) and -53.8% for susceptance (16.40% to 7.58%). Its saw-cut series ends at 175°C, and neither the reduced means nor their direction are assigned to an unmeasured fibre-bridging mechanism.

SFC2 (AR55/SF0.5%) has the largest reported MAPD change, with conductance increasing by +135.9% and susceptance by +107.0%. One specimen cannot establish an optimal AR–dosage configuration or performance across other thermal histories.

SFC4 (AR55/SF0.75%) has negative changes in conductance (-22.9%) and susceptance (-31.2%), as does SFC3. This two-specimen pattern does not isolate fibre dosage as the determining factor.

The similar MAPD and RMSD directions in Table 6.133 reflect their related deviation-based definitions. They are not independent validation and do not identify an underlying physical mechanism.

Table 6.133: MAPD vs RMSD: Damage Sensitivity Pattern Comparison

Configuration	RMSD Change	MAPD Change	Consistency
AR65/SF0.5% (Cond)	+100.1%	+95.4%	Same positive direction
AR65/SF0.75% (Cond)	-39.8%	-43.8%	Same negative direction
AR55/SF0.5% (Cond)	+136.5%	+135.9%	Same positive direction
AR55/SF0.75% (Cond)	-22.4%	-22.9%	Same negative direction

The two AR55 records average +56.5% and the two AR65 records +25.8% for conductance; the 0.50% pair averages +115.6% and the 0.75% pair -33.4%. These unreplicated grouped means are confounded by specimen identity and temperature coverage and do not establish primary material effects.

In summary, MAPD follows a direction similar to RMSD: positive in the two 0.50% specimens and negative in the two 0.75% specimens. Conductance has the larger reported effect in these comparisons. MAPD remains a dataset-specific descriptive index, with percentage and near-zero-baseline limitations.

6.12.2.3 AMPD Response

Absolute Mean Percentage Deviation (AMPD) quantifies the magnitude of percentage deviations without retaining their sign. Its matched intact–saw-cut response differs between conductance and susceptance, so the two channels are reported separately.

Figures 6.53 and 6.54 present the AMPD comparison for conductance and susceptance. Conductance has positive matched changes in the two 0.50% records and negative changes in the two 0.75% records, whereas susceptance has positive changes in all four records.

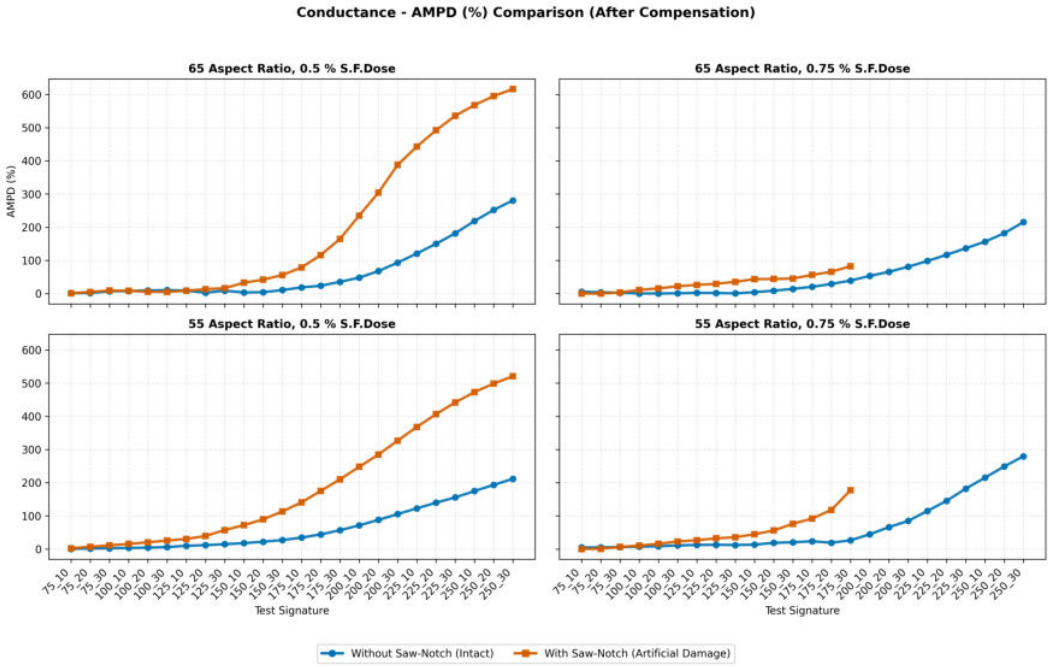

Figure 6.53: AMPD response after compensation: matched intact and saw-cut conductance records.

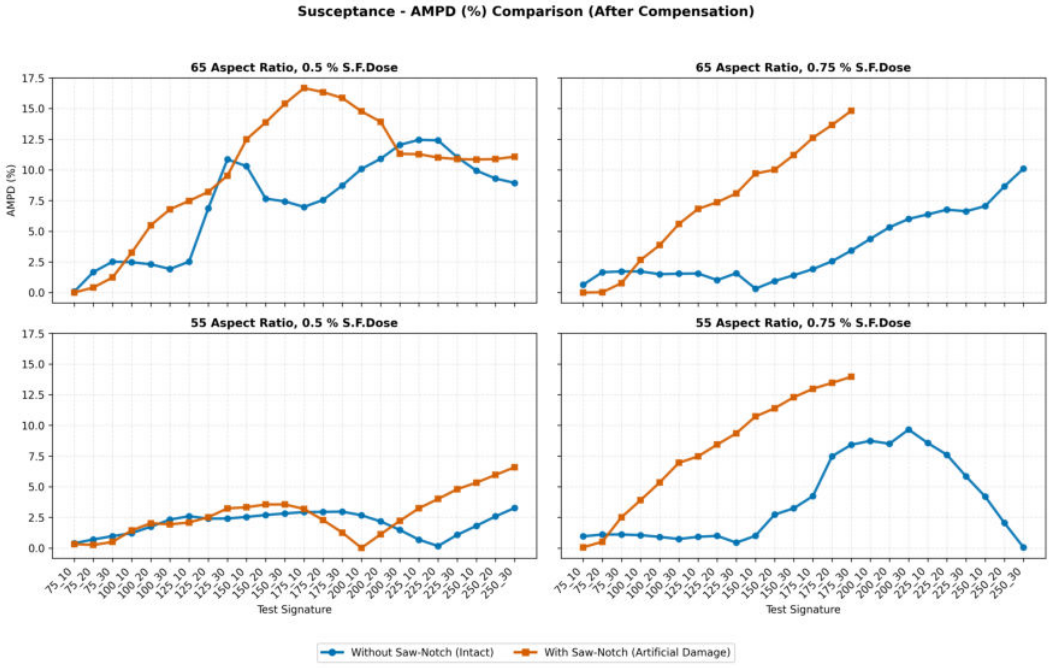

Figure 6.54: AMPD response after compensation: matched intact and saw-cut susceptance records.

Table 6.134 shows conductance changes of +202.2% and +201.1% for SFC1 and SFC2, respectively, and negative changes for SFC3 and SFC4. The AMPD percentages are larger than the corresponding RMSD and MAPD percentages, but differences in

index definition preclude a direct sensitivity ranking.

Table 6.134: AMPD Damage Sensitivity: Conductance Signal (After Compensation)

SFC	AR	SF	Intact Mean (%)	Saw-cut Mean (%)	Change	Direction
1	65	0.5%	65.37	197.56	**+202.2%**	Positive
3	65	0.75%	51.70	32.15	-37.8%	Negative
2	55	0.5%	63.36	190.76	**+201.1%**	Positive
4	55	0.75%	65.99	47.70	-27.7%	Negative

Table 6.135 shows positive changes for all four specimens: +102.3% and +111.0% for SFC3 and SFC4, and +35.1% and +36.1% for SFC1 and SFC2. This differs from the conductance direction and requires channel-specific interpretation.

Table 6.135: AMPD Damage Sensitivity: Susceptance Signal (After Compensation)

SFC	AR	SF	Intact Mean (%)	Saw-cut Mean (%)	Change	Direction
1	65	0.5%	7.37	9.96	+35.1%	Positive
3	65	0.75%	3.53	7.15	**+102.3%**	Positive
2	55	0.5%	1.98	2.70	+36.1%	Positive
4	55	0.75%	3.77	7.96	**+111.0%**	Positive

Table 6.136 highlights the channel-dependent pattern. Conductance has the larger positive change in the two 0.50% specimens (about +202%), whereas susceptance is positive in the two 0.75% specimens (about +102% to +111%) while conductance is negative. This four-specimen comparison supports retaining both channels; it does not establish a dosage-based channel-selection rule.

Table 6.136: AMPD matched intact–saw-cut comparison by signal type

SFC	Configuration	Conductance Change	Susceptance Change	Larger positive change
1	AR65/SF0.5%	**+202.2%**	+35.1%	Conductance
3	AR65/SF0.75%	-37.8%	**+102.3%**	Susceptance
2	AR55/SF0.5%	**+201.1%**	+36.1%	Conductance
4	AR55/SF0.75%	-27.7%	**+111.0%**	Susceptance

Table 6.137 shows the conductance AMPD progression. At 250°C, SFC1 reaches 593.11% in the saw-cut record and 250.58% in the intact record. These large values reflect the percentage-based definition and are compared within the same index; they do not establish a cross-index sensitivity ranking.

SFC1 (AR65/SF0.5%) has a +202.2% conductance change (65.37% to 197.56%) and a +35.1% susceptance change (7.37% to 9.96%). The saw-cut conductance AMPD

Table 6.137: AMPD temperature progression for matched intact and saw-cut conductance records

Configuration	State	75°C	125°C	175°C	225°C	250°C
AR65/SF0.5%	Intact	3.45	6.88	26.03	150.89	250.58
	Damaged	5.05	12.89	119.97	490.33	593.11
AR65/SF0.75%	Intact	4.16	1.59	29.63	117.28	184.65
	Damaged	1.25	30.44	68.29	–	–
AR55/SF0.5%	Intact	1.62	12.16	45.22	139.37	193.27
	Damaged	6.73	42.38	175.35	405.47	497.54
AR55/SF0.75%	Intact	5.37	12.58	23.02	147.46	247.89
	Damaged	2.50	31.56	129.07	–	–

reaches 593.11% at 250°C. Conductance has the larger effect for this specimen, but the result is not a general channel recommendation.

SFC3 (AR65/SF0.75%) has a -37.8% conductance change (51.70% to 32.15%) and a +102.3% susceptance change (3.53% to 7.15%). The opposite channel directions differ from the RMSD and MAPD results for this specimen and show why AMPD must be interpreted channel by channel.

SFC2 (AR55/SF0.5%) has a +201.1% conductance change (63.36% to 190.76%) and a +36.1% susceptance change (1.98% to 2.70%). Its saw-cut conductance AMPD reaches 497.54% at 250°C. Similarity to SFC1 is a two-specimen observation and does not isolate fibre dosage as the cause.

SFC4 (AR55/SF0.75%) has a +111.0% susceptance change (3.77% to 7.96%) and a -27.7% conductance change (65.99% to 47.70%). The same direction occurs in SFC3, but replicated configurations are required before assigning it to fibre dosage or claiming detection reliability.

Table 6.138 compares the reported AMPD, RMSD and MAPD directions. AMPD differs from the other two indices because its susceptance change is positive in the two 0.75% records while its conductance change is negative. This channel-dependent result does not establish AMPD as a generally preferable index.

Table 6.138: AMPD vs RMSD/MAPD: Pattern Comparison

Index	0.5% SF (Conductance)	0.75% SF (Conductance)	0.75% SF (Susceptance)
RMSD	+118%	-31%	-49%
MAPD	+116%	-33%	-42%
AMPD	**+202%**	-33%	**+107%**

In summary, AMPD has the largest reported deviation-index effect in the two 0.50% specimens and a positive susceptance change in the two 0.75% specimens.

The direction is channel-dependent. These observations do not establish a reliable conductance/susceptance selection rule for other SFRC configurations.

6.12.2.4 Correlation-Coefficient Response

The Correlation Coefficient measures the Pearson correlation between the baseline and current signals. Values near 1.0 indicate similar linear variation, while values near zero or negative indicate weak or inverse linear association. Its matched direction is determined from the present records rather than prescribed from the structural state.

Figures 6.55 and 6.56 compare CC for conductance and susceptance. CC decreases in the two 0.50% specimens and increases in the two 0.75% specimens, demonstrating a configuration-associated reversal within the analysed records.

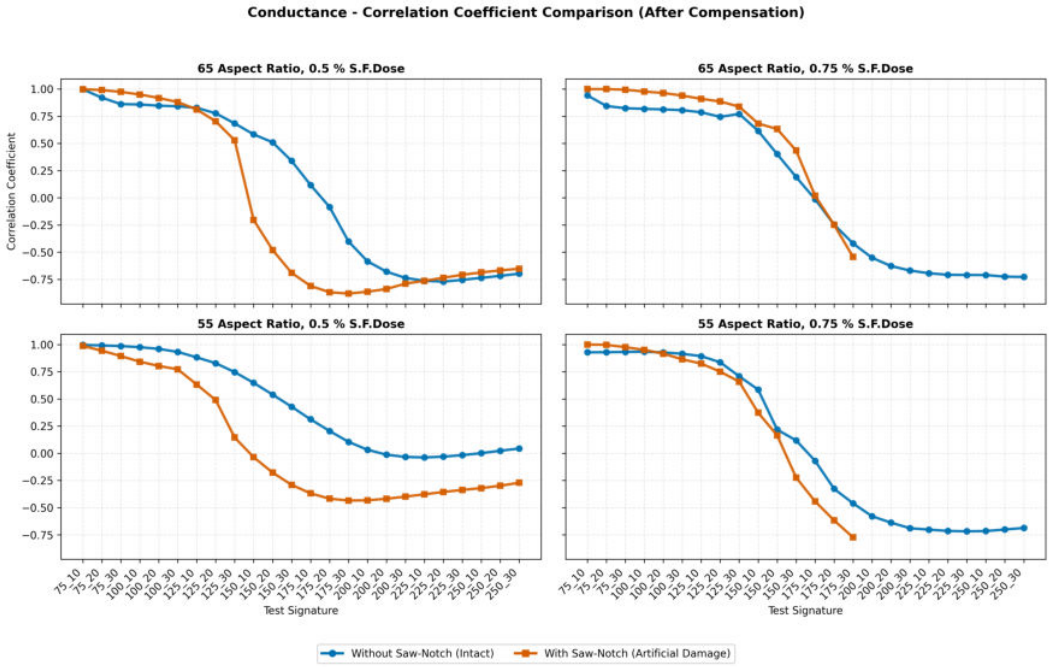

Figure 6.55: Correlation Coefficient (CC) response after compensation: matched intact and saw-cut conductance records.

Table 6.139 shows opposite matched directions: positive changes of +764.4% and +433.7% for SFC3 and SFC4, and negative changes of -228.4% and -85.0% for SFC1 and SFC2. Because the percentage is unstable when the signed reference is close to zero, these values are interpreted with their underlying CC values rather than against a prescribed damage direction.

Table 6.140 shows smaller absolute matched changes in susceptance: +17.5% for SFC3 and +20.1% for SFC4, compared with -0.5% for SFC1 and -8.7% for SFC2. The

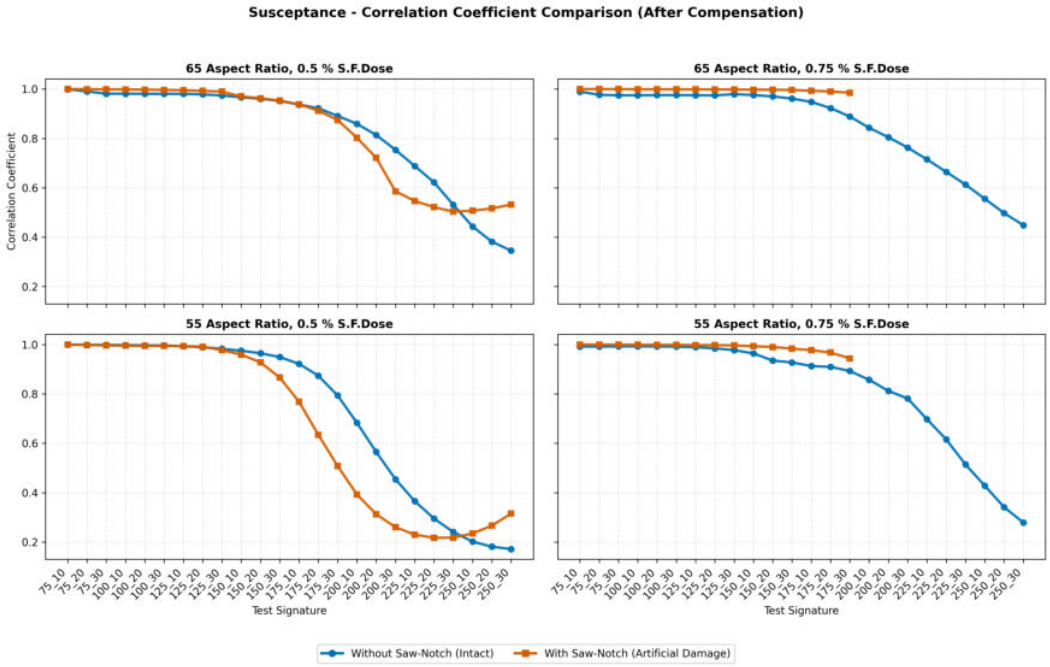

Figure 6.56: Correlation Coefficient (CC) response after compensation: matched intact and saw-cut susceptance records.

Table 6.139: Correlation Coefficient Damage Sensitivity: Conductance Signal (After Compensation)

SFC	AR	SF	Intact Mean	Saw-cut mean	Change	Behaviour
1	65	0.5%	0.0934	-0.1200	-228.4%	Normal
3	65	0.75%	0.0732	0.6325	**+764.4%**	Reversed
2	55	0.5%	0.4376	0.0655	-85.0%	Normal
4	55	0.75%	0.0802	0.4279	**+433.7%**	Reversed

larger susceptance CC levels of 0.67–0.99 reflect that channel and baseline; they are not a performance rating.

Table 6.140: Correlation Coefficient Damage Sensitivity: Susceptance Signal (After Compensation)

SFC	AR	SF	Intact Mean	Saw-cut mean	Change	Behaviour
1	65	0.5%	0.8298	0.8258	-0.5%	Minimal
3	65	0.75%	0.8487	0.9969	+17.5%	Reversed
2	55	0.5%	0.7328	0.6687	-8.7%	Normal
4	55	0.75%	0.8237	0.9896	+20.1%	Reversed

Table 6.141 shows larger CC changes in conductance and smaller changes in susceptance, with directions depending on the specimen group. In the two 0.75% specimens, CC is positive while RMSD, MAPD and AMPD are negative. This makes

CC a complementary descriptor of the present signatures, not an independently validated indicator.

Table 6.141: Correlation Coefficient Damage Sensitivity: Signal Type Comparison

SFC	Configuration	Conductance Change	Susceptance Change	Pattern
1	AR65/SF0.5%	-228.4%	-0.5%	Conductance sensitive
3	AR65/SF0.75%	+764.4%	+17.5%	Both positive
2	AR55/SF0.5%	-85.0%	-8.7%	Both negative
4	AR55/SF0.75%	+433.7%	+20.1%	Both positive

Table 6.142 shows CC values near 1.0 at the first stage and lower values at later stages. The saw-cut sequences vary by specimen: the two 0.50% records change sign earlier, while the two 0.75% records end at 175 °C. The unequal coverage precludes a degradation-rate or dosage conclusion.

Table 6.142: Correlation-coefficient temperature progression for matched intact and saw-cut conductance records

Configuration	State	75°C	125°C	175°C	225°C	250°C
AR65/SF0.5%	Intact	0.927	0.763	-0.123	-0.763	-0.717
	Damaged	0.988	0.682	-0.853	-0.736	-0.669
AR65/SF0.75%	Intact	0.870	0.768	-0.227	-0.704	-0.721
	Damaged	0.998	0.878	-0.258	–	–
AR55/SF0.5%	Intact	0.991	0.819	0.207	-0.029	0.023
	Damaged	0.941	0.422	-0.407	-0.357	-0.297
AR55/SF0.75%	Intact	0.930	0.813	-0.285	-0.711	-0.701
	Damaged	0.991	0.745	-0.611	–	–

For SFC1 (AR65/SF0.5%), the mean CC changes from 0.0934 in the intact state to -0.1200 in the saw-cut state, a -228.4% change. Both sequences move from 0.93–0.99 at 75 °C to negative values at 250 °C. At 175 °C the values are -0.853 and -0.123, respectively. These measured differences do not establish a degradation mechanism or rate.

SFC3 (AR65/SF0.75%) has a CC increase from 0.0732 to 0.6325 (+764.4%). The saw-cut value is also higher at the first measured stage (0.998 versus 0.870). CC measures similarity to the selected baseline, so an increase is not equivalent to structural improvement. No fibre-bridging mechanism is inferred.

SFC2 (AR55/SF0.5%) has a CC change from 0.4376 to 0.0655 (-85.0%). The saw-cut values remain below the intact values over the reported sequence; at 175°C they are -0.407 and 0.207, respectively. This is within-specimen separation rather than a reliability estimate.

SFC4 (AR55/SF0.75%) has a CC increase from 0.0802 to 0.4279 (+433.7%) and begins with a saw-cut value of 0.991 compared with 0.930 in the intact state. The direction is reported as a property of this matched comparison and is not attributed to fibre content or bridging.

Table 6.143 compares CC with RMSD, MAPD and AMPD. In the two 0.75% specimens the deviation indices are negative while CC is positive. This is a complementary direction within the dataset; it does not establish performance for other high-fibre-content materials.

Table 6.143: Observed directions of the correlation coefficient and RMSD in the matched records

Configuration	RMSD change	CC change	Observed relation
AR65/SF0.5%	+100%	-228%	Opposite directions
AR65/SF0.75%	-40%	+764%	Opposite directions
AR55/SF0.5%	+137%	-85%	Opposite directions
AR55/SF0.75%	-22%	+434%	Opposite directions

In summary, CC decreases in the two 0.5% specimens (-85% to -228%) and increases in the two 0.75% specimens (+434% to +764%). The reversal differs from several deviation indices and makes CC configuration-dependent in this dataset. Fibre bridging was not measured as the cause, and no dosage-specific interpretation rule is established.

6.12.2.5 CCD Response

Correlation Coefficient Deviation (CCD) is calculated from the correlation coefficient and represents departure from perfect positive correlation. Its value is algebraically dependent on CC; it is therefore not treated as independent confirmation of the same signature difference.

Figures 6.57 and 6.58 present the matched CCD records for conductance and susceptance. The magnitude and direction differ by specimen and channel, including near-zero susceptance values that restrict percentage interpretation.

Table 6.144 shows positive matched changes for SFC1 and SFC2 and negative changes for SFC3 and SFC4. SFC2 has the largest reported value (+232.7%). This two-versus-two pattern is not treated as a causal dosage effect.

Table 6.145 contains small susceptance CCD values (0.00–0.16), including rounded zeros for the two 0.75% records. These near-zero values make ratios and threshold interpretation unstable; they do not prove that the channel is intrinsically insensitive.

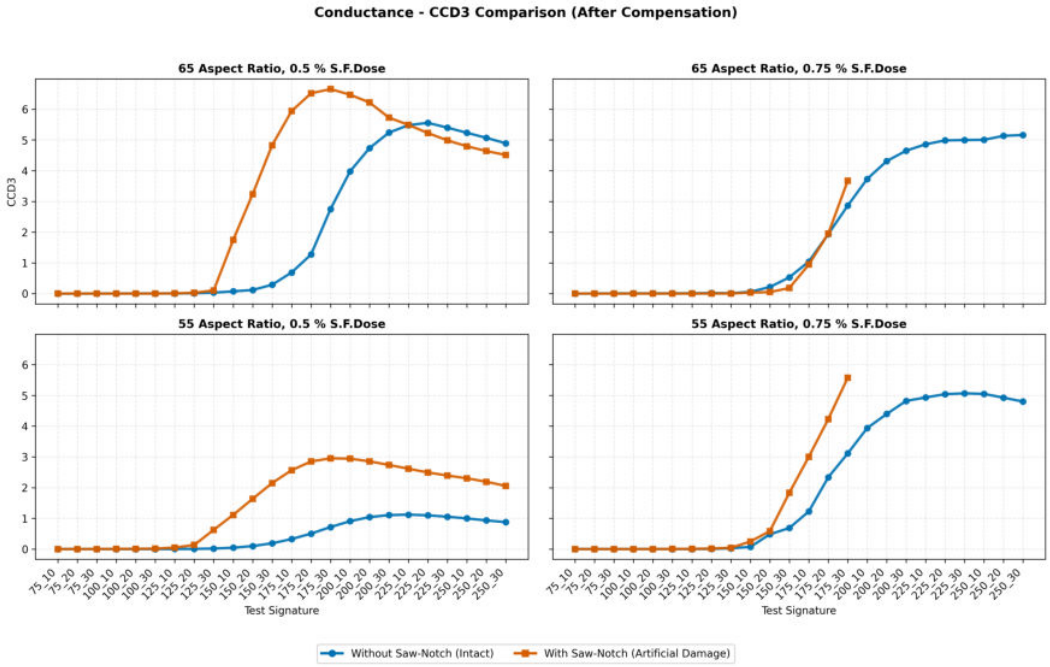

Figure 6.57: CCD response after compensation: matched intact and saw-cut conductance records.

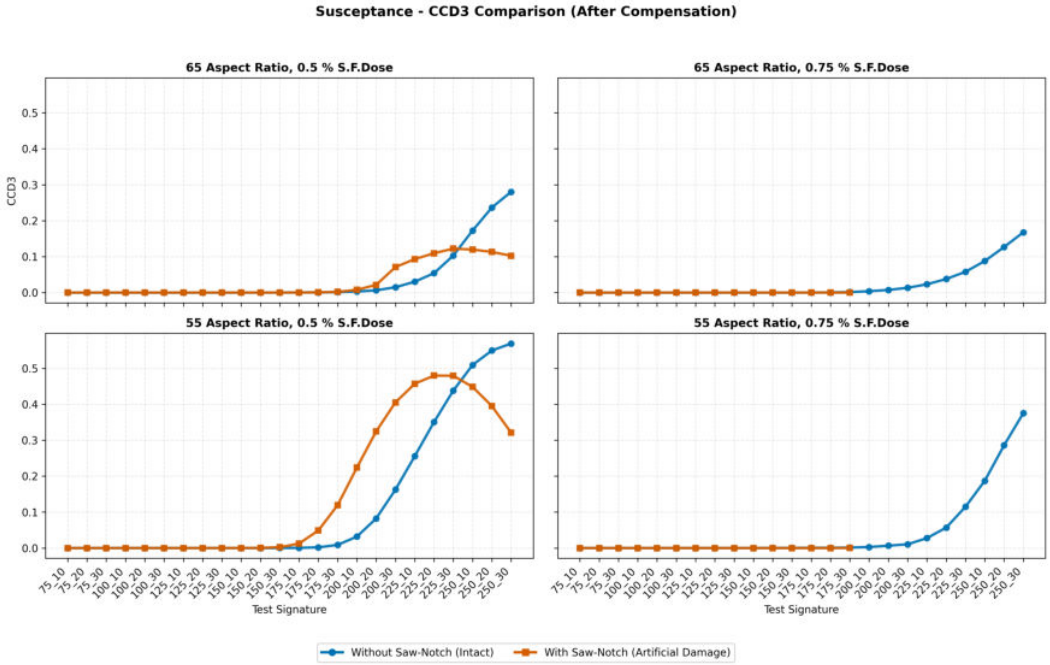

Figure 6.58: CCD response after compensation: matched intact and saw-cut susceptance records.

Table 6.146 shows larger CCD magnitudes in conductance. Susceptance CCD approaches zero in selected 0.75% records, limiting percentage and threshold interpretation; this does not establish a universally superior channel.

Table 6.144: CCD Damage Sensitivity: Conductance Signal (After Compensation)

SFC	AR	SF	Intact Mean	Saw-cut Mean	Change	Observed direction
1	65	0.5%	2.1178	3.2132	+51.7%	Positive
3	65	0.75%	2.0640	0.4556	-77.9%	Negative
2	55	0.5%	0.4592	1.5278	**+232.7%**	Positive
4	55	0.75%	2.1211	1.0352	-51.2%	Negative

Table 6.145: CCD Damage Sensitivity: Susceptance Signal (After Compensation)

SFC	AR	SF	Intact Mean	Saw-cut Mean	Change	Observed result
1	65	0.5%	0.0376	0.0318	-15.5%	Negative
3	65	0.75%	0.0220	0.0000	-100.0%	Rounded to zero
2	55	0.5%	0.1233	0.1549	+25.6%	Positive
4	55	0.75%	0.0446	0.0000	-100.0%	Rounded to zero

Table 6.146: CCD Damage Sensitivity: Signal Type Comparison

SFC	Configuration	Conductance Change	Susceptance Change	Larger magnitude
1	AR65/SF0.5%	+51.7%	-15.5%	Conductance
3	AR65/SF0.75%	-77.9%	-100% (zero)	Neither
2	AR55/SF0.5%	+232.7%	+25.6%	Conductance
4	AR55/SF0.75%	-51.2%	-100% (zero)	Neither
Average (0.5% SF only)		+142.2%	+5.1%	**Conductance**

Table 6.147 shows CCD values near zero at selected early stages and larger values later. At 175 °C, SFC2 has values of 2.789 (saw-cut) and 0.515 (intact), a within-specimen separation rather than a validated discrimination grade.

Table 6.147: CCD temperature progression for matched intact and saw-cut conductance records

Configuration	State	75°C	125°C	175°C	225°C	250°C
AR65/SF0.5%	Intact	0.001	0.016	1.571	5.479	5.064
	Damaged	0.000	0.046	6.371	5.233	4.647
AR65/SF0.75%	Intact	0.003	0.013	1.946	4.947	5.099
	Damaged	0.000	0.002	2.189	–	–
AR55/SF0.5%	Intact	0.000	0.008	0.515	1.090	0.935
	Damaged	0.000	0.269	2.789	2.499	2.182
AR55/SF0.75%	Intact	0.000	0.010	2.223	5.013	4.924
	Damaged	0.000	0.020	4.269	–	–

SFC1 (AR65/SF0.5%) has a +51.7% conductance CCD change and a -15.5% susceptance change. At 175°C, the corresponding conductance values are 6.371 for the saw-cut record and 1.571 for the intact record. Conductance has the larger reported

separation for this specimen, without establishing a general channel preference.

SFC3 (AR65/SF0.75%) has a -77.9% conductance CCD change, from 2.0640 to 0.4556, while the saw-cut susceptance mean rounds to 0.0000. The near-zero result limits ratio interpretation and does not demonstrate loss of detection capability or a fibre-bridging mechanism. Its saw-cut series ends at 175°C.

SFC2 (AR55/SF0.5%) has the largest conductance CCD change (+232.7%, from 0.4592 to 1.5278). Its saw-cut CCD exceeds the intact value from 125 °C onwards in the reported sequence. This does not establish an optimal material configuration.

SFC4 (AR55/SF0.75%) has a -51.2% conductance CCD change, while its saw-cut susceptance mean rounds to zero. The rounded value does not by itself establish loss of detection capability. At 175°C, the conductance CCD values are 4.269 for the saw-cut record and 2.223 for the intact record; this stage-level difference and the negative mean change show that the relationship varies across the measured range.

Table 6.148 compares CCD with the deviation-based indices. The two 0.50% records have positive mean changes and the two 0.75% records have negative mean changes for the listed quantities. With one specimen per configuration, this two-versus-two pattern does not establish fibre dosage as the determinant of index behaviour.

Table 6.148: CCD vs RMSD: Pattern Consistency

Configuration	RMSD Change	CCD Change	Pattern
AR65/SF0.5%	+100%	+52%	Both positive
AR65/SF0.75%	-40%	-78%	Both negative
AR55/SF0.5%	+137%	+233%	Both positive (CCD higher)
AR55/SF0.75%	-22%	-51%	Both negative

In summary, conductance CCD is positive in the two 0.50% specimens and negative in the two 0.75% specimens. Susceptance values approach zero in selected records. The result is channel- and configuration-dependent and does not support a general low-dosage application rule.

6.12.2.6 CCD^3 Response

Cubic Correlation Coefficient Deviation (CCD^3) is the algebraic cube of CCD. The transformation compresses CCD values below unity and magnifies values above unity; consequently, it changes the numerical contrast but does not provide an independent measurement or an independently validated gain in sensitivity.

Figures 6.59 and 6.60 present the matched CCD^3 results for conductance and susceptance. Cubing CCD magnifies values above unity and compresses values below

unity, so the apparent scale change is algebraically dependent on CCD rather than independent evidence.

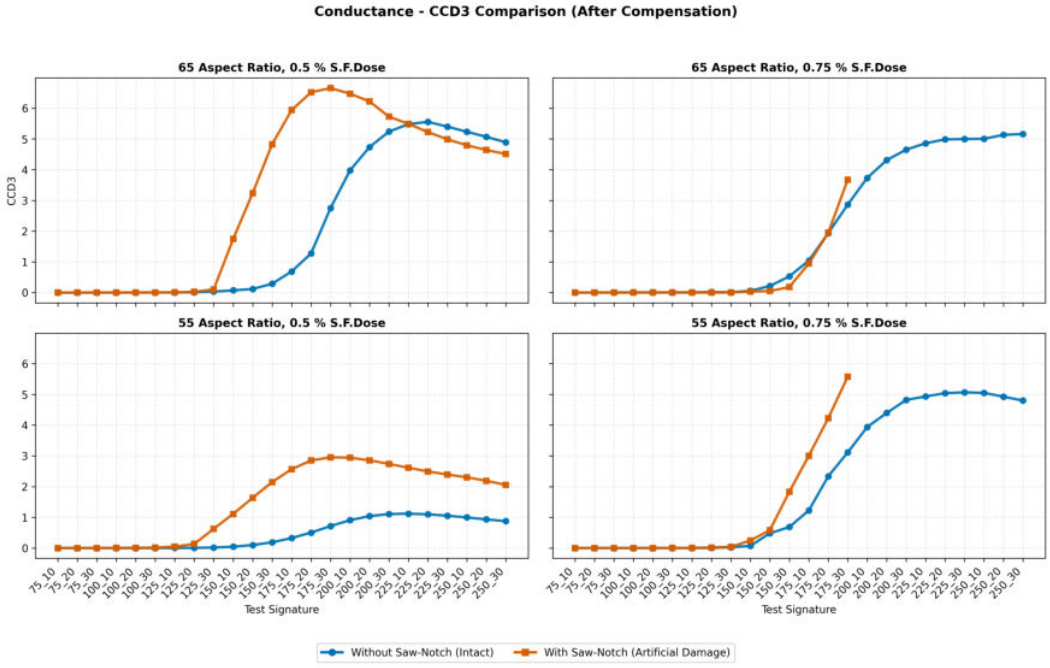

Figure 6.59: CCD[3] response after compensation: matched intact and saw-cut conductance records.

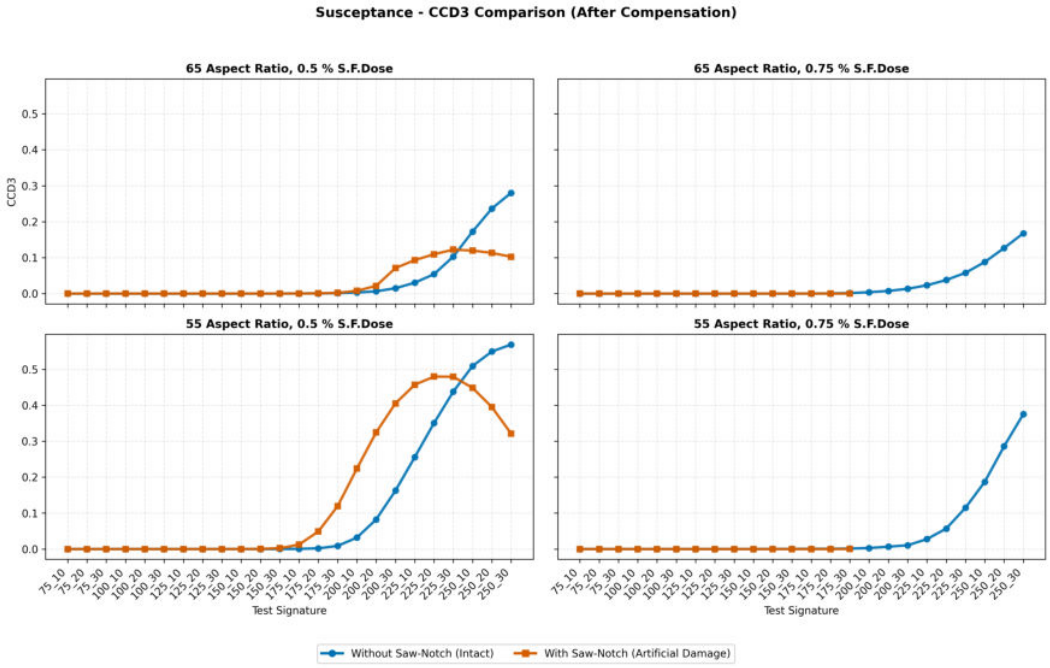

Figure 6.60: CCD[3] response after compensation: matched intact and saw-cut susceptance records.

Table 6.149 has the same directions as CCD because the values are obtained by a monotonic cubing transformation. The two 0.50% specimens have positive changes, including +232.7% for SFC2, while the two 0.75% specimens have negative changes.

Table 6.149: CCD^3 Damage Sensitivity: Conductance Signal (After Compensation)

SFC	AR	SF	Intact Mean	Saw-cut Mean	Change	Observed direction
1	65	0.5%	2.1178	3.2132	+51.7%	Positive
3	65	0.75%	2.0640	0.4556	-77.9%	Negative
2	55	0.5%	0.4592	1.5278	**+232.7%**	Positive
4	55	0.75%	2.1211	1.0352	-51.2%	Negative

The susceptance values are small and round to zero in the two 0.75% records, which limits ratio interpretation. SFC2 has a positive reported change of +25.6%; the remaining directions vary. Rounded zeros do not establish loss of detection capability.

Table 6.150: CCD^3 Damage Sensitivity: Susceptance Signal (After Compensation)

SFC	AR	SF	Intact Mean	Saw-cut mean	Change	Observed direction
1	65	0.5%	0.0376	0.0318	-15.5%	Negative
3	65	0.75%	0.0220	0.0000	-100.0%	Rounded to zero
2	55	0.5%	0.1233	0.1549	+25.6%	Positive
4	55	0.75%	0.0446	0.0000	-100.0%	Zero signal

SFC1 (AR65/SF0.5%) has a +51.7% conductance CCD^3 change and values of 6.371 (saw-cut) and 1.571 (intact) at 175 °C. Susceptance has a smaller magnitude and opposite direction in selected records; no general channel recommendation is made.

SFC3 (AR65/SF0.75%) has a -77.9% conductance change, while the reported saw-cut susceptance value is 0.0000. The near-zero value limits ratio interpretation; it does not prove loss of detection capability for a material class.

SFC2 (AR55/SF0.5%) has the largest conductance CCD^3 change in the four-specimen comparison, +232.7% (0.4592 to 1.5278), while susceptance changes by +25.6%. Conductance has the larger reported effect for this specimen; no optimal configuration or general channel preference follows from this comparison.

SFC4 (AR55/SF0.75%) has a -51.2% conductance change and a reported near-zero saw-cut susceptance value. Together with SFC3, this is an observed two-specimen direction and not proof that higher fibre dosage prevents a positive response.

In summary, CCD^3 preserves the direction of CCD because it is a cubic transformation of the same correlation deviation. It is not independent evidence. Conductance values are larger in these records, while near-zero susceptance values restrict interpretation.

6.12.2.7 CCV Response

Correlation Coefficient Value (CCV) is a correlation-derived metric used here to compare the intact and saw-cut signatures. Its matched mean change is positive for all four specimens in both channels; this reported direction is evaluated without imposing a universal expected sign.

Figures 6.61 and 6.62 present the matched CCV comparison for conductance and susceptance. The saw-cut mean exceeds the intact mean in each of the eight specimen–channel comparisons.

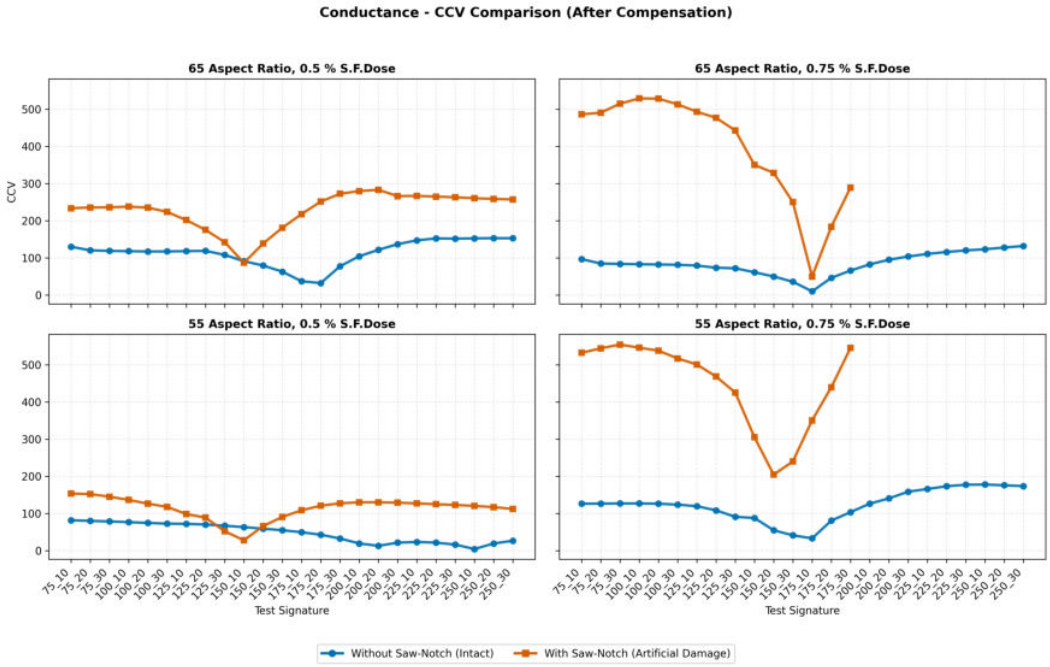

Figure 6.61: CCV response after compensation: matched intact and saw-cut conductance records.

Table 6.151 shows positive conductance changes in all four specimens, ranging from +101.1% to +369.9%. Unlike several other deviation indices, CCV is also positive for the two 0.75% specimens in this dataset.

Table 6.151: CCV Damage Sensitivity: Conductance Signal (After Compensation)

SFC	AR	SF	Intact Mean	Saw-cut Mean	Change	Direction
1	65	0.5%	113.41	228.03	+101.1%	Positive
3	65	0.75%	84.12	395.27	**+369.9%**	Positive
2	55	0.5%	47.27	113.32	+139.7%	Positive
4	55	0.75%	122.51	447.29	**+265.1%**	Positive

Table 6.152 likewise shows positive susceptance changes in all four specimens,

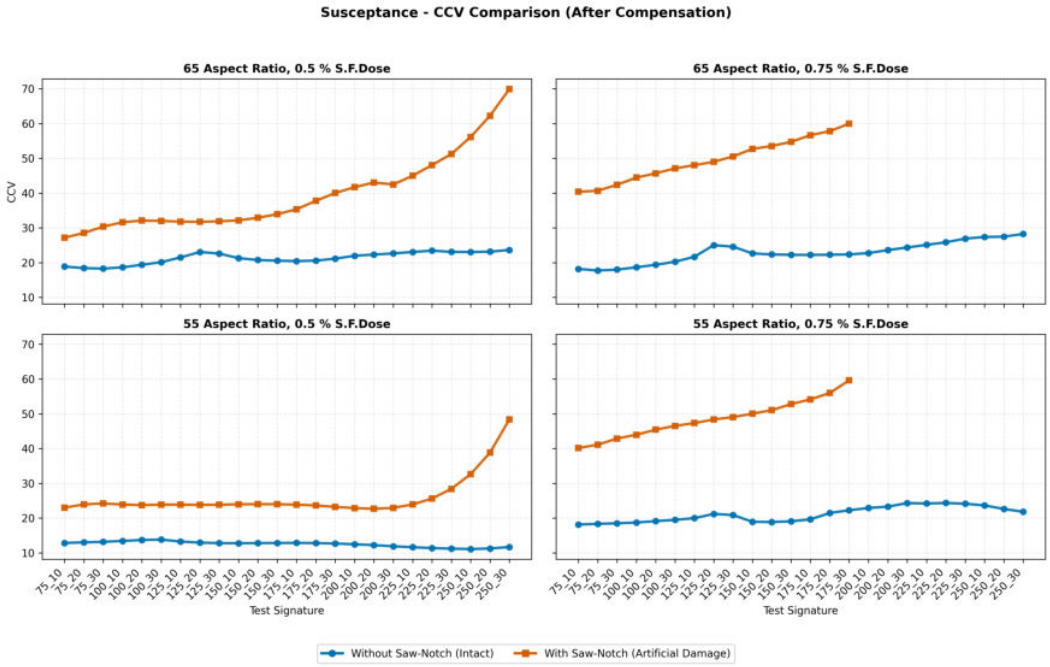

Figure 6.62: CCV response after compensation: matched intact and saw-cut susceptance records.

from +85.3% to +130.4%. The consistent direction across the eight specimen–channel comparisons makes CCV a candidate for replicated evaluation, not a validated universal detector.

Table 6.152: CCV Damage Sensitivity: Susceptance Signal (After Compensation)

SFC	AR	SF	Intact Mean	Saw-cut Mean	Change	Direction
1	65	0.5%	21.34	39.54	+85.3%	Positive
3	65	0.75%	22.89	49.58	+116.6%	Positive
2	55	0.5%	12.53	25.96	+107.3%	Positive
4	55	0.75%	21.08	48.56	**+130.4%**	Positive

Table 6.153 shows positive changes in both channels for all four specimens. Conductance has the larger change in the two 0.75% specimens, whereas the channel magnitudes are closer in the two 0.5% specimens. This is a same-direction result within the dataset, not proof of configuration-independent detection.

SFC1 (AR65/SF0.5%) has increases of +101.1% in conductance CCV (113.41 to 228.03) and +85.3% in susceptance CCV (21.34 to 39.54). At 250°C, the conductance values are 152.92 (intact) and 258.91 (saw-cut).

SFC3 (AR65/SF0.75%) has the largest conductance CCV change, +369.9% (84.12 to 395.27), and a +116.6% susceptance change. This direction differs from several other deviation indices for the same specimen; the experiment does not isolate fibre dosage as

Table 6.153: CCV intact–saw-cut comparison by signal type

SFC	Configuration	Conductance Change	Susceptance Change	Result
1	AR65/SF0.5%	+101.1%	+85.3%	Both positive
3	AR65/SF0.75%	**+369.9%**	+116.6%	Both positive
2	AR55/SF0.5%	+139.7%	+107.3%	Both positive
4	AR55/SF0.75%	**+265.1%**	+130.4%	Both positive
All four specimens have positive matched changes in both channels.				

the cause.

SFC2 (AR55/SF0.5%) has increases of +139.7% in conductance CCV (47.27 to 113.32) and +107.3% in susceptance CCV. At 250°C, the conductance values are 16.46 (intact) and 116.27 (saw-cut).

SFC4 (AR55/SF0.75%) has increases of +265.1% in conductance CCV (122.51 to 447.29) and +130.4% in susceptance CCV. As for SFC3, the positive direction contrasts with several other indices, but no material mechanism is inferred from the two specimens.

Table 6.154 compares CCV with the deviation-based indices. CCV has a positive matched change in all four tested specimens, including the two 0.75% records in which several deviation indices change in the opposite direction.

Table 6.154: Direction of CCV and other deviation-index changes in the tested specimens

Index	SF 0.5% Response	SF 0.75% Response	Observed direction
RMSD	Positive (+100-137%)	Negative (-22 to -40%)	No
MAPD	Positive (+95-136%)	Negative (-23 to -44%)	No
CCD	Positive (+52-233%)	Negative (-51 to -78%)	No
CCV	Positive (+101–140%)	Positive (+265–370%)	Positive in all four specimens

In summary, CCV is positive in all eight reported specimen–channel combinations. The two 0.75% specimens have the largest effects (+265% to +370%). This consistent direction makes CCV a candidate for replicated evaluation, but it does not establish universal sensitivity, a primary-indicator role or transfer to high-fibre-content structures generally.

6.12.2.8 MSE Response

MSE quantifies the squared deviation between the baseline and current signals and therefore weights larger pointwise deviations more heavily than a linear absolute-difference measure. Its matched direction is reported from the measurements rather than prescribed by structural state.

Figures 6.63 and 6.64 presents the visual comparison of MSE damage sensitivity for both conductance and susceptance signals. The plots reveal that specimens in the saw-cut state consistently show higher MSE values at elevated temperatures, with the divergence becoming most pronounced at test signatures above 175°C.

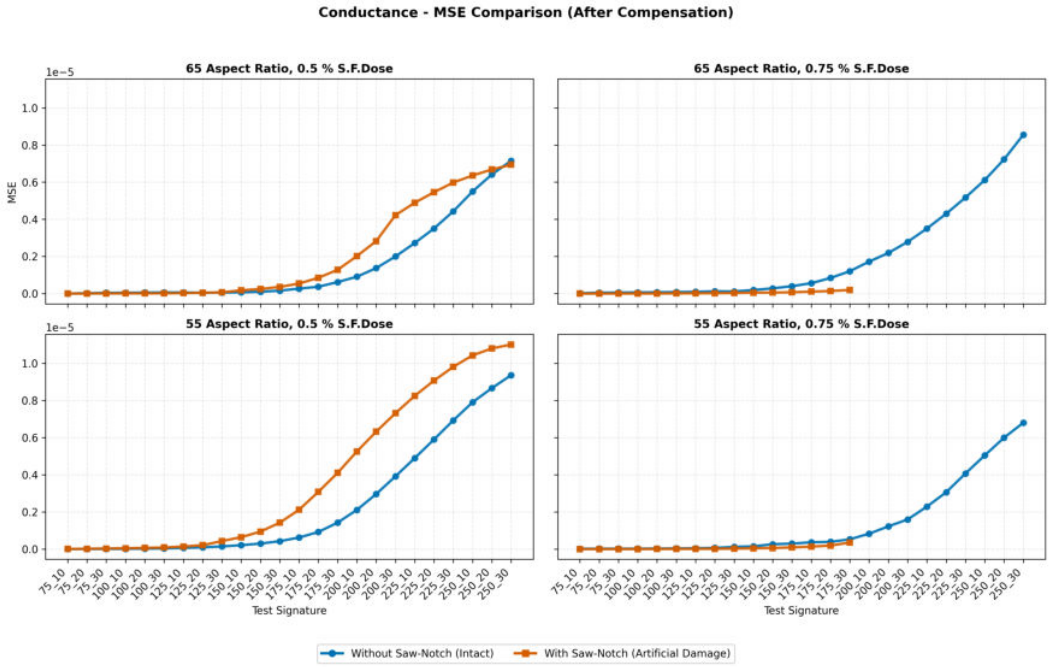

Figure 6.63: MSE response after compensation: matched intact and saw-cut conductance records.

The conductance signal analysis in Table 6.155 reveals the familiar SF-dependent pattern observed for RMSD, MAPD, and CCD. The 0.5% SF configurations show positive response (+36.3% for SFC1 and +60.9% for SFC2), while the 0.75% SF configurations show strongly negative response (-97.5% for SFC3 and -95.6% for SFC4).

Table 6.155: MSE Damage Sensitivity: Conductance Signal (After Compensation)

SFC	AR	SF	Intact Mean	Saw-cut mean	Change
1	65	0.5%	∼0 (1e-5 scale)	∼0 (1e-5 scale)	+36.3%
3	65	0.75%	∼0 (1e-5 scale)	∼0 (1e-5 scale)	-97.5%
2	55	0.5%	∼0 (1e-5 scale)	∼0 (1e-5 scale)	+60.9%
4	55	0.75%	∼0 (1e-5 scale)	∼0 (1e-5 scale)	-95.6%

Table 6.156 shows changes of +125.0% for SFC2 and +110.1% for SFC1, compared with -93.4% for SFC3 and -90.0% for SFC4. These directions are configuration-associated observations within the tested records.

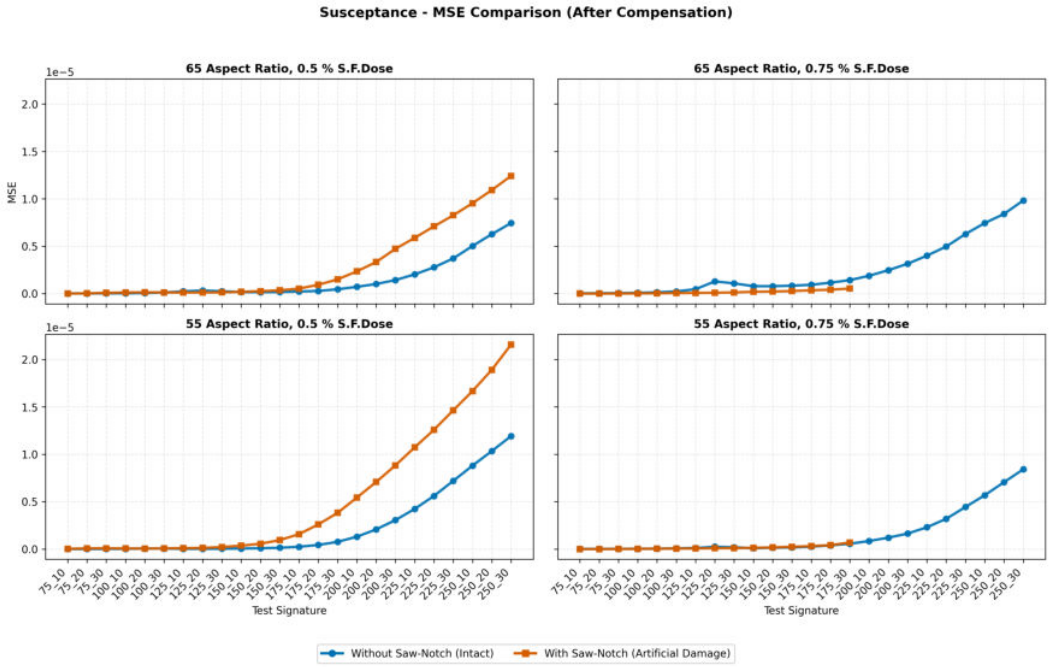

Figure 6.64: MSE response after compensation: matched intact and saw-cut susceptance records.

Table 6.156: MSE Damage Sensitivity: Susceptance Signal (After Compensation)

SFC	AR	SF	Intact Mean	Saw-cut mean	Change
1	65	0.5%	∼0 (1e-5 scale)	∼0 (1e-5 scale)	+110.1%
3	65	0.75%	∼0 (1e-5 scale)	∼0 (1e-5 scale)	-93.4%
2	55	0.5%	∼0 (1e-5 scale)	∼0 (1e-5 scale)	**+125.0%**
4	55	0.75%	∼0 (1e-5 scale)	∼0 (1e-5 scale)	-90.0%

For the two 0.50% specimens, Table 6.157 gives an average change of +117.5% in susceptance and +48.6% in conductance. Both channels have negative changes for the two 0.75% specimens. The signs do not constitute success or failure criteria outside this dataset.

Table 6.157: MSE Damage Sensitivity: Signal Type Comparison

SFC	Configuration	Conductance Change	Susceptance Change	Larger reported change
1	AR65/SF0.5%	+36.3%	+110.1%	Susceptance
3	AR65/SF0.75%	-97.5%	-93.4%	Neither
2	AR55/SF0.5%	+60.9%	+125.0%	Susceptance
4	AR55/SF0.75%	-95.6%	-90.0%	Neither
Average (0.5% SF)		+48.6%	+117.5%	**Susceptance**
Average (0.75% SF)		-96.6%	-91.7%	Neither

SFC1 (AR65/SF0.5%) has conductance and susceptance changes of +36.3%

and +110.1%, respectively. The figure shows larger later-stage saw-cut values. This single-specimen result does not establish effectiveness for low-dosage applications.

SFC3 (AR65/SF0.75%) has negative conductance and susceptance changes of -97.5% and -93.4%. The saw-cut curve crosses below the intact curve in selected stages. No dosage mechanism or general application exclusion is inferred.

SFC2 (AR55/SF0.5%) has the largest reported MSE changes, +125.0% in susceptance and +60.9% in conductance. The plot shows the largest absolute difference in selected later stages, but the unreplicated configuration does not establish optimal AR–dosage conditions.

SFC4 (AR55/SF0.75%) has negative changes of -95.6% in conductance and -90.0% in susceptance, similar in direction to SFC3. The two-record pattern does not establish that dosage prevents a positive response or that fibre bridging controls the squared deviation.

The comparison between MSE and RMSD is presented in Table 6.158. For the four tested configurations, the two indices have the same reported direction within each specimen, while their percentage magnitudes differ because MSE and RMSD use different scaling. This agreement is descriptive of the analysed records and does not establish an SF-content effect.

Table 6.158: MSE vs RMSD: Pattern Consistency

Configuration	**RMSD Change**	**MSE Change (Susceptance)**
AR65/SF0.5%	+100%	+110%
AR65/SF0.75%	-40%	-93%
AR55/SF0.5%	+137%	+125%
AR55/SF0.75%	-22%	-90%
Pattern	Consistent: positive for 0.5% SF, negative for 0.75% SF	

In summary, MSE is positive in the two 0.50% specimens and negative in the two 0.75% specimens, with a larger susceptance effect in the former pair. The reversed direction precludes a transferable channel or dosage recommendation.

6.12.2.9 Variance Response

Variance measures dispersion around the mean of a signature. Unlike MSE, it does not directly compare pointwise values with a baseline. Its direction after the saw-cut is therefore determined empirically rather than assumed to increase.

Figures 6.65 and 6.66 present the matched variance responses for conductance and susceptance. The observed directions are configuration- and channel-dependent and differ from those of several deviation-based indices.

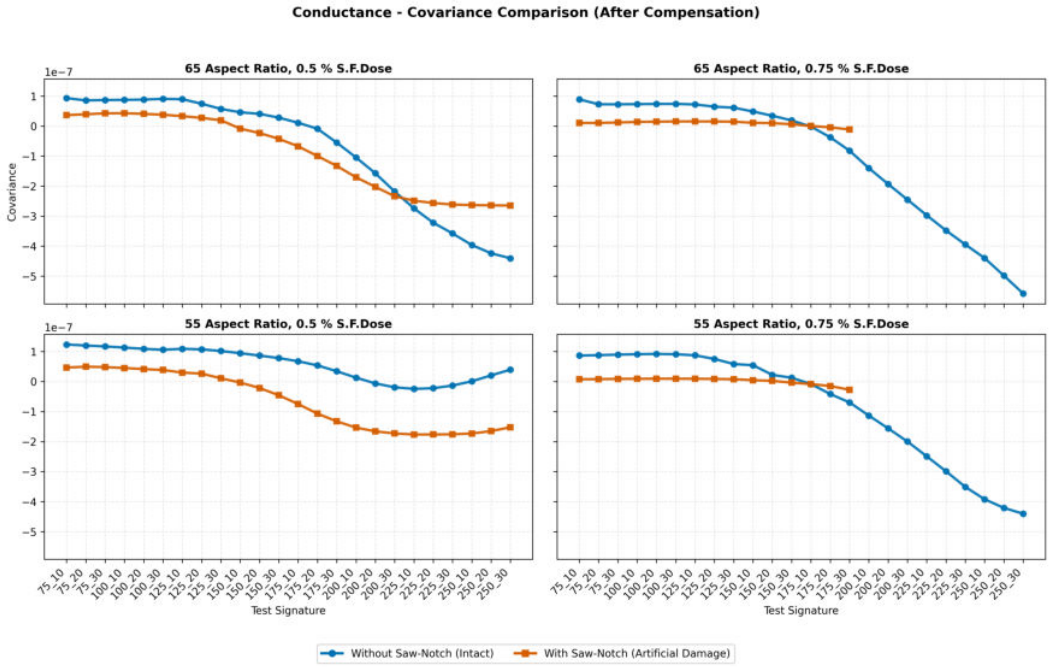

Figure 6.65: Variance response after compensation: matched intact and saw-cut conductance records.

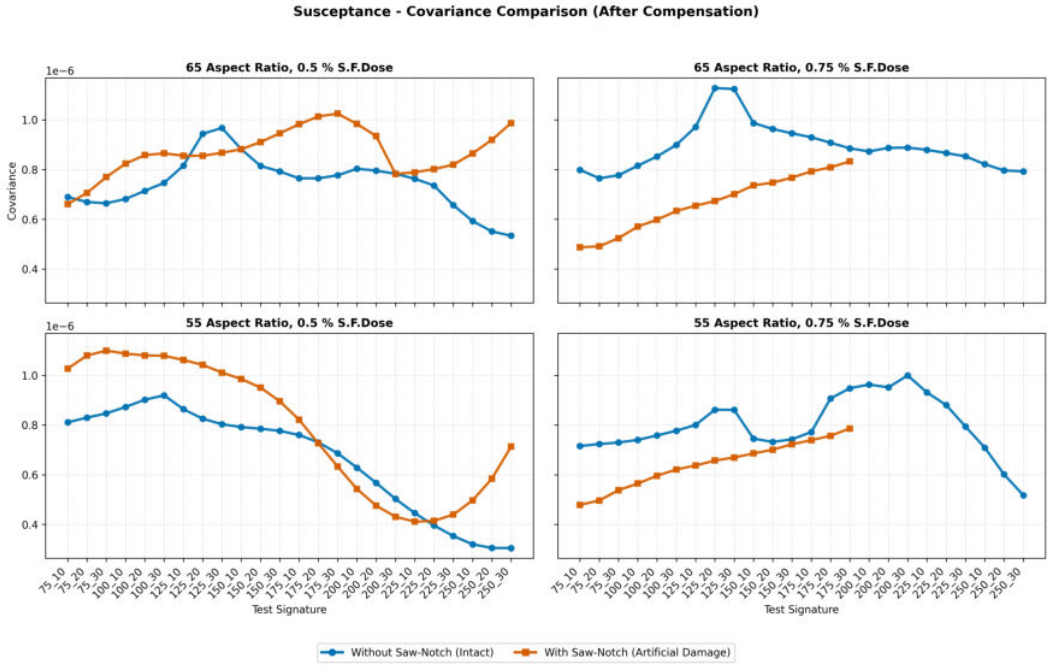

Figure 6.66: Variance response after compensation: matched intact and saw-cut susceptance records.

Table 6.159 shows the opposite direction to RMSD, MAPD and MSE: +108.7% for SFC3 and +102.6% for SFC4, compared with -18.1% for SFC1 and -210.6% for SFC2.

Table 6.159: Variance Damage Sensitivity: Conductance Signal (After Compensation) – REVERSED PATTERN

SFC	AR	SF	Intact Mean	Saw-cut mean	Change
1	65	0.5%	∼0 (1e-7 scale)	∼0 (1e-7 scale)	-18.1%
3	65	0.75%	∼0 (1e-7 scale)	∼0 (1e-7 scale)	**+108.7%**
2	55	0.5%	∼0 (1e-7 scale)	∼0 (1e-7 scale)	-210.6%
4	55	0.75%	∼0 (1e-7 scale)	∼0 (1e-7 scale)	**+102.6%**

The susceptance signal analysis in Table 6.160 shows lower magnitude changes but maintains the reversed pattern. The 0.5% SF configurations show positive response (+16.8% for SFC1 and +19.1% for SFC2), while the 0.75% SF configurations show negative response (-25.1% for SFC3 and -19.4% for SFC4).

Table 6.160: Variance Damage Sensitivity: Susceptance Signal (After Compensation)

SFC	AR	SF	Intact Mean	Saw-cut mean	Change
1	65	0.5%	∼0 (1e-6 scale)	∼0 (1e-6 scale)	+16.8%
3	65	0.75%	∼0 (1e-6 scale)	∼0 (1e-6 scale)	-25.1%
2	55	0.5%	∼0 (1e-6 scale)	∼0 (1e-6 scale)	+19.1%
4	55	0.75%	∼0 (1e-6 scale)	∼0 (1e-6 scale)	-19.4%

The signal type comparison in Table 6.161 reveals complementary behaviour between the two signals. For 0.75% SF configurations, conductance provides positive response while susceptance shows negative. For 0.5% SF, susceptance provides modest positive response while conductance shows negative. This complementary pattern suggests potential for combined signal analysis.

Table 6.161: Variance Damage Sensitivity: Signal Type Comparison – Complementary Pattern

SFC	Configuration	Conductance Change	Susceptance Change	Observed pattern
1	AR65/SF0.5%	-18.1%	+16.8%	Susceptance
3	AR65/SF0.75%	+108.7%	-25.1%	Conductance
2	AR55/SF0.5%	-210.6%	+19.1%	Susceptance
4	AR55/SF0.75%	+102.6%	-19.4%	Conductance
Pattern: Conductance for 0.75% SF, Susceptance for 0.5% SF				

For SFC1 (AR65/SF0.5%), conductance changes by -18.1% and susceptance by +16.8%. This differs from the conductance direction observed for RMSD and MAPD in the same specimen. The two channels therefore provide different descriptions of the matched records, but the comparison does not establish a preferred channel or validated detection capability.

SFC3 (AR65/SF0.75%) has a +108.7% conductance change and a -25.1% susceptance change, opposite to the conductance direction of several deviation indices. This shows that variance and deviation measures describe different properties of the same signatures; it does not establish failure of those indices or a dosage-specific selection rule.

SFC2 (AR55/SF0.5%) has the largest negative conductance change (-210.6%) and a positive susceptance change (+19.1%). The same specimen has the largest RMSD change (+137%), illustrating that variance and deviation metrics describe different properties of the paired signatures. These specimen-level directions are not an optimal/worst material ranking.

For SFC4 (AR55/SF0.75%), the conductance change is +102.6% and the susceptance change is -19.4%. The conductance direction matches SFC3 and differs from RMSD. Because each configuration is represented once, this does not establish a dosage effect or an index-selection rule.

The comparison between Variance and RMSD is presented in Table 6.162. This reveals a complementary relationship where the indices show opposite sensitivity patterns based on SF content.

Table 6.162: Observed variance and RMSD directions in the matched records

Configuration	RMSD change	Variance change (cond.)	Observed relation
AR65/SF0.5%	+100%	-18%	Opposite directions
AR65/SF0.75%	-40%	+109%	Opposite directions
AR55/SF0.5%	+137%	-211%	Opposite directions
AR55/SF0.75%	-22%	+103%	Opposite directions

In summary, the signed variance-related index has positive conductance changes in the two 0.75% specimens (+103% to +109%) and negative changes in the two 0.5% specimens (-18% to -211%); susceptance has different directions. The reversal is complementary to several deviation indices in this dataset but does not establish a dosage-specific channel rule.

6.12.2.10 RMS Response

Root Mean Square (RMS) quantifies overall signal magnitude. Unlike deviation-based indices, it does not compare the signature pointwise with a baseline. Its direction after the saw-cut is therefore reported from the measurements without assigning a signal-transmission mechanism.

Figures 6.67 and 6.68 present the RMS comparison for conductance and susceptance. The saw-cut values are lower than the intact values in all eight reported

specimen–channel combinations; this is a within-dataset direction, not evidence of universal sensitivity.

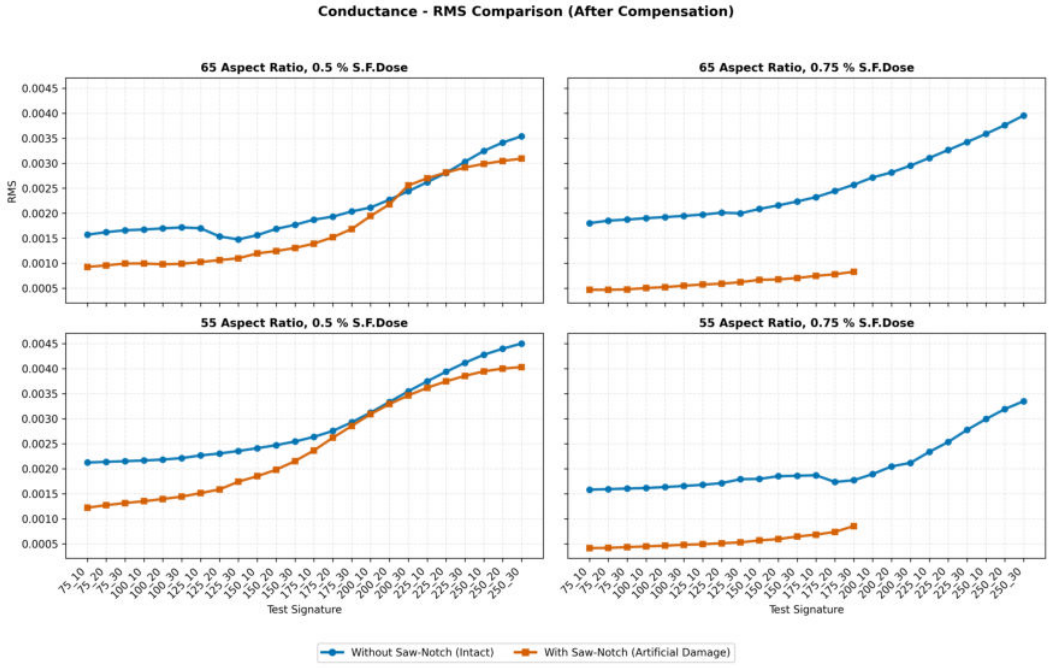

Figure 6.67: RMS response after compensation: matched intact and saw-cut conductance records.

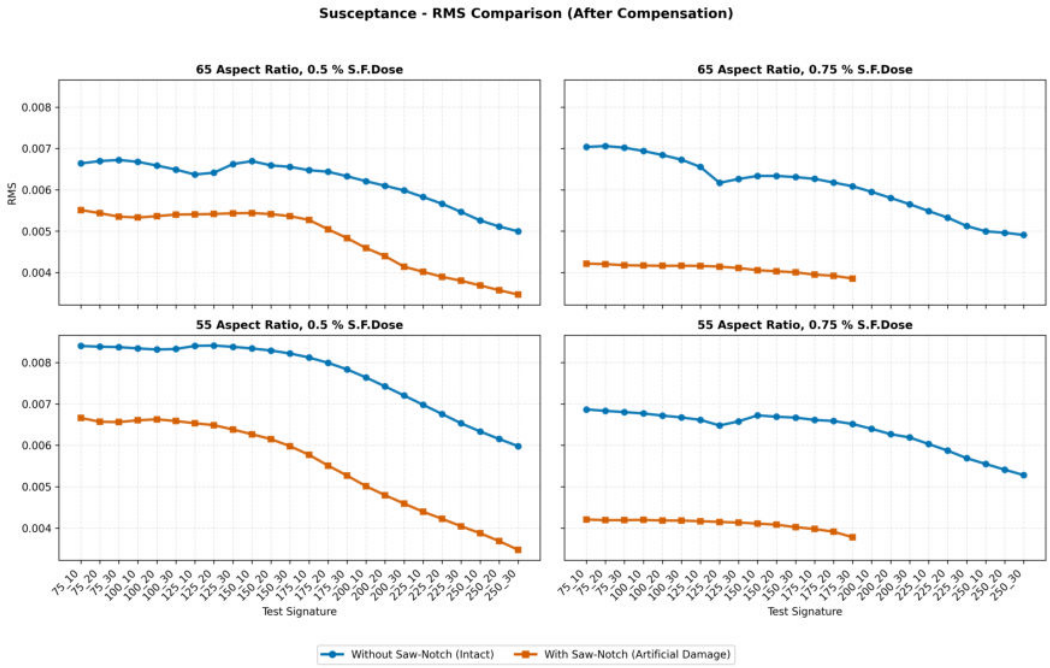

Figure 6.68: RMS response after compensation: matched intact and saw-cut susceptance records.

The conductance comparison in Table 6.163 shows a negative matched response in all four specimens. The decreases are -75.7% for SFC3 and -73.0% for SFC4, compared with -18.4% for SFC1 and -15.5% for SFC2. These magnitudes describe the tested records and do not isolate a fibre-dosage effect.

Table 6.163: Conductance RMS comparison after compensation

SFC	AR	SF	Intact mean	Saw-cut mean	Change
1	65	0.5%	0.0021	0.0017	-18.4%
3	65	0.75%	0.0025	0.0006	**-75.7%**
2	55	0.5%	0.0029	0.0025	-15.5%
4	55	0.75%	0.0020	0.0006	**-73.0%**

The susceptance signal analysis in Table 6.164 shows more uniform sensitivity across all configurations, with changes ranging from -22.4% to -35.6%. Unlike conductance, susceptance RMS shows more balanced sensitivity across SF levels.

Table 6.164: Susceptance RMS comparison after compensation

SFC	AR	SF	Intact mean	Saw-cut mean	Change
1	65	0.5%	0.0062	0.0048	-22.4%
3	65	0.75%	0.0061	0.0041	-32.9%
2	55	0.5%	0.0077	0.0055	-28.7%
4	55	0.75%	0.0064	0.0041	**-35.6%**

Table 6.165 shows a negative change in all eight specimen–channel comparisons. RMS is therefore one of two indices with a consistent direction across the four tested specimens, alongside CCV, although the two indices describe different properties of the signatures.

Table 6.165: RMS intact–saw-cut comparison by signal type

SFC	Configuration	Conductance Change	Susceptance Change	Both Negative?
1	AR65/SF0.5%	-18.4%	-22.4%	✓
3	AR65/SF0.75%	-75.7%	-32.9%	✓
2	AR55/SF0.5%	-15.5%	-28.7%	✓
4	AR55/SF0.75%	-73.0%	-35.6%	✓
Result: 8/8 measurements show RMS decrease upon damage				

SFC1 (AR65/SF0.5%) has decreases of -18.4% in conductance RMS (0.0021 to 0.0017) and -22.4% in susceptance RMS (0.0062 to 0.0048). The intact values remain higher over the reported sequence, providing a consistent direction for this specimen.

SFC3 (AR65/SF0.75%) has the largest conductance RMS decrease, -75.7% (0.0025 to 0.0006), and a -32.9% susceptance change. RMS describes signal magnitude; the experiment does not establish fibre bridging or transmission efficiency as the mechanism.

SFC2 (AR55/SF0.5%) has a -15.5% conductance RMS change (0.0029 to 0.0025) and a -28.7% susceptance change. Its RMSD change is much larger in relative magnitude, illustrating that baseline deviation and signal magnitude are not interchangeable measures.

SFC4 (AR55/SF0.75%) has changes of -73.0% in conductance RMS and -35.6% in susceptance RMS. The similar conductance magnitude in SFC3 is a dosage-associated pattern in two specimens, not evidence of an optimal material configuration.

Table 6.166 compares RMS with the other indices. RMS decreases in every reported specimen–channel combination, while several deviation indices reverse direction between the two dosage groups.

Table 6.166: RMS vs RMSD: Opposite Sensitivity Patterns by SF Content

Configuration	RMSD Change	RMS Change (Cond.)	Direction comparison
AR65/SF0.5%	+100%	-18%	Opposite directions
AR65/SF0.75%	-40%	-76%	Both negative
AR55/SF0.5%	+137%	-16%	Opposite directions
AR55/SF0.75%	-22%	-73%	Both negative

In summary, RMS decreases in all eight reported specimen–channel combinations and is therefore one of two same-direction candidates in this dataset, alongside CCV. The two 0.75% specimens have the largest conductance changes (-73% to -76%). RMS describes signal amplitude rather than a direct physical energy loss, and the four-specimen result does not establish a primary-indicator role for other structures.

6.12.2.11 Skewness Response

Skewness quantifies asymmetry of the amplitude distribution around its mean. It supplies shape information distinct from magnitude-based measures, but its signed direction after the saw-cut is determined from the records rather than prescribed in advance.

Figures 6.69 and 6.70 presents the visual comparison of skewness damage sensitivity for both conductance and susceptance signals. The plots reveal complex behaviour with significant divergence between intact and damaged states, though the patterns vary substantially across configurations.

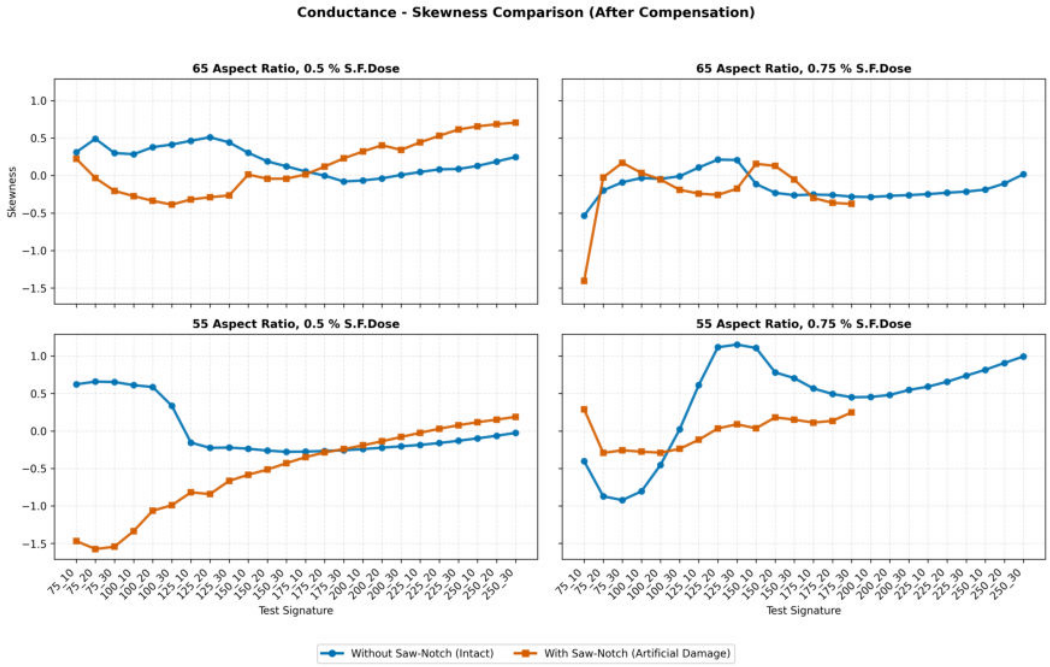

Figure 6.69: Skewness response after compensation: matched intact and saw-cut conductance records.

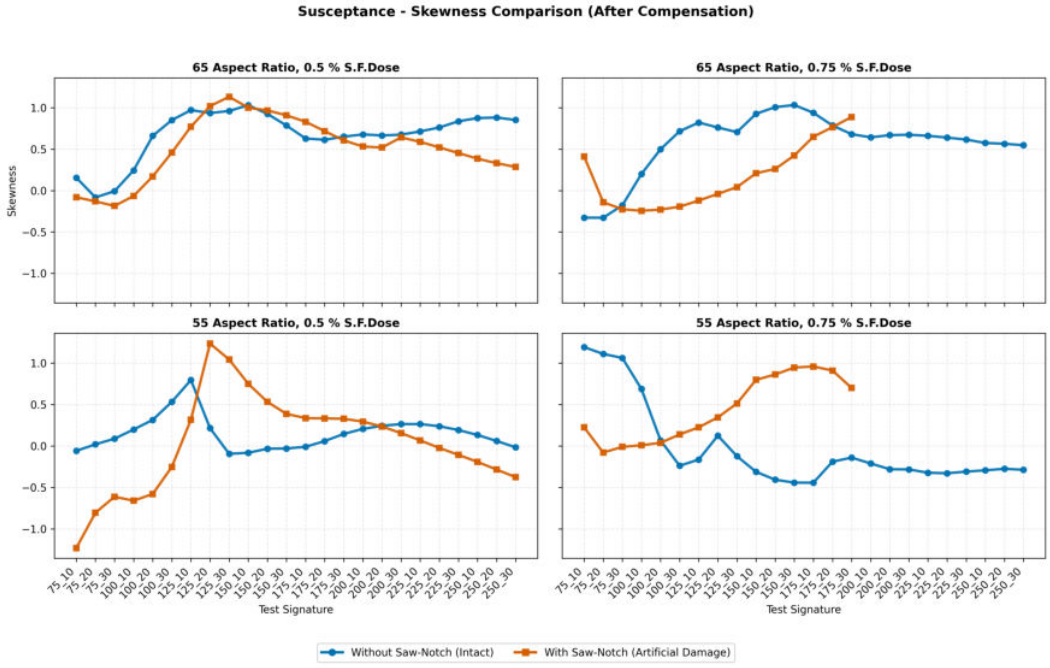

Figure 6.70: Skewness response after compensation: matched intact and saw-cut susceptance records.

The conductance signal analysis in Table 6.167 reveals predominantly negative changes across configurations. The values are presented in terms of mean skewness rather than percentage change, as some baseline values are near zero making percentage

calculations misleading.

Table 6.167: Skewness Damage Sensitivity: Conductance Signal (After Compensation)

SFC	AR	SF	Intact Mean	Saw-cut mean	ΔSkew	Direction
1	65	0.5%	+0.203	+0.130	-0.073	Decrease
3	65	0.75%	-0.149	-0.197	-0.048	More negative
2	55	0.5%	-0.001	-0.524	-0.522	Strong decrease
4	55	0.75%	+0.406	-0.013	-0.419	Sign change

The susceptance signal analysis in Table 6.168 shows more varied response patterns. Most configurations show negative changes, except for SFC4 (AR55/SF0.75%) which shows substantial positive change due to near-zero baseline.

Table 6.168: Skewness Damage Sensitivity: Susceptance Signal (After Compensation)

SFC	AR	SF	Intact Mean	Saw-cut mean	ΔSkew	Direction
1	65	0.5%	+0.677	+0.515	-0.162	Decrease
3	65	0.75%	+0.576	+0.163	-0.412	Strong decrease
2	55	0.5%	+0.152	+0.037	-0.115	Decrease
4	55	0.75%	-0.033	+0.439	+0.472	Sign change

The signal type comparison in Table 6.169 reveals that skewness shows configuration-dependent sensitivity with generally negative response (more negative skewness upon damage). The one exception is SFC4 susceptance, which shows positive response due to baseline being near zero.

Table 6.169: Skewness Damage Sensitivity: Signal Type Comparison

SFC	Configuration	Conductance Δ	Susceptance Δ	Observed direction
1	AR65/SF0.5%	-0.073	-0.162	Both negative
3	AR65/SF0.75%	-0.048	-0.412	Both negative
2	AR55/SF0.5%	-0.522	-0.115	Both negative
4	AR55/SF0.75%	-0.419	+0.472	Opposite directions

SFC1 (AR65/SF0.5%). demonstrates modest skewness sensitivity with conductance decreasing by 0.073 (from +0.203 to +0.130) and susceptance decreasing by 0.162 (from +0.677 to +0.515). Both signals show the signal remaining positive but becoming less right-skewed upon damage. The figure analysis reveals distinct separation between intact and damaged curves, with specimens in the saw-cut state showing a dip to negative values early in the temperature progression before recovering. This configuration shows consistent but moderate skewness sensitivity.

SFC3 (AR65/SF0.75%) shows small conductance change (-0.048) but substantial susceptance change (-0.412). The conductance skewness remains negative for both states, shifting from -0.149 to -0.197. Susceptance shows a larger shift from +0.576 to +0.163, indicating significant loss of positive skewness upon damage. The figure analysis notes more oscillating behaviour between intact and damaged curves for this configuration, but with clear distinctions maintained throughout the temperature range.

SFC2 (AR55/SF0.5%) has the largest absolute conductance skewness change, -0.522, from -0.001 to -0.524; the susceptance change is -0.115. The near-zero conductance baseline produces a misleading percentage (-36,435%), so the absolute change and trajectory are reported instead.

SFC4 (AR55/SF0.75%) has opposite channel directions. Conductance changes by -0.419, from +0.406 to -0.013, while susceptance changes by +0.472, from -0.033 to +0.439. The channels therefore describe different changes in distribution asymmetry for this record; neither is designated as the preferred damage indicator.

The interpretation of skewness versus other indices is presented in Table 6.170. Unlike magnitude-based indices like RMS or deviation-based indices like RMSD, skewness captures shape changes that may provide complementary diagnostic information.

Table 6.170: Skewness Interpretation: Shape vs Magnitude Information

Index Category	**Measures**	**Example**
Deviation-based	How much signal deviates from baseline	RMSD, MAPD
Energy-based	Signal magnitude/power	RMS
Shape-based	**Distribution asymmetry**	**Skewness**

In summary, Skewness decreases in seven of eight specimen–channel comparisons. Conductance is negative in all four specimens, while SFC4 susceptance is positive (+0.472). The index supplies complementary shape information, but near-zero baselines limit percentage and threshold interpretation; no general channel recommendation is made.

6.12.2.12 Peak-to-Peak Response

Peak-to-Peak (P2P) is the difference between the maximum and minimum amplitude of a signature. It is simple to compute but discards the location and shape of intermediate spectral features. Its matched direction varies among the four specimens and is not assumed to increase after the saw-cut.

Figures 6.71 and 6.72 presents the visual comparison of Peak-to-Peak damage sensitivity for both conductance and susceptance signals. The plots reveal strong

positive divergence for 0.5% SF configurations, with specimens in the saw-cut state reaching values over 1300% compared to 650% for intact.

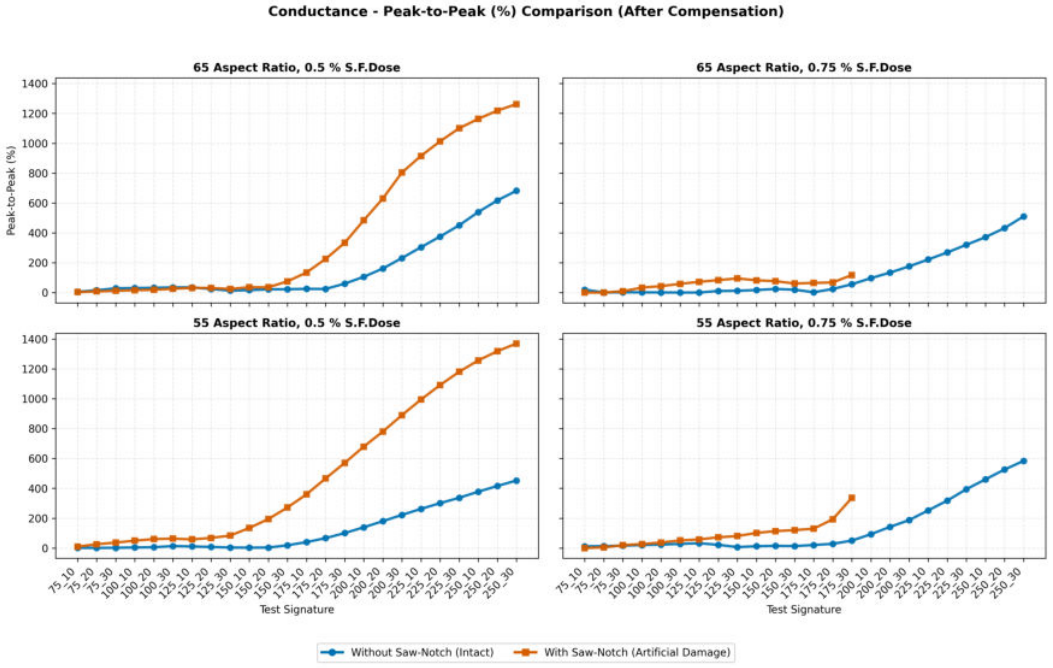

Figure 6.71: Peak-to-Peak response after compensation: matched intact and saw-cut conductance records.

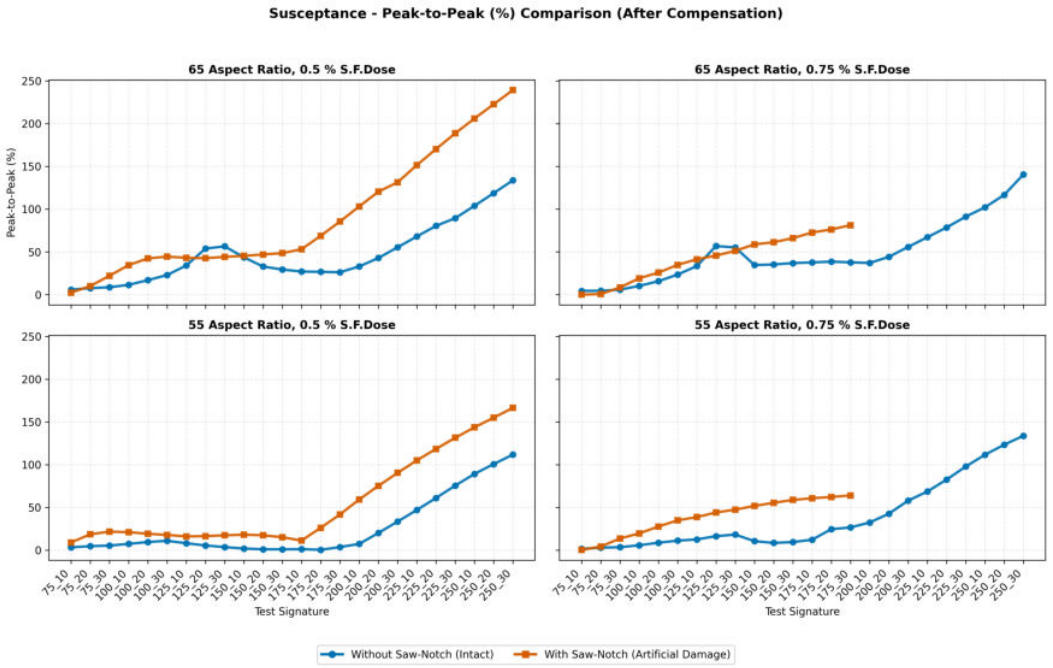

Figure 6.72: Peak-to-Peak response after compensation: matched intact and saw-cut susceptance records.

The conductance signal analysis in Table 6.171 reveals the familiar SF-dependent pattern observed for RMSD and MAPD. The 0.5% SF configurations show very strong positive response (+148.9% for SFC1 and +304.8% for SFC2), while the 0.75% SF configurations show negative response (-49.1% and -34.2%).

Table 6.171: Peak-to-Peak Damage Sensitivity: Conductance Signal (After Compensation)

SFC	AR	SF	Intact Mean	Saw-cut mean	Change
1	65	0.5%	160.69	399.97	+148.9%
3	65	0.75%	113.58	57.77	-49.1%
2	55	0.5%	123.61	500.34	**+304.8%**
4	55	0.75%	136.23	89.64	-34.2%

The susceptance signal analysis in Table 6.172 shows similar pattern but with lower overall sensitivity. The 0.5% SF configurations show positive response (+91.9% and +117.4%), while 0.75% SF shows minimal response (-11.5% and +1.1%).

Table 6.172: Peak-to-Peak Damage Sensitivity: Susceptance Signal (After Compensation)

SFC	AR	SF	Intact Mean	Saw-cut mean	Change
1	65	0.5%	47.05	90.31	+91.9%
3	65	0.75%	48.51	42.91	-11.5%
2	55	0.5%	25.50	55.43	**+117.4%**
4	55	0.75%	38.41	38.82	+1.1%

For the two 0.50% specimens, Table 6.173 gives an average change of +226.8% in conductance and +104.7% in susceptance. Both channels have negative or near-zero changes for the two 0.75% specimens. These signs do not constitute success or failure criteria outside this dataset.

Table 6.173: Peak-to-Peak Damage Sensitivity: Signal Type Comparison

SFC	Configuration	Conductance Change	Susceptance Change	Larger reported change
1	AR65/SF0.5%	+148.9%	+91.9%	Conductance
3	AR65/SF0.75%	-49.1%	-11.5%	Neither
2	AR55/SF0.5%	+304.8%	+117.4%	Conductance
4	AR55/SF0.75%	-34.2%	+1.1%	Susceptance
Average (0.5% SF)		+226.8%	+104.7%	**Conductance**
Average (0.75% SF)		-41.7%	-5.2%	Neither

SFC1 (AR65/SF0.5%) has increases of +148.9% in conductance Peak-to-Peak (160.69 to 399.97) and +91.9% in susceptance. At 250°C, the conductance values are

612.78 (intact) and 1214.52 (saw-cut).

SFC3 (AR65/SF0.75%) has a -49.1% conductance change (113.58 to 57.77) and a -11.5% susceptance change. The direction matches RMSD and MAPD for this specimen, but a fibre-bridging mechanism was not measured directly.

SFC2 (AR55/SF0.5%) has the largest conductance Peak-to-Peak change, +304.8% (123.61 to 500.34), and a +117.4% susceptance change. At 250°C, the conductance values are 415.00 (intact) and 1314.48 (saw-cut). This specimen-level maximum does not establish an optimal configuration.

SFC4 (AR55/SF0.75%) has a -34.2% conductance change and a +1.1% susceptance change. Together with SFC3, the conductance result forms a two-specimen dosage-associated pattern; it does not prove that dosage controls the response.

Table 6.174 shows that Peak-to-Peak and RMSD have the same conductance direction in each specimen, while their relative magnitudes differ.

Table 6.174: Peak-to-Peak vs RMSD: Pattern Comparison

Configuration	RMSD Change	P2P Change (Cond.)	Observed direction
AR65/SF0.5%	+100%	+149%	Both positive
AR65/SF0.75%	-40%	-49%	Both negative
AR55/SF0.5%	+137%	+305%	Both positive
AR55/SF0.75%	-22%	-34%	Both negative

In summary, Peak-to-Peak conductance increases by +149% to +305% in the two 0.50% specimens and decreases by -34% to -49% in the two 0.75% specimens. Its calculation is simple, but the reversed direction and unreplicated configurations preclude a general signal, dosage or primary-indicator recommendation.

6.12.2.13 Covariance Response

Covariance measures the joint variability of the baseline and current signals. The matched intact–saw-cut change describes how their co-variation differs between the two tested states; it is not an independent physical measurement or validation channel.

Figures 6.73 and 6.74 presents the visual comparison of covariance damage sensitivity for both conductance and susceptance signals. The plots reveal that covariance values are very small (scaled by 1e-7 for conductance, 1e-6 for susceptance), requiring careful interpretation of relative changes rather than absolute magnitudes.

The conductance signal analysis in Table 6.175 reveals a pattern that is REVERSED compared to RMSD, identical to Variance. The 0.75% SF configurations show positive response (+108.7% for SFC3 and +102.6% for SFC4), while the 0.5% SF configurations show negative response (-18.1% for SFC1 and -210.6% for SFC2).

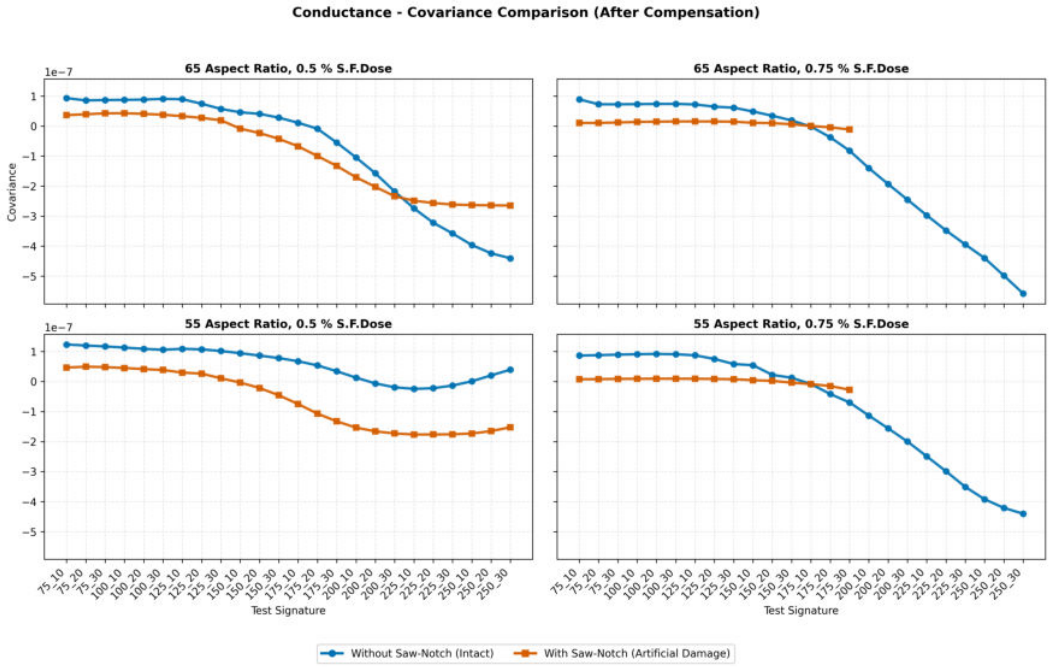

Figure 6.73: Covariance response after compensation: matched intact and saw-cut conductance records.

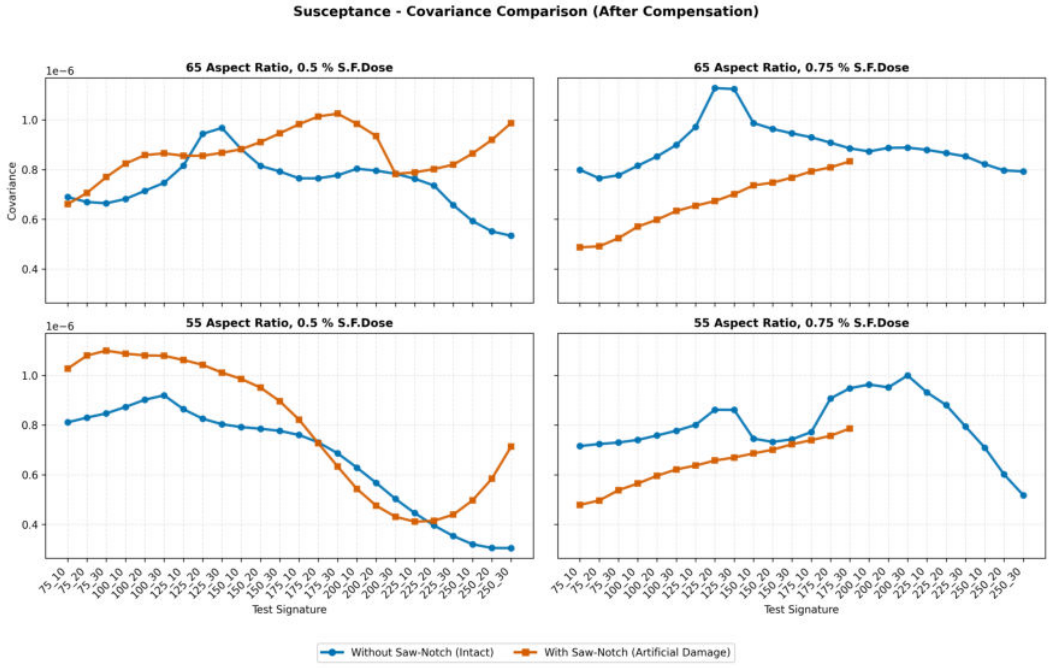

Figure 6.74: Covariance response after compensation: matched intact and saw-cut susceptance records.

The susceptance signal analysis in Table 6.176 shows lower magnitude changes with the opposite pattern: positive for 0.5% SF (+16.8% and +19.1%) and negative for 0.75% SF (-25.1% and -19.4%).

Table 6.175: Covariance Damage Sensitivity: Conductance Signal (After Compensation) – REVERSED PATTERN

SFC	AR	SF	Intact Mean	Saw-cut mean	Change
1	65	0.5%	∼0 (1e-7 scale)	∼0 (1e-7 scale)	-18.1%
3	65	0.75%	∼0 (1e-7 scale)	∼0 (1e-7 scale)	**+108.7%**
2	55	0.5%	∼0 (1e-7 scale)	∼0 (1e-7 scale)	-210.6%
4	55	0.75%	∼0 (1e-7 scale)	∼0 (1e-7 scale)	**+102.6%**

Table 6.176: Covariance Damage Sensitivity: Susceptance Signal (After Compensation)

SFC	AR	SF	Intact Mean	Saw-cut mean	Change
1	65	0.5%	∼0 (1e-6 scale)	∼0 (1e-6 scale)	+16.8%
3	65	0.75%	∼0 (1e-6 scale)	∼0 (1e-6 scale)	-25.1%
2	55	0.5%	∼0 (1e-6 scale)	∼0 (1e-6 scale)	+19.1%
4	55	0.75%	∼0 (1e-6 scale)	∼0 (1e-6 scale)	-19.4%

The signal type comparison in Table 6.177 reveals complementary behaviour between the two signals, identical to the Variance index pattern. For 0.75% SF, conductance provides positive response while susceptance shows negative. For 0.5% SF, susceptance provides modest positive response while conductance shows negative.

Table 6.177: Covariance Damage Sensitivity: Signal Type Comparison – Complementary Pattern

SFC	Configuration	Conductance Change	Susceptance Change	Larger Magnitude
1	AR65/SF0.5%	-18.1%	+16.8%	Susceptance
3	AR65/SF0.75%	+108.7%	-25.1%	Conductance
2	AR55/SF0.5%	-210.6%	+19.1%	Susceptance
4	AR55/SF0.75%	+102.6%	-19.4%	Conductance
Pattern: Conductance for 0.75% SF, Susceptance for 0.5% SF				

SFC1 (AR65/SF0.5%) has a -18.1% conductance change and a +16.8% susceptance change. The opposite directions resemble the corresponding variance comparison and differ from RMSD.

SFC3 (AR65/SF0.75%) has a +108.7% conductance change and a -25.1% susceptance change. The values match the reported variance comparison and have the opposite conductance direction to RMSD; no dosage mechanism is inferred.

SFC2 (AR55/SF0.5%) has the largest absolute conductance change, -210.6%, and a +19.1% susceptance change. The direction differs from its positive RMSD change, illustrating that covariance and baseline-deviation indices describe different signature properties.

SFC4 (AR55/SF0.75%) has a +102.6% conductance change and a -19.4% suscep-

tance change. The common direction with SFC3 is a within-dataset pattern and does not establish a dosage-specific application rule.

The comparison between Covariance and Variance is presented in Table 6.178. The two indices show identical patterns, confirming that they capture related statistical properties.

Table 6.178: Covariance vs Variance: Identical Patterns

Configuration	Variance (Cond)	Covariance (Cond)	Match?
AR65/SF0.5%	-18.1%	-18.1%	Identical
AR65/SF0.75%	+108.7%	+108.7%	Identical
AR55/SF0.5%	-210.6%	-210.6%	Identical
AR55/SF0.75%	+102.6%	+102.6%	Identical

In summary, Covariance has the same reported values and dosage-group directions as the signed variance-related index: positive conductance changes in the two 0.75% specimens and negative changes in the two 0.5% specimens, with different susceptance directions. This within-dataset pattern does not establish a dosage-specific channel-selection rule.

6.12.2.14 Within-Dataset Comparison of the Thirteen SHM Indices

This section compares all thirteen indices reported in Sections D.2.01–D.2.13. The ordering is limited to the four specimens, two channels, available temperature ranges and adopted aggregation; it is not a general implementation ranking.

The thirteen SHM indices are grouped here by calculation form. Deviation-based indices (RMSD, MAPD, AMPD, MSE and Peak-to-Peak) quantify difference from a baseline; correlation-based indices (CC, CCD, CCD^3 and CCV) describe linear similarity or derived correlation quantities; RMS describes signal magnitude; and Variance, Covariance and Skewness describe distributional properties. Their matched directions are determined from the present records rather than assumed from category membership.

CCV is positive and RMS negative in all eight reported specimen–channel combinations. Their consistent direction makes them candidates for further replicated evaluation, but it does not establish configuration-independent reliability or a general monitoring foundation.

Table 6.179 presents the performance of indices with a consistent direction in the four tested specimens across all configurations.

Indices Positive in the Two 0.5% Specimens.

Table 6.179: Indices with a Consistent Direction in the Four Tested Specimens: Performance Across All Configurations

Index	Direction	SF 0.5% Avg	SF 0.75% Avg	Larger Channel	Scope
CCV	Increase	+120%	+318%	Conductance	Positive in all four specimens
RMS	Decrease	-22%	-74%	Both	Negative in all four specimens

Five deviation-based indices are positive in the 0.50% specimens and negative in the 0.75% specimens. The numerical ranges are preserved in Table 6.180; the signs refer only to the matched direction in this dataset and are not application-level judgements.

Table 6.180 summarises the dosage-group directions of selected indices.

Table 6.180: Observed dosage-group direction of selected deviation indices

Index	0.5% SF Maximum	0.75% SF Response	Larger Channel	Observed Pattern
Peak-to-Peak	+305%	-49%	Conductance	Direction reverses
RMSD	+137%	-40%	Conductance	Direction reverses
MAPD	+136%	-44%	Conductance	Direction reverses
MSE	+125%	-98%	Susceptance	Direction reverses
AMPD	+121%	Mixed	Signal-dependent	Channel-dependent

Variance and Covariance show conductance changes of +103% to +109% in the two 0.75% specimens and -18% to -211% in the two 0.5% specimens. Their matching values reflect related calculations in this dataset; no dosage-specific channel rule is inferred.

The correlation-based indices have different directions and magnitudes. CC is closer to unity in selected 0.75% records, while CCD and CCD^3 follow the dosage-associated direction of RMSD. Selected susceptance CCD values are near zero, limiting percentage comparisons. CCV retains the same direction in all four tested specimens.

Skewness provides shape information and is negative in seven of eight specimen–channel comparisons. Near-zero baseline values make percentage and one-sided threshold interpretation unstable, so it is retained as complementary descriptive evidence.

Table 6.181 preserves the reported ordering but recasts its final column as a within-dataset role rather than a recommendation.

The same-direction CCV and RMS observations may be combined as a consistency check within these records, but they are derived from the same signatures and are not independent confirmation. The remaining index magnitudes and reversals describe the tested configurations. No general low- or high-dosage application rule follows without replicated and externally evaluated specimens.

Conductance has the larger effect for several deviation indices in these records, while susceptance is larger for selected MSE and AMPD comparisons. Variance and

Table 6.181: Within-dataset comparison of the thirteen SHM indices

Order	Index	Direction coverage	Max effect	Observed pattern
1	CCV	8/8 same direction	+370%	Positive in all four specimens and both channels
2	RMS	8/8 same direction	-76%	Negative in all four specimens and both channels
3	Peak-to-Peak	4/8 same direction	+305%	Positive in the 0.50% pair
4	CC	6/8 same direction	+20%	Configuration- and channel-dependent
5	RMSD	4/8 same direction	+137%	Positive in the 0.50% pair
6	MAPD	4/8 same direction	+136%	Positive in the 0.50% pair
7	MSE	No (4/8)	+125%	Positive in 0.5% pair
8	Variance	No (4/8)	+109%	Positive in 0.75% pair
9	Covariance	No (4/8)	+109%	Positive in 0.75% pair
10	AMPD	No (6/8)	+121%	Signal-dependent
11	CCD	No (4/8)	+233%	Positive in 0.5% pair
12	CCD^3	No (4/8)	+233%	Positive in 0.5% pair
13	Skewness	Partial (7/8)	Variable	Supplementary

Covariance also change direction by channel. Both channels should therefore be retained; no universal signal preference is established.

The within-dataset SHM-index comparison is summarised as follows.

Across the four specimens, CCV and RMS retain the same response direction, whereas several deviation and distribution indices reverse by configuration or channel. These patterns justify a study-specific comparison of multiple indices but do not establish causal dosage effects, transferable thresholds or reliable performance across other structural configurations.

6.12.3 Consolidated Matched Changes of the Secondary SHM Indices

The preceding sections present the detailed temperature response of RMSD, CCV and RMS. The remaining ten indices (MAPD, AMPD, CC, CCD, CCD^3, MSE, Variance, Skewness, Peak-to-Peak and Covariance) were analysed using the same matched-record procedure; their consolidated intact–saw-cut differences are summarised in Table 6.182.

The detailed per-index comparisons establish the values summarised in Table 6.182. The representative indices are discussed in the preceding sections, while this table retains the measured direction and range of the remaining indices.

6.12.4 Material Effects on Damage Detection

The matched intact–saw-cut analysis shows configuration-associated differences among the thirteen indices. The following AR 55–AR 65 and 0.50–0.75% comparisons are descriptive because each combination is represented by one specimen and the factors

Table 6.182: Consolidated matched changes of the ten secondary SHM indices for all four SFRC specimens

Index	**SFC1**		**SFC3**		**SFC2**		**SFC4**		**Direction**	**Direction coverage**	**Processing change**
	Mean	Max	Mean	Max	Mean	Max	Mean	Max			
MAPD	+95.4%	+74.3%	-43.8%	-53.8%	+135.9%	+107.0%	-22.9%	-31.2%	SF-dep.	No	33%
AMPD	+202.2%	+35.1%	-37.8%	+102.3%	+201.1%	+36.1%	-27.7%	+111.0%	Mixed	No	38%
CC	-228.4%	-0.5%	+764.4%	+17.5%	-85.0%	-8.7%	+433.7%	+20.1%	Reversed	No	Stab.
CCD	+51.7%	-15.5%	-77.9%	-100.0%	+232.7%	+25.6%	-51.2%	-100.0%	SF-dep.	No	40%
CCD^3	+51.7%	-15.5%	-77.9%	-100.0%	+232.7%	+25.6%	-51.2%	-100.0%	SF-dep.	No	67%
MSE	+36.3%	+110.1%	-97.5%	-93.4%	+60.9%	+125.0%	-95.6%	-90.0%	SF-dep.	No	50%
Variance	-18.1%	+16.8%	+108.7%	-25.1%	-210.6%	+19.1%	+102.6%	-19.4%	Reversed	No	60%
Skewness	-0.073	-0.162	-0.048	-0.412	-0.522	-0.115	-0.419	+0.472	Decrease	Partial	50%
Peak-to-Peak	+148.9%	+91.9%	-49.1%	-11.5%	+304.8%	+117.4%	-34.2%	+1.1%	SF-dep.	No	43%
Covariance	-18.1%	+16.8%	+108.7%	-25.1%	-210.6%	+19.1%	+102.6%	-19.4%	Reversed	No	60%

are not independently replicated.

6.12.4.1 Aspect-Ratio-Group Comparison

The study compares two fibre aspect ratios, AR 55 and AR 65, at two dosages. The tables report the associated index differences; they do not isolate a population-level aspect-ratio effect.

For the 0.50% specimen pair, the AR 55 specimen has the larger reported matched change for the deviation indices in Table 6.183.

Table 6.183: Matched changes of deviation-based indices for the 0.50% fibre pair

Index	AR55 Change	AR65 Change	Larger reported change
RMSD	+137%	+100%	AR55 specimen
MAPD	+136%	+95%	AR55 specimen
Peak-to-Peak	+305%	+149%	AR55 specimen
MSE (suscept.)	+125%	+110%	AR55 specimen

The numerical difference cannot be attributed to fibre geometry or matrix homogeneity because specimen variability, sensor installation and dosage are not independently controlled through replication.

For CCV and RMS, the AR ordering differs by fibre dosage and index, as shown in Table 6.184.

Table 6.184: Matched CCV and RMS changes for the two aspect ratios and fibre dosages

Index	AR55/0.5%	AR65/0.5%	AR55/0.75%	AR65/0.75%	Observed ordering
CCV (cond.)	+140%	+101%	+265%	+370%	SF-dependent
RMS (cond.)	-15%	-18%	-73%	-76%	Similar

For CCV at 0.50% SF, the AR 55 specimen has the larger effect (+140% versus +101%), whereas at 0.75% SF the AR 65 specimen has the larger effect (+370% versus +265%). RMS values are closer. The reversal precludes a single AR ranking and does not establish an AR–dosage interaction statistically.

Table 6.185 compares the reported correlation-based changes for the matched specimen pairs. The values are descriptive because each aspect ratio is represented by one specimen at each dosage.

Within the 0.5% pair, the reported CCD changes are +233% for SFC2 (AR55) and +52% for SFC1 (AR65). This is a comparison of two specimens and does not establish superior AR-dependent behaviour.

Table 6.185: Matched changes of selected correlation-based indices by aspect ratio

Index	AR55 Average	AR65 Average	Observed comparison
CCD (cond., 0.5% SF)	+233%	+52%	Larger for AR55 specimen
CC (cond.)	Similar	Similar	No clear ordering

Variance and Covariance are positive in the two 0.75% records and negative in the two 0.50% records. Within the 0.75% pair, the AR65 value exceeds the AR55 value by six percentage points.

Table 6.186: Matched Variance and Covariance changes for the 0.75% fibre pair

Index	AR55 Change	AR65 Change	Reported difference
Variance	+103%	+109%	AR65 specimen: +6 pp
Covariance	+103%	+109%	AR65 specimen: +6 pp

The reported ordering depends on index and dosage: the AR 55/0.50% specimen is larger for several deviation indices, CCV reverses its AR ordering at 0.75%, and the Variance/Covariance difference is small. No aspect ratio is recommended for general monitoring from this unreplicated comparison.

6.12.4.2 Fibre-Dosage-Group Comparison

The two 0.50% specimens and two 0.75% specimens show different directions for several indices. These specimen-group patterns are reported without treating dosage as the sole or most critical cause because each AR–dosage combination has one physical specimen.

Deviation-based indices show positive matched changes for the two 0.50% specimens and negative changes for the two 0.75% specimens. Variance and Covariance show the opposite conductance pattern. Table 6.187 records this within-dataset reversal; it is not evidence of a universal dosage dichotomy.

Table 6.187 presents this reported contrast using representative indices from each category.

The two 0.50% specimens have positive changes from +95% to +305% for the listed deviation indices, whereas the two 0.75% specimens have negative changes from -22% to -98%. A negative change is an observed direction, not proof that an index fails generally for 0.75% SF.

The experiment did not measure crack bridging, electrical continuity or fibre-network evolution, so no mechanism is assigned to the reversed direction.

The observed direction for the two 0.75% specimens.

Table 6.187: Observed index-direction reversal between the two dosage groups

Index Category	Example	0.5% SF Response	0.75% SF Response	Pattern
Deviation-based	RMSD	+137%	-40%	Standard
Deviation-based	Peak-to-Peak	+305%	-49%	Standard
Reversed-pattern	Variance	-211%	+109%	Reversed
Reversed-pattern	Covariance	-211%	+109%	Reversed
Positive in all four specimens	CCV	+140%	+370%	Both positive
Negative in all four specimens	RMS	-17%	-75%	Both negative

Table 6.188: Deviation-Based Indices: SF Dose Effect (Conductance Signal)

Index	0.5% SF (Avg)	0.75% SF (Avg)	Difference
Peak-to-Peak	+227%	-42%	269 pp
RMSD	+119%	-31%	150 pp
MAPD	+116%	-34%	150 pp
MSE	+49%	-97%	146 pp
CCD	+142%	-65%	207 pp

The negative response means that the matched saw-cut value is lower than the intact value under the stated baseline and aggregation. It is not identified as measurement error, but neither does the four-specimen design establish a fundamental limitation for all high-fibre-content materials.

Variance and Covariance show the reversed direction: positive conductance changes of +103% to +109% for the two 0.75% specimens and negative changes for the two 0.50% specimens. This is a complementary description of the tested records, not evidence that either group or index succeeds or fails generally.

Table 6.189: Reversed conductance-index directions in the two fibre-dosage groups

Index	0.5% SF Response	0.75% SF Response	Complementary to
Variance	-114%	+106%	RMSD, MAPD
Covariance	-114%	+106%	Peak-to-Peak, MSE

The opposite directions are complementary descriptions of the present records. They do not establish index-selection rules for another structure.

CCV and RMS retain the same direction in both dosage groups, with larger absolute effects in the two 0.75% specimens. This does not establish dosage-independent operation beyond the tested records.

The CCV and RMS group averages differ as listed in the table. Enhanced electromagnetic coupling or a beneficial effect of fibre density was not independently measured and is not inferred.

The observed specimen-group pattern differs by signal channel. Conductance

Table 6.190: Indices retaining one direction across the four tested specimens

Index	0.5% SF Avg	0.75% SF Avg	Enhancement	Direction
CCV (cond.)	+120%	+318%	+198 pp	Positive
RMS (cond.)	-17%	-75%	+58 pp abs.	Negative

has the larger change for several deviation indices in the two 0.50% records, while some 0.75% comparisons reverse by channel. CCV and RMS retain their directions in both channels. These results support channel-specific reporting, not a dosage-based channel-selection rule.

The two dosage groups show different directions for several indices, while CCV and RMS retain the same direction in all four specimens. This is a study-specific observation, not proof that dosage determines index behaviour or that a given index should be selected or excluded for an untested structure.

6.12.4.3 Configuration-Associated Index Patterns

This subsection synthesises the patterns reported in Sections D.2–D.3.2. Because one specimen represents each configuration, the comparison ranks the observed records but cannot support material-design, field-threshold or general index-selection recommendations.

SFC2 (AR 55/SF 0.50%) has the largest matched percentage change for several deviation-based indices in the reported dataset. Table 6.191 retains these values as a specimen-level comparison.

Table 6.191: Reported index effects for SFC2 (AR 55/SF 0.50%)

Index	AR55/SF0.5% effect	Dataset comparison	Signal
Peak-to-Peak	+305%	Largest listed change	Conductance
CCD	+233%	Largest listed change	Conductance
CCV	+140%	AR65/0.75% is larger	Conductance
RMSD	+137%	Largest listed change	Conductance
MAPD	+136%	Largest listed change	Conductance
MSE	+61% (cond), +125% (susc)	Susceptance is larger	Mixed

SFC2 provides five of the six largest values listed in the table. This observation does not establish an AR, dosage, homogeneity or electrical-network mechanism, and it is not a basis for specifying an SFRC mixture.

The 0.50% specimens show positive matched changes for several deviation indices, whereas the 0.75% specimens show reversed directions. CCV and RMS retain the same direction across the four specimens. Table 6.192 summarises these dataset-specific

patterns; the category boundaries and effects are not transferred to existing structures.

Table 6.192: Within-dataset index directions grouped by fibre dosage

Tested group	First index	Second index	Signal	Reported change
$\leq$0.5%	Peak-to-Peak	RMSD	Conductance	+200% to +305%
$\geq$0.75%	CCV	RMS	Conductance	+265% to +370%
All four tested specimens	CCV	RMS	Both	+85% to +370%

CCV, RMS and Peak-to-Peak describe different aspects of the recorded signatures, but they are calculated from the same measurements and are not independent validation channels. Their opposite or configuration-dependent directions can be used to compare the present records; a logical damage-decision rule requires testing on independent specimens.

Table 6.193 retains the channel associated with the larger reported effect for each comparison. This is a dataset summary rather than a universal preference, and both channels remain necessary because their responses differ.

Table 6.193: Signal channel associated with the reported within-dataset effects

Index	Larger reported effect	Dataset observation	Other channel
CCV	Conductance	Larger reported change	Smaller reported change
RMS	Conductance	Larger reported change	Smaller reported change
Peak-to-Peak	Conductance	Larger reported change	–
RMSD	Conductance	Larger reported change	–
MAPD	Conductance	Larger reported change	–
MSE	Susceptance (0.5% SF)	+125% vs +49%	Smaller conductance change
Variance	Conductance (0.75% SF)	Positive response	Susceptance for 0.5% SF
Covariance	Conductance (0.75% SF)	Positive response	Susceptance for 0.5% SF

The following table preserves the reported ordering by effect magnitude and computational form. It is not an implementation priority for an untested structure.

Table 6.194: Within-dataset ordering of selected indices

Rank	Index	Observed scope	Max effect	Computation
1	CCV	Positive in all four specimens	+370%	Moderate
2	RMS	Negative in all four specimens	-76%	Simple
3	Peak-to-Peak	SF $\leq$ 0.5%	+305%	Very Simple
4	RMSD	SF $\leq$ 0.5%	+137%	Moderate
5	Variance	SF $\geq$ 0.75%	+109%	Simple

The configuration-associated comparison is summarised as follows.

The four specimens exhibit configuration-associated differences in index magnitude and direction. SFC2 has the largest reported effect for several deviation indices,

while CCV and RMS retain the same direction in all four specimens. Replicated testing is required before attributing these patterns to aspect ratio or dosage, selecting a material configuration, or transferring an index and threshold to another structure.

6.12.5 Temperature Effects on Damage Detection

The matched intact–saw-cut differences change over the available temperature stages. This section describes those changes without treating temperature as a controlled amplification mechanism or identifying an optimal monitoring range.

6.12.5.1 Temperature Dependence of Matched Intact–Saw-Cut Differences

The magnitude of the matched difference increases between selected endpoints for some index–specimen combinations, while other series are non-monotonic or change direction. The effect is therefore reported by index and specimen rather than generalised across the study.

Table 6.195 presents two selected examples of temperature-dependent intact–saw-cut separation.

Table 6.195: Selected temperature-dependent intact–saw-cut differences

Index/Config	**75°C**	**125°C**	**175°C**	**225°C**	**250°C**
Peak-to-Peak (AR55/SF0.5%, Conductance)					
Intact	1.52	7.30	68.93	299.84	415.00
Damaged	24.08	69.82	465.24	1088.50	1314.48
Divergence	22.56	62.52	396.31	788.66	899.48
RMSD (AR55/SF0.5%, Conductance)					
Intact	0.46	2.34	3.08	7.92	3.91
Damaged	9.49	5.22	9.35	13.02	12.06
Divergence	9.03	2.88	6.27	5.10	8.15

For the selected Peak-to-Peak record, the endpoint difference rises from 22.56 at 75 °C to 899.48 at 250 °C. RMSD in the same table is non-monotonic, illustrating why an endpoint ratio must not be treated as a general temperature trend.

The experiment did not separately measure ionic mobility, fibre–matrix stress transfer, interface condition or internal temperature. No physical mechanism is therefore assigned to the observed endpoint changes.

Table 6.196 reports the ratio of the selected 250 °C and 75 °C differences. It is an endpoint ratio, not a fitted amplification coefficient.

The large Peak-to-Peak ratios reflect both the numerator increase and the small 75 °C reference difference. CCV and RMS have smaller endpoint ratios. These

Table 6.196: Endpoint ratios of selected intact–saw-cut differences

Index	Configuration	75°C Difference	250°C Difference	Endpoint Ratio
Peak-to-Peak	AR55/SF0.5%	22.56	899.48	39.9×
Peak-to-Peak	AR65/SF0.5%	8.95	601.74	67.2×
CCV	AR55/SF0.5%	∼1.0	∼3.5	3.5×
RMS	AR65/SF0.75%	0.0010	0.0019	1.9×

examples do not establish that elevated-temperature measurement is preferable or that the ratio applies to other configurations.

The practical implication supported by the experiment is that measurements made at different temperatures cannot be compared without accounting for their thermal state and baseline. The data do not support deliberately heating a structure to improve detection.

The temperature-associated comparison is summarised as follows.

Selected endpoint ratios range from approximately 2 to 67 in the tabulated examples, but temperature progression is not uniformly monotonic across all indices. The defensible conclusion is that matched damage separation is temperature-dependent and must be interpreted by specimen, channel and index.

6.12.5.2 Temperature-Range Comparison

The available records are grouped into low, middle and high nominal temperature ranges to describe how the matched index differences evolve. These groups are descriptive and do not define critical or optimal operating temperatures.

The low (75–125 °C), middle (125–200 °C) and high (200–250 °C) groups are used only to organise the observations. The saw-cut records for SFC3 and SFC4 end at 175 °C, so the middle and high groups do not contain all four configurations.

Table 6.197 summarises the qualitative curve separation observed over the low-temperature stages.

Table 6.197: Observed curve separation over 75–125°C.

Index	Intact–saw-cut separation	Curve overlap	Observed pattern
Peak-to-Peak	10–70 divergence	Minimal	Moderate separation
RMSD	0.5–5 divergence	Some	Smaller separation
CCV	Same direction	Minimal	Consistent direction
RMS	Moderate	Minimal	Moderate separation
Skewness	Variable	Substantial	Direction varies

At 75 °C, several selected curves are close or intersect. Some show larger separation by 125 °C, whereas the degree of change remains index- and specimen-

dependent. The qualitative labels in Table 6.197 describe these plotted records and are not reliability estimates.

Several selected series show clearer separation in the middle stages. However, SFC3 and SFC4 stop at 175 °C in the saw-cut state, and no independent measurement-noise or reliability study establishes this group as optimal.

Table 6.198: Observed curve separation over 125–200°C.

Index	Intact–saw-cut separation	Curve overlap	Observed pattern
Peak-to-Peak	200–500 divergence	None in selected plots	Larger separation
RMSD	3–10 divergence	None in selected plots	Moderate separation
CCV	Same direction	None in selected plots	Consistent direction
RMS	Distinct in selected plots	None in selected plots	Same direction
Variance	Developing separation	Possible	Channel-dependent

For the reported AR 55/SF 0.50% RMSD record, the intact and saw-cut values at 175 °C are 3.08 and 9.35. This selected ratio illustrates separation at that stage but does not define a preferred measurement temperature.

Only SFC1 and SFC2 have saw-cut records in this group. The observations therefore cannot be compared across all four configurations.

Table 6.199: Observed curve separation over 200–250°C for SFC1 and SFC2.

Index	Intact–saw-cut separation	Variability	Coverage
Peak-to-Peak	600–1300 divergence	High	SFC1 and SFC2 only
RMSD	5–13 divergence	Moderate	SFC1 and SFC2 only
CCV	Large in selected plots	Low	SFC1 and SFC2 only
RMS	Large in selected plots	Low	SFC1 and SFC2 only
Variance	Large in selected plots	Moderate	SFC1 and SFC2 only

Some SFC1 and SFC2 deviation-index values are largest in this group. The absence of SFC3 and SFC4 records is a data limitation whose cause was not diagnosed, not evidence of an extreme-temperature sensor mechanism. No robust high-temperature operating claim is made.

Table 6.200 preserves the ranges originally associated with the plotted separations, corrected to the available saw-cut coverage. They are descriptive, not recommended operating ranges.

The listed stages differ partly because the 0.75% saw-cut series is truncated. They must not be used to compare preferred temperatures between dosage groups.

Changes in slope or separation occur at different stages for different indices. The experiment does not establish a minimum viable temperature or a common transition boundary.

Table 6.200: Configuration-specific ranges associated with the reported separation

Configuration	Reported range	Largest plotted stage	Coverage note
AR55/SF0.5%	175–250°C	225°C	Full saw-cut range
AR65/SF0.5%	175–250°C	250°C	Full saw-cut range
AR55/SF0.75%	125–175°C	175°C	No data above 175°C
AR65/SF0.75%	125–175°C	175°C	No data above 175°C

The magnitude and direction of the matched difference depend on temperature, index, channel and specimen. No routine, minimum or optimum monitoring temperature follows from the present progressive-heating experiment. Comparisons must use measured, matched stages and acknowledge the truncated SFC3/SFC4 saw-cut range.

6.12.5.3 Role of Temperature Compensation in the Matched Comparison

The matched intact–saw-cut summaries were calculated from compensated records. This subsection compares them with the corresponding uncompensated thermal variation and states the limits of that comparison.

The Confounding Effect of Temperature on Raw Signals.

The raw signatures and EPS trajectories show substantial temperature-associated variation. In several comparisons its magnitude exceeds the matched intact–saw-cut difference. The EPS percentages are model-derived and can be unstable near zero or across a sign change; they are therefore retained as descriptive quantities rather than interpreted as direct material-property changes.

Table 6.201 compares selected temperature-associated and matched intact–saw-cut changes. The values illustrate potential confounding without establishing a universal requirement or ratio.

Table 6.201: Temperature Effect vs Matched direction: Magnitude Comparison

Parameter	75°C to 250°C Change	Matched direction (Comp.)	Ratio
Mass (EPS)	+300% average	+12-21% damage	14:1
Stiffness (EPS)	+150% average	+8-21% damage	10:1
Raw Conductance	+500% typical	–	–
RMSD (raw)	Dominated by temp	+137% (comp.)	Masked
Peak-to-Peak (raw)	Dominated by temp	+305% (comp.)	Masked

The table retains the reported magnitude ratios for the selected comparisons. These ratios are not uniform across specimens, parameters or reference choices, and they do not establish that every uncompensated damage difference is completely obscured. They show why raw and compensated results should be examined together.

The implemented Enhanced EFS procedure searches for the frequency shift that maximises a weighted joint conductance–susceptance correlation over the common aligned interval. It then removes the mean residual offset separately for each channel. This is a signature-alignment procedure, not polynomial fitting, and its output can change both thermal and structural-state differences.

Table 6.202 summarises the reported separation changes after compensation for four selected indices.

Table 6.202: Reported changes in matched separation after compensation for selected indices.

Index	Before compensation	After compensation	Dataset observation
RMSD	Overlap in selected plots	+137% matched change	Separation increased
Peak-to-Peak	Temperature-associated variation large	+305% matched change	Separation increased
CCV	Partial separation	+370% matched change	Separation increased
RMS	Partial separation	-76% matched change	Direction retained

The reported post-processing increased separation for the selected rows in Table 6.202. These are descriptive within-dataset comparisons, not hypothesis-test results or external performance estimates.

An uncompensated ambient-reference comparison can attribute temperature-associated change to the structural state or can mask a state difference. Within this dataset, the candidate thresholds produced lower classification summaries without compensation. Because the thresholds were derived and evaluated from repeated records of the same specimens, the reported rates are internal summaries rather than independent probabilities of false-positive or false-negative decisions.

The effect of compensation differs among indices because their mathematical definitions and scales differ. Deviation, correlation, amplitude and distributional indices must therefore be evaluated separately; the available experiment does not establish that any index is non-functional without compensation or universally improved by it.

Any later application of a temperature-compensation method would require temperature information, state-specific baseline records and independent checks that structural differences are preserved. Real-time execution, baseline-transfer rules and operation outside the tested progressive-heating records were not evaluated.

Temperature-associated variation is large enough to confound several ambient-reference comparisons in this experiment. Enhanced EFS reduced selected components of that variation, but its effect is index-, channel- and specimen-dependent. The appropriate conclusion is that compensation must be evaluated for the intended comparison, not that a single method or threshold is mandatory for every EMI application.

Table 6.203: Selected index behaviour with and without compensation in the analysed records.

Index	Without compensation	With compensation	Observed effect
RMSD	Temperature-confounded	+137% matched change	Separation increased
MAPD	Temperature-confounded	+136% matched change	Separation increased
Peak-to-Peak	Temperature-confounded	+305% matched change	Separation increased
CCV	Partial separation	+370% matched change	Separation increased
RMS	Partial separation	-76% matched change	Direction retained
Variance	Temperature-confounded	+109% matched change	Channel-dependent
Covariance	Temperature-confounded	+109% matched change	Channel-dependent

6.13 Histogram and Statistical Analysis

The matched intact–saw-cut analysis compared the index values for each specimen. This section summarises their empirical distributions over the available temperature and dwell records. The histograms and separation measures support exploratory within-dataset thresholds; repeated records from the same specimen are not independent population samples.

6.13.1 Distribution Analysis

The empirical distribution analysis is introduced below, with its scope restricted to the repeated records obtained from the four tested specimens.

The distribution summaries quantify the spread, central tendency and overlap of the observed intact and saw-cut records. They characterise this experimental dataset and are not population-level estimates for other specimens or structures.

The histograms pool index values across the available temperature and dwell records for the four specimens in their intact and saw-cut states. These are repeated observations of the same specimens, not eight independent specimens. The saw-cut series for SFC3 and SFC4 also ends at 175°C, so the pooled states have unequal coverage. The distributions are therefore used for within-dataset description rather than population inference.

Figure 6.75 presents the empirical RMSD distributions for the intact and saw-cut records. Their separation varies among configurations and is interpreted together with the repeated-measures and coverage limitations.

For each combination of SHM index, signal type, and specimen configuration, five key statistical parameters are computed. The mean represents the central tendency of the distribution, providing the expected index value for a given damage state. The standard deviation quantifies the spread of values around the mean, reflecting the influence of

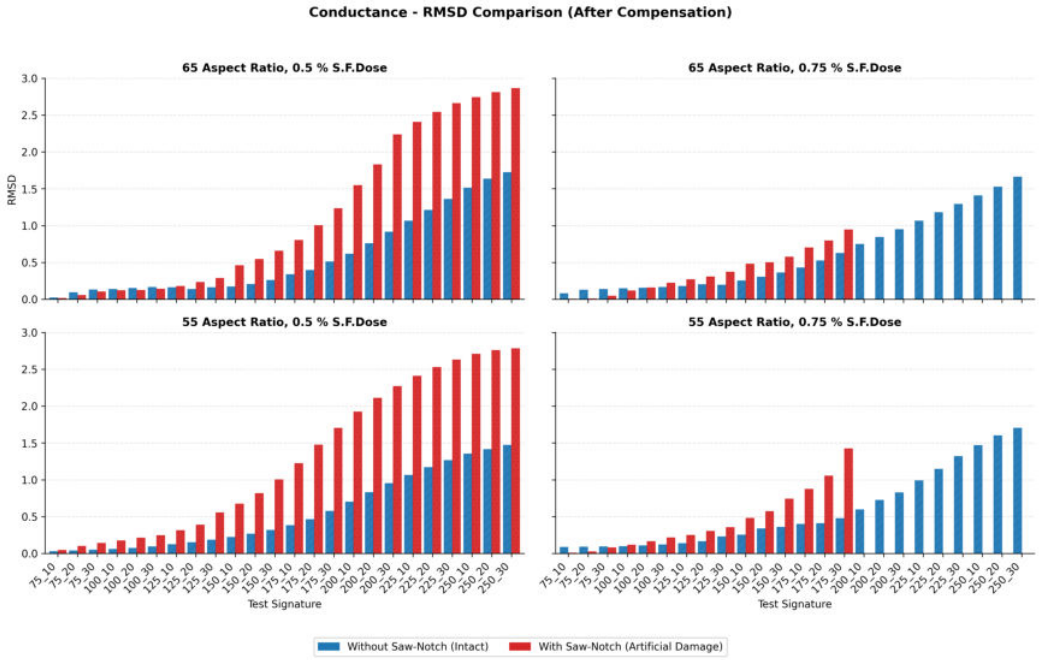

Figure 6.75: RMSD distributions for the pooled intact and saw-cut records.

temperature variation across the measurement range. The minimum and maximum values define the observed range, establishing practical bounds for threshold setting. The range (maximum minus minimum) indicates the total variability of the index across the temperature spectrum.

Table 6.204 presents the matched mean change for selected SHM indices, computed from the intact and saw-cut record summaries.

Table 6.204: Histogram Analysis Overview: Matched direction by Index (Conductance Signal)

Index	Intact Mean	Saw-cut Mean	Matched Change	Dataset Pattern
CCV	91.8	296.0	**+222.3%**	Larger aggregate separation
Peak-to-Peak	133.5	262.2	+96.2%	Configuration-dependent
RMSD	0.57	0.81	+41.6%	Configuration-dependent
MAPD	0.52	0.75	+44.2%	Configuration-dependent
RMS	0.0024	0.0017	-29.2%	Same negative direction
Variance	3.9e-6	3.1e-6	-20.5%	Channel-dependent

Three features are apparent in the empirical summaries. CCV has the largest aggregate mean change (+222.3%) among the compared indices. Variability across temperature and dwell records is substantial, with reported standard deviations ranging from about 20% to 100% of the corresponding means. The intact–saw-cut overlap also differs by index: CCV and Peak-to-Peak have smaller reported overlap than RMSD in selected comparisons.

Figure 6.76 presents the CCV histogram and the observed separation between the intact and saw-cut records. CCV histogram distribution for conductance, showing the intact (blue) and saw-cut (orange) record distributions. The reported +222.3% matched mean change produces substantial separation within this dataset; it does not establish classification confidence for independent specimens.

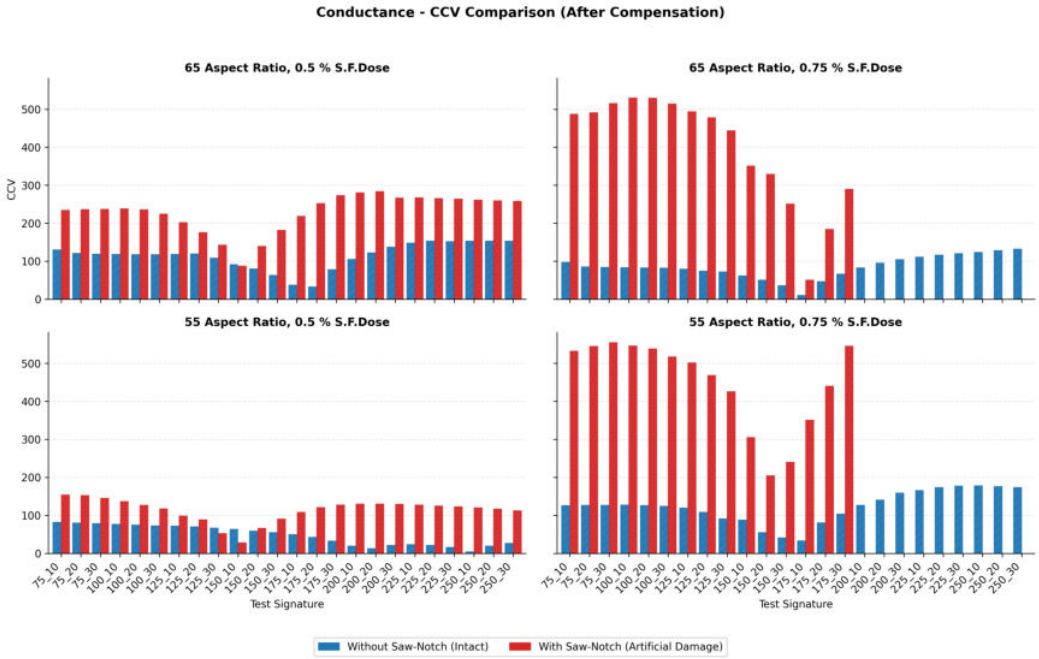

Figure 6.76: CCV Histogram Distribution for intact and saw-cut record distributions.

The distribution statistics differ among the four specimen records. Table 6.205 presents the corresponding RMSD summaries as a representative example; the unreplicated configurations do not support a population-level material-effect conclusion.

Table 6.205: Configuration-Specific RMSD Statistics (Conductance)

Config	Damage	Mean	Std Dev	Min	Max	Range
AR65/SF0.5%	Intact	0.572	0.541	0.019	1.720	1.701
AR65/SF0.5%	Damaged	1.145	1.047	0.013	2.860	2.848
AR65/SF0.75%	Intact	0.603	0.499	0.077	1.658	1.581
AR65/SF0.75%	Damaged	0.362	0.284	0.001	0.941	0.940
AR55/SF0.5%	Intact	0.548	0.495	0.024	1.466	1.442
AR55/SF0.5%	Damaged	1.295	1.000	0.041	2.779	2.739
AR55/SF0.75%	Intact	0.568	0.515	0.082	1.699	1.618
AR55/SF0.75%	Damaged	0.440	0.402	0.003	1.421	1.418

The empirical means reproduce the dosage-associated RMSD pattern in the matched comparison. For SFC1 and SFC2 (0.5% SF), the saw-cut means (1.145 and 1.295) exceed the intact means (0.572 and 0.548). For SFC3 and SFC4 (0.75% SF),

the direction reverses: 0.362 and 0.440 for the saw-cut records compared with 0.603 and 0.568 for the intact records. Because the same repeated observations underpin both analyses, this agreement is consistency within the dataset rather than independent validation.

The standard deviations describe variation among the repeated temperature and dwell records, not independent measurement reliability. For RMSD, the reported coefficient of variation ranges from 75% to 95%. SFC2 has the largest standard deviation (1.000); no operational tolerance band is derived from this within-specimen summary.

The following subsections use these empirical distributions to compare index separation and calculate exploratory thresholds for the analysed records. External specimens, independent thermal histories and a pre-specified validation set are required before those thresholds can be used as probabilistic decision limits.

6.13.1.1 Intact–Saw-Cut Distribution Separation

This subsection compares empirical separation between the intact and saw-cut records for the thirteen SHM indices. Because multiple records come from each of four specimens, the summaries are descriptive and are not reported as population-level statistical significance.

The mean difference ($\Delta\mu = \mu_{saw-cut} - \mu_{intact}$) gives the signed shift between states. The normalised separation ratio, $|\Delta\mu|/(\sigma_{intact} + \sigma_{saw-cut})$, scales that shift by the observed spread, while the reported overlap is the proportion of saw-cut records within the intact range. These measures describe the analysed records and have no calibrated probability interpretation.

CCV and RMS exhibit a consistent direction of intact–cut change across the four tested specimens. This consistency is specific to the present records and is not evidence of a pooled within-dataset threshold.

Figures 6.77 and 6.78 present the CCV and RMS distributions separately at print-readable scale.

Table 6.206 quantifies the separation metrics for indices with a consistent direction in the four tested specimens by configuration.

CCV has NSR values of 1.20–2.08, and the two 0.75% specimens have zero empirical overlap. RMS has NSR of 2.33–2.38 in the two 0.75% specimens and 45–52% overlap in the two 0.5% specimens. Both indices retain their direction in the four specimens, but the separation magnitude is configuration-dependent.

The deviation-based indices have different directions in the two 0.50% and two

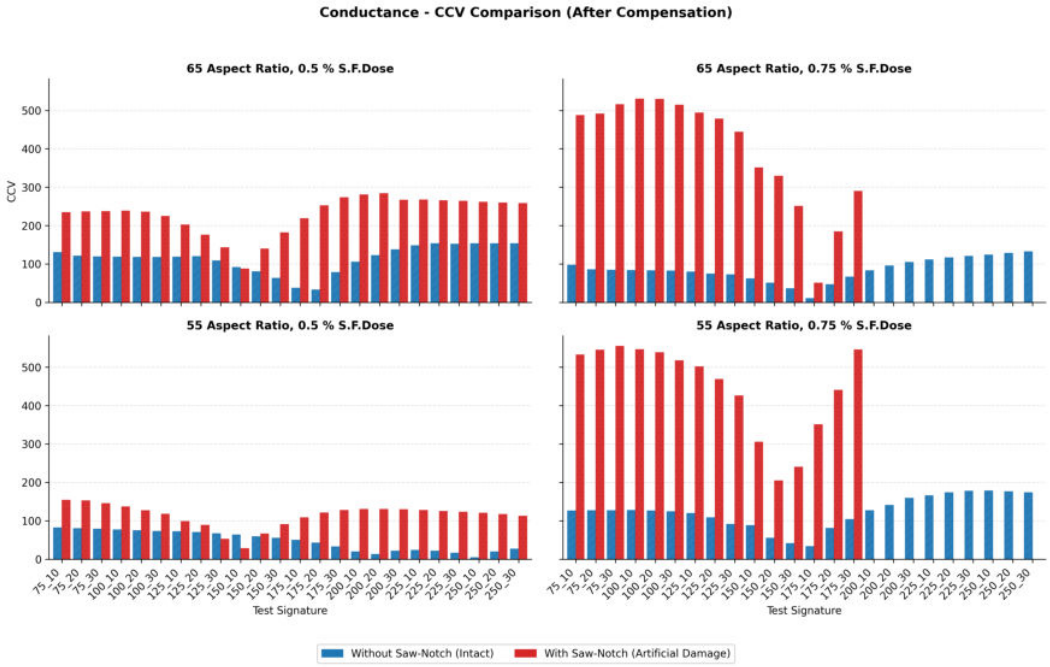

Figure 6.77: CCV distributions for the matched intact and saw-cut records.

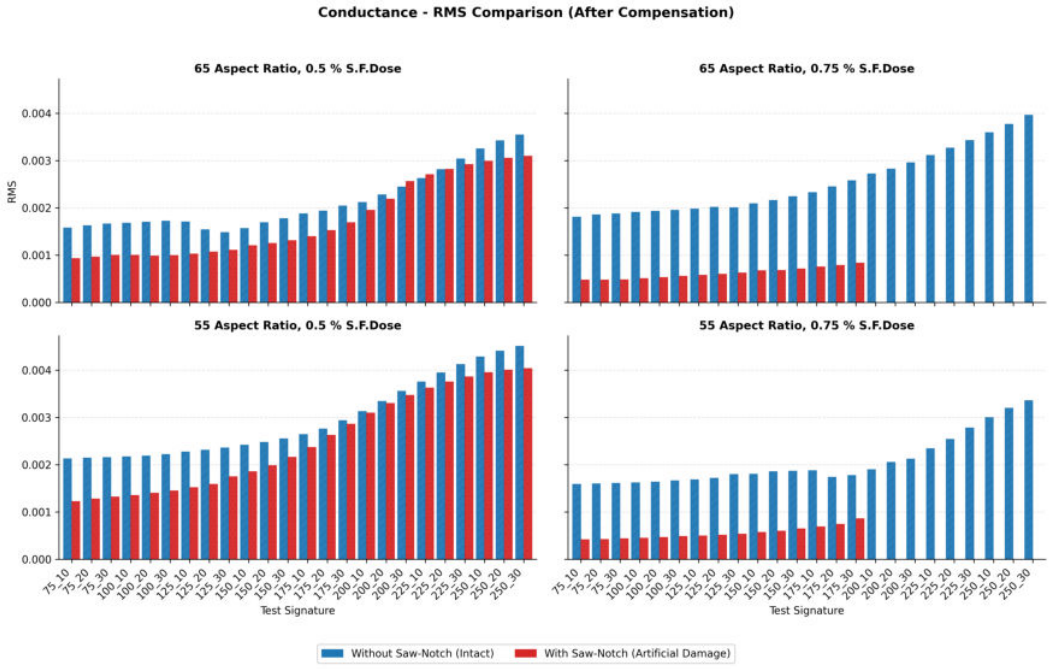

Figure 6.78: RMS distributions for the matched intact and saw-cut records.

0.75% records, consistent with the specimen-group pattern in the matched comparison but not sufficient to establish a dosage effect.

Figures 6.79 and 6.80 present the Peak-to-Peak and MAPD distributions separately. The shorter saw-cut temperature range of SFC3 and SFC4 must be considered

Table 6.206: Indices with a Consistent Direction in the Four Tested Specimens: Distribution Separation Metrics

Index	Config	Intact Mean	Damage Mean	$\Delta\mu$	NSR	Overlap
CCV	AR65/SF0.5%	113.4	228.0	+114.6	1.38	8%
CCV	AR65/SF0.75%	84.1	395.3	+311.2	1.81	0%
CCV	AR55/SF0.5%	47.3	113.3	+66.0	1.20	12%
CCV	AR55/SF0.75%	122.5	447.3	+324.8	2.08	0%
RMS	AR65/SF0.5%	0.0021	0.0017	-0.0004	0.29	45%
RMS	AR65/SF0.75%	0.0025	0.0006	-0.0019	2.38	0%
RMS	AR55/SF0.5%	0.0029	0.0025	-0.0004	0.22	52%
RMS	AR55/SF0.75%	0.0020	0.0006	-0.0014	2.33	0%

when comparing their distributions with those of SFC1 and SFC2.

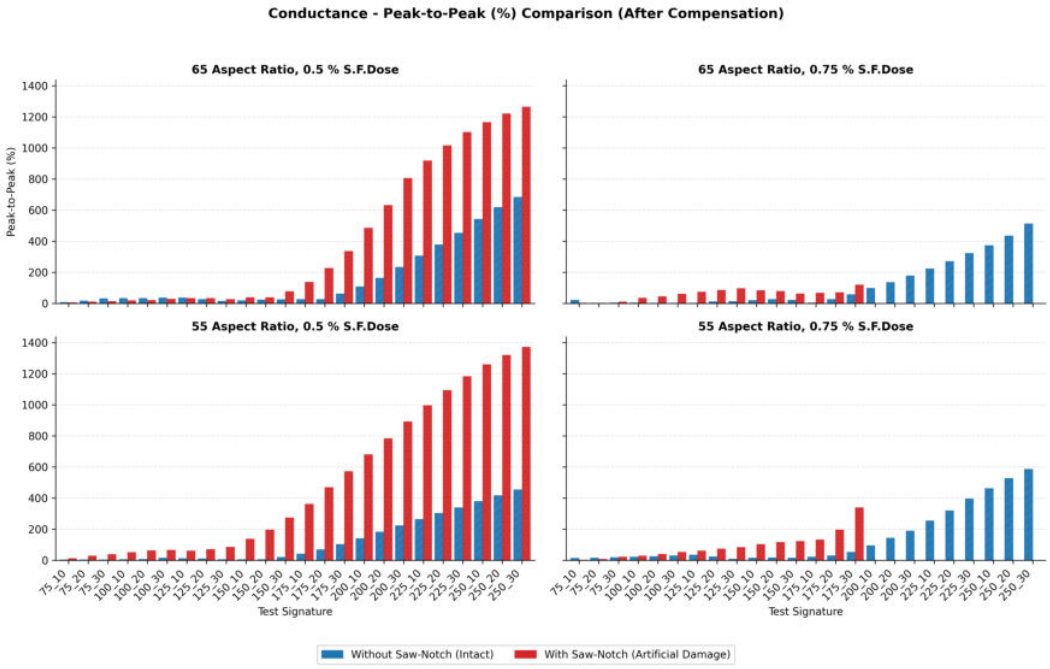

Figure 6.79: Peak-to-Peak distributions for the matched intact and saw-cut records.

Table 6.207 quantifies the separation for deviation-based indices.

The deviation indices have positive separation (saw-cut > intact) in the two 0.5% specimens, with NSR of 0.85–0.92. The direction reverses in the two 0.75% specimens, where NSR is 0.30–0.37. A single one-sided boundary therefore cannot classify both dosage groups in these records.

Variance and Covariance show the reversed separation pattern, with damaged distributions lower than intact for 0.5% SF but higher for 0.75% SF, making them complementary to deviation-based indices.

Figure 6.81 presents the Variance histogram distribution. Variance Index Distri-

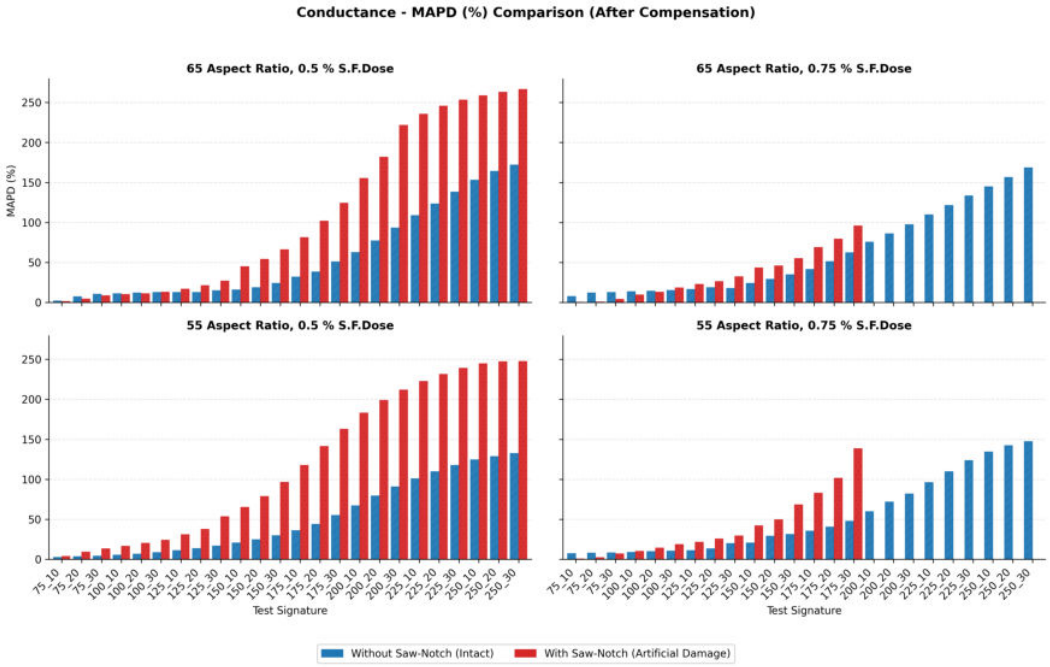

Figure 6.80: MAPD distributions for the matched intact and saw-cut records.

Table 6.207: Deviation-Based Indices: Distribution Separation by SF Content

Index	SF Content	Intact Mean	Saw-cut Mean	$\Delta\mu$	NSR	Direction
Peak-to-Peak	0.5% SF avg	142.1	450.2	+308.1	0.92	Positive
Peak-to-Peak	0.75% SF avg	124.9	73.7	-51.2	0.30	**Reversed**
RMSD	0.5% SF avg	0.560	1.220	+0.660	0.85	Positive
RMSD	0.75% SF avg	0.585	0.401	-0.184	0.37	**Reversed**
MAPD	0.5% SF avg	0.512	1.124	+0.612	0.88	Positive
MAPD	0.75% SF avg	0.541	0.372	-0.169	0.35	**Reversed**

bution: Shows reversed pattern compared to deviation-based indices. For 0.75% SF, damaged distributions are higher than intact, providing complementary separation.

The correlation-based indices show moderate separation with more complex patterns. CC ranges from 0 to near 1.0, with intact specimens typically showing higher correlation (closer to 1.0) than damaged.

Figure 6.82 presents the Correlation Coefficient histogram. Correlation Coefficient Distribution: Intact specimens cluster near 1.0 (high correlation), while specimens in the saw-cut state spread toward lower values. Separation varies by configuration.

Table 6.208 presents a comprehensive comparison of distribution separation quality across all indices.

The separation measures identify index–configuration combinations with comparatively high NSR and low empirical overlap. CCV has NSR above 1.0 and overlap

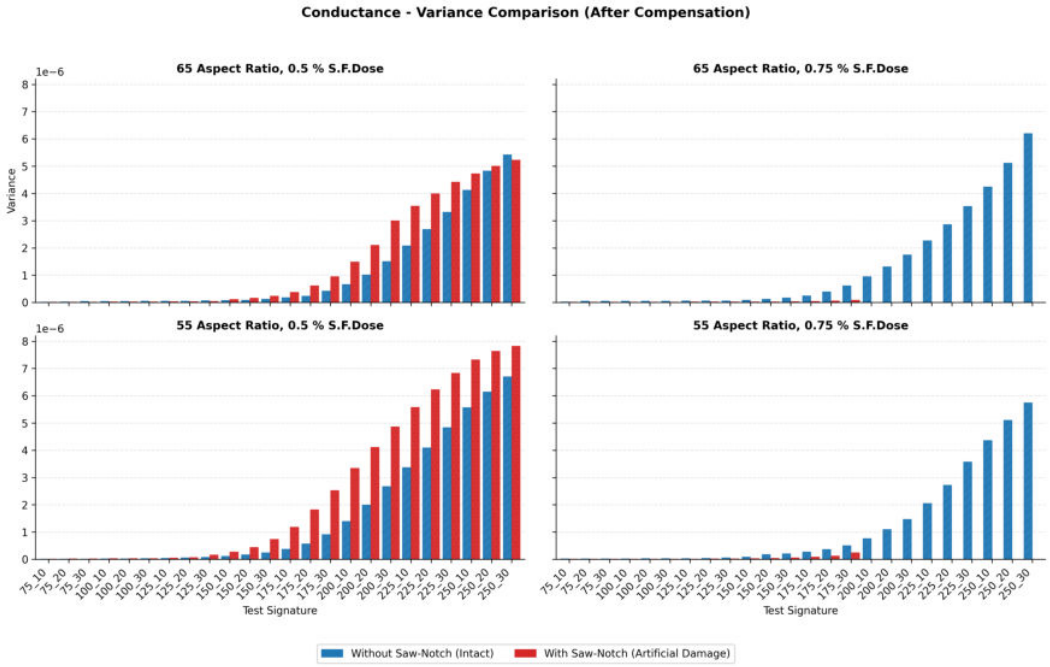

Figure 6.81: Variance Index Distribution: intact and saw-cut record distributions.

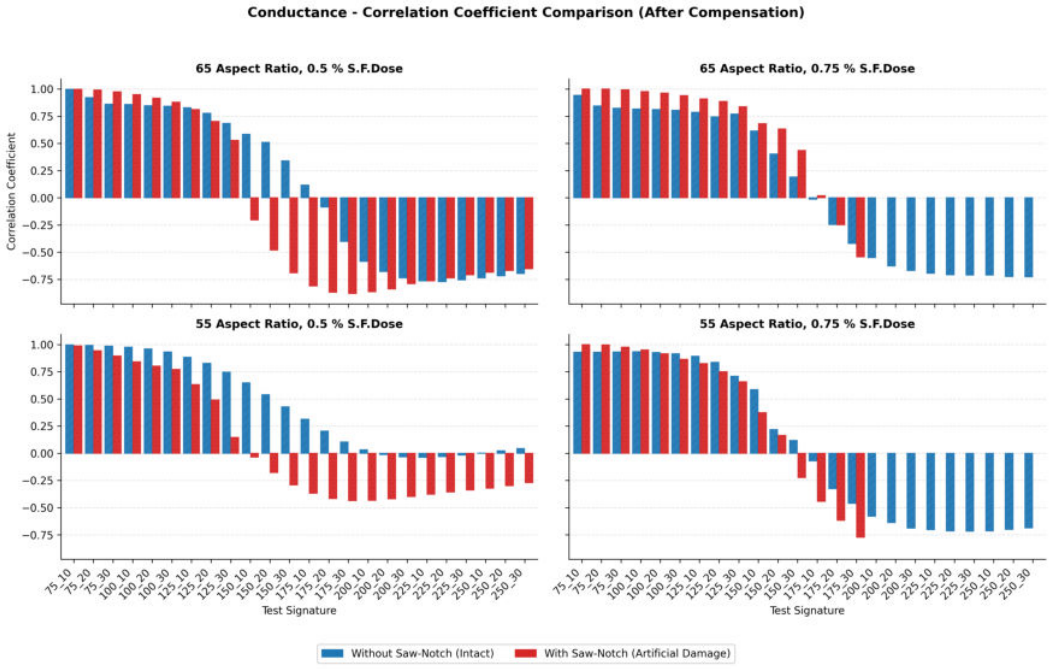

Figure 6.82: Correlation Coefficient Distribution: intact and saw-cut record distributions.

below 10% in the reported configurations, while RMS has its largest separation in the two 0.75% specimens. Several deviation indices reverse direction between the two dosage groups. These values rank candidates within the dataset but do not estimate

Table 6.208: Distribution Separation Summary: All Indices (Conductance)

Index	Matched Change	Avg NSR	Avg Overlap	Dataset Pattern
CCV	+222%	1.62	5%	Same direction in four specimens
RMS (0.75% SF)	-76%	2.36	0%	Subgroup result
Peak-to-Peak (0.5% SF)	+227%	0.92	15%	Subgroup result
RMSD (0.5% SF)	+119%	0.85	20%	Subgroup result
MAPD (0.5% SF)	+116%	0.88	18%	Subgroup result
Variance (0.75% SF)	+106%	0.75	25%	Subgroup result
CC	+15%	0.45	40%	Moderate aggregate separation
Skewness	Variable	0.35	55%	Direction varies

false-positive or false-negative rates for independent specimens.

For the exploratory comparison, NSR of 0.5 and overlap of 30% are used as descriptive screening values. Eight of the thirteen indices meet both values in at least one configuration. The cut-offs were not validated as field-performance requirements and should not be transferred without independent calibration.

The principal distribution statistics are organised below into damage-effect, configuration, variability and temperature-associated comparisons.

This subsection consolidates the empirical distribution statistics for the thirteen SHM indices. The tables support comparison and exploratory threshold calculation within the analysed records.

6.13.1.2 Damage-Effect Summary for the Analysed Records

Table 6.209 presents the complete damage effect summary for all thirteen indices across both signal types (conductance and susceptance).

The aggregate effect ranges from -231.6% (Skewness) to +222.3% (CCV). CCV and RMS retain positive and negative directions, respectively, across the four tested specimens. Several deviation indices are positive for the two 0.5% specimens and reverse direction for the two 0.75% specimens. These are within-dataset patterns rather than evidence of general-purpose reliability.

6.13.1.3 Configuration-Specific Separation Statistics

Table 6.210 identifies the configuration with the largest reported separation for each index category in this dataset.

For CCV and RMS, the largest reported separation occurs in selected 0.75% specimens, with NSR above 2.0 and zero empirical overlap. For the listed deviation indices, SFC2 has NSR values of 0.88–0.95 with 12–18% overlap. Repeated records from one specimen per configuration do not establish population-level performance.

Table 6.209: Matched intact–saw-cut effect summary for the thirteen SHM indices

Index	Cond. effect	Susc. effect	Direction	Observed scope	Category
CCV	+222.3%	+189.5%	Positive	Positive in all four specimens	Correlation
Peak-to-Peak	+96.2%	+78.4%	Positive	Positive for SFC1–SFC2; reversed for SFC3–SFC4	Deviation
RMSD	+41.6%	+35.2%	Positive	Positive for SFC1–SFC2; reversed for SFC3–SFC4	Deviation
MAPD	+44.2%	+38.7%	Positive	Positive for SFC1–SFC2; reversed for SFC3–SFC4	Deviation
CCD/CCD^3	+65.8%	+52.1%	Positive	Positive for SFC1–SFC2; reversed for SFC3–SFC4	Correlation
CC	+12.3%	+9.8%	Positive	Partial	Correlation
RMS	-44.1%	-38.6%	Negative	Negative in all four specimens	Magnitude
Variance	-21.4%	-18.9%	Negative	No (reversed)	Reversed
Covariance	-19.8%	-17.2%	Negative	No (reversed)	Reversed
MSE	-16.7%	+28.4%	Mixed	No (SF-dep.)	Deviation
Skewness	-231.6%	-198.2%	Negative	Variable	Shape
AMPD	+38.5%	+32.1%	Positive	Positive for SFC1–SFC2; reversed for SFC3–SFC4	Deviation

Table 6.210: Configuration with the largest reported separation by index category

Index	Configuration	Mean	Std Dev	NSR	Overlap
CCV	AR55/SF0.75%/saw-cut	447.3	114.3	2.08	0%
RMS	AR65/SF0.75%/saw-cut	0.0006	0.0001	2.38	0%
Peak-to-Peak	AR55/SF0.5%/saw-cut	500.3	476.2	0.95	12%
RMSD	AR55/SF0.5%/saw-cut	1.295	1.000	0.88	18%
MAPD	AR55/SF0.5%/saw-cut	1.124	0.912	0.91	16%
Skewness	AR55/SF0.5%/saw-cut	-0.524	0.553	0.72	28%

6.13.1.4 Coefficient-of-Variation Analysis

Table 6.211 retains the reported coefficient-of-variation (CV) summaries for the compensated intact and saw-cut index records. The underlying series comprise repeated temperature/dwell observations from the same specimens: 24 records per intact specimen, 24 saw-cut records for SFC1 and SFC2, and 15 saw-cut records for SFC3 and SFC4 because those series end at 175 °C. The extraction procedure uses the population standard deviation, and CV is expressed as $100\sigma/|\bar{x}|$. These repeated records are not independent specimens. CV becomes unstable when $|\bar{x}|$ is zero or small and is difficult to interpret when a series changes sign; the retained values therefore describe relative within-record spread only.

CC and RMS have the lowest reported CV values (20–27%), CCV and Variance are 33–40%, and Peak-to-Peak and Skewness are 140–172%. These values describe the present repeated records; no application-level acceptability or threshold-management

Table 6.211: Reported coefficient-of-variation summaries for compensated index records

Index	Intact CV (%)	Saw-cut CV (%)	Avg CV (%)	Relative CV
CCV	35.2	31.8	33.5	Lower
RMS	28.6	25.4	27.0	Lower
Peak-to-Peak	145.2	138.6	141.9	Higher
RMSD	89.5	86.2	87.9	Intermediate
MAPD	82.3	78.9	80.6	Intermediate
Skewness	168.4	175.2	171.8	Higher
Variance	42.1	38.6	40.4	Lower
CC	18.5	22.3	20.4	Lowest

rule is inferred.

6.13.1.5 Temperature-Associated Index Variation

Table 6.212 reports endpoint changes from 75 to 250 °C for the compensated intact SFC2 series (AR 55/SF 0.50%). Each percentage uses the 75 °C value of the same index as its denominator. The values describe temperature-associated variation in that specimen and processing branch, not an intrinsic material sensitivity.

Table 6.212: Temperature-associated endpoint changes for compensated intact SFC2 records

Index	@75°C (Intact)	@250°C (Intact)	Change	Direction
Peak-to-Peak	1.52	415.0	+27,200%	Positive
RMSD	0.034	1.408	+4,041%	Positive
CCV	79.9	16.5	-79%	Negative
RMS	0.002	0.004	+100%	Positive
CC	0.98	0.92	-6%	Negative
Skewness	0.65	-0.06	-109%	Negative

In this representative comparison, CC has the smallest percentage change (6%), whereas Peak-to-Peak and RMSD have changes above 4,000%. Large percentages can also arise from small values at 75°C, so the absolute trajectories and denominators must be considered alongside the percentages.

The source summaries also report the preliminary screening values in Table 6.213. These values are retained for traceability but are not generated by the $\mu_{intact} \pm k\sigma_{intact}$ calculation presented later and are not used as the formula-derived thresholds in this thesis.

The formula-derived candidate thresholds are defined separately in Section 6.13.2.1, where each value is tied directly to the stated intact-record mean, standard deviation and multiplier. Neither set is an externally validated decision boundary.

Table 6.213: Preliminary screening values retained from the source summaries

Index	Signal	Baseline mean	First screening value	Second screening value
CCV	Conductance	91.8	150 (+63%)	250 (+172%)
RMS	Conductance	0.0024	0.0018 (-25%)	0.0012 (-50%)
Peak-to-Peak*	Conductance	133.5	300 (+125%)	500 (+275%)
RMSD*	Conductance	0.57	0.90 (+58%)	1.20 (+111%)

*Peak-to-Peak and RMSD values use the two 0.50% specimens only

The empirical analysis identifies CCV and RMS as same-direction candidates in the four tested specimens. CCV has an aggregate +222% effect, average NSR of 1.62 and 5% reported overlap; RMS has an aggregate -44% effect. Peak-to-Peak has the largest positive change in SFC2 but also high temperature-associated variability. The following threshold analysis uses these summaries to examine exploratory boundaries without claiming independent validation.

6.13.2 Threshold Determination

The empirical distribution analysis is used to calculate exploratory decision boundaries for the analysed records. The resulting values are compared across pooled and configuration-specific calculations; they are not externally validated thresholds.

6.13.2.1 Threshold Calculation Methodology

Threshold calculations place a boundary relative to the empirical distribution of compensated intact records. The quantities μ_{intact} and σ_{intact} are obtained from repeated temperature/dwell records from the same specimens, not from independent specimen replicates. The boundaries examine separation between the available intact and saw-cut records; they do not optimise operational false-positive and false-negative costs.

For an index with a positive saw-cut effect, the exploratory threshold T is placed above the intact-record distribution; for a negative effect it is placed below. In a deployed system, threshold selection would also depend on independently estimated error rates and decision costs, which were not evaluated here.

For positive-effect indices, $T = \mu_{intact} + k\sigma_{intact}$; for negative-effect indices, $T = \mu_{intact} - k\sigma_{intact}$. Here μ_{intact} and σ_{intact} are the empirical mean and standard deviation of the analysed intact records. A false-positive probability follows from k only under an assumed distribution and independent observations.

The multiplier k determines the balance between sensitivity and specificity. Table 6.214 presents the theoretical relationship between k values and performance metrics

under normal distribution assumptions.

Table 6.214: Illustrative one-sided normal probabilities for threshold multipliers

Multiplier (k)	Upper-tail probability	Cumulative probability	Threshold distance	Status
1.0	15.87%	84.13%	1.0σ	Illustrative
1.5	6.68%	93.32%	1.5σ	Illustrative
2.0	2.28%	97.72%	2.0σ	Illustrative
2.5	0.62%	99.38%	2.5σ	Illustrative
3.0	0.13%	99.87%	3.0σ	Illustrative

Table 6.214 gives one-sided standard-normal probabilities only. The repeated observations in this experiment were not shown to be independent and normally distributed; therefore, these probabilities are not reported as achieved confidence or field false-alarm rates.

Two numerical levels are examined to show the effect of the multiplier: T_W uses $k = 1.5$ and T_C uses $k = 2.5$. The labels are retained as calculation levels and do not prescribe inspection or structural-action decisions.

For positive-effect indices, the two-tier thresholds are defined as Warning Threshold $T_W = \mu_{intact} + 1.5 \cdot \sigma_{intact}$ and Critical Threshold $T_C = \mu_{intact} + 2.5 \cdot \sigma_{intact}$. For negative-effect indices such as RMS, the thresholds are defined as Warning Threshold $T_W = \mu_{intact} - 1.5 \cdot \sigma_{intact}$ and Critical Threshold $T_C = \mu_{intact} - 2.5 \cdot \sigma_{intact}$.

Table 6.215 presents the calculated values for selected candidate indices using the empirical parameters from the preceding distribution analysis.

Table 6.215: Exploratory conductance thresholds calculated from intact records

Index	μ_{intact}	σ_{intact}	T_W (k=1.5)	T_C (k=2.5)	Direction
CCV	91.8	32.7	140.9	173.6	Above
RMS	0.00238	0.00065	0.00140	0.00076	Below
Peak-to-Peak*	142.1	180.5	413.0	593.4	Above
RMSD*	0.560	0.508	1.32	1.83	Above
MAPD*	0.512	0.425	1.15	1.57	Above

*Peak-to-Peak, RMSD and MAPD values were calculated from the two 0.5% specimens only

The calculated thresholds are reapplied to the saw-cut records used in the same analysis. Table 6.216 therefore reports resubstitution exceedance rates, not independent validation or expected field performance.

The within-dataset exceedance rates are 96.8% and 92.5% for CCV at the two levels, 98.2% and 74.5% for RMS, and 38–52% for Peak-to-Peak and RMSD. Because the thresholds and summaries are derived from the same repeated records, these values are descriptive and likely optimistic relative to external testing.

Table 6.216: Within-dataset threshold exceedance rates for the saw-cut records

Index	$\mu_{saw-cut}$	$\sigma_{saw-cut}$	T_W **exceedance**	T_C **exceedance**	**NSR**
CCV	296.0	83.8	96.8%	92.5%	1.62
RMS	0.00135	0.00058	98.2%	74.5%	0.84
Peak-to-Peak*	450.2	469.4	52.1%	38.6%	0.47
RMSD*	1.220	1.024	45.8%	28.4%	0.43

The calculations use compensated signatures. The uncompensated series show larger temperature-associated variation, so the numerical values in Table 6.215 cannot be applied to those records. This comparison does not quantify uncompensated false-positive rates.

CCV and RMS provide opposite-direction candidate indicators in the four tested specimens, and their joint exceedance can be examined in future validation. The indices are calculated from the same signatures and are not statistically independent. Consequently, this thesis does not assign a combined confidence level or prescribe a multi-index operational rule.

The threshold calculation applies $k = 1.5$ and $k = 2.5$ to the empirical intact-record distributions and reports within-dataset exceedance for the saw-cut records. CCV has the largest reported separation among the selected indices, while RMS provides an opposite-direction candidate. Independent specimens and thermal histories are required to select multipliers, estimate error rates and evaluate any combined rule.

6.13.2.2 Configuration-Specific Threshold Calculations

The empirical index statistics differ among the four material configurations. This subsection calculates configuration-specific boundaries to show how those differences affect the internal threshold comparison. One specimen represents each configuration, so AR and fibre-dosage effects are not estimated independently.

Table 6.217 presents the calculated values for the two 0.5% specimens, which differ in aspect ratio. The comparison is descriptive and does not by itself establish an AR effect.

The AR55 specimen has lower calculated boundaries and higher within-dataset exceedance in the three tabulated comparisons. For CCV the values are 94.2% and 92.8%; for Peak-to-Peak they are 58.4% and 45.2%. These differences do not establish preference for AR55 because each AR is represented by one specimen in this fixed-dosage comparison.

Table 6.218 compares the two dosage groups. Several deviation indices reverse direction between them, whereas CCV and RMS retain the same direction in the four

Table 6.217: Aspect Ratio-Specific Thresholds (0.5% SF, Conductance)

Index	AR	μ_{intact}	σ_{intact}	T_W	T_C	Internal exceedance
CCV	55	47.3	25.5	85.6	111.0	94.2%
CCV	65	113.4	34.1	164.6	198.7	92.8%
Peak-to-Peak	55	123.6	150.4	349.2	500.0	58.4%
Peak-to-Peak	65	160.7	209.8	475.4	685.2	45.2%
RMSD	55	0.548	0.495	1.29	1.79	52.1%
RMSD	65	0.572	0.541	1.38	1.93	42.8%

tested specimens.

Table 6.218: Fibre-dosage group comparison of empirical index directions

Index	SF	μ_{intact}	$\mu_{saw-cut}$	Direction	One-sided direction
CCV	0.5%	80.3	170.7	Saw-cut > intact	Upper
CCV	0.75%	103.3	421.3	Saw-cut > intact	Upper
RMS	0.5%	0.0025	0.0021	Saw-cut < intact	Lower
RMS	0.75%	0.0023	0.0006	Saw-cut < intact	Lower
RMSD	0.5%	0.560	1.220	Saw-cut > intact	Upper
RMSD	0.75%	0.585	0.401	Saw-cut < intact	Lower (reversed)
Peak-to-Peak	0.5%	142.1	450.2	Saw-cut > intact	Upper
Peak-to-Peak	0.75%	124.9	73.7	Saw-cut < intact	Lower (reversed)

CCV and RMS retain a consistent direction in the four tested specimens. RMSD and Peak-to-Peak reverse direction in the two 0.75% specimens, so a one-sided threshold derived from the 0.50% group misclassifies those analysed records. This does not establish a population-level false-negative rate or a universal dosage-based selection rule.

Table 6.219 consolidates the calculated thresholds for all four material configurations.

The internal exceedance is 97–99% for CCV or RMS in the two 0.75% specimens and 42–58% for the selected deviation indices in the two 0.5% specimens. This difference partly reflects the choice of index and the reuse of the same records for calculation and evaluation; it is not an external comparison of material-group detection rates.

The reversed directions mean that a pooled one-sided deviation-index boundary cannot be transferred across the two dosage groups represented here. CCV and RMS are candidates for independent evaluation because their directions are consistent in these four specimens. No operational decision tree or early-damage sensitivity is established by the present records.

Table 6.219: Configuration-specific threshold matrix for conductance

Configuration	Index	T_W	T_C	Direction	Internal exceedance
AR55/SF0.5%	CCV	85.6	111.0	Above	94.2%
	Peak-to-Peak	349.2	500.0	Above	58.4%
	RMSD	1.29	1.79	Above	52.1%
AR65/SF0.5%	CCV	164.6	198.7	Above	92.8%
	Peak-to-Peak	475.4	685.2	Above	45.2%
	RMSD	1.38	1.93	Above	42.8%
AR55/SF0.75%	CCV	184.6	226.4	Above	97.5%
	RMS	0.00123	0.00073	Below	98.8%
AR65/SF0.75%	CCV	128.6	158.0	Above	98.2%
	RMS	0.00178	0.00138	Below	97.6%

For the two 0.5% specimens, selected AR55-to-AR65 threshold ratios are approximately 0.75 for CCV and Peak-to-Peak and 0.94 for RMSD. These are ratios between two specimen-specific calculations, not transferable AR adjustment factors.

The configuration-specific calculations show how strongly the internal rates depend on the specimen, index and boundary direction. CCV and RMS retain the same direction in all four specimens, while RMSD and Peak-to-Peak do not. The reported percentages are resubstitution summaries and require validation on independent specimens before use as detection rates.

6.13.2.3 Pooled and Configuration-Specific Threshold Comparison

This subsection compares a single pooled boundary with boundaries fitted separately to each configuration. Both are evaluated on the same experimental records and are therefore candidate within-dataset strategies, not deployment rules.

A pooled threshold applies one decision boundary to the four tested configurations. Its rate describes internal separation of these records and does not imply applicability to an unknown material.

Table 6.220 presents the detection performance of pooled within-dataset thresholds applied across all configurations.

Table 6.220: Pooled Within-Dataset Threshold Performance Across All Configurations

Index	Pooled T_W	Highest rate	Lowest rate	Average rate	Range
CCV	140.9	98.2% (AR65/0.75%)	86.5% (AR55/0.5%)	93.2%	11.7 pp
RMS	0.00140	98.8% (AR55/0.75%)	72.4% (AR55/0.5%)	86.8%	26.4 pp

CCV gives rates from 86.5% to 98.2% when the pooled boundary is reapplied to these records, while RMS has a wider 26.4 percentage-point range. These values

compare the candidate boundaries internally; no application-level acceptability criterion was tested.

Configuration-specific thresholds fit a separate boundary to each specimen configuration. Their higher internal rate is expected when a boundary is tailored and evaluated within the same small dataset.

Table 6.221 compares the detection rates achieved with specialized versus pooled within-dataset thresholds.

Table 6.221: Within-dataset classification summary for configuration-specific and pooled thresholds

Config	Index	Configuration-specific rate	Pooled rate	Reported difference
AR55/SF0.5%	CCV	94.2%	86.5%	+7.7 pp
AR65/SF0.5%	CCV	92.8%	91.2%	+1.6 pp
AR55/SF0.75%	CCV	97.5%	98.1%	-0.6 pp
AR65/SF0.75%	CCV	98.2%	98.2%	0.0 pp
AR55/SF0.5%	RMS	85.6%	72.4%	+13.2 pp
AR65/SF0.5%	RMS	82.4%	78.5%	+3.9 pp
AR55/SF0.75%	RMS	98.8%	92.1%	+6.7 pp
AR65/SF0.75%	RMS	97.6%	95.8%	+1.8 pp

The largest reported difference between pooled and configuration-specific boundaries occurs for the AR 55/SF 0.50% RMS records. Because the boundaries were not evaluated on held-out specimens, the apparent gain may include overfitting and is not evidence that configuration-specific thresholds will transfer better.

The two candidate threshold constructions differ in the amount of configuration-specific information used.

Table 6.222: Descriptive comparison of pooled and configuration-specific threshold constructions

Factor	Pooled Approach	Specialized Approach
Implementation Complexity	Low	High
Material Documentation Required	None	Complete
Average internal rate (CCV)	93.2%	95.7%
Average internal rate (RMS)	86.8%	91.1%
Applicable to untested materials	Not established	Not established
Configuration mismatch risk	Present	Present
Threshold Tables Required	1	4+

The pooled and configuration-specific results show how boundary choice changes the internal classification summary. Neither strategy is recommended for new, existing, mixed or critical infrastructure from this experiment. Application-specific baselines and

evaluation on independent specimens are required before either boundary can be used for a structural decision.

Table 6.223 retains the numerical candidate thresholds derived from the present records.

Table 6.223: Candidate pooled thresholds derived from the present dataset

Index	Signal	Warning	Critical	Direction	Average internal rate
CCV	Conductance	141	174	Above	93.2%
RMS	Conductance	0.0014	0.0008	Below	86.8%
Peak-to-Peak*	Conductance	413	593	Above	51.8%
RMSD*	Conductance	1.32	1.83	Above	47.5%

*Peak-to-Peak and RMSD values were calculated from the two 0.5% specimens only

Pooled and configuration-specific boundaries produce different internal rates, with the latter usually higher because it is more closely fitted to each configuration. The comparison is useful for designing an independent validation study but does not establish a transferable threshold strategy.

6.13.3 Statistical Evaluation Summary

The following conclusions are restricted to the analysed records and do not constitute independent validation.

The histogram and threshold analysis in Sections E.1 and E.2 quantifies separation among repeated temperature and dwell records from the four specimens. It does not provide independent validation because records from a specimen are correlated and the same dataset is used to derive and evaluate the thresholds.

Table 6.224 retains the reported ranking and separation metrics. The rank describes this dataset and is not a general performance hierarchy.

Table 6.224: Within-dataset separation metrics for selected SHM indices

Rank	Index	Saw-cut Effect	NSR	Overlap	Internal Exceedance	Scope
1	CCV	+222%	1.62	5%	93-98%	Positive in all four specimens
2	RMS	-44%	2.36*	0%*	87-99%*	Negative in all four specimens
3	Peak-to-Peak**	+96%	0.92	15%	52-58%	0.5% subset
4	RMSD**	+42%	0.85	20%	43-52%	0.5% subset
5	MAPD**	+44%	0.88	18%	45-55%	0.5% subset

*RMS metrics reported for the 0.75% specimens; **deviation-index summaries from the 0.5% specimens

CCV has the largest aggregate effect in the reported comparison, while RMS has strong separation for the two 0.75% specimens. These values identify candidates for replicated testing; they do not establish an optimal primary or confirmatory indicator.

CCV has a positive and RMS a negative matched response across the reported specimen–channel combinations. Their magnitudes vary substantially among configurations. The same-direction result is useful within this experiment but does not establish universality or independent classification reliability.

RMSD, MAPD and Peak-to-Peak change direction between the 0.50% and 0.75% specimen groups. Applying a one-sided boundary derived from the former group to the latter records therefore misclassifies those records. With one specimen per configuration, the reversal cannot be attributed solely to fibre dosage and cannot support rules for unknown materials.

The coefficient-of-variation summaries show substantial temperature-associated variability in several indices. The candidate thresholds are calculated from compensated records and describe only that processing branch. They are not applied to uncompensated data or treated as externally valid decision limits.

Table 6.225 retains the internal classification summaries obtained by applying candidate boundaries to the analysed records. These are resubstitution results, not reliability estimates.

Table 6.225: Within-dataset classification summaries for candidate threshold strategies

Boundary set	**First index**	**Second index**	**Saw-cut exceedance**	**Intact exceedance**
Pooled (four specimens)	CCV	RMS	90.0%	6.7%
Configuration-specific (0.5% SF)	CCV + Peak-to-Peak	RMS	95.2%	4.2%
Configuration-specific (0.75% SF)	CCV	RMS	97.8%	2.3%
Multi-index confirmation	CCV AND RMS	–	88.5%	$<1\%$

The rates in Table 6.225 are retained as outputs of the candidate boundaries applied to the analysed records. They must not be read as expected detection or false-positive probabilities for new specimens.

The experiment used 24 heated records plus an ambient baseline for a complete state-specific series; it did not establish a minimum baseline size. Real-time operation and transfer of the reported numerical boundaries were not tested. Independent specimens and application-specific calibration are required before operational classification.

Only four physical specimens were tested, with one specimen representing each AR–dosage configuration. Temperature and dwell records are repeated observations, not specimen replicates, so the experiment does not establish population-level statistical power. The progressive 75–250 °C history excludes cooling, sub-ambient exposure and fire conditions. The artificial saw-cut represents one controlled discontinuity. SFC3 and

SFC4 also have no saw-cut records above 175 °C.

The empirical statistical evaluation is summarised as follows.

The empirical statistical evaluation provides a within-dataset comparison of candidate indices and threshold constructions. CCV and RMS show consistent directions in the four tested specimens, while several other indices are configuration- or channel-dependent. The reported boundaries remain exploratory until evaluated on independent specimens; the analysis therefore supports further validation rather than field implementation.

6.14 Conclusions

This section consolidates the findings of the progressive-heating experiment while retaining the limits imposed by the four-specimen design, the artificial saw-cut and the available temperature ranges.

6.14.1 Temperature Effect Conclusions

The conductance and susceptance signatures changed with nominal temperature and dwell time in both structural states. The direction and magnitude of the change were not identical for every specimen or signal channel. Temperature is therefore a confounding influence in comparisons made against an ambient signature, but the present observations do not isolate a single material, sensor or interface mechanism responsible for that influence.

The EPS trajectories were also temperature-sensitive. Large percentage changes, reversals and sign crossings occurred in some mass-like, stiffness-like and dissipative terms. These behaviours must be read as changes in the adopted coupled representation rather than direct changes in physical mass, stiffness or damping. Ratios based on a near-zero reference are especially unstable and are not used to establish a material mechanism.

Matched intact–saw-cut differences varied with temperature, specimen, index and signal channel. Some combinations showed a larger separation at later stages, whereas others showed weaker or reversed changes. The results therefore support temperature-resolved assessment within the tested records, not a general claim that heating always amplifies damage sensitivity.

All four intact series extend to 250 °C. In the saw-cut state, SFC1 and SFC2 extend to 250 °C, while SFC3 and SFC4 extend only to 175 °C. Comparisons involving all four specimens are consequently restricted to the common measured range through 175 °C.

The experiment does not establish a universally preferred monitoring temperature.

The Enhanced EFS procedure reduced frequency misalignment and constant vertical offset for many records, but its effect depended on the specimen, channel and derived quantity. Compensation did not uniformly reduce every index or EPS trajectory, and it can also alter a damage-sensitive difference. Its usefulness is therefore judged from the matched intact–saw-cut records, not from visual spectral overlap or a generic improvement percentage alone.

Within the tested progressive-heating programme, temperature and dwell time materially affected the coupled EMI response and must be considered when interpreting the saw-cut comparison. Enhanced EFS provided a useful post-processing route for selected records, while residual variation, truncated high-temperature coverage and model-dependent EPS behaviour remain explicit limitations.

6.14.2 Compensation Algorithm Conclusions

The Enhanced EFS procedure combines joint frequency alignment of conductance and susceptance with channel-wise removal of a constant mean offset. Its performance is evaluated on the same four specimens used to develop the analysis; the results constitute an internal experimental assessment rather than external validation.

The procedure generally improved alignment with the selected state-specific baseline, but the degree of reduction varied among channels, specimens and derived quantities. A reduction in thermal-baseline difference does not by itself prove that a structural-state difference has been preserved. For this reason, the compensated results are assessed together with the raw records and the matched intact–saw-cut comparison.

Baseline selection follows the analysis question. Intact thermal records are aligned to the ambient intact record of the same specimen, and saw-cut thermal records are aligned to the corresponding ambient saw-cut record. Structural-state assessment then compares intact and saw-cut records matched by specimen, temperature and dwell time. The present experiment does not determine a minimum number of measurements for another structure or a baseline-renewal interval.

Conductance and susceptance enter the joint shift objective but retain separate weights and residual offsets. Their responses and derived indices are therefore reported by channel; equivalence between the two channels is not assumed.

The analysed records produced different classification summaries before and after compensation. These values are retained as descriptive outputs of the adopted thresholds, not as proof of a four-fold performance improvement or a transferable false-positive rate.

Table 6.226 retains the reported within-dataset classification summaries. These percentages describe the analysed records and thresholds; because repeated temperature and dwell records arise from the same four specimens, they are not independent field-performance estimates.

Table 6.226: Within-dataset classification summaries before and after compensation

Within-Dataset Metric	**Without Compensation**	**With Compensation**	**Reported Change**
Saw-cut threshold exceedance	$<$20%	85-93%	+65-73 pp
Intact-record exceedance	$>$50%	6.7%	-43+ pp
CV (Temperature Variability)	100-170%	20-35%	5× reduction
NSR (Separation Ratio)	Not calculated	0.85-2.36	Calculated
Candidate boundary evaluation	Not applied	Applied	Within dataset

The implemented procedure searches a joint conductance–susceptance correlation objective on an interpolated shift grid, retains the common frequency interval after each trial shift and then removes the channel-wise mean residual offset. The implementation details document reproducibility of the present analysis; computational suitability for an embedded or real-time system was not tested.

No independent noise-injection, temperature-uncertainty or parameter-sensitivity experiment was performed. Robustness is therefore limited to the variation represented by the recorded specimen, temperature and dwell sequences.

The methodological contribution is the application of the Enhanced EFS procedure to the paired conductance and susceptance records of this SFRC thermal programme. Transfer to other materials, sensors, temperature histories or field conditions requires independent evaluation.

Enhanced EFS reduced selected temperature-associated differences in the analysed signatures and improved separation for several within-dataset comparisons. It did not produce uniform improvement for every index or EPS quantity, and the reported classification rates are not external validation. The procedure is therefore retained as a study-specific compensation method whose results must be interpreted alongside the raw records and the limitations of the experimental design.

6.14.3 Damage Detection Conclusions

The thirteen SHM indices provide different descriptions of the matched intact–saw-cut records. Their behaviour is summarised within the four tested specimens; rankings and classification rates are not treated as independent validation or as universal selection rules.

CCV and RMS retained a consistent response direction across the four tested specimens in the analysed channel and matched range. Peak-to-Peak, RMSD, MAPD and other deviation measures were more configuration- and channel-dependent. The numerical effect and classification summaries reported in Parts D and E describe this dataset only and must be read together with the mathematical dependence among related indices.

The observed consistency of CCV and RMS does not establish universality beyond these specimens. The reversed direction of several deviation-based indices in the 0.75% specimens shows why a threshold direction selected from another configuration can misclassify the present records. It does not establish a population-level effect of fibre dosage because each configuration is represented by one specimen.

Conductance and susceptance produced different magnitudes and, for some indices, different response directions. Channel-specific tables must therefore govern interpretation. The present results do not justify a generally preferred channel.

The empirical threshold analysis reports within-dataset classification rates for the candidate boundaries. Temperature and dwell records from the same specimen are correlated observations, and the same experimental programme was used to derive and evaluate the thresholds. The rates therefore describe separation in the analysed dataset and are not estimates of performance on independent specimens.

Different response patterns were observed between the 0.50% and 0.75% specimens. Because aspect ratio, dosage, local material variability and sensor installation were not independently replicated, these differences are descriptive and no fibre-bridging or electrical-continuity mechanism is assigned from this experiment alone.

The two-tier boundaries derived in the empirical threshold analysis are exploratory and study-specific. They demonstrate how the present records can be separated under the stated preprocessing and baseline rules; they require evaluation on independent specimens before being used as decision limits.

The structural change is a 3 mm-wide, 30 mm-deep artificial saw-cut. It is a controlled discontinuity and does not represent the range of crack morphologies, distributed deterioration or field boundary conditions.

The matched analysis distinguishes the intact and saw-cut records for several index–channel combinations within the tested programme. CCV and RMS were directionally consistent across the four specimens, while other indices were more configuration-dependent. These findings support further replicated evaluation; they do not establish universal indices, externally validated thresholds or field performance.

6.14.4 Material Configuration Conclusions

The four specimens combine two aspect ratios (AR 55 and AR 65) with two fibre dosages (0.50% and 0.75%). With one specimen per configuration, the results show configuration-associated patterns but cannot separate aspect-ratio, dosage, specimen and sensor-installation effects statistically.

Differences between the AR 55 and AR 65 specimens are reported for the individual indices in Parts B–E. Because dosage and specimen identity vary concurrently and no replicate specimens were tested, those differences are not evidence of a general aspect-ratio effect and are not assigned a fibre-geometry mechanism.

The 0.50% and 0.75% specimens exhibited different directions for several deviation-based indices, while CCV and RMS retained a consistent direction in the analysed records. These patterns are relevant to this specimen set and show that an index and threshold cannot be transferred between configurations without checking its direction. They do not establish dosage as the causal or dominant parameter.

Table 6.227 preserves the reported configuration-associated summaries while removing their use as material-design recommendations.

Table 6.227: Within-dataset index summaries by material configuration

Within-dataset criterion	Associated config.	Index	Rate	Effect summary
Maximum sensitivity	AR55/SF0.5%	Peak-to-Peak	58%	+305%
Maximum detection rate	AR65/SF0.75%	CCV + RMS	98%	+370%
Cross-config. consistency	All four	CCV + RMS	90%	+222% avg
Balanced performance	AR55/SF0.5%	CCV + Peak-to-Peak	75%	+260% avg

Where the material configuration differs from the tested specimens, neither the reported thresholds nor the apparent ranking should be transferred without a new baseline and independent validation. CCV and RMS are retained as candidates for such validation because their direction was consistent here, not because universal performance has been demonstrated.

Application to a structure containing multiple SFRC configurations would require configuration-specific baseline measurements and a sampling design that distinguishes material variation from damage. The present four-specimen experiment does not establish zone-level thresholds.

The monitored-response differences are insufficient to recommend an SFRC mixture for structural design. Material selection must remain governed by structural and durability requirements; a separate replicated programme would be needed to optimise a mixture for EMI monitoring.

The four configurations produced different index responses, including direction reversals in some deviation measures. The table retains the reported within-dataset summaries, but the study does not establish an optimal mixture, independent aspect-ratio or dosage effects, or transferable detection reliability.

6.14.5 PZT Sensor Performance Conclusions

This subsection distinguishes what the thermal records establish about the embedded JPS response from properties that were not measured independently.

Usable signatures were obtained from all four JPS-instrumented specimens throughout the intact sequence to 250 °C. In the saw-cut sequence, SFC1 and SFC2 also extend to 250 °C, whereas SFC3 and SFC4 end at 175 °C. The available records confirm operation only at the stages actually measured; they do not identify why the two saw-cut series terminate or establish a general sensor temperature limit. No intermediate cooling programme was used, so reversibility after cooling and long-term depolarisation were not tested in this campaign.

The EPS values describe the equivalent response of the coupled PZT–jacket–interface–SFRC system under the fixed formulation in Section 3.11. Their temperature-dependent and, in some cases, sign-changing trajectories must not be interpreted as direct measurements of specimen mass, static stiffness or material damping. The four single-specimen configurations do not permit the observed EPS differences to be separated uniquely into sensor, interface and material contributions.

The experiment did not measure an effective sensing radius or its variation with temperature. The acquired range of 30–557.4 kHz and 5275 points per signature defines the electrical interrogation used here; it does not by itself establish spatial resolution or a temperature-invariant sensing zone.

The signatures retained for analysis contained identifiable resonance structure and could be processed by the adopted EFS and index calculations. A separate signal-to-noise-ratio test and an independent repeatability campaign were not reported; therefore, numerical SNR or repeatability limits are not claimed.

The sensors were embedded in protective jackets rather than surface-bonded directly to the concrete. The campaign did not include a destructive post-test interface examination or a separate high-temperature bond-strength test. Interface change therefore remains one possible contributor to the measured admittance variation and cannot be excluded from the interpretation.

The furnace controller had a stated accuracy of approximately ±2 °C, and measurements were taken after 10, 20 and 30 min at each nominal stage. Internal uniformity at

the JPS location was not independently measured. The three dwell records consequently represent observations during progressive heating and are not treated as independent specimen replicates or proof of thermal equilibrium.

Any extension beyond the laboratory specimens would require collocated temperature measurement, state-specific baselines and independent checks of the sensor package, lead and interface for the intended temperature and exposure duration. The present four-specimen dataset does not establish field-deployment specifications.

Long-term exposure, repeated heating–cooling fatigue, spatial sensing range, internal temperature gradients and post-test interface condition were not independently characterised. Measurements above 250 °C were outside the protocol, and the missing saw-cut records for SFC3 and SFC4 prevent a four-specimen comparison above 175 °C.

The embedded JPS arrangement yielded analysable thermal signatures over the available ranges and showed that temperature dependence cannot be neglected in EMI interpretation. The Enhanced EFS procedure reduced selected components of this dependence, but neither universal sensor reliability nor field applicability follows from the present dataset. Conclusions are limited to the tested specimens, acquisition range, structural states and progressive-heating protocol.

6.15 Recommendations

The present findings identify the experiments required before the temperature-compensated EMI approach can be transferred beyond the four tested specimens. The following recommendations are therefore framed as research needs rather than established operating guidance.

6.15.1 Recommendations for Researchers

Future work should include replicated heating and cooling cycles, measurements below 75 °C and, where the sensor package and furnace permit, measurements above 250 °C. Internal specimen temperature should be measured so that dwell-time evolution can be distinguished from thermal equilibrium and irreversible thermal history.

The response of other fibre materials, geometries and dosages should be investigated with replicated specimens. Index direction and compensation performance should be re-established for each material system rather than transferred from the present steel-fibre configurations.

Data-driven compensation or classification should be considered only after a larger independent dataset is available. Specimen-level separation of training, validation

and test data is essential so that temperature and dwell records from the same specimen do not appear in more than one partition.

The 3 mm-wide, 30 mm-deep saw-cut should be complemented by controlled crack widths, distributed cracking and other independently characterised deterioration modes. Such testing is required to determine which observed spectral and index changes are specific to the present artificial discontinuity.

Replicated multi-sensor experiments could assess spatial variability, sensor-to-sensor variation and localisation capability. Those experiments should separate host response from differences in the JPS package, lead, interface and installation position.

Enhanced EFS should be compared with alternative alignment and environmental-compensation methods on independent records. The evaluation should report both removal of state-specific thermal drift and preservation of known structural-state differences.

Any field study should begin with a documented baseline, collocated temperature measurements and independent inspection evidence. Seasonal variation, moisture, boundary conditions, loading and sensor ageing must be evaluated before laboratory thresholds are considered for decision-making.

Alternative frequency bands, feature-selection methods and time–frequency representations may be examined, but their parameters must be selected using training data and verified on independent specimens. Comparisons should retain both conductance and susceptance because the present study found channel-dependent behaviour.

Long-term repeatability, cooling-path hysteresis, moisture interaction, sensor-package durability, damage severity and uncertainty propagation remain unresolved. These questions define the principal boundary between the present laboratory evidence and a deployable monitoring method.

The immediate priority is replicated experimental validation with measured internal temperature, independent structural evidence and specimen-level statistical separation. Broader sensing, modelling and field-integration studies should follow only after those controls are established.

6.15.2 Conditions for Future Implementation

The present results show that a thermal baseline cannot be ignored. A future implementation would require temperature measurement at the monitored location, a baseline for each structural state under evaluation and verification that compensation does not remove the structural difference of interest. Enhanced EFS is the method assessed here; no polynomial compensation model was used.

CCV and RMS are candidates for further evaluation because their response direction was consistent across the four tested specimens. Other indices remain informative but were more dependent on configuration, signal channel or mathematical scaling. None is designated as universally applicable.

The warning and critical boundaries reported in the empirical threshold analysis are study-specific analytical levels. Before any operational use, they require evaluation on independent intact and saw-cut specimens under the intended temperature history, followed by uncertainty and false-classification analysis.

The experiment establishes measurements at 10, 20 and 30 min during progressive heating, not a universally adequate stabilisation time or preferred monitoring temperature. A future protocol must determine equilibrium and repeatability for the actual element geometry and exposure conditions.

The embedded JPS, lead and interface require separate durability and repeatability evaluation for the intended temperature and exposure duration. The current experiment does not establish sensor spacing, sensing radius, service life or an upper operating limit for another installation.

Independent visual, mechanical or non-destructive evidence should accompany future EMI assessment so that an admittance change is not assigned uniquely to damage. Multi-method integration and localisation were not tested in the present programme.

The results support continued development of temperature-aware EMI monitoring, but not direct deployment rules. Independent specimens, application-specific baselines, verified sensor durability and external threshold validation are required before the method can inform structural decisions.

6.16 Potential Applications and Transfer Requirements

The laboratory results identify contexts in which temperature-aware EMI monitoring may merit further study. They do not constitute validation for an infrastructure class, and the study-specific thresholds are not transferred to the following applications.

6.16.1 Infrastructure Applications

SFRC bridge elements experience changing environmental and mechanical conditions that would require temperature, moisture, loading and boundary-condition effects to be separated. A bridge pilot would need replicated sensor locations, independent condition evidence and a site-specific baseline before the present method could be assessed.

Application to building elements would require validation at the substantially

different temperature histories and boundary conditions encountered in service. The current progressive-heating records do not establish performance for ambient building monitoring or life-safety decisions.

The present test did not reproduce a fire curve, cooling phase or thermally degraded concrete. Post-fire assessment is therefore a future research context only and would require direct mechanical and material characterisation in addition to EMI measurements.

Tunnel elements provide a possible setting for embedded monitoring, but installation variability, moisture, sustained loading and access constraints would require dedicated evaluation. No tunnel-specific detection or localisation capability was tested.

Bridges, buildings, fire-affected elements and tunnels are possible validation contexts rather than demonstrated applications. Transfer requires application-specific baselines, independent damage evidence and replicated field measurements.

6.16.2 Industrial Applications

Structures near process heat are a potential context for temperature-aware EMI monitoring, but their temperature gradients, exposure duration and boundary conditions differ from the progressive furnace test. The present data cannot be used outside 75–250 °C or as evidence of performance under sustained service exposure.

Any study near furnaces or kilns would require measured temperature at the sensor and host, protection of the JPS and lead, and independent assessment of thermal damage. The current experiment does not establish behaviour under thermal cycling or refractory-service conditions.

Vibration, electromagnetic interference, moisture and operational loading may all affect an industrial EMI record. Their influence and interaction with Enhanced EFS must be tested before a change in an index can be interpreted structurally.

Combined chemical and thermal exposures were outside the experimental scope. Dedicated durability tests would be required to distinguish environmental changes in the sensor package and interface from changes in the host SFRC.

Future implementation studies should establish site-specific acquisition bands, baselines, sensor protection, repeatability and independent condition evidence. No real-time, wireless or automated decision system was evaluated in this thesis.

Industrial facilities provide possible test environments for the method, not validated deployment domains. The laboratory findings define questions for those studies but do not supply transferable thresholds or operating specifications.

6.16.3 Future Technology Integration

The following possibilities are outside the experimental verification of this thesis. They are retained to identify the evidence that would be needed for later system development.

A networked system would require verified acquisition hardware, synchronised temperature records, data-quality checks and secure communication. The present study analysed laboratory records offline and did not test wireless or distributed operation.

Real-time use of Enhanced EFS would require timing, memory and numerical-stability tests on the intended hardware, together with checks that frequency alignment and mean-offset removal preserve structural-state differences. These implementation tests were not performed.

Automated classification would require a larger dataset containing independent specimens, structural states and environmental histories. Model development must separate specimens across training and evaluation partitions and report uncertainty; the study-specific empirical thresholds are not substitutes for that validation.

Remote storage or analysis could support long-term monitoring, but it introduces data integrity, traceability and security requirements beyond this thesis. No cloud platform or automated maintenance workflow was evaluated.

The present contribution is limited to a laboratory investigation of embedded-JPS signatures, Enhanced EFS compensation and matched saw-cut comparisons. A broader monitoring system would require localisation, independent condition confirmation, long-term sensor assessment and application-specific decision criteria.

Networked acquisition, real-time compensation and automated classification remain future development paths. Their feasibility and performance cannot be inferred from the current four-specimen dataset without new experimental and implementation evidence.

CHAPTER 7

MACHINE LEARNING AND DEEP LEARNING FOR STRENGTH PREDICTION

7.1 General

The electromechanical impedance (EMI) technique, measured via the jacketed piezoelectric sensor (JPS) and the non-bonded piezoelectric sensor (NBPS), was evaluated in the preceding chapters to track the hydration, compressive damage, tensile degradation, and thermal response of steel-fibre-reinforced concrete (SFRC). These experimental programmes yielded extensive datasets comprising conductance (G) and susceptance (B) spectra, alongside the derived equivalent mass (m), stiffness (k), and damping (c). While individual spectra provide direct resonance shifts and statistical indices, the high dimensionality of the dataset and the non-linear relationship between the EMI features and the target mechanical properties demand advanced computational processing.

The data-driven framework developed for the three principal experimental programmes (the hydration monitoring, the compressive damage, and the split-tensile damage programmes) is presented in this chapter. Classical machine learning (ML) and deep learning (DL) architectures are implemented to map the high-dimensional frequency data directly to the mechanical targets.

7.2 Unified ML/DL Framework and Data Pipeline

The end-to-end framework adopted for the prediction tasks is illustrated in Figure 7.1. The pipeline initiates with the raw EMI spectra recorded by the LCR meter, advances through feature engineering and normalisation, and culminates in a trained model capable of generating a continuous-valued strength prediction from an unseen spectrum.

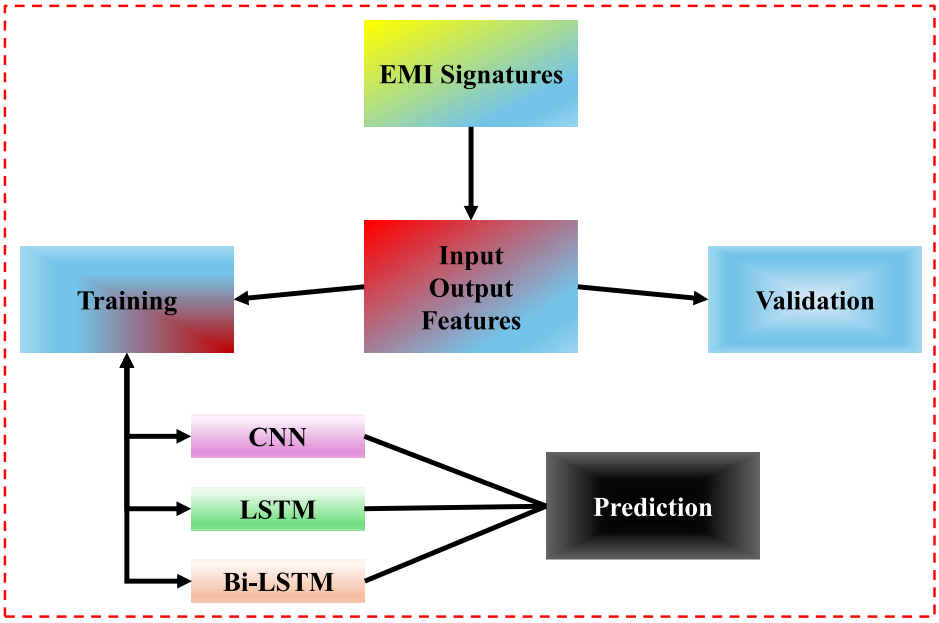

Figure 7.1: Unified ML/DL framework for EMI-based SHM of SFRC.

7.2.1 Dataset Construction

The three prediction applications were constructed from their corresponding experimental programmes. The compressive application used NBPS measurements from the cube series and the associated destructively measured compressive strengths. The hydration application used the age-indexed JPS measurements and the corresponding compressive-strength development, whereas the split-tensile application paired the NBPS cylinder measurements with the measured splitting-tensile strengths. Each acquisition covered 30–500 kHz at 100 Hz intervals, providing 4701 frequency points. This case-specific construction retains the experimental meaning of each target while allowing the three applications to be discussed within one computational framework.

7.2.2 Feature Engineering and Normalisation

The feature matrix was assembled from excitation frequency, conductance G, susceptance B, the real and imaginary components of structural admittance (X' and Y'), and the equivalent model parameters (c, m and k). Fibre aspect ratio and dosage identified the material configuration, while curing age was included for the hydration application. The destructively measured compressive or splitting-tensile strength served as the response variable for the relevant application. Features were standardised using z-score normalisation to place variables of different magnitudes on a common numerical scale; the response was also standardised in the two deep learning applications.

For the 2D deep learning architectures, the scaled one-dimensional feature vectors were wrapped row-by-row into numerical $N \times N$ matrices. The transformation maintains frequency order within successive matrix rows and provides a consistent computational input shape; it does not convert the spectrum into a physical spatial field. Zero padding was applied where necessary so that every sample presented the same matrix dimensions to the evaluated architectures.

7.2.3 Training and Validation Protocol

In each application, the validation partitions were drawn at random from the frequency-point observations without grouping by specimen. The classical compressive-strength models were assessed using five-fold cross-validation, while the deep learning applications used an 80 % training and 20 % validation partition. Deep learning employed the Adam optimiser with an initial learning rate of 1×10^{-3}, a batch size of 32 and early stopping with a patience of 5 epochs. The reported metrics therefore compare the candidate models under the validation design adopted for each experimental dataset.

7.3 Classical Machine Learning Models

Direct mathematical insights into the correlation between individual EMI features and mechanical degradation are provided by classical ML algorithms. The following model groups were evaluated, spanning from linear baselines to non-parametric kernel structures.

7.3.1 Linear Regression Family

Standard Linear Regression, Robust Linear Regression, and Stepwise Linear Regression were implemented as reference baselines. These algorithms presume a linear mapping between the feature vector and the target, establishing a foundational error bound against which the non-linear models were assessed.

7.3.2 Support Vector Machines

Four SVM formulations were evaluated: a Linear SVM and three Gaussian-kernel SVMs executed at distinct kernel scale resolutions (Fine, Medium, and Coarse).

7.3.3 Ensemble Boosted Trees

An Ensemble Boosted Tree regressor was deployed. Boosted Trees sequentially fit weak regression-tree learners to the residuals of their predecessors, isolating non-linear feature interactions without requiring explicit kernel specification.

7.3.4 Gaussian Process Regression

Four Gaussian Process Regression (GPR) variants were trained using distinct covariance kernels: Squared Exponential, Matérn 5/2, Exponential, and Rational Quadratic. The GPR architecture generates both a point prediction and a probabilistic uncertainty bound.

The comprehensive workflow for classical ML model development, progressing from dataset acquisition through feature structuring to k-fold validation, is delineated in Figure 7.2.

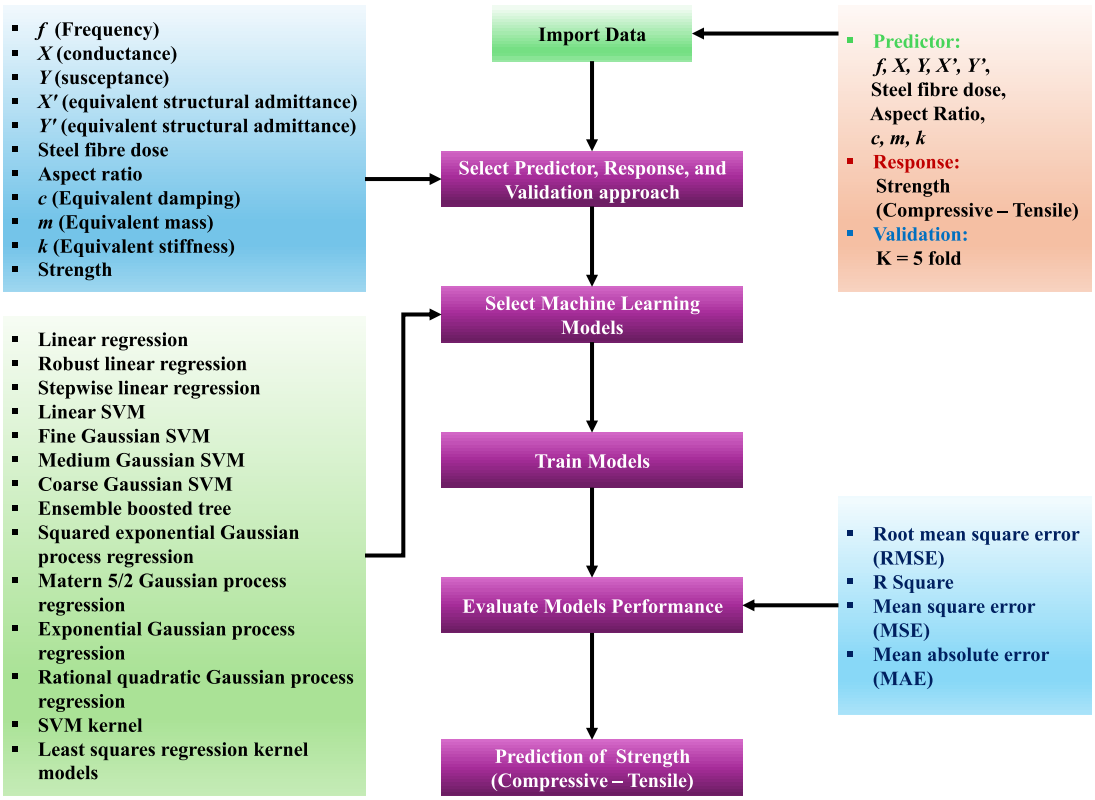

Figure 7.2: Workflow for the development and validation of machine learning algorithms for SFRC strength prediction.

7.4 Deep Learning Architectures

Three primary deep learning paradigms were implemented to capture the highly non-linear EMI correlations: the 2D CNN, the 2D LSTM, and the 2D Bi-LSTM. For the compressive strength assessment within the hydration study, hybrid variants (2D CNN–LSTM and 2D CNN–Bi-LSTM) were additionally evaluated.

7.4.1 2D Convolutional Neural Network (2D CNN)

A hierarchical feature-learning strategy forms the core of the 2D CNN architecture. Spatial filters are applied by convolutional layers to detect resonance peak formations, followed by pooling layers that down-sample the resulting feature maps. The extracted feature hierarchies are subsequently integrated into the final regression output by fully connected dense layers. The Rectified Linear Unit (ReLU) activation function, which zeroes negative values to induce non-linearity, is applied sequentially after each convolution block (Equation 7.1):

$$y_{i,j,k} = \max(0, x_{i,j,k}), \tag{7.1}$$

where $y_{i,j,k}$ represents the activated output at position (i, j) of the k-th feature map.

The topological layout of the architecture is illustrated in Figure 7.3. The network initiates with a primary convolutional block applying 16 filters via a 5×5 spatial kernel with zero padding, immediately followed by batch normalisation, ReLU activation, and a 2×2 max-pooling operation. A secondary convolutional block subsequently applies 32 filters through a tighter 3×3 kernel, again followed by normalisation and ReLU activation. The resulting multidimensional feature maps are flattened into a 1D tensor and passed through a dense layer comprising 64 ReLU neurons, regulated by a 0.2 dropout rate to penalise dominant weights. The network terminates at a single-neuron dense layer that outputs the continuous strength prediction.

7.4.2 2D Long Short-Term Memory (2D LSTM)

Memory cells engineered to track ordered dependencies characterise the LSTM architecture. Within each discrete LSTM cell, an input gate, a forget gate and an output gate are modulated by sigmoid and hyperbolic tangent activation functions to regulate information flow. In the present implementation, each row of the reshaped frequency-feature matrix is evaluated as one step in a computational sequence. This ordering

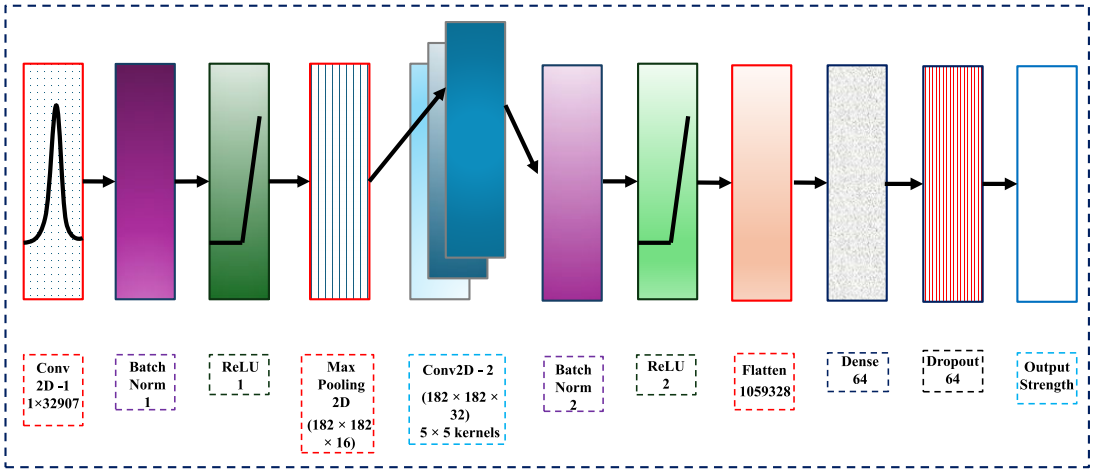

Figure 7.3: Schematic of the 2D Convolutional Neural Network (2D CNN) architecture implemented for strength prediction.

represents the arranged spectral input and is distinct from the physical curing-time axis.

The complete LSTM topology (Figure 7.4) commences by restructuring the standardised sensor arrays into $N \times N$ spatial grids. Sequence processing is executed by a primary LSTM layer containing 8 interconnected memory units configured to return the full temporal sequence. To restrict overfitting, a 0.2 dropout penalty is enforced, after which the sequential features are enhanced via a time-distributed dense layer containing 16 ReLU units. The temporal context is ultimately consolidated by a secondary LSTM layer comprising 16 units that return the final condensed state vector. A regression synthesis is performed through an 8-neuron ReLU dense layer, culminating in the single-node continuous output prediction.

7.4.3 2D Bidirectional LSTM (2D Bi-LSTM)

Sequence processing in both forward and backward temporal directions is facilitated by the Bi-LSTM architecture, allowing the network to evaluate preceding and subsequent frequency shifts simultaneously.

The bidirectional architecture is detailed in Figure 7.5. Following the initial restructuring of the sensor data into $N \times N$ grids, the data tensor is fed into a primary Bi-LSTM layer equipped with 12 memory units per direction, configured to return the complete dual-directional sequence. A 0.2 dropout layer regulates the tensor before it enters the secondary Bi-LSTM layer, which further consolidates the contextual data using 12 units per direction and returns a singular state vector. The isolated features are synthesised through a primary dense layer of 32 ReLU units (subjected to a 0.2 dropout) and a secondary dense layer of 16 ReLU units. The network concludes with

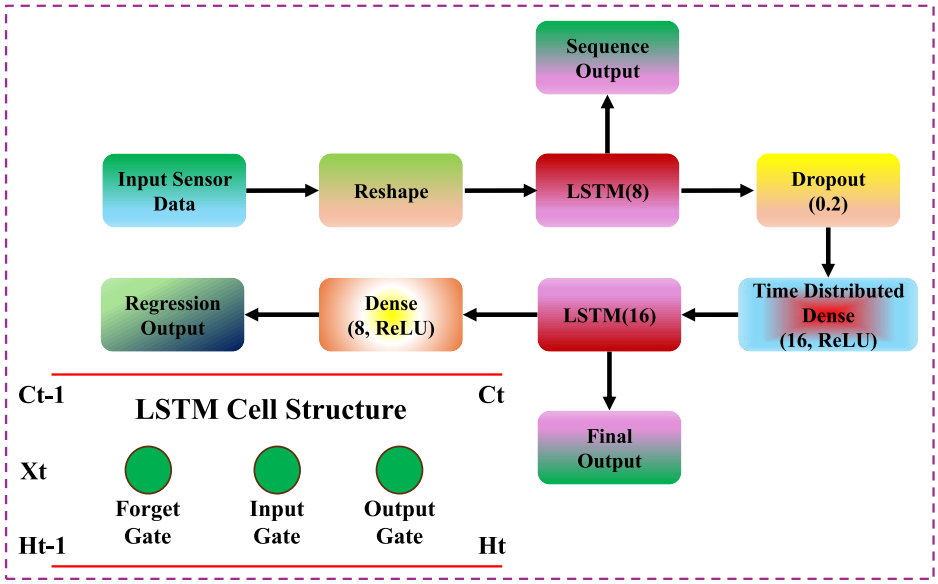

Figure 7.4: Block diagram of the 2D LSTM architecture illustrating internal cell gate operations.

the standard single-neuron regression output.

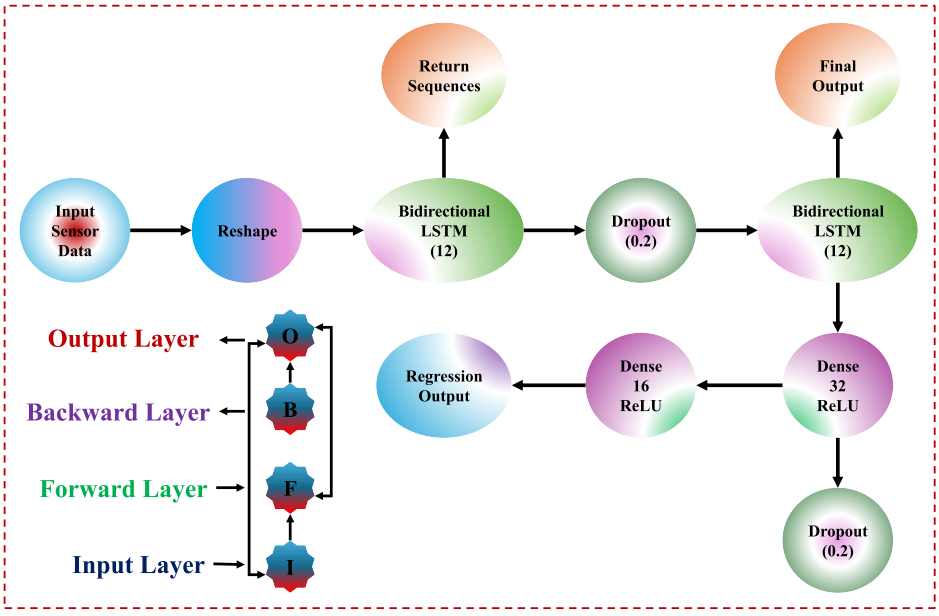

Figure 7.5: 2D Bidirectional Long Short-Term Memory (2D Bi-LSTM) architecture configured for sequential sensor data evaluation.

7.4.4 Hybrid DL Architectures

Two hybrid configurations were trained specifically for the complex hydration datasets: the 2D CNN–LSTM, where a convolutional front-end acts as a spatial feature

extractor passing compressed representations to a sequential LSTM back-end; and the 2D CNN–Bi-LSTM, which swaps the standard LSTM for a bidirectional back-end to capture dual-directional temporal nuances.

7.5 Evaluation Metrics

The predictive performance of the machine learning and deep learning architectures was evaluated using standard regression error metrics. These metrics quantify the residual deviations between the experimentally measured structural strengths (y_i) and the model-predicted values ($\hat{y}_i$) across N validation samples, where $\bar{y}$ represents the arithmetic mean of the experimentally observed values.

The Root Mean Square Error (RMSE) and Mean Squared Error (MSE) quantify the average squared magnitude of the prediction errors:

$$\text{RMSE} = \sqrt{\frac{1}{N}\sum_{i=1}^{N}(y_i - \hat{y}_i)^2}, \qquad \text{MSE} = \frac{1}{N}\sum_{i=1}^{N}(y_i - \hat{y}_i)^2 \tag{7.2}$$

Because the squared formulation applies a disproportionate penalty to large residuals, RMSE and MSE are sensitive to isolated prediction errors. Reporting them together with MAE and R^2 provides complementary information on error magnitude and overall agreement.

The Mean Absolute Error (MAE) computes the average absolute magnitude of the residuals without quadratic scaling:

$$\text{MAE} = \frac{1}{N}\sum_{i=1}^{N}|y_i - \hat{y}_i| \tag{7.3}$$

The MAE provides a direct linear metric of average error across all tested specimens, preserving an intuitive baseline scale that is less sensitive to extreme outliers.

The coefficient of determination (R^2) evaluates the proportion of total variance in the destructive strength measurements explained by the electromechanical admittance models:

$$R^2 = 1 - \frac{\sum_{i=1}^{N}(y_i - \hat{y}_i)^2}{\sum_{i=1}^{N}(y_i - \bar{y})^2} \tag{7.4}$$

An R^2 value approaching unity indicates close agreement between the predictions and the measured strengths over the response range represented in the validation data.

7.6 Predictive Modelling of the Compressive Programme

The predictive framework was first applied to compressive-strength data obtained from 39 SFRC cube specimens monitored using the reusable Non-Bonded Piezoceramic Sensor (NBPS). The measured EMI response and the corresponding destructive-test strengths provide paired predictor and response data throughout the investigated material configurations.

The AR 65 and AR 55 series were modelled separately so that performance could be compared for the two fibre families without combining their configuration labels. Within each aspect-ratio series, the plain-concrete control and the six fibre dosages formed the material configurations represented in the feature matrix. The classical algorithms were then applied to the processed EMI descriptors to compare linear, kernel-based, ensemble and probabilistic regression formulations.

The performance error bounds of the classical ML algorithms for the aspect ratio 65 and aspect ratio 55 series are presented in Tables 7.1 and 7.2, respectively. The linear regression baselines returned error margins of RMSE ≈ 4.5 % and $R^2 \approx 0.40$, highlighting the severe non-linearity of the EMI spectra mapping. Non-linear models rapidly closed this error gap; specifically, the Fine Gaussian SVM achieved an $R^2 = 0.9904$ with an RMSE of 0.5790 % for the AR 65 series. The highest overall accuracy among the classical architectures was registered by the Squared Exponential Gaussian Process Regression, yielding an RMSE of 0.1648 % ($R^2 = 0.9992$) on the AR 65 validation set.

The comparison follows a deliberate progression from simple reference models to increasingly flexible non-linear models. Linear and robust regressions establish the baseline mapping obtainable without a non-linear kernel. The Gaussian SVM results then show how kernel scale changes the balance between local spectral sensitivity and a smoother regression response, while the GPR variants provide an additional comparison across alternative covariance functions. This sequence allows the examiner to relate the numerical improvement directly to model class rather than viewing the tables as an isolated ranking.

The two aspect-ratio datasets show the same principal pattern: the linear formulations produce similar baseline errors, the Fine Gaussian SVM markedly reduces those errors, and all four GPR variants achieve the strongest reported agreement. The close AR 65 and AR 55 results indicate that the model comparison is repeatable across the two separately evaluated fibre families within the present compressive programme. Tables 7.1 and 7.2 retain the complete numerical evidence for this comparison.

Table 7.1: Performance comparison of classical ML algorithms for the aspect ratio 65 SFRC cube series.

ML Model (AR 65 cubes)	**RMSE (%)**	**MSE (%)**	**R^2 (Val.)**	**MAE (%)**
Linear Regression	4.5503	20.7049	0.4087	3.8023
Robust Linear Regression	4.5537	20.7366	0.4078	3.7947
Stepwise Linear Regression	4.4778	20.0508	0.4274	3.7907
Linear SVM	4.6245	21.3857	0.3893	3.7038
Fine Gaussian SVM	0.5790	0.3353	0.9904	0.5050
Medium Gaussian SVM	0.9744	0.9494	0.9729	0.8344
Coarse Gaussian SVM	2.5724	6.6171	0.8110	1.8267
Ensemble Boosted Tree	2.2859	5.2254	0.8508	2.2721
Squared Exp. Gaussian Process	0.1648	0.0272	0.9992	0.0077
Matérn 5/2 Gaussian Process	0.1652	0.0273	0.9992	0.0079
Exponential Gaussian Process	0.2177	0.0474	0.9986	0.0143
Rational Quadratic Gaussian Proc.	0.1659	0.0275	0.9992	0.0078
SVM Kernel	1.0153	1.0308	0.9706	0.5284
Least Squares Regression Kernel	0.6562	0.4305	0.9877	0.3444

A comparison of the AR 65 and AR 55 tables shows similar relative behaviour among the algorithms. In both datasets, the linear models provide the reference performance, the Gaussian SVM variants improve the fit, and the GPR models give the lowest reported errors. The close results across the two independently evaluated aspect-ratio series support the consistency of this model-ranking pattern within the compressive programme.

Table 7.2: Performance comparison of classical ML algorithms for the aspect ratio 55 SFRC cube series.

ML Model (AR 55 cubes)	**RMSE (%)**	**MSE (%)**	**R^2 (Val.)**	**MAE (%)**
Linear Regression	4.4828	20.0957	0.4261	3.7984
Robust Linear Regression	4.4816	20.0843	0.4264	3.7900
Stepwise Linear Regression	4.4778	20.0506	0.4274	3.7906
Linear SVM	4.5648	20.8376	0.4049	3.6996
Fine Gaussian SVM	0.5860	0.3434	0.9902	0.5060
Medium Gaussian SVM	0.9829	0.9660	0.9724	0.8426
Coarse Gaussian SVM	2.5871	6.6930	0.8089	1.8300
Ensemble Boosted Tree	2.2859	5.2254	0.8508	2.2721
Squared Exp. Gaussian Process	0.1984	0.0394	0.9989	0.0093
Matérn 5/2 Gaussian Process	0.2369	0.0561	0.9984	0.0104
Exponential Gaussian Process	0.2271	0.0516	0.9985	0.0149
Rational Quadratic Gaussian Proc.	0.2033	0.0413	0.9988	0.0093
SVM Kernel	0.8708	0.7582	0.9783	0.5054
Least Squares Regression Kernel	0.6920	0.4789	0.9863	0.3516

7.6.1 Comparative Analysis of Support Vector Machine Kernels

The predicted-versus-actual compressive strength correlations for the Gaussian Support Vector Machine (SVM) kernels are mapped in Figure 7.6 (AR 65 series) and Figure 7.7 (AR 55 series). Support Vector Regression constructs an optimal hyperplane within a transformed feature space by mapping the input electromechanical admittance vectors $\mathbf{x} \in \mathbb{R}^P$ via non-linear kernel transformations. The Gaussian radial basis function (RBF) kernel is formulated as:

$$K(\mathbf{x}_i, \mathbf{x}_j) = \exp\left(-\gamma \|\mathbf{x}_i - \mathbf{x}_j\|^2\right) = \exp\left(-\frac{\|\mathbf{x}_i - \mathbf{x}_j\|^2}{2\sigma^2}\right) \tag{7.5}$$

where $\gamma = 1/(2\sigma^2)$ defines the kernel scale parameter and σ represents the kernel bandwidth relative to the input dimensionality P.

The scaling of the Gaussian kernel parameter governs the flexibility of the regression boundary. In the Fine Gaussian SVM, the bandwidth is constrained to $\sigma = \sqrt{P}/4$, generating localized kernel responses that capture fine spectral variations across narrow frequency bands. As recorded in Tables 7.1 and 7.2, the Fine Gaussian model achieved $R^2 = 0.9904$ (RMSE $= 0.5790\%$) for the AR 65 series and $R^2 = 0.9902$ (RMSE $= 0.5860\%$) for the AR 55 series. The predicted values align closely along the $1:1$ ideal agreement line across the entire compressive range (10–70 MPa).

Increasing the kernel bandwidth to the Medium Gaussian configuration ($\sigma = \sqrt{P}$) broadens the spatial influence of each support vector, producing a smoother regression surface ($R^2 = 0.9729$ for AR 65; $R^2 = 0.9724$ for AR 55). However, when the bandwidth is expanded to the Coarse Gaussian formulation ($\sigma = 4\sqrt{P}$), the model exhibits excessive regularisation. The coarse kernel over-smoothes high-frequency resonance shifts, resulting in an increased RMSE of 2.5724% ($R^2 = 0.8110$) for AR 65 and 2.5871% ($R^2 = 0.8089$) for AR 55, with noticeable prediction scatter around intermediate compressive levels.

The non-parametric Gaussian Process Regression (GPR) models demonstrated the strongest reported mapping across the evaluated kernels (Squared Exponential, Matérn 5/2, Exponential and Rational Quadratic), consistently achieving $R^2 \geq 0.9984$ and RMSE $\leq 0.2369\%$. The Squared Exponential GPR achieved the lowest overall error, with RMSE $= 0.1648\%$, MSE $= 0.0272\%$ and $R^2 = 0.9992$. The four covariance functions therefore provide closely comparable high-accuracy alternatives for the present compressive-strength dataset.

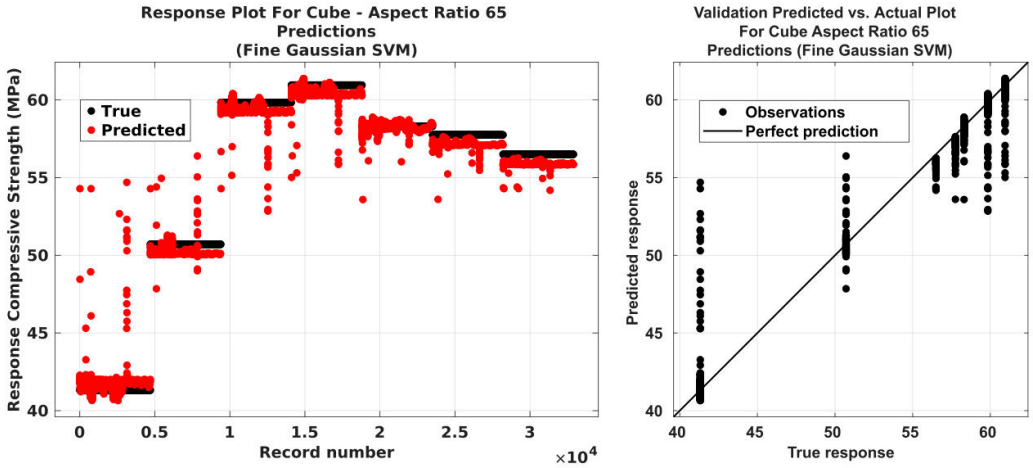

(a) Fine Gaussian SVM

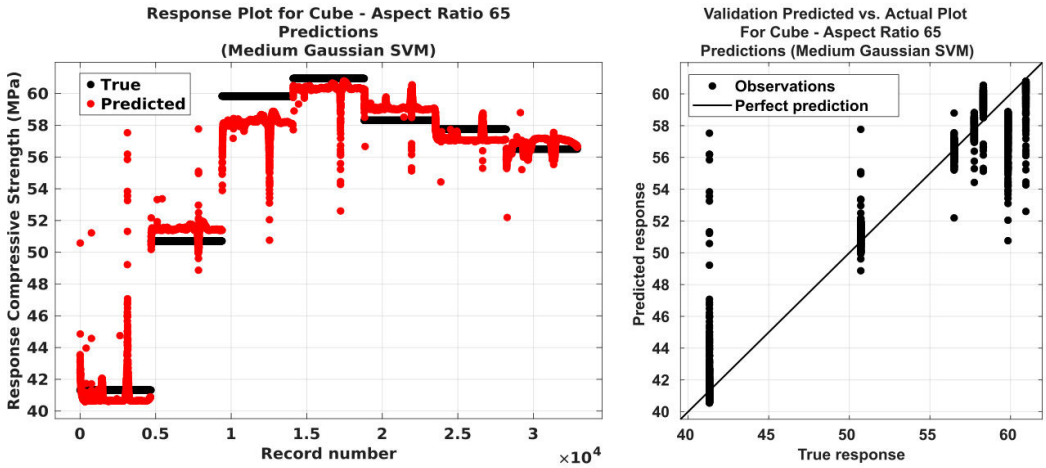

(b) Medium Gaussian SVM

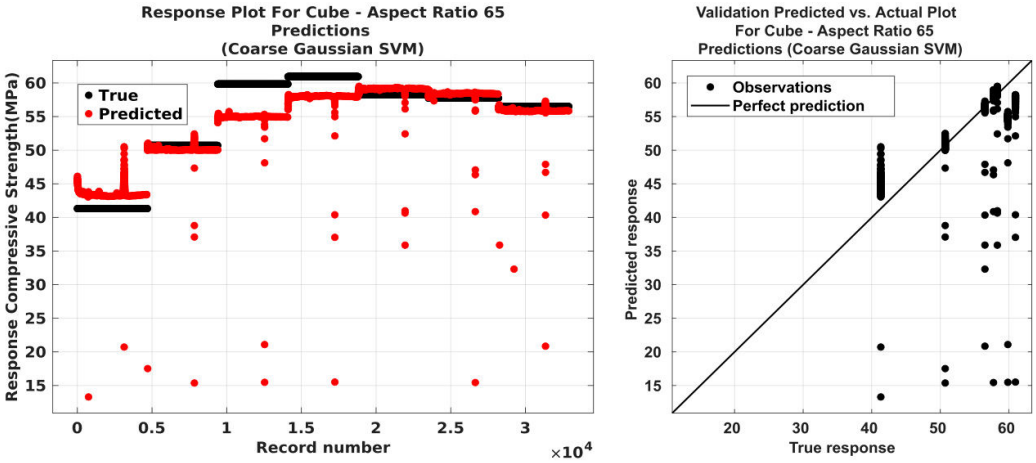

(c) Coarse Gaussian SVM

Figure 7.6: Predicted versus actual compressive strength of SFRC cubes (AR 65 series) demonstrating tracking error across three Gaussian kernel scales.

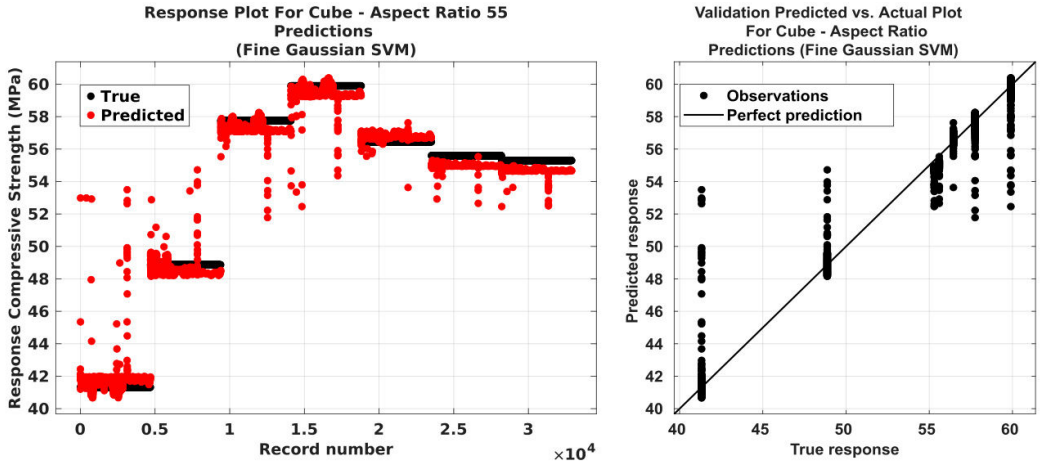

(a) Fine Gaussian SVM

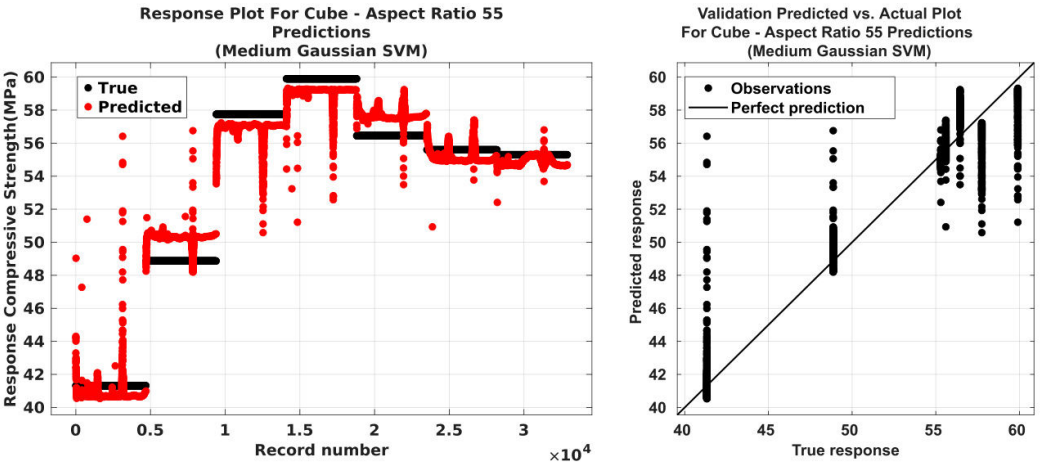

(b) Medium Gaussian SVM

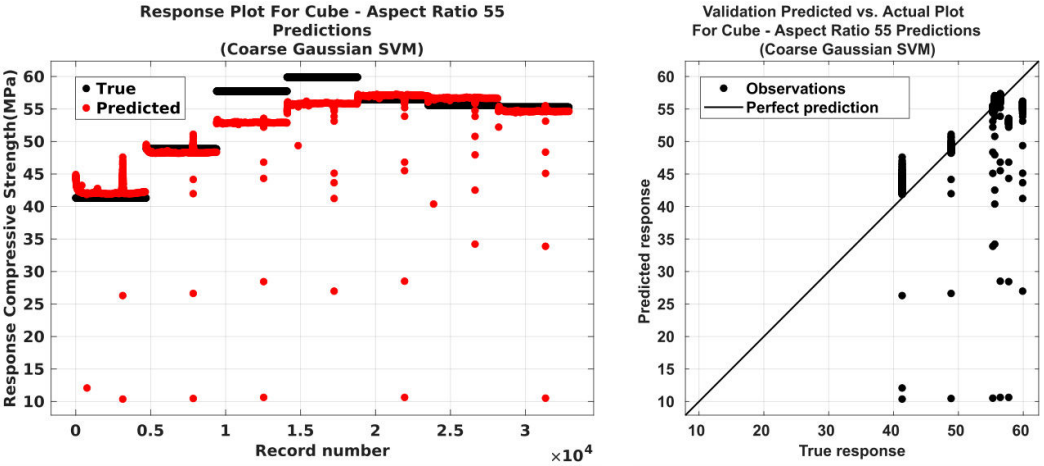

(c) Coarse Gaussian SVM

Figure 7.7: Predicted versus actual compressive strength of SFRC cubes (AR 55 series) demonstrating tracking error across three Gaussian kernel scales.

7.7 Predictive Modelling of the Hydration Programme

The deep learning architectures (2D CNN, 2D CNN–LSTM and 2D CNN–Bi-LSTM) were applied to the hydration signatures recorded by the four JPS-instrumented specimens (SFC1–SFC4). Their validation metrics are summarised in Table 7.3. Every architecture achieved an R^2 above 0.95 on its corresponding held-out validation subset, demonstrating strong predictive agreement across the four hydration datasets.

Table 7.3: Validation performance of the three deep learning architectures for hydration compressive strength prediction

JPS Sensor	Deep Learning Model	MSE (%)	R^2 (Val.)
JPS1	2D CNN	0.004760	0.9952
	2D CNN–LSTM	0.005624	0.9944
	2D CNN–Bi-LSTM	0.008332	0.9917
JPS2	2D CNN	0.138618	0.9612
	2D CNN–LSTM	0.015047	0.9849
	2D CNN–Bi-LSTM	0.043636	0.9563
JPS3	2D CNN	0.006447	0.9935
	2D CNN–LSTM	0.006295	0.9937
	2D CNN–Bi-LSTM	0.008666	0.9913
JPS4	2D CNN	0.007976	0.9920
	2D CNN–LSTM	0.007548	0.9925
	2D CNN–Bi-LSTM	0.006354	0.9937

Training behaviour is documented through the loss histories and prediction plots. Figure 7.8 presents the 2D CNN result for SFC1. Under the early-stopping criterion, the loss curves approach a stable level rapidly, indicating efficient numerical optimisation for this hydration dataset.

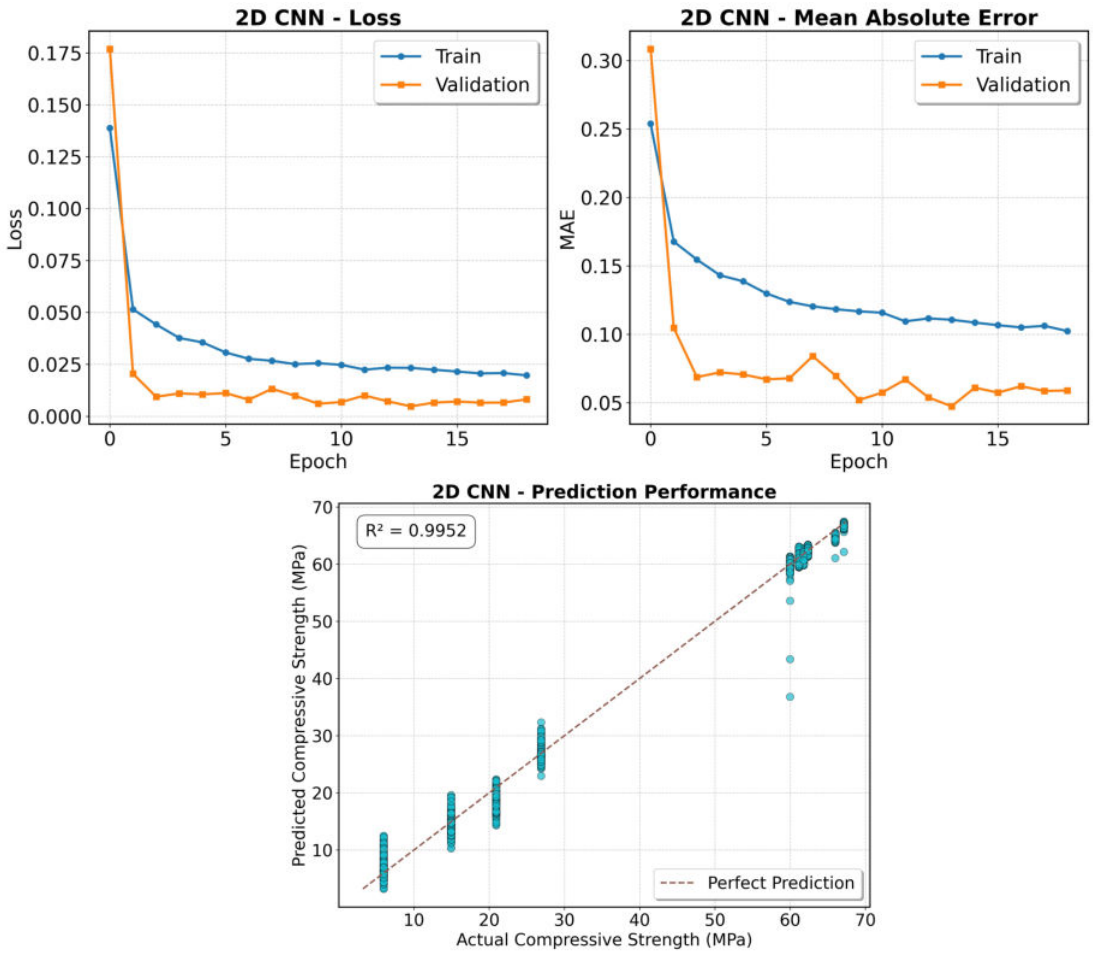

Figure 7.8: SFC1 training and prediction performance: 2D CNN.

The loss curves in Figure 7.8 show rapid parameter optimisation during the initial training cycles, with the training and validation mean absolute error reducing below 0.10 within the first five epochs. Both curves then approach comparatively stable levels, indicating that the reported performance is not taken from an isolated early-epoch minimum.

The prediction scatter remains close to the ideal response line across the represented strength range of 10–70 MPa, although the spread is more visible at the lower strength levels. The R^2 value therefore summarises the overall association and does not imply identical absolute error at every curing state. This distinction is retained when the recurrent architectures are compared with the CNN result.

The hybrid 2D CNN–LSTM combines convolutional feature extraction with recurrent processing of the ordered feature matrix. Its SFC1 convergence profile in Figure 7.9 reaches a stable error minimum and provides a direct comparison with the CNN-only architecture.

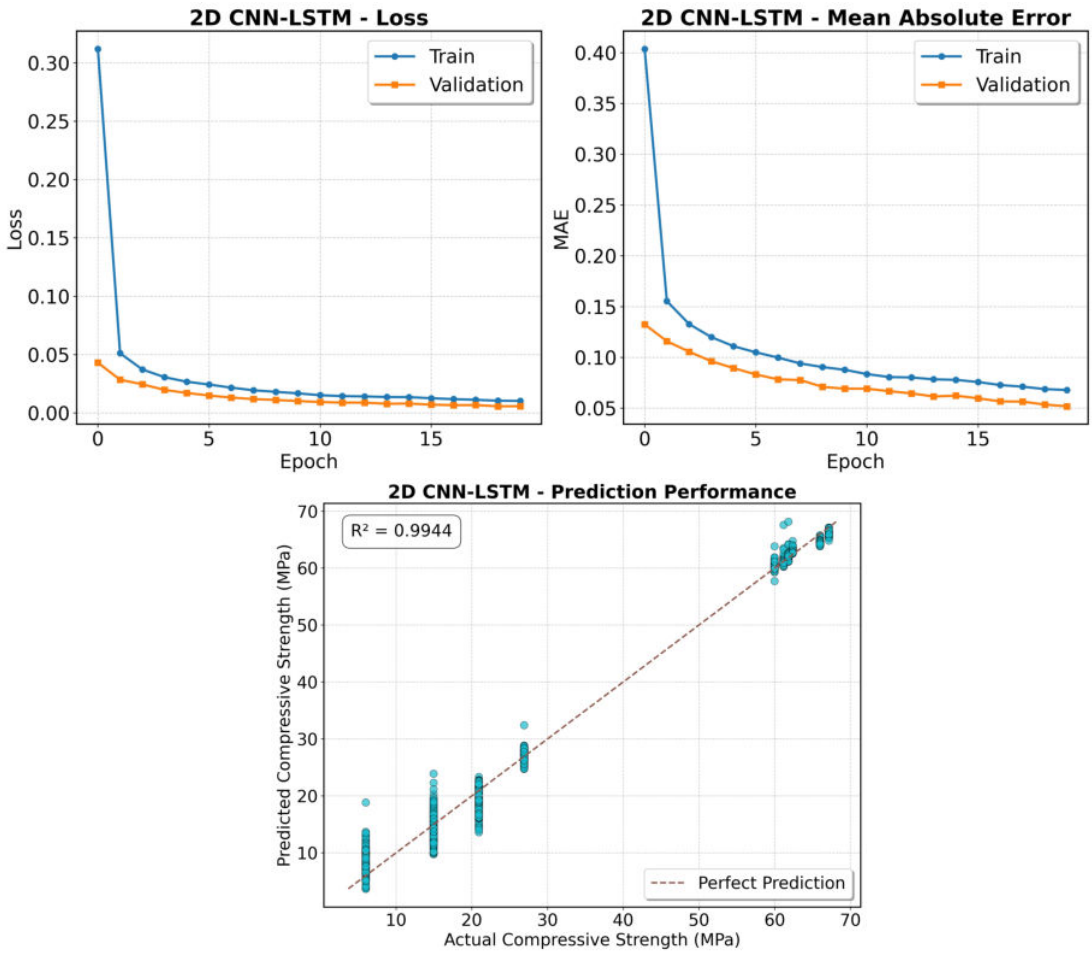

Figure 7.9: SFC1 training and prediction performance: 2D CNN–LSTM.

The CNN–LSTM convergence profile in Figure 7.9 shows a stable validation-loss trajectory after the initial decline. The prediction points cluster closely around the diagonal and yield $R^2 = 0.9944$, including close agreement over the intermediate strength range of 20–35 MPa. Because several observations occur at common target-strength levels, the plot is interpreted as performance within the analysed SFC1 dataset rather than as independent external validation.

The Bi-LSTM evaluates the arranged frequency-feature sequence in both forward and reverse directions. This provides an alternative representation of dependencies within the input matrix and allows its validation performance to be compared directly with the unidirectional and convolutional models.

The 2D CNN–Bi-LSTM result is presented in Figure 7.10. Its validation correlation provides evidence that bidirectional processing can represent the ordered EMI feature matrix effectively for the SFC1 prediction task.

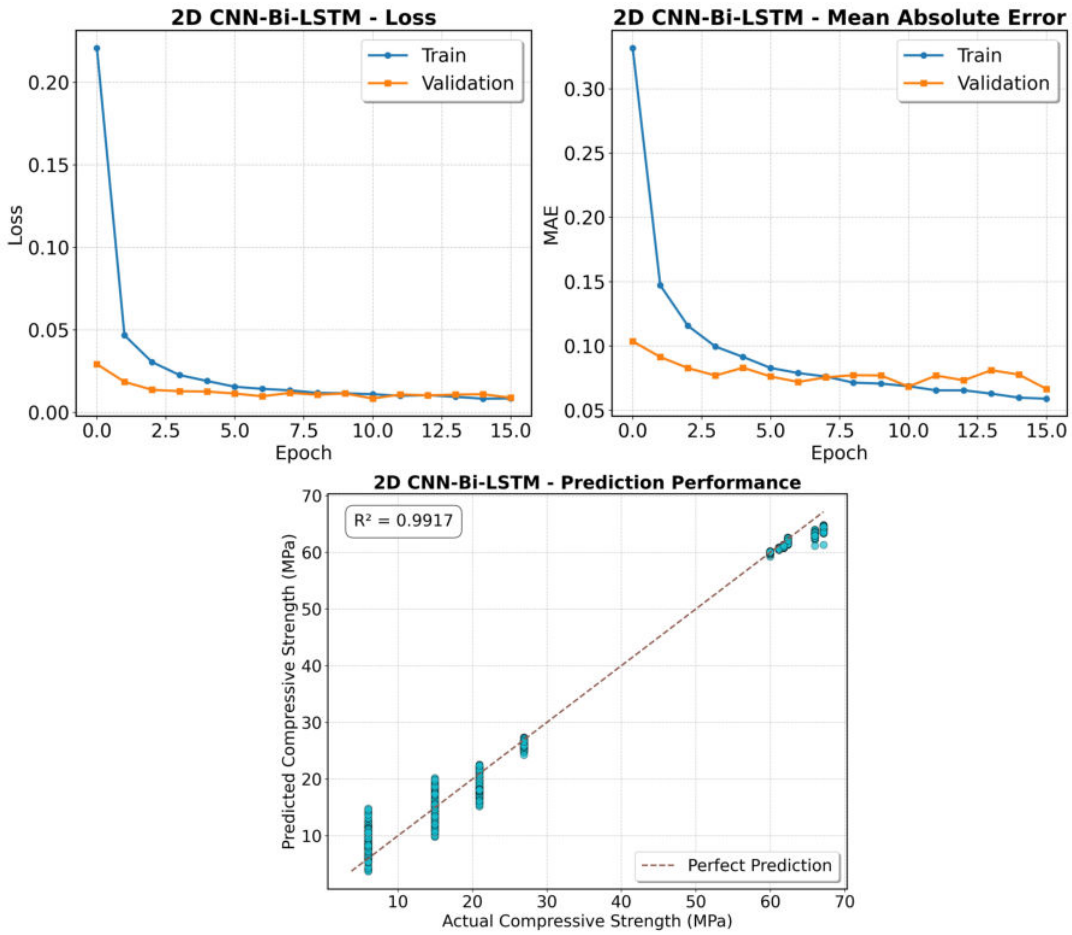

Figure 7.10: SFC1 training and prediction performance: 2D CNN–Bi-LSTM.

The convergence response in Figure 7.10 remains stable and achieves $R^2 = 0.9917$. The mean absolute error curves decay consistently without abrupt spikes, while the prediction plot shows close agreement over the validation subset.

Taken together, the three SFC1 plots compare convolutional, recurrent and bidirectional processing under the same experimentally labelled hydration application. Their similar high R^2 values show that more than one architecture can represent the measured EMI–strength association, while the MSE values in Table 7.3 identify the best-performing model separately for each JPS dataset.

A consolidated assessment of the R^2 and MSE thresholds achieved across all JPS configurations is visualised in Figure 7.11. The 2D CNN secured the lowest absolute error for JPS1, whereas the hybrid CNN–LSTM dominated the predictive performance for the JPS2 and JPS3 sensors.

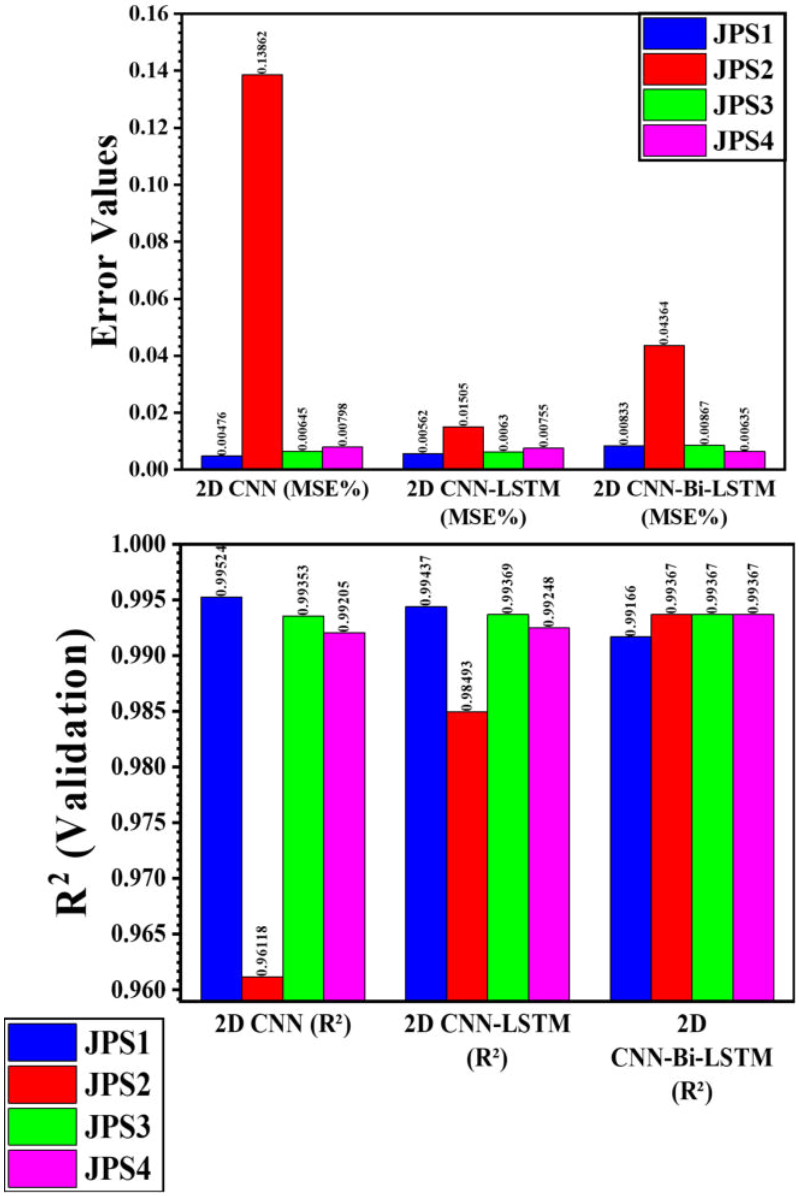

Figure 7.11: MSE and R^2 comparison across the four JPS hydration datasets.

The bar charts in Figure 7.11 summarise the error distributions across the four JPS datasets. The 2D CNN gives the lowest MSE for JPS1, the CNN–LSTM gives the lowest value for JPS2 and JPS3, and the CNN–Bi-LSTM gives the lowest value for JPS4. The consistently high R^2 values show that the framework achieved strong validation agreement for each of the four tested specimen–sensor configurations.

The relative ordering of the architectures varies among JPS1–JPS4, so model selection is made from the measured validation performance of each dataset rather than from one universal ranking. This configuration-specific comparison preserves the combined influence of material composition, curing age and the coupled JPS–specimen

response represented in each experimental series.

7.8 Predictive Modelling of the Split-Tensile Programme

The robustness of the framework was finally subjected to the split-tensile test data recorded via the NBPS modules. The core 2D CNN, 2D LSTM, and 2D Bi-LSTM architectures were trained against the AR 65 and AR 55 cylinder series.

The regression alignment between the network-predicted and experimentally measured tensile strengths is plotted in Figure 7.12 for AR 65 and Figure 7.13 for AR 55. All reported validation scores exceed $R^2 = 0.995$, demonstrating a strong association between the NBPS measurements and splitting-tensile strength over the tested response range.

The split-tensile application evaluates whether the measured EMI descriptors can predict the destructive-test response of the cylinder series. The three architectures process the same experimentally paired predictor and target data, allowing their validation errors to be compared without assigning a specific fracture mechanism to an individual network architecture.

The nine-subplot matrix in Figure 7.12 presents the individual training, error, and prediction scatter characteristics for the 2D CNN, 2D LSTM, and 2D Bi-LSTM models on the AR 65 cylinder series. Across all three models, validation loss functions stabilised within 25 epochs. The right-hand column demonstrates tight alignment between predicted and experimentally measured tensile strengths (4.0–6.5 MPa), with the 2D CNN model attaining the highest individual correlation ($R^2 = 0.9984$).

For the AR 65 series, the 2D CNN records the lowest reported error, with $R^2 = 0.9984$ and MSE $= 0.001571\,\%$. The LSTM and Bi-LSTM results remain close, but their higher MSE values establish the CNN as the best-performing architecture for this dataset under the adopted validation procedure.

The corresponding performance matrix for the AR 55 cylinder series is illustrated in Figure 7.13. The recurrent 2D LSTM gives the strongest result for this dataset, reaching $R^2 = 0.9996$ and an MSE of 3.76×10^{-4} %. The steadily decreasing validation MAE and the close predicted–measured alignment show stable optimisation and accurate prediction over the represented tensile-strength range.

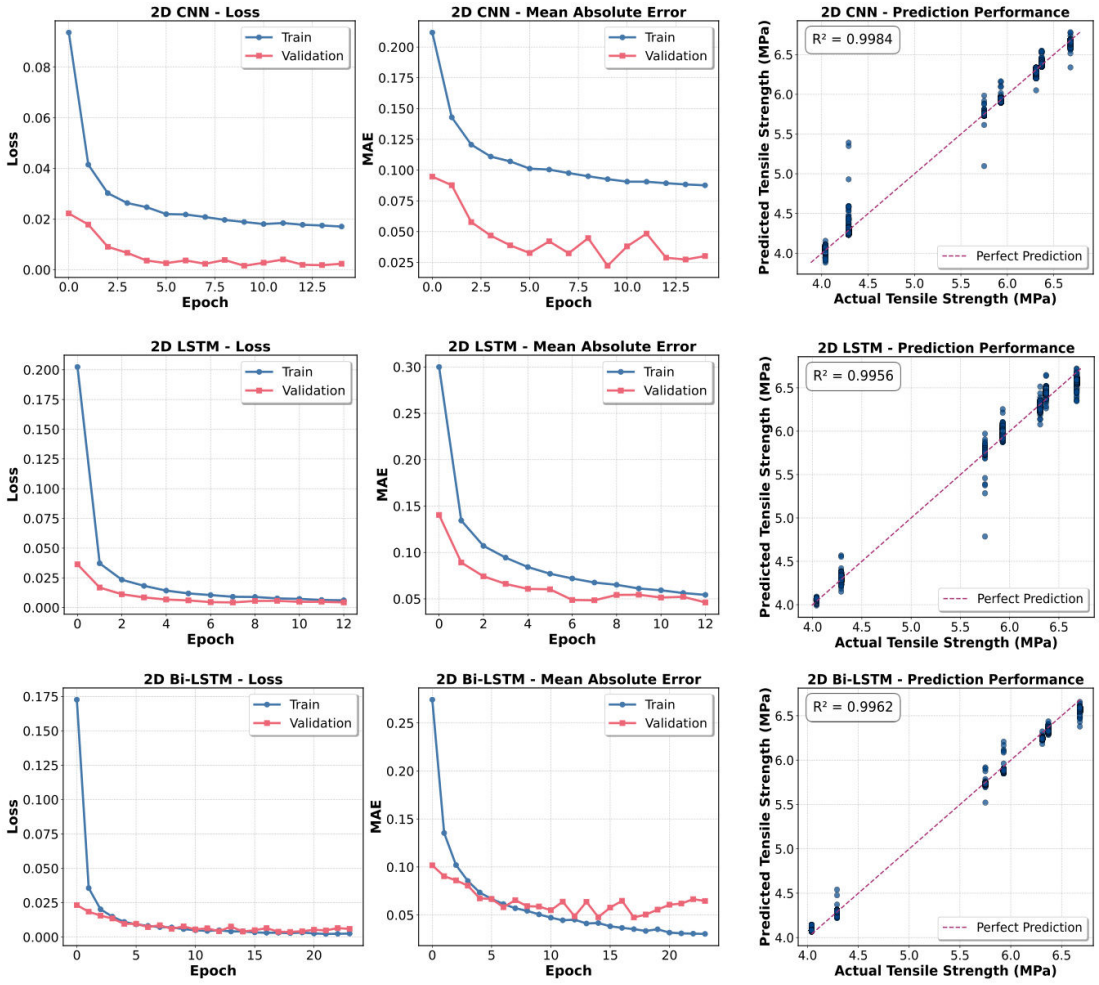

Figure 7.12: Network-predicted versus destructively measured tensile strength for SFRC cylinders (AR 65 series).

Table 7.4: Validation performance boundaries of the applied DL architectures for split-tensile strength prediction

Specimen	**DL Model**	**MSE (%)**	R^2 **(Val.)**
	2D CNN	0.001571	0.9984
Cylinder AR 65	2D LSTM	0.004340	0.9956
	2D Bi-LSTM	0.003746	0.9962
	2D CNN	0.002928	0.9970
Cylinder AR 55	2D LSTM	0.000376	0.9996
	2D Bi-LSTM	0.004049	0.9959

The quantitative MSE and R^2 metrics specify the relative performance of the evaluated architectures. The 2D CNN produces the lowest error for the AR 65 dataset, whereas the 2D LSTM produces the lowest error for AR 55. The comparison therefore identifies a dataset-specific best model while showing that all three architectures retain

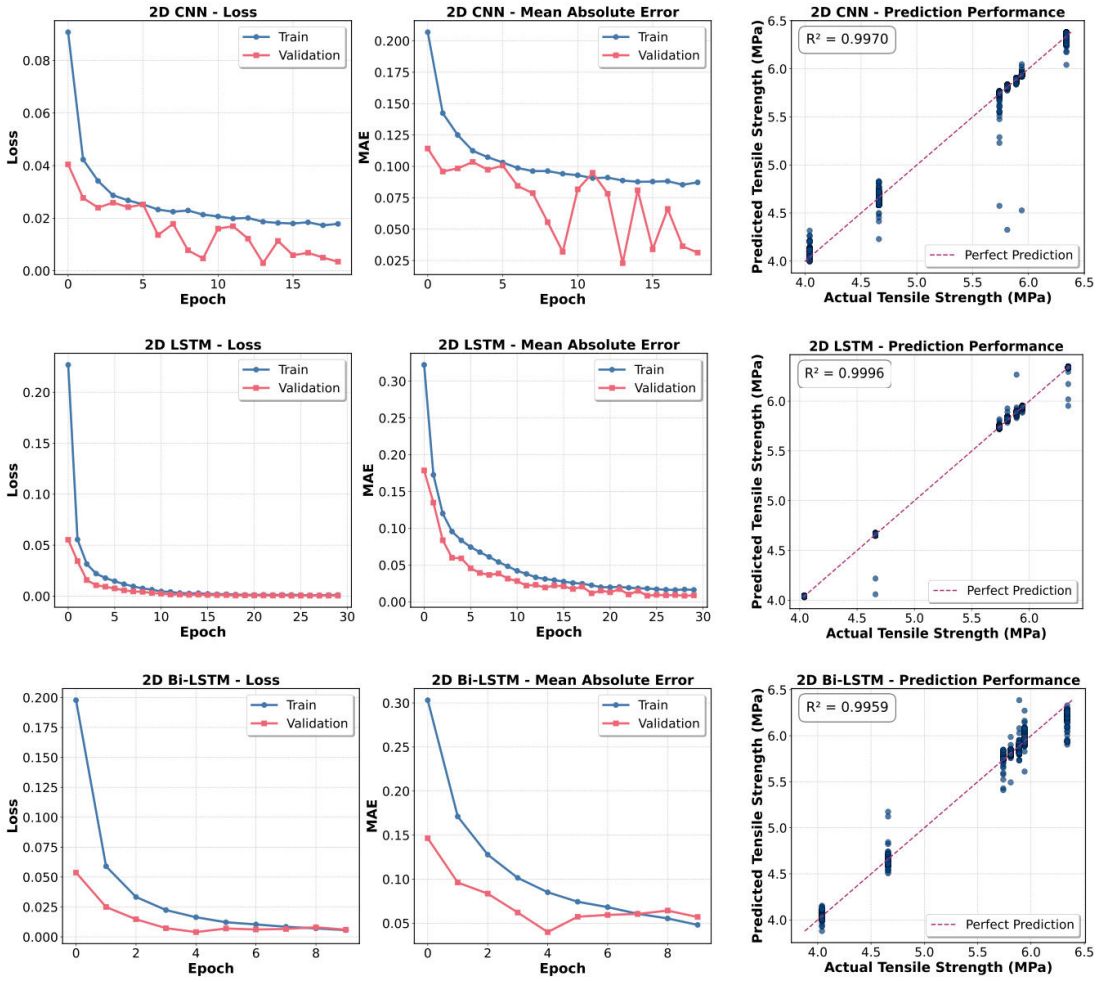

Figure 7.13: Network-predicted versus destructively measured tensile strength for SFRC cylinders (AR 55 series).

high predictive agreement for both aspect-ratio series.

The AR 55 result demonstrates the value of evaluating recurrent processing alongside convolutional processing rather than selecting one architecture in advance. Its near-linear prediction trajectory ($R^2 = 0.9996$) provides the strongest numerical agreement in the AR 55 comparison, while the AR 65 comparison favours the CNN. These complementary outcomes are retained as empirical model-performance results for the two cylinder datasets.

The graphical comparison of the aggregated network performance across both cylinder typologies is visualised in Figure 7.14.

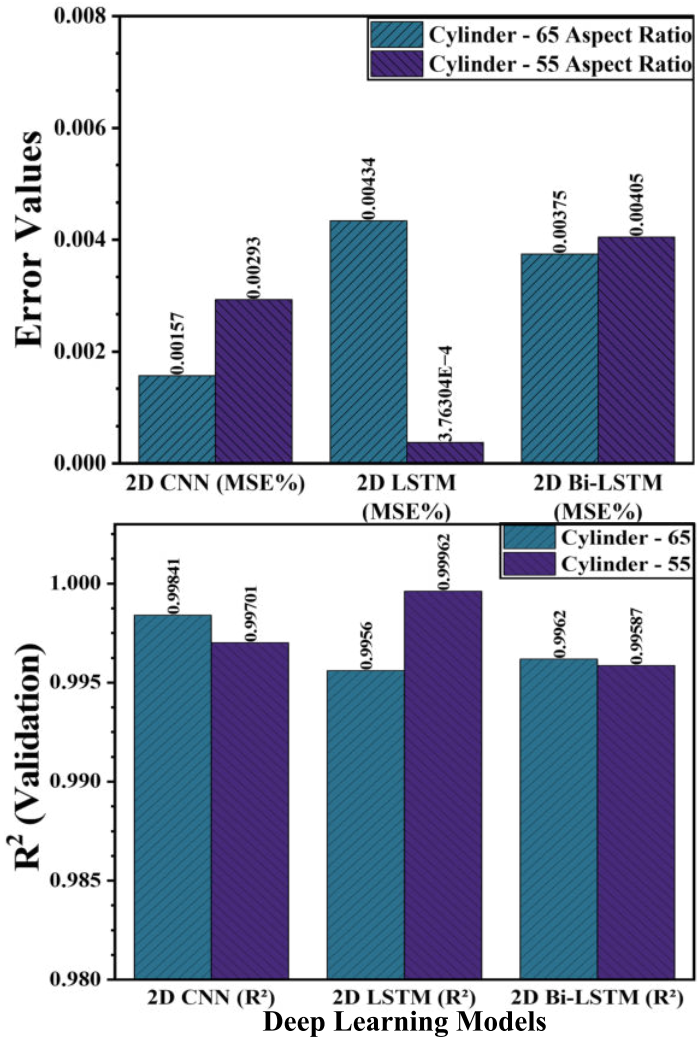

Figure 7.14: Quantitative evaluation of deep learning architectures based on MSE and R^2 for both split-tensile cylinder series.

Figure 7.14 provides a direct comparison of the MSE and R^2 metrics for the AR 65 and AR 55 cylinder series. The 2D CNN achieves the lowest error for AR 65, while the 2D LSTM achieves the lowest error for AR 55. The figure therefore makes the change in relative model ranking visible without obscuring the consistently high validation agreement of all three architectures.

The architecture ranking is interpreted within each measured aspect-ratio dataset. Fibre geometry remains an experimental descriptor of the SFRC series, while CNN and LSTM are alternative numerical mappings of the supplied EMI features. This distinction permits a clear performance comparison without treating network type as a direct representation of a particular cracking mechanism.

7.9 Physical Interpretability of the AI Framework

The physical basis of the prediction tasks is provided by the experimental pairing of EMI measurements with destructively measured compressive or splitting-tensile strengths. Conductance, susceptance and the equivalent model parameters supply complementary descriptors of the coupled sensor–interface–specimen response. As established in Chapter 3, the equivalent m, k and c terms are model-derived quantities and are interpreted comparatively rather than as direct bulk material properties.

Within this evidence framework, the high validation R^2 values show that the evaluated models reproduce the measured strength responses closely over the tested ranges. The physical interpretation continues to come from the experimental programmes and their measured mechanical responses, while the machine learning and deep learning architectures provide alternative data-driven mappings from the assembled EMI descriptors to strength.

7.10 Comparative Analysis and Computational Cost

The absolute computational strain of the deep learning framework was benchmarked on a cloud-based node provisioned with an NVIDIA T4 GPU, executing identical early-stopping constraints. The network weight volumes, epoch convergence rates, and aggregate training durations are documented in Table 7.5.

Table 7.5: Computational benchmarking and architectural training durations for the deep learning models

Architecture	**Trainable weights**	**Epoch time**	**Conv. epoch (Cyl. 55)**	**Conv. epoch (Cyl. 65)**	**Total training**	R^2 **(Cyl. 55 / Cyl. 65)**
2D CNN	∼85k	∼9 s	19	15	∼3 min	0.9970 / 0.9984
2D LSTM	∼215k	∼25 s	30	13	∼14 min	0.9996 / 0.9956
2D Bi-LSTM	∼380k	∼40 s	10	24	∼21 min	0.9959 / 0.9962

The 2D CNN is the most computationally efficient architecture, using the fewest trainable weights ($\sim$ 85k) and completing training in approximately 3 minutes. The 2D LSTM requires approximately 14 minutes and yields the highest reported R^2, 0.9996, for the AR 55 series. The 2D Bi-LSTM has the largest parameter count ($\sim$ 380k) and longest training duration ($\sim$ 21 min), without improving the reported MSE and R^2 values over the best CNN or LSTM result.

7.11 Summary

The data-driven framework produced strong predictive agreement between EMI-derived inputs and the measured mechanical responses of the tested SFRC specimens. For the compressive programme, the non-linear SVM and GPR formulations markedly improved on the linear baselines. For hydration and split-tensile prediction, the CNN, LSTM and hybrid architectures achieved high validation R^2 values, with the best-performing architecture determined separately for each experimental dataset.

Together, the three applications demonstrate the feasibility of using JPS and NBPS measurements for data-driven strength prediction within the investigated laboratory programmes. The framework combines experimentally measured targets, case-specific EMI datasets and transparent model comparisons, providing a coherent computational component of the proposed non-destructive assessment methodology.

CHAPTER 8

CONCLUSIONS, LIMITATIONS AND FUTURE SCOPE

8.1 Conclusion

This thesis establishes an integrated laboratory framework for monitoring SFRC using embedded JPS and reusable NBPS measurements, resonance characteristics, statistical indices, EPS, temperature compensation and data-driven modelling. The investigation comprises four studies: long-term hydration monitoring, compressive-damage assessment, splitting-tensile-damage assessment and controlled elevated-temperature testing. Together, these studies examine changes associated with curing, mechanical loading, fibre configuration, temperature, dwell time and structural state.

JPS measurements supported continuous observation of curing and thermal response, whereas the reusable NBPS enabled paired interrogation before and after destructive loading. The EPS formulation represented the local coupled sensor–interface–concrete response around the selected resonance. E–EFS reduced temperature-associated mismatch in the available matched comparisons, and the ML/DL studies related measured descriptors to assigned mechanical responses within each study-specific dataset.

The following subsections present the principal findings in relation to the three research objectives and within the tested experimental and validation scope.

8.1.1 Conclusions on Objective 1

Objective 1 addressed the detection and characterisation of curing- and loading-related changes using JPS and NBPS measurements. The principal conclusions are:

- Long-term hydration monitoring was demonstrated for the tested configurations. The four embedded JPS configurations tracked conductance, susceptance, resonance characteristics, statistical indices and EPS development from day 1 to day 180. The measurements captured rapid early-age evolution followed by pro-

gressively slower long-term change, consistent with the accompanying strength-development trend.

- The JPS response was sensitive to configuration-specific material development. The four sensor–specimen systems produced distinct response histories rather than one universal response. This shows the importance of establishing a baseline for each installed configuration while confirming that the embedded sensors retained useful sensitivity throughout the curing programme.

- EPS provided an additional interpretation of the measured signatures. The stiffness-like response developed systematically during curing, and the reported SFC1 and SFC2 stiffness–strength relations achieved in-sample R^2 values of 0.94 and 0.96. These results show that the local equivalent representation of the coupled sensor–interface–concrete response can support interpretation of the measured material-development trend.

- Reusable NBPS interrogation distinguished pre-loading and post-loading states. The cube and cylinder programmes each comprised 39 specimens distributed across thirteen mixture configurations. Paired measurements showed changes in resonance position, peak conductance, RMSD, MAPD and EPS quantities following destructive loading, demonstrating sensitivity of the coupled NBPS–specimen response to the altered structural state.

- The compressive-strength results identified a dosage-dependent trend. The AR 55 and AR 65 series increased from the plain-concrete control to their maximum measured mean at 0.75% fibre. The corresponding values were 59.90 MPa for AR 55 and 60.95 MPa for AR 65, representing increases of 44.9% and 47.5% relative to the 41.32 MPa control.

- The splitting-tensile results showed continued benefit over the tested dosage range. The largest measured means occurred at the upper tested dosage of 1.50%, reaching 6.34 MPa for AR 55 and 6.68 MPa for AR 65. These values correspond to increases of 56.9% and 65.3% relative to the common 4.04 MPa control.

- The mechanical programmes revealed configuration-dependent resonance behaviour. Some high-dosage cylinder records exhibited an upward post-loading resonance shift. This observation shows that the measured local response did not follow one shift direction across all tested fibre configurations.

- Resonance features, statistical indices and EPS quantities described different aspects of the same coupled response. Their joint interpretation supported comparison of the tested pre-loading and post-loading states without treating one scalar index as a universal damage measure.

Objective 1 was achieved within the tested laboratory programmes: JPS measurements tracked curing-related development, while NBPS measurements distinguished paired structural states and supported comparison across the investigated SFRC configurations. The established local response characterisation provides an experimental basis for future multi-sensor studies of spatial localisation.

8.1.2 Conclusions on Objective 2

Objective 2 investigated the influence of temperature and heating time and evaluated compensation of temperature-associated signature variation. The principal conclusions are:

- The thermal programme established a detailed repeated-measurement archive. Four JPS-instrumented cubes were assessed in intact and saw-cut states through the available 75–250 °C range and at 10-, 20- and 30-minute dwell times. The resulting 182 documented acquisitions retain the combined influence of configuration, structural state, temperature and dwell time.

- Heating time influenced the measured response. Conductance and susceptance signatures continued to evolve across the dwell sequence at the same nominal temperature. The magnitude and direction of this evolution varied among configurations, showing that dwell time is an essential part of elevated-temperature measurement description.

- Temperature produced both frequency and amplitude variation. The observed response could not be represented adequately by frequency translation alone. The joint behaviour of conductance and susceptance supported a compensation procedure that considered both channels and retained their individual residual behaviour.

- E–EFS improved within-state alignment for every available matched comparison. The implemented procedure used 25-fold interpolation, a defined shift-search interval, joint conductance–susceptance correlation and channel-offset correction. Across the available temperature-averaged RMSD results, the processed value

was lower than the corresponding unprocessed value for every intact and saw-cut cell.

- Compensation strengthened matched structural-state comparison. After processing, saw-cut conductance RMSD exceeded the corresponding intact value for all four configurations from 125 to 175 °C and for the available 0.50% configurations from 200 to 250 °C. This provides a configuration- and temperature-resolved basis for comparing the tested structural states.

- EPS extended the thermal interpretation beyond statistical distance. The mass-like, stiffness-like and damping-like terms recorded configuration-dependent evolution in intact and saw-cut states. Their use with the measured spectra and statistical indices provided an additional description of the local coupled system.

- The thermal study defined a reproducible analysis sequence. Baseline selection, shift estimation, offset correction, matched structural-state comparison and multi-index interpretation were organised into one traceable procedure for evaluation on independent specimens in future work.

Objective 2 was achieved within the tested thermal programme by documenting temperature- and dwell-associated variation and by applying a compensation procedure that reduced baseline mismatch in the available matched records. The results provide a basis for further replicated thermal and environmental validation.

8.1.3 Conclusions on Objective 3

Objective 3 evaluated data-driven modelling of the measured response. The analysis produced three study-specific regression applications, and the principal conclusions are:

- EMI-derived descriptors were used to model the measured mechanical responses in all three applications. Hydration-age compressive strength, cube compressive strength and cylinder splitting-tensile strength were represented within their respective recorded datasets.

- Hydration-model performance depended on the JPS configuration. The 2D CNN produced the lowest reported MSE for JPS1, the 2D CNN–LSTM for JPS2 and JPS3, and the 2D CNN–Bi-LSTM for JPS4. Model architecture was therefore evaluated separately for each sensor–specimen dataset.

- Squared-exponential Gaussian Process Regression produced the lowest reported RMSE and the highest reported R^2 for both the AR 55 and AR 65 cube-compression datasets under the adopted validation procedure.
- The split-tensile datasets favoured different deep-learning architectures. The 2D CNN produced the lowest reported error for AR 65, while the 2D LSTM produced the lowest reported error for AR 55. The result retains the dataset-specific model ranking.
- The reported prediction plots and validation metrics showed high agreement within the analysed datasets. The selected EMI/EPS descriptors contained information related to the assigned mechanical-strength labels over the investigated response ranges.
- Model ranking depended on the experimental dataset, input representation and validation design. Classical and deep-learning methods were therefore compared within each application rather than assigned one universal order.
- The documented workflow of data organisation, preprocessing, architecture comparison and quantitative assessment can be extended using group-wise specimen separation and independent external testing.

Objective 3 was achieved within the available study-specific datasets by relating piezoelectric measurements to the assigned mechanical responses and comparing the reported model performance. Independent specimen-group and external validation remain the next stages before application beyond the investigated datasets.

8.1.4 Principal Contributions of the Thesis

The main contributions arising from the complete investigation are:

- experimental evaluation of an embedded JPS configuration for long-term hydration and elevated-temperature monitoring of SFRC;
- demonstration of reusable NBPS interrogation across the tested cube and cylinder mixture matrices;
- integration of resonance features, statistical indices and EPS quantities within one interpretation framework;

- implementation and evaluation of E–EFS using joint conductance–susceptance alignment and offset correction;
- development of a structured intact–saw-cut comparison across temperature and dwell-time records;
- comparison of classical machine-learning and deep-learning architectures across hydration, compression and splitting-tensile applications; and
- integration of experimental sensing, temperature-compensated interpretation and data-driven prediction within one thesis framework.

8.2 Limitations

The conclusions are interpreted within the following experimental boundaries:

- The hydration and thermal programmes contain one retained JPS-instrumented cube per configuration; additional independent specimens will enable population-level inference.
- The material scope is defined by the investigated M30 matrix, hooked steel-fibre families, dosage ranges, specimen geometries and laboratory loading procedures.
- NBPS remounting, clamp force, contact pressure and repeated engage–disengage variability were not quantified separately from structural-state change.
- Sensor fabrication, curing and thermal exposure were limited to the laboratory procedures adopted in this study. The findings therefore apply to the reported JPS and NBPS materials, geometries, protective assemblies and coupling arrangements, and to the specified curing regime. The progressive thermal sequence also combines temperature, dwell time, moisture evolution and cumulative heating history, while the saw-cut 0.75% records end at 175 °C.
- EPS quantities represent the local coupled sensor–specimen system around the selected resonance and require separate validation before interpretation as bulk material properties.
- The data-driven results apply to the available datasets; specimen-group provenance, retained preprocessing objects and independent external testing remain priorities for confirmation.

- Field performance, lifecycle cost, service-life extension and environmental benefit were outside the measured scope of the laboratory programme.

8.3 Future Scope

The following research directions build directly on the reported results and limitations:

- increase independent replication for each material, sensor and structural-state configuration;
- quantify NBPS clamp force, remount dispersion, surface condition, curvature and long-cycle reuse through repeatability and reproducibility testing;
- apply multi-sensor arrays to members with controlled damage coordinates to extend local response detection towards spatial localisation;
- conduct controlled heating–cooling and simultaneous thermo-mechanical programmes with moisture and post-heating mechanical measurements;
- evaluate E–EFS on independent environmental cycles using predeclared matched comparisons and uncertainty limits;
- extend the material matrix to other concrete grades, fibre families, hybrid systems and structural scales;
- retain complete ML datasets, specimen-group assignments, preprocessing objects, model artefacts and seeds, followed by group-wise validation and an independent external test set;
- benchmark prediction latency, memory and energy demand on named hardware before embedded or edge deployment; and
- undertake staged field trials after laboratory repeatability and specimen-level validation have been established.

8.4 Social, Economic and Environmental Relevance

8.4.1 Social Relevance

The monitoring approaches developed in this thesis can support safer and more objective assessment of concrete infrastructure. Embedded sensing offers the possibility

of observing material development from within a member, while reusable interrogation can provide targeted assessment without permanently installing a sensor at every test location. Following field validation, these capabilities can assist engineers in identifying changes earlier, prioritising detailed inspection and directing maintenance resources towards the locations of greatest concern.

The work is particularly relevant to infrastructure for which access is difficult or interruption is costly. More frequent quantitative information can complement visual inspection and destructive testing, strengthen maintenance planning and contribute to the resilience of facilities serving the public. The thesis therefore provides a laboratory foundation for monitoring approaches that place safety, traceability and informed engineering judgement at the centre of condition assessment.

8.4.2 Economic Relevance

The NBPS concept demonstrates laboratory reuse across large cube and cylinder programmes, reducing the need to dedicate a permanently bonded sensor to every specimen. This reuse principle can support economical quality-control and targeted inspection strategies. JPS monitoring can also provide information during curing and subsequent exposure without repeated sensor installation.

The potential economic value lies in enabling condition-informed testing and maintenance. Earlier identification of significant change can help avoid unnecessary intervention while allowing detailed investigation to be prioritised when evidence warrants it. A formal cost-benefit analysis was not part of this study, but the experimental results establish the technical basis required for future lifecycle-cost evaluation.

8.4.3 Environmental Relevance

Monitoring that supports timely repair and continued safe use of an existing structure can reduce unnecessary demolition, replacement and material consumption. Reusable sensors also align with more efficient use of monitoring hardware. These potential benefits are relevant to concrete infrastructure because repair decisions influence cement, aggregate, steel, transport and construction demand.

The thesis does not assign a measured carbon saving; instead, it provides the sensing and interpretation foundation needed for a future lifecycle assessment. Such an assessment can quantify whether monitoring-supported maintenance extends service life, reduces replacement frequency and lowers embodied environmental impact.

8.4.4 Alignment with the Sustainable Development Goals

The contributions align with the following United Nations Sustainable Development Goals:

SDG 9 Industry, Innovation and Infrastructure: the JPS, NBPS, compensation and data-driven components contribute to innovation in infrastructure monitoring and support the development of more resilient engineering systems.

SDG 11 Sustainable Cities and Communities: improved condition information can support safer, more reliable and better-maintained infrastructure serving urban communities.

SDG 12 Responsible Consumption and Production: reusable sensing and maintenance-informed decision making can promote more efficient use of monitoring equipment and construction resources.

SDG 13 Climate Action: monitoring-supported repair and service-life extension have the potential to reduce premature reconstruction and its associated emissions, subject to confirmation through lifecycle assessment.

8.5 Closing Remarks

This thesis presents a progression from sensor development and experimental measurement to EPS interpretation, temperature compensation and data-driven prediction. The combined JPS and NBPS studies produced evidence spanning curing, compression, splitting tension and elevated temperature. Within the investigated datasets, the measured signatures supported direct comparison, statistical assessment, EPS interpretation and study-specific regression.

The work contributes to the development of traceable SHM methods for SFRC. It establishes tested sensing configurations, a structured analysis procedure and defined directions for replicated validation and field evaluation. The proposed extensions in replication, environmental testing, model validation and lifecycle assessment provide a basis for future research on safe, economical and sustainable monitoring of concrete infrastructure.

BIBLIOGRAPHY

1. Miguel Abambres and Eva OL Lantsoght. Ann-based shear capacity of steel fiber-reinforced concrete beams without stirrups. *Fibers*, 7(10):88, 2019.

2. Hojjat Adeli and C Yeh. Perceptron learning in engineering design. *Computer-Aided Civil and Infrastructure Engineering*, 4(4):247–256, 1989.

3. D. Ai and J. Cheng. A deep learning approach for electromechanical impedance based concrete structural damage quantification using two-dimensional convolutional neural network. *Mechanical Systems and Signal Processing*, 183:109634, 2023.

4. D. Ai, H. Zhu, and H. Luo. Heating-time hysteresis effect on electromechanical impedance signature and its compensation. *Smart Materials and Structures*, 30(2):025026, 2021.

5. Demi Ai, Chengxing Lin, and Hongping Zhu. Embedded piezoelectric transducers based early-age hydration monitoring of cement concrete added with accelerator/retarder admixtures. *Journal of Intelligent Material Systems and Structures*, 32(8):847–866, 2021.

6. Demi Ai, Fang Mo, Yihang Han, and Junjie Wen. Automated identification of compressive stress and damage in concrete specimen using convolutional neural network learned electromechanical admittance. *Engineering Structures*, 259:114176, 2022.

7. Demi Ai, Fang Mo, Feng Yang, and Hongping Zhu. Electromechanical impedance-based concrete structural damage detection using principal component analysis incorporated with neural network. *Journal of Intelligent Material Systems and Structures*, 33(17):2241–2256, 2022.

8. Demi Ai, Fang Mo, Jiabao Cheng, and Lixun Du. Deep learning of electromechanical impedance for concrete structural damage identification using 1-d convolutional neural networks. *Construction and Building Materials*, 385:131423, 2023.

9. Osama Alazzawi and Dansheng Wang. Health monitoring of an assembly-type structure using raw time-domain emi signals and a novel hybrid deep learning algorithm. *Smart Materials and Structures*, 33(2):025038, 2024.

10. Aneta Antolik and Daria Jóźwiak-Niedźwiedzka. Asr induced by chloride-and formate-based deicers in concrete with non-reactive aggregates. *Construction and Building Materials*, 400:132811, 2023.

11. Dattar Singh Aulakh and Suresh Bhalla. Non-bonded piezo sensor configuration for strain modal analysis based shm. In *Health Monitoring of Structural and Biological Systems XVI*, volume 12048, pages 334–340. SPIE, 2022.

12. Dattar Singh Aulakh and Suresh Bhalla. Piezo sensor-based operational strain modal analysis of structures: Transition from lab to field application. *Measurement*, 239:115398, 2025.

13. Tushar Bansal and Visalakshi Talakokula. Deterioration of structural parameters due to corrosion in prestressed concrete identified by smart probe-based piezo sensor. *Engineering Research Express*, 3(1):015011, 2021.

14. Tushar Bansal and Visalakshi Talakokula. Comparative analysis of very-early age hydration process: Lc3 vs. conventional and blended cement pastes using embedded piezo sensors. *Measurement*, 229:114433, 2024.

15. N. Banthia and R. Gupta. Hybrid fiber reinforced concrete (hyfrc): fiber synergy in high strength matrices. *Materials and Structures*, 37:707–716, 2004.

16. Sushmita Baral, Sailesh Adhikari, Prateek Negi, and Suresh Bhalla. Development and evaluation of reusable piezo sensors for health monitoring of thin-walled steel structures. *Journal of Civil Structural Health Monitoring*, 12(3):647–657, 2022.

17. Mouhcine Benaicha, Olivier Jalbaud, Adil Hafidi Alaoui, and Yves Burtschell. Correlation between the mechanical behavior and the ultrasonic velocity of fiber-reinforced concrete. *Construction and Building Materials*, 101:702–709, 2015.

18. A. Bentur and S. Mindess. *Fibre Reinforced Cementitious Composites*. CRC Press, 2nd edition, 2007.

19. S Bhalla and A Gupta. An embeddable piezo composite concrete vibration sensor for structural health monitoring of reinforced concrete structures and process of preparation thereof. *Indian Patent*, (412929), 2022.

20. Suresh Bhalla and Chee Kiong Soh. Electromechanical impedance modeling for adhesively bonded piezo-transducers. *Journal of intelligent material systems and structures*, 15(12):955–972, 2004.

21. Suresh Bhalla and Chee Kiong Soh. Structural health monitoring by piezo-impedance transducers. i: Modeling. *Journal of Aerospace Engineering*, 17(4):154–165, 2004.

22. Bureau of Indian Standards. IS 516:1959 methods of tests for strength of concrete. New Delhi, 1959.

23. Bureau of Indian Standards. IS 2386 (Part III):1963 methods of test for aggregates for concrete: specific gravity, density, voids, absorption and bulking. New Delhi, 1963.

24. Indian Standard. Plain and reinforced concrete-code of practice. *New Delhi: Bureau of Indian Standards*, 2000.

25. I S BIS. 8112 2013 ordinary portland cement 43 grade specifications. *Bureau of Indian Standards, New Delhi, India*, 2013.

26. Bureau of Indian Standards. IS 12269:2013 ordinary Portland cement, 53 grade—specification. New Delhi, 2013.

27. B I S IS. 383 (2016) coarse and fine aggregate for concrete-specification. *Bureau of Indian Standards, New Delhi*, 2016.

28. I Standard IS. 10262 (2019): Concrete mix proportioning-guidelines (second revision), 2019.

29. Zhiyuan Chen, Xin Wang, Kaidi Jiang, Xiuwen Zhao, Xia Liu, and Zhishen Wu. The splitting tensile strength and impact resistance of concrete reinforced with hybrid bfrp minibars and micro fibers. *Journal of Building Engineering*, 88:109188, 2024.

30. Kai Cui, Denvid Lau, and Jun Chang. Advancements in energy harvesting through building materials: A critical review. *Journal of Building Engineering*, 98:111412, 2024.

31. M. Di Prisco, G. Plizzari, and L. Vandewalle. Fibre reinforced concrete: new design perspectives. *Materials and Structures*, 42:1261–1281, 2009.

32. Marco di Prisco, Matteo Colombo, and Daniele Dozio. Fibre-reinforced concrete in fib model code 2010: principles, models and test validation. *Structural Concrete*, 14(4):342–361, 2013.

33. Marco di Prisco, Terje Kanstad, Giovanni Plizzari, Fausto Minelli, and Andreas Haus. Eurocode 2–annex l–european harmonized standard for steel fibre reinforced concrete. In *RILEM-fib International Symposium on Fibre Reinforced Concrete*, pages 539–551. Springer, 2021.

34. A Dinesh, D Suji, et al. Electro-mechanical investigations of steel fiber reinforced self-sensing cement composite and their implications for real-time structural health monitoring. *Journal of Building Engineering*, 51:104343, 2022.

35. B. S. Divsholi and Y. Yang. Application of reusable pzt sensors for monitoring initial hydration of concrete. In *Sensors and Smart Structures Technologies for Civil, Mechanical, and Aerospace Systems*. SPIE, 2009.

36. Aashank Dogra, Sheikh Hazim, Arpit Goyal, Ayush Bhatia, and Shruti Sharma. Developing embeddable self-sensing cementitious composite sensor incorporating carbon based materials for smart structural health monitoring. *Journal of Building Engineering*, page 113278, 2025.

37. C. R. Farrar and K. Worden. An introduction to structural health monitoring. *Philosophical Transactions of the Royal Society A*, 365:303–315, 2007.

38. Weihang Gao, Caiyan Zhang, and Lin Chen. Monitoring mechanical behaviors of clt connections under reciprocating loading based on pzt-enabled active sensing and machine learning algorithms. *Smart Materials and Structures*, 32(2):024001, 2023.

39. Danying Gao, Lu Wang, and Wei Ma. Flexural tensile property and damage evolution of hooked-end steel fiber reinforced concrete with low fiber dosage and concrete strength. *Journal of Building Engineering*, 99:111680, 2025.

40. Himanshi Gayakwad and Jothi Saravanan Thiyagarajan. Structural damage detection through emi and wave propagation techniques using embedded pzt smart sensing units. *Sensors*, 22(6):2296, 2022.

41. V. Giurgiutiu and A. Zagrai. Damage detection in thin plates and aerospace structures with the electro-mechanical impedance method. *Structural Health Monitoring*, 4(2):99–118, 2005.

42. Ramesh Gomasa, Visalakshi Talakokula, Sri Kalyana Rama Jyosyula, and Tushar Bansal. A review on health monitoring of concrete structures using embedded piezoelectric sensor. *Construction and Building Materials*, 405:133179, 2023.

43. K. Balamonica, T. Jothi Saravanan, C. Bharathi Priya, and N. Gopalakrishnan. Piezoelectric sensor–based damage progression in concrete through serial/parallel multi-sensing technique. *Structural Health Monitoring*, 19(2):339–356, 2019.

44. Viktor Gribniak, Pui-Lam Ng, Vytautas Tamulenas, Ieva Misiūnaitė, Arnoldas Norkus, and Antanas Šapalas. Strengthening of fibre reinforced concrete elements: Synergy of the fibres and external sheet. *Sustainability*, 11(16):4456, 2019.

45. H. Gu, G. Song, H. Dhonde, Y. L. Mo, and S. Yan. Concrete early-age strength monitoring using embedded piezoelectric transducers. *Smart Materials and Structures*, 15(6):1837, 2006.

46. Shuqi Guo, Yahong Ding, Xianggang Zhang, Ping Xu, Jiuwen Bao, and Chenglu Zou. Tensile properties of steel fiber reinforced recycled concrete under bending and uniaxial tensile tests. *Journal of Building Engineering*, 96:110467, 2024.

47. Ashok Gupta, Dattar Singh Aulakh, Divya Singh Rawat, and Suresh Bhalla. Reusable miniature piezo-magnetic sensor for rapid application of electro-mechanical impedance technique on steel structures. In *Journal of Physics: Conference Series*, volume 2647, page 252026. IOP Publishing, 2024.

48. İsmail Hocaoğlu. A novel cost-effective method for self-estimation of crack occur time by piezoelectric measurement of glass powder-modified cementitious mortar. *Journal of Building Engineering*, 86:108967, 2024.

49. S. Hochreiter and J. Schmidhuber. Long short-term memory. *Neural computation*, 9(8):1735–1780, 1997.

50. Arnaud Huijer, Christos Kassapoglou, and Lotfollah Pahlavan. Acoustic emission monitoring of carbon fibre reinforced composites with embedded sensors for in-situ damage identification. *Sensors*, 21(20):6926, 2021.

51. T. C. Huynh and J. T. Kim. Quantification of temperature effect on impedance monitoring via piezoelectric tendon anchor. *Smart Materials and Structures*, 26(12):125004, 2017.

52. Trushna Jena, Abhineet Kumar Raj, T Jothi Saravanan, and Tushar Bansal. Deep learning neural networks for monitoring early-age concrete strength through a surface-bonded pzt sensor configuration. *Measurement*, 241:115698, 2025.

53. Zilong Jia, Jie Zhong, Cheng Zhang, Xiaomei Wang, Xiaoying Du, and Yvpei Li. Mechanical, electrical, and piezoresistive properties of modified conductive recycled fine aggregate smart mortar. *Journal of Building Engineering*, 98:111075, 2024.

54. K. Y. Koo, S. Park, J. J. Lee, and C. B. Yun. Automated impedance-based structural health monitoring incorporating effective frequency shift for compensating temperature effects. *Journal of Intelligent Material Systems and Structures*, 20(4):367–377, 2009.

55. Eva OL Lantsoght. How do steel fibers improve the shear capacity of reinforced concrete beams without stirrups? *Composites Part B: Engineering*, 175:107079, 2019.

56. Y. LeCun, Y. Bengio, and G. Hinton. Deep learning. *nature*, 521(7553):436–444, 2015.

57. Chen Liang, Fan Ping Sun, and Craig A Rogers. Coupled electro-mechanical analysis of adaptive material systems—determination of the actuator power consumption and system energy transfer. *Journal of intelligent material systems and structures*, 5(1):12–20, 1994.

58. Y. Y. Lim, S. T. Smith, and C. K. Soh. Wave propagation based monitoring of concrete curing using piezoelectric materials: Review and path forward. *NDT & E International*, 99:50–63, 2018.

59. Yee Yan Lim, Scott T Smith, Ricardo Vasquez Padilla, and Chee Kiong Soh. Monitoring of concrete curing using the electromechanical impedance technique: review and path forward. *Structural Health Monitoring*, 20(2):604–636, 2021.

60. V. M. Malhotra and N. J. Carino. *Handbook on Nondestructive Testing of Concrete*. CRC Press, 2nd edition, 2004.

61. Jonathan Melchiorre, Leo D'Amato, Federico Agostini, and Antonino Maria Rizzo. Acoustic emission onset time detection for structural monitoring with u-net neural network architecture. *Developments in the Built Environment*, 18:100449, 2024.

62. Mayank Mishra, Paulo B Lourenço, and Gunturi Venkata Ramana. Structural health monitoring of civil engineering structures by using the internet of things: A review. *Journal of Building Engineering*, 48:103954, 2022.

63. Wongi S Na and Jongdae Baek. A review of the piezoelectric electromechanical impedance based structural health monitoring technique for engineering structures. *Sensors*, 18(5):1307, 2018.

64. A. E. Naaman. Engineered steel fibers with optimal properties for reinforcement of cement composites. *Journal of Advanced Concrete Technology*, 4(1):241–252, 2006.

65. Sadjad Naderi and Mingzhong Zhang. 3d meso-scale modelling of tensile and compressive fracture behaviour of steel fibre reinforced concrete. *Composite Structures*, 291:115690, 2022.

66. M. C. Naoum, G. M. Sapidis, N. A. Papadopoulos, and M. E. Voutetaki. An electromechanical impedance-based application of real-time monitoring for the load-induced flexural stress and damage in fiber-reinforced concrete. *Fibers*, 11(4):34, 2023.

67. Maria C Naoum, Nikos A Papadopoulos, George M Sapidis, and Maristella E Voutetaki. Efficacy of pzt sensors network different configurations in damage detection of fiber-reinforced concrete prisms under repeated loading. *Sensors*, 24(17):5660, 2024.

68. A. Narayanan and K. V. L. Subramaniam. Early age monitoring of cement mortar using embedded piezoelectric sensors. *Smart Materials and Structures*, 25(7):075011, 2016.

69. Mahdi Nematzadeh, Morteza Tayebi, and Hojjat Samadvand. Prediction of ultrasonic pulse velocity in steel fiber-reinforced concrete containing nylon granule and natural zeolite after exposure to elevated temperatures. *Construction and Building Materials*, 273:121958, 2021.

70. M. Ohtsu. Recommendation of rilem tc 212-acd: acoustic emission and related nde techniques for crack detection and damage evaluation in concrete. *Materials and Structures*, 43:1187–1189, 2010.

71. Sinno Jialin Pan and Qiang Yang. A survey on transfer learning. *IEEE Transactions on knowledge and data engineering*, 22(10):1345–1359, 2009.

72. Lukesh Parida, Sumedha Moharana, Victor M Ferreira, Sourav Kumar Giri, and Guilherme Ascensão. A novel cnn-lstm hybrid model for prediction of electro-mechanical impedance signal based bond strength monitoring. *Sensors*, 22(24):9920, 2022.

73. Lukesh Parida and Sumedha Moharana. Structural health monitoring for 3d-printed civil infrastructures: A review of challenges, applications and future directions. *Smart Materials and Structures*, 2024.

74. G. Park, D. J. Inman, and H. H. Cudney. The effects of temperatures on the piezoceramic-based structural health monitoring. *Proceedings of the SPIE*, 3668:104–112, 1999.

75. G. Park, H. Sohn, C. R. Farrar, and D. J. Inman. Overview of piezoelectric impedance-based health monitoring and path forward. *Shock and Vibration Digest*, 35(6):451–463, 2003.

76. Aditya Parpe and T Jothi Saravanan. Emi-based multi-sensing technique for monitoring load influence and damage in structural elements using smart sensing units: A numerical and experimental study. *Journal of Vibration Engineering & Technologies*, 12(3):4845–4866, 2024.

77. D. S. Rabelo et al. Temperature effects on the electromechanical impedance signature: a comparative study. *Journal of Intelligent Material Systems and Structures*, 28(6):724–739, 2017.

78. C. E. Rasmussen and C. K. I. Williams. *Gaussian processes for machine learning*. MIT press, 2006.

79. R Vidya Sagar, Jayant Srivastava, and RK Singh. A probabilistic analysis of acoustic emission events and associated energy release during formation of shear and tensile cracks in cementitious materials under uniaxial compression. *Journal of Building Engineering*, 20:647–662, 2018.

80. Mike Schuster and Kuldip K Paliwal. Bidirectional recurrent neural networks. *IEEE transactions on Signal Processing*, 45(11):2673–2681, 1997.

81. Aruna Senapathi and Abheetha Peiris. A comprehensive study of steel fiber alternatives on mechanical properties, long-term performance, and durability of ultra-high-performance concrete: A review. *Journal of Building Engineering*, page 112900, 2025.

82. Bin Shi, Xueqin Chen, Ye Lu, Xiang Wang, Kang Yao, and Qiao Dong. Smart cement-based materials from resistance-based self-sensing to capacitance-based self-sensing: A comprehensive review. *Journal of Building Engineering*, page 113093, 2025.

83. A. K. Singh, S. Bhalla, and A. Gupta. Physical equivalent structural parameter extraction for health monitoring. *Mechanical Systems and Signal Processing*, 170:108846, 2022.

84. Indrajeet Singh, Nirendra Dev, and Shilpa Pal. Damage identification in concrete under impact loading at varying temperatures using voltage strain relations technique: an experimental and numerical study. *Materials Research Express*, 10(5):055702, 2023.

85. H. Sohn, C. R. Farrar, F. M. Hemez, et al. A review of structural health monitoring literature: 1996–2001. *Los Alamos National Laboratory Report*, 2003.

86. Wei Sun, Jun Du, Pizhong Qiao, Baoxin Qi, Shi Yan, and Hongwei Tan. Smart piezoelectric module-based wave energy measurement for crack damage evaluation of concrete beams. *Measurement*, 221:113463, 2023.

87. M. A. Sutton, J. J. Orteu, and H. Schreier. *Image Correlation for Shape, Motion and Deformation Measurements*. Springer, 2009.

88. V. Talakokula, S. Bhalla, and A. Gupta. Monitoring early hydration of reinforced concrete structures using structural parameters identified by piezo sensors via electromechanical impedance technique. *Mechanical Systems and Signal Processing*, 99:129–141, 2018.

89. Fan Wu and Fu-Kuo Chang. Debond detection using embedded piezoelectric elements in reinforced concrete structures-part i: experiment. *Structural Health Monitoring*, 5(1):5–15, 2006.

90. Hernán Xargay, Marianela Ripani, Paula Folino, Nicolás Núñez, and Antonio Caggiano. Acoustic emission and damage evolution in steel fiber-reinforced concrete beams under cyclic loading. *Construction and Building Materials*, 274:121831, 2021.

91. Dongyu Xu, Huaicheng Chen, Yan Hu, Dandan Sun, Peng Du, and Peng Liu. Ultrasonic monitoring and property prediction of cement hydration with novel omnidirectional piezoelectric ultrasonic transducer. *Journal of Building Engineering*, 72:106612, 2023.

92. Qixiang Yan, Xiaolong Liao, Chuan Zhang, Yifeng Zhang, Shuangsheng Luo, and Dongmei Zhang. Intelligent monitoring and assessment on early-age hydration and setting of cement mortar through an emi-integrated neural network. *Measurement*, 203:111984, 2022.

93. Zeliang Yang, Demi Ai, and Hongping Zhu. Heterogeneous mesoscale concrete model bonded with pzt sensor for electromechanical admittance-based structural damage identification. *Smart Materials and Structures*, 34(3):035039, 2025.

94. Duo Zhang, Wentao Wang, and Victor C Li. Microcrack characterization of loaded engineered cementitious composites via optical scans and photogrammetric analyses. *Construction and Building Materials*, 318:126000, 2022.

95. C. Zhang, Q. Yan, X. Liao, et al. Deep hybrid neural network-aided electromechanical impedance method for automated damage detection of lining concrete. *Structural Health Monitoring*, 2024.

96. Chuan Zhang, Qixiang Yan, Xiaolong Liao, Yunhui Qiu, Yifeng Zhang, and Ping Wang. Deep hybrid neural network-aided electromechanical impedance method for automated damage detection of lining concrete under freeze-thaw cycling. *Structural Health Monitoring*, 24(3):1725–1751, 2025.

97. Jianjian Zhu, Zhongqing Su, Zhibin Han, Zifeng Lan, Qingqing Wang, and Mabel Mei-po Ho. An ensemble approach for enhancing generalization and extendibility of deep learning facilitated by transfer learning: principle and application in curing monitoring. *Smart Materials and Structures*, 32(11):115022, 2023.

98. R. F. Zollo. Fiber-reinforced concrete: an overview after 30 years of development. *Cement and Concrete Composites*, 19(2):107–122, 1997.

99. Xuexue Zou, Ruijian Zhu, Xing Chen, Qianping Ran, and Zengmei Wang. Pvdf piezoelectric sensor based on solution blow spinning fibers for structural stress/strain health monitoring. *Smart Materials and Structures*, 33(4):045006, 2024.

100. Shuang Zou, Kunpeng Zheng, Zhenping Sun, and Jingbin Yang. Influence of hooked-end steel fiber shape parameters on fiber-matrix bond strength: A quantitative analysis. *Journal of Building Engineering*, page 113608, 2025.

APPENDIX A

SUPPLEMENTARY TEMPERATURE-STUDY RESULTS

A.1 Scope of the Supplementary Results

This appendix supplements Chapter 6 with equations and tabulated results from the progressive-heating experiment. Chapter 3 defines RMSD, MAPD, CC and covariance; the present appendix gives the remaining implemented SHM-index equations used in the temperature comparison. It also reports the temperature-averaged Equivalent Structural Parameter (EPS) results for the intact and saw-cut states. The tabulated values retain the experimental coverage of the four specimens. A dash denotes an unavailable temperature stage; no value is inferred for an unmeasured stage.

A.2 Additional SHM-Index Equations

The definitions below complete the thirteen-index set reported in Chapter 6 without repeating the four equations already given in Section 3.12. They reproduce the implemented calculations for both conductance and susceptance signatures.

Let b_i denote the selected baseline signature, x_i the comparison signature, and $d_i = x_i - b_i$ for $i = 1,\ldots,N$. The corresponding means and population standard deviations are denoted by $\bar{b}$, $\bar{x}$, $\bar{d}$ and σ_d. The nine equations not stated in Chapter 3 are:

$$\mathrm{AMPD}(\%) = 100\,\frac{|\max_i |x_i| - \max_i |b_i||}{\max_i |b_i|}, \tag{A.1}$$

$$\mathrm{CCD} = 1 - \mathrm{CC}, \tag{A.2}$$

$$\mathrm{CCD}^3 = (1 - \mathrm{CC})^3, \tag{A.3}$$

$$\mathrm{CCV} = \frac{\sqrt{|\mathrm{Cov}(b,x)|}}{\bar{b}\,\bar{x}}, \tag{A.4}$$

$$\mathrm{MSE} = \frac{1}{N}\sum_{i=1}^{N} d_i^2, \tag{A.5}$$

$$\mathrm{Var}(d) = \frac{1}{N}\sum_{i=1}^{N} (d_i - \bar{d})^2, \tag{A.6}$$

$$\mathrm{RMS}(x) = \sqrt{\frac{1}{N}\sum_{i=1}^{N} x_i^2}, \tag{A.7}$$

$$\mathrm{Skew}(d) = \frac{1}{N}\sum_{i=1}^{N} \left(\frac{d_i - \bar{d}}{\sigma_d}\right)^3, \tag{A.8}$$

Defining the signature range as $R(z) = \max_i(z_i) - \min_i(z_i)$, the peak-to-peak amplitude deviation is

$$\mathrm{P2P}(\%) = 100\,\frac{|R(x) - R(b)|}{R(b)}. \tag{A.9}$$

The implementation returns an undefined value when a required normalising quantity is zero. CCD and CCD^3 are deterministic transformations of CC and therefore do not constitute independent confirmations of structural change.

A.3 Temperature-Averaged EPS Results

Tables A.1–A.6 reproduce the after-compensation temperature means for the equivalent mass-like, stiffness-like and damping-like parameters. These fitted quantities describe the adopted coupled representation and are not interpreted as direct bulk material properties. Percentage changes referenced to values close to zero are correspondingly treated with caution.

Table A.1: Intact-state mean equivalent mass-like parameter after compensation (kg).

Temperature (°C)	SFC1/JPS1	SFC2/JPS2	SFC3/JPS3	SFC4/JPS4
Ambient	0.034995	0.026626	0.0368	0.032954
75	0.027774	0.0050223	0.027243	0.02965
100	0.022573	-0.020265	0.018644	0.023553
125	0.011319	-0.051456	0.012228	0.018816
150	0.011564	-0.053765	0.010646	0.015601
175	0.0084314	0.1678	0.0045807	0.0032415
200	-0.011	0.10574	-0.012525	-0.013304
225	-0.02924	0.12469	-0.027559	-0.020665
250	-0.02859	0.061702	-0.071345	-0.012316

Table A.2: Intact-state mean equivalent stiffness-like parameter after compensation ($\mathrm{N\,m^{-1}}$).

Temperature (°C)	SFC1/JPS1	SFC2/JPS2	SFC3/JPS3	SFC4/JPS4
Ambient	84321	68218	90546	79339
75	66923	12868	67033	71384
100	54389	-51921	45873	56706
125	27274	-1.3184×10^5	30088	45301
150	27863	-1.3775×10^5	26194	37560
175	20315	4.2991×10^5	11271	7804
200	-26505	2.7092×10^5	-30819	-32030
225	-70453	3.1947×10^5	-67808	-49753
250	-68888	1.5809×10^5	-1.7555×10^5	-29651

Table A.3: Intact-state mean equivalent damping-like parameter after compensation.

Temperature (°C)	SFC1/JPS1	SFC2/JPS2	SFC3/JPS3	SFC4/JPS4
Ambient	-673.25	-370.83	-1644.5	-3595.3
75	-735.66	248.18	1451.8	-821.29
100	-1524.9	2713.5	-1335.5	-589.62
125	699.65	235.06	369.75	-1755.2
150	-54.064	-299.9	-1133.7	-1028
175	-969.15	53.792	-390.85	-496.44
200	-526.3	175.73	-1133.7	-719.21
225	-110.36	-394.97	-291.84	-403.97
250	-360.6	-430.15	-476.78	-883.35

Table A.4: Saw-cut-state mean equivalent mass-like parameter after compensation (kg).

Temperature (°C)	SFC1/JPS1	SFC2/JPS2	SFC3/JPS3	SFC4/JPS4
Ambient	0.037653	0.031584	0.042277	0.043809
75	0.032569	0.021539	0.043796	0.037884
100	0.025664	0.01579	0.038712	0.037792
125	0.023031	0.010593	0.036096	0.03456
150	0.016813	0.0019623	0.031838	0.031693
175	0.010467	-0.0034907	0.029158	0.028919
200	0.0086534	-0.00094894	–	–
225	0.0084095	0.0069561	–	–
250	0.011523	-0.0427	–	–

Table A.5: Saw-cut-state mean equivalent stiffness-like parameter after compensation ($\mathrm{N\,m^{-1}}$).

Temperature (°C)	SFC1/JPS1	SFC2/JPS2	SFC3/JPS3	SFC4/JPS4
Ambient	85511	76906	88632	93205
75	73965	52447	91816	80599
100	58284	38449	81157	80403
125	52305	25792	75673	73527
150	38184	4778	66747	67427
175	23771	-8499.7	61128	61526
200	19652	-2310.6	–	–
225	19098	16938	–	–
250	26168	-1.0397×10^5	–	–

Table A.6: Saw-cut-state mean equivalent damping-like parameter after compensation.

Temperature (°C)	SFC1/JPS1	SFC2/JPS2	SFC3/JPS3	SFC4/JPS4
Ambient	-1222.1	-496.55	-756.33	-739.09
75	-1000.9	-825.93	-728.99	-696.79
100	-744.35	-431.36	-623.03	-627.82
125	-621.36	-524.83	-607.38	-610.26
150	-634.68	5151.7	-607.91	-619
175	-287.18	-327.88	-652.74	-738.07
200	-273.83	-322.99	–	–
225	-358.49	-862.93	–	–
250	-367.29	-431.65	–	–

A.4 Experimental Coverage and Interpretation Limits

The intact series extends to 250 °C for SFC1–SFC4. In the saw-cut state, SFC1 and SFC2 extend to 250 °C, whereas SFC3 and SFC4 extend to 175 °C. Comparisons involving all four specimens are therefore limited to the common measured range through 175 °C. Intact and saw-cut observations are repeated states of the same specimens rather than independent specimen groups. The results describe the tested progressive- heating programme and artificial saw-cut; they do not establish transferable thresholds or isolate independent effects of fibre aspect ratio and dosage.

PLAGIARISM VERIFICATION

turnitin Page 1 of 365 - Cover Page Submission ID trn:oid:::27535:149135156

Wesam Al Agha

Thesis_Wesam Al Agha

plag check

Document Details

Submission ID
trn:oid:::27535:149135156

Submission Date
Aug 23, 2026, 6:03 PM GMT+5:30

Download Date
Aug 23, 2026, 6:13 PM GMT+5:30

File Name
Thesis Wesam Al Agha.pdf

File Size
28.0 MB

352 Pages

98,140 Words

509,753 Characters

3% Overall Similarity

The combined total of all matches, including overlapping sources, for each database.

Match Groups

250 Not Cited or Quoted 2%
Matches with neither in-text citation nor quotation marks

44 Missing Quotations 0%
Matches that are still very similar to source material

0 Missing Citation 0%
Matches that have quotation marks, but no in-text citation

0 Cited and Quoted 0%
Matches with in-text citation present, but no quotation marks

Top Sources

1% Internet sources
2% Publications
1% Submitted works (Student Papers)

03.09.2026

Candidate's Signature

Shilpa Pal
3/9/26

Signature of Supervisor(s)

ANNEXURE

Responses to the comments of the foreign examiner

The candidate sincerely thanks the examiner for the careful evaluation of the thesis and for the valuable comments. Each comment is followed by the candidate's reply, with reference to the relevant sections and pages of the thesis. The minor corrections made in the updated thesis are listed at the end.

1. Some conclusions should remain clearly limited to the tested materials, specimen sizes, sensor configurations, thermal histories and data partitions. In particular, the very high predictive coefficients obtained for some models should be interpreted as performance within the available datasets, rather than evidence of general applicability.

Reply:

The candidate thanks the examiner for the positive assessment of the work and for this observation. The conclusions in Chapter 8 are presented "within the tested experimental and validation scope" (Section 8.1, p. 344), and Section 8.2 (p. 349) lists the boundaries that apply to them, including the replication level, the material scope, the progressive heating sequence and the validation design of the data-driven models. The high R^2 values of Chapter 7 are interpreted as agreement within the analysed datasets (pp. 335 and 348).

2. The candidate should revise the wording of Objective 1 and its related conclusions to clearly distinguish among damage detection, damage characterization and damage localization. A single sensor position can detect a change in the local coupled response, but it cannot determine the spatial position of the damage. If localization was not experimentally demonstrated, the term should be removed or explicitly presented as future work requiring a sensor array.

Reply:

The candidate thanks the examiner for this important comment. Objective 1 (Section 1.7, p. 6) is to assess and investigate damage detection and localization using piezoelectric sensors. EMI is a local monitoring technique: it measures the local high-frequency response of the region around the sensor (pp. 3 and 15), not the global response of the element. The thesis therefore uses the three terms as follows:

- ✓ **Detection:** recognising a change in the measured response between a reference state and a later state (Chapters 5 and 6).

- ✓ **Characterisation:** describing that change through the resonance shift, the statistical indices and the equivalent structural parameters, including Δs (Section 5.3.5, p. 83).
- ✓ **Localisation:** attributing the detected change to the region of the sensor. The investigation showed that the changes between the healthy and damaged states reflect the localised sensitivity of the sensing mechanism, and that Δs is a localised indicator, not a volumetric measure of the whole specimen (p. 81).

As the examiner rightly notes, one sensor position cannot determine the position of damage elsewhere in the element. The thesis does not claim this (abstract, pp. vii–viii); covering a whole element requires an array of sensors, which, in line with the examiner's suggestion, is explicitly presented as future work (Section 8.1.1, p. 346; Section 8.3, p. 350). The wording of Objective 1 is therefore retained, with its scope stated in the abstract and the conclusions.

No change was needed in the thesis.

3. The thesis should also include a concise clarification of the statistical unit and replication level used in each experimental programme. In particular, the hydration and thermal studies rely on one retained JPS instrumented cube per configuration. Therefore, conclusions from these tests should be described as specimen specific observations, not population level trends.

Reply:

The candidate thanks the examiner for this observation. The statistical unit and the replication level are stated in Section 3.13.2, "Experimental Units and Replication" (p. 39). The compressive and splitting-tensile programmes used three specimens per configuration (39 cubes and 39 cylinders), whereas the hydration and thermal programmes used one JPS-instrumented cube per configuration, so their repeated measurements are not replicates. The hydration and thermal results are therefore reported as specimen-specific observations (pp. 40 and 102), and this is the first limitation listed in Section 8.2 (p. 349).

No change was needed in the thesis.

4. For the machine learning analysis, the candidate should clearly state how training, validation and test observations were separated. Measurements from the same physical specimen should not appear in different partitions. The thesis should also specify whether normalization and feature preprocessing were fitted

only on the training data and should report the relevant random seeds or data group assignments to ensure reproducibility.

Reply:

The candidate thanks the examiner for this comment. The classical models for cube compressive strength were assessed by five-fold cross-validation, and the two deep-learning applications (hydration and splitting-tensile strength) by a random division into 80 % training and 20 % validation data (Section 7.2.3, p. 322).

A) **Partitioning:** an observation is one frequency point of a recorded signature, and the divisions were drawn at random without grouping by specimen. Observations of the same specimen therefore occur in both the training and the validation data, and no separate test set was held out.

B) **Normalisation:** for the classical models, the standardisation of the predictors is part of each fold's model fit; in the deep-learning applications, the z-score scaler was fitted on the complete dataset before the division.

C) **Seeds and group assignments:** these were not retained with the datasets; their retention, with group-wise validation and an independent external test set, is proposed in Section 8.3 (p. 350).

Consequently, the R^2 values describe agreement within the tested datasets, not performance on new specimens (pp. 335 and 348). In the updated thesis, Sections 7.2.2 and 7.2.3 (pp. 321–322) state the random, non-grouped division and the standardisation of the response in the deep-learning applications. No page number has changed.

5. In Chapter 7, the definitions and units of the reported prediction errors should be checked. In particular, the use of percentages for MSE should be explained and applied consistently. The candidate should also distinguish between validation performance and independent external validation when discussing the high R^2 values.

Reply:

The candidate thanks the examiner for noticing this. RMSE, MSE and MAE are defined by Equations 7.2 and 7.3 (Section 7.5, p. 327) and are used in Chapter 7 as error indices for comparing the prediction models of the same dataset. In the EMI literature reviewed in Section 2.4 (p. 13), MSE is listed among the published statistical indices of signature difference (Parida et al., 2022; Parida and Moharana, 2024), alongside RMSD and MAPD. Consistent with this index usage, the regression error indices are reported in the same format as the other statistical indices of the thesis; the "%" in

Tables 7.1–7.4 is part of this reporting format and does not denote a percentage of the measured strength, and the ranking of the models is not affected. In the deep-learning applications, the response was standardised (p. 321), so the MSE values in Tables 7.3 and 7.4 are dimensionless.

On the second point, every R^2 value in Chapter 7 is a validation result obtained within the corresponding dataset, by five-fold cross-validation or on the 20 % validation subset; no independent external dataset was tested (pp. 335, 348 and 349).

No change was needed in the thesis.

6. Finally, the thermal conclusions should more consistently acknowledge that the progressive heating programme combines temperature, moisture evolution, and cumulative thermal history. The incomplete high temperature records for the 0.75% fibre configurations should be clearly indicated wherever comparisons are made.

Reply:

The candidate thanks the examiner for this valuable comment. The eight temperature stages were applied consecutively to the same specimens without intermediate cooling, so the experiment "represents a progressive heating history rather than independent exposure at each temperature" (Section 6.4.3, p. 104). The combined effect of temperature, dwell time, moisture evolution and cumulative heating history is stated in Section 8.2 (p. 349); heating–cooling programmes with moisture measurement are proposed in Section 8.3 (p. 350).

The saw-cut records of the two 0.75% configurations (SFC3 and SFC4) end at 175 °C, whereas the intact records cover 75–250 °C. This is indicated in the abstract (p. viii), where the saw-cut results are introduced (pp. 164 and 181), and in the conclusions, which limit the 200–250 °C statement to the 0.50% configurations (p. 347).

No change was needed in the thesis.

7. A final editorial review is recommended to standardize terminology, abbreviations, equation notation, figure captions, and the distinction between an EMI signature change and confirmed structural damage.

Reply:

The candidate thanks the examiner for this recommendation. Symbols and abbreviations are defined in the List of Symbols, Abbreviations and Nomenclature and are used with these meanings throughout the thesis. The distinction between an EMI signature

change and confirmed structural damage is maintained: the signature is treated as the response of the coupled measurement system (p. 110), damage states are defined by the test protocol (destructive loading in Chapter 5 and the saw-cut in Chapter 6), and the abstract states that "An uncompensated signature therefore cannot be treated as a damage response without comparison at the same temperature" (p. viii). The editorial corrections made in the updated thesis are listed below.

Corrections made in the updated thesis

The following corrections change wording only. No result, figure, table value or page number has changed.

A) Page 336: "… for the JPS2 and JPS4 sensors" has been corrected to "… for the JPS2 and JPS3 sensors", in agreement with Table 7.3.

B) Page 25 (Section 3.2.1): two sentences that referred to tables not included in the thesis have been reworded.

C) Sections 7.2.2 and 7.2.3 (pp. 321–322): the text now states that the response was standardised only in the two deep-learning applications and that the validation partitions were drawn at random without grouping by specimen (see the reply to comment 4).

Responses to the comments of the Indian examiner

The candidate sincerely thanks the examiner for the careful evaluation of the thesis, for the positive assessment of the experimental programme, the E–EFS approach and the organisation of the thesis, and for the valuable comments and questions. Each comment given in Annexure-I of the report is followed by the candidate's reply, with reference to the thesis. Written answers to the questions proposed for the viva-voce examination (Item 10) are given at the end.

1. Clarify the distinction between damage detection, damage quantification and damage localisation in the context of the present study.

Reply:

In this study, the three terms have the following meaning.

✓ **Damage detection** is the recognition that the measured EMI response has changed between a reference state and a later state: healthy and loaded specimens in Chapter

5, and intact and saw-cut specimens at the same temperature and dwell time in Chapter 6.

- ✓ **Damage quantification** is the expression of the size of that change through the statistical indices and the stiffness-based index Δs (Section 5.3.5, p. 83); these are relative measures of the local sensor–specimen response, not measures of crack size or global stiffness loss (pp. 81 and 84).
- ✓ **Damage localisation** is the identification of where the change occurs. In the present study it is local: the detected change is attributed to the region of the sensor, because a local EMI response is influenced by the material and cracking within the sensing region (pp. 15 and 81). Determining the position of damage elsewhere in a member requires several sensor positions and is the extension proposed in Section 8.3 (p. 350).

No change was needed in the thesis.

2. Clarify the physical interpretation and limitations of the EPS/E–EFS-based indicators and the extent to which they may be regarded as empirical damage indices.

Reply:

A) **EPS:** the equivalent mass m, stiffness k and damping c are obtained from the lumped-parameter mechanical impedance model of Section 3.11 (p. 36) around the selected resonance. They are the mass-like, stiffness-like and damping-like terms of the local coupled system of the PZT, its bonding or contact layer and the adjacent concrete, not bulk properties of the specimen (pp. 107 and 349). They describe only the region near the sensor (p. 81), depend on the model and the selected resonance, are specific to each installation (p. 67) and vary with temperature.

B) **E–EFS:** the Enhanced Effective Frequency Shift (Section 6.2, p. 98) is a signal-processing procedure, not a physical model. It aligns a heated signature with its reference by frequency shifting and offset correction (p. 346), so that records can be compared at the same temperature; it reduces the temperature-associated mismatch but does not identify the physical cause of a change.

C) **Empirical character:** the EPS have a physical basis in the impedance model, but their use as damage indicators is empirical and comparative within the tested specimens (Sections 5.6, 7.9 and 8.2).

No change was needed in the thesis.

3. Explain clearly the transformation of EMI data into the input format used for the one-dimensional and two-dimensional deep-learning models.

Reply:

All deep-learning models in Chapter 7 used the same two-dimensional input; no separate one-dimensional model was trained. The one-dimensional form is the feature vector of each observation before reshaping. The transformation (Sections 7.2 and 7.4, pp. 321–325) has five steps:

A) **Acquisition:** conductance G and susceptance B at 100 Hz intervals (p. 321).

B) **Derived quantities:** the structural-admittance components and the equivalent parameters c, m and k at each frequency.

C) **Feature vector (one-dimensional):** each frequency point is one observation with its features (frequency, G, B, X', Y', c, m, k, fibre aspect ratio and dosage, and curing age in the hydration study) and the measured strength as target.

D) **Standardisation:** z-score normalisation of the features, and of the response in the deep-learning applications (p. 321).

E) **Reshaping (two-dimensional):** each vector is written row by row into an $N \times N$ matrix with zero padding (p. 322); the 2D CNN processes it as a single-channel image, and the 2D LSTM and 2D Bi-LSTM read its rows sequentially (pp. 324–325).

The matrix is a computational arrangement, not a physical spatial field, and its row order is not a time axis (pp. 322 and 325).

No change was needed in the thesis.

4. The list of publications arising from the thesis appears at two different places, i.e., on page X and page 369. The list on page X appears to be incomplete, particularly with respect to the conference publications. It is recommended that the complete list of publications arising from the thesis be consolidated and presented at one place only for consistency and clarity.

Reply:

The candidate thanks the examiner. The two lists serve different purposes. The List of Publications on p. x is the list of publications arising from this thesis: the three journal articles, the paper in *Materials Today: Proceedings* (2023), presented at ICCMS-2022, and the presentation at ICAMNOP-2023; their first pages and the conference certificates

are reproduced under Proofs of Publications and Certificates in the updated thesis. The list on p. 369 of the evaluated copy belongs to the candidate's Curriculum Vitae (pp. 384–387 in the updated thesis), which also records earlier work unrelated to this thesis. The publications arising from the thesis are therefore presented at one place, p. x.

No change was needed in the thesis.

Answers to the questions raised by the Indian examiner

1. How can EMI measurements from multiple piezoelectric sensors be used to identify the location as well as severity of damage in an SFRC element?

Answer: EMI sensing is local: the admittance of a PZT sensor is governed mainly by the structure in a limited region around it (Park et al., 2003), which is why the single-sensor measurements of this thesis detected changes near the sensor (p. 81). With several sensors on an SFRC element:

A) **Baselines:** a baseline signature is recorded for every sensor, and later signatures are compared at the same temperature or after E–EFS compensation.

B) **Index:** at each inspection, an index of change (RMSD, MAPD or the change in k) is computed for every sensor.

C) **Location:** the damaged zone is identified from the sensors showing the largest change above a threshold set from the undamaged element; interpolation over the sensor grid refines the position.

D) **Severity:** the magnitude of the change at the nearest sensors indicates the severity, after calibration on members with damage of known extent.

The multi-sensor step builds on the local response characterisation established in this thesis (p. 346) and is proposed in Section 8.3 (p. 350).

2. How would the EMI response be expected to change during a realistic fire exposure followed by cooling, compared with the progressive heating procedure adopted in the thesis?

Answer: In the thesis, the specimens were heated in eight stages from 75 to 250 °C without intermediate cooling, with signatures recorded after 10, 20 and 30 min at each stage (Section 6.4.3, p. 104). A realistic fire differs in its faster and higher temperature rise, the temperature gradient through the section and the subsequent cooling.

A) **During heating:** a largely reversible temperature effect on the PZT, its jacket and the concrete, as observed in Chapter 6, would combine with irreversible damage

(moisture loss, microcracking and weakening of the fibre–matrix bond), both larger and faster than in the present programme.

B) **During and after cooling:** the reversible part would recover, but not necessarily along the heating path (cooling-path hysteresis, p. 316); the difference remaining at the same temperature would indicate the permanent damage.

C) **Sensor survival:** above the tested range, depolarisation of the PZT and damage to the jacket, adhesive and leads become possible, so the sensor package and the E–EFS procedure would need qualification, as proposed in Sections 6.15 (p. 315) and 8.3 (p. 350).

3. What are the principal sources of uncertainty associated with the use of the reusable NBPS configuration?

Answer: The NBPS is not bonded to the specimen: the PZT is bonded to an aluminium carrier that is held against the specimen with PTFE shims (Section 3.4.2, pp. 27–28), so the signature depends on the contact as well as on the specimen. The principal sources of uncertainty are:

- ✓ remounting: position, alignment and contact area at each installation;
- ✓ contact pressure: clamp force and contact pressure were not measured (p. 349);
- ✓ surface condition and geometry: roughness, dust, moisture and cylinder curvature;
- ✓ wear of the PZT–carrier bond and of the shims after repeated use;
- ✓ environment and instrumentation: temperature, humidity, lead position and LCR-meter settings;
- ✓ specimen variability: the random distribution of fibres near the contact zone.

These effects were limited by using the same sensor, marked position, shims and procedure for each specimen and by comparing each specimen with its own baseline (p. 28); a repeatability study is proposed in Section 8.3 (p. 350).

4. How do changes in EMI response relate to changes in stiffness and strength? What are the limitations of using EMI as an indirect indicator of these properties?

Answer: The PZT transducer is mechanically coupled to the host, so its electrical admittance reflects the mechanical impedance of the concrete near the sensor. An increase in local stiffness, as during hydration, generally shifts the resonance to higher frequencies, whereas a loss of local stiffness, as from cracking, generally shifts it to lower frequencies and lowers the peak; the equivalent stiffness k quantifies this change.

Strength is related to stiffness only indirectly, through the elastic modulus (for example, $E_c = 5000\sqrt{f_{ck}}$ in IS 456). In this study, k increased with curing age together with compressive strength (R^2 = 0.94 and 0.96 for JPS1 and JPS2, p. 67).

Advantages of the EMI technique in this study:

- ✓ non-destructive and repeatable interrogation of the same specimen during curing, loading and heating;
- ✓ high sensitivity to local changes in stiffness and damage near the sensor;
- ✓ several descriptors (resonance, statistical indices and EPS) from one measurement;
- ✓ reusability of the NBPS, without a permanently bonded sensor on every specimen (p. 351).

Limitations of the EMI technique in this study:

- ✓ the response is local, whereas strength is a property of the whole specimen;
- ✓ the relation with stiffness and strength is indirect and installation-specific (p. 67);
- ✓ temperature, moisture and contact conditions also alter the signature (Chapter 6);
- ✓ the direction of the frequency shift differs between fibre configurations (p. 345);
- ✓ the EPS are model-based parameters of the coupled system, not material constants (p. 349).

Proofs of Publications and Certificates

Construction and Building Materials 489 (2025) 142296

Contents lists available at ScienceDirect

Construction and Building Materials

journal homepage: www.elsevier.com/locate/conbuildmat

Electro-mechanical impedance-based equivalent structural health monitoring of steel fibre cementitious materials under long curing age effect

Wesam Al Agha, Shilpa Pal *, Nirendra Dev

Department of Civil Engineering, Delhi Technological University, Delhi 110042, India

ARTICLE INFO

Keywords:
Concrete
Fibre aspect ratio
Electro-mechanical impedance technique (EMI)
Jacketed piezo sensor (JPS)
Curing
Equivalent structural parameters
Strength
Deep Learning

ABSTRACT

Monitoring the hydration of fibre cement-based materials is a motivational field in structural health monitoring (SHM), but there is still a gap compared with conventional destructive test-based curing. This research develops the SHM approach to integrating an electro-mechanical impedance (EMI) system, which uses lead zirconate titanate (PZT) devices embedded in steel fibre cement-based material (SFCM). A novel piezoceramic sensor, jacketed piezo sensors (JPS), was fabricated to measure EMI signatures by the specimens of hooked-end steel fibre contents (0.5 % and 0.75 %), produced with aspect ratios of 55 and 65 fibre at long curing time monitoring (1, 3, 7, 14, 28, 60, 90, 120, 150, and 180 days). The significance of utilized hooked-end steel fibres on compressive strength and SHM technique is measured. During hydration, the experiments investigate electrical signature changes such as resonance frequency and peak conductance. More importantly, the sensor's signature is examined using statistical metrics for both qualitative and quantitative assessment, such as root mean square deviation (RMSD), mean absolute percentage deviation (MAPD), cross-correlation coefficient (CC), and coefficient of variance (CoV). Consequently, it is indicated that a 28-day curing time is vital for achieving optimal stiffness and strength in SFCM. A deep learning framework accomplished outstanding compressive strength prediction (R^2=0.99) with immediate convergence, developing EMI-based analysis. The insights consist of a main reference for future jacketed PZT curing applications of SFCM, highlighting the beneficial impact of understanding the strength growth process and focusing on observation, calibration, and validation of structural parameters identification as equivalent stiffness, damping, and mass.

1. Introduction

Concrete is the predominant construction material in civil engineering due to its versatility, cost-effectiveness, and simplicity of handling. Nevertheless, fibre-reinforced concrete (FRC) is an effective cement-based composite that significantly decreases the quasi-brittleness characteristic of plain concrete. Steel fibres have been thoroughly studied for insignificant concrete specimens under varied loading conditions and in large reinforced concrete (RC) structural elements [1]. Incorporating steel fibres in concrete enhances its strength, hardness, cracking resistance, and tensile performance since the randomly distributed fibres effectively limit the unstable development of cracks at both micro and macro levels [2,3]. Studies demonstrate that fibres significantly enhance crack control since FRC displays strain-softening behavior even after macro-cracks growth [4–6]. Moreover, concrete with randomly distributed hooked-end steel fibres is a kind of FRC that exhibits less plastic shrinkage cracking and enhanced impact resistance and toughness compared to conventional concrete qualities [7]. Like other fibres incorporated into the concrete matrix, hooked-end fibres enhance post-cracking properties, particularly regarding ductility in tensile response [8]. Steel fibres reduce the initiation and propagation of microcracks [9,10]; hence, fibre-reinforced concrete demonstrates enhanced strain capacity under both tensile and compressive forces [11,12]. Nevertheless, hooked-end steel fibres significantly enhance tensile strength in direct tension testing, whereas splitting and bending tests demonstrate their advantageous effect on ultimate splitting and flexural tensile strength [13–15]. Monitoring the hydration process of steel fibre cement-based materials is vital since it profoundly influences the structures' mechanical characteristics and long-term performance [16,17]. Creating an effective and non-invasive

* Corresponding author.
E-mail addresses: wesamalagha_2k21phdce16@dtu.ac.in, wesamalagha1@gmail.com (W. Al Agha), shilpapal@dtu.ac.in (S. Pal), nirendradev@dce.ac.in (N. Dev).

https://doi.org/10.1016/j.conbuildmat.2025.142296
Received 12 January 2025; Received in revised form 5 April 2025; Accepted 14 June 2025
Available online 26 June 2025
0950-0618/© 2025 Elsevier Ltd. All rights are reserved, including those for text and data mining, AI training, and similar technologies.

Measurement 258 (2026) 119201

Contents lists available at ScienceDirect

Measurement

journal homepage: www.elsevier.com/locate/measurement

Ml-integrated reusable piezoceramic sensors for steel fibre concrete structural health monitoring

Wesam Al Agha, Nirendra Dev, Shilpa Pal *

Department of Civil Engineering, Delhi Technological University, Delhi 110042, India

ARTICLE INFO

Keywords:
Concrete
Steel fibre
Electro-mechanical impedance technique (EMI)
Non-bonded surface sensors (NBPS)
Damage
Equivalent structural parameters
Strength
Machine learning

ABSTRACT

This research develops a novel non-destructive measurement approach integrating electro-mechanical impedance (EMI) technology with innovative reusable non-bonded surface piezoelectric sensors (NBPS) for steel fibre cement-based materials (SFCM). The measurement of SFCM structural health monitoring faces significant limitations due to reliance on destructive testing methods. Therefore, this experimental program can systematically provide damage assessment of SFCM specimens containing hooked-end steel fibres at six dosage levels (0.25, 0.5, 0.75, 1, 1.25, and 1.5 %) with aspect ratios of 55 and 65, evaluating both healthy and damaged states over 28 days. EMI signature analysis focused on resonance frequency shifts and peak conductance variations, with damage quantification achieved through statistical metrics including RMSD and MAPD. Results demonstrate that specimens with an aspect ratio of 65 consistently outperformed those with an aspect ratio of 55, achieving optimal compressive strength of 60.95 MPa at 0.75 % fibre content (47.5 % improvement). Machine learning frameworks accomplished outstanding compressive strength prediction (R^2 = 0.99) with immediate convergence, developing EMI-based analysis. The validated EMI-NBPS system offers a transformative non-destructive solution for structural health monitoring, enabling immediate strength assessment and damage detection in fibre-reinforced cementitious materials for construction quality control and infrastructure monitoring applications. This paper will serve as a primary reference for non-bonded PZT in SFCM damage monitoring due to the crucial process of strength changes, focusing on the observation, calibration, and validation of selecting structural parameters, including equivalent stiffness, damping, and mass.

1. Introduction

In recent decades, damage assessments throughout steel fibre reinforcement have demonstrated it as a viable approach for enhancing the crack resistance of concrete. The fibres improve performance by connecting cracks and redistributing stress over them. The integration of randomly distributed steel fibres within concrete substantially enhances the structural integrity of reinforced concrete (RC) components. This enhancement develops from the fibres' capacity to manage to crack and increases strength, primarily via the crack-bridging mechanism [1]. The performance of steel fibre-reinforced cement-based materials (SFCM) varies by many characteristics, such as fibre type, aspect ratio, and volume fraction. Nonetheless, the use of SFCM in structural engineering continues to be challenged in defining reliable design frameworks. Structural failures in civil engineering infrastructure present considerable economic and safety challenges, prompting further development of nondestructive technologies to identify early-stage damage in SFRC systems. Structural health monitoring (SHM) has developed into a vital framework for proactive safety management, integrating periodic assessments with sensor-based surveillance to enhance the long-term sustainability of structures. Lead Zirconate Titanate (PZT) piezoelectric sensors are frequently introduced into concrete frameworks during the fabrication process because of their compatibility with wet mixtures. This integration allows for the real-time evaluation of parameters such as stress, strain, and corrosion [2]. This combined strategy, utilizing both planned maintenance and integrated sensing technologies, improves the precision of damage detection while reducing operational delays to increase the safety and resilience of existing composite structures [2]. Nonetheless, immediate identification of damage in concrete structures is crucial for performing timely repairs and preventing significant functional deterioration. As an alternative to traditional nondestructive testing, SHM systems utilize integrated sensory networks, which comprise sensors and smart materials that are fully integrated within the structure. This network enables automated, ongoing evaluations, setting SHM apart from traditional periodic NDT

* Corresponding author.
E-mail addresses: wesamalagha_2k21phdce16@dtu.ac.in, wesamalagha1@gmail.com (W. Al Agha), nirendradev@dce.ac.in (N. Dev), shilpapal@dtu.ac.in (S. Pal).

https://doi.org/10.1016/j.measurement.2025.119201
Received 5 July 2025; Received in revised form 26 August 2025; Accepted 30 September 2025
Available online 1 October 2025
0263-2241/© 2025 Elsevier Ltd. All rights are reserved, including those for text and data mining, AI training, and similar technologies.

Journal of Vibration Engineering & Technologies (2026) 14:164
https://doi.org/10.1007/s42417-025-02311-9

ORIGINAL PAPER

Electromechanical Impedance–Based Tensile Damage Assessment of Steel Fibre Concrete Using Reusable Piezoceramic Sensors: An Experimental and Deep Learning Approach

Wesam Al Agha[1] · Shilpa Pal[1] · Nirendra Dev[1]

Received: 3 October 2025 / Revised: 4 December 2025 / Accepted: 26 December 2025
© Springer Nature Singapore Pte Ltd. 2026

Abstract

Purpose This study develops a reusable non-bonded piezoceramic sensor (NBPS) system for split-tensile structural health monitoring of steel fibre concrete structures. The research addresses critical limitations in conventional destructive testing methodologies by integrating electromechanical impedance (EMI) signatures with deep learning regression for non-destructive tensile performance evaluation.

Methods The enhanced monitoring system evaluated both healthy and damaged steel fibre concrete cylinders at six volumetric dosages (0.25–1.5%) and two aspect ratios (55, 65) after 28 days of curing. EMI signatures, including resonance frequency, conductance peak, and stiffness-loss index (Δs), were compiled into conventional tensile and processed using RMSD metrics. Equivalent structural parameters were computed via a calibrated Hixon model, and deep learning networks were trained on raw EMI data for tensile strength prediction.

Results The maximum tensile strength of 6.68 MPa was achieved at 1.50% fibre content and an aspect ratio of 65, representing a 65.3% enhancement over plain M30 concrete. The calibrated model confirmed predominantly stiffness-controlled damage mechanisms through equivalent spring-mass-damper system analysis. LSTM achieved exceptional prediction accuracy with $R^2 = 0.9996$ and MAE less than 0.02, significantly outperforming CNN and Bi-LSTM architectures in processing raw EMI signatures.

Conclusion The NBPS-EMI-DL system provides fast, identical, repeatable, and non-destructive tensile diagnostics for steel fibre concrete structures. The validated correlation between EMI signatures and structural damage progression enables automated quality control and establishes pathways for closed-loop structural health monitoring of fibre-reinforced concrete infrastructure.

Keywords Electro-mechanical impedance (EMI) · Structural health monitoring · Non-bonded surface piezoceramic sensor (NBPS) · Steel fibre concrete · Tensile damage · Deep learning

Abbreviations

G	Conductance
B	Susceptance
j	Imaginary unit
ω	Angular frequency
$\bar{\epsilon}^{T}_{33}$	Complex electric permittivity
$\bar{Y}^{E}$	Complex Young's modulus of elasticity of the PZT patch
T	Complex tangent ratio
v	Poisson's ratio
GA	Real part
BA	Imaginary part
f	Frequency
G_i	Conductance process
LCR	Inductance capacitance and resistance
CTM	Compression testing machine
IS	Indian Standard
RMSD	Root mean square deviation
CNN	Convolutional neural networks
LSTM	Long short-term memory

✉ Wesam Al Agha
wesamalagha_2k21phdce16@dtu.ac.in;
wesamalagha1@gmail.com

Shilpa Pal
shilpapal@dtu.ac.in

Nirendra Dev
nirendradev@dce.ac.in

[1] Department of Civil Engineering, Delhi Technological University, Delhi 110042, India

Published online: 14 March 2026

Second International Conference on
Construction Materials and Structures

Jointly Organized by

Certificate of Presentation

This is to certify that ***Mr. Wesam Al Agha*** of ***Delhi Technological University, Department of Civil Engineering*** has presented a paper entitled ***"Challenges for Structural Health Monitoring of Concrete Curing Using Piezoelectric Sensor and Electromechanical Impedance (EMI) Technique: A Critical Review"*** in the Second International Conference on Construction Materials and Structures (ICCMS-2022) during 13-19 December, 2022.

Prof. J. Sudhakumar
NIT Calicut (India)

Dr. Blessen Skariah Thomas
NIT Calicut (India)

Prof. Kevin Paine
University of Bath (U.K)

Dr. Sudharshan N. Raman
Monash University (Malaysia)

Dr. Alexander S. Brand
Virginia Tech. USA

Dr. Miriam Velay-Lizancos
Purdue University (USA)

Dr. Ali Kashani
University of New South Wales (Australia)

Dr. A. Bahurudeen
BITS Pilani (India)

Publication

ELSEVIER
Scopus

Technical Support

ARTICLE IN PRESS

Materials Today: Proceedings xxx (xxxx) xxx

Contents lists available at ScienceDirect

Materials Today: Proceedings

journal homepage: www.elsevier.com/locate/matpr

Challenges for structural health monitoring of concrete curing using piezoelectric sensor and electromechanical impedance (EMI) technique: A critical review

Wesam Al Agha, Shilpa Pal *, Nirendra Dev

Department of Civil Engineering, Delhi Technological University, Delhi, 110042, India

ARTICLE INFO

Article history:
Available online xxxx

Keywords:
Electromechanical Impedance (EMI)
Concrete
Piezoelectric patches (PZT)
Curing
Early-age

ABSTRACT

Monitoring the strength of early-age concrete is crucial by assessing an accurate time of removing construction formwork and loads on the structural elements, as well as the high technology strength identifications. This high technology is based on electromechanical impedance (EMI). EMI technique might also be monitored for efficient and verifiable effects, such as the curing phenomenon in situ investigation level. The curing effect on concrete strength elements has been significantly detected using piezoelectric patches (PZT) as smart material devices in electromechanical impedance investigation. This EMI approach is also becoming a sustainable solution for diagnostic demands in order to determine the signature characteristics at earlier phases of the concrete strength growth. In 2005, the first investigation on the curing problem was published, then became increasingly well-known in many relevant studies. Consequently, this paper presents the most recent state-of the- art curing studies by EMI technology. The literature reviews categorized relevant information into vital concrete curing challenges to be highlighted in future research. State-of-art listed the critical outputs and findings as installation techniques, computing technology integration, modelling, analysis techniques, signal processing, and environmental factors. In conclusion, EMI technology might potentially be transformed into a self-contained monitoring device to detect early damage in concrete. Similarly, the appropriate research gaps might examine more experiments and simultaneously provides an explanation for more research problems in the field of structural health monitoring.
© 2024 Elsevier Ltd. All rights reserved.
Selection and peer-review under responsibility of the scientific committee of the International Conference on Advances in Construction Materials and Structures.

1. Introduction

Concrete hydration is a complex multi-phase process in which the cement interaction starts from the fresh condition process into a hardened one. Long-term failure is possible since casting and curing are done incorrectly [1]. Therefore, monitoring the hydration process from the casting step is vital to ensure the optimum rate of strength increase [2]. Several non-destructive testing (NDT) techniques might be used for surveillance in concrete identification parameters, including ultrasonic spectrum analysis of surface waves, ultrasonic pulse velocity, microwave ground penetrating radar, and nuclear energy-based approaches [3,4]. However, these tools are expensive and sometimes difficult to install the measurement equipment in the field. Nevertheless, the Electromechanical Impedance (EMI) method for monitoring concrete's hardening has been considered beneficial [5]. The direct and converse piezoelectric properties of the PZT patch are the fundamentals of this method. Applying alternating voltage into a piezoelectric patch occurred as causing the vibration effect and placing a mechanical strain on the host structure [6]. This PZT patch is modulated due to changes in its vibrational behaviour brought by the host structure's resonant response. Vibration waves are affected by the host's size, geometry, and damping qualities [7]. The signature output is sometimes illustrated as unstable electrical impedance throughout the electricity channel of instruments. The essential technique to learn in the lab and site is how can be monitoring the fresh concrete's strength growth [5]. There are timely removal of formwork, loading of structural parts, and evaluation of batch quality that

* Corresponding author.
E-mail addresses: wesamalagha_2k21phdce16@dtu.ac.in, wesamalagha1@gmail.com (W. Al Agha), shilpapal@dtu.ac.in (S. Pal), nirendradev@dce.ac.in (N. Dev).

https://doi.org/10.1016/j.matpr.2023.06.451
2214-7853/© 2024 Elsevier Ltd. All rights reserved.
Selection and peer-review under responsibility of the scientific committee of the International Conference on Advances in Construction Materials and Structures.

Please cite this article as: W. Al Agha, S. Pal and N. Dev, Challenges for structural health monitoring of concrete curing using piezoelectric sensor and electromechanical impedance (EMI) technique: A critical review, Materials Today: Proceedings, https://doi.org/10.1016/j.matpr.2023.06.451



ICAMNOP - 2023

International Conference on
Atomic, Molecular, Material, Nano, and Optical Physics with Applications

20th - 22nd December, 2023

Organized by:
Department of Applied Physics, Delhi Technological University, Delhi, India

Certificate

This is to certify that

Prof./Dr./Mr./Ms. WESAM AL AGHA

has presented Poster / Oral Presentation in the **"International Conference on Atomic, Molecular, Material, Nano and Optical Physics with Applications (ICAMNOP-2023)"** held at Delhi Technological University, Delhi, India during 20th-22nd December, 2023.

Prof. Rinku Sharma
President, ICAMNOP-2023

Prof. A. S. Rao
Chairperson, ICAMNOP-2023

Prof. Vinod Singh
Convener, ICAMNOP-2023

Metrohm

Curriculum Vitae

WESAM AL AGHA
Department of Civil Engineering, Delhi Technological University (DTU)
Shahbad Daulatpur, Main Bawana Road, Delhi–110042, India
Email: wesamalagha1@gmail.com • Roll No.: 2K21/PHD/CE/16
ORCID: 0000-0001-9460-1365 • Google Scholar: Wesam Al Agha

EDUCATIONAL QUALIFICATIONS

Year	Degree	University / Institution	Division / Grade
2021–2026	Ph.D. Civil Engg.	Delhi Technological University (DTU), Delhi, India	First Division
2019–2021	M.Tech Structural Engg.	SRM Institute of Science and Technology (SRMIST), Chennai, India	First Class with Distinction (CGPA: 9.65/10)
2012–2017	B.Sc. Civil Engineering	University of Damascus, Damascus, Syria	First Division (69.19%)

RESEARCH & PROFESSIONAL EXPERIENCE

- **Doctoral Research Scholar (2021–2026):** Department of Civil Engineering, Delhi Technological University (DTU), Delhi, India.
  - Developed reusable Non-Bonded Piezo Sensor (NBPS) ecosystems for structural health monitoring (SHM) of steel fibre reinforced concrete (SFRC), reducing sensor consumption by 78-fold.
  - Formulated the Enhanced Effective Frequency Shift (Enhanced EFS) temperature compensation framework for operational SHM up to 250 °C.
  - Extracted Equivalent Structural Parameters (EPS: mass, stiffness, damping) via electromechanical impedance (EMI) analytical modeling.
  - Implemented deep learning pipelines (2D CNN, LSTM, Bi-LSTM, CNN–LSTM, GPR, SVM, Boosted Trees) on EMI signatures for automated mechanical degradation tracking.
- **M.Tech in Structural Engineering (2019–2021):** SRM Institute of Science and Technology, Chennai, India.
  - Investigated flexural capacity, local buckling behavior, and connector mechanics in Steel–Concrete–Steel (SCS) sandwich composite sections.
  - Conducted nonlinear finite element and dynamic analysis of steel–concrete composite and RC structures using ABAQUS, ETABS, and SAP2000.
  - Evaluated structural energy dissipation systems (FVD, LRBI, BRB) and 3D soil–structure interaction (SSI) dynamics.
- **Professional & Academic Leadership (Damascus, Syria):**
  - Structural engineering consultancy and design of reinforced concrete structures in Damascus.
  - Organizer and Session Chair, *Damascus International Conference* (2023) and *Third International Conference on Construction Engineering* (2025), Damascus, Syria.

PUBLICATIONS

A. Peer-Reviewed SCI/SCIE Journals (Q1/Q2):

1. **W. Al Agha**, S. Pal, and N. Dev, "Electro-mechanical impedance-based equivalent structural health monitoring of steel fibre cementitious materials under long curing age effect," *Construction and Building Materials*, vol. 489, p. 142296, 2025. DOI: 10.1016/j.conbuildmat.2025.142296. **(SCI Q1, Impact Factor: 8.0)**
2. **W. Al Agha**, N. Dev, and S. Pal, "ML-integrated reusable piezoceramic sensors for steel fibre concrete structural health monitoring," *Measurement*, vol. 258, p. 119201, 2026. DOI: 10.1016/j.measurement.2025.119201. **(SCI Q1, Impact Factor: 6.1)**
3. **W. Al Agha**, S. Pal, and N. Dev, "Electromechanical Impedance-Based Tensile Damage Assessment of Steel Fibre Concrete Using Reusable Piezoceramic Sensors: An Experimental and Deep Learning Approach," *Journal of Vibration Engineering & Technologies*, vol. 14, p. 164, 2026. DOI: 10.1007/s42417-025-02311-9. **(SCI Q2, Impact Factor: 3.5)**

B. Scopus-Indexed Journals & Conference Proceedings:

4. **W. Al Agha**, S. Pal, and N. Dev, "Challenges for structural health monitoring of concrete curing using piezoelectric sensor and electromechanical impedance (EMI) technique: A critical review," *Materials Today: Proceedings*, 2023. DOI: 10.1016/j.matpr.2023.06.451.
5. **W. Al Agha** and N. Umamaheswari, "Analytical study of irregular reinforced concrete building with shear wall and dual framed-shear wall system by using Equivalent Static and Response Spectrum Method," *Materials Today: Proceedings*, 2020. DOI: 10.1016/j.matpr.2020.12.525.
6. **W. Al Agha**, W. A. Almorad, N. Umamaheswari, and A. Alhelwani, "Study the seismic response of reinforced concrete high-rise building with dual framed-shear wall system considering the effect of soil structure interaction," *Materials Today: Proceedings*, 2020. DOI: 10.1016/j.matpr.2020.12.111.
7. R. Kant, **W. Al Agha**, W. A. Almorad, M. S. Thakur, and N. Umamaheswari, "Study on seismic performance of reinforced concrete multi-storey building considering soil–structure interaction effect," *Materials Today: Proceedings*, 2021. DOI: 10.1016/j.matpr.2021.11.475.
8. R. Kant, **W. Al Agha**, M. S. Thakur, and N. Umamaheswari, "Comparative study on seismic performance of steel–concrete composite structure without and with buckling-restrained braces," *Materials Today: Proceedings*, 2021. DOI: 10.1016/j.matpr.2021.11.461.
9. R. Kant, **W. Al Agha**, M. S. Thakur, and N. Umamaheswari, "Impact of the lead rubber base isolators on reinforced concrete building," *IOP Conference Series: Materials Science and Engineering*, vol. 1026, p. 012004, 2020. DOI: 10.1088/1757-899X/1026/1/012004.
10. **W. Al Agha** and N. Umamaheswari, "Comparative study on seismic performance of reinforced concrete building with and without fluid viscous dampers," *International Journal of Engineering Research And Management (IJERM)*, 2020.

INTERNATIONAL CONFERENCES & PRESENTATIONS

- **Third International Conference on Construction Engineering** (Damascus, Syria): Organizer and Session Chair, 23–24 Feb 2025.
- **Damascus International Conference** (Damascus, Syria): Organizer and Session Chair, 28–30 Nov 2023.
- **ICAMNOP-2023** (Delhi Technological University, DTU, Delhi, India): *"Investigation of Steel Fibre Reinforced Concrete Elements under Elevated Temperature"*, 20–22 Dec 2023.
- **ICARAE 2021** (Cape Town, South Africa): Presented papers on seismic performance with soil–structure interaction and steel–concrete composite structures with buckling-restrained braces, 26–28 Nov 2021.
- **Saveetha Engineering College Conference** (Saveetha, India): Presented paper on Lead Rubber Base Isolators — **Awarded Best Paper Award**, 20 Aug 2020.
- **Ramco Institute of Technology Web Conference** (India): Presented study on Fluid Viscous Dampers for seismic control, 21 July 2020.
- **Eswari Engineering College Conference** (India): Presented 2 papers on seismic response and soil–structure interaction, 01 June 2020.

TECHNICAL & COMPUTATIONAL SKILLS

- **Structural Analysis & FEA Software:** ETABS, SAP2000, ABAQUS, COMSOL Multiphysics, AutoCAD
- **Artificial Intelligence & Machine Learning:** Python, MATLAB, TensorFlow, Keras, Scikit-learn (2D CNN, LSTM, Bi-LSTM, GPR, SVM)
- **Experimental Testing & Diagnostic Techniques:** Electromechanical Impedance (EMI) Sensing, PZT Transducers (NBPS, SBPS, JPS), Universal Testing Frame (Galdabini Sun/60), Digital Image Correlation (DIC)
- **Data Analytics & Typesetting:** OriginLab, LaTeX, MS Office Suite

PERSONALITY & PROFESSIONAL ATTRIBUTES

- Exceptional research discipline, analytical rigor, and strong theoretical foundation.
- Proven capability to formulate, manage, and execute complex multi-faceted experimental and computational research programs simultaneously.
- Self-motivated, goal-oriented, and highly committed to scientific standards and project deadlines.
- Proficient with cutting-edge experimental instrumentation, data synthesis, and technical reporting.
- Collaborative team player with excellent cross-disciplinary communication skills.

HONOURS & AWARDS

- **Best Paper Award:** International Conference on Innovative Solutions and Challenges in Civil Engineering, Saveetha Engineering College, India (2020).
- **First Class with Distinction:** Awarded for outstanding academic performance in M.Tech Structural Engineering (CGPA: 9.65 / 10), SRMIST, Chennai.
- **High-Impact Publication Record:** Multiple Q1/Q2 first-author papers in prestigious international SCI journals (Impact Factors up to 8.0).

ACADEMIC REFERENCES

- **Prof. Shilpa Pal**, Professor, Department of Civil Engineering, Delhi Technological University (DTU), Delhi, India. Email: shilpapal@dtu.ac.in
- **Prof. Nirendra Dev**, Professor, Department of Civil Engineering, Delhi Technological University (DTU), Delhi, India. Email: nirendradev@dtu.ac.in

(Signature)

Name: WESAM AL AGHA
Place: DELHI, INDIA